STRUCTURE-PROPERTY RELATIONS OF MIXED-ALKALI AND ION-EXCHANGE SILICATE GLASSES

by

Courtney Calahoo

Submitted in partial fulfillment of the requirements
for the degree of Doctor of Philosophy

at

Dalhousie University
Halifax, Nova Scotia
June 2016

Dedicated to my forefathers Louis Karaconti Calahoo, who had an awe-inspiring amount of adventuresome spirit and Michel Calahoo, who always knew things would get better.

Contents

List of Tables

List of Figures

Abstract

Improvement of the mechanical properties of glass was undertaken by furthering understanding of the fundamental relationships between composition, structure and mechanical response. Glasses which were known to already have desirable mechanical properties were made and analysed in order to establish correlations between different properties.

Ion exchange (IE), where a smaller ion is replaced by a larger ion without subsequent structural relaxation, causes surface compressive stresses which increase strength and scratch resistance significantly. Micro-Raman spectroscopy was employed to directly measure the volumetric negative strain (contraction) and compressive stress as a function of IE processing temperature by observing changes in Raman peaks correlated with Si-O bond lengths and Si-O-Si bond angles. From the Raman data, the strain of the glass network and consequent stress was calculated relative to several reference states. The reference state of relaxed, fully exchanged glass produced results which matched the complex experimental behaviour.

The mechanical response of the IE layer was probed using nano-indentation. Stiffness and hardness were measured as a function of distance from the surface and IE temperature. Additionally, elastic recovery and resistance to plastic deformation were determined. Low IE temperatures (which the Raman results indicated contained the most compressive stress) were observed to improve mechanical properties more than higher IE temperatures, likely due to increased thermal relaxation.

The mixed-modifier effect (MME), a deviation from additivity when two or more different types of modifying cations are combined, is known to exist in in static, dynamic and mechanical properties. Yet, the underlying mechanism of the MME is poorly understood, thus, a comprehensive study of several mixed-modifier glass series was undertaken to better elucidate the complex relationships between these three categories of properties. The most significant predictor of the MME was the valence(s) of the mixed cations. Furthermore, the MME in conductivity, packing fraction, bulk modulus, hardness and fracture toughness was related to relative cationic field strength and ionic radii. The MME in shear modulus, Young's modulus and Poisson's ratio was related to structural connectivity rather than the properties of the modifier cations.

List of Abbreviations and Symbols Used

α material-dependent constant related to bond strength

χ goodness of fit

ΔE_{a} difference in activation energies between two cations

ΔCN difference in coordination number between two cations

$\Delta\nu$ shifted Raman shift

ΔF_{c} difference in cationic strength between two ions

$\delta G/\delta K$ deviation from linearity of shear modulus over deviation in bulk modulus

ϵ strain

γ surface energy density

κ ionic conductivity

λ wavelength

λ_0 excitation source or laser wavelength

λ_1 modulated wavelength after interaction with material

μ Poisson's ratio

μ_j mobility of ion j

μ_m reduced mass

ν Raman shift or frequency

ν_0 fundamental Raman frequency

ω_e elastic recovery

ρ density, usually of sample

ρ_{a} density of air

ρ_{glass} density of glass

ρ_{l} density of immersion liquid

$\S_V^R$ material-independent geometric constant for Vickers-produced radial cracks

σ stress

σ_{st} strength

θ angle of reflection

A pre-exponential factor

a cation-oxide bond distance

A_0 electrode area in ionic conductivity measurements

A_{p} projected area of the indent

B LNDC or linear strain per change in alkali concentration

c_0 critical crack length

C_{F} Faraday's constant

$C_{\mathrm{M^+avg}}$ average concentration of invading ion

C_{M^+} concentration of invading ion

c_{avg} average radial crack length, including indent width

c_j volume concentration of ion j

d proportionality constant between crack length (c_0) and Young's modulus (Y)

d_L lattice spacing in a crystal

F force (N)

F_c cationic field strength

G shear modulus

H hardness from nano-indentation

h Planck's constant

h_S displacement into the surface (μm)

H_V Vickers hardness from micro-indentation

K bulk modulus

k Boltzmann's constant

K_H Hooke's force constant

K_{Ic} fracture toughness in mode I

L length of material

M_i molar mass of the component

m_{a} mass of air

m_{i} apparent immersed mass of glass

m_{l} mass of displaced liquid

N number of data points in model

n number of homonuclear Si-O-Si bonds or bridging oxygens

$N(\mathrm{O}^{2-})$ fraction of free oxygen

N_{A} Avogadro's number

P load or pressure

P_{add} value of material property predicted from the additivity law

P_{exp} experimental value of a material property

R resistivity

R^2 correlation coefficient

R_{DC} DC bulk resistance

R_{O} oxygen-second-nearest-neighbour-oxygen or O-Si-O

r_{O} Si-O bond-length

R_{i} ionic radius

T temperature

t flight time of waves through material

T_{f} fictive temperature

T_{g} glass transition temperature

T_{h} thickness of sample

T_{m} melting temperature

t_j transport number of ion j

V volume

V_{f} packing fraction

V_{L} longitudinal velocity

V_{m} molar volume

V_{sound} sound velocity

V_{T} shear or transverse velocity

W width of material

x relative mol-% or mol fraction of modifier weighted over total modifier

Y Young's modulus (GPa)

Y^* effective Young's modulus

Z valency of ion

Z' real component of impedance

Z" imaginary component of impedance

z_j charge of ion j

ZAF correction factor for WDS

Δr_c difference in ionic radii between two cations

E_a activation energy (of ion movement)

AC alternating current

BO bridging oxygen

CN coordination number

CTE coefficients of thermal expansion

DC direct current

DSM dynamic structure model

EDS energy dispersive spectroscopy

EXAFS extended X-ray absorption fine structure

FWHM full-width half maximum

HF high-frequency

HT high temperature

ICP-OES inductively coupled plasma optical emission spectrometry

IE ion-exchange or ion-exchanged

IR infrared

ISE indent size effect

LCD liquid crystal display

LF low-frequency

LNDC linear network dilation coefficient

LT low temperature

MAE mixed-alkali effect

MAEE mixed alkaline-earth effect

MME mixed-modifier effect

MRN modified random network

NBO non-bridging oxygen

NMR nuclear magnetic resonance

O_i oxygen fraction of component

PXRD powder X-ray diffraction

RF radio frequency

WDS wavelength-dispersive spectroscopy

Acknowledgements

First, I would like to thank my supervisor, Prof. Josef Zwanziger, who allowed me a wide berth in pursuing the research I was interested in; it may have been more difficult at times but I believe it gave me legs to stand on in the next step of my career path. Next, I would like to thank all of the scientists I have had the pleasure to collaborate with: Prof. Ian S. Butler, Dr. XiaoFang Zhang, and Dr. Ulrike Werner-Zwanziger. I would also like to thank the members of my committee: Prof. Daniel Boyd, Prof. Mark Obrovac and Prof. Peng Zhang, whose fresh perspectives on my research have been helpful.

Next, I would like to thank all of the Dalhousie University staff who over the years have helped in various ways: allowed me to use their instruments, taught me how to run my own experiments, maintained equipment, ran experiments for me, made equipment or simply helped me in a bind. This includes Dr. Dan MacDonald, Andy George and Todd Carter, who have all given me their guidance that only decades of working in their respective fields can, Mike Boutilier, Michel Johnson, Daniel Chevalier, Cathy Ryan, Barry Moore, Ryan MacKinnon, Brian Millier, Prof. Mary-Anne White, Prof. Kevin Plucknett, Dr. Julian O'Flynn, Dr. Cathy Whitman, Dr. Robbie Sanderson, Prof. Jeff Dahn, Dr. Tim Hatchard, Prof. Mark Obrovac, Prof. Alan Doucette, Dr. Dennis Orton, Andrew Crowell, Prof. Heather Andreas and Prof. Daniel Boyd. All of these people made my research possible.

I wish to thank my family, my Dad and Mom, for never doubting me and finding the right way to teach me things, by example. I want to thank my Aunt Cynthia for showing me there is more than one way to be happy in this world. I must thank my friends for being great people and enthusiastically commiserating with me about the hardships of being an adult. Last, but not least, I must thank Carl, who I truly believe I could have not done this without, but I know he would tell me that's not true. Thank you.

Chapter 1

Introduction

Despite glass being an inert, natural and cradle-to-cradle recyclable material made from abundant starting materials,[1] it still has a large negative impact on the environment. Global glass production exceeds 80 million tonnes per year; considering that each tonne takes approximately 1.7 MWh to melt and that most of our existing sources of power are fossil-fuels,[1] it quickly becomes clear how the large carbon footprint (1 kg CO_2/kg glass) of glass is relevant. High-strength glass makes up approximately 20% of global glass production[2] and is required in a wide-variety of applications: solar panels, lining of batteries, accelerated devices, hard discs, surgery equipment, lightweight construction, and composite materials.[3]

Unfortunately, many glass systems known to have useful mechanical properties, such as high strength and hardness, also have high working temperatures. The current state-of-the-art glasses being used for LCD screens, solar panel covers and electroluminescent displays have softening temperatures of 850–1050 °C,[4,5] making their average working temperatures 1250 °C. If that temperature were reduced even by 10% without a loss in strength, approximately 14 million MWh and 2.5 million tonnes of CO_2 would be saved per year in the high-strength sector alone.[1] Consequently, it is important to find novel glass compositions which have lower melting-temperatures or require less volume without sacrificing mechanical and chemical properties.

Improving the mechanical properties of glass has potentially wide-sweeping implications for applications and energy use alike. As a consequence, many different avenues to this end are being explored, whether by modifying the processing of the material, the material's surface or chemical composition. It is known that the molecular structure of a glass is influential on the mechanical and chemical behaviour of the material,[3] thus, it is critical to investigate which structural features improve these important properties. This is done in two ways, first, by synthesizing and characterizing novel low-melting glass systems with improved properties and second, by examining already-known systems with desirable properties.

1.1 Glass Properties

Despite the length of time glass has been in use, it remains a controversial material. First synthesized in 3000 B.C., complete theories of significant properties such as the glass transition and glass structure continue to elude scientists today.[6] Nonetheless, glass can be defined as a *solid with liquid like structure*,[7] meaning it is devoid of any long-range order. One of the simplest, yet most informative representations of any material is a phase diagram. In the V-T diagram in Fig. 1.1, a material begins as a molten mixture (a) and is allowed to cool at a slow rate along the path abc below the melting temperature (b), then crystallization (d) occurs, shown here as a thick black line.

However, as long as the crystal growth rate is slow and there is a sufficiently low amount of nucleation sites in the melt, the liquid volume will continue on shrinking without crystallization and will remain a liquid below its melting temperature (b) forming a supercooled liquid. After cooling below the supercooled liquid region, the liquid undergoes the glass transition into an amorphous solid shown at both (g) and

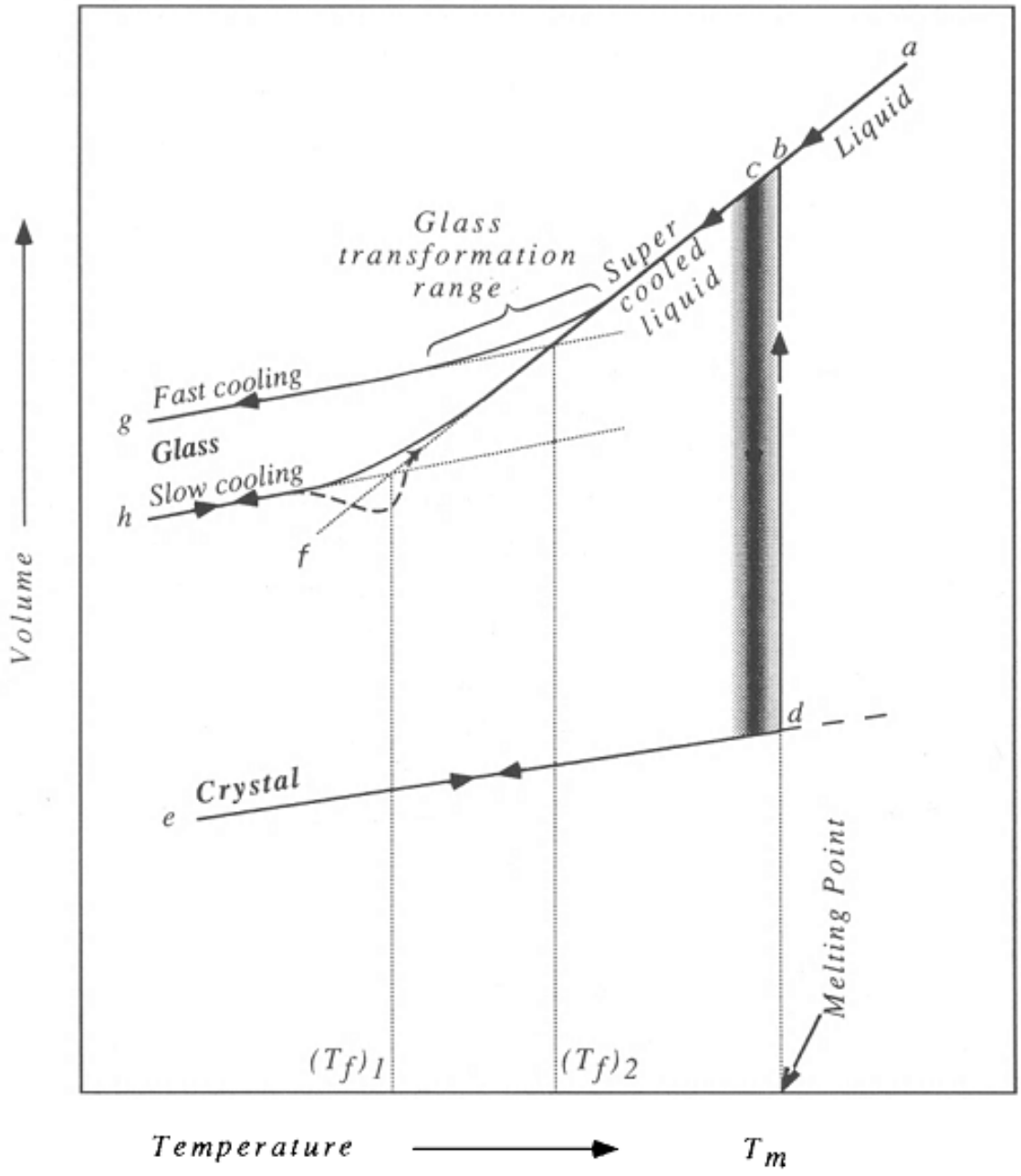

Figure 1.1: The volume-temperature (V-T) diagram for a glass-forming liquid, taken with permission from Varshneya [7].

(h). At some point the cooling-curve derivative shallows and begins to parallel that of the crystal, the temperature at this change in slope is considered to be the glass transition temperature (T_g).[8] The volume, amount of disorder and glass transition temperature of the solid depend on cooling rate. Thus it is important when comparing glass data to ensure the synthesis procedures are consistent.[8,9] In fact, depending on the cooling rate and the glass transformation range, different samples will have unique fictive temperatures, which are denoted by $(T_f)_1$ and $(T_f)_2$ at the bottom and represent the configurational state "frozen" in at that temperature.

1.1.1 Glass Structure

Even though other theories exist,[10,11] Zachariasen's Random Network Model, put forward in 1932 has overtaken all other hypotheses to become the most accepted theory of glass structure. Zachariasen[12] realised the similarities between crystals and their corresponding glasses, leading him to suggest that glass is composed of the same local units as a crystal, but in a random, open structure. To achieve this, he imagined corner-sharing polyhedra that differed only in interpolyhedral bond angles whilst the angles within the polyhedra themselves stayed much the same, as shown in Fig. 1.2.

As a result of this preservation of local structure, corresponding crystals with roughly the same molecular formula as the glass are important in the study of glass as they represent one possible stable geometry and conformation. Density, mechanical properties and thermal properties are known to be similar to that of the analogous crystal and lead to the idea that the atomic forces in both amorphous and crystalline solids must be similar.[7] Crystal compounds are used for comparison in NMR and Raman spectroscopy as well as for computing relevant properties using density functional theory.[14]

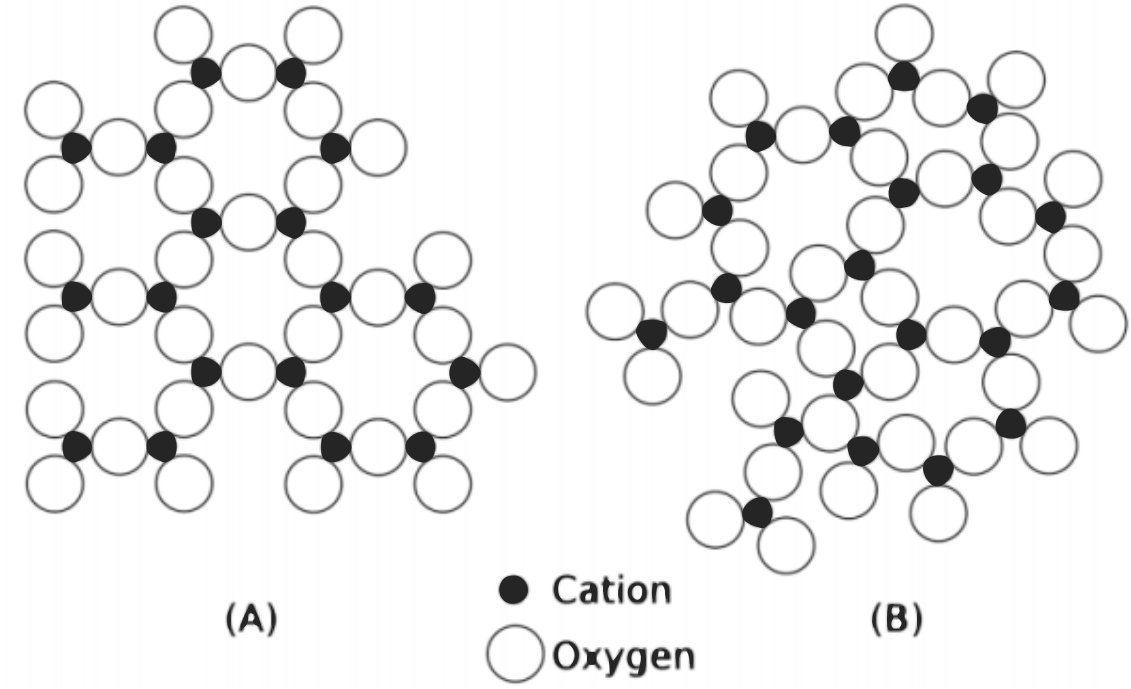

Figure 1.2: Representation of the crystalline structure (A) and the glass structure (B) of an oxide M_2O_3 according to the Random Network Theory, with permission from Dr. Vincent Martin [13].

1.1.2 Glass Materials

Materials used in glass synthesis are divided into two categories; formers create the framework structure and, in the case of oxide glass, contain bonds with a significant covalent character, whereas modifiers, in contrast, form mostly ionic bonds and reduce the connectivity of the covalent network. Classifying which materials are glass network formers provides information about bond strength and molecular structure. Sun[15] concluded that the glass transition must occur because of the material's inability to rearrange, thereby meaning the higher the bond strength the better the glass former. Dietzel[16] classified oxide materials based on the field strengths exerted on the oxygen by the cation. Using either of these organization schemes, silica (SiO_2) is a network former, while most alkali and alkaline metals are network modifiers with the most modifier-like being at the bottom of their respective column in the periodic table. Finally, zinc, and depending on their coordination number, Mg and Ca are intermediates. Both of these classification systems, Sun's[15] and Dietzel's,[16] are different ways of saying that silicon forms the most covalent bonds with oxygen, while alkali metals are easily ionizable and bond with oxygen through mostly coulombic forces. Other oxides such as B_2O_3, P_2O_5 and Al_2O_3 form more covalent oxides bonds and are glass formers as well. Silica is the most commonly used and studied glass former for several reasons: it maintains its local structure with very few exceptions[17,18] (B_2O_3 undergoes a coordination change from 3-fold to 4-fold under pressure or in presence of large amounts of network modifier), makes glasses over large compositional ranges (Al_2O_3 has a small glass-forming region) and is highly chemically durable (high P_2O_5 glasses are highly hygroscopic). Consequently, in this work, SiO_2 was chosen as the only glass former to simplify analysis of the network structure and to allow the influence of the modifier to be studied in isolation.

The introduction of a modifier, such as sodium oxide, breaks up the silica network and converts a site with one bridging oxygen (BO) into two non-bridging oxygen sites (NBO) as shown in Fig. 1.3. The size and charge of the modifier as well as the network environment will determine the number of oxygen atoms in the cation's coordination sphere. However, this value is not always agreed upon, often the cut-off distance is somewhat blurred.[16,19]

1.1.3 Glass Topology

Glasses are unique in that they truly lack the long-range order typical of single crystals and the grain boundaries that are characteristic of polycrystalline materials. If annealed properly, "miscible" glasses are homogeneous throughout. Nonetheless, there are many possible glass topologies; Fig. 1.4 shows four ways to describe glass topology that will be discussed herein: degree of polymerization, channel formation, structural dimensionality and packing density.[3]

Degree of polymerization or condensation refers to the amount of homonuclear former bonds, in this case, Si-O-Si bonds (also called BOs due to the 'bridging' oxide bond). Pure silica is completely polymerized, every oxygen is a BO, and has high network connectivity. On the other hand, added modifier creates NBOs and reduces network connectivity. This extends into network dimensionality, where pure silica would be connected in three-dimensions, while glasses with more modifier will have chain-like structures and lower network dimensionality.

In 1938, Warren and Biscob[19] studied X-ray diffraction patterns of soda-silica glass and discovered the modifier occupies the interstitial sites between the network tetrahedra. This led to the idea that at sufficient modifier content, ion channels would begin to form which facilitate ionic diffusion throughout the material.[20] A

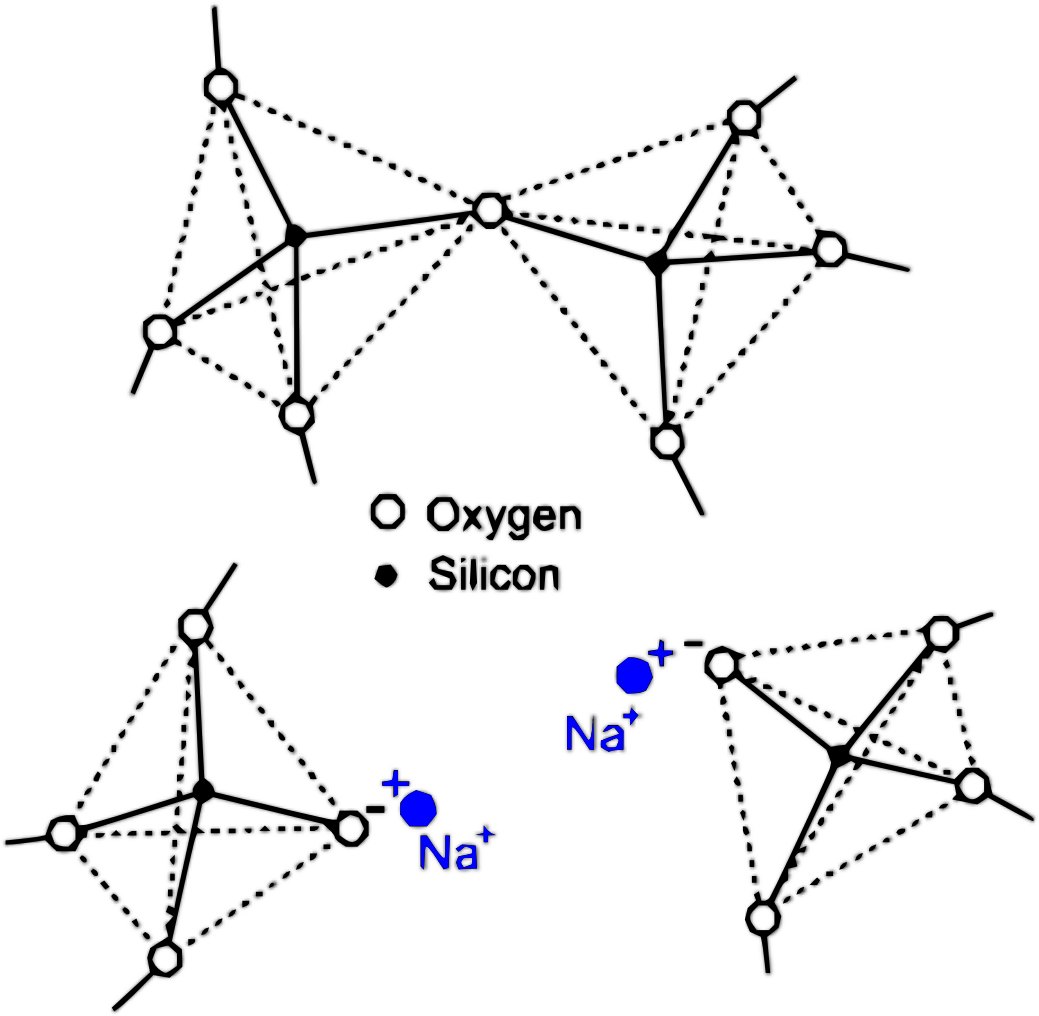

Figure 1.3: The Na^+ cation breaks the Si-O-Si chains creating non-bridging oxygens (NBOs), with permission from Dr. Vincent Martin [13].

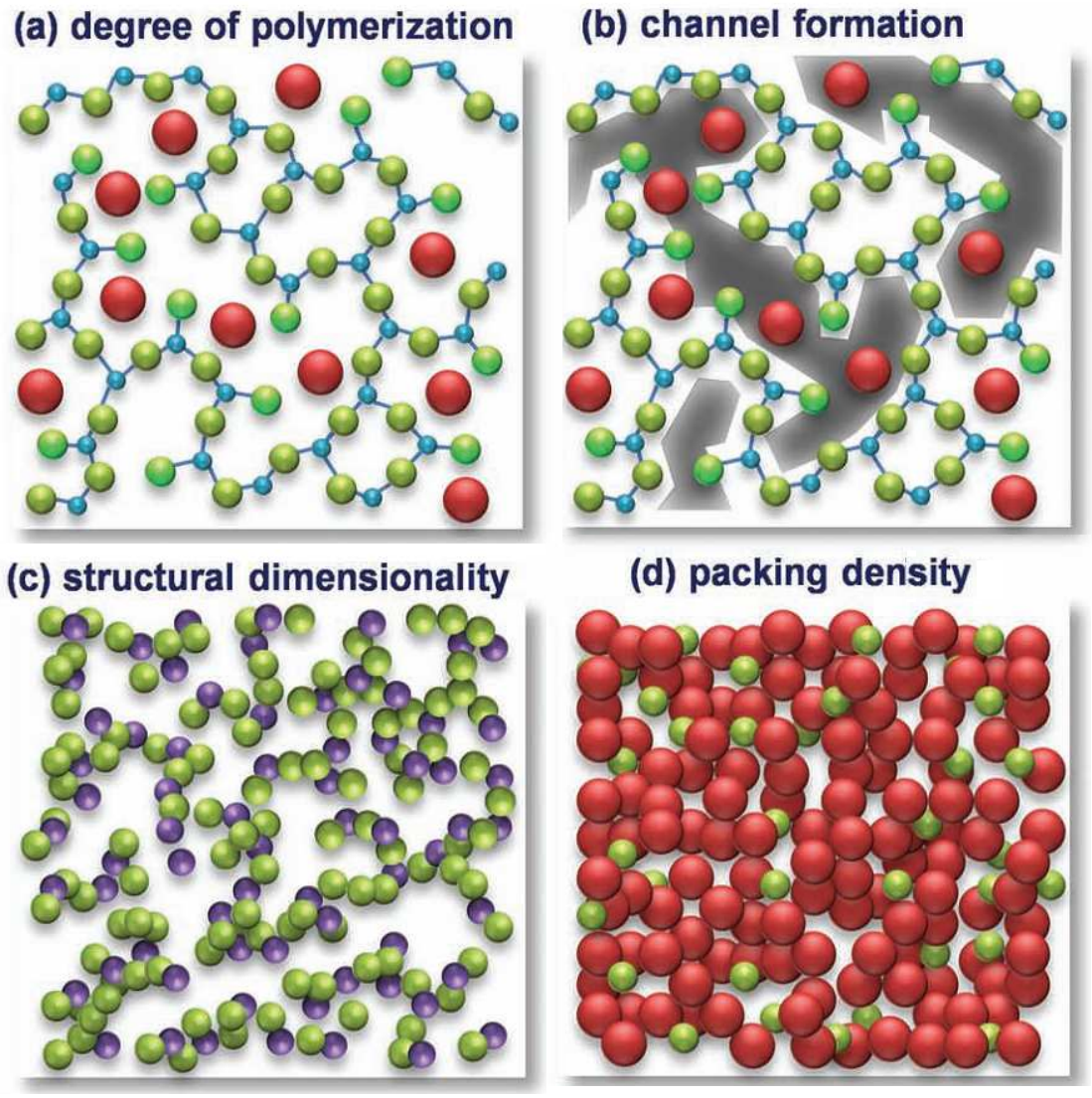

Figure 1.4: Methods of description of the topology of an amorphous solid, from Wondraczek *et al.* [3].

visual representation of this is seen in Fig. 1.4b, where the white-coloured space includes the network former and the dark-coloured space includes the ion channel. Experimentally, initial additions of the modifier are enclosed in the silica network cages until 10-12% mol cation, at which point the modifier ions begin to open up the cages to form channels.[20]

Packing density is a notion used in many fields and essentially measures the volume filled by atoms vs. free volume. The packing fraction (V_f) can be calculated using the volume of each ion ($\frac{4}{3}\pi R_\mathrm{i}^3$) weighted by the mole fraction of each oxide (x_i),[21]

$$V_\mathrm{f} = \frac{1}{V_\mathrm{m}} \sum_i N_\mathrm{A} x_\mathrm{i} \frac{4}{3} \pi R_\mathrm{i}^3, \tag{1.1}$$

where N_A is Avogadro's number, R_i is the Shannon-Prewitt ionic radius of the expected coordination number in oxide crystals[22] and V_m is the molar volume. V_f describes the compactness of the structure; a higher value indicates less open space within the structure. Calculation of V_f assumes that the ionic radii for a given coordination number are the same in a glass as they are in a crystal, which is usually a reasonable approximation.[20,21] The real difference between many crystalline and glassy materials is the spread of bond lengths and CN; for example, K^+ is found in octahedral sites in $K_2Si_2O_5$,[23] yet in glasses, it has been found to have 5–7[24,25] or 8–9[7,15,16] neighbours. Finally, network compactness and connectivity have been found to be inversely correlated.[3,26]

1.1.4 Q^n denotation

A system of naming prevalent in the glass community is the Q^n species classification, where n represents the number of Si-O-Si bonds; for example vitreous silica would theoretically only be composed of Q^4-units, where a silicon atom is bonded to four

other silicon atoms (through oxygen linkages). With the addition of a modifier, the number of Si-O-Si bonds and n would be reduced accordingly. A higher Q-species implies more cross-linking in the network; Q^2 units are considered strings of SiO_4 tetrahedra, while higher Q-species make the network 3-dimensional and increase connectivity.

1.2 Mechanical Properties

1.2.1 Fracture Strength

One of the goals of this work is to understand the origin and improve the strength of glass, σ_{st}, the maximum stress incurred before failure. It is a practical property measured over many, usually hundreds, of samples; it takes into account the inherent material properties and the specific conditions of each glass piece. Considering only the bonds in any glass, the glass should be very strong; in fact, depending on the theory, the predicted tensile strength for silica glass is between 10–35 GPa, yet in reality, a rod from the factory will have a breaking strength of 4.5×10^{-2} GPa.[27] It is abundantly clear there is another factor contributing other than bond strength alone.

In a comparison[9] of a commercial glass rod to one severely sandblasted and another acid etched then lacquered, it is easily recognizable that the surface condition plays a large role in strength. While the factory rod had a tensile strength of 4.5×10^{-2}, the breaking stress of the sand blasted rod was more than two times lower (1.8×10^{-2} GPa) and the acid etched rod had nearly three orders of magnitude higher strength (1.7 GPa) than either rod.[27] The rod which had the cracked, weakened surface removed by acid and sealed with lacquer actually possessed strength within the range predicted by interatomic forces alone.

The first step towards understanding the importance of the surface condition was made by Inglis,[28] who proposed that scratches act as stress concentrators where local stresses exceed the ultimate tensile strength of the material, which leads to crack propagation and fracture. Later Griffith[29] expanded upon this idea and for brittle materials described a critical crack length (c_0) and tensile strength (σ_{st}); if the flaw length is equal to or larger than c_0, the material will fail at σ_{st}. Interestingly, for glass the relationship between surface flaw length and strength is linearly dependent on only the material's Young's modulus (Y) and surface energy density, (γ), $c_0 = 2Y\gamma/\pi\sigma_{\mathrm{st}}^2$.[29] Surface energy quantifies the work needed to break the bonds of a material and create two new surfaces, thus a way to increase surface energy density is to increase the bond strength or number of bonds per unit area.

If a glass is homogeneous, it will always begin to crack at the surface and always as a result of tension. According to Griffith's theory,[29] it is impossible to prevent microcracks below the critical length (c_0) from forming, where cracks of length greater than the critical length will propagate and cracks with lengths less than c_0 will not, so only crack propagation, not formation, can be mitigated. Based on Griffith's crack theory and strength studies, Phillips[9] takes Griffith's equation and substitutes the crack length (c_0) with a proportionality constant, d, between crack length (c_0) and Young's modulus (Y), $d = Y/c_0$, showing Y and c_0 are related inversely:

$$\sigma_{st} = \left(\frac{2Y\gamma}{\pi c_0}\right)^{1/2} \rightarrow \sigma_{st} = Y\left(\frac{2\gamma}{\pi d}\right)^{1/2}, \tag{1.2}$$

where γ is surface energy density. Consequently, it can be said that increasing Young's modulus will directly increase the breaking strength, but also indirectly by reducing average crack length. In fact, the breaking strengths (σ_{st}) and Young's moduli of glasses do possess a clear linear relationship.[9] Consequently, there is a strong connection between strength and Y, and the optimization of Young's modulus can be

thought of as equivalent to improving the overall strength of glasses.

1.2.2 Elastic moduli

Young's modulus, Y, is defined as the stiffness of the material under uniaxial compression or tension, and is equal to the slope on a stress-strain curve.[30] Strength, σ_{st}, is the upper limit of the stress-strain curve before failure, while toughness is the area under the curve and is described as a solid's ability to absorb energy before fracture.[7,30] Although elastic modulus, strength and toughness are different, their intimate relationship is represented in the stress-strain curve in Fig. 1.5. At temperatures well below T_g, glass is a mostly elastic material (i.e., it obeys Hooke's law and deforms reversibly);[7] there is little visco-elastic deformation and it is a brittle material that experiences catastrophic failure at the high limit of stress as shown by the far-left curve in Fig. 1.5. For a brittle, elastic material such as glass, the changes in dimensions are very small and can be treated as an continuum. Brittleness does not make glass a soft material;[9] in fact, glasses tend to have some of the highest elastic moduli and compressive strengths compared to other materials,[30] it only means that glass experiences almost no visco-elastic deformation and has low toughness.

On the other extreme, an uncrosslinked polymer such as low-density polyethylene (LDPE) has low strength, stretches easily (high ductility), yet breaks quickly (low toughness) when under tensile stress. Finally, a metal such as titanium has high marks in all three mechanical properties; it fractures at a high stress, yet undergoes sufficient plastic deformation without catastrophic failure.

The Poisson ratio, μ, is a dimensionless quantity that relates transverse strain to axial strain. For a homogeneous, isotropic material where a force is applied along the length (L), the width (W) changes accordingly, μ is ratio of the perpendicular strains

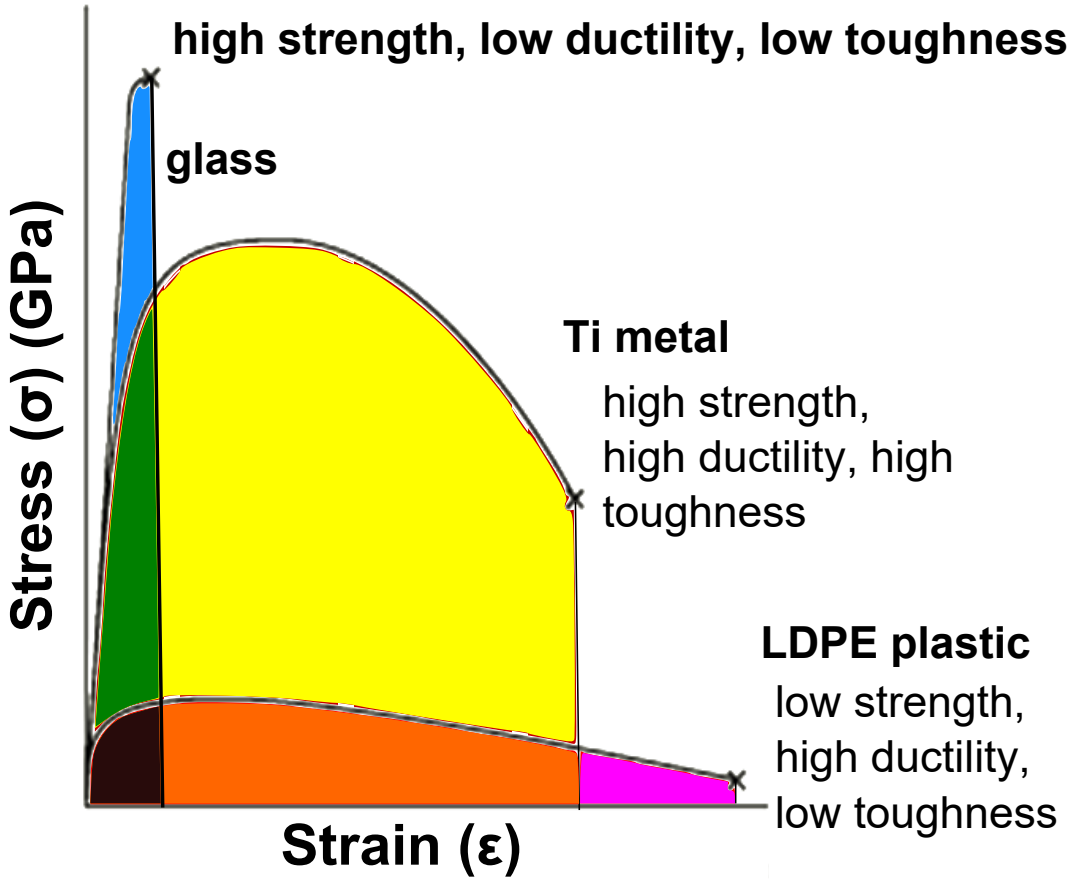

Figure 1.5: The stress-strain curve for three materials with different mechanical behaviour. The coloured areas under the curves are fracture toughnesses or energies absorbed by the material during deformation (GPa×strain = J/m^3). The three areas are different colours for each material, glass, Ti metal and LDPE plastic, while the other colours are mixtures and show area overlap for clarity.

and is defined as,

$$\mu = -\frac{\Delta W/W}{\Delta L/L}. \tag{1.3}$$

The Young's moduli and Poisson ratios of oxide glasses are typically found in the range of 40–100 GPa and 0.2–0.3, respectively. Bulk modulus (K) is the resistance to uniform compression; it is the change in relative volume under infinitesimal changes in pressure, meaning it is shape-conserving. In contrast, shear modulus (G) is volume-conserving, it is the resistance to change in shape. K and G are typically 40–85 and 20–40 GPa, respectively for oxide glasses. If any two of the elastic moduli are known (Young's modulus, Poisson ratio, bulk modulus or shear modulus) it is possible to calculate the other two.

1.2.3 Hardness

Like strength, hardness is a practical measurement: it is a material's resistance to permanent deformation following indentation, formulated as force (F) divided by the *projected* area of the indent (A_p), $H = F/A_\mathrm{p}$.[31] Since most materials can be indented, it provides an easy point of comparison and measures a property akin to scratch resistance, which is very important in applications. Although the processes which occur during indentation are complex, they can be separated into an elastic densification component (K) and a plastic response component (αG). Hardness has been found to be proportional to $(\alpha GK)^{1/2}$, where α is a material-dependent constant related to bond strength.[32,33] Moreover, it may be more complicated than that, since plastic behaviour can take two routes as well, permanent densification or shear flow.

The load used during indentation is also significant. As a result, reported hardness values typically include the type of tip and load in kgf (kilogram-force, simply the weight of the load), then kgf can be converted to Newtons using the force of gravity

and thereby hardness is also often reported in GPa. Micro-hardnesses of oxide glasses are typically found in the range of 4–10 GPa. At low indent loads, such as the 0.5 N (0.05 kgf) used in nano-indentation, the indentation size effect (ISE) has been found to affect hardness measurements in glasses. The ISE has been defined as an increase in hardness at decreasing indent penetration depths, typically beginning below one micron.[34] The effect is thought to be caused by dislocation strengthening (necessary to accommodate plastic deformation) and/or friction between the indenter and specimen.[34–36] Although most publications have focused on the ISE in bulk metallic glasses,[36–38] it has been found to exist, albeit with a small magnitude, in silicate glass and fused quartz.[39–42] Plastic deformation in amorphous metals is known to occur through highly localized "shear bands" rather than dislocations.[36]

1.2.4 Fracture Toughness

Fracture toughness in mode I (K_{Ic}) or the resistance to crack propagation under tensile stress can also be measured during indentation according to,[43–45]

$$K_{\mathrm{Ic}} = \S_V^R \left(\frac{Y}{H}\right)^{1/2} \cdot \frac{P}{c_{\mathrm{avg}}^{3/2}}, \tag{1.4}$$

where c_{avg} is the average radial crack length (including indent width), P is the pressure or load of the indenter and $\S_V^R$ is a material-independent geometric constant for Vickers-produced radial cracks. This semi-empirical model for K_{Ic} assumes that entirely plastic flow, not densification, occurs from indentation; if densification does occur, Eq. 1.4 overestimates fracture toughness.[46,47] Densification only varies the constant $\S_V^R$, but would likely not affect overall trends signicantly. Furthermore, the crack length must be greater than the indent diagonal. An evaluation of Eq. 1.4 on a variety of ceramics showed it to be accurate within 30% compared to conventional

fracture toughness measurements, while the precision of fracture toughness measurements were found to be much better; on the order of 10% at the 95% confidence level.[43]

1.3 Relation of Glass Topology to Mechanical Properties

In general, Young's modulus is the easiest elastic modulus to predict as it is mainly determined by the average bond disassociation energy and packing fraction, so much that Makishima and Mackenzie's[21] calculations of Y solely from these properties for several silicate compositions matched well with experiments.[3,21] Nonetheless, the other elastic moduli were not so well-correlated to experiments, nor did the model work well for other glass systems indicating that other factors are at play.[21,48]

The degree of polymerization has two effects in silicates; first, it dictates the level of network connectivity, which has been inversely correlated with Poisson's ratio and directly correlated with all other elastic moduli, especially shear modulus.[3,26,49,50] Generally, the introduction of an alkali is typically associated with a decrease in Young's modulus,[51] however, Si-O-Si bonds are known to be flexible, so depending on the modifier more NBOs compared to BOs can actually increase Young's and bulk moduli.[52,53] The strength and type of bonds is important for all mechanical properties, thus, it can greatly matter which NBOs are being exchanged for Si-O-Si bonds. For silicates, network dimensionality is primarily related to the degree of polymerization, yet, highly-coordinated modifiers can increase the covalence of NBO-modifier bonds, thereby increasing dimensionality and therefore Y and K. In metallic glasses, Wondraczek *et al.*[3] found that atomic packing density was correlated with Poisson's ratio and, to a lesser extent, Young's modulus.

Free volume is strongly correlated with μ and K, but may also be important for Y

as the highest values found for Y are metallic glasses.[3,54] Despite having comparatively low interatomic bond energies,[55] metallic glasses compensate with a much higher atomic packing densities than most oxide glasses. Essentially, there are more bonds per volume, so even though the bonds are weaker, the bond density compensates through sheer abundance.[3]

In general hardness is proportional to K and Y, such that the addition of sodium and potassium to silicates is known to lower the Vickers hardness, while the addition of alkaline-earths increases the hardness due to the differences in NBO bonding.[7] Ion channels also play a role as plastic flow has actually been seen to increase above a certain amount of modifier, at which point modifiers are in strongly bound groups that move cooperatively.[56] Crack propagation will be hindered by stronger and/or more abundant bonds, therefore increasing fracture toughness. There has been a multitude of studies performed with the aim of understanding the relationship between surface condition and strength, yet, all theories follow a similar law: a chain is only as strong as its weakest link.[57] This explains how a stronger connection under strain, such as a covalent bond, would hinder crack propagation. As for compactness, the correlation with K_{Ic} is explained by the antagonism of crack depth and surface energy; a material with more atoms will produce more surface area for the same depth of crack compared to a high free-volume material.[9]

Finally, chemical heterogeneity is thought to increase compactness or packing fraction as more geometries are possible, so disorder may affect mechanical properties as well. Wondraczek *et al.* also demonstrate how structural inhomogeneity has been used in metallic glasses to increase elastic modulus and strength, but has not been exploited in oxide glasses.[3] Structural disorder is defined as diversity in one or more of these categories: coordination, topology (e.g., the presence of certain structural units such as rings, chains, or layers), and/or chemical composition.[3]

Without long-range order, glass mechanical properties are determined entirely by their topology which is dominated by chemical composition. In summation, glass response to mechanical stress is chiefly controlled by the chemical composition of the material. Consequently, to improve glass mechanical properties, the relationship between mechanical properties and chemical composition merits further investigation.

1.4 Mixed-Modifier Effect

Tuning the chemical composition is the most fundamental method of varying the properties of a glass. Industry is limited in which components are feasible to use, due to safety and cost considerations. Nonetheless, one modification of chemical composition has wide-spread applicability to nearly every kind of glass used commercially. Most glasses, with the exception of those used in some specialized scientific applications, use an alkali or alkaline earth oxide as a component; these lower the melting and glass transition temperatures (T_{g} and T_{m}) of the glass mixture, thereby introducing significant energy savings and increasing the workability window.

Interestingly, by adding more than one type of alkali or alkaline earth ion, there is a deviation from the law of additivity, typically called the mixed-alkali effect (MAE), but which can be more broadly termed the mixed-modifier effect (MME). Many properties, including ion conductivity, elastic modulus, hardness, chemical durability, viscosity, density, molar volume, and refractive index exhibit the MME;[58] it can be found in most commercially utilized glass systems including phosphates, borates, germanates, aluminosilicates and silicates.[59–63] The departures from linearity for mechanical properties are significant, e.g., Young's modulus (±20%) and hardness (±10%), with a positive improvement of 4–6 times in chemical durability due to decreased modifier extraction.[58] To put this in perspective, the ubiquitous ion-exchange glass

Table 1.1: Summary of properties for mixed alkali glasses, described qualitatively and approximately quantitatively, reproduced from Day [58].

Property	Deviation from linearity (additivity) w/ addition of 2nd alkali
ion conductivity[a]	large, 10–10^5 orders of magnitude (dependent on T)
density	small, $\approx \pm 10\%$
refractive index	small,$\approx \pm 10\%$
molar volume	slight, $\approx \pm 5\%$
hardness	small,$\approx \pm 10\%$
thermal expansion	small, $< \pm$ 10%, usually positive dev.
chemical durability	moderately higher, alkali extraction lowered by 4-6 times
strength	no reported data
elastic modulus	small, $\approx \pm 20\%$, deviation temperature dependent
compressibility	no reported data

[a]From ref [64].

found on hand-held screens made by Corning^{TM} has an improvement of 22% in Vickers hardness[5] vs. non-exchanged glass. The ion-exchange treatment is a fairly costly one, leading to its use only in high stress applications, however, the MME could be exploited to improve mechanical properties without any additional cost or processing — it is simply a matter of optimizing the modifier content. Table 1.1 surveys the many properties the MME affects; the significant departure ($\pm$20%) from linearity shown by the elastic modulus is of the most interest to the present study. Although the original paper[64] called the deviation in Y small, this is compared to the deviations in dynamic properties, which have several orders of magnitude deviations. However, a 20% increase is signicant for applications. Finally, larger amounts of total alkali increase the magnitude of the MAE, in such differing properties as molar volume and ionic conduction.[64–67] In fact, only after 10% total modifier is the MME prounounced and there is evidence that the MME is proportional to the total alkali content;[58,61,67] essentially, by increasing alkali content, there are more opportunities for ions to become "trapped" in ill-fitting configurations.[65]

In this work, the MAE or %-deviation is quantified by comparing the experimental

value, P_{exp} with the predicted value determined by additivity alone, P_{add},

$$\%-deviation = \frac{P_{\text{exp}}(x) - P_{\text{add}}(x)}{P_{\text{add}}(x)} \times 100\%. \tag{1.5}$$

The value at x predicted by addivity alone is determined using the two pure-alkali endpoints, $P(0)$ and $P(1)$, according to Eq. 1.6,

$$P_{\text{add}}(x) = P(0) + [P(1) - P(0)]x. \tag{1.6}$$

This construction consists of drawing a straight line between the two endpoints of the series and evaluating the distance each experimental data point is from the line of additivity. While the law of additivity is linear to the first approximation for most properties, density is known to display a non-linear 2nd-order behaviour according to:[7,68]

$$\rho = \frac{1}{\sum_i x_i V_{m,i}} \sum_i x_i \rho_i V_{m,i}. \tag{1.7}$$

Most publications about the MME to date have focussed on ion transport properties such as ionic conductivity, viscosity and diffusion, likely because they have markedly large (several orders of magnitude) negative deviations from linearity, perhaps indicating that these properties are most directly related to the origins of the MME. Yet, despite many decades of interest and publications in this field, no comprehensive understanding of ion diffusion in amorphous solids exists,[69] making the MME doubly difficult to understand. Initially, Greaves[20] proposed the modified random network (MRN) model: when two differently-sized ions share an ion channel, such as K^+ and Cs^+, diffusion is limited due to energetic factors; it requires more energy for an atom to hop into the adjacent space recently vacated by a differently-sized atom.[24] Later, Greaves and Ngai[70] attributed the MME to cooperative ion motion

by including an extra term for the energy needed to change a structural unit from one conformation to another. However, the elastic stain energy of the silicate network required for accommodation of the new ion was neglected. Although this model fit their potassium-cesium silicate data well, the MME in other mixed-ion compositions cannot be explained in this way.[61] Additionally, several authors have found that structural parameters, such as modifier and former bond distances ($R_{\text{M-O}}$ and $R_{\text{F-O}}$), vary significantly with alkali ratio; however, this finding is tempered by the fact that the local cation environment changes similarly for an increase of modifier in a single-modifier glass.[61,70]

Subsequently, the explanation of the MME has shifted from being structural and static in nature to being entirely dynamic and treating the role of the network as active. Currently, the theory which is used to explain most of the properties of the MME is the dynamic structure model (DSM),[71,72] which does not rely on interactions between differing ions as others have in the past.[70,73–76] It proposes that moving ions are actively changing the local structure of the glass, *i.e.*, there is relaxation of ion sites to their new occupants, even below T_{g}, and the energy and time needed to accommodate the different types of sites is responsible for the diminished hopping rate.

Nevertheless, no theory has been able to explain completely the deviation from linearity for both dynamic and static properties. In this case, dynamic properties are those involving ion transport and network dilation, while static properties are similar to those termed thermodynamic in thermodynamically stable materials, such as density and packing fraction. Considering that properties like density, hardness and ionic conductivity all have differing magnitudes of deviation from linearity, it is difficult to find a phenomenological model that explains the mixed-modifier behaviour and its relationship to applied stress. While the DSM is a possible explanation of the MME

observed in dynamic properties, it does not fully predict the effect on mechanical properties, which are dependent on a combination of static properties, *i.e.*, packing fraction, and dynamic properties, *i.e.*, ion diffusion during plastic flow. Nonetheless, it would be useful to understand and predict the MME's role in mechanical properties. One of the goals of this work is to relate the MME in dynamic (ion conduction) and static (glass structure) properties to that in mechanical properties.

It is not clear how the MME in ionic conduction and mechanical properties are interrelated. Several authors state that mixed-modifier glasses have reduced ion mobility in the ion channels, thus there is less plasticity and higher resistance to shear.[24,46,77]. Additionally, ionic motion is thought to help relax applied stresses, such as those in observed in measurements of internal friction.[78] Thus, if this model is correct, mechanical properties which involve ion motion, such as hardness and toughness, are expected to be affected. Finally, as per the DSM, the strain energy of the network incurred during ion conduction should be correlated with mechanical properties, such as stiffness, which depends on bond strength and bond density.

Additionally, both mechanical properties and ionic conduction depend on the glass structure. Conductivity has been shown to increase with the amount of NBOs, although with diminishing effect after the initial 20% modifier;[61,79,80] thus, the connectivity of the network plays a role in both sets of properties. Furthermore, molar volume has been known to correlate negatively with conductivity in single-alkali glasses,[61] therefore compactness may play a role in both mechanical, structural and ion tranport properties as well. Although most of the current data indicate that the alkali environment in the mixed glasses is the same as in single-alkali compositions,[20,61,81,82] in mixed-modifier glasses the energetic differences from variations in field strength are often stronger than the entropy of mixing, hence, they form regions

of mostly one type of modifier or another.[81] Mixed-modifier glasses have more disorder and usually a higher V_f, therefore given the current "ion hopping" explanation of the MME for ionic conduction, chemical heterogeneity may affect conductivity as well.

Thus far, the differences in mass, size, cationic field strength, ion distribution, bonding and coordination environment between the two modifiers have been considered in terms of the nature of the MME.[58,64,83] They play a role in predicting the strength of the MME and location of the maximum deviation. Initially, mass differences were considered to be of the highest importance, since then this idea has been ruled out.[84–86] Next, size differences were thought to be the predictor of the MME, with larger differences translating to larger MMEs.[87–91] On the other hand, there were cases of very differently-sized ions not having correspondingly large deviations from linearity, which was attributed to the ions having separate interpenetrating channels without competing.[83]

Dietzel[83] used cationic field strength (F_c), defined as Z/a^2, where Z is the valency of the ion and a is cation-oxide bond distance, to predict the strength of the MME. He stated that the difference (ΔF_c), not F_c itself is the decisive factor.[83]. He also used the stability of the mixed crystal phases to predict which mixed alkali combinations are more stabilizing: combinations with small ΔF_c, yet large differences in radii, have no corresponding crystal compounds, perhaps indicating their instability. Indeed, dynamic processes, such as diffusion, control crystallization and the final crystalline state, thus it seems likely that for glasses static and dynamic processes could be controlled by the same forces. A small ΔF_c indicates instability and possible phase separation due to competition at the NBO site and the absence of the stabilization which comes from two different type atoms bonding to Si-O^-. Conversely, a large ΔF_c increases NBO stabilization and is thought to increase the energy required for

ion transport properties and lead to the higher E_a.[83,92]

Although authors[83,86] used springs to illustrate their point about stabilization, it may be better thought of as electron density on the oxygen transferring from the more ionic bond (less electronegative cation) towards the more covalent bond (more electroegative cation), therefore the more covalent bond would become shorter, while the ionic bond would become longer (the oxygen atom in the middle would increase in size due to the added electron density); thus, there may be a zero net sum for bond lengths and static properties. However, Dietzel[83] also reported that ions with different CN can encourage better packing and affect static properties in a different way as well. Authors have shown that for many mixed-modifier compositions the local cationic structure does not change significantly with mixing, yet different degrees of mixing and even induced cation CN changes in the presence of a second ion have been observed.[20,24,81] Consequently, differences in cationic field strength (ΔF_c) and CN (ΔCN) between the two cations may affect static properties, while the former is more likely to influence ion transport properties.

1.4.1 Mixed Alkaline-Earth Effect

Although the MME usually refers to deviations from linearity in alkali metal-containing glasses, there is mounting evidence that an analogous effect occurs in alkaline-earth-containing glasses as well.[93–98] There were some initial studies of conductivity and viscosity which indicated that no departure from linearity existed for mixed alkaline-earth glasses.[58,99,100] Most studies of the mixed-alkaline-earth effect (MAEE) have examined complex glass systems involving two different alkaline-earth ions along with other additives, such as Al^{+3},[94,96,98] Na^{+}[93,95–98] or F^{-}[94]. Additionally, few studies

have investigated ion transport properties in mixed-alkaline-earth glasses.[95,99] Consequently, there is a need to understand the MAEE separate from the influences of other components, especially additional alkali ions and Al_2O_3 as they have both been known to affect the strength of the MME in mixed-alkali and mixed-alkaline earth glasses alike.[62,95]

1.5 Ion-Exchange

As discussed earlier, the surface condition is plays an important in the breaking strength of glass (see Section 1.2.1). It follows that there are two major ways to improve the breaking strength of glass; either prevent flaws above the critical limit from forming, such as by the application of a protective polymer coating, or increase the Young's modulus and surface energy density of the material.

The ion-exchange (IE) process enhances mechanical and optical properties, most notably increasing strength up to 4-6 times, thereby broadening the scope of high-stress applications where glass can be used: hand-held media device screens, heat-resistant fireplace windows, waveguides, micro-optics, airplane cockpit and high-speed train windshields, drug-delivery equipment, and eye-glasses.[101–104] As glass is a brittle material, the reason for failure is rarely insufficient stiffness; the surface condition usually plays a larger role, where tiny flaws act as local tensile-stress concentrators and give rise to fracture. Ion-exchange offers a solution to this problem: it increases scratch-resistance by generating an opposing compressive stress at the surface. Uniquely, IE produces high stresses, several hundreds of MPa,[101,104–106] over a shallow case depth, ≤ 100 μm, which allows objects that cannot undergo thermal tempering, e.g., irregularly-shaped and thin glass objects, to be strengthened nevertheless. Due to the compositional gradient, birefringence can be used to produce

waveguides and the resulting changes in refractive index have been measured optically;[103] nonetheless, the resulting stress profile is important as different stress states can affect the refractive index further.[107,108]

The IE process is performed by placing the target object in a molten salt bath, *e.g.,* KNO_3, and the exchange is driven by ion-concentration differences between the inside of the glass and salt bath. When performed below the glass transition temperature, T_g, IE induces compressive stress on the glass network due to a larger ion filling a cavity recently vacated by a smaller ion, while preventing significant relaxation or accommodation of the larger invading ion. Commercial IE glasses such as Corning Gorilla® and Schott Robax® have smaller ions, such as Na^+ or Li^+ ions, respectively, replaced with larger K^+ ions which can yield strength enhancements up to 2–4 times, improve hardness by 8–20% and decrease fragment size substantially.[106,109] Additionally, the refractive index of the exchange-layer can be altered over a shallow depth by introducing an ion with a different polarizability.[104,110,111]

Many experimental studies use birefringence to probe directly the compressive stress found in the IE layer; stresses are typically on the order of hundreds of MPa up to 1 GPa spread over case depths of 20-1000 μm.[101,105,106,112,113] The duration of the IE treatment affects both the magnitude and location of the maximum compressive stress; the maximum stress has been shown to decrease and migrate further from the glass surface with increasing IE duration. The maximum induced stress occurs when IE is performed at temperatures well below the T_g, roughly 120–250 °C[105,112,113] below. Nonetheless, substantial compressive stress, approximately half of the maximum, has been observed even when IE took place only 30 °C below T_g, yet for the same amount of time as the maximum compressive stress.[105,114] Finally, even temperatures 135 °C below T_g have shown significant stress relaxation over a long enough period, 72-216 h,[101,105,112,113,115] highlighting the possibility that the glass network will relax the

applied stress, despite being well below T_g. It is important to remember that T_g is a broad transition and that the viscosity of the material is still significant at these temperatures.

1.5.1 Linear Network Dilation Coefficient

A recognized problem in understanding the physical properties of IE glasses is the anomalous behaviour of the linear network dilation coefficient (LNDC), B, defined as the linear strain per unit change in alkali concentration, where V_m is the molar volume and C_{M^+} is the concentration of invading cation:[102,116–118]

$$B = \frac{1}{3}\left(\frac{1}{V_m}\frac{\partial V_m}{\partial C}\right) = \frac{1}{3}\frac{\partial \ln V_m}{\partial C_{M^+}}. \tag{1.8}$$

As the molar volume of the exchange layer of an IE glass cannot be measured directly, B for IE glasses is typically calculated from the optically measured stress, σ, using the following relation:[119,120]

$$\sigma(z) = -\frac{BY}{1-\mu}\left[C_{M^+}(z) - C_{avg}\right]. \tag{1.9}$$

It is dependent on Young's modulus (Y), Poisson's ratio (μ), stress as a function of distance from the IE surface (σ(z)), concentration of substituting ion, (C_{M^+}(z)) and average concentration of substituting ion (C_{M^+avg}). These last two terms enforce that the total stress in the glass, compressive and tensile, sum to zero. Additionally, if there is no concentration gradient, the stress is also zero. Conversely, V_m and the corresponding B, can be calculated from combined Metropolis Monte Carlo and molecular dynamics simulations.[116,121]

The observed anomalous behaviour comes about when B for IE glasses is compared

to the corresponding as-melted mixed-alkali glasses; B is always 2–5 lower in IE glasses. B depends on the IE temperature, where the lowest B is typically found at processing temperatures of approximately $0.8T_g$.[120,122] For example, an $Na^+ \leftrightarrow K^+$ exchange in a silicate glass has a measured LNDC of $3–5\times10^{-4}$ (mol-% $K_2O)^{-1}$ compared with a LNDC of 1.3×10^{-3} (mol-% $K_2O)^{-1}$ for the as-melted series.[102] This order-of-magnitude discrepancy is likely because the molar volume of an IE-glass is less than the corresponding as-melted composition; models have shown that the local molar volume in an IE glass is approximately half of the as-melted composition and this has been used to calculate the experimentally-observed LNDC, about 2-4 lower than the bulk as-melted glasses.[116,117,121,123] Nonetheless, thus far, the molar volume of the exchange layer in an IE glass has not been measured experimentally, nor has any specific mechanism for stress generation or relaxation been reported, only mechanisms from simulations have been suggested.

It has been reported that if the exchange is performed below T_g, the ion coordination number is similar to what is expected from the bulk as-melted composition.[116,117,124] However, there is some disagreement as to whether the glass network connectivity remains unaltered.[104,116,117,125] Investigations of IE glasses using micro-Raman[104,125] and X-ray absorption[124] spectroscopy have both observed changes in the topological structure. Furthermore, it has been proposed that changes in Q^n-populations could reduce the accumulation of compressive stress within the IE layer.[126] Kreski *et al.*[117] used simulations to show the topological structure of the IE glasses remains the same, *i.e.,* like the untreated material, yet they possess the local cation environment of the invading ion, thereby leading to constraints on the possible molar volume. On the other hand, a computational study by Tandia *et al.*[116] attributed the LDNC anomaly to differences in local cation site between as-melted and IE glasses.

Computational studies[116,117] also discuss how the compressive stress and relaxation manifests structurally. Kreski *et al.*[117] attributed the residual strain in the system to an increase in cation coordination sphere size, evidenced by oxygen atoms being pulled towards the alkali site and a re-orientation of SiO_4 tetrahedra, namely an *increase* in ∠Si-O-Si beyond what is found in the as-melted potassium end-member composition. Tandia *et al.*[116] describe the relaxation of the structure as a two step process: an initial fast rearrangement of the cation site towards a mixed-alkali as-melted structure indicated by an elastic expansion, followed by a slow process towards the as-melted potassium end-member structure manifested as an irrecoverable densification without network expansion. The first step is thought to induce the strain found in IE glasses, while the slow rate of the second step is responsible for the lower molar volume and LNDC anomaly seen in IE glasses. Another study corroborates by explaining the network is expanding elastically initially and then plastically contracting to relax stress.[127]

Several authors have attributed the anomalous behaviour of the LNDC to a slow plastic relaxation of the network.[115,126,128–130] Although the densification due to IE is thought to be irreversible on the laboratory time scale, back-exchange simulations, where the invading ion is re-exchanged for the original ion type, showed the structural changes to be nearly completely reversible or elastic. Since this mechanism involves two different rate-steps, exchange and back-exchange, it may be more accurately described as non-linear elasticity.[116,117,121]

An important question for fundamental and applied research alike is whether there exists a maximum obtainable compressive stress. One study states that the lower limit on molar volume is responsible for the limit of achievable compressive stress.[117] Another study states the slow rate of relaxation limits the achievable maximum compressive stress; the authors propose a way of overcoming this problem by

performing IE at higher temperatures, therefore having more energy to relax the local environment around the invading ion, leading to a larger volume increase and compressive stress.[116] Although this may sound counter-intuitive, it is possible to obtain compressive stress during expansion of the material; the equilibrium state of the IE glass changes from the untreated structure to an as-melted mixed-alkali composition upon ion-exchange. Consequently, as long as the molar volume of the IE glass is increasing at a *slower* rate than the as-melted composition upon the addition of the larger ion, it can still be under compression while expanding. Finally, a review of the future of IE points out that relaxation is likely responsible for the compression maximum being below the surface and that these structural mechanisms require further investigation.[102] It is clear that understanding the origin of the compressive stress maximum as well as its position within the case depth is important to the continued improvement of the IE process.

1.6 Central Question of the Thesis

The overall goal of this work is to better understand the relationship between the mechanical properties and molecular structure of glass and thereby, to be able to tune these properties for future applications. The MME has previously been shown to exist in both mechanical and static properties, highlighting it as an avenue of investigation. In order to explore this question, the relationships between structural, static, dynamic and mechanical properties had to be examined; mechanical properties involve both static and dynamic phenomena, while the MME influences both types of properties through difference mechanisms, thus, it was necessary to evaluate the factors which are most important in regards to the mechanical response. Additionally, the molecular structure of the relevant glasses had to be investigated and related to all the other properties. Although modifiers are added to nearly every commercial glass

composition, no comprehensive understanding of their role exists. Thus, in addition to characterizing the MME in glass, part of this investigation has been to better understand the role of the modifier in glass, specifically alkali and alkaline-earth ions in a silicate network. By examining the relationships between all these properties, the mechanisms of the MME may be clearer and more useful when optimizing compositions. Also, given the improved mechanical properties of IE glasses, the structure and mechanical properties of ion-exchange glasses were studied in order to compare to the "as-melted" relaxed mixed-modifier glasses.

First and foremost, it is expected that the MME will be present in all mixed-modifier glasses, whether alkali or alkaline-earth ions or a combination is used; additionally, it is expected to exist in all properties, although it will be stronger in dynamic properties compared to static ones. Consequently, it is expected that mechanical properties involving plasticity, such as hardness and fracture toughness, will have larger deviations from linearity in comparison to elastic moduli, which only involve infinitesimal strains. The same relationships between glass structure (such as packing density, network connectivity and dimensionality and packing density) and mechanical properties found in simpler glasses are predicted to hold for mixed-modifier compositions.

The manifestation of the MME in glass structure is more difficult to predict as many experiments indicate the environment of the cation in a mixed-modifier glass to be similar to that of a single-modifier glass. The identities of the two modifiers are likely to matter greatly, as previous studies indicate that the difference in mass or field strength will determine how greatly the introduction of the second ion affects the environment of the initial modifier. The role of the MME in the SiO_2 network itself is difficult to predict, still, small deviations from linearity in molar volume and packing fraction are expected, thus the compactness and perhaps even connectivity

is affected by the presence of more than one cation.

On the other hand, the network structure and the environment of the substituting ion in IE glasses will have large differences in comparison to the corresponding "as-melted" composition. There is measurable compressive stress in IE glasses, thus, in addition to increased mechanical properties, a corresponding strain within the glass structure also exists. Finally, since the composition is mixed, there may be some evidence of the MME in IE glasses as well.

In order to investigate the role of the MME in mechanical properties, several mixed-modifier silicate series were made and their physical properties characterized. The difference here, by comparison to previous studies, is that mechanical properties and ionic conduction were investigated together, thereby allowing for better quantification of the dynamic component in the MME of mechanical properties. The compositions of the glass series were selected thus: modifier pairs were chosen to isolate modifier differences and similarities, such as in size, charge, covalency, and/or field strength. Moreover, the glass structure was characterized and related to static and dynamic properties, again allowing for better separation of the two components. This way, the MME in these two apparently different properties could be related and taken advantage of when choosing novel compositions.

A single-alkali silicate glass was ion-exchanged and characterized. The structural changes induced by IE were studied by Raman spectroscopy and related to an "as-melted" glass of the same relative alkali concentration. Using nano-indentation the Young's modulus and hardness in the IE layer were measured and again related to those in the corresponding "as-melted" glasses. The changes in properties and structure of the IE glasses could be extreme cases of the MME and were related to the MME in conventionally-made glasses.

Chapter 2

Techniques and Methods

2.1 Sample Preparation

Glass synthesis can be simply described as heating the components, usually metal oxides or carbonates, until melted, then rapidly cooling the melt until frozen. Since glass is a kinetically-controlled state rather than a thermodynamic one, the conditions of cooling are likely the most important step in the glass-making process. Depending on the method and rate of cooling many physical processes can occur: crystallization can be prevented or encouraged, phases can separate, thermal stresses can be introduced, in addition to the different fictive temperatures (see Section 1.1) representing energetically-different conformations and volumes that can also be produced. In this work, all glasses were heated to the same temperature, only the length of heating was varied. With few exceptions, the same cooling method was also used, the melt was simply poured in a metal mold, cooling in air to room temperature. In some series, the endmembers of the mixed-modifier series required the "squash-melt" method; where after pouring, the melt was quickly pressed between two metal plates to prevent crystallization and/or phase separation.

Fig. 2.1 is a ternary phase diagram of all the glass compositions made; all were silicates, but depending the modifiers, different amounts of total modifier had to be used to prevent crystallization or to ensure melting at temperatures below softening temperature of the Pt crucible used for melting. Several mixed-modifier silicate series

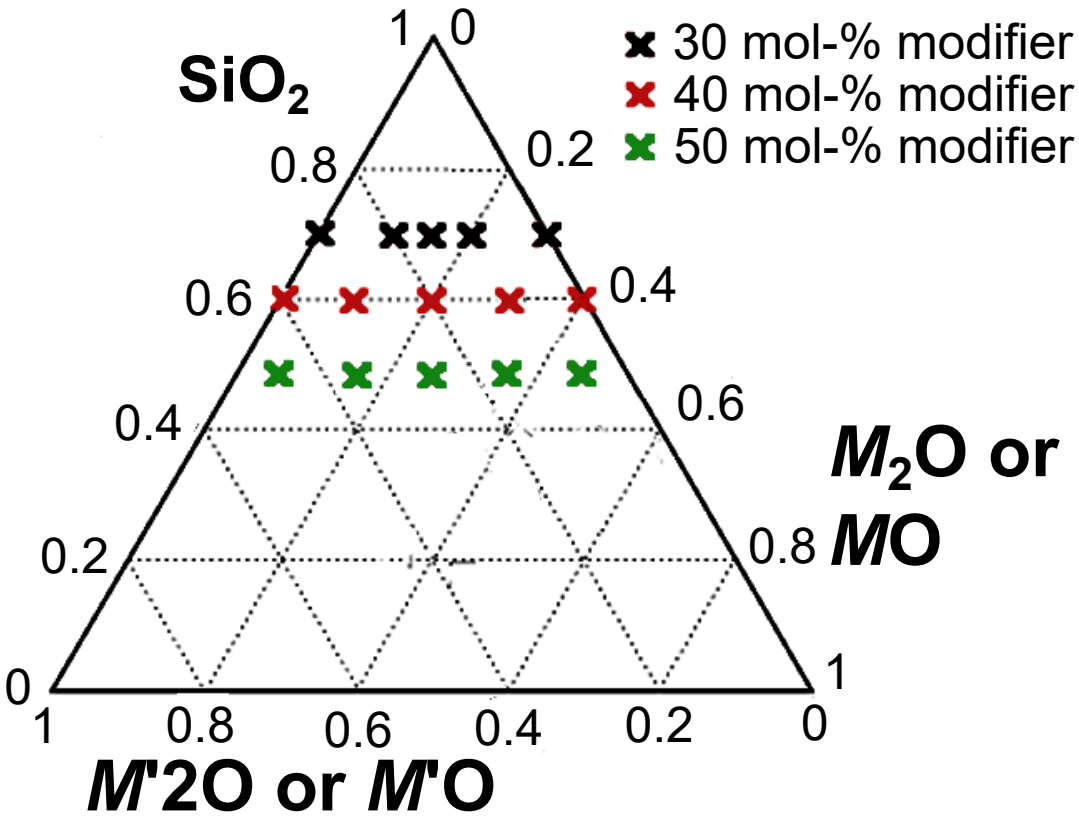

Figure 2.1: Ternary composition diagram of silicate glasses made in this study, where M_2O = Li_2O, K_2O and/or Rb_2O and MO = MgO, CaO, BaO and/or ZnO, while M'_2O or $M'O$ just denotes a different alkali or alkaline earth oxide.

were made, mixed-alkali, mixed alkaline-earth and mixed alkali alkaline-earth oxide combinations; M_2O or MO with a second M'_2O or $M'O$, where M_2O = Li_2O, K_2O and/or Rb_2O and MO = MgO, CaO, BaO and/or ZnO, while M'_2O or $M'O$ just denotes a different alkali or alkaline-earth oxide than the first.

For this work, the most representative glass series are MgO-CaO-SiO_2 and Li_2O-K_2O-SiO_2; the relevant phase diagrams can be found in Figs. 2.2 and and 2.3, respectively. Phase diagrams can be a useful tool for predicting glass-forming regions and evaluating melting temperatures. For example, MgO-CaO-SiO_2 system (Fig. 2.2) has many different crystal phases, seven in total which contain all three component oxides, indicating that the system likely has a propensity to form glass; in fact, if a line

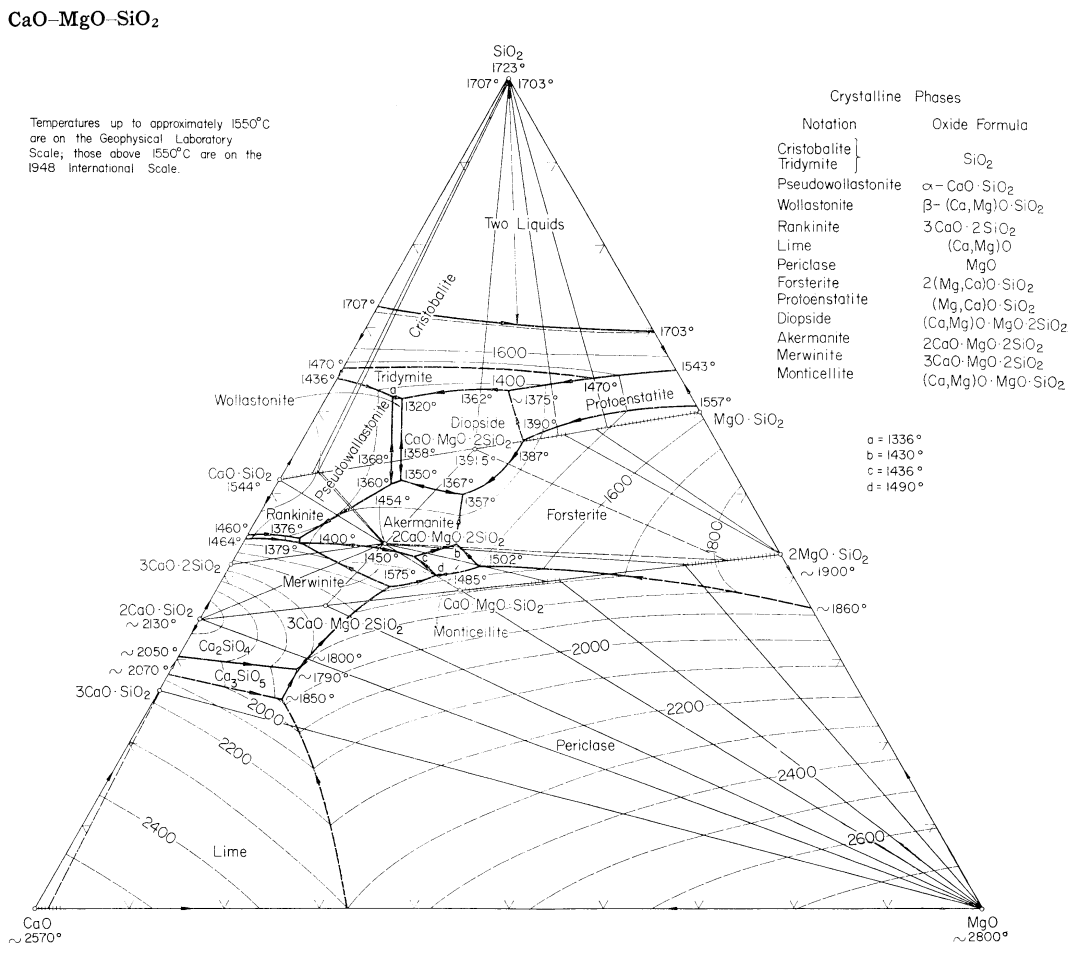

Figure 2.2: Liquidus projection of the MgO-CaO-SiO_2 system. Reproduced with permission from the American Ceramic Society [131].

is drawn from MgO-SiO_2 to CaO-SiO_2, which corresponds to the xMgO-$(50-x)$CaO-SiO_2 series studied within, at least four crystal phases are passed through. Also, this region has a lower melting temperature than other regions. In addition to having many crystal phases, a deep eutectic can also indicate high glass-forming capability, which can also be seen in the Li_2O-K_2O-SiO_2 system (Fig. 2.3), where the melting temperature decreases from 1100 to 750 °C for the line that corresponds to the present $x$$Li_2O$-$(40-x)$$K_2O-60SiO_2$ series.

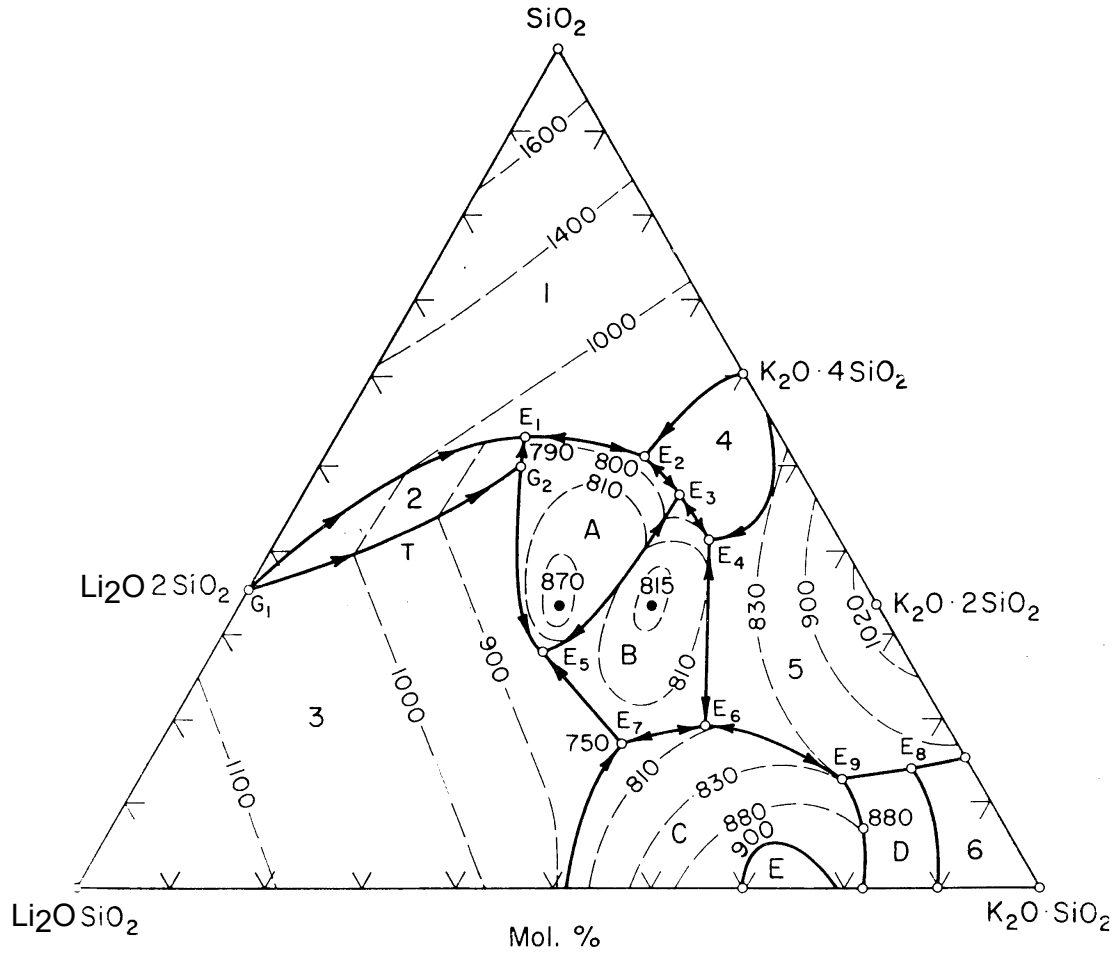

Figure 2.3: Liquidus projection of the $Li_2O{\cdot}SiO_2$–$K_2O{\cdot}SiO_2$–SiO_2 system. Reproduced with permission from the American Ceramic Society [131].

A common glass synthesis procedure would be as follows: the $x$$Li_2O$-(30−$x$$K_2O$)-70$SiO_2$ series was made from stoichiometric amounts of SiO_2, Li_2CO_3 and K_2CO_3 that were shaken together, or in some cases ball milled, to ensure good mixing. Thereafter, the mixture was heated until melted. However, due to the decomposition of the carbonate species and the evolution of CO_2 gas, the temperature was slowly increased (approximately 2 °C/min) between 700 and 1150 °C until the volume was greatly reduced. Unfortunately, since the starting volume of the reagents was large in comparison to the Pt crucible, this process had to be done twice to obtain a large mass of melted glass. Thereafter, the mixture was heated more quickly, at 6 °C/min until a final temperature of 1550 °C was reached. In the hope of saving time, an alternate strategy was sometimes adopted; only a small amount, roughly 1/4, of starting powder was added initially to allow for normal heating rates without sample loss to thermal decomposition bubbling, then once at the highest temperature, small amounts of sample, roughly 1/4 again, were added to the crucible and placed back into the oven, approximately every 5 minutes. The thermal decomposition "bubbling over" problem can be practically approached one of two ways, either by allowing slow removal of large amounts of CO_2, or by having smaller amounts evolve from a lower viscosity liquid (at higher temperatures).

Once the melt had equilibriated at this elevated temperature for 60–120 minutes, it was quickly removed from the furnace, poured into a brass mold and quenched in air. Glasses containing high relative amounts of Li_2O in the Li_2O-MgO or ZnO in the Li_2O-ZnO mixed-modifier series saw tendencies to crystallize and/or phase separate and the melt needed to be quickly pressed between two metal plates to obtain a clear homogeneous piece of glass.

To check mass loss, the mass of the crucible containing the extra melt and the

produced glass piece were measured. The second most important step in glass making is annealing to remove thermal stress, where the sample is heated near to T_g, usually $\geq 0.85T_g$, and cooled *slowly* to room temperature. However, usually for most glasses made herein T_g was not known for the annealing process, therefore, consecutively higher annealing temperatures were used until no birefringence was observed. The bulk glass pieces of the $x\mathrm{Li_2O}$-$(30-x\mathrm{K_2O})$-$70\mathrm{SiO_2}$ series were annealed between temperatures of 350–450 °C overnight to remove residual internal stress and allowed to cool down very slowly. The optical properties of glass are very sensitive to stress, thus the progression of the annealing process can be checked using a light table; residual stress creates rainbow fringe lines that can be observed between two cross-polarizers.[132] If significant residual stress was present the glass was annealed again at a higher temperature, usually 25–50 °C higher. Generally, compositions with higher silicon dioxide content required the highest temperatures, in addition refractory materials like MgO and CaO also increased the annealing temperatures significantly.

The bulk glass would then be cut (removing any bubbles, cloudy or crystalline top layer) using a Buehler low-speed saw with a LapCraft diamond-tipped blade and ethanol for cooling. High relative $\mathrm{Li_2O}$ concentration in the $\mathrm{Li_2O}$-BaO series typically created "cloudy" tops of the glass cube, while high MgO content in the MgO-CaO series produced white crystals on top. This localization of phase separation and/or crystallization is likely due to the difference in cooling rates between the surfaces of the glass exposed to the air vs. metal plate. Finally the piece would be polished with silicon carbide paper and diamond paste of different grain sizes (15 through 1 micron) suspended in oil or Buehler MetaDi polishing fluid until the piece was smooth and entirely transparent. Typically, each grit size took 20–30 minutes to polish three samples using a Graton Vanderwilt Polishing Machine from the Mico Instrument Company. Given the hygroscopic nature of series containing high amounts

of K_2O, they required special care, such as handling them with gloves and storage in desiccators. Furthermore, measurements needed to be completed quickly to avoid corrosion due to moisture.

Glasses present unique sample verification challenges; how can one know that their glass is indeed the structure and composition they desired to synthesize? Although several analysis techniques can be used in combination, no single technique gives a comprehensive view of the structure. For this reason, all measurements, from elemental analysis, mechanical properties, static properties and ionic conductivity were made on the same sample all from the same melt. This is both disadvantageous as only one sample was made per composition, yet advantageous in that it is valid to compare the trends between properties to ascertain which properties are correlated. There are a few exceptions, where high K_2O and Rb_2O-containing samples in the Li-K and Li-Rb series had to be remade for ionic conductivity measurements, thus these data are the least reliable. These samples were made five years prior to the ionic conductivity measurements and suffered from hygroscopicity. It is clear from the hygroscopic nature of some glasses that the structure does change over time, yet for glasses which are inert to water attack their structure is not expected to change over lab time-scales.

2.2 Ion-exchange Procedure

A large piece of base glass, $30Li_2O$-$70SiO_2$, was cut into several smaller pieces, approximately $1 \times 1.5 \times 0.5$ cm; each piece was ion-exchanged in a fresh bath of KNO_3 ($\geq$ 99%, APS) in an N_2 atmosphere. The N_2 was used to prevent the oxidation of the nitrate to the carbonate or oxide form which was seen to occur in a similar experiment involving $Ca(NO_3)_2$. Six samples were ion-exchanged for 72 hours, each at a

different temperature between 360–480 °C; the conditions include temperatures both below and above the glass transition temperature, T_g, of this glass composition (measured to be 459 °C). An IE processing time of 72 hours was chosen because soda-lime glass exchanged at that time scale showed significant and differing case depths for a range of IE temperatures.[101] After 72 hours, the samples were removed from the oven; examination of the specimens through crossed polarizers revealed no significant additional residual strain generated by this procedure. The mass of the samples was measured before and after the exchange treatment.

2.3 Elemental Analysis

2.3.1 Inductively Coupled Plasma Optical Emission Spectrometry

Some of the glass compositions were confirmed by inductively coupled plasma optical emission spectrometry (ICP-OES). This technique was used initially due to lithium being present in many of the samples, which is too light an element to be detectable by X-ray or electron methods such as WDS or energy dispersive spectroscopy; ICP-OES is well-suited in this case since it has very low detection limits for most elements (between 5–50 ppm-wt depending on the element analyzed).[133]

ICP-OES as its name implies involves two stages: the creation of plasma from inductive coupling with RF electromagnetic fields, whose heat and energy transfer induce electronic excitation, which is followed by the detection of the atomic emission spectrum. The plasma is usually created using an Ar gas quartz torch with a copper load coil surrounding the top of the torch which is connected to an RF generator (27–40 MHz). Once the Ar is flowing, the load coil is "turned on" and creates AC fields which "swirl" the charged particles in the Ar gas back and forth further (the Ar

gas is already swirling from a nozzle which flows perpendicular to the flame), thus, when a small spark is applied to the gas, it creates some free electrons and Ar ions which continue to be accelerated by and inductively coupled to the AC fields. The addition of energy from the RF coil continues, more ions and electrons are created and recombined continuously, creating a plasma with at least <1% free electrons.

Due to the configuration of the load coil, the inductive region where most of the acceleration of particles occurs is in a donut-shaped region near the base of the Ar torch. As a result, the sample is introduced into the middle of the "donut" which avoids the white argon continuum emission. The solvated sample is introduced as an aerosol or fine mist where first the liquid evaporates, the solid analytes vaporize into a gas, and then atomized into its elements. These processes all happen in what is termed the "preheating zone" which is only roughly 3300 K and achievable by furnace and flames alone. However, the plasma is much hotter, about 6800 K, and has sufficient energy to excite electronic transitions of atoms and ions causing ionization of the analyte, which can be important as in some cases only the emission of ions, not atoms can be easily detected.

When the electrons relax down to a lower energy state, they emit characteristic wavelengths of light which are detected either monochromatically one wavelength at a time or dispersed and measured simultaneously. Once the light has been separated it is then detected by photo-multiplier tubes or charge-coupled devices. Although overlap between atomic emission lines can occur, there are usually several different emission lines to choose from. Finally, to obtain quantitative information, calibration curves of atomic emissions from standards of known concentrations must be used. If the analyte is too concentrated (5–6 orders of magnitude larger than the detection limit) non-linearities in the calibration curves can occur due to self-absorption of the emitted light. As long as the analyte is in concentrations 100 times larger than the

detection limit, errors of 1% or less are achieved.

ICP-OES was performed by Daniel Chevalier from the Minerals Engineering Centre. Glass powders were solvated before analysis; Al and Si analysis samples were prepped by Li-borate fusion, while the other elements were prepped using near total acid digestion.

2.3.2 Wavelength-Dispersive Spectroscopy

Wavelength-dispersive spectroscopy (WDS) was also used for confirmation of compositions as it is well-suited for elemental analysis of solids, including crystalline and amorphous minerals. Although it uses the same working principles as energy dispersive spectroscopy, WDS has much higher resolution at the detector and therefore higher sensitivity and accuracy when reporting chemical analyses. In an ideal system, it can have 10s of ppm by weight sensitivity, however, in the current case, quantitative spot analysis had errors closer to 0.2–1 wt-%. Another strength of WDS is its ability to perform spatial compositional analysis with resolution of 1–2 μm in diameter.[134]

In WDS, free electrons are generated by a heated piece of metal (usually tungsten) with a low work function; a large potential, usually 15–20 kV, directs accelerating electrons toward the sample and magnets serve to collimate it into an electron beam. The primary electrons from the source interact with the sample in several ways to produce: secondary electrons, backscattered electrons, Auger electrons, heat, sometimes low energy light and most-importantly X-rays.[135] The essential interaction involves free electrons from the cathode ray gun colliding with and ejecting core electrons of atoms, and the outer, higher energy electrons cascading down to fill the lower energy "hole" and emitting a characteristic X-ray (and secondary electron).[136] The main advantage of WDS are the "analytical" crystals which act as X-ray filters based on

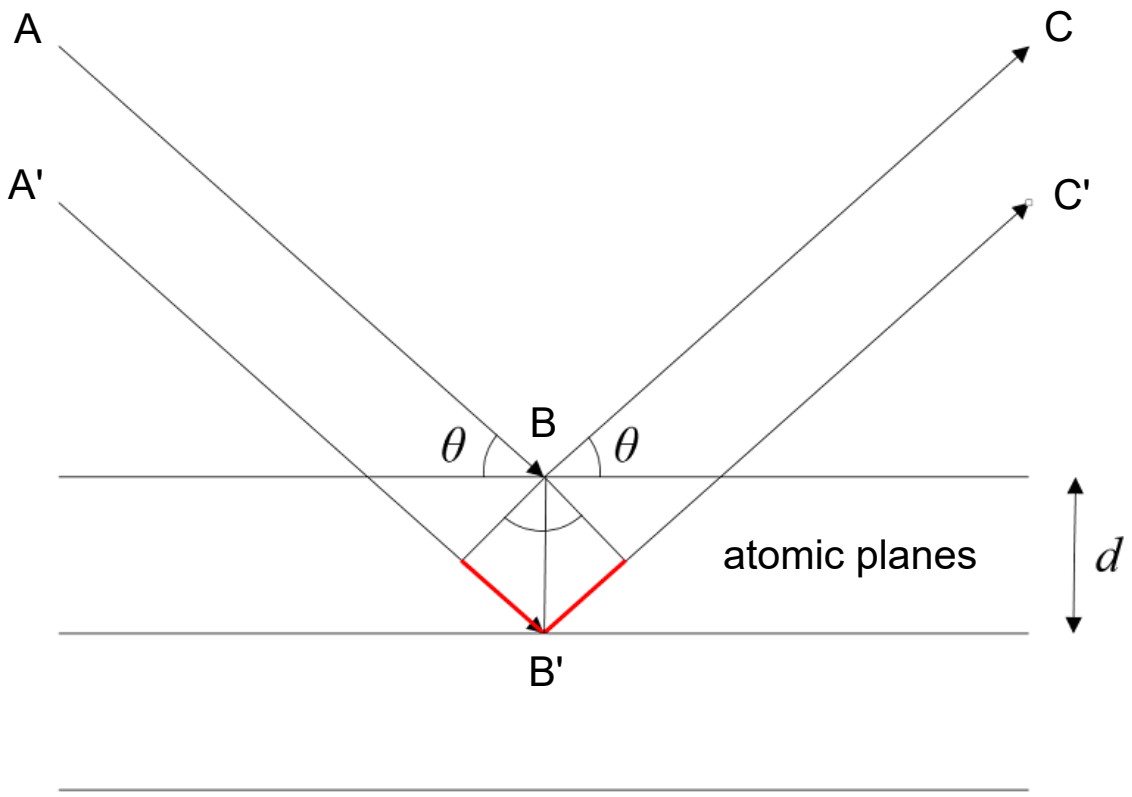

Figure 2.4: Bragg diffraction: diffracted rays are in phase when distance $A'B'C'$ differs from ABC by an integral number of wavelengths. Two rays are reflected at an angle θ by planes of atoms separated by a distance d_{L}. The difference in distance traveled between the two rays, shown as red line segments, is equal to $2dsin\theta$; for constructive interference to occur this distance must equal an integer multiple of the wavelength λ. Modified and reproduced from Dr. Carl Romao's thesis with permission [138].

Bragg's law (see Fig. 2.4), which can be moved and rotated to lie on Rowland's circle in order to pass only the target X-rays to the detector (see Fig. 2.5). In most WDS set-ups several different "analytical" crystals are used to detect a wide range of and several elements simultaneously. Two types of detectors (gas proportional counter type and gas flow proportional type) were used, however, they both work similarly, where X-rays hit and excite electrons from a gas, which are accelerated towards a wire anode and create an electrical current upon collision which is proportional to the energy of the X-ray from the sample.[137]

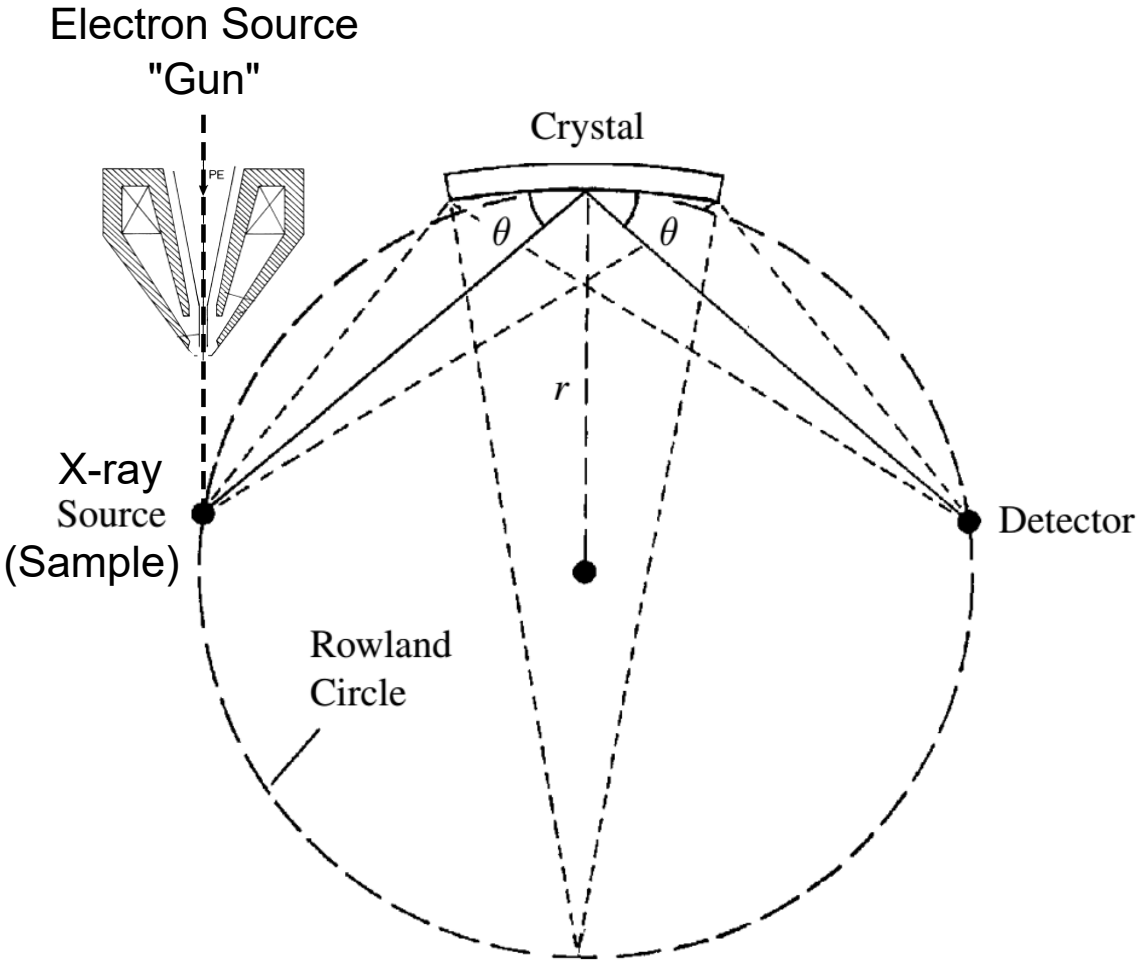

Figure 2.5: Rowland circle geometry: a constant Bragg angle is obtained when the source, crystal and detector lie on the circumference of a circle. Modified and reproduced from Reed [137], pg. 91.

Another advantage of WDS is the use of standards containing the elements of interest; the counts of X-rays of the unknown sample are compared to the counts of the standard and corrected for the matrix effects of the sample. The correction factor is composed of atomic number, absorption and fluorescence terms (typically called ZAF).[137] For the present samples, the largest correction factor comes from the backscattering which is dictated by atomic number, although for Mg, which absorbs long λ, absorption can also be important. Additionally, characteristic X-ray overlaps can occur and care must be taken during calibration to model the overlaps in a similar standard sample.

Hard limitations of this technique include only being able to analyze elements including and heavier than boron, which means it could not be used to directly detect Li in the samples. In general, analyses of samples with lower atomic number are less precise, due to atoms with fewer electrons being less ionizable and producing less X-ray intensity as a result. Thus, in the present work, oxygen has the most error of the detectable elements. Practically speaking, it is exceedingly important for samples to be uniformly flat as to ensure the correct sample-detector distance and angle are used to filter the target X-ray wavelength. Additionally, ideal samples are homogeneous laterally or perpendicular to the electron beam as it excites a 3-d teardrop shape below the surface.[135] The electron beam dwell time affects the X-ray counts, which is of importance for linescans, where the dwell time of the beam is known with less certainty, making the technique less quantitative. Finally, samples which are insulating must be carbon-coated to prevent a buildup of charge at the surface, however, electrons or even ions within the sample are also migrating away from the electron beam, so a balance must be struck between having high X-ray counts or an analyses that is representative of the initial material.

2.3.3 Collection of WDS data

For most samples, the common "point and shoot" method was used, where five different spots were analyzed quantitatively, *i.e.* for the same length of time and voltage as the standards. However, in cases when spatial information was also important, for example in the IE glasses or long-term conductivity experiments, either a line of quantitative points or linescan, respectively, was used.

In order to ensure that the edge of the IE samples were analyzed, the following procedure was adopted. Once the ion-exchange procedure was done, the samples were washed with water and thoroughly dried, then placed in epoxy to obtain an epoxy disc. The discs were then roughly polished with 30 μm diamond paper until the epoxy and glass surface were flush, whereby the top IE layer was mechanically removed and the compositional profile exposed. The exposed surface was then polished down to 1 μm, as shown in Fig. 2.6a. Case depth is defined, per metallurgy, as the thickness of the hardened layer of a specimen; it increases with distance away from the IE surface or specimen edge as shown in Fig. 2.6b. Fig. 2.6b is not optical, but was collected using the same microprobe instrument that was used for WDS analysis; it is possible to loosen the constraints of the "analytic" crystal to obtain a map of X-ray density. Although this is similar to the image obtained in energy dispersive spectroscopy, it is lower resolution than typical micrographs.

Quantitative point analysis was performed at approximately nine μm intervals from the IE surface (with the exception of the 390 °C sample, which had approximately seven μm intervals), as calculated from the XYZ stage data of the WDS instrument; an illustrative example can be found in Fig. 2.6b, where x's represent points of analyses. The translation of the WDS stage is accurate to $\pm$ 1 μm.

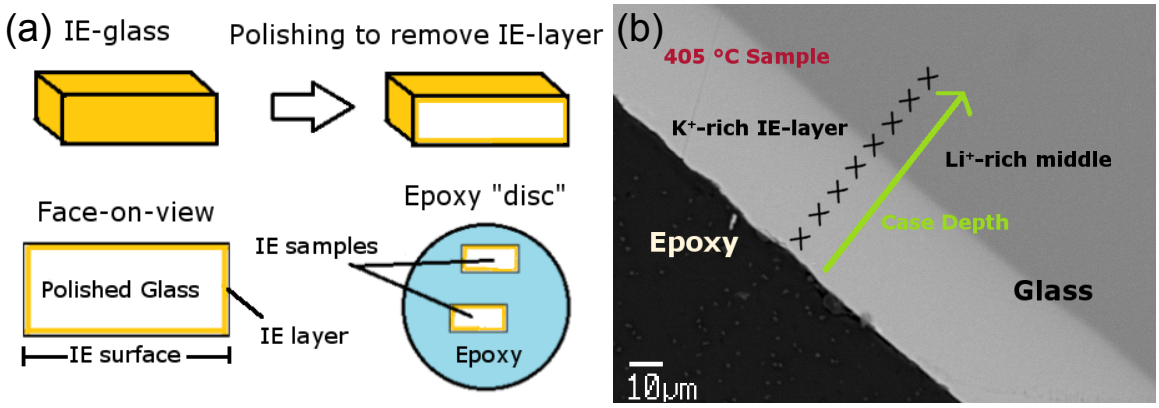

Figure 2.6: (a) Procedure for IE layer exposure and epoxy "disc" preparation for analyses. (b) Example of procedure for both WDS and Raman analyses, showing the case depth. The K^+-rich region appears lighter in colour.

WDS data was collected by Dr. Dan MacDonald in the Department of Geology at Dalhousie University; a JEOL 8200 Superprobe was used with a 15 kV running voltage and the proper standards for ZAF correction. All samples were carbon coated before analyses. The quantitative point analyses has errors of 0.2–1 mol-%. In the case of long-term conductivity experiments, the linescan type of analysis used (rather than quantitative point analysis), the error is larger, at most 3 mol-% since in this case the material volume which the electron beam excites is known with less certainty.

2.4 Density

Density was measured by the Archimedean method using a Mettler Toledo density kit and analytical balance. According to the kit's manual, the density of the glass (ρ_{glass}) can be obtained using the mass of the sample in air (m_{a}), mass of displaced liquid (m_{l}), density of the liquid of immersion (ρ_{l}) and density of the air (ρ_{a}), which is taken to be 0.001 g/cm^3.

$$\rho_{\text{glass}} = \left(\frac{m_{\text{a}}}{m_{\text{l}}}\right)\rho_{\text{l}} + \rho_{\text{a}} \tag{2.1}$$

The Archimedean principle states that the buoyant force acting on an object immersed in a liquid equals the weight of the displaced liquid, meaning the difference between the samples mass in air (m_{a}) and apparent immersed mass (m_{i}) is equal to the mass of the displaced liquid, m_{l}. The above equation now becomes,

$$\rho_{\mathrm{glass}} = \left(\frac{m_{\mathrm{a}}}{m_{\mathrm{a}} - m_{\mathrm{i}}}\right)\rho_{\mathrm{l}} + \rho_{\mathrm{a}} \tag{2.2}$$

Therefore, using the mass measured in air, the apparent mass immersed in the solid and the density of the immersion liquid, it is possible to calculate the density of a solid. In this study, the immersion liquid was absolute ethanol and the temperature-dependent density of the ethanol was obtained from literature values.[143] Each sample was measured three times giving a standard error between 0.008–0.015 g/cm^3.

Glass scientists also often report the molar volume (V_{m}), which is the volume a mole of glass occupies. It is considered a more direct analysis of changes in free space, since unlike V_{f} it does not involve assumptions about the size of the ionic radius in the glass from appropriate oxide crystal data (Shannon-Prewitt ionic radii[22]). Molar volumes were calculated using the analyzed composition data according to Eq. 2.3,[7]

$$V_{\mathrm{m}} = \frac{\sum_i x_{\mathrm{i}} M_{\mathrm{i}}}{\rho}, \tag{2.3}$$

where x_{i} and M_{i} are the mole fractions and molar masses of the component oxides.

Finally, from the density data, the molar volume of oxygen(V_{o}) can be determined:[94]

$$V_{\mathrm{o}} = \frac{\sum_i x_{\mathrm{i}} M_{\mathrm{i}}}{\rho \sum x_{\mathrm{i}} \mathrm{O}_{\mathrm{i}}}, \tag{2.4}$$

where $\Sigma x_{\mathrm{i}}\mathrm{O}_{\mathrm{i}}$ is the *total* mole fraction of oxygen in the glass.

2.5 Raman Spectroscopy

Raman spectroscopy is an inelastic spectroscopic technique; it uses light to probe the vibrational energies of the chemical bonds of a material. If one treats a bond like a simple harmonic oscillator, then there is a characteristic vibration that corresponds to specific atoms and bond strength, represented respectively by the reduced mass (μ_m) and the Hookes force constant (K_{H}) in the classical vibration equation:[144]

$$\nu_0 = \frac{1}{2\pi}\sqrt{\frac{K_{\mathrm{H}}}{\mu_m}} \tag{2.5}$$

However, Eq. 2.5 applies most accurately to motions of isolated bonds in a molecule, whereas in solids composed of a lattice of interconnected bonds, the vibrations are going to result from the motions of several atoms. Generally, in glasses and network solids, high energy stretches are considered to be more isolated than lower energy bending vibrations.

Of course, there is some anharmonicity present in the potential energy well, but it plays a small role as Raman spectroscopy looks mainly at the fundamental vibration transition, $\nu(0\rightarrow1)$ and anharmonicity is only significant at higher levels. Raman spectroscopy is used to measure the number of relative Q^n-species as well as the weakening or strengthening of silicate bonds.[145–149] Raman is inelastic as the working principle involves the interaction and most importantly, transfer of energy between a photon and the vibrational energy levels of a solid. When a photon, of energy ν, is absorbed by a solid, the vibrational ground state is excited to a virtual state equal to $h\nu$ where from it quickly relaxes back to the ground state and releases a photon of the same energy as the absorbed light. The virtual state is a superposition of the higher and lower energy vibrational eigenstates and cannot be measured.[150] This elastic scattering is called Rayleigh scattering and makes up the majority of

interactions that occur, however, there is a small amount of light that undergoes Raman scattering and is transferred from the excitation frequency (laser) to the vibrations of the bonds in the sample. This transfer will force the solid to return to a different vibrational level, one above or below the original ground state. Furthermore, it will increase or decrease the wavelength of the light emitted, called Stokes and anti-Stokes shifts respectively, compared with the incident photon.[144] This is the basis of Raman spectroscopy; the modulated emission, λ_1, and original excitation source, λ_0, can be subtracted to obtain the frequency of the resultant vibrational transition, normally reported in wavenumbers, $\widetilde{\nu}$, with units of cm^{-1}. There is no particular reason to use wavenumbers other than convenience; they allow spectroscopists to refer to peaks in units from 0–4000 cm^{-1}.

$$\nu(\mathrm{cm}^{-1}) = \left(\frac{1}{\lambda_0(\mathrm{nm})} - \frac{1}{\lambda_1(\mathrm{nm})}\right) \cdot 10^7 = \frac{1}{\lambda}(\mathrm{cm}^{-1}) \tag{2.6}$$

Finally, only certain transitions are Raman-active; transitions that involve a change in polarization, such as a symmetric stretch of an electron cloud, are detected.[150] In a crystal, the fewer peaks observed, the more symmetric the environment as very symmetric crystals will have few to no Raman modes.[151] However, since glasses are disordered, essentially all motions of atoms involve a change in polarizability and dipole moment, leading to all Raman and IR modes, respectively, being active to a certain degree.

Despite glasses being disordered, the local symmetry of SiO_2 tetrahedra are actually quite ordered or near to tetrahdral, so much that fused quartz or pure silica glass has quite low intensity Raman spectra.[24] However, upon the introduction of modifier, the symmetry of the SiO_4^{4-} tetrahedra decreases and the modes are known to increase in Raman intensity when large, structurally disruptive cations such as K^+ are present, in comparison to smaller cations such as Li^+, which tend to affect the SiO_2

structure less.[145] More generally, these differences in Raman intensity are related to the Raman cross-section, which relates spectral peak intensity to vibration counts in the structure. As the Raman cross-section is a result of changes in polarizability, and Q^n-units differ in charge and volume, they also differ in cross-section.[146,152,153] There is even evidence to suggest that the identity of the cation in a NBO can affect the strength of the Raman effect, although that is likely a minor contribution in comparison to the type of Q^n-species.[154] Nevertheless, the normalized cross-section, which relates the intensity of a Raman-active mode to its population, for a given Q^n-species can be determined empirically from known compositions and assumed to be roughly constant across a glass series.[146] However, if the Q^n-distributions are unknown for a composition, the relative intensities of each Q^n peak can be compared within a spectrum, which is essentially assigning a cross-section of one to all structural units. This is generally physically inaccurate, however, if the cross-section for each Q^n-species is fairly constant, the relative increase or decrease of Raman intensity of each Q^n peak *within* a spectrum can be indicative of structural variation *within* a glass series.

Raman spectra were collected at room temperature using a Nicolet NXR 9650 FT-Raman spectrometer using a 1064 nm excitation laser with a spectral resolution of 2 cm^{-1} and 256 scans. The resulting spectra were baseline corrected and deconvoluted using Renishaw Wire or Fityk[155] software programs.

2.5.1 Micro-Raman Spectroscopy

For the IE samples, Raman spectra were collected using a Renishaw inVia micro-Raman spectrometer with a 514.5 nm argon-ion laser for 12 scans of 10 s each with a resolution of 1 cm^{-1}. The laser spot size was approximately five microns in diameter. Spectroscopic profiles across the IE samples were acquired as follows: the first point

was as close to the interface between the epoxy and the glass as possible without obtaining a large fluorescence signal observed when the epoxy was excited by the laser. This point is estimated to be approximately six microns from the edge. Afterwards, the focal point of the laser was translated inward between 10-100 μm (smaller steps within the IE layer, larger past the layer); the step distance was determined by the scale on the eyepiece of the microscope and instrument viewing screen. Some distinct features were noted on the sample surface and the sample stage was moved accordingly, as a result the error is estimated to be roughly $\pm$ 1 μm. The procedure is similar to the one used for the WDS point analyses, thus, Fig. 2.6b can be applied again here, where $\times$'s represent points of Raman analyses. Baseline correction and peak deconvolution were performed using the Wire software program from Renishaw.

2.5.2 Non-bridging Oxygens per Silicon Atom and Free Oxygen

The Q^n distribution from Raman spectroscopy can be used to determine the observed non-bridging oxygens per silicon atom ($[NBO]/[Si]_{obs}$), where Q^3 has one NBO, Q^2 has two NBOS, etc. In this work, when [NBO]/[Si] is discussed without a subscript, it refers to the observed value. The $[NBO]/[Si]_{obs}$ can be compared with the expected $[NBO]/[Si]_{calc}$ determined from the compositional analyses. Generally, these values match quite well, however, there has been significant differences in silicates containing high cationic strength ions, such as Li_2O-SiO_2 and MgO.[156] If the extra oxygen atoms are assumed to be sequestered in the modifier as O^{2-} (for example oxygen surrounded by only lithium ions), the fraction of total oxygen which is free O^{2-}, $N(O^{2-})$ can be calculated thusly,[156]

$$N(O^{2-}) = \frac{[NBO]/[Si]_{calc} - [NBO]/[Si]_{obs}}{4 + [NBO]/[Si]_{calc}}. \tag{2.7}$$

2.6 Mechanical Properties

2.6.1 Elastic Moduli

The Poisson ratio (μ) can be determined from the shear or transverse (V_{T}) and longitudinal (V_{L}) wave velocities according to,[157]

$$\mu = \frac{1 - 2(V_{\mathrm{T}}/V_{\mathrm{L}})^2}{2 - 2(V_{\mathrm{T}}/V_{\mathrm{L}})^2}. \tag{2.8}$$

From the Poissons ratio, density (ρ), and the longitudinal wave velocity, it is possible to calculate the Youngs modulus,

$$Y(GPa) = V_{\mathrm{L}}^2 \rho \frac{(1+\mu)(1-2\mu)}{(1-\mu)}. \tag{2.9}$$

The shear modulus (G) is directly and only dependent on the transverse velocity and density,

$$G = V_{\mathrm{T}}^2 \rho. \tag{2.10}$$

The wave velocities were measured using Panametrics NDT ultrasonic thickness gauge, Model 25. The gauge emits high frequency sound waves and measures the time of flight through the material using a piezoelectric crystal as the transmitter and receiver. First, the thickness of the glass was measured to the nearest hundredth of a mm using digital calipers and input into the Ultrasonic Thickness Gauge. The transducer was then placed against the polished glass sample using the appropriate Panametric coupling fluid (propylene glycol for longitudinal waves and molasses-like goop for shear waves) and the sound velocity (V_{sound}) was computed using Eq. 2.11,[157]

where T_h is the thickness and t is the flight time through the material:

$$V_{sound} = \frac{2T_h}{t}. \tag{2.11}$$

Frequency-appropriate delay lines are used in the ultrasonic transducers that prevent the piezoelectric element from vibrating before a return signal can be received.[157] Often longitudinal waves are prematurely reflected from the glass/transducer interface, so this delay improves the near-surface resolution of the signal. Another consideration is dispersion effects, however, in this case, the frequencies used (MHz) are far below the energies (THz) required for dispersion to be a significant phenomenon.[157]

The ultrasonic method was used at room temperature to measure the longitudinal and shear wave velocities through the glass series, which along with density (section 2.4) can be used to calculate all four elastic moduli: Young's modulus (Y), Poisson's ratio (μ), shear modulus (G) and bulk modulus (K). A Panametric NDT transducer was used with the respective coupling fluids and 3–5 measurements were made per sample leading to errors of about 2%.

2.6.2 Vickers Hardness and Fracture Toughness

Hardness is the ratio of force over projected area of the indent, thus, the shape of indenter tip plays a large role in the hardness values obtained. There are many different scales of hardness depending on the shape of the indenter used for deformation, each type of hardness test, eg. Vickers, Knoop, Berkovich, adds a geometrical factor which converts the 3-dimensional indenter shape to projected area. Vickers hardness (H_V) is used heavily in micro-indentation while the Berkovich tip is used in nano-indentation, despite having the same projected area-to-depth ratio, the Berkovich tip is three-sided, making it easier to grind to the fine point needed for nano-indentation.[158,159]

Although the geometric factor of each tip type takes the projected area-to-depth ratio into consideration, it is still difficult to compare results from different types of indenter tips; in fact, only because Vickers and Berkovich have the same projected area-to-depth ratios can meaningful comparisons be made between micro- and nano-hardness.

Vicker's hardness (H_{V}) measurements were performed in air using a Leco V-100A Hardness Tester; each sample was indented 6–8 times with a load of 1 or 5 kg for 15 seconds (softer glasses required larger loads for cracking to occur) and analyzed optically immediately after indentation. Although it is generally important to only compare hardness values indented at the same force, almost all samples were measured using 1 kg or 5 kg; both which are small enough they are expected to be in the linear range for the mechanical response. The visible crack lengths were measured as quickly as possible after indentation to calculate fracture toughness using Eq. 1.4. Hardness measurements had errors of less than 0.2 GPa, while the precision of fracture toughness measurements at the 95% confidence level were found to be on the order of 5–15%.

2.6.3 Nano-Indentation

As the name implies, nano-indentation can use much smaller loads and produces smaller indents than typical hardness measurements, on the order of 10–100 mN and 10–1000 nm, respectively.[160] In fact, loads of only a nanonewton and displacements of 0.1 nm have been measured accurately.[160,161] These attributes make nano-indentation the clear choice for characterising the mechanical properties of thin films and surfaces, such as the IE case depth. Unlike traditional hardness testing, which involves indentation and imaging of the indent at a later time, nano- or ultra-low load indentation

is able to measure Y and H continuously. It measures the load (P) and displacement into the surface (h_S) during one complete cycle of loading and unloading, allowing real-time determination of F and A_p. A small harmonic vibration of the tip is also added to measure the contact stiffness at any point during the indentation. The underlying equations that allow the determination of stiffness and hardness from nano-indentation assume a mostly elastic contact between the indenter tip and sample, resulting in sink-in only (where the material around the indenter deforms below the original surface plane) rather than pile-up of the material around the indent.[161] This is generally a valid assumption for the indentation of hard ceramics[160] and/or glasses.

Interestingly, in the case of IE glasses, an ISE (Section 1.2.3) was reported in the Young's modulus and hardness for loads less than 10 and 120 mN, respectively, and hardness for penetration depths less than 500 nm.[162] Consequently, the ISE in nano-indentation measurements is not expected above these loads and penetration depths.

Although nano-indentation offers insights regarding a size scale immeasurable by conventional methods, it is also complicated by its high sensitivity. There are two important "rules" to follow when nano-indenting a bulk material. Firstly, it is important that the surface roughness of the sample is $\leq 5\%$ of the indent depth;[163] 1 μm grit sand paper like the one used here has been shown to have an average surface roughness of ≤ 52 nm for Pyrex[164] and ophthalmic glass lenses[165]. Consequently, an indent with a depth larger than approximately 1 μm will satisfy the "5% rule". Secondly, it is important that the sample is as perpendicular to the indent tip as possible. Hardness and to a lesser degree, Young's modulus, have been known to increase when the sample is indented at an angle. Sample tilt causes the actual contact area between the indenter tip and sample to be larger than the expected projected area

for a given depth (A_p). The equations used to calculate Y and H both use the projected area, however, Y depends on the square root, while H varies linearly with A_p; thus, hardness is always predicted to be affected more by errors in determining the projected area.[160,161,163] A tilt between 1–5° results in an overestimation of 2.0–10.4% and 3.2–9.6% for hardness and stiffness, respectively.[163] As a consequence, a tilt of only 1° or less is considered acceptable.

It was necessary to have the surrounding epoxy upon which to indent, as it was feared indenting near an entirely free edge would negatively affect the indenter. Additionally, it was of paramount importance that all of the indents near the interface be successful; observing the transition from epoxy to glass ensured that the measured mechanical properties were those of the material at the beginning of the case depth. However, indenting continuously from one material to another mechanically different type of material introduced some unique challenges. Firstly, the difference between the mechanical properties of epoxy and glass made it difficult to polish the two materials evenly; finding a continuous straight, clean interface between the epoxy and glass for several indents could be challenging. Additionally, the initial positioning of the indenter tip on the sample needed to be accurate and involved many separate calibrations of the tip's position. Also, due to the mechanics of polishing, it is more likely that the edges of the sample are polished more compared to the sample middle and there is a slope downwards from the middle towards the edge. Although WDS showed the edges to be mostly flat (the technique is sensitive to micron-size changes in height), nano-indentation errors still occurred, presumably caused by elevation differences or "gap" found between the two materials. These issues led to larger uncertainties for indents made near the edge compared to indents made further from the edge of the specimen.

Indents were made in two configurations: "face-on", perpendicular to the case

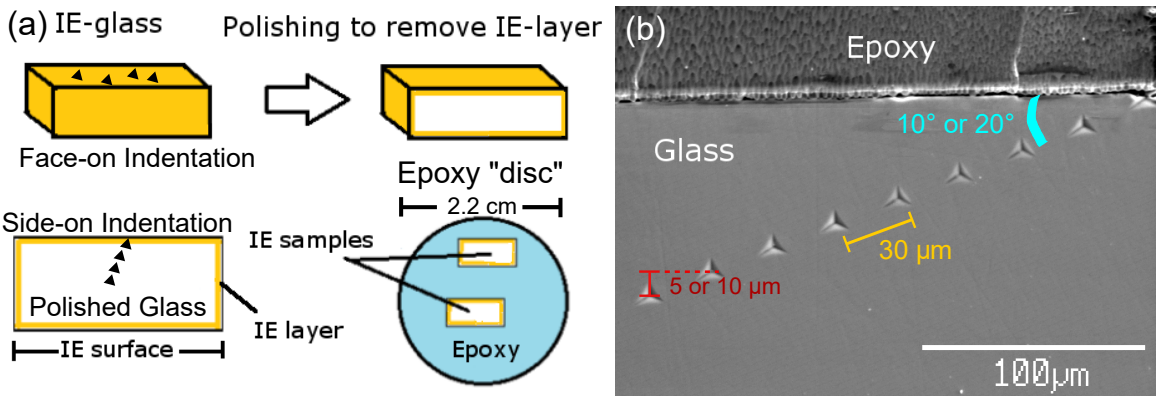

Figure 2.7: (a) Schematic of removing IE layer and embedding in epoxy disc procedure, along with face-on vs. side-on indentation. (b) An example of the nano-indentation procedure. Image captured using an electron microprobe. The indents were made at an angle, 10 or 20°, to ensure adequate spacing between indents while allowing several indents to be within the IE layer. For a 10 or 20° the lateral spacing between indents was 5.3 or 10.7 μm. The error in the lateral spacing is between 0.1–2 μm as the error compounds with increasing indent number.

depth and "side-view", a cross-section of the case depth. For the cross-section, an angled procedure was used (as shown in Fig. 2.7) where an angle of 10 or 20° resulted in approximately 5 or 10 μm lateral spacing perpendicular to the epoxy-glass interface, yet still maintaining a large space between each indent, roughly 30 μm. This procedure allowed for adequate sampling of the case depth, while placing sufficient distance between each indent. According to the conventions used for indentation,[163,166,167] the indents should be spaced apart 10–30 times more than the indent depth. In this case, the indent depth was 2 μm; thus, the lower limit of the convention was used because a shorter string of indents made it easier to find a suitable location for indentation along the epoxy-glass interface. The angle between the string of indents and the epoxy-glass interface was set manually; the "zero" was set by visually aligning the epoxy-glass interface of the sample with the internal axes of the indenter actuator.

Using images collected from WDS and/or an optical microscope, the angle of the string of indents was determined for each IE temperature and was found to be at most $\pm$ 1.5° from the target angle. Although an angle difference of 1.5° is significant over

long length scales, it is of less importance nearest the edge where significant changes in mechanical properties are expected to occur. Nonetheless, the optically *measured* angle values were used to determine the lateral space between each indent. Since the angles were inspected visually, an error of $\pm$ 0.25° is estimated, translating to an error range of $\pm$ 0.1–2 μm as the error compounds with increasing indent number. Indent images like the one in Fig. 2.7 also were used to ascertain whether visible pile-up had occurred around the indents.

Nano-indentation was performed at room temperature by Dr. XiaoFang Zhang using an Agilent G200 Nano-indenter using the Agilent Nanosuite G-series, "Continuous stiffness measurement (CSM), standard hardness, modulus and tip cal" module. A calibrated and certified diamond tip Berkovich indenter with a tip radius $\leq$ 20 nm was used. The surface approach velocity for each indent was 10 nm·sec^{-1}, while the allowable drift rate and surface detection (stiffness criteria) were preset to 0.05 nm·sec^{-1} and 200 N·m^{-1}, respectively. Y and H were calculated by the software using equations from Oliver and Pharr's seminal paper;[40] when determining Y, a typical Poisson's ratio for glass, 0.3, was assumed for all samples.[168] Although the Poisson's ratio (μ) is likely to be affected by changes in composition and perhaps stress, a significant decrease in μ from 0.3 to 0.25 results in an decrease in Y of only 2.3%, thus, a constant μ is considered to be reasonable.

2.7 Ionic Conductivity

Ionic conductivity (κ) was determined by electrical impedance measurements made with a Solartron SI 1260 impedance/gain phase analyzer and the Corrware Zplot software program.[169,170] DC or static ionic conductivity can be measured using the

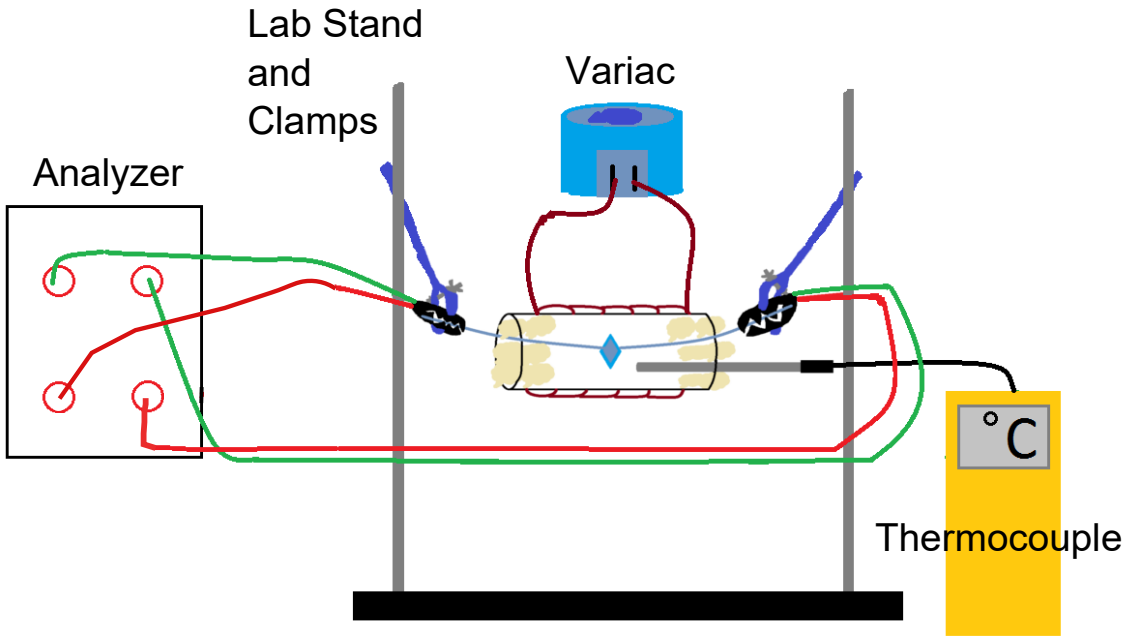

Figure 2.8: Schematic of the set-up used for conductivity measurements, including wire connections. Analyzer is connected to a computer.

relation,

$$\kappa = \frac{1}{R_{\mathrm{DC}}}\left(\frac{T_{\mathrm{h}}}{A_0}\right), \tag{2.12}$$

where T_{h} is the thickness of the sample and A_0 is the electrode area and R_{DC}, is the DC bulk resistance detetmined from a Nyquist plot (the imaginary component (Z") vs. the real component (Z') of the impedance, where the phase between the two components indicates the type of electrical element, resistor vs. capacitor), from the intersection of the curve with the real axis (where $Z" = 0$, not at origin).[171] The measurement and heating apparatus was constructed by the author with common materials found in the lab, see Figs. 2.8 and 2.9. Connections from the sample to the analyzer were made as according to the Solartron and ZPlot manuals.[169,170]

Sample slices were cut from larger bulk samples; they were measured with a digital micrometer and had areas of 0.3–0.8 cm^2 and thicknesses of 0.5–0.8 mm. Inorganic

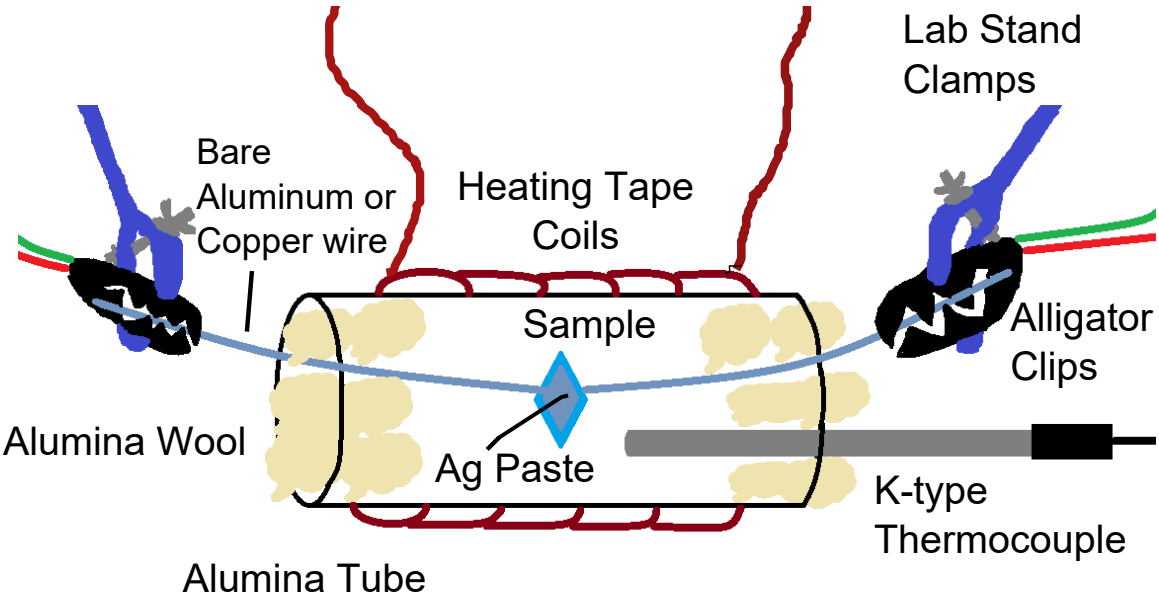

Figure 2.9: Sample holder of the conductivity set-up.

silver paste, Pyroduct 597-A, was applied as an electrode and acted as an adhesive to attach bare aluminum or copper wires to the sample ($\leq$ 6 cm in length). This Ag paste uses water as the solvent, so care was made to either put the samples in the drying oven quickly after application, or in the case of extremely hygroscopic samples, Ag epoxy paste was used instead, which worked well for relatively conductive samples, *i.e.*, ones which contained only K_2O or Rb_2O as the modifier. Generally the paste was applied across the face of the entire sample, therefore, the face of the sample was assumed to be equal to the area of the electrode. Although this may introduce some error since the paste may not reach the exact edge, the electrode error is applied to all κ and was found to affect the activation energy (E_a) very little.

All connections were checked using an ohmmeter to ensure low resistance between sample and wires, and high (infinite) resistance over the sample. The longer leads attached to the analyzer (red and green) were soldered to alligator clips to allow easy attachment and detachment of new samples. They were shielded and under 1 m in length in order to prevent stray induction, inductive coupling, and to ensure that the

analyzer received the analog signals at the correct time.[169] The alligator clips were then held in place by adjustable rubber-coated lab clamps; in this way, the relatively light sample and bare wires could be suspended in the alumina tube (sample holder) without touching the sides. Additionally, alumina wool was "stuffed" into either end of the sample holder, which acted as both a thermal and electrical insulator.

Heating came from heating tape wrapped around the outside of the alumina tube and was controlled by a Variac (variable voltage output). The temperature was measured by a K-type thermocouple, whose end was placed as close as possible to the sample without contact (impedance measurements indicated if the thermocouple *was indeed* in contact with thermocouple tip). Additionally, when the sample was attached, only the side without the thermocouple needed to have the alumina wool plugs removed, thus this at least left the side with the thermocouple undisturbed.

Although the author acknowledges that this set-up is simple, several steps were taken to help ensure reliability. Since the set-up is only a two electrode configuration, the main concerns are surface conduction (if the the glasses have high resistivity, $R >$ 100 MΩ) and problems with the electrode-glass interface (barrier layers or non-ohmic contacts).[171] The set-up was verified by measuring the κ of two commercial soda-lime samples of different thickness (cut from the same rod) and the conductivity was found to change proportionally to the ratio of thicknesses of the samples, Figs 2.10 and 2.11. This indicates that the impedance measured was *only* a property of the sample, not any external sources, such as metal-electrode contacts, connections, wires, etc. from the set-up.[171] Additionally, the activation energy (E_a) of Sc_2WO_{12} was measured and compared favourably to literature values (90 vs. 101 kJ/mol).[138,172] Finally, the only other point to consider is that glass samples with high resistivity ($R >$ 100 MΩ) are susceptible to conductance along the surface, rather than through the material; however, no evidence, such as large decreases in conductivity with increased

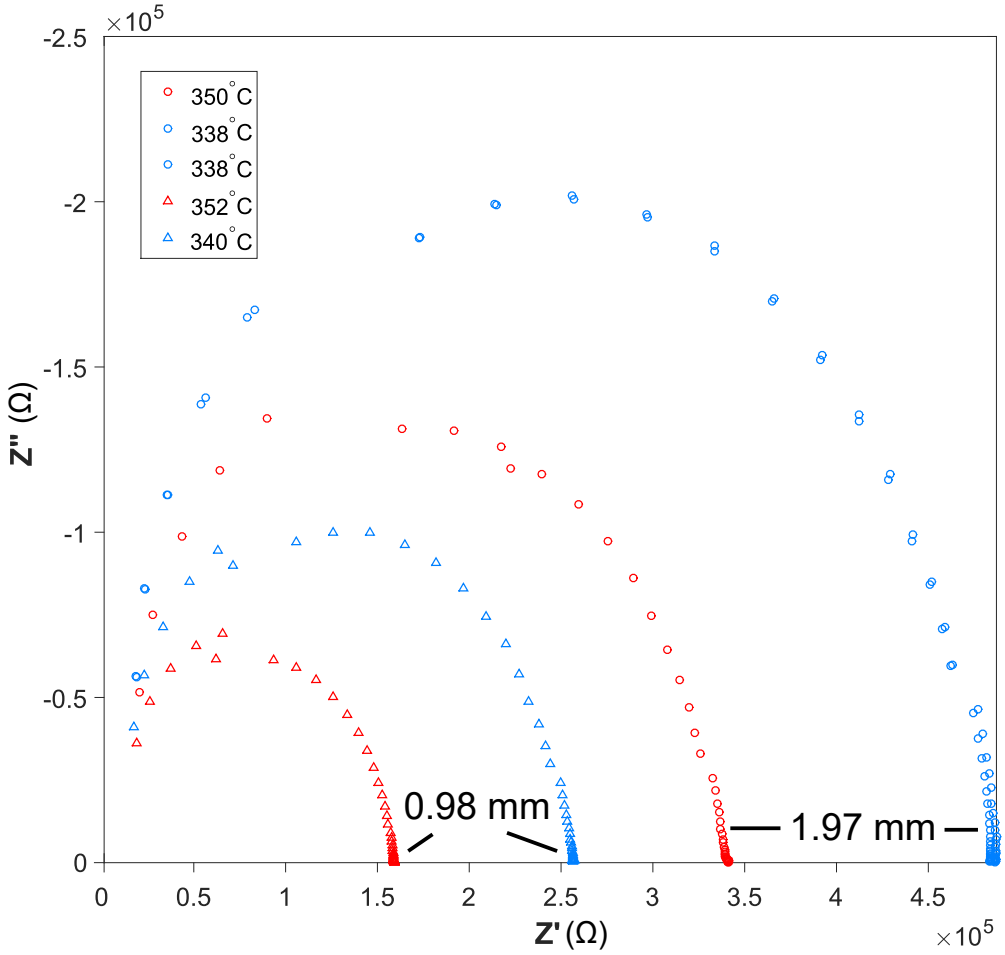

Figure 2.10: Nyquist plot for the evaluation of conductivity apparatus using two soda-lime pieces of different lengths, 0.98 and 1.97 mm.

temperature, of this phenomenon was observed (see Figs. 5.9, D.5, D.23, D.14, D.33, D.43, D.63, D.53, D.72 and D.82).[171]

AC impedance measurements were made while decreasing the frequency from 3 MHz to 100 Hz, and an amplitude of 3000 mV was used as it gave the best signal to noise ratio. It is important to use high enough amplitude to minimize noise, yet still minimize the non-linear response; the effect of using excessive potential pertubation amplitude is most clearly observed in the real part of the impedance as a function of

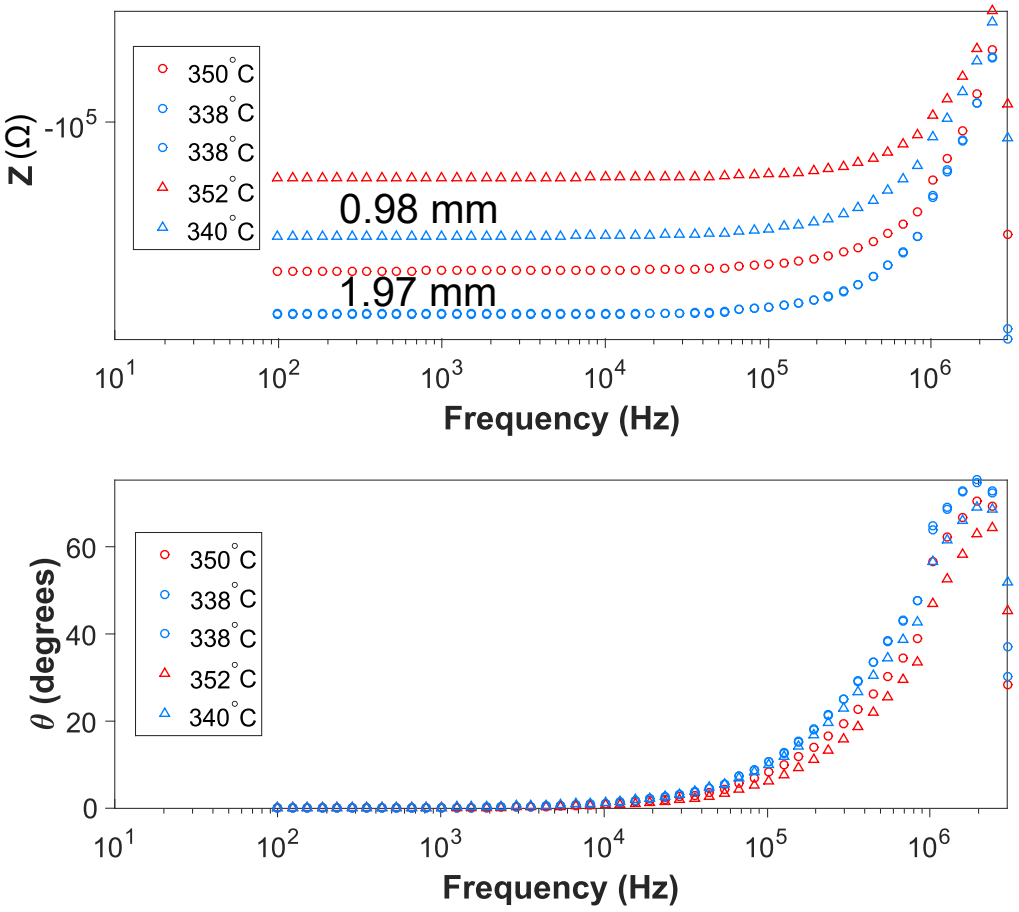

Figure 2.11: Bode plots for the evaluation of conductivity apparatus using two soda-lime pieces of different lengths, 0.98 and 1.97 mm.

frequency.[173] To ensure the linear response region was being probed, several different amplitudes, 50–3000 mV, were tested and the Bode representation did not alter significantly, see Figure 2.12.

The instrument was corrected using a "nulling" run where the impedance of teflon was measured as the "open circuit" high resistance limit as shown in Fig. 2.13. This also ensured that no current leakage through extraneous paths occurs, such as through the leads and sample holder. Although a low resistance limit correction (a shorted circuit of Al wire) was initially used, it was found to be of little use and created artefacts at the high-frequency limit as shown in Fig. 2.14 and was discarded from the procedure. Finally, the instrument was rated to measure resistance ranges of 10mΩ to 100MΩ with 5 digit resolution.[169]

Temperatures between 175–675 °C were used in order to have a sufficiently large temperature range over which to measure κ yet remain well-below T_g (usually 200–300 °C below) and high enough that κ could be measured reliably (lower limit $\approx 10^{-10}$S·cm^{-1}). The temperature was measured using a K-type thermocouple which was placed 2 cm from the sample and alumina wool was used as thermal insulation to maintain thermal equilibrium. Additionally, tests were performed to ensure sufficient time to reach thermal equilibrium after each temperature step. Fig. 2.15 shows the impedance 5–101 mins after increasing the heat, *i.e.*, increasing the voltage of the Variac; although there is some change after 43 mins, it is not proportional, for example, 79 minutes has a higher resistance or intersection with the Z' axis than 43 minutes. Consequently, 30 minutes was chosen as acceptable, as the differences are small relative to the differences seen for for each temperature step (≈30 °C).

Finally, since κ is temperature dependent, the activation energies can be obtained

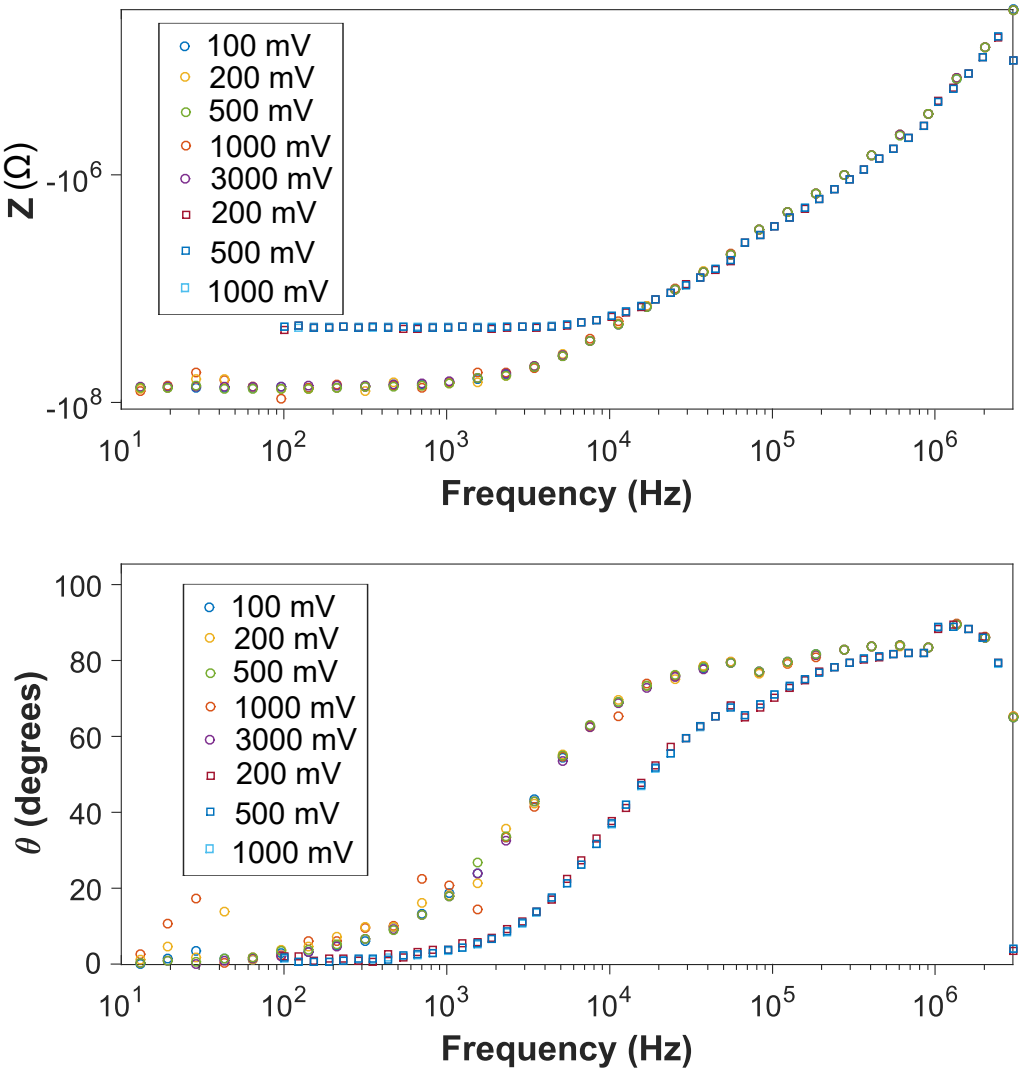

Figure 2.12: Bode plots for the evaluation of conductivity apparatus using different AC amplitudes (voltages) for two different glass compositions, ☐ is soda-lime, while ◯ is $30Li_2O$-$70SiO_2$.

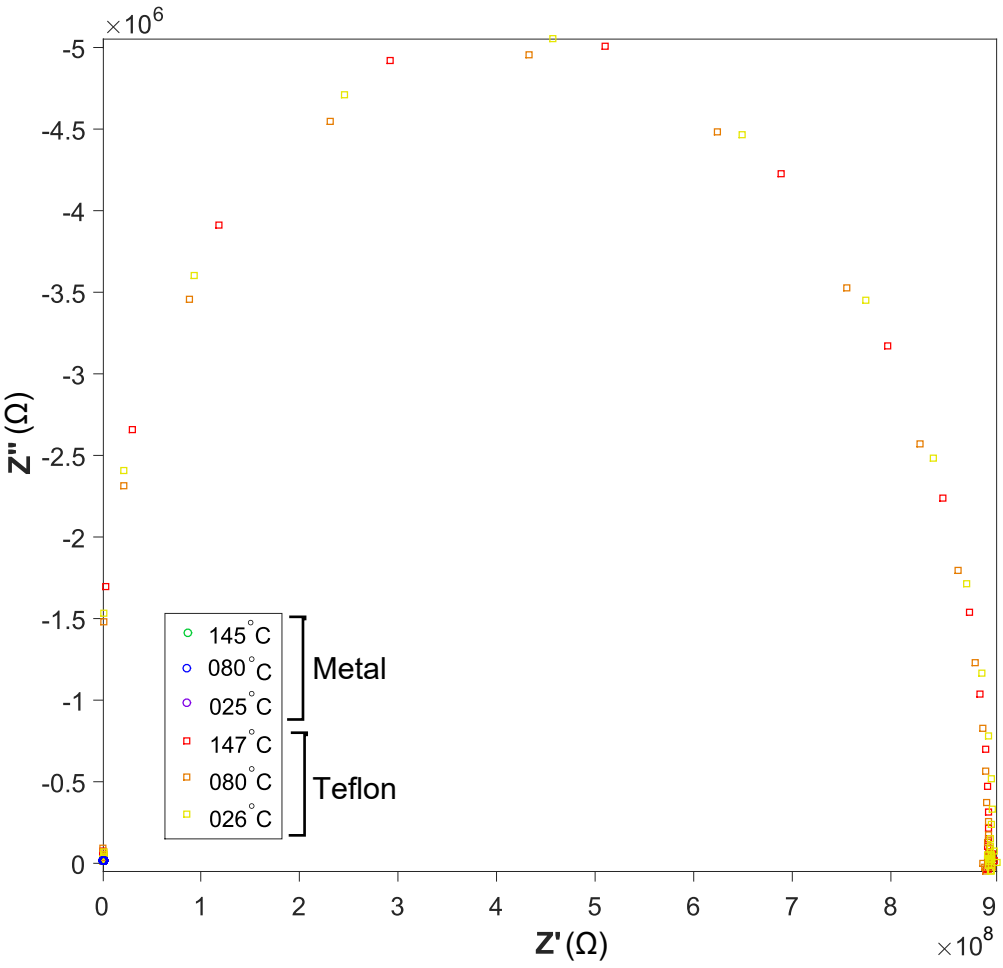

Figure 2.13: Nyquist plot of materials used to make nulling files (teflon and Al wire) for conductivity measurements.

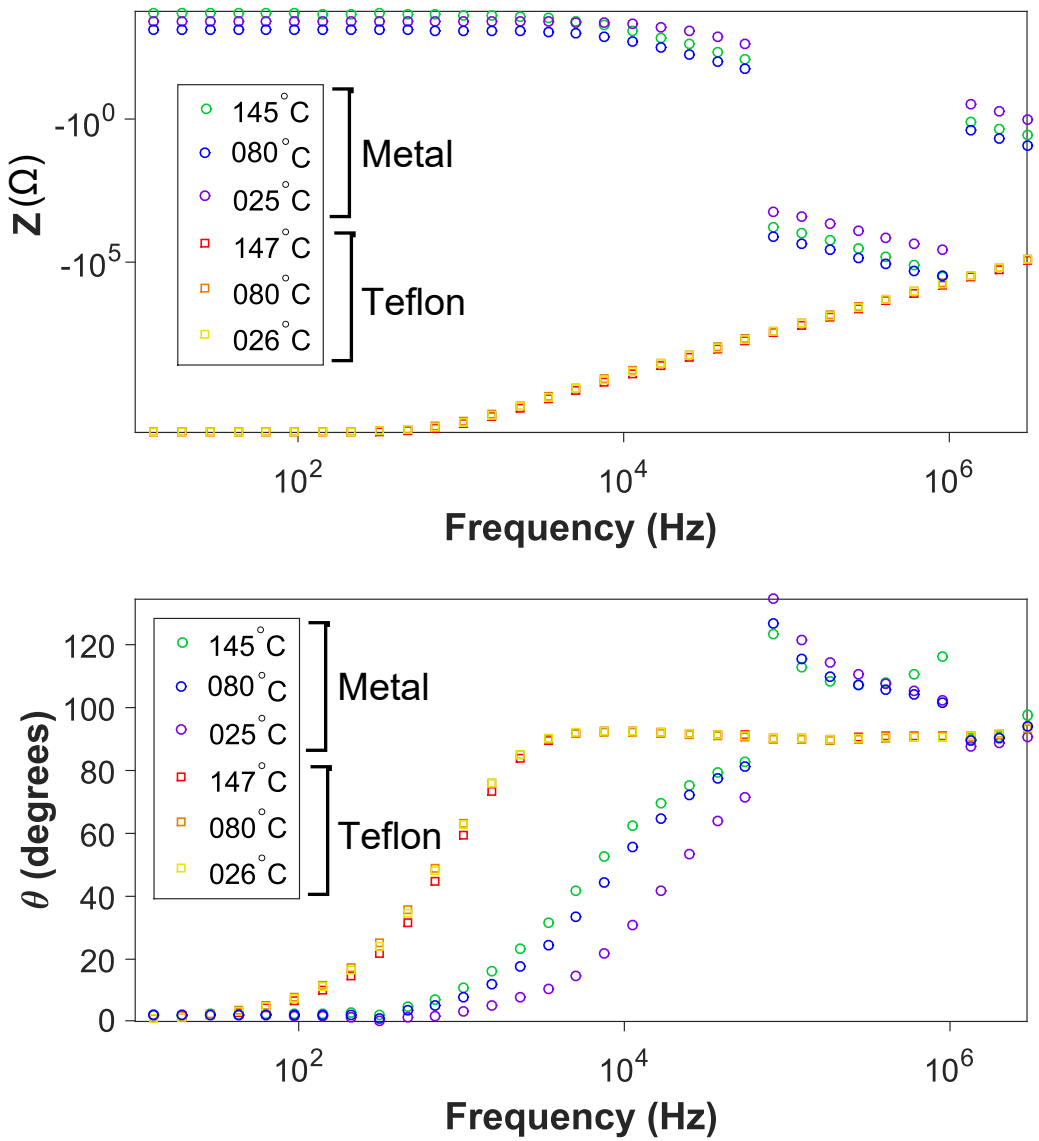

Figure 2.14: Bode plots of materials used to make nulling files (teflon and Al wire) for conductivity measurements.

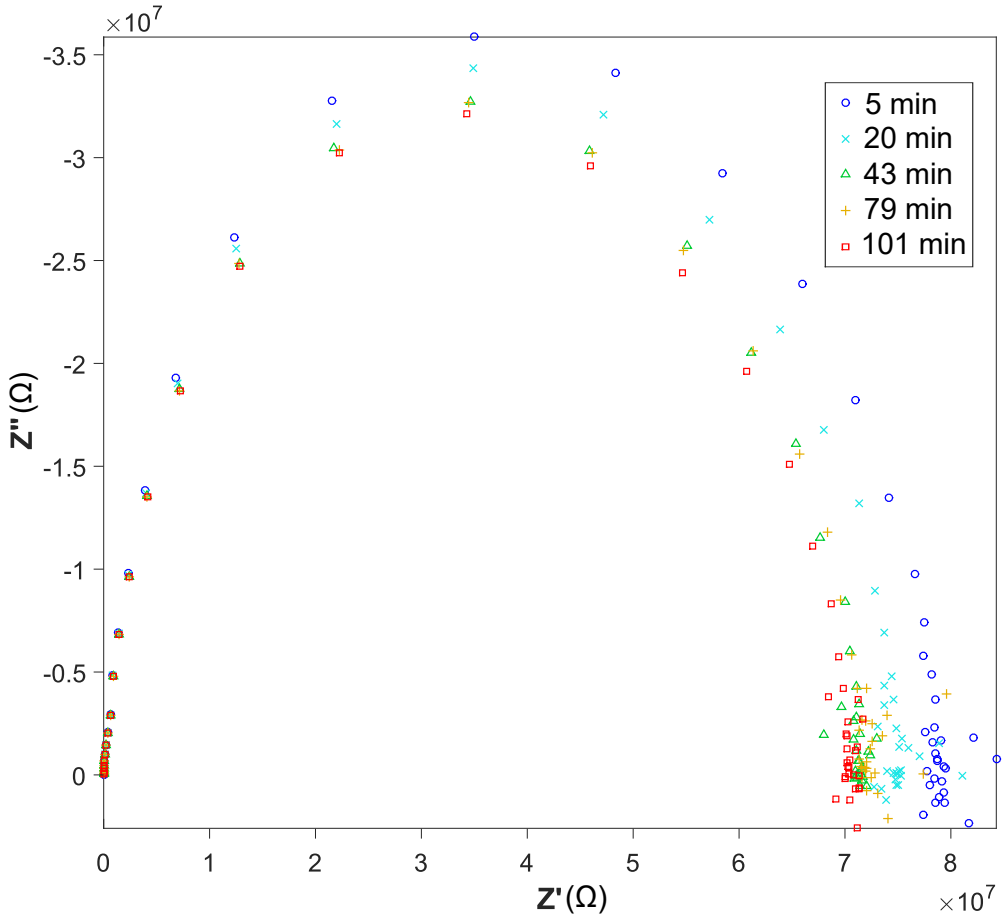

Figure 2.15: Nyquist plot for the evaluation of conductivity apparatus as a function of heating time.

from conductivity data by plotting $1/T$ vs. $\ln\kappa T$ according to the Arrhenius equation:

$$\kappa = \frac{A}{T} exp\left(- \frac{E_{\mathrm{a}}}{kT} \right) \tag{2.13}$$

where A and E_{a} are the pre-exponential factor and activation energy, while k and T are Boltzmann's constant and temperature, respectively. Although $\ln\kappa T$ should be used to determine E_{a}, often $\log\kappa$ is plotted as well for easier comparison between data sets.

The conductivity is the concentration-weighted sum of the mobilities (μ_j) of all types of ions,[174]

$$\kappa = C_{\mathrm{F}} \sum z_j c_j \mu_j, \tag{2.14}$$

where C_{F} is the Faraday constant, z_j is the charge and c_j is volume concentration of ion. Moreover, the fraction of the conductivity due to a specific type of ion can be determined, termed the *transport number*, t_j,

$$t_j = \frac{z_j c_j \mu_j}{\sum z_j c_j \mu_j}. \tag{2.15}$$

In a binary electrolyte solution cations and anions move in *equal and opposite directions* to maintain electroneutrality, therefore, Eq. 2.15 becomes,

$$t_j = \frac{\mu_j}{\mu_+ + \mu_-}. \tag{2.16}$$

However, in a solid, which has a rigid, non-deformable sublattice of esentially immobile anions, it becomes more difficult to determine the movement of ions.[175] Furthermore, unlike in solutions, the degree of dissociation, *i.e.*, the concentration of

mobile ions, is less clear, especially in glasses where terms like interstitial and defect are difficult to define. There has been some work done on this problem which relates the measured prefactor (A) to a calculated one to determine the percentage of ions mobile in the glass structure.[176,177] Thus far, most studies of transport numbers in amorphous solids have focused on ions with low E_a such as Li^+, where the extra energy needed to make the ion mobile (termed charge carrier formation enthalpy) is relatively small for a solid electrolyte.[178,179] Although t_j has been measured in solids using complex impedance measurements like those described in this Section, they have been performed on solid electrolyte polymers with both an cation and anion charge carrier; during these experiments, three arcs are measured in the Nyquist plot (Z' vs. Z'').[178,179] Out of nearly 80 samples measured within, only a handful of conductivity measurements showed more than a single near-semicircular arc.

Nonetheless, in the cases where t_j has been measured in a network forming glass, it has been very near to unity, indicating that cations are the only mobile species in the material.[180,181] However, in these cases, DC was applied and the apparatus involved the sample being attached to a galvanic cell. Rather than t_j, mixed-alkali studies of conductivity have used isotopic tracers to determine the diffusivity of each cation without an applied potential.[58,182–185] Finally, long-term DC studies have shown if two types of cations with different mobilities are present, rather than anions moving, the more mobile cation will move towards the anode first, subsequently in order to maintain charge balance, the less mobile cation will move the opposite direction to fill the region recently vacated by the more mobile cation.[186]

2.7.1 Long-Term Conductivity

Since different types of ions have different mobilities, they conduct at different rates towards the electrodes allowing for qualitative assessment of the relative mobility of each type of cation using a long-term DC potential and compositional analysis. In order to determine which cation was the dominant mobile species at different compositions and temperatures, pieces of sample were placed under an electric potential for a month and then analyzed at the edges (near electrodes) for changes in composition by WDS. Fresh slices of samples were cut and silver electrodes applied which were attached with copper wires to a 3V DC battery pack (in parallel for several samples at once). Connections were checked to ensure low resistance existed in wires and and high resistance at opposite sides of sample. Additionally, before being placed in the oven, voltages on the wires near the sample were found to be about 3V. Once the apparatus was in the oven, again similar checks were made. The samples were left in the oven at low temperature (500 °C) and high temperature (600 °C) for 30 days; in the case of high temperature run, the voltage was observed to decrease over time by nearly 1V. After 30 days the samples were placed in epoxy, cut and polished to 1 μm for elemental analysis; using WDS, linescans were performed parallel to ion movement (perpendicular to electrodes) near sample edges. Like quantitative analysis, diopside was used as the external standard, however the experimental error for this linescan type of analysis is larger, at most 3%.

Chapter 3

Structural Mechanisms of Compression in the Ion-Exchanged Layer in Lithium Silicate[i]

3.1 Background

As ion-exchanged glass is used heavily in applications, it is important to fully understand the structural changes that lead to its enhanced mechanical properties. One of the major foci in this field is to improve further upon this enhancement, whether by using a specialized IE treatment or different materials. The goal of the present chapter is to explain the structural mechanisms which result in compressive stress in hopes of providing insight into improving the IE process.

As mentioned in Section 1.5, no studies to date have directly investigated the structural changes induced by the IE process; they have either calculated the change in molar volume from the optically measured stress (Section 1.5.1) or are computational only in nature.[102,116–118,120,121] As the case depth is on the order of tens of microns, many typical analysis techniques are unsuited to examining the local structure of the IE layer, one exception being micro-Raman spectroscopy. This has the advantage that it can probe the molecular structure with < 1 μm lateral spatial resolution.[188] Moreover, the energies of Raman vibrations can be related to external

[i]This chapter was adapted from Calahoo *et al.*[187] ICP-OES, SEM-WDS and DSC experiments were performed by Dan Chevalier, Dr. Dan MacDonald, and Dr. Cathy Whitman, respectively. All other experiments, data analyses and writing of the manuscript were done by the author.

Si-O-Si bond-angles between SiO_4 tetrahedra and internal Si-O bond-lengths within each tetrahedron;[145,146,148,189,190] thus, Raman spectroscopy offers a unique insight into the silica network structure. Unfortunately, Raman spectroscopy is incapable of directly measuring changes in the alkali environment due to the ionic nature of the alkali-oxygen bond, however, it can investigate how the connectivity of the glass network is affected by IE and IE temperature alike.

In this study, the effect of ion exchange treatment temperature on structural modifications in IE glass is determined using Raman spectroscopy. The structural mechanisms that lead to compression within the silica network are explored, as is the type of mechanical behaviour they exhibit. Using a well-developed relationship between the Si-O-Si bond angle, Si-O bond length, and Raman shifts, the reduction in network molar volume and increase in compressive stress were estimated. Based on the effect of the ion exchange temperature, the existence of a threshold energy below which the compressive stress manifests as the re-orientation of silica tetrahedra only, and above which, the system relaxes by increasing the Si-O bond-length, is proposed. Finally, the linear network dilation coefficient (Section 1.5.1) is revisited in terms of these new data, and an explanation given for its underestimation and overestimation of stress at low and high temperatures, respectively.

In this study, a simple binary lithium silicate, $30Li_2O$-$70SiO_2$ was used as the base glass. The samples were thermally ion-exchanged in KNO_3, $Li^+ \leftrightarrow K^+$, at six different temperatures between 360–480 °C, spanning the glass transition temperature, for 72 hours each. Micro-Raman spectroscopy and Wavelength Dispersive Spectroscopy (WDS) were used to examine the structure and composition, respectively, in order to address the issues mentioned above. This system was chosen for three reasons: simplicity of composition in comparison to many commercially-available IE glasses;[104] technological relevance, (Schott's Robax® is a commercially-available IE glass that

involves Li^+-for-K^+ substitution); and amenability to analysis, as the Raman spectra show significant differences between glasses in the lithium and potassium disilicate region.[145,189,190]

3.2 Experimental

The base glass, $30Li_2O$-$70SiO_2$, was prepared using Li_2CO_3 ($\geq$ 99%, Sigma-Aldrich) and SiO_2 (purum p.a., Sigma-Aldrich) by the conventional melt-quench method, melting at 1550 °C in a Pt crucible for 2 hours, quenching in air, followed by annealing at 415 °C overnight. Additionally, the bulk as-melted xLi_2O-$(30-x)K_2O$-$70SiO_2$ series was made for comparison, using a similar procedure, except annealing between 415–450 °C overnight and using dried (400 °C, 2 hrs), granular K_2CO_3 ($\geq$ 99%, ACP) as an additional starting material. Samples with large amounts of K_2CO_3 were seen to bubble rapidly at $\approx$ 800 °C, as supported by K_2CO_3 having a decomposition temperature of $\geq$900 °C;[191] thus, small batch sizes, 7g, were used. Homogeneity and complete relaxation were confirmed optically using crossed polarizers to detect residual strain.

The compositions of the as-melted series were confirmed by ICP-OES performed by Daniel Chevalier (Section 2.3.1). Additionally, T_g measurements were made by Dr. Cathy Whitman on the $30Li_2O$-$70SiO_2$ and $20Li_2O$-$10K_2O$-$70SiO_2$ bulk glasses using differential scanning calorimetry with a heating rate of 10 °C in an Ar environment. The Netzsch DSC 404 F1 Pegasus instrument has a precision of $\pm$ 2 °C.

The composition of the base glass, $30Li_2O$-$70SiO_2$, was measured from WDS by Dr. Daniel MacDonald (see Section 2.3.2). IE (see Section 2.2) occurred at six temperatures ranging from well-below T_g to temperatures essentially at T_g; T_g was found to be 459 °C, while IE temperatures were 360, 390, 405, 420, 450, and 480 °C. Since WDS has a spatial resolution of 1–2 μm, it was also used to confirm that the IE

was successful and create a quantitative composition profile across the IE layer (see Section 2.3.3). WDS is incapable of measuring any elements lighter than boron, thus, lithium content was not measured directly, but calculated from the oxygen, silicon and potassium content assuming correct stoichiometry. Sanidine ($KAlSi_3O_8$) was used as the standard in WDS to accurately determine K, Si and O concentrations.

Finally, micro-Raman spectra of the IE glasses were collected in the laboratory of Prof. Ian S. Butler at McGill University using a Renishaw inVia micro-Raman spectrometer (Section 2.5). The important feature of micro-Raman is it allowed the vibrational spectra of the IE layer to be analyzed as a function of case depth and composition, using a procedure similar to that of WDS (Section 2.3.3).

3.3 Results

3.3.1 Elemental Analysis

The analyzed compositions for the as-melted mixed alkali series are presented in Table 3.1. Although lithium was only measured indirectly for the $30Li_2O$-$70SiO_2$ sample, the elemental analysis from WDS is consistent with the nominal composition.

Table 3.1: Verification of glass composition from ICP-OES and WDS[a]

Nominal Composition	Actual Composition		
	Li_2O	K_2O	SiO_2
$30Li_2O$-$70SiO_2$[a]	31.4	0.4	68.5
$20Li_2O$-$10K_2O$-$70SiO_2$	19.4	11.8	68.4
$15Li_2O$-$15K_2O$-$70SiO_2$	14.5	15.1	70.1
$30K_2O$-$70SiO_2$	0.0	27.9	70.9

[a]Calculated from WDS results

Fig. 3.1 shows the K_2O mole fraction in the IE glasses as a function of case depth

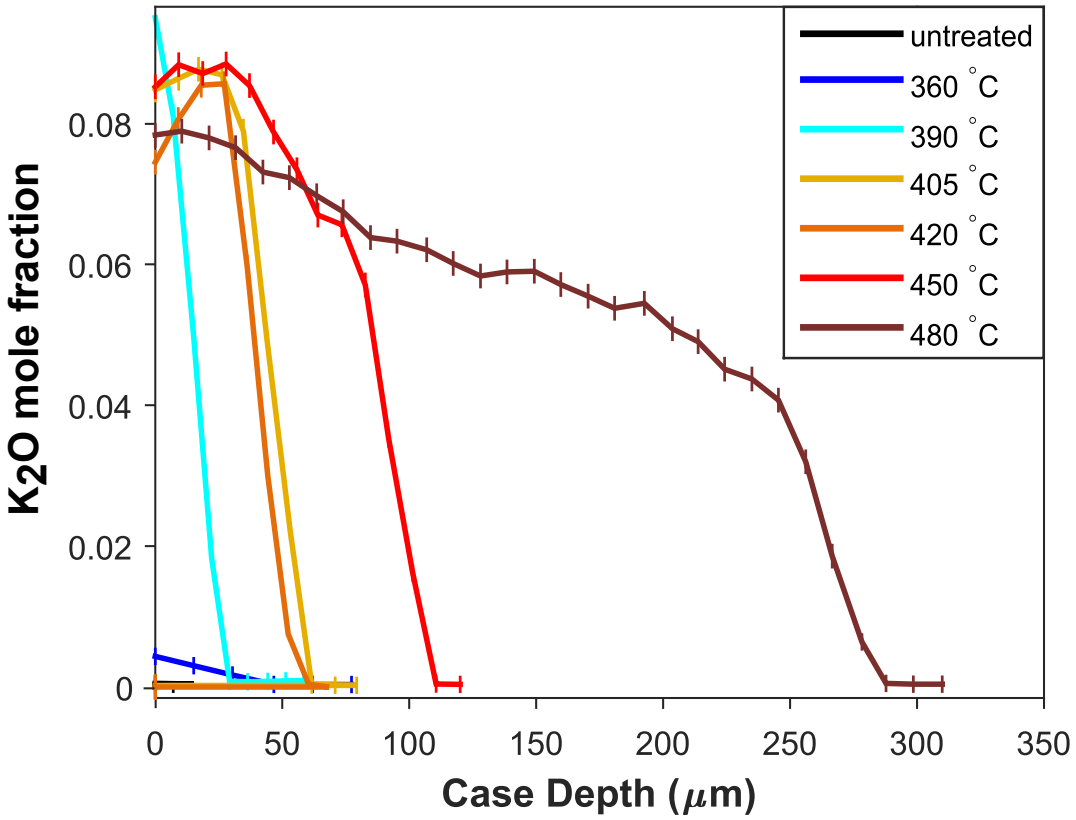

Figure 3.1: K_2O mole fraction of IE glasses as a function of distance from the IE surface or edge, determined by Wavelength-Dispersive Spectroscopy (WDS). Error estimates depend on the mass of the analyte, which can be converted to mole fraction for this glass system. When K_2O has a mole fraction ≥ 0.01, the error is $1.0–1.6\times10^{-3}$ mole fraction, while for a mole fraction < 0.01, the error is 0.4×10^{-3} mole fraction.

(defined as IE layer thickness) as measured by WDS; the complete elemental analysis results can be found in Appendix A.1. The WDS results show the highest K_2O content found in the IE glasses to be 9.3–9.5% (for only two points sampled by WDS), while 8.0–8.5% is the common K_2O content near the IE surface. The maxima near the surface in the 405 and especially the 420 °C sample are not expected from diffusion theory,[192] unless large amounts of Li^+ are transferring from the glass to the salt bath, and are likely an artefact of the surface condition. A mole fraction of 0.085 for K_2O corresponds to a relative Li_2O fraction of 0.72, therefore all the IE-glass compositions are in the range of 0.72–1 Li_2O total alkali fraction.

3.3.2 Raman Spectra

Micro-Raman spectra collected at increasing depths from the IE surface are shown in Fig. 3.2a–g) for different conditions: untreated (no IE) and six different treatment temperatures between 360–480 °C. For comparison, Fig. 3.2h) presents the Raman spectra of the mixed-alkali as-melted bulk series, xLi_2O-$(30-x)K_2O$-$70SiO_2$. The effect of the invading K^+ ions on the glass structure is noticeable in temperatures at and above 390 °C. Most clearly, the high-frequency (HF) region peaks (900–1200 cm^{-1}) shift to higher wavenumbers and the low-frequency (LF) peak at approximately 480 cm^{-1} decreases in intensity as K_2O content increases near the edge of the sample. Comparing these observations to the as-melted series in Fig. 3.2h), the trends are similar as the series goes from lower to higher K_2O content, with the exception of the narrowing of the major band in the LF-region. Fig. 3.3a) compares the Raman spectra collected past the IE layer into the untreated portion of the sample, indicating samples were mostly unaffected by the ion-exchange process past the case depth, when the temperature was far enough below T_g, 459°C. However, the 450 and 480 °C samples did show some differences in the Raman spectra past the case depth. On the other hand, the comparison of the Raman spectra at the edge of each sample, Fig. 3.3b), shows the temperature-dependence of the IE process.

3.4 Discussion

3.4.1 Raman Shift Assignments

Silicate glass structure is often described in terms of Q^n-units, where n refers to the number of bridging oxide (BO) bonds, i.e., Si-O-Si bonds, found around a tetrahedral SiO_4-unit. The three low-frequency (LF) region Raman peaks at approximately 480,

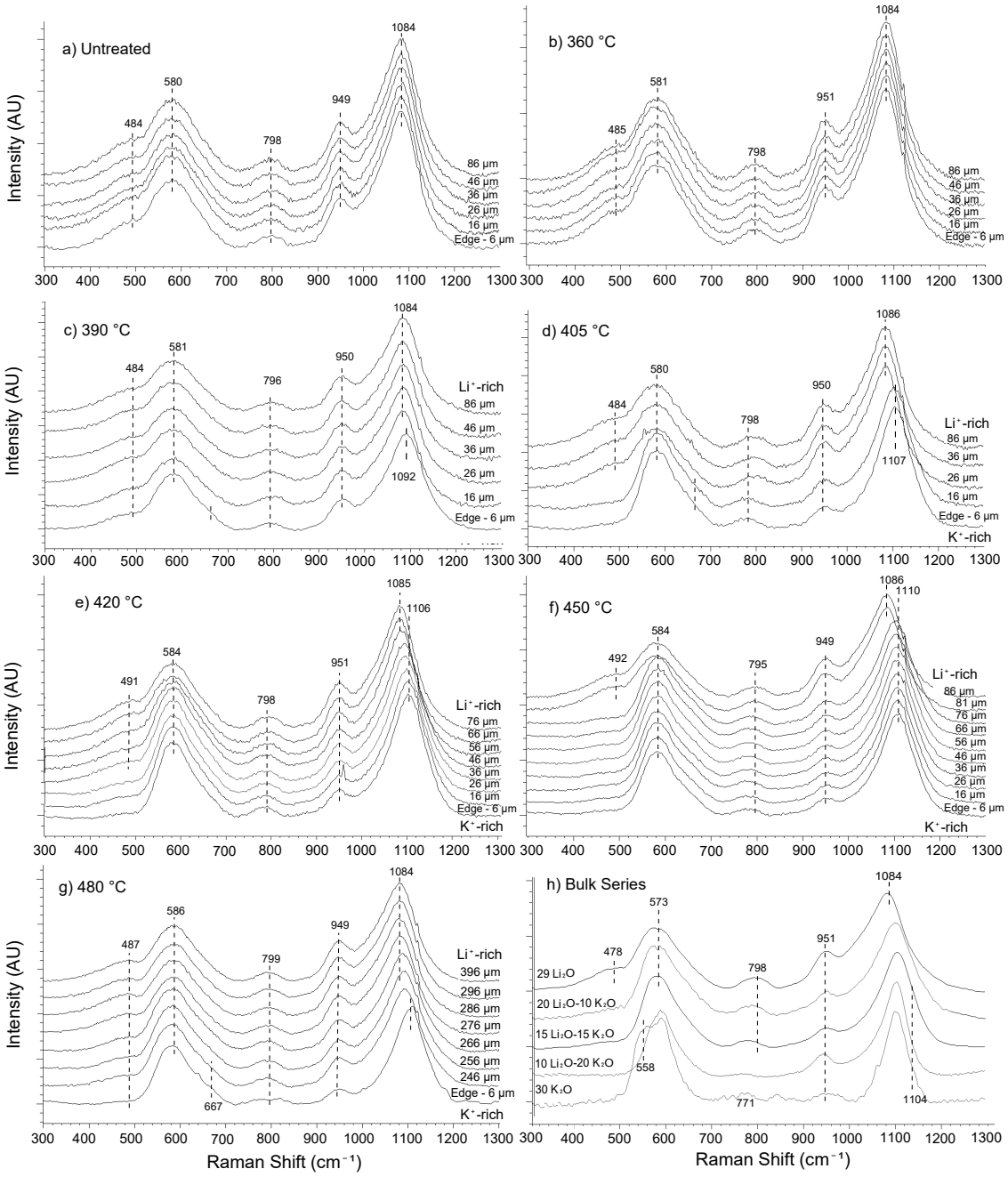

Figure 3.2: Micro-Raman spectra of the IE glasses treated at different temperatures at increasing depths from the glass surface: (a)untreated (b)360 °C (c)390 °C (d)405 °C (e)420 °C (f)450 °C and (g)480 °C. Where IE has occurred, the edge of the glass is relatively K^+-rich compared to deeper into the specimen, which closely matches the spectra of the untreated parent glass shown in (a). The error in the stage movement, corresponding to increasing case depth is ± 1 μm. The Raman spectra of the as-melted mixed-alkali xLi_2O-$(1–x)K_2O$-70SiO2 series as a function of composition are shown in (f).

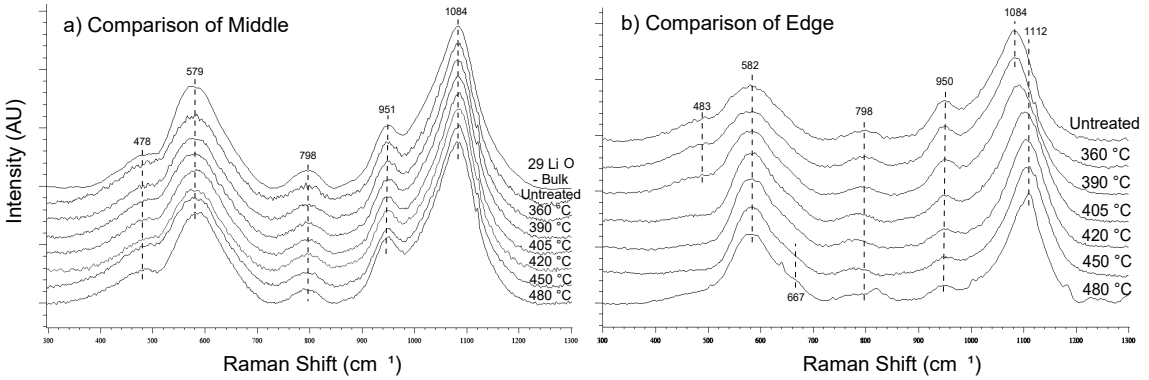

Figure 3.3: (a)Comparison of micro-Raman spectra collected far from the edge of each IE specimen, 360 °C–480 °C and untreated, with as-melted $30Li_2$–$70SiO_2$, indicating the effect of the IE process is negligible past the IE layer. (b)Comparison of micro-Raman spectra collected at the edge (highest K^+ conc.) of each IE specimen, 360 °C–480 °C and untreated, showing the effect of heat and K^+-concentration.

570 and 630 cm^{-1} have been assigned to symmetric Si-O-Si stretching plus bending of Q^4, Q^3 and Q^2-units, respectively.[145,190] These vibrations are thought to be somewhat dependent on long-range interactions, in addition to being dependent on the external Si-O-Si bond angle, where a shift to higher wavenumbers indicates a reduction in angle.[145,148,190] Within the alkali and alkali-earth silicates, only K_2O-SiO_2 was seen to have easily resolved 570 and 630 cm^{-1} bands.[190] In the mid-frequency region, there is a single peak between 790–800 cm^{-1}, identified as a highly depolarized or antisymmetric Si-motion in a cage;[190] it has been observed to shift to lower wavenumber with increased alkali content.

Peaks in the high frequency (HF) region are due to localized Si-O stretches within the silicate tetrahedra; as a result peaks in the HF-region can be used for quantification of Q^n-species in the glass structure. In the case of the HF bands, the Raman shift is a function of internal Si-O bond-length, where with the exception of Q^4-units, a higher wavenumber corresponds to a shorter Si-O bond. The three peaks in the HF-region at approximately 945, 1040, 1090 and 1120 cm^{-1} were assigned to symmetric Si-O^- stretches of Q^2, Q^4, Q^3 and $Q^{3'}$-units, respectively (that is, Q^3 with two

different second-neighbour environments).[145,189,190]

There is some disagreement in the literature about the assignment of the HF shoulder at ≈ 1120 cm $^{-1}$ ($Q^{3'}$ vs. $Q^{4'}$ [145,149,193]). Matson *et al.* observed the ≈ 1150 cm^{-1} shoulder in high-alkali silicates and assigned it as a distinct $Q^{3'}$-species due to its having the same polarization ratio as the main Q^3 peak, its merging with the main Q^3 peak at the disilicate region and the fact that its intensity does not correlate with the intensity of the known LF Q^4 peak at ≈ 480 cm^{-1}. As the near-disilicate composition used here, $30Li_2O$-$70SiO_2$, is known to be mostly composed of Q^3-units and the Raman peak intensity of shoulder at 1115 cm^{-1} was actually found to correlate *negatively* with the LF Q^4 peak at ≈ 480 cm^{-1}, the shoulder was assigned as $Q^{3'}$. Compared to other alkalis, Li_2O-SiO_2 has been found to possess a structure more similar to pure silica even at high modifier concentrations; their spectra retain the LF Q^4 peak (480 cm^{-1}) longer and the HF Q^n peaks have more equal Raman scattering efficiencies.[145] The Raman shift assignments are summarized in Table 3.2.

Table 3.2: Raman shifts (ν) and assignments for fitted peaks

Wavenumber (cm^{-1})	Vibrational Mode	Q-species
460–480	$(Si\text{-}O\text{-}Si)_s$ stretch	Q^4
560–580	$(Si\text{-}O\text{-}Si)_s$ stretch	Q^3
605–650	$(Si\text{-}O\text{-}Si)_s$stretch	Q^2
780–795	antisymmetric Si-motions in cage	
945–950	(O-Si-O) stretch	Q^2
1030–1070	$(O\text{-}Si\text{-}O)_s$ stretch	Q^4
1085–1110	$(O\text{-}Si\text{-}O)_s$ stretch	Q^3
1115–1160	$(O\text{-}Si\text{-}O)_s$ stretch	$Q^{3'}$ [a] or $Q^{4'}$ [b]

[a]From ref [145] [b]From ref [149]

3.4.2 Fitting and Error Analysis

The fits for the middle of the untreated specimen and the edge of the 450 °C sample are shown in Fig. 3.4. It was challenging to fit the IE spectra due to the compositional

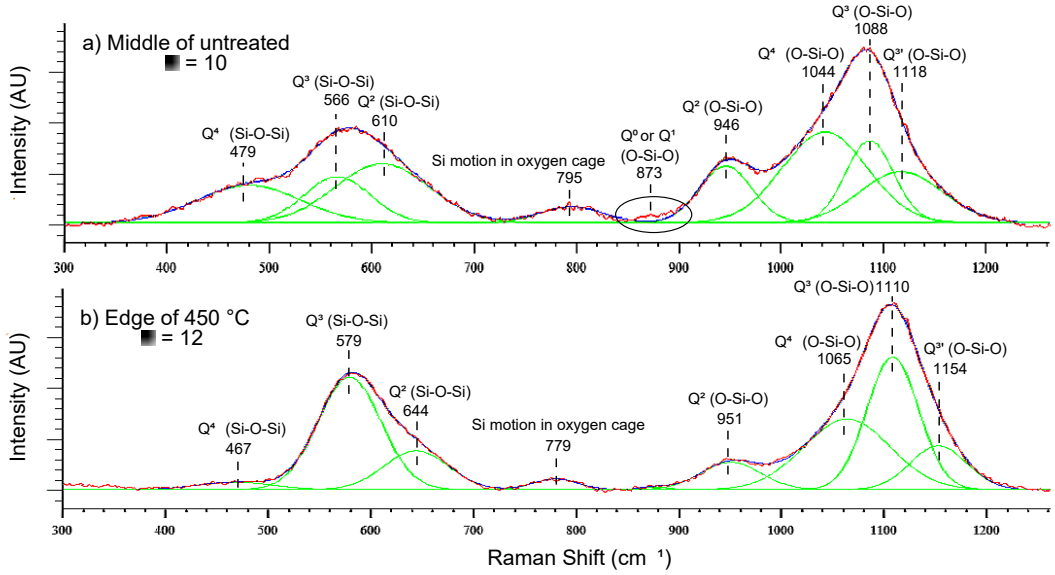

Figure 3.4: Peak deconvolution for two samples: (a) middle of untreated parent glass, $30Li_2O$-$70SiO_2$ and (b) edge (highest K^+ conc.) of IE glass at 450 °C treatment. Lines are only guides for the eyes.

gradient, nonetheless, eight peaks were found to fit all the spectra reasonably well, with a maximum $\chi^2 \leq 12$ (where χ is goodness of fit, defined as the difference between the experimental fitting residual and expected residual calculated from number of data points in spectrum), while still having valid peak assignments. No restrictions were placed on the fits other than using pure Gaussian lineshapes[190] and limiting the possible peak width of the HF-region peaks to $\leq$ 100 cm^{-1}, which is supported by literature peak bandwidths.[149,190]

The errors for these fits in peak area and position, are standard errors calculated at the 95% confidence level using the spectra from the compositional plateau found past the IE layer. As Raman spectra were collected beyond where K^+ was able to

diffuse into the glass structure, there is a plateau in the fitted peak values, where the Raman spectra are essentially replicates of the untreated glass, $30Li_2O$-$70SiO_2$, collected from different spots along the surface. These errors are then applied to the entire sample, including the mixed-alkali gradient region near the edge. As each IE temperature has a plateau past the case depth, there is a unique error corresponding to that sample. Overall, this strategy appears reasonable as most of the error is due to the fitting procedure rather than the data collection. In the case of the 480 °C sample, the compositional plateau near the edge was used instead of the pristine plateau nearer the middle; this larger variance in composition may be responsible for some of the larger errors seen for 480 °C in Fig. 3.7a).

3.4.3 Area Fraction

Although Raman spectroscopy is not a quantitative analysis technique, it is possible to compare relative peak areas within a spectrum in order to gain semi-quantitative indications of network connectivity, *i.e.*, Q^n distribution. The spectra of the IE samples were collected consecutively, one point after another along the surface, maintaining experimental parameters for each sample. The Q^n distributions determined from the relative area of the four localized HF-region peaks are shown in Fig. 3.5. In this case, the Q^3 and $Q^{3'}$-units were grouped together, to make the graphs clearer and easier to compare to literature. The errors were tabulated from the plateau spectra of the middle region of each sample as explained in the previous section. As the Q^3 fraction is actually composed of two peaks, Q^3 and $Q^{3'}$, it generally has twice the error of the other two Q^n-units in Fig. 3.5. In the case of the as-melted mixed-alkali series, Fig. 3.5h), the errors were simply taken to be ±10% of the area fraction per literature procedures.[149] It is encouraging that although the errors for the IE glasses and the as-melted series were determined by different routes, they are comparable.

For exchange temperatures $\geq$ 390 °C, a clear effect of the invading K^+-ions is observed: at the edge of the ion-exchange glass, where there is the highest concentration of K^+-ions, there is a higher area-fraction of Q^3-species, 0.55, in comparison to the middle of the glass, 0.45. Along with the decrease in Q^3-species, there is a concurrent increase in Q^2 and Q^4-species towards the middle of the sample. This trend is similar to the disproportionation reaction, $2Q^3 \leftrightarrow Q^2 + Q^4$, that is known to occur in bulk glasses.[145,194] The area-fraction of ion-exchanged glasses can also be compared directly to the as-melted mixed-alkali glasses shown in Fig. 3.5h). There is a slight increase in Q^3-species compared to what is expected from the corresponding as-melted compositions; this indicates that the IE glass Q^n populations exceed those in the corresponding as-melted mixed-alkali compositions and more similar to as-melted compositions with greater concentrations of K^+.

Using the expected Q^n-population[195] for a glass with the untreated composition, $30Li_2O$-$70SiO_2$, and the spectral area of the assigned Raman peaks, normalized cross-sections (see end of Section 2.5) were determined for each Q^n-species in the untreated sample ($Q^4 = 1.44$, $Q^3 = 0.70$ and $Q^2 = 1.50$); it was then applied to the corresponding peak area in the IE samples to produce a normalized Q^n-population, which will be used in the rest of the paper. Additionally, the structural changes are expected to be small in an IE glass, further validating the application of the normalized cross-sections estimated from the untreated sample to the IE spectra.

3.4.4 Non-Bridging Oxygens per Silicon Atom

Using the normalized Q^n-distribution, the non-bridging oxygens per silicon atom $\big([NBO]/[Si]\big)$ of the different IE-samples can be calculated, as shown in Fig. 3.6. The [NBO]/[Si] ratio gives a more comprehensive picture of what is occurring in

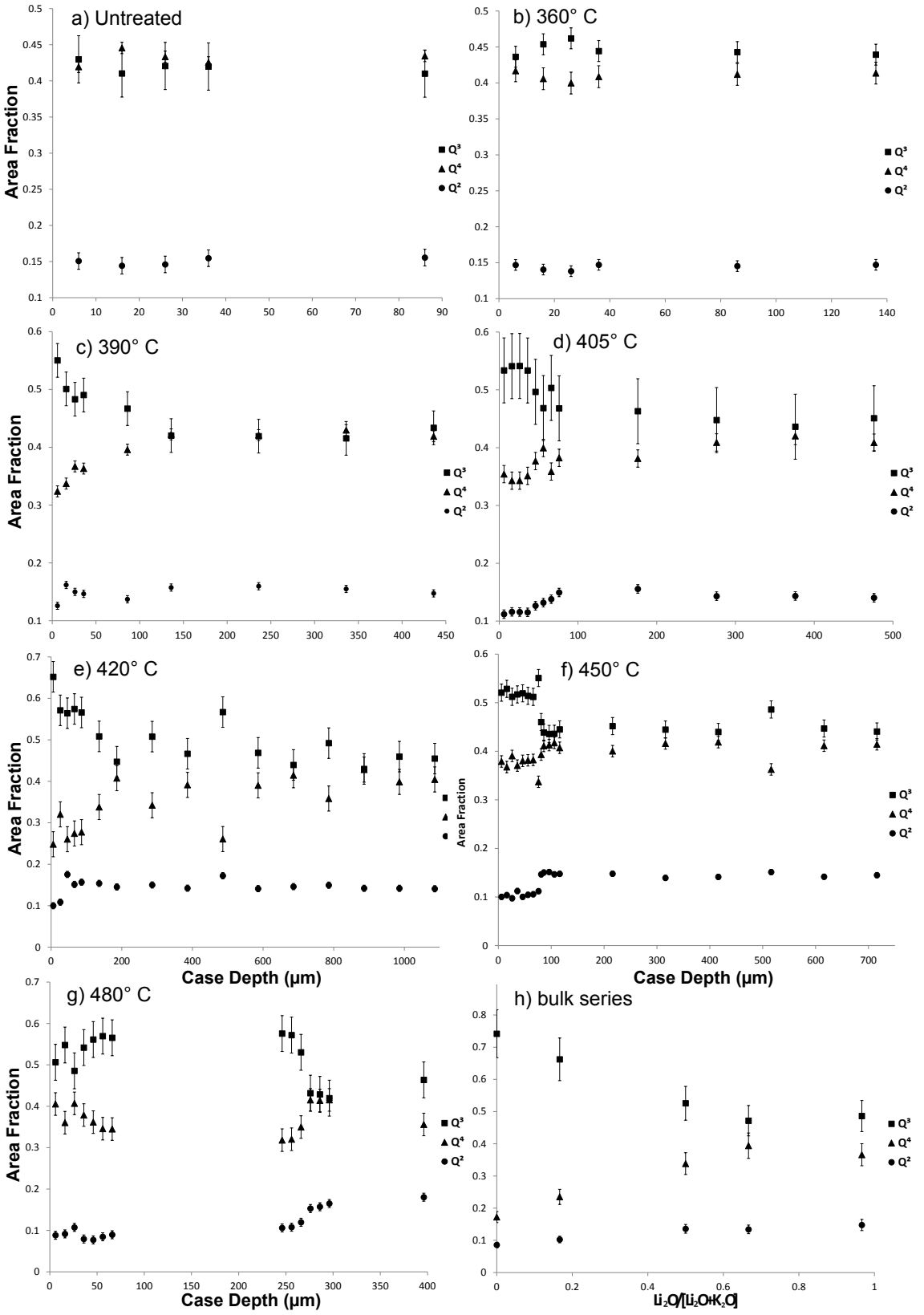

Figure 3.5: Normalized area of the HF-region Raman Peaks corresponding to Q^2(⧫), Q^3(■), and Q^4-unit(▲) fractions for all IE temperatures, untreated and 360–480 °C (a–g) as a function of case depth from the IE surface in comparison with the Q^n-fractions of the bulk, xLi_2O-$(30-x)K_2O$-$70SiO_2$ series in (h).

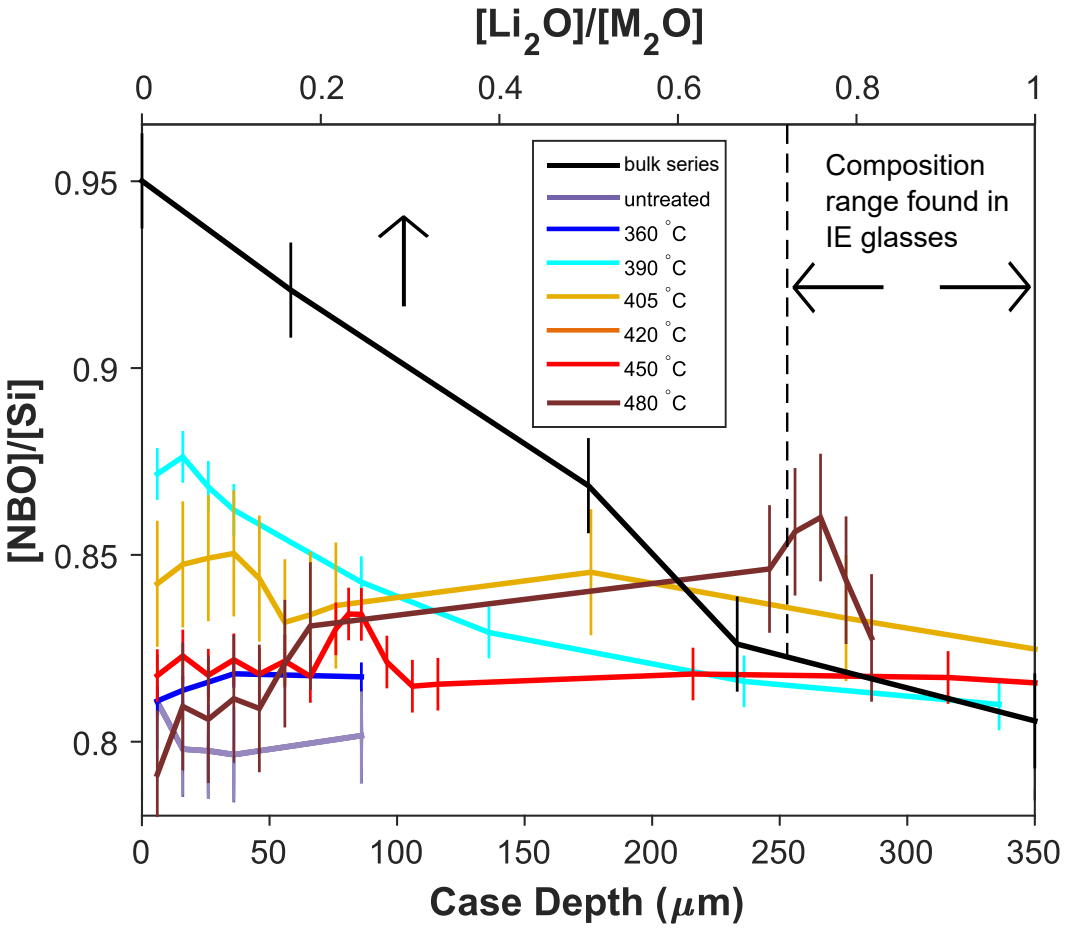

Figure 3.6: Connectivity, or non-bridging oxygen per silicon atom, [NBO]/[Si], for ion-exchanged glasses, untreated (purple) and 360–480 °C (dark blue–red), as a function of depth from IE surface (bottom axis) in comparison with [NBO]/[Si] in the bulk series (black) as a function of composition (top axis). All [NBO]/[Si], including the as-melted series, were determined from Raman spectroscopy and the calculated normalized cross-sections. For comparison, the range of $[Li_2O]/[M_2O]$ found in the IE glasses is also marked.

the glass structure compared to the Q^n populations alone. Fig. 3.6 also includes the [NBO]/[Si] ratio of the as-melted mixed-alkali series (plotted against composition along the top axis) for comparison, which match the [NBO]/[Si] determined from composition in Table 3.1 quite well. Fig. 3.6 indicates that as-melted glasses with similar compositions to that of the IE layer ($[Li_2O]/[Li_2O+K_2O]$ of 0.72–1) would have [NBO]/[Si] of 0.8–0.82. Samples treated at higher temperature, 450 and 480 °C, have an [NBO]/[Si] ratio of approximately 0.81 near the outer edge, which is fairly close to what was found for the compositionally equivalent as-melted glass, 0.82. Both of these temperatures are near enough to T_g to relax the structure towards that of the as-melted sample. However, the 480 °C sample shows a steady increase in [NBO]/[Si] from 0.81 to 0.87 with increasing case depth until decreasing sharply near the transition from IE layer to pristine composition. Additionally, for the samples treated at lower temperature (390–420 °C) the [NBO]/[Si] ratio is higher, especially near the outer edge, than what was found for the corresponding as-melted mixed-alkali composition. Consequently, this increased [NBO]/[Si] may be a feature found within all unrelaxed IE layers. This result indicates a *reduction* in connectivity, which is the opposite of what is normally associated with enhanced mechanical properties. These larger than expected ratios indicate a modification in how the charge balance of the glass is being maintained; there are Si-O-Si bonds being converted into $Si\text{-}O^-M^+$, perhaps simply to accommodate the substituting K^+-ion which has twice the desired oxygen coordination number of Li^+ (8 vs. 4).[16] Computational studies have showed the invading cation oxygen coordination to be somewhere between what is found in the untreated and as-melted compositions.[116]

Additionally, the WDS results (presented in Appendix A.1) show less SiO_2 content within the IE layer in comparison to the middle of the sample, which may be due to larger ions blocking ion channels, preventing the smaller ions from leaving, creating

a build-up of "extra" ions leading to more NBOs. In any case, the peak area data show clear evidence for structural rearrangement, *i. e.,* breaking and forming bonds, becoming more similar to the as-melted mixed-alkali structure and is supported by other experimental literature.[104,125] Nonetheless, the differences in connectivity between the IE layer and as-melted mixed-alkali series is likely not responsible for the improved mechanical properties seen in IE glasses.

3.4.5 Shifted Raman Shifts

For the present purpose, a useful way to represent peak positions is the shift of the Raman shift, $\Delta\nu$, defined as the difference between the Raman shift of a peak in a sample, ν_{s} and the shift of the corresponding peak of the untreated or the endpoint composition of the as-melted series, $30Li_2O$-$70SiO_2$, $\nu_{30\mathrm{Li_2O}}$.

$$\Delta\nu = \nu_{\mathrm{s}} - \nu_{30\mathrm{Li_2O}} \tag{3.1}$$

$\Delta\nu$ is a quantifiable measure of the any structural changes caused by the replacement of the Li^+ with K^+ ions in the IE samples. It was determined at each depth from the IE surface for all eight major peaks identified from fitting, Fig. 3.7 and Fig. 3.8. The three LF-peaks at 480, 560 and 610 cm^{-1} presented in Fig. 3.7a-c) are assigned to symmetric Q^4, Q^3 and Q^2 Si-O-Si stretches, respectively, and have been correlated to the external Si-O-Si angle.[145,146,148,189,190] The plots in Fig. 3.8a–d) show the $\Delta\nu$ of the four peaks in the HF-region, 945, 1040, 1090 and 1125 cm^{-1}. As stated earlier, the positions of these peaks are correlated with the Si-O bond-length of the structural Q^n-units found in the glass. The errors were calculated for each temperature using the method described in Section 3.4.2. Typically, the error was on the order of $\pm$0.5–2.5 cm^{-1}, with the outer, 480 and 1120 cm^{-1}, and weaker, 795 cm^{-1}, peak fits having

Table 3.3: Shifted Raman shifts, $\Delta\nu$, for the as-melted mixed-alkali silicate with the same composition as the edge of the IE-samples, $\approx 21Li_2O\text{-}9K_2O\text{-}70SiO_2$.

Shift Range (cm^{-1})	Q^n-species	$\Delta\nu$ (cm^{-1})	Error (cm^{-1})
460-480	Q^4	-10	2.6
560-580	Q^3	3	1.1
605-650	Q^2	3	2.5
780-795	Si motions in cage	-8	1.2
945-950	Q^2	2.5	0.5
1030-1070	Q^4	15	1.7
1085-1110	Q^3	10.5	0.5
1115-1160	$Q^{3'}$	8	2.9

the largest variance.

Raman shifts for the as-melted mixed-alkali series can be found in Fig 6.2 in Appendix A. The $\Delta\nu$ for the as-melted composition which corresponds to the highest K^+ composition found in the IE glasses (approximately $21Li_2O\text{-}9K_2O\text{-}70SiO_2$) is tabulated in Table 3.3. The error in the as-melted $\Delta\nu$ is the average error found for each peak in the ion-exchanged samples.

First of all, in Figs. 3.7 and 3.8, the shift $\Delta\nu$ is generally farther from the baseline, i.e., the untreated glass, for the samples treated at the highest temperatures. Beginning with Fig. 3.7a) (the 480 cm^{-1} peak), this fit is noisier than the rest, but it can be said with confidence that the low and high temperatures, 390, 450 and 480 °C, have spectral peaks which shift to lower wavenumbers than expected from the equivalent untreated composition. In contrast, the other two LF-region peaks, 560 and 610 cm^{-1} (Fig. 3.7b) and c)), have much larger increases in $\Delta\nu$, 7–16 and 12–45 cm^{-1} respectively, for all temperatures, compared with the untreated $\Delta\nu$, only 3 cm^{-1}, for both bands. Fig. 3.7d) shows that the negative $\Delta\nu$ value indicates replacing Li^+ with K^+ reduces the frequency of the Q^4-motion in a cage. Once more, the higher temperature samples, 405–480 °C have a larger deviation from the untreated sample of the same composition. Fig. 3.8 shows the higher temperatures, 420–480 °C, to

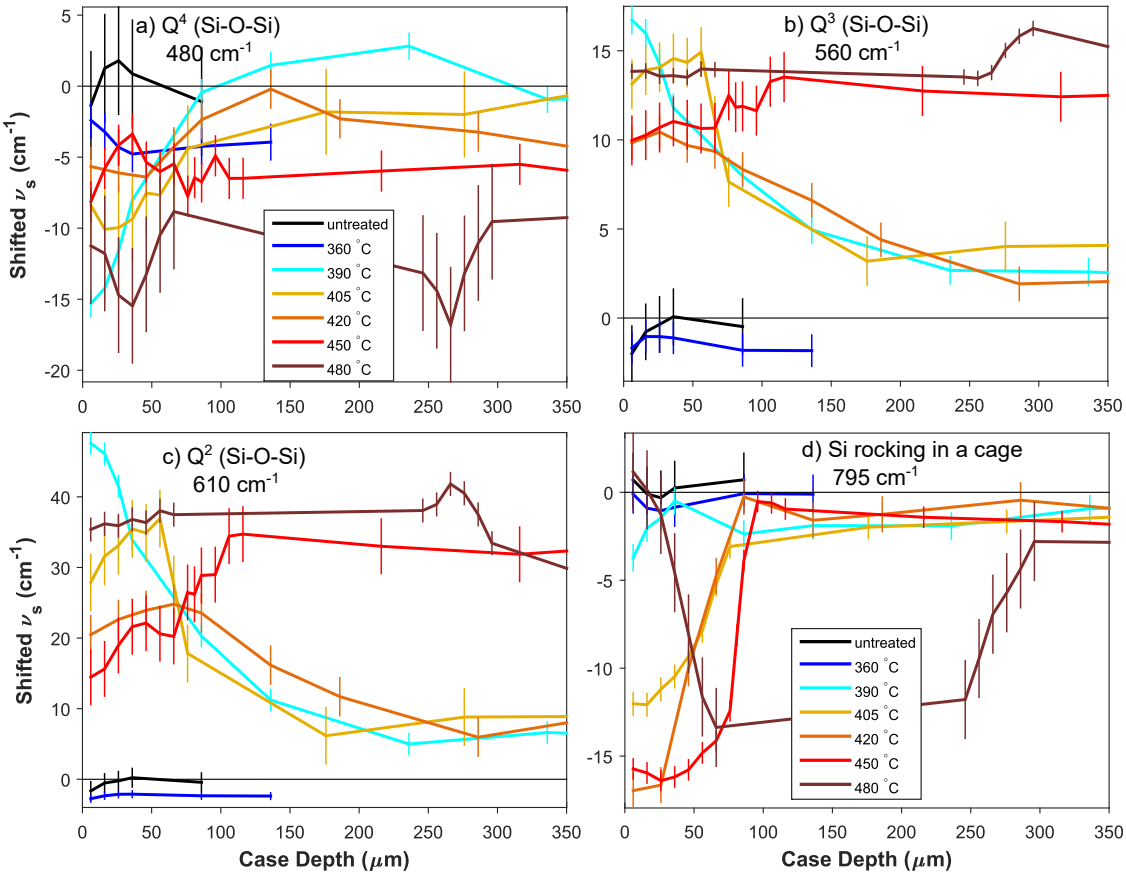

Figure 3.7: Shifted Raman shifts ($\Delta\nu$) for the low frequency Raman modes. $\Delta\nu$ is the difference between the Raman shift in the IE layer and the untreated parent glass for a given mode, plotted here as a function of ion-exchange depth for all IE-temperatures. Colors: untreated (black) and 360–480 °C (purple–red). The positions of the first three Raman peaks in the LF-region are known to correlate with Si-O-Si bond angle in Q^n-species: (a)480 cm^{-1} Q^4, (b)560 cm^{-1} Q^3, (c)610 cm^{-1} Q^2, while the fourth peak is attributed to Si-rocking in a cage (d)795 cm^{-1}.

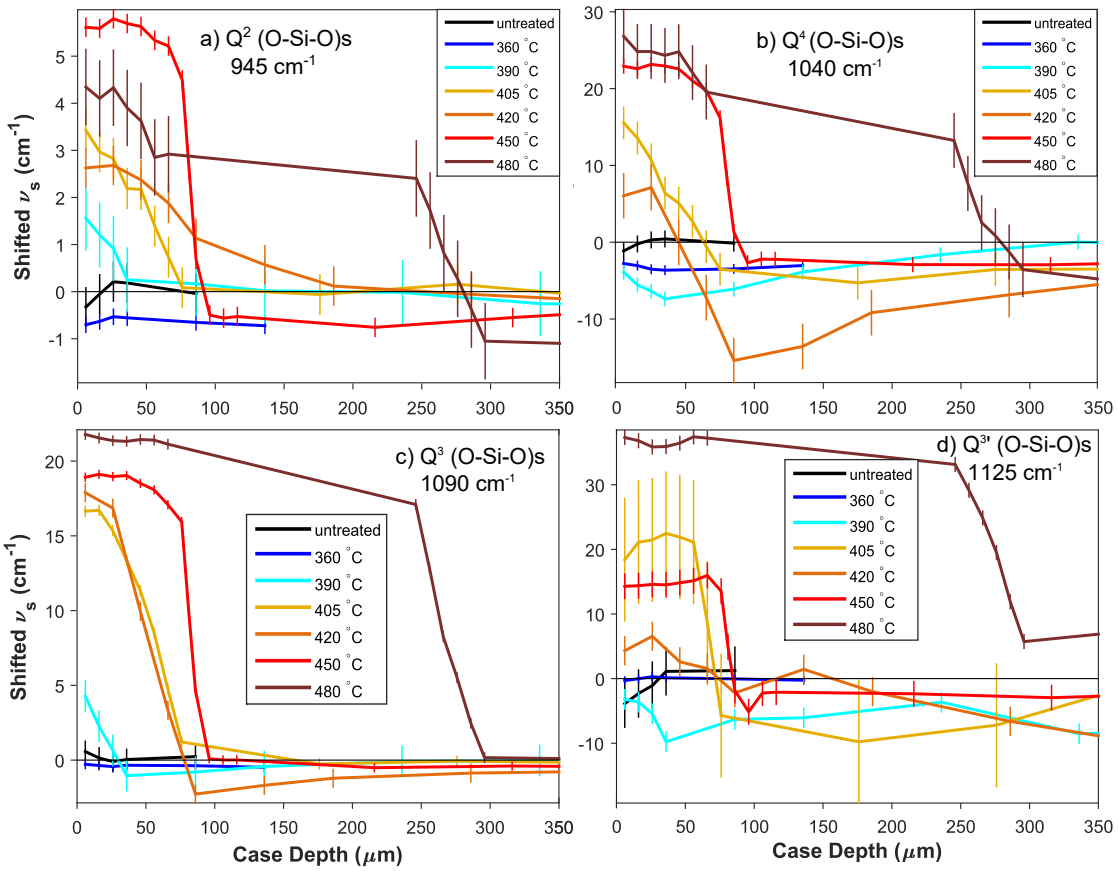

Figure 3.8: As in Fig. 3.7 but for the high frequency Raman modes. The positions of the four Raman peaks in the HF-region are known to correlate with Si-O bond-length in Q^n-species: (a)945 cm^{-1} Q^2, (b)1040 cm^{-1} Q^4, (c)1090 cm^{-1} Q^3 and (d)1125 cm^{-1} $Q^{3'}$.

have larger $\Delta\nu$ in comparison to the untreated composition. Overall, a larger deviation from the potassium-free composition is seen in the IE-samples, especially for the high-temperature conditions, in comparison to the equivalent untreated composition.

3.4.6 Raman-Crystal Calibrations

The Raman peaks of the IE glasses can be compared to those found in crystals of similar composition to understand how much the external Si-O-Si angles are changing. A calibration curve of Si-O-Si bond angle vs. Raman shift was made using literature crystal data (Fig. 3.9). It was found that although a reliable trend ($R^2 = 0.88$) exists for alkali silicate crystals, where a higher wavenumber indicates a smaller Si-O-Si angle, there is no relation between Si-O-Si bond angle and Raman shift in SiO_2 polymorphs. This may be due to a lack of steric constraints in SiO_2 structures, where calculations have shown the energy per molecule in fused quartz varies only by 0.2 eV for a range of 120° to 180°.[196–198] As a result, little can be said about the ∠Si-O-Si of Q^4-units, consequently, an average ∠Si-O-Si (149°) is assumed for *all* IE and as-melted glasses alike. Additionally, the Raman peak position correlated with ∠Si-O-Si of Q^4-units, Fig. 3.7a), changes less than the other Q^n-unit peaks, Fig. 3.7b-c).

Alkali silicate crystals, in contrast, appear to have more constraints and fewer possible crystal structures, for example, lithium and sodium silicates are iso-structural. Nonetheless, the relationship between Si-O-Si bond-angle and Raman shift in alkali-silicate crystals can be used to convert the shifted Raman shift, $\Delta\nu$, into an estimate of Si-O-Si bond-angle modification induced by the IE process. For example, the LF-region Q^2 and Q^3 Raman peaks positions increase by 35 and 14 cm^{-1}, respectively, at the surface of the 480 °C sample, which corresponds to a decrease of $-7°$ (-5%) and $-3°$ (-2%) in the Si-O-Si bond-angle. In the case of an IE temperature of 390°C, a

$\Delta\nu$ of 48 and 17 cm^{-1} were observed, indicating a bond angle decrease of $-9°$ (-7%) and $-3°$ (-2%) for Q^2 and Q^3-units, respectively. This indicates that the Si-O-Si bond-angles of Q^2-units are more affected by the IE-temperature in comparison to Q^3-units, which is also observed in $\Delta\nu$, Fig. 3.7.

Like the LF-region peaks, the HF-region Raman peaks can be compared to crystal data to determine the approximate conversion between wavenumber and bond-length, Fig. 3.10. However, unlike Fig. 3.9, SiO_2 polymorphs have a stronger correlation between Si-O bond-length and Raman shift, $R^2 = 0.83$, while alkali silicates show a weaker trend between Si-O bond-length and Raman shift, $R^2 = 0.63$. It is interesting to note the trends are opposite for SiO_2 polymorphs compared to alkali silicates; although a negative relationship between bond-length and Raman shift is commonly seen, the opposite relationship observed in SiO_2 polymorphs, where the bond-length is increasing with wavenumber is more difficult to explain. Using the trends in Fig. 3.10, $\Delta\nu$'s of the 480 °C sample (4, 22, 37 cm^{-1}) translate into a bond-length decrease of -5×10^{-4}Å (-0.2%), -2×10^{-3}Å (-0.1%) and -3×10^{-3} Å (-0.2%) for Q^2, Q^3 and $Q^{3'}$-units, respectively. Q^4-units, on the other hand, saw a large increase in Si-O bond-length of 4.43×10^{-1}Å (2.9%). A strain of 2.9% is larger than most in brittle ceramics, with the exception of structural phase transitions; otherwise, the material would fail much before those high of strains. Consequently, it seems like the structure of the IE-glass is changing as well as being strained, such as increasing the number of NBOs, in addition to a less electronegative K^+ replacing Li^+. In this case, temperature appears to have a linear effect on Si-O bond-length.

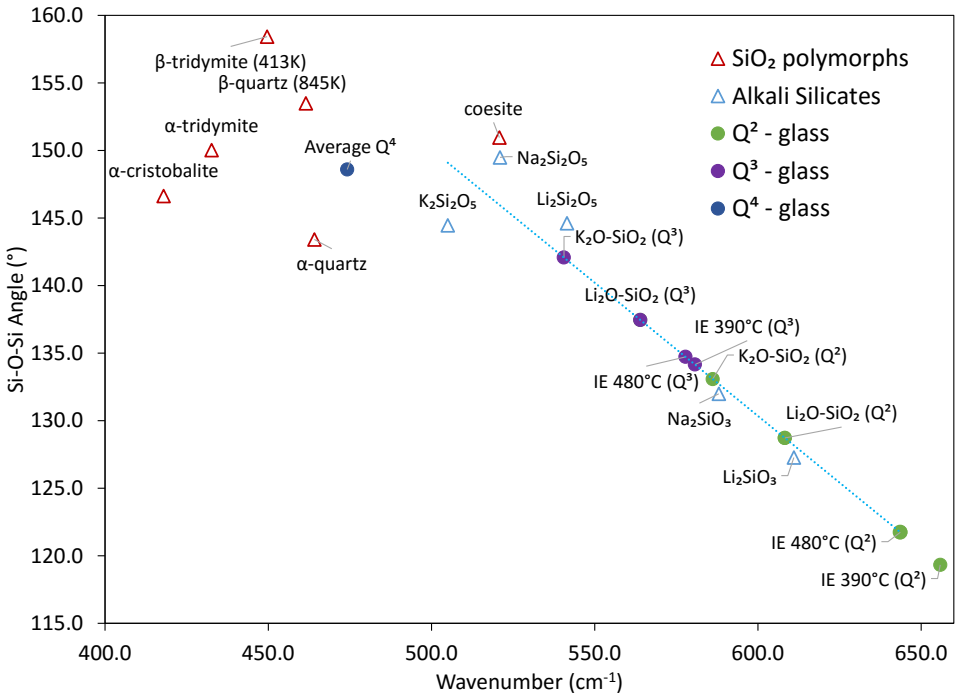

Figure 3.9: Calibration curve comparing average Si-O-Si bond-angle in crystal structures from literature to literature Raman data. Na_2SiO_3[189,201–203]; Li_2SiO_3[189,203–207]; $K_2Si_2O_5$[23,189]; $Na_2Si_2O_5$[189,208,209]; $Li_2Si_2O_5$[189,207,210,211]; coesite[212–216]; α-quartz[215–232]; α-cristobalite[233–238]; β-cristobalite[235,237–240]; α-tridymite[241–243]; β-quartz[218,219,227,228,244–246]; β-tridymite[242,243,247]. Literature values are available in Appendix A.2. SiO_2 polymorph crystals (△) do not have a correlation between Si-O-Si bond-angle and Raman shift, therefore, an average ∠Si-O-Si is suggested for the Q^4-units(●) in Li_2O-SiO_2, K_2O-SiO_2 and IE glasses based on the average measured Raman shift. The alkali silicate crystals (△) line-of-best-fit, $R^2 = 0.87$, was used to calculate the corresponding Si-O-Si bond-angles for the Q^2(●) and Q^3-units(●) in the Li_2O-SiO_2, K_2O-SiO_2 and IE glasses from the measured Raman shift. Errors in ∠Si-O-Si determined from the fit are ±4° (±3%) for both Q^2 and Q^3-units. For the Raman and crystal data, at least two separate literature values were averaged; however, for α and β-tridymite has one experimental and one calculated value.[243] Additionally, the crystal data only contains one value for the structures of $K_2Si_2O_5$ and $Na_2Si_2O_5$. As of now, the crystal structure of K_2SiO_3 remains unavailable.

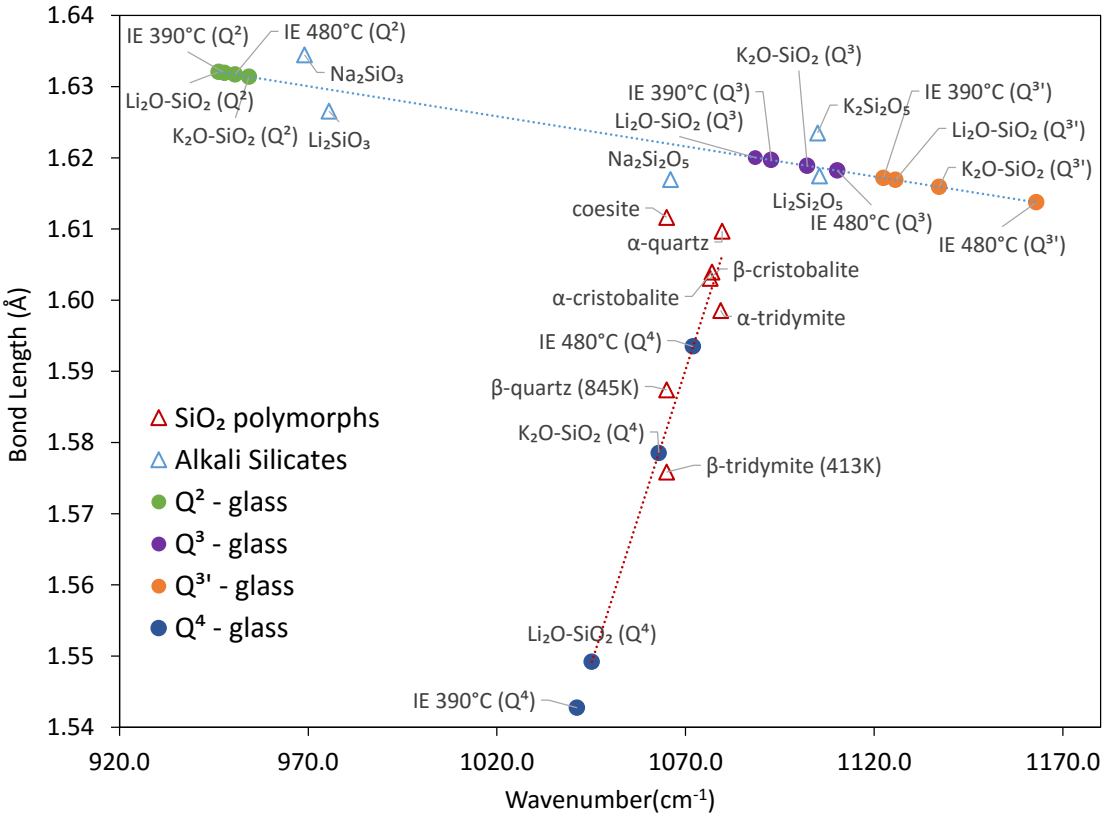

Figure 3.10: Calibration curve comparing average Si-O bond-length in crystal structures from literature to literature Raman data. Na_2SiO_3[189,201–203]; Li_2SiO_3[189,203–207]; $K_2Si_2O_5$[23,189]; $Na_2Si_2O_5$[189,208,209]; $Li_2Si_2O_5$[23,189,207,210,211]; coesite[212–216,248]; α-quartz[215–232]; α-cristobalite[233–238]; β-cristobalite[235,237–240]; α-tridymite[241–243]; β-quartz[218,219,227,228,244–246]; β-tridymite[242,243,247]. Literature values are available in Appendix A.2. SiO_2 polymorph crystals (△) line-of-best-fit, $R^2 = 0.83$, was used to calculate the corresponding Si-O bond-length for the Q^4-units(●) in the Li_2O-SiO_2, K_2O-SiO_2 and IE glasses from the measured Raman shift. High-pressure phases, coesite and stishovite, were excluded as they did not fit the trend. Alkali silicate crystals (△) line-of-best-fit, $R^2 = 0.63$, was used to calculate the corresponding Si-O bond-lengths for the Q^2(●), Q^3(●) and $Q^{3'}$-units(●) in the Li_2O-SiO_2, K_2O-SiO_2 and IE glasses from the measured Raman shift. Errors in $\langle d(\text{Si-O})\rangle$ determined from the fits are $\pm 5\times10^{-3}$ Å ($\pm 0.3\%$) for both Q^2 and Q^3-units, and $\pm 6\times10^{-3}$ Å ($\pm 0.4\%$) for Q^4-units. For the Raman and crystal data, at least two separate literature values were averaged; however, for α and β-tridymite has one experimental and one calculated value.[243] Additionally, the crystal data only contains one value for the structures of $K_2Si_2O_5$ and $Na_2Si_2O_5$. As of now, the crystal structure of K_2SiO_3 remains unavailable.

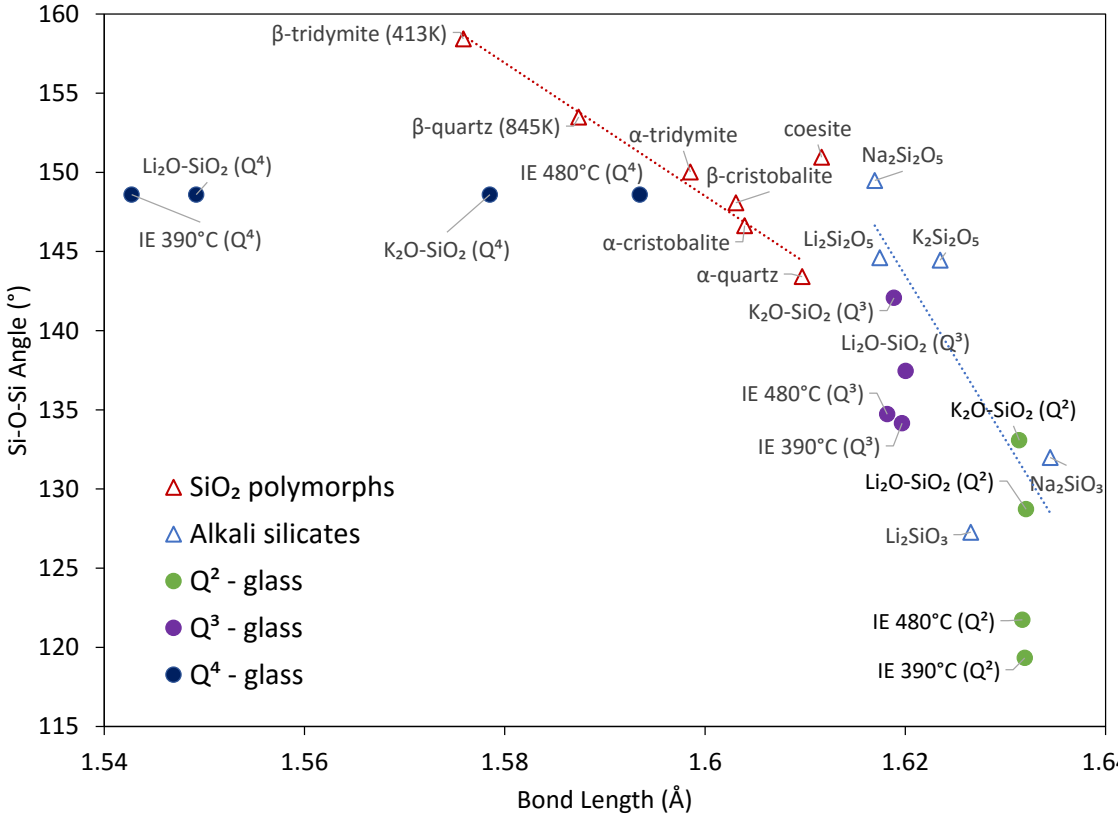

Figure 3.11: Relationship between average Si-O bond-length and Si-O-Si bond-angle in silicate crystal structures from literature. Na_2SiO_3[201,202]; Li_2SiO_3[204–206]; $K_2Si_2O_5$[23]; $Na_2Si_2O_5$[208]; $Li_2Si_2O_5$[23,210,211]; coesite[212,213]; α-quartz[217–225]; α-cristobalite[233,234]; β-cristobalite[239,240]; α-tridymite[241–243,249]; β-quartz[218,219,244,245]; β-tridymite[242,247]. At least two separate literature values were averaged for each crystal structure, wih the exception of $Na_2Si_2O_5$ and $K_2Si_2O_5$. The line-of-best-fit for SiO_2 polymorph crystals (△) has an $R^2 = 0.98$ (once the high-pressure phase coesite is removed), while the alkali silicate crystals' (△) trend has an $R^2 = 0.63$. This is simply to show a negative correlation between $\langle d(\text{Si-O})\rangle$ and ∠Si-O-Si, although there is a different relationship for Q^4-units(●) in comparison with Q^2(●) and Q^3-units(●). The $\langle d(\text{Si-O})\rangle$ and ∠Si-O-Si for Li_2O-SiO_2, K_2O-SiO_2 and the IE glasses are those calculated from the measured Raman shifts as shown in the previous section. As of now, the crystal structure of K_2SiO_3 remains unavailable.

3.4.7 Relaxation Mechanisms

Plotting Si-O-Si bond-angle versus average Si-O bond-length of literature crystal data in Fig. 3.11, there appears to be a negative correlation for SiO_2 polymorphs and alkali silicates alike, such that as ∠SiOSi decreases, $\langle d(\text{Si-O})\rangle$ increases. Indeed, the IE glasses exhibit bond-angle reductions in Q^2 and Q^3-units concurrently with the lengthening of Q^4 d(Si-O). The Q^2 and Q^3-units neighbouring the ion-channels must accommodate the larger ion, both in space and coordination number, leading to reduction in network volume by collapsing the SiO_4 tetrahedra towards one another. IE likely causes the ion-channels within the glass to be more rigid than in the corresponding as-melted glass-structure, so it follows that the NBO or Si-O^- bond-lengths in Q^2 and Q^3-units are constrained and unable to dilate, while Q^4-units have more freedom. Consequently, the changes in ∠Si-O-Si in the Q^2 and Q^3-units necessitated by the larger invading ion are accommodated by dilation of the Q^4 network.

The IE-glass values determined from the Raman spectra in the previous section are included to demonstrate that they lie in the expected region of the graph compared to the crystal data. The Si-O-Si bond-angles of the Q^4-units are held constant since no correlation was found between Raman shift and ∠Si-O-Si; however, due to the relationship between ∠Si-O-Si and $\langle d(\text{Si-O})\rangle$, it may be fair to extend the negative correlation between ∠Si-O-Si and $\langle d(\text{Si-O})\rangle$ to Q^4-units as well. Nevertheless, all following calculations still hold the ∠Si-O-Si in Q^4-units to be constant.

Furthermore, calculations[196,250] have shown the ∠Si-O-Si to shift to smaller angles as R_O/r_O decreases, where R_O is the oxygen-second-nearest-neighbour-oxygen or O-Si-O separation and r_O is the Si-O bond-length, thus reinforcing the idea that ∠Si-O-Si and $\langle d(\text{Si-O})\rangle$ are negatively correlated. Hill and Gibbs similarly state that ∠Si-O-Si are determined by Si-O bond-lengths, d(Si-O), and Si-next-nearest-Si interactions,

Si$\cdots$Si; larger Si$\cdots$Si-separations are correlated with longer d(Si-O) and larger $\angle$Si-O-Si, as fit in the following:[251]

$$\log d(\mathrm{Si}\cdots\mathrm{Si})/\text{Å} = \log 2\langle d(\mathrm{Si}-\mathrm{O})\rangle/\text{Å} + b\log\sin\left(\frac{1}{2}\angle\mathrm{Si}-\mathrm{O}-\mathrm{Si}\right) \tag{3.2}$$

In fact, by assuming the variance in $d(\mathrm{Si}-\mathrm{O})$ is small and using the general relationship in Eq. 3.2, Hill and Gibbs found clear linear correlations for both crystalline SiO_2 polymorphs (N = 161, R^2 = 0.98) and alkali silicate crystals (N = 87, R^2 = 0.93) alike. Moreover, the authors found that the slope, b, differed very little for SiO_2 polymorphs and silicates, 0.808 in comparison to 0.809; hence, the relationship in Eq. 3.2 can be applied to all Q^n-species present in the IE glasses. As the d(Si-O) and $\angle$Si-O-Si have been determined from the Raman data using correlations in Figs. 3.9 and 3.10, it is now possible to calculate the changes in Si$\cdots$Si. To accomplish this, Eq. 3.2 must be modified using experimental Q^n-species fractions, x_{Q^n}, in addition to being summed over all possible Q^n-interactions, to obtain the average $\langle d(\mathrm{Si}\cdots\mathrm{Si})\rangle$ separation:

$$\log\langle d(\mathrm{Si}\cdots\mathrm{Si})\rangle = \sum_{o,p=2}^{4} x_{Q^o}x_{Q^p}\left[\log 2\langle d(\mathrm{Si}-\mathrm{O})_{Q^o}\rangle + 0.81\log\sin\left(\frac{1}{2}\angle\mathrm{Si}-\mathrm{O}-\mathrm{Si}_{Q^p}\right)\right] \tag{3.3}$$

The $\langle d(\mathrm{Si}\cdots\mathrm{Si})\rangle$ separation was found by this approach to be 3.05 Å and 3.02 Å for untreated and 390 °C samples respectively; although 0.03 Å appears to be a small reduction in $\langle d(\mathrm{Si}\cdots\mathrm{Si})\rangle$, it results in an approximate 2% reduction in silica network volume, $\delta V_{\mathrm{network}}$, as determined by Eq.3.4.

$$\delta V/V^{\mathrm{network}} = 3\frac{\langle d(\mathrm{Si}\cdots\mathrm{Si})\rangle - \langle d(\mathrm{Si}\cdots\mathrm{Si})\rangle_{\mathrm{ref}}}{\langle d(\mathrm{Si}\cdots\mathrm{Si})\rangle_{\mathrm{ref}}}, \tag{3.4}$$

where the reference state is the pristine middle section of each treated glass. The pristine middle sections of the high temperature IE treatments, 450 and 480 ° were found

to change structurally, compared to the untreated 30% Li_2O glass. The $\delta V/V^{\text{network}}$ results for all IE samples, untreated and 360–490 °C are shown in Fig. 3.12. The network is seen to densify at low IE temperatures, 390–420 °C, and then at IE temperatures $\geq T_g$, relaxation and expansion occur due to larger K^+-ions entering. In fact, IE temperatures near or above T_g, 450 and 480 °C, show a large increase in network volume near the edge, indicating large structural rearrangement.

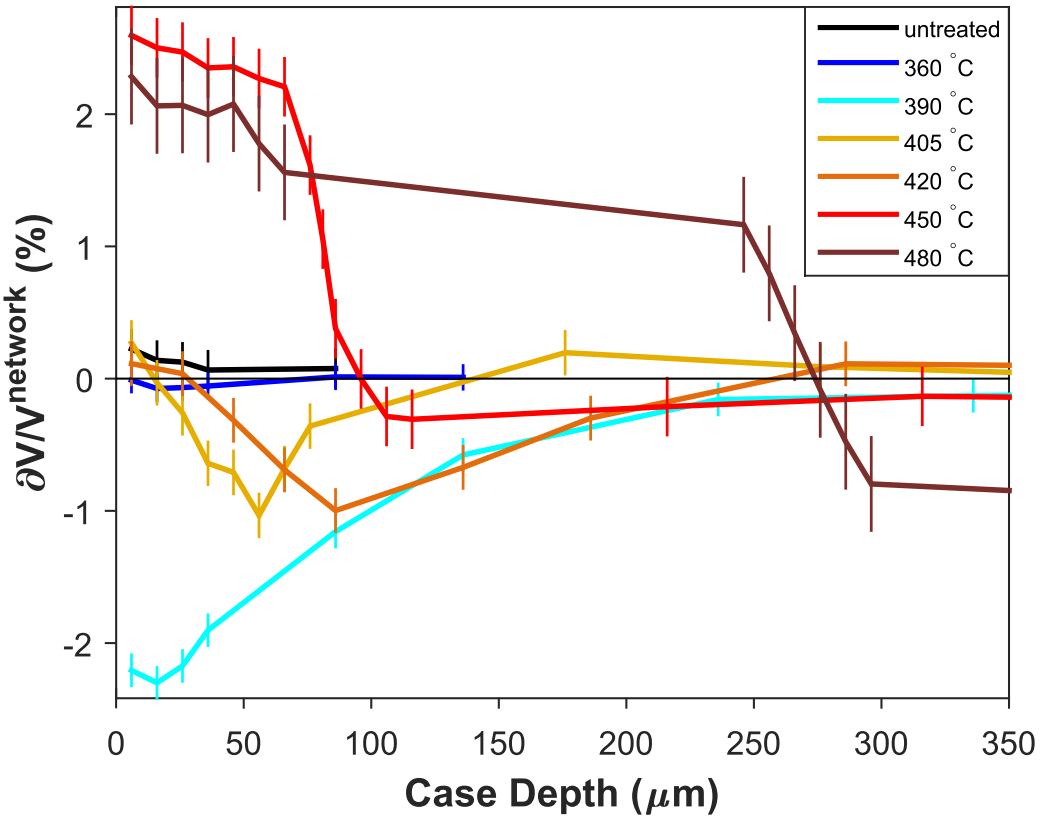

Figure 3.12: Relative densification or reduction in molar volume of the silica network, $\delta V/V^{\text{network}}$, determined from Eq. 3.4 as a function of distance from the IE-edge and IE-temperatures, untreated (black) and 360–480 °C (dark blue–red).

It is difficult to estimate the stress present in IE-glass without measuring it directly, however, to a first approximation, the reduction in Si $\cdots$ Si separation can be thought as the result of an uniformly applied stress. Since the surface is free to move,

the stress is anisotropic, nevertheless, only the volume change is able to measured and the stress must be treated as hydrostatic. In this case, the stress (σ) can be estimated as $\delta P/3$, where δP is the effective hydrostatic pressure due to the IE process, and use the bulk modulus $K = -\delta P/(\delta V/V)$ together with Eq. 3.4 to estimate stress. For the value of the bulk modulus the value of the 20% Li_2O- 10% K_2O bulk glass was used as representative. It is then possible to compare the results determined here to stresses reported in literature.[101,106] In this case, the ion volumes are assumed to stay constant and to not participate in the stress. Fig. 3.13 shows the calculated axial stress for all IE-samples. First of all, these values are in good agreement with literature, which reports compressive stresses of approximately 350–970 MPa.[101,105,106,117] Our data agrees with literature expectations,[105] where the maximum compressive stress was found in the lowest temperature sample in which significant concentration of K^+ entered, in this case, 390 °C. Since the current IE procedure was done at higher temperatures relative to T_g than in commercially available IE glasses, it is not surprising that the highest stress determined solely from the Raman spectra, $\approx$ 300 MPa, is at the lower end of literature values.

Secondly, Figs. 3.12 and 3.13 reveal a more complete understanding of the structural mechanisms than the shifted Raman shift, $\Delta\nu$, plots alone, Figs. 3.7 and 3.8. In general, the $\Delta\nu$'s linked to d(Si-O) increase dramatically with higher temperatures, while $\Delta\nu$'s linked to $\angle$SiOSi stay relatively constant as a function of temperature. The reduction in $\angle$SiOSi occurs as soon as any invading ion is present, even at lower temperatures, while the lengthening of d(Si-O) is a relaxation mechanism that can only occur when enough energy is present in the network. Furthermore, the effects of temperature and relaxation can be seen in Figs. 3.12 and 3.13, where the most densification or maximum compressive stress is seen to be lower and progressively further from the IE surface with increasing temperature. Although the $\angle$SiOSi for

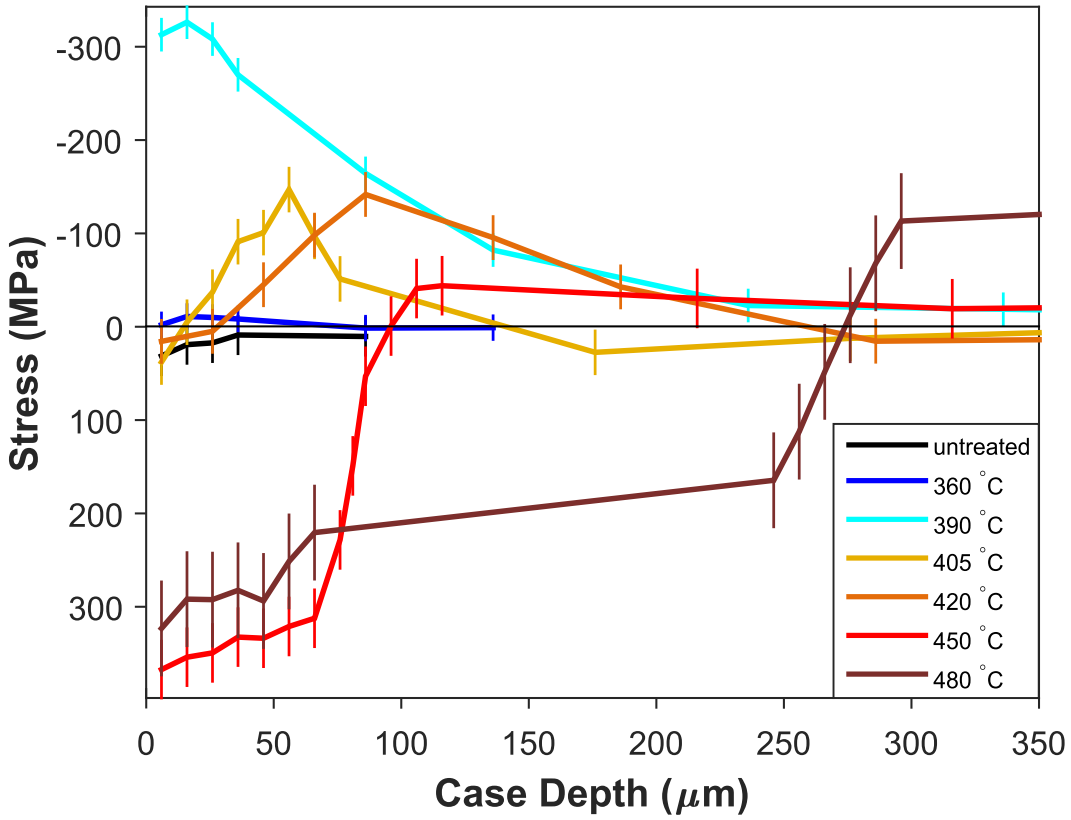

Figure 3.13: Axial stress along one dimension, σ_{ii}, determined from Eq. 1.9 as a function of distance from the IE-edge and IE-temperatures, untreated (black) and 360–480 °C (dark blue–red).

Q^4-units is not known and held constant, it is likely that an increase in average d(Si-O) would facilitate a decrease in ∠SiOSi as indicated by the trend in Fig. 3.11; this makes the estimate of the reduction in network volume conservative as it does not include reduction of the Q^4 ∠SiOSi. Since Fig. 3.12 shows there to be an expansion of the network at high IE temperatures, Fig. 3.13 shows a large tensile stress as a result, which may be overestimated since the structure was seen to clearly change at IE temperatures ≥ 450 °C. On the hand, the 480 °C sample was observed to have cracking after the IE process, so perhaps this is indicative of the large tensile stresses formed at the edge. It could also be mismatch between thermal expansion coefficients of Li- and K-containing regions,[252,253] although the effect is expected to be small in

comparison to the compressive stress from the compositional effects. Finally, the stresses in Fig. 3.13 match what is seen experimentally; the reduction and migration of maximum stress from the edge has been well-documented.[102,105,115]

This compaction followed by dilation of the silica network may indeed be the two-step relaxation process discussed earlier:[116,121] a fast local rearrangement followed by a slow relaxation towards the structure of the as-melted potassium end-member. However, the data presented here indicate the reverse order of rearrangements; rather than an expansion followed by an irrecoverable densification, an elastic compaction, i.e., Si-O-Si bond-angle reduction, followed by a plastic dilation, i.e., Si-O bond-lengthening at higher temperatures, is observed. This disagreement may be explained simply by noting re-orientation of SiO_4 tetrahedra requires less energy than bond-length changes. The first step likely involves non-linear elasticity, where the deformation would recover entirely on laboratory-length time scales if the load is removed.[116] This is solely based on the fact that there appears to be a preferred relationship between $\angle$SiOSi to d(Si-O) as shown in Fig. 3.11, which leads to the conclusion that the compressive stress manifested as reduction in $\angle$SiOSi may be relieved in one of two ways: either the load can be removed and the $\angle$SiOSi returned to the "rest" position, or the d(Si-O) can increase. Finally, this relaxation mechanism may, in conjunction with viscous flow at the IE temperature, be an explanation for the lower-than-expected stress commonly seen in IE glasses, where the practically achievable compressive stress is significantly lower than that predicted from the as-melted composition.[116] There may exist a temperature-dependent stress threshold, where when breached, the structure yields and lengthens the d(Si-O) in response.

3.4.8 Linear Network Dilation Coefficient

Although $\delta V/V^{\text{network}}$ determined from the reduction in average $d(\text{Si}\cdots\text{Si})$ separation is a reasonable measurement of changes in the silica network, it does not describe the change in molar volume due to the volumes of the ions. The *total* molar volume, V_M^{total}, is a combination of the densification of the network as well as the volume increase expected from $\text{Li}^+ \leftrightarrow \text{K}^+$ substitution. Estimation of the relative change in total molar volume, $\Delta V_M/V_M$, was done by summing the weighted relative changes in partial molar volumes V_M^i between the IE and bulk of each glass component, SiO_2, Li_2O and K_2O. For the silica contribution the $\delta V/V^{\text{network}}$ from Eq. 3.4 was used. The lithium oxide contribution, $\Delta V_M^{\text{Li}_2\text{O}}$ between IE and bulk environments, was assumed to be negligible because the environments of lithium in the IE layer and lithium in the bulk glass should be quite similar. For potassium we estimate the change in partial molar volume, as potassium substitutes for lithium, as approximately $V_M^{\text{K}_2\text{O}} - V_M^{\text{Li}_2\text{O}}$. The result is

$$\frac{\Delta V_M}{V_M} \approx x_{\text{SiO}_2}\delta V/V^{\text{network}} + x_{\text{K}_2\text{O}}\frac{V_M^{\text{K}_2\text{O}}(\text{bulk}) - V_M^{\text{Li}_2\text{O}}(\text{bulk})}{V_M}. \tag{3.5}$$

Now it is possible to determine the LNDC (B) in Eq. 1.8 by plotting $\frac{1}{3}\Delta V_M^{\text{total}}$ versus mole fraction of K_2O ($x_{\text{K}_2\text{O}}$ or $C_{\text{K}^+}(z)$); Fig. 3.14 compares the LNDC for the as-melted mixed-alkali series with increasingly higher-temperature IE glasses. It is clear that the IE-samples have a much shallower slope than the corresponding as-melted series because of the limited relaxation of the network during IE. The final B values and R^2 values are tabulated in Table 3.4, which shows B to be quite close to what is expected from the literature[102,116,117], roughly 2–4 times smaller compared with the as-melted mixed-alkali series.

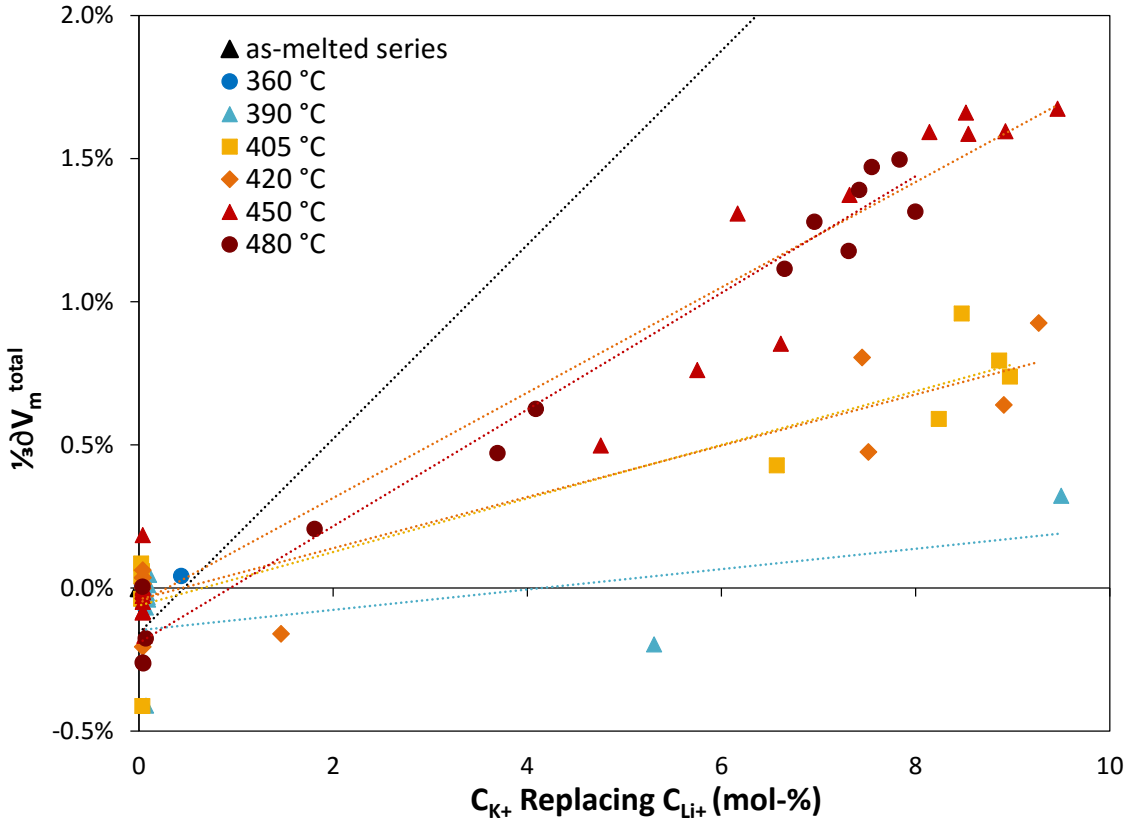

Figure 3.14: Determination of LNDC using Eq. 3.5 for all IE-temperatures, untreated (black) and 360–480 °C (dark blue–red).

Table 3.4: LNDC or B[102,120], error (ΔB) and correlation-coefficient (R^2) calculated using bulk Li_2O as the reference (Eq. 3.5 and Fig. 3.14) for as-melted series in comparison with IE glasses at increasing temperatures

Sample	B (mol-% K_2O)$^{-1}$	ΔB (mol-% K_2O)$^{-1}$	R^2
xLi_2O-(30−x)K_2O-70SiO_2	3.4×10^{-3}	2×10^{-4}	0.994
390 °C	6×10^{-4}	2×10^{-4}	0.65
405 °C	9×10^{-4}	1×10^{-4}	0.85
420 °C	1.0×10^{-3}	2×10^{-4}	0.85
450 °C	2.0×10^{-3}	1×10^{-4}	0.95
480 °C	2.04×10^{-3}	6×10^{-5}	0.98

The LNDC appears to depend positively on IE-temperature, indicating $\Delta V_M^{\text{total}}$ is more sensitive to K_2O content at higher temperatures. For example at equal concentrations of the substituting K^+-ions, $C_{K^+} \approx 10$, the $\Delta V_M^{\text{total}}$ is larger at 480 °C in comparison to the 405 °C sample. This result is consistent with the proposed mechanism for stress manifestation during $Li^+ \leftrightarrow K^+$ exchange: an initial reduction in Si$\cdots$Si separation caused by reduction in $\angle$SiOSi followed by an increase in Si$\cdots$Si separation due to lengthening of d(Si-O). The LT samples (390–425 °C) show only a small increase in $\Delta V_M^{\text{total}}$ with increasing K^+ concentration, indicating that the network densifies (by decrease of $\angle$SiOSi) to accommodate the increased volume of the invading ion and that little structural relaxation (i.e., increase in $\langle d(\text{Si-O})\rangle$) occurs. Additionally, the lower correlation coefficient for these LT samples can be explained by the antagonistic two-step process. The increase in structural relaxation with temperature can explain the temperature-sensitivity of the LNDC in Fig. 3.14 and Table 3.4.

Another consequence of the LNDC anomaly is manifested when compressive stress is calculated using B in Eq. 1.9: if the LNDC for the as-melted mixed-alkali series is used, the compressive stresses obtained are also 2–4 times higher than the stresses measured photoelastically in IE glasses.[102,116–118] To illustrate this point further, Fig. 3.15 shows the stress, $\sigma(z)$, calculated using Eq. 1.9, with B determined from $\Delta V_M^{\text{total}}$ in Eq. 3.5 and the mole fraction of K^+, $C_{K^+}(z)$), from WDS. Studies of IE glasses have shown tension of < 100 MPa past the case depth,[102] therefore, the average mole fraction of K^+, C_{avg}, was artificially set to generate tension between 10–50 MPa. This is simply extending the sampling range beyond what was measured using WDS, for example, a longer distance would result in a lower average mole fraction of K^+, C_{avg}.

Fig. 3.15, by comparison to Fig. 3.13 shows how Eq. 3.5 overestimates the stress

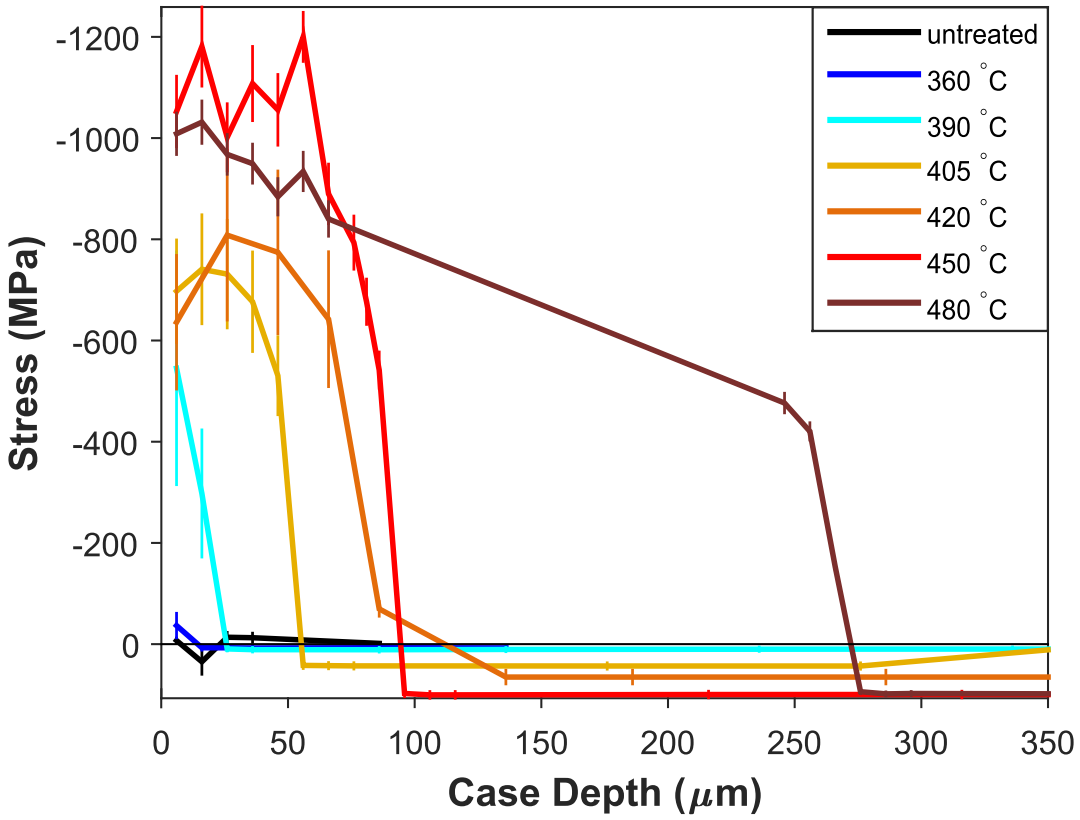

Figure 3.15: Stress determined from Eq. 1.9 and B when bulk Li_2O is the reference state (from Eq. 3.5 and Fig. 3.14), as a function of case depth for all IE-temperatures, 360–480 °C (dark blue–red) and untreated composition (black).

at the IE surface, since it equates a positive $\partial V_M^{\text{total}}$ to compressive stress, but if lengthening Si-O bonds are indeed a relaxation mechanism, that is not always the case. Overall, the molar volume will always increase compared to the untreated lithium silicate due to larger ions filling smaller interstices, as shown by finite element modelling,[102] but a larger $\Delta V_M^{\text{total}}/\Delta C_{\text{K}^+}(z)$ means more relaxation has occurred and less compressive stress is present. This can be seen clearly in Fig. 3.14, where the highest temperature IE sample with the largest thermal relaxation also has the largest value of $\Delta V_M^{\text{total}}/\Delta C_{\text{K}^+}(z)$. Additionally, Eq. 1.9 likely underestimates the stress at low temperatures, since the total molar volume, $\Delta V_M^{\text{total}}$, is similar to the initial untreated molar volume resulting in a small B, yet the Raman data shows the silica network to be stressed and densified due to dilation of the ion channels.

The method of estimating stress from the change in molar volume per change in alkali ion from a bulk lithium-modified glass does not account for the reduction in network molar volume that occurs from compressive stress. The IE glass with the highest maximum compressive stress is one where there is no change in molar volume compared to the untreated sample, indicating the silica network has densified without being able to relax (that is, a decrease in ∠SiOSi with no relaxation in Si-O bond lengths). For the IE structure to have the most stress, it should be furthest from its equilibrium state, i.e., the as-melted mixed-alkali composition corresponding to the final IE composition, not the initial untreated structure. In such a state the partial molar volume of K_2O would be quite similar to what it is in a pure potassium silicate glass. It is therefore interesting to consider an alternative method of determining B, using $V_M^{\text{K}_2\text{O}}$(bulk) as the reference state:

$$\frac{\Delta V_M}{V_M} \approx x_{\text{SiO}_2}\delta V/V^{\text{network}} + x_{\text{K}_2\text{O}}\Delta_K. \tag{3.6}$$

Here ΔK is the reduction in molar volume for K^+ in the IE layer compared to in a

relaxed K^+ site. The similar factor in Eq. 3.5 was the difference between a relaxed K^+ site and a Li^+ site, which is clearly large and positive.

The closer the IE structure is to the as-melted mixed-alkali structure, the less stress is present in the glass. If B is calculated using $\frac{1}{3}\Delta V_M^{\text{total}}$ determined from Eq. 3.6 and an estimate of $\Delta_K \approx -0.1$, an LNDC which changes from negative to positive with increasing temperature is obtained, shown in Fig. 3.16. The exact B values when the K_2O reference is used are tabulated in Table 3.5. When the glass is stressed the first and second terms are negative, however, at higher temperatures, the network is no longer densifying, in fact, $\Delta V_M^{\text{total}}$ is positive, thus, there is a sign change despite the second term remaining negative. Although counter-intuitive, the LNDC is negative at low IE temperatures because the reference state is bulk K_2O; it is a direct result of the network densifying and $V_M^{K_2O}(\text{IE}) \leq V_M^{K_2O}(\text{IE})$. Furthermore, $\frac{1}{3}\Delta V_M^{\text{total}}$ always remains below zero; in fact, high IE temperatures 450 and 480 °C are seen to approach zero or equilibrium V_M of the as-melted $20Li_2O$-$10K_2O$-$70SiO_2$ composition. Additionally, the IE glass always has a larger V_M^{total} than that of the untreated 30% Li_2O glass, which has a $\frac{1}{3}\Delta V_M^{\text{total}}$ of −3.0% relative to the as-melted $20Li_2O$-$10K_2O$-$70SiO_2$ composition. The high temperature IE treatments show the structure to relax, *i.e.*, have larger $\frac{1}{3}\Delta V_M^{\text{total}}$, significantly. Overall, in either reference state, bulk Li_2O (*see Eq. 3.5*) or K_2O (*see Eq. 3.6*), *lower* values of the LNDC should be equated with more compressive stress, rather than higher values per Eqs. 1.8 and 1.9.

The stress determined from Eq. 1.9 using the alternative B with bulk K_2O as the reference is shown in Fig. 3.17. In this alternative formulation, Eq. 1.9 does not include the negative sign in the front, to account for the change in perspective from K^+ dilation to K^+ contraction. The change in reference state gives a stress profile which matches quite well with the experimental profile measured from the Raman data

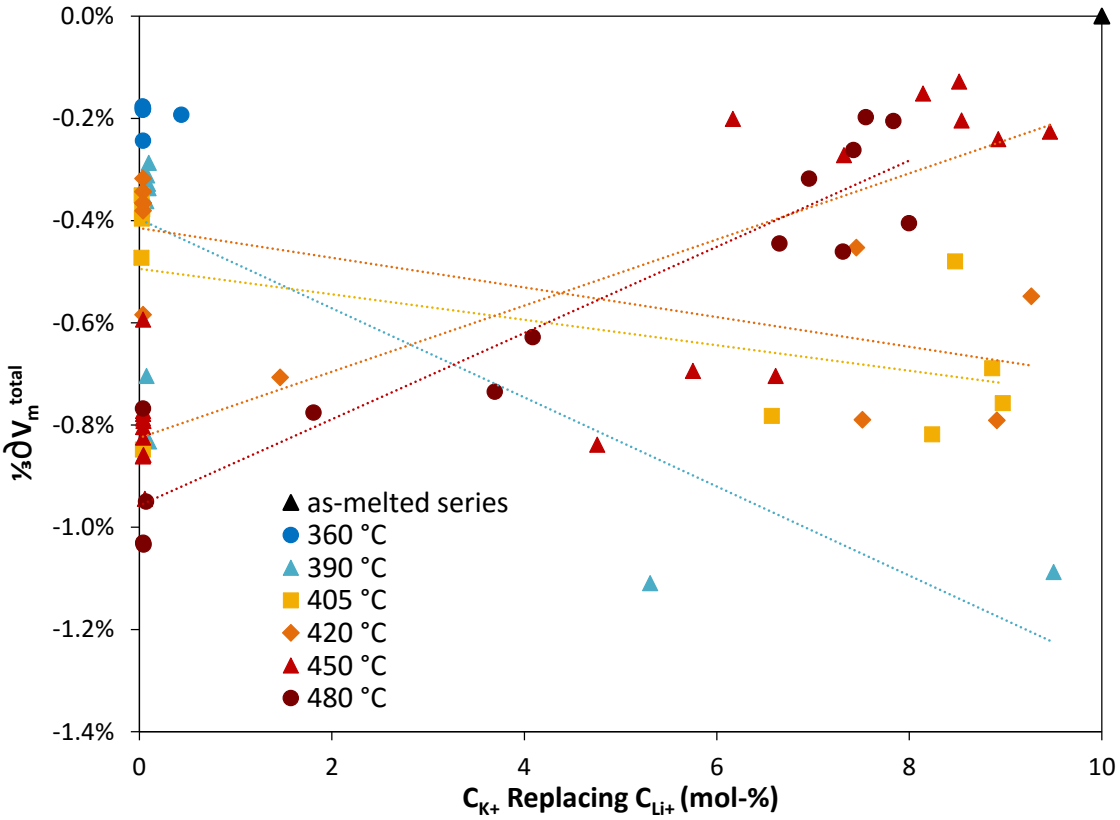

Figure 3.16: Determination of LNDC, B, using Eq. 3.6 and mol-% of substituting ion, K^+, (from WDS) for all IE temperatures, untreated (black) and 360–480 °C (dark blue–red).

(Fig. 3.13) as well as what is expected from literature: the stress maximum decreases and migrates inwards with increasing IE temperature. The change in sign for B allows for the complex behaviour expected in the stress profile. This reformulation ensures that a compressive stress or decrease in ${\Delta V_M}^{\text{total}}$ always exists for the ion interstice (although that may not be true at high IE temperatures like 450 and 480 °C) and most importantly allows the direction of the $\Delta V_M^{\text{network}}$ to be significant, rather than overwhelmed by the increase in ion volume when bulk Li_2O is used as the reference state.

As mentioned before the maximum achievable stress occurs when the most ion-exchange has occurred without expansion, thus, an IE glass with a similar molar

Table 3.5: LNDC or $B^{102,120}$, error (ΔB) and correlation-coefficient (R^2) calculated using bulk K_2O as the reference (Eq. 3.6 and Fig. 3.16) for as-melted series in comparison with IE glasses at increasing temperatures

Sample	B (mol-% K_2O)$^{-1}$	ΔB (mol-% K_2O)$^{-1}$	R^2
xLi_2O-$(30-x)K_2O$-$70SiO_2$	3.4×10^{-3}	2×10^{-4}	0.994
390 °C	-6×10^{-4}	3×10^{-4}	0.64
405 °C	-2×10^{-4}	1×10^{-4}	0.36
420 °C	-2×10^{-4}	2×10^{-4}	0.21
450 °C	7.7×10^{-4}	1×10^{-4}	0.75
480 °C	8.5×10^{-4}	8×10^{-5}	0.90

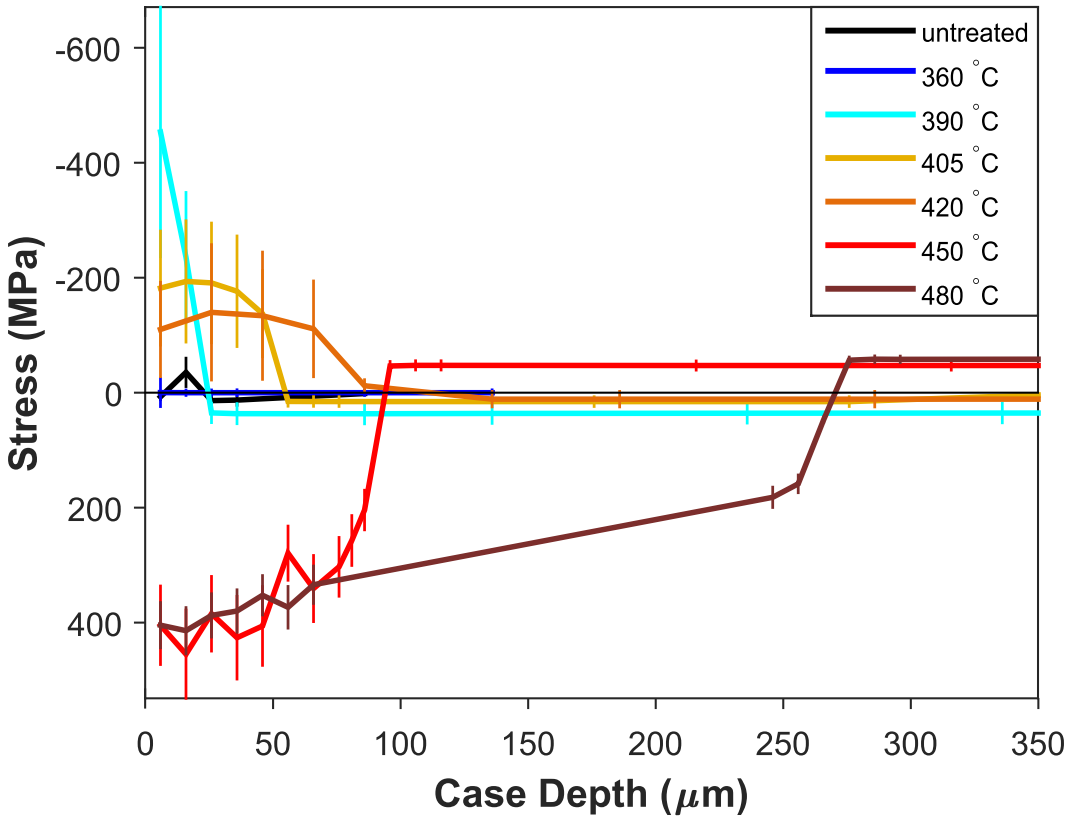

Figure 3.17: Stress determined from Eq. 1.9 and B when bulk K_2O is the reference state as a function of case depth for all IE-temperatures, 360–480 °C (dark blue–red) and untreated composition (black).

volume to the starting material should have the most enhanced mechanical properties. This condition puts a lower bound on possible molar volume, since the IE volume cannot be smaller than the starting volume as well as a corresponding higher bound on *possible* compressive stress. As a result, using a *bulk* as-melted glass system with a higher LNDC may appear beneficial to achieving more stress, since there would be a larger difference in molar volume between the starting and equilibrium structure. However, that difference is only the *possible* compressive stress, not necessarily what is achievable through IE. For example, let us consider two different glass systems, alkali aluminosilicate versus alkali silicate, where the LNDC of the *bulk* as-melted mixed-alkali aluminosilicate series in lower than the corresponding silicate series, yet the aluminosilicate series has higher, almost double, compressive stress.[118] It is possible to have a system where upon the addition of the larger ion, the molar volume of the IE glass is increasing at a slower rate compared to its as-melted equilibrium structure, only the *difference* between the two structures matters, so a system can still have a lower as-melted LNDC and higher compressive stress. Additionally, aluminosilicate crystals and glasses are known to be stiffer than corresponding silicate crystals[254] and glasses.[99,255] In fact, the higher stiffness of the aluminosilicate network may be responsible for its lower LNDC; a more rigid network may result in a smaller molar volume change as a function of mixed composition. Since stiffness converts strain to stress, it is important to consider the strain, i.e., the reduction in molar volume compared to the equilibrium structure, as well as the stiffness when determining the compressive stress. Thus, the structure with the most achievable stress must have the largest difference in V_M between the IE and equilibrium structure as well as the highest stiffness.

The difficulty with comparing these results with literature stems from the fact that experimental studies are limited to calculating B from the measured stress using

Eq. 1.8, so they obtain a higher B for a higher measured stress.[102,118] On the other hand, computational studies obtain B from the molar volume change in Eq. 1.8, however, these studies have great trouble calculating reasonable stresses, since IE glasses are "forbidden glasses" where the structure is not achievable through thermal routes alone.[116,117,123,256] The current study uniquely provides a method to experimentally determine the changes in molar volume of the silica network during the IE process which can be spatially compared to the expected compressive stress profile. Given that the compressive IE layer cannot be separated from the bulk, which is under low-level tension, it is difficult to use other techniques commonly used to measure density such as pycnometry. Considering that the IE layer is much less volume compared to the bulk, great care would have to be taken to ensure that the changes in the IE layer were being measured, furthermore, the spatial accuracy of Raman spectroscopy would be lost.

Nonetheless, proof of a lower LNDC for the IE glass in comparison to the as-melted value indicating higher compressive stress may be found in how the LNDC depends logarithmically on the amount of ion-exchange which has occurred. Many studies have considered the dependence of the LNDC on the starting fraction of K_2O in the untreated glass (larger starting K_2O-fraction means less IE can occur); the LNDC has been shown computationally[116,121,123] and experimentally[118] to vary more when only small amounts of alkali have been exchanged, while at high amounts of exchange, B is fairly constant. All other things being equal, time and temperature for each starting composition, the greatest compressive stress would be expected to be found at the largest amount of ion-exchange; this is also where B is not changing greatly with amount of IE. A structure with the most stress and an invariant B while exchange occurs would indicate a structure whose molar volume is unchanging despite larger ions being present. One computational study[123] found Young's modulus to depend

positively on the amount of exchange, i.e., concentration of K^+, despite B remaining constant at high amounts of exchange, proving further the most enhanced mechanical properties occur where the most ion-exchange has occurred *without* an increase in expansion. The explanation as to why B varies so much at small amounts of ion-exchange may simply be that there is some ability for the network to expand elastically and accommodate the larger invading ions, as is proposed by many authors[116,127,127], however, very quickly the critical volume is reached and the network must densify to accommodate the larger ions.

3.5 Summary

The structure of an ion-exchanged glass was probed using micro-Raman spectroscopy and compared to the compositionally-equivalent as-melted mixed-alkali series, xLi_2O-$(30-x)K_2O$-$70SiO_2$. The Q^ndistribution in the IE glasses exhibited conversion of Q^2-units and Q^4-units to Q^3 as IE progressed, additionally, a net conversion of BOs to NBOs was observed at temperatures near or above T_g . The identified Raman peaks were shown to shift the most for high-temperature samples, indicating a positive correlation between temperature and structural modifications. Additionally, the low-frequency region Raman peaks known to correlate with external Si-O-Si bond angle showed a decrease in bond angle for Q^2 and Q^3-units as a function of K^+ concentration or exchange depth, a maximum of $-9.4°$ (-7.3%) and $-3.3°$, (-2.4%), respectively for the lowest IE-temperature where exchange occurred, 390 °C. On the other hand, the peaks corresponding to Q^4 $\angle$SiOSi did not change significantly following ion-exchange. The high-frequency region peaks showed an increase in wavenumber, indicating a slight shortening of average Si-O bond-length for Q^2 (-0.02%) and Q^3-units (-0.1%) and substantial lengthening in Q^4-units ($+2.9\%$) at high temperatures, while low-temperatures and far enough from the IE surface in high-temperatures displayed

much less significant modification of the $\langle d(\text{Si-O})\rangle$.

The calculated $\angle$SiOSi and $\langle d(\text{Si-O})\rangle$ were used to calculate the Si$\cdots$Si separation, which was treated as being equivalent to network molar volume. By comparing the IE samples with the untreated material, $30Li_2O$-$70SiO_2$, the reduction in network molar volume was used along with the bulk modulus to determine the compressive axial stress, which exhibited trends similar to experimental stress profiles. The subsurface maximum stress both decreased and migrated inward as temperature increased. Additionally, the calculated maximum stress was similar to reported values and was found at the lowest temperature where significant IE occurred. A two-step structural modification process is proposed, where at low-energy conditions, i.e., well below T_g or at low concentrations of substituting ion, the network tetrahedra collapse towards each other, leading to reduction in Si$\cdots$Si separation or silica network volume; however, above the energy-threshold, the Si-O bonds lengthen in order to relax some of the compressive stress which leads to a much less-reduced network molar volume. This analysis has demonstrated that micro-Raman spectroscopy could be used as a rapid in-situ measurement tool for the determination of stress in IE glass.

When the increase in cation interstice size was included in the molar volume calculation, LNDCs for the IE glasses were determined and found to match those reported in literature. Additionally, a second stress profile was determined using the LNDCs, showing more clearly that the LNDC model overestimates stress at temperatures near or above T_g and underestimates it when well below T_g. Since the LNDC depends directly on molar volume, it does not account for the first-step in the structural rearrangement process, i.e., the reduction of the network molar volume due to compressive stress. The current LNDC model uses the bulk lithium silicate structure as the reference equilibrium state, however, when bulk potassium silicate was used instead, a more realistic stress profile was obtained. This change of reference state

demonstrates how an IE glass with a *higher* LNDC has relaxed towards to the equilibrium state and will have *less* compressive stress, rather than more σ as is currently predicted. The maximum *possible* stress exists when the most ion-exchange has occurred without expansion, however, the *actual* compressive stress is a function of the *difference* between the molar volume of the IE and equilibrium structure as well as the stiffness of the network. The underestimation of stress in IE glass by the LNDC model could have important implications for the prediction of stress in commercial IE glass.

Overall, the Raman data show evidence for two different structural-alteration regimes for a lattice under compression: decreased external Si-O-Si bond-angles followed by increase in Si-O bond-length. This may indicate a limit of the maximum stress achievable through ion-exchange; it appears that once the strain limit is reached, the material relaxes and reduces the compressive stress accordingly. Moreover, the higher temperatures required to exchange the ions deeper into the material could aid structural relaxation. Nonetheless, this phenomenon may be unique to silicate structures and other glass network-formers, such as aluminosilicates which show twice the compressive stress, should be examined for similar trends.

Chapter 4

Mechanical Response of the Surface of Ion-Exchanged Lithium Silicate Glass[i]

4.1 Background

Although the mechanical advantages conferred by the IE process are well-exploited, the elastic properties *at the surface* are not well-characterised. The goal of this chapter is to establish the effect of compressive stress and compositional variation on the mechanical properties stiffness and hardness *within the IE layer*. Given the significance of the surface condition with respect to breaking strength, it is important to understand how the IE process and resulting compression change both the elastic and plastic response of the material at the surface.

Although it is expected that IE will improve the stiffness and hardness, it is difficult to know by how much and the reason for this improvement. The treatment has been known to enhance strength,[101] however, as discussed earlier, this property is dependent on several factors, stiffness being only one. Conversely, hardness of IE glasses has been well-studied and a 8–20% increase is expected.[162,258] Although both stiffness and hardness pertain to a material's ability to resist deformation, the main difference is that the former is entirely elastic, while the latter contains both elastic

[i]This chapter was adapted from Calahoo *et al.*[257] ICP-OES, SEM-WDS, DSC and nano-indentation experiments were performed by Dan Chevalier, Dr. Dan MacDonald, Dr. Cathy Whitman and Dr. XiaoFang Zhang, respectively, while sample preparation, bulk mechanical experments, data analysis and writing of the manuscript was done by the author.

and plastic deformation components.[259,260] Nonetheless, because glass is a brittle material indentation mostly probes the elastic response; in fact, Oyen[260] determined from nano-indentation data that the deformation resistance was 84% elastic and 14% plastic for fused silica.

In glasses containing more than one type of alkali, a concurrent reduction in ion mobility[261] and increase in hardness[46] due to the mixed-alkali effect is known to occur. The IE process is expected to produce similar structural changes whereby ion movement is hindered leading to a decrease in plasticity and increase in hardness. Additionally, the compressive stress is likely to limit the mobility of the glass network and ions further, increasing hardness again. In general, the stiffness of a material increases upon compression.[262,263] Finally, compression increases the effective tensile strength of a material as external tensile forces must perform work against the compression in order to return the material to an unstressed state. Densification of the glass network is expected from IE, likely leading to higher bond density as well.

4.2 Experiments

In order to investigate the effect of ion exchange on mechanical properties *near the surface*, simple binary $30Li_2O$-$70SiO_2$ glasses were prepared and ion-exchanged with K^+ and were subsequently polished upon one face to expose the composition profile of the IE layer. Furthermore, to better understand the temperature dependence and thermal relaxation of stress, the IE procedure was performed at several different temperatures, ranging from well below to above the glass transition temperature, T_g, of the starting composition. The same IE glasses studied in Chapter 3 were used in this Chapter, please Section 3.2 for further experimental details and Section 3.3.1 for compositional analysis. Additionally, the corresponding bulk as-melted mixed-alkali series

($x\mathrm{Li_2O}$-$(30-x)\mathrm{K_2O}$-$70\mathrm{SiO_2}$) was synthesized and its mechanical properties were determined using the ultrasonic method and micro-hardness indentation (Sections 1.2.2 and 1.2.3, respectively).

Nano-indentation was then performed by Dr. XiaoFang Zhang on the IE glasses to obtain the stiffness and hardness as a function of case depth and IE temperature. Please see Section 2.6.3 for a detailed explanation of the indentation procedure.

4.3 Results

4.3.1 Displacement Plots

Plots of stiffness or hardness vs. displacement into the surface are shown in Fig. 4.1 for the edge of the sample exchanged at 390 °C. These plots readily show the transition from the surrounding epoxy to the glass sample. For clarification purposes, there are two types of distance being discussed; there is indent depth or displacement into surface, which is between 100–2000 nm, contrasted with lateral distance from the sample edge or case depth, usually between 5–100 μm. In the displacement depth plots of 390 °C (Fig. 4.1), indents 1 & 2 were made on the epoxy, measuring stiffness and hardness values of $\leq$ 10 and $\leq$ 0.25 GPa, respectively. Next, indent 3 shows where the tip first measures the epoxy and then at a larger displacement contacts the glass sample. Conversely, indent 4 in Fig. 4.1 was on the glass, yet near enough to the interface that the glass is weak and appears to fail at large penetration depths, $>$ 1400 nm.

Continuing with increasing indent number or lateral distance from the edge, indents 5 and 6 demonstrate larger-than-expected Y and H values at low indent depths, 100–600 nm, and then significantly lower Y and H values for larger displacements

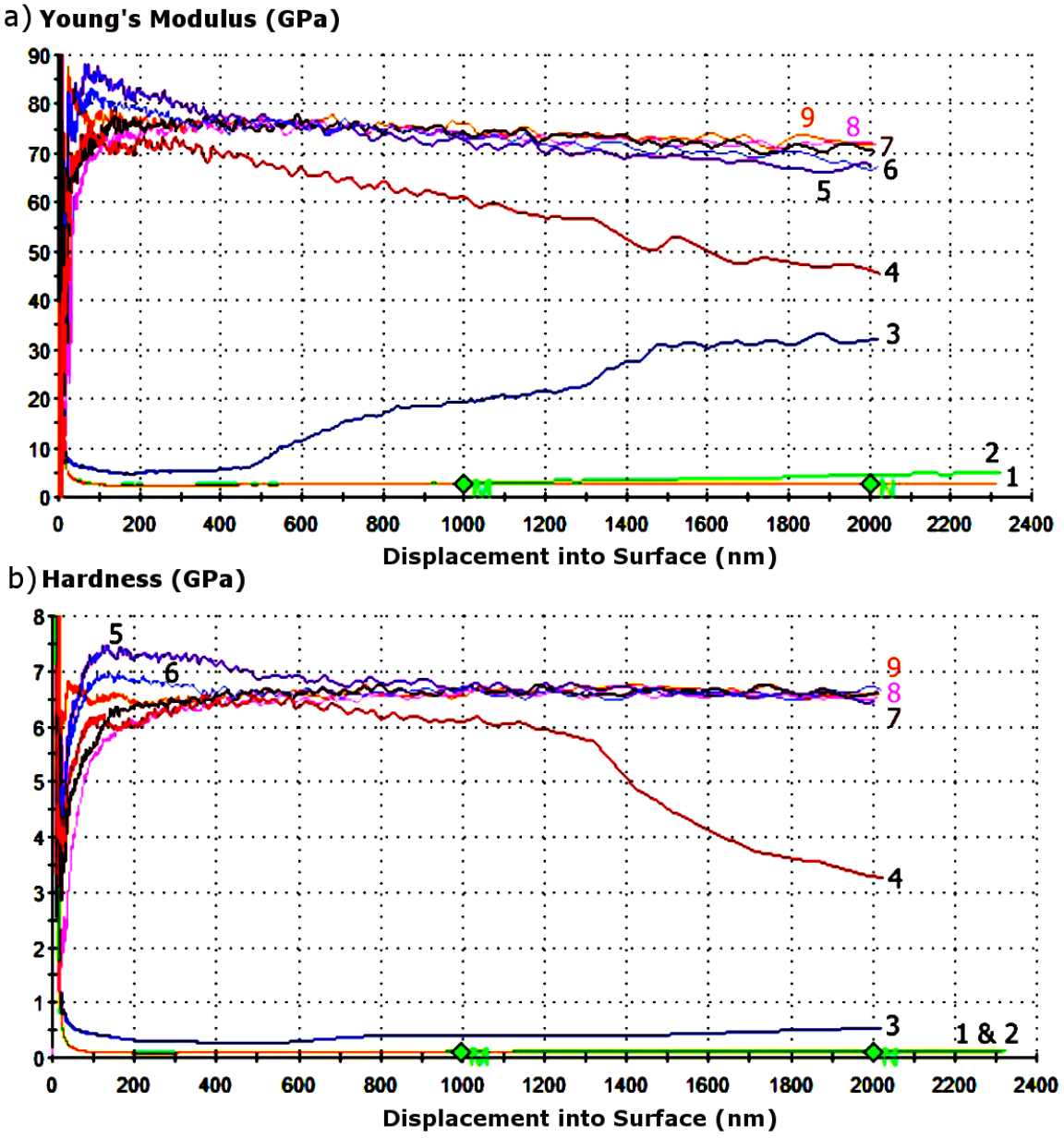

Figure 4.1: Young's modulus (a) and hardness (b) vs. displacement into surface for the 390 °C IE sample. Indents 1 and 2 were made on the epoxy surrounding the sample, indents 3 and 4 were made on the epoxy-glass interface, and indents 5–9 were made on the glass. Additional plots of Young's modulus and hardness as a function of displacement for each sample are available in Appendix B.

into the surface, 1500–2000 nm. A downwards slope with increasing indent depth is ISE behaviour, although normal ISE behaviour usually stops above a certain indent depth, after which a displacement-independent value is obtained. In this case, a sharper slope is found between 100–500 nm, while a shallower slope continues for the remainder of the depth of the indent (500–2000 nm). As mentioned in Section 2.6.3, an ISE is not expected in IE glasses for indents deeper than 500 nm,[162] so it may be that the steeper slope found between 100–500 nm is the typical ISE, however, without more information, the behaviour will be called ISE-*like*.

At higher indent numbers (7–9), *i.e.*, further from the edge, hardness no longer shows an ISE-like behaviour, *only* stiffness maintains the downwards slope. WDS analysis showed [K_2O] to be significant in the 25 μm nearest the edge, thus, indents 8 and 9 are likely near the end of the IE layer. Although they are not shown, indents made past the case depth do not possess this type of behaviour—that is, the Young's modulus and hardness are independent of indent depth (for penetration depths greater than 200 nm) outside of the IE layer. Other IE temperatures (420–480 °C) can be found in Figs. B.2, B.3 and B.4, respectively, in Appendix B. In contrast, Young's modulus as a function of indent depth for the middle of the untreated sample, $30Li_2O$-$70SiO_2$, is reported in Fig. B.1 in Appendix B; it shows a constant stiffness value past an indent depth of 200 nm.

Although only one displacement plot is shown (Fig. 4.1) all other IE temperatures were found to show this decrease in Young's modulus and hardness (near the edge *only*) with increasing penetration depth within the IE layer as well. This ISE-like behaviour could be caused by several factors. First, as discussed earlier, nano-indentation assumes that no pile-up of the material occurs around the indent; if pile-up occurs, it has been known to result in erroneously large H values.[163] The empirical rule developed by Pharr can be used,[161] where if the final-to-maximum

displacement ratio is less than 0.7, no pile-up is expected for the indent. Essentially, the lower limit of h_f/h_{max} corresponds to fully elastic behaviour, while the upper limit indicates plastic deformation.[264] Fig. 4.2 shows the displacement curve for the 390 °C sample, demonstrating that pile-up is expected for indents 3–4, since the final displacement after unloading is more than 0.7 of the maximum displacement, while pile-up is *not* expected for indents 5–10. The shape of indent 4 is similar to that seen for a multi-layered material with a harder layer on top.[160] This agrees with what was observed in WDS images of the indents; when indents were made completely on the glass no evidence of pile up, however, indents straddling the epoxy-glass interface were seen to have pile-up, even on the glass side. The other IE temperatures, 405–480 °C, showed similar behaviour in the displacement curves and WDS images, thus pile-up is not the reason for ISE-like behaviour when indents are made at least 10 μm from the sample edge.

Tilting of the indenter tip, which can be caused by an incline of the surface resulting from polishing, can also increase measured Y and H. An example of this is seen clearly for indent 2 (green) in the 480 °C sample (Fig. B.4 in Appendix B) where based on studies of effects of tip tilting,[163] the tilt can be estimated to be 10°. It is also possible that tilting could occur from the compositional gradient found in the IE glasses resulting in varying degrees of stiffness or hardness on opposite sides of the indenter tip. However, the ISE-like behaviour is found even when the compositional gradient is small relative to the indent size; elemental analysis from WDS reveals a plateau of fairly constant mixed-alkali composition, approximately $10K_2O$-$20Li_2O$-$70SiO_2$, in the IE glasses over several of 10s of microns. Only the the tail-edge of the diffusion profile is likely to have a steep compositional gradient. Finally, the micrographs also show the indents to be symmetric, not asymmetric as would be expected from a tilted indent. Consequently, it appears unlikely the ISE-like

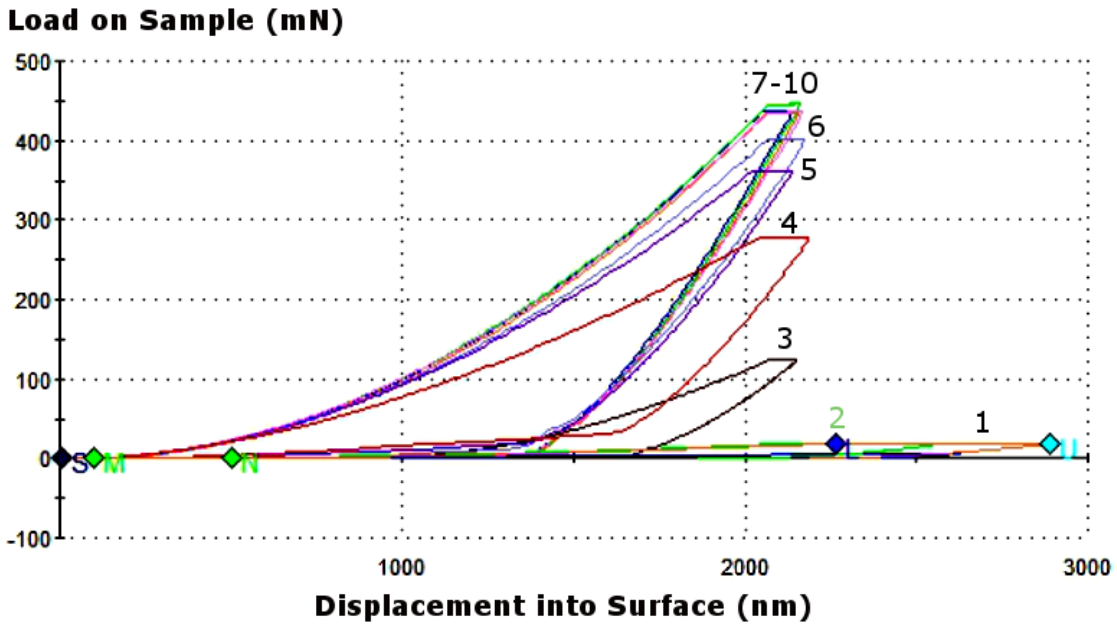

Figure 4.2: Load-displacement curve produced from nano-indentation for the 390 °C IE sample. Indents 1 and 2 are clearly on the epoxy, while indents 3 and 4 are near the epoxy-glass transition, likely indent 3 is on the epoxy, while indent 4 is on the glass, but near the sample edge (< 10 μm). Indent 5–8 are fully into the case depth of the IE glass, while indents 9–10 are likely past the case depth and into the untreated region of the IE sample (known from WDS results).

behaviour in the IE layer could be a result of the compositional gradient. Nonetheless, since it is possible that the sample is sloped at the edge from polishing and there was piling up observed around indents made along the epoxy-glass interface, a possible error of 6–10%[163] was estimated for the Y and H data measured within 20 μm of the sample edge (as seen in the following case depth plots).

4.3.2 Case Depth Dependence

Since samples exchanged at all IE temperatures displayed ISE-like behaviour far enough from the sample edge where no pile-up or incline from polishing was expected, the mechanical properties were evaluated over two indent depth ranges: a shallow (150–300 nm) and a deep (1500–2000 nm) displacement. The indent shape is the same for both displacements, only the depth range over which the mechanical values are averaged is different. Fig. 4.3 shows the stiffness as a function of case depth for a deep indent; each data point is a different indent further from the edge of the sample and the penetration into the surface of each indent is deep (1500–2000 nm). The "zero" was set for each IE temperature at the beginning of the sharp increase in stiffness, however, due to sampling resolution, the actual epoxy-glass interface may be shifted 2–5 μm to the right.

First of all, the stiffness of the untreated ($30Li_2O$-$70SiO_2$) composition (70 GPa) matches the value measured ultrasonically for the bulk sample (75 GPa). Valid nano-indentation is reported to have an accuracy of better than 10% when compared to bulk values.[265] Strikingly, the untreated sample is much more compliant in the 30 μm nearest the sample edge. This is likely because there are fewer constraints, such as bonding to the rest of the bulk material, at the edge. Several studies have examined nano-indentation near an interface or free edge;[266–269] they found that the material's

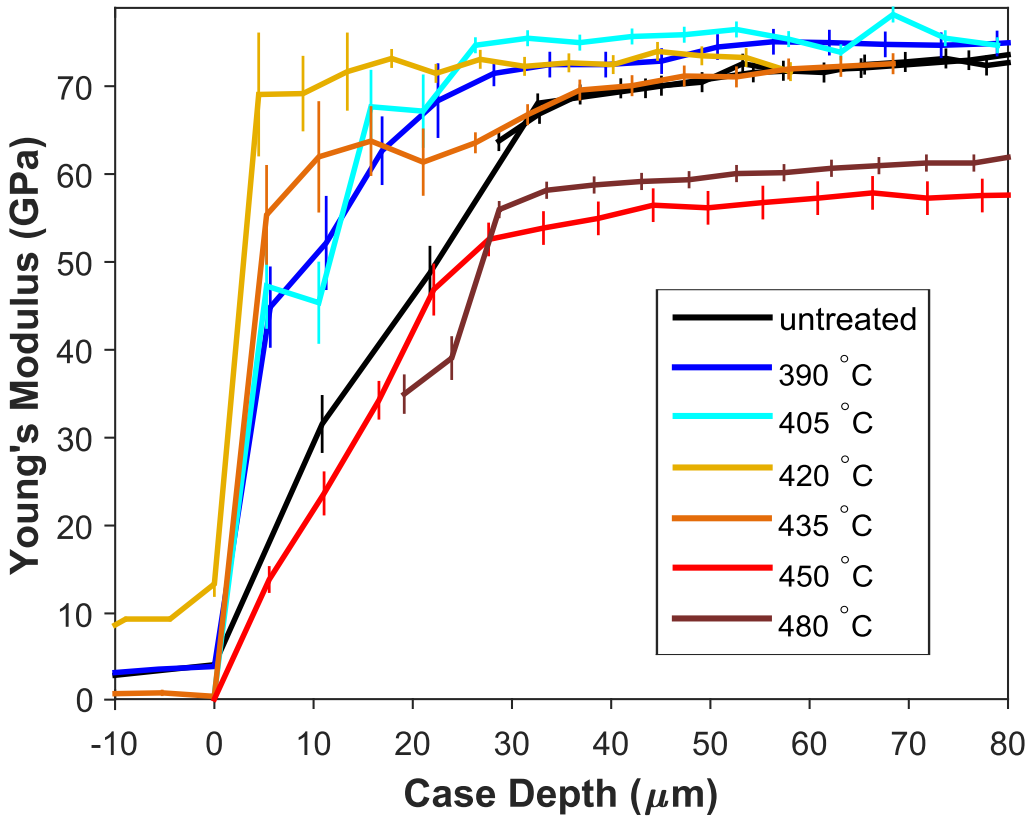

Figure 4.3: Comparison of the Young's modulus for all IE temperatures, 390–480 °C (dark blue–dark red) with two untreated (black) lithium silicate glasses, at a *deep* displacement depth of 1500–2000 nm.

mechanical properties were somewhere between those of the two phases. For example, indenting a polymer matrix near a glass fibre leads to increased apparent elastic modulus, while indenting the same polymer near a free edge caused a decrease in apparent elastic modulus.[268] More importantly, the stiffness and hardness of fused silica were seen to decrease linearly when indented near a free edge.[266] Although indentation is occurring in the glass near epoxy, the large disparity in mechanical properties between glass and epoxy is similar to a free edge.

Jakes *et al.*[266] attributed the lower Y to an additional effect called *structural compliance*, which is negatively correlated with distance from the sample edge while being independent of the depth of the indent. When the material is more compliant and plastic (as will be shown), it is possible that the assumptions which are integral to determining mechanical properties from nano-indentation may break down since they presume an elastic response. However, Jakes *et al.* used atomic force microscopy to image the indents, thereby, proving the material is less stiff and hard near an edge—it is not an artefact of the continuous depth-sensing analysis.

Low IE temperatures, 390–405 °C, enhance the stiffness near the edge (0–30 μm) and even have higher Young's moduli in comparison to the untreated sample beyond that first 30 μm (Fig. 4.3). This second result is somewhat surprising for the 390 and 405 °C samples, since the stiffness is enhanced past the depth of the IE layer as determined by WDS. Possibly the additional thermal treatment for 72 hours led to densification and increased Y.

The sample exchanged at 420 °C shows the most complex behaviour; it has the most improved stiffness nearest the edge, but then appears to rejoin the Young's modulus of the untreated sample around 55 μm (approximately where the IE layer ends). The sample exchanged at 435 °C shows a very similar behaviour, only with

less enhancement near the edge. It is somewhat surprising that samples exchanged at these middle IE temperatures, 420 and 435 °C, appear to be returning to the baseline Young's modulus of the untreated sample, when both of these samples are in fact mixed-alkali within the case depth for the data shown. They do not have the Y expected for an as-melted mixed-alkali composition, as Y was observed to decrease with the addition of K_2O in the bulk Li_2O-K_2O-SiO_2 series. Instead these IE temperatures appear to have similar stiffnesses to the starting material, 30%Li_2O, perhaps indicating some, but incomplete relaxation of the compressive stresses due to thermal treatments near, but still below T_g (465 °C).

Finally, samples exchanged at 450 and 480 °C demonstrate the result of significant thermal relaxation—that is, there is no improved Y near the edge and the final Young's modulus is well below that found for the untreated sample. In fact, the stiffness for these two samples, 55–60 GPa, is lower than expected from the measurements on the compositionally equivalent bulk glass, 72 GPa. In part, this discrepancy may be due to heating the glass well-above its initial fictive temperature ($T_f \approx 415$ °C). Additionally, cracking was observed between the indents in the sample exchanged at 450 °C, which may contribute to it having *lower* stiffness than the sample exchanged at 480 °C.

The stiffness as a function of case depth averaged over a shallow indent range (150-300 nm) is shown in Fig. 4.4. The trends are very similar as those seen for the deep indent data (Fig. 4.3), albeit somewhat noisier. IE temperatures well-below T_g, 390–435 °C, show enhanced stiffness near the edge in comparison with the untreated sample, while samples exchanged at high temperatures, 450 and 480 °C have stiffnesses below that of the untreated material (as expected for the corresponding as-melted mixed-alkali compositions). The main difference is that *all* samples, even the untreated composition, are much stiffer near the edge (first 30 μm) at shallow

indent depths. Additionally, the stiffness values measured here are 13–40% higher than those averaged over deep displacements, demonstrating the ISE-like behaviour seen in the displacement plots in Fig. 4.1. Finally, samples exchanged at low temperatures, such as 390 and 420 °C, have high stiffnesses near the edge (0–15 μm), perhaps indicating more pronounced ISE-like behaviour in this region, in addition to agreeing with the results from face-on nano-indentation (Table 4.1).

Table 4.1 also contains the hardnesses from micro-indentation for the untreated and IE samples. As expected, IE improved the mechanical properties, however, the trends in hardness are different whether nano- or micro-indentation was used. In comparison with the untreated sample, IE temperature 390 °C shows increased hardness during face-on nano-indentation, yet a decrease in H_{V} when micro-indentation is performed. Conversely, the sample exchanged at 420 °C shows the opposite trend; nano-indentation indicates a degraded hardness, while micro-indentation shows improved H. Both indentation techniques begin to measure decreased stiffness and hardness at high IE temperatures, 435–450 °C.

Table 4.1: Average Y and H from face-on (before removal of IE layer) nano-indentation of the middle of the sample in comparison to H_{V} from micro-indentation

Sample	Y (GPa)	H (GPa) (nano)	H_{V} (GPa) (micro)
untreated	74.9(5)	6.65(5)	5.2(1)
390 °C	78.9(4)	6.91(4)	5.07(6)
405 °C			5.4(1)
420 °C	77.0(8)	6.0(1)	5.25(8)
435 °C			5.1(1)
450 °C	67.7(9)	5.2(1)	

Fig. 4.5 displays the hardness as a function of case depth averaged over a deep displacement (1500-2000 nm). In this case, the "zeroes" were set from the Y data in Fig. 4.3, thus, it is possible to compare the stiffness and hardness data at the same case depth since they come from the same indent. As expected, the untreated composition is softer near the edge (0–30 μm) than at the middle of the sample. The

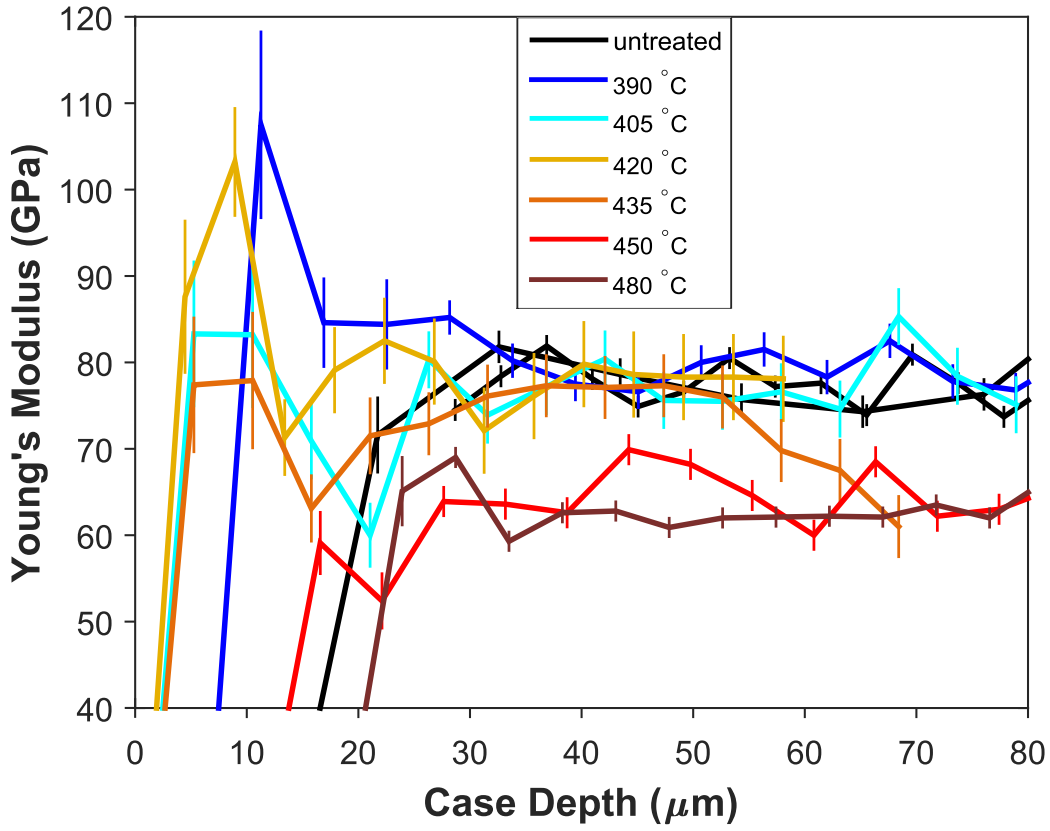

Figure 4.4: Comparison of the Young's modulus for all IE temperatures, 390–480 °C (dark blue–dark red) with two untreated (black) lithium silicate glass samples, at a *shallow* displacement depth of 150–300 nm.

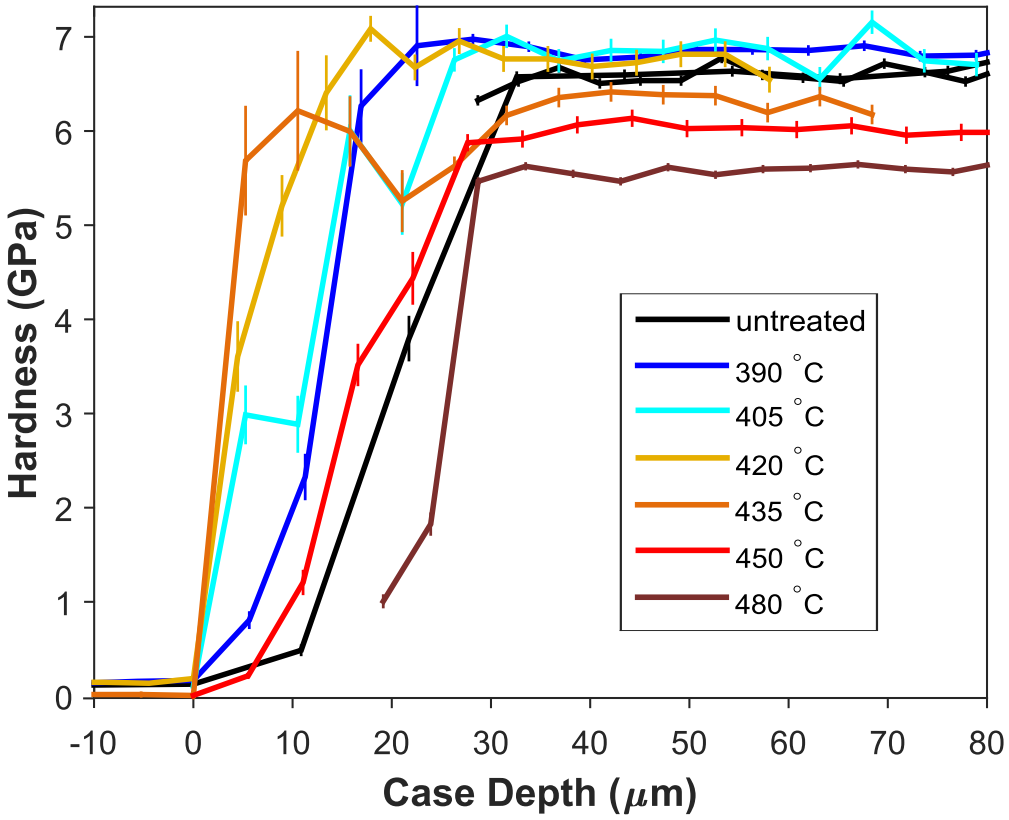

Figure 4.5: Comparison of the hardness for all IE temperatures, 390–480 °C (dark blue–dark red) with two untreated (black) lithium silicate glass samples, at a *deep* displacement depth of 1500–2000 nm.

nano-hardness of the 30% Li_2O sample is significantly higher than what was found by micro-indentation of the bulk composition, 6.5 vs. 5.2 GPa. Although this is a large discrepancy (25%), the load is known to greatly affect the hardness values obtained due to the ISE.[34] In fact, nano- vs. micro-indentation has been seen to have a difference of 22% for IE glasses,[162] and 10–440% for other materials.[270,271]

In terms of the effect of IE temperature, the hardness data have strikingly similar trends to the stiffness data; the low IE temperatures (390 and 405 °C) are harder near the edge and beyond the case depth, the middle IE temperatures (420 and 435 °C) offer enhanced hardness near the edge *only*, while the high IE temperatures (450 and

480 °C) are thermally relaxed ($T >> T_f$) and have lower hardness throughout their case depths, as was observed by Svenson *et al.*.[272] The notable differences are that the 435 °C sample has higher hardness near the edge, yet lower hardness further into the case depth, both in comparison to the hardness of the untreated composition. Additionally, as expected the 480 °C sample is softer than the 450 °C sample. It appears that an IE temperature of 420 °C is a turning point, after which the hardness decreases predictably with increasing IE temperature. Based on the composition profiles from WDS, the case depth where the hardness of IE samples matches the untreated is approximately where the IE layer ends without the lag observed in the Young's moduli measurements in Fig. 4.3.

The hardness data as function of case depth averaged over a *shallow* indent depth (150–300 nm) is shown in Fig. 4.6. Temperatures below T_g (459 °C) where significant IE occurred, 390–435 °C, show increased hardness compared to the untreated sample *near the edge*, however, the hardnesses decrease with increasing case depth until they are approximately equal to the untreated value. Conversely, temperatures near or above T_g, 450 and 480 °C, show decreased hardness compared to the untreated sample throughout the case depth. Additionally, the low-temperature IE sample (390 °C) has the largest increase in hardness which agrees with the results from nano-indentation done perpendicular to the IE layer (Table 4.1).

4.3.3 Normalization

To quantify the improvement in mechanical properties induced by IE, the data were normalized with respect to the untreated composition, Y/Y_0 and H/H_0, and is plotted in Figs. 4.7 and 4.8, respectively.

These figures demonstrate the improvement of stiffness and hardness compared

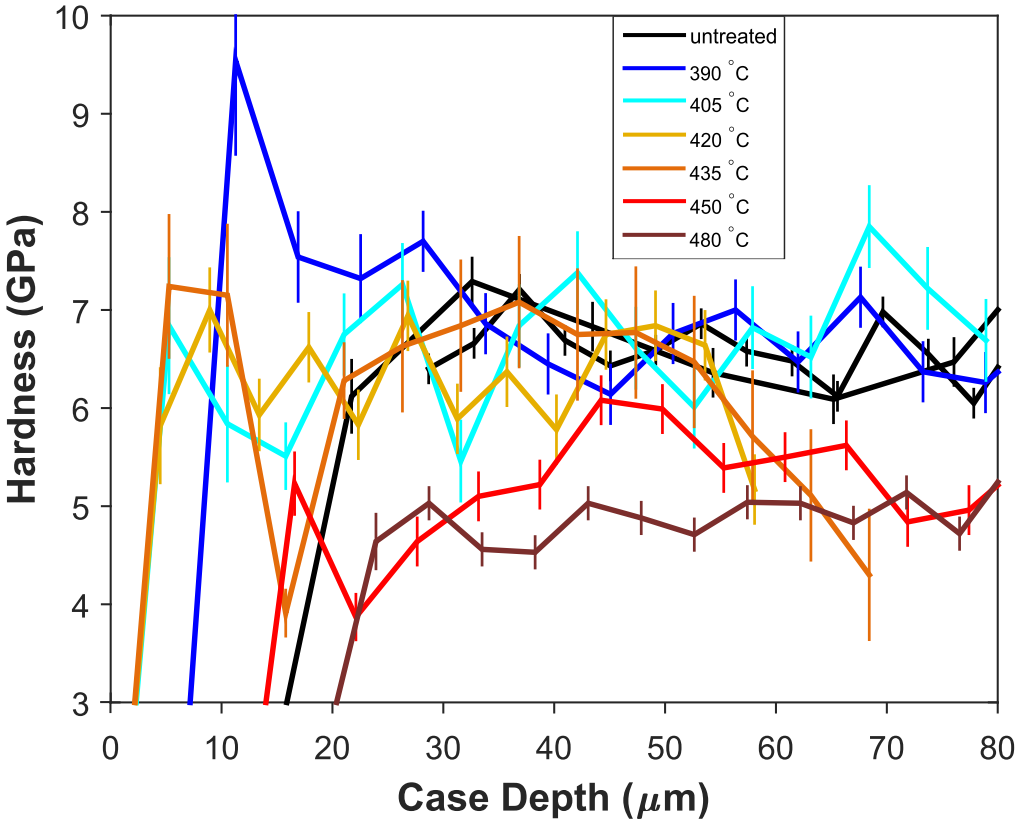

Figure 4.6: Comparison of the hardness for all IE temperatures, 390–480 °C (dark blue–dark red) with two untreated (black) lithium silicate glass samples, at a *shallow* displacement depth of 150–300 nm.

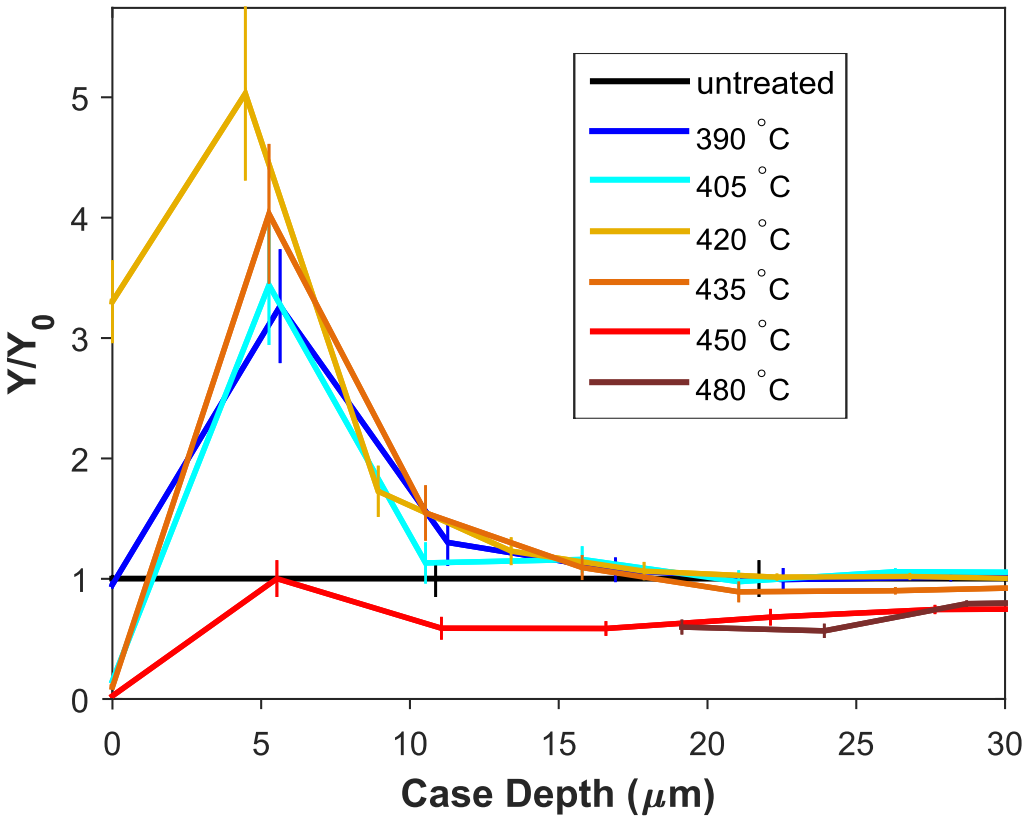

Figure 4.7: Improvement in Young's modulus in comparison to the untreated lithium silicate glass (Y/Y_0) as a function of case depth for all IE temperatures, 390–480 °C (dark blue–dark red). Only deep indent data (1500–2000 nm) were used. Values above unity indicate enhancement, such as for IE temperatures below T_g (459 °C) where significant IE occurred, 390–435 °C, while high IE temperatures, 450 and 480 °C, saw significant thermal relaxation and have values below one, signifying decreased stiffness.

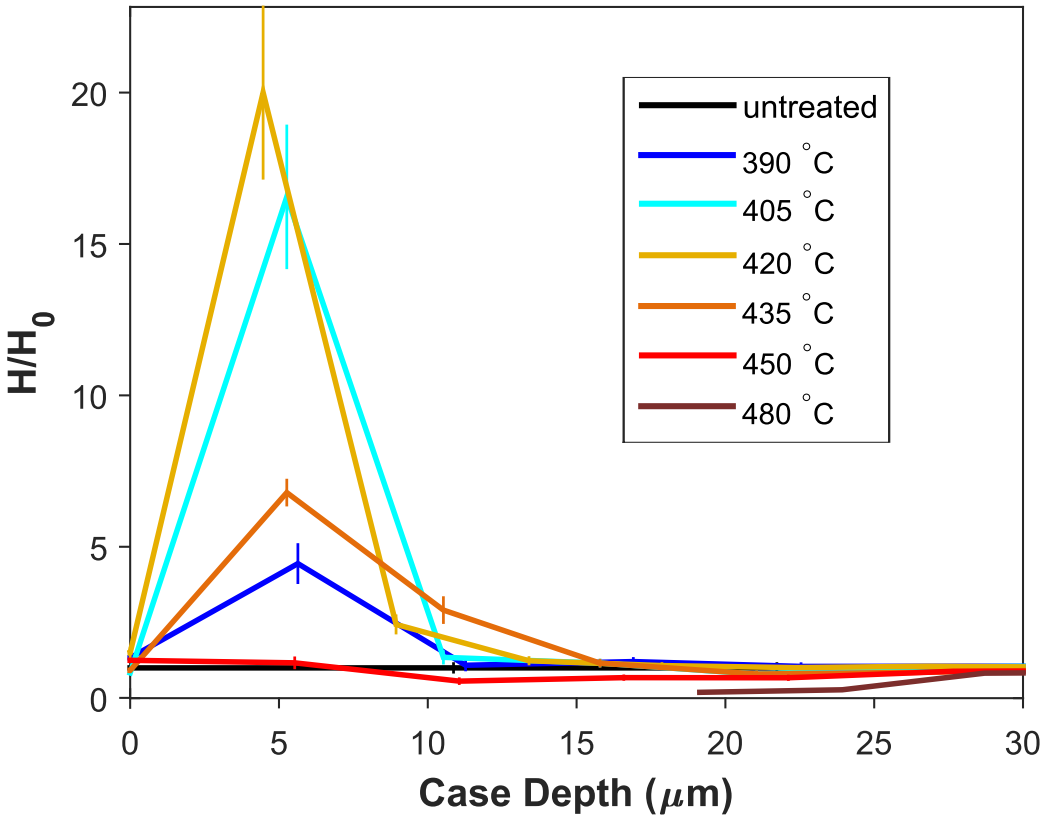

Figure 4.8: Improvement in hardness in comparison to the untreated lithium silicate glass (H/H_0) as a function of case depth for all IE temperatures, 390–480 °C (dark blue–dark red). Only deep indent data (1500–2000 nm) were used. Values above unity indicate enhancement, such as for IE temperatures below T_g (459 °C) where significant IE occurred, 390–435 °C, while high IE temperatures, 450 and 480 °C, saw significant thermal relaxation and have values below one, signifying reduced hardness.

to the untreated composition at the same case depth. First, all of the improvement is in the first 25 μm nearest the edge. Secondly, IE temperatures below T_g where compressive stress is expected (390–435 °C) have normalized mechanical properties greater than unity, while high IE temperatures (450 and 480 °C) have Y/Y_0 and H/H_0 values below unity, indicating degraded mechanical properties. Both of these observations are expected from the deep indent data in Figs. 4.3 and 4.5, however, the normalization plots clearly indicate that hardness has improved vastly in comparison to the stiffness near the sample edge. Hardness was seen to improve 5–20 times, while stiffness has only a 3–5 fold enhancement compared to the mechanical properties of the untreated composition.

4.4 Discussion

Generally, the IE process appears to negate the free edge effect, *i.e.*, Y and H near the edge approach similar values to those found in the middle of the untreated composition. IE at 420 °C gives the most enhancement in Y near the immediate edge, while the low IE temperatures 390 and 405 °C result in higher Y values further into the case depth (Fig. 4.3). It is possible that the improvements in stiffness are due to high compressive stresses found at low thermal treatments and possible crack healing known to occur as a result.[273] For an industrial piece of float-glass, cracks are typically on the order of 10 μm in depth.[101] Thus, based on Griffith's work,[29] the sample exchanged at 420 °C is expected to arrest cracks at higher stresses, *i.e.*, be stronger, than the other IE samples. Conversely, the IE temperatures 390 and 405 °C result in higher Y after the first 10 μm, thus, they would likely arrest deeper cracks most effectively. However, the trends seen for Y in Figs. 4.3 and 4.7 are different from those observed in compressive stress.[105,272] In a separate experiment micro-Raman spectroscopy was used to determine that IE temperature 390 °C has the highest compressive stress,

while the 405 and 420 °C samples have lower compressive stresses spread over a wider case depth.

Although bulk modulus (volumetric stiffness) depends linearly on pressure,[262] it is not immediately clear how the uniaxial stiffness will behave; for a brittle material, it is difficult to measure the changes in Y as a function of pressure. As a result, nanoindentation of IE glass actually offers a unique example of measuring the effect of compression on Y. Young's moduli of borates and borosilicates show a strong dependence on isostatic pressure, increasing by 10% with only 500 MPa of applied pressure.[274] However, even at low pressures, borates are known to undergo a structural change from BO_3 to BO_4 units[275] leading to a more constrained network and increased rigidity.[276] In contrast, no significant structural transformation is expected in SiO_2, as no permanent densification was observed for pressures up to approximately 10 and 2 GPa for pure silica and $10Na_2O$-$90SiO_2$, respectively.[277]

However, it is important to recognize compressive stress is not expected to change the stiffness greatly; for most materials, the bulk modulus (K) has only a small dependence on pressure (P), where $K(P) = K(0) + 4P$ (for isostatic stress, $\sigma = 3P$).[262] Thus, if there were an axial stress of 500 MPa in the IE glass, an increase of only 2 GPa would be expected in K. Assuming that Poisson's ratio (μ) remains approximately constant under compression, this translates to an increase of only 3 GPa for Y. Yet, the deep indent plots of Y and H show enhancements of 20–40 GPa near the edge (0–30 μm) and 5–8 GPa further into the case depth. It is important to remember there are also compositional effects from the MAE occurring in these glasses; a mixed Na-Li silicate system was seen to increase Y up to 36% in comparison to the single alkali end-member.[46] Although compression may be affecting the stiffness, the MAE likely plays a larger role.

Evaluating hardness, the 405 and 420 °C samples are the most improved near the immediate edge (0–10 μm), while the samples exchanged at 390–405 °C have higher hardnesses further into the case depth. Once more these results do not align with the trends found for face-on nano-indentation and compressive stress; the 390 °C sample would be expected to have the highest hardness especially near the edge. This disagreement is more surprising for hardness, as it is expected to strongly depend on compressive stress. Indentation hardness involves plastic deformation in directions perpendicular to the load, therefore, shear stresses (which has both compressive and tensile components) must occur. Consequently, compressive stress increases hardness simply by forcing the tensile stresses to first overcome the opposing compressive stress *before* deforming permanently. However, the MAE is known to limit ion mobility and improve the hardness compared to the single-alkali end member, even more than the stiffness (47%).[46] Thus, compositional effects could be responsible for some of the observed enhancement as well as the differences between trends in Fig. 4.8 versus compressive stress.

Comparing the results when nano-indentation was performed perpendicular to the case depth (Table 4.1) versus when it was performed along the cross-section (Figs. 4.3 and 4.5), the sample exchanged at 390 °C showed similar improvements in both cases, while the 420 °C sample did not. IE temperature 420 °C saw improvements in both stiffness and hardness in the side-on case, yet face-on measurements showed only Y to be higher, while H was actually lower than the untreated sample. Furthermore, the IE temperature 450 °C sample has a much lower hardness for face-on measurements in comparison to the side-on values. These differences may be a matter of position and scale; the face-on measurements are made far from a free edge and only probe the topmost 2 μm. Relaxation is known to occur at the immediate edge,[101,105] thus high IE temperatures likely have relaxation occurring in the few topmost microns that

the cross-section view does not observe. Nonetheless, it is interesting that hardness appears to be more affected by relaxation at the immediate edge in comparison to stiffness. This result agrees with the above idea that stiffness is more affected by composition and the resulting MAE in comparison with hardness which depends heavily on compressive stress.

The micro-indentation results in Table 4.1 show a different trend, where the hardness decreases for the sample exchanged at 390 °C likely because the resulting indent was deeper than the IE layer, leading to worse mechanical properties due to the mixed composition within the layer as well as the tensile stress expected beyond the IE layer. On the other hand, IE temperature samples 405 and 420 °C saw enhanced hardness due to a thicker IE layer relative to indent size. Overall, the results from nano-indentation of the cross-section (normalized hardness in Fig. 4.8) agree well with the hardness trends found for micro-indentation; samples exchanged at 405 and 420 °C have the most improved hardness in comparison with the untreated composition. This demonstrates how the improved hardness observed in the first 10 μm of the IE layer, a relatively small volume, is a predictor of the micro-mechanical behaviour of the material. In contrast, the 390 and 435 °C samples saw improvement in nano-hardness, yet not in the micro-hardness measurements. This disagreement is likely due to the difference in size of indents, where the low cumulative compressive stress was overcome by micro-indentation, but not nano-indentation. This demonstrates how the indentation process damages the material, thereby relaxing the compressive stress as penetration occurs, leading to results that are dependent on indent penetration depth as corroborated by the displacement plots (Fig. 4.1) and following section.

Given that the side-on nano-indentation procedure yielded hardness trends that matched those of the micro-hardness experiments, it may be supposed that the nano-indentation trends for Y are also valid on the micron scale. This is interesting because

it is generally difficult to probe the mechanical properties, especially Young's modulus, of a thin layer such as the IE case depth. Thus far, studies have only performed face-on nano-indentation perpendicular to the case-depth,[162] which is shown here to not accurately reflect the material's micron-scale behaviour. Consequently, the behaviour of Y shown here can be used in mechanical modelling of the IE layer, such as in the case of the determination of the linear network dilation coefficient (LNDC) which has been shown to correlate negatively with Y.[105] Generally, Y has been considered to be invariant with compression within the IE layer, which is a reasonable assumption sufficiently far from the free edge (> 30 μm); Y only increases about 6% past this case depth. Nonetheless, the free edge effect causes significant decreases in stiffness near the edge and should be taken into consideration when modelling surfaces. However, it is worth noting that near the free edge, a constant Y is a *more* valid assumption for IE glasses than it is for an untreated sample as IE appears to negate most of the free edge effect.

4.4.1 ISE-like Behaviour

In order to better evaluate the ISE-like anomaly, its magnitude was quantified by comparing the Y and H values evaluated over shallow indent displacements to the corresponding values at deep indent displacements. Fig. 4.9 plots the stiffness value averaged over a shallow indent depth (150–300 nm) divided by the stiffness value averaged over a deep indent range (1500-2000 nm), $Y_{\text{shallow}}/Y_{\text{deep}}$. These values come from the *same* indent, the stiffness is being averaged at different indent depth ranges only.

In Fig. 4.9, unity represents the absence of ISE-like behaviour; the stiffness measured at shallow indents depths is the same as for deep indent displacements. All

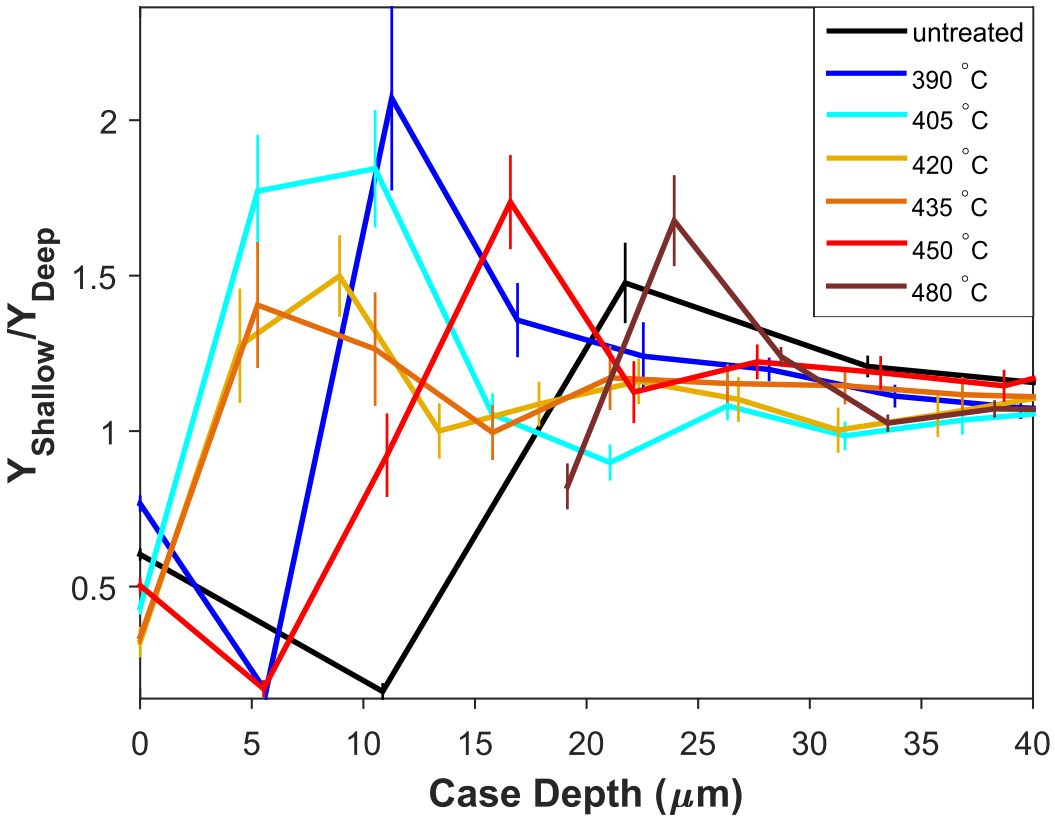

Figure 4.9: Evaluation of the ISE in Young's modulus by comparing values averaged over shallow vs. deep indent displacements ($Y_{\text{shallow}}/Y_{\text{deep}}$) as a function of case depth for all IE temperatures, 390–480 °C (dark blue–dark red) with the untreated (black) lithium silicate glass. Values above unity indicate a ISE-like behaviour, while values below one, signify a reverse ISE-like behaviour, where the stiffness is lower at shallow indent depths.

IE temperatures have little to no ISE ($Y_{\text{shallow}}/Y_{\text{deep}}$ of approximately 1–1.15) for case depths greater than 40 μm, which is smaller than those reported for fused silica (1.25[41]) and bulk metallic glasses (1.4[38]) alike. When $Y_{\text{shallow}}/Y_{\text{deep}}$ is greater than unity, it is indicative of ISE-like behaviour—the material is stiffer at shallow displacements, while a value below one represents a behaviour sometimes referred to as reverse ISE-like behaviour[34]—the material is more compliant at shallow displacements. As a reminder, the "zero" position is the same one used in the plot of stiffness vs. case depth in Fig. 4.3.

Perhaps one of the most interesting observations about Fig. 4.9 is that the untreated sample itself shows complex behaviour near the edge of the sample, $\leq$ 30 μm. This indicates that ISE-like behaviour may be inherent to measurements made near the sample edge, which as discussed earlier could be caused by tip tilting due to inclines near the edge. If that is the case, hardness is expected to be more affected by sample tilt compared with stiffness. Fig. 4.10 shows the same type of shallow vs. deep indent plot, but for hardness ($H_{\text{shallow}}/H_{\text{deep}}$). Comparing the ISE-like behaviour of stiffness and hardness (Figs. 4.9 and 4.10), it is observed that the values and trends are almost identical for all IE temperatures except 390 and 480 °C. Interestingly, those IE temperatures do have the expected dependence for Y and H *if* tip tilting occurred. For example, 390 °C has a $H_{\text{shallow}}/H_{\text{deep}}$ of 4 and a $Y_{\text{shallow}}/Y_{\text{deep}}$ of 2, while 480 °C has a $H_{\text{shallow}}/H_{\text{deep}}$ of 2.5 and a $Y_{\text{shallow}}/Y_{\text{deep}}$ of 1.6. As a consequence, those samples are likely experiencing tip tilting, either as a result of sloping near the edge or a compositional gradient, as discussed earlier. Nonetheless, it demonstrates that the complex behaviours of the untreated and other IE temperature samples are likely due to another physical phenomenon.

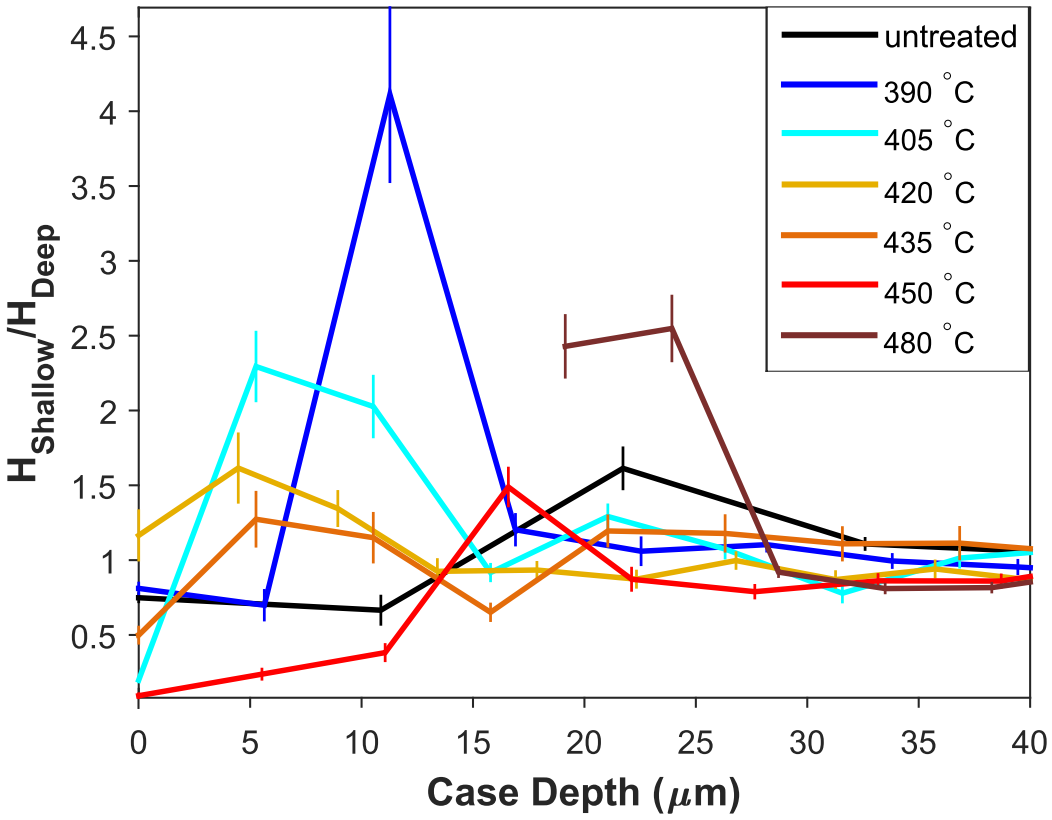

Figure 4.10: Evaluation of the ISE in hardness by comparing values averaged over shallow vs. deep indent displacements ($H_{\text{shallow}}/H_{\text{deep}}$) as a function of case depth for all IE temperatures, 390–480 °C (dark blue–dark red) with the untreated (black) lithium silicate glass. Values above unity indicate a ISE-like behaviour, while values below one, signify a reverse ISE-like behaviour, where the hardness is lower at shallow indent depths.

Although a complex behaviour such as the one exhibited by the untreated sample is rarely observed in an amorphous, isotropic material such as glass, it is important to realise that the ISE has been shown to be very sensitive to the surface condition.[34] There have been several articles on the difficulties and importance in preparing a flawless surface for nano-indentation.[278–281] In fact, when a single crystal of Cu was polished in two different manners (colloidal silica vs. electropolishing) the magnitude of the ISE was seen to reduce significantly;[279] using the notation here, the $H_{\text{shallow}}/H_{\text{deep}}$ decreased from 1.7 to 1.2 because of surface preparation technique alone. As a consequence, it may be less surprising that the untreated sample shows ISE-like behaviour near the edge, where surface flaws are present. Additionally, since stiffness and hardness are known to decrease near a free edge,[266] it may simply be that the geometry of the indenter is such that a deeper indent probes closer to the material's edge.

Although it is interesting to attempt to understand the reason why ISE-like behaviour is occurring near the edge in all samples, the answer lies out of the scope of this investigation. The origins of the ISE are not fully understood for bulk amorphous materials; here there exists the added complexity of examining the behaviour of the surface under compression. Not only does the surface condition change under compression, but the compressive stress profile may be changing as the indenter tip displaces the material, thereby affecting the values of Y and H measured at different indent depths. This is indicated by the differences observed between the side-view nano-hardness (Fig. 4.8) and micro-hardness (Table 4.1) results. In this study, the behaviour of the untreated sample serves as a baseline to observe the effect of the IE on the mechanical properties at the edge.

Considering $Y_{\text{shallow}}/Y_{\text{deep}}$ for the untreated sample in Fig. 4.9, it shows reverse

ISE-like behaviour very close to the edge, first 10 μm, followed by a positive ISE-like behaviour peak, before going to unity. The lowest IE temperature, 390 °C, has a migration of the "zig-zag" towards the edge, where IE temperatures 405–435 °C immediately have ISE-like behaviour (positive values) at the edge and then at high IE temperatures, 450 and 480 °C, the zig-zag migrates away from the edge and back towards the untreated sample. The most thermally relaxed IE temperature (480 °C) shows nearly the same behaviour within the case depth as the untreated composition. The same migration with increasing IE temperature occurs in the $H_{\text{shallow}}/H_{\text{deep}}$ plot in Fig. 4.10, although the zig-zag itself tends to be less pronounced for hardness. Additionally, the ISE-like behaviour persists further into the case depth for the stiffness in comparison to the hardness for most IE temperatures, which agrees with what was observed in the displacement plots in the Results section.

The migration of the ISE peak towards the sample edge in both Y and H may indicate that IE is having a significant effect on the surface condition. For IE temperatures where significant exchange occurring while still being below T_{g} (405–435°C), the immediate ISE-like behaviour at the edge is likely due to the compressive stress at the edge. In addition to mitigating the concentrated tensile stress at crack tips and arresting crack propagation, compressive stress has been known to promote crack closure, which depending on the extent of closure also leads to significant strengthening.[273] The low IE temperatures, 390 and 405 °C, have the largest values (although some of the height in the 390 °C sample in the $H_{\text{shallow}}/H_{\text{deep}}$ plot may be from another physical process), perhaps indicating that compressive stress leads to larger changes at the surface and more pronounced ISE-like behaviour near the edge. Concurrently, the indenter tip may release compressive stress, *i.e.*, microcracking, as it displaces material. Finally, the peak for the high IE temperatures (450 and 480 °C) in Figs. 4.9 and 4.10 migrates back towards the untreated zigzag, demonstrating as

the structure relaxes and compressive stress decreases to zero, the same indentation behaviour and surface condition reappear; the role of the surface in the indentation behaviour is the same for a completely relaxed composition, the untreated or 480 °C sample.

4.4.2 Elasticity and Plasticity

One of the goals of this study was to ascertain which mechanical response, elastic or plastic, is more enhanced from the IE process; stiffness is a measure of the elastic response solely, while hardness contains both elastic and plastic components. Although the exact proportions of elastic and plastic resistance to deformation are unknown for these samples, glass is expected to respond mostly elastically, 84% compared with only 14% plastic response.[260] As a result, if the improvement is elastic in nature, *i.e.*, increase in bond density and/or strength, the stiffness and hardness should increase similarly after the IE process. Conversely, if resistance to plastic deformation increases, the hardness should be enhanced more than the stiffness. The previous two normalization plots, Figs. 4.7 and 4.8 display clearly that H has a much greater enhancement, indicating that IE increases resistance to plasticity to a greater degree than elasticity.

However, Y or H alone do not fully characterize a material's mechanical response; in fact, the ratio of the two properties (H/Y^*, where $Y^* = Y/(1-\mu^2)$ and μ is the same Poisson's ratio value that was used to convert Y^* to Y in the nano-indentation procedure) has been found to better predict elastic vs. plastic behaviour.[282] According to Musil *et al.*'s nano-indentation of superhard coatings, H/Y^* is approximately proportional to elastic recovery (ω_e), while H^3/Y^{*2} is correlated with resistance to plastic deformation.[283–285]

Fig. 4.11 displays the effect of IE temperature on elastic recovery or H/Y^*. It can be seen that for all IE temperatures, with the exception of 480 °C, IE improved the elastic recovery near the edge (0–30 μm) compared to the untreated composition. Interestingly, past 30 μm of case depth none of the IE temperatures lowered the elastic recovery (H/Y^*) in comparison to the untreated sample, despite both of the samples exchanged at 450 and 480 °C having lower Y and H in that region. Initially, an increase in IE temperature enhances elastic recovery closer to the immediate edge until the sample exchanged at 405 °C, which has the most improved elastic response closest to the edge. Thereafter, high IE temperatures (435–480 °C) decrease the elastic recovery at the edge. The sample exchanged at 420 °C has the most consistently large elastic recovery improvement, while the 390 °C sample has a slightly higher peak elastic recovery (excluding the 450 °C sample). This trend is closer to that seen in the compressive stress profile and face-on nano-indentation results; the sample exchanged at 390 °C should display the most enhanced mechanical response, while 405–420 °C should have a smaller, but broader improvement. It is surprising that the sample exchanged at 450 °C shows such an improvement in ω_e far into the case depth, however, it is only a consequence of the sample having an unexpectedly low Y in Fig. 4.3 probably due to cracking.

The resistance to plastic deformation, H^3/Y^{*2}, shows similar trends (Fig. 4.12). Once more, with the exception of 480 °C, there is a positive relationship between enhanced mechanical response and increasing IE temperature. However, unlike elastic recovery which was roughly the same for all IE temperatures past a case depth of $\geq$ 30 μm, high IE temperature samples (435 and 480 °C) show decreased resistance to plastic deformation compared to the untreated sample in this region. Again, the sample exchanged at 450 °C shows an unexpected improvement in H^3/Y^{*2} far into the case depth. All the same, perhaps the effects of composition are observable here; when

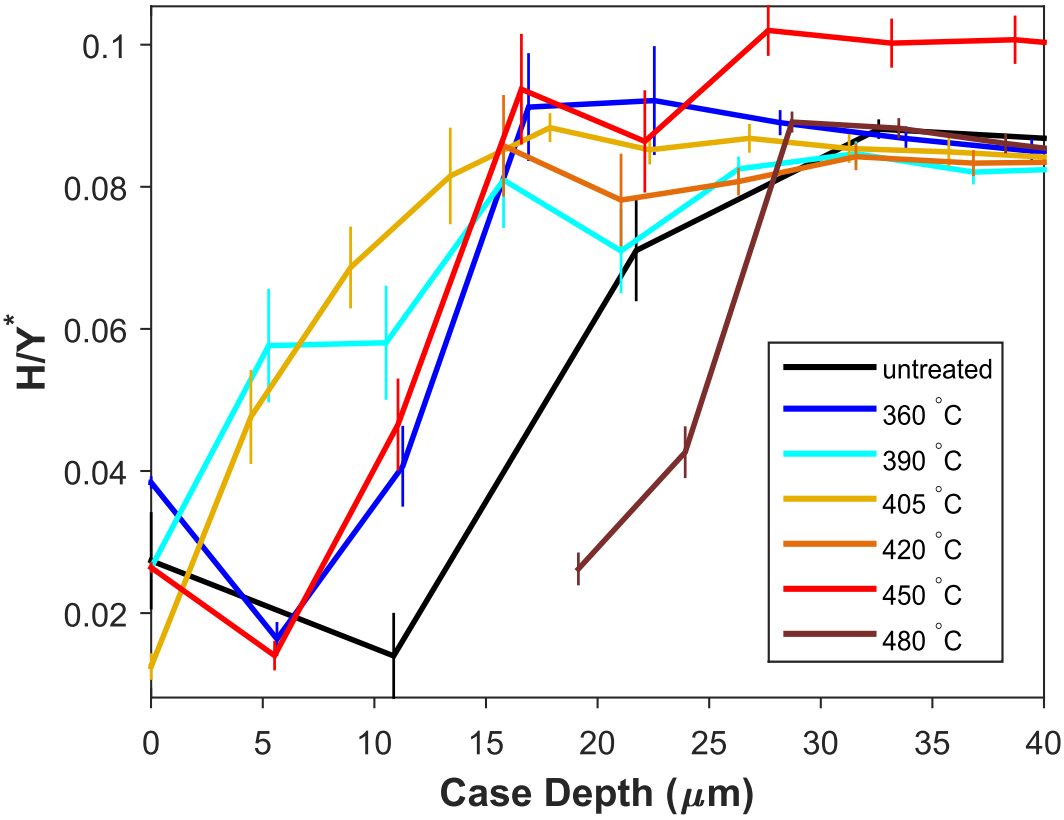

Figure 4.11: H/Y^*, which is proportional to elastic recovery (ω_e), as a function of case depth for all IE temperatures, 390–480 °C (dark blue–dark red) in comparison with the untreated lithium silicate glass (black). Only deep indent data (1500–2000 nm) were used.

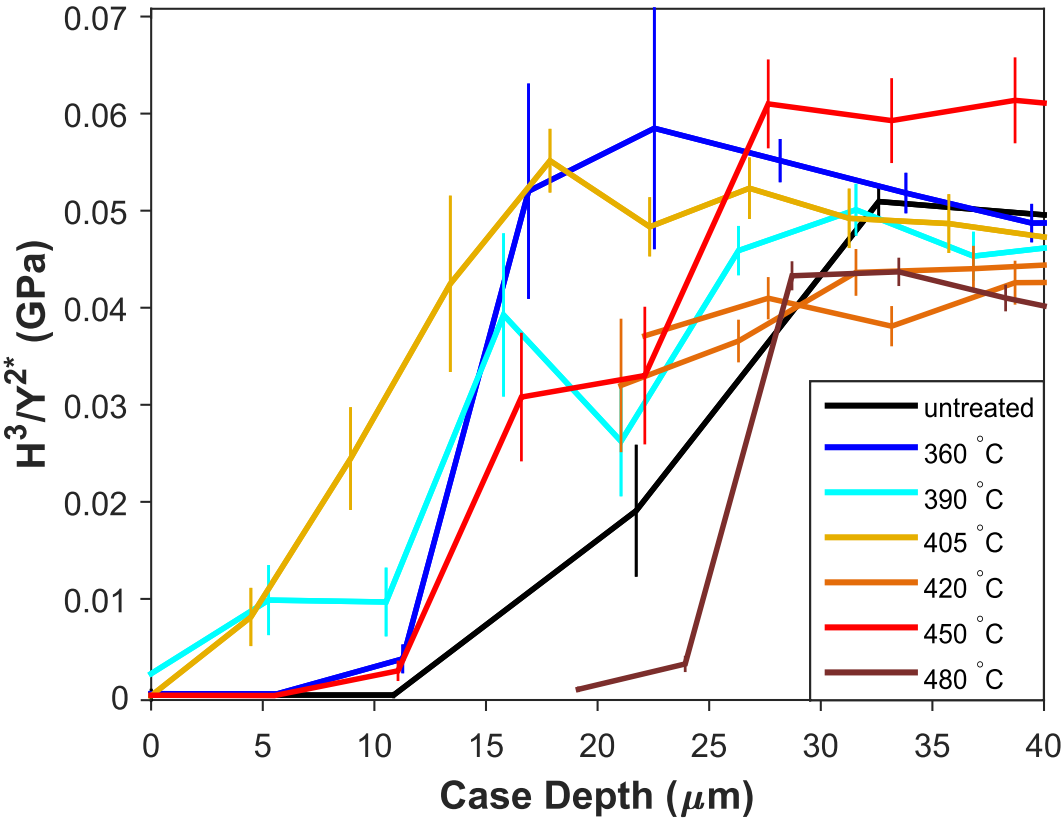

Figure 4.12: H^3/Y^{*2} (correlated with resistance to plastic deformation) as a function of case depth for all IE temperatures, 390–480 °C (dark blue–dark red) in comparison with the untreated lithium silicate glass (black). Only deep indent data (1500–2000 nm) were used.

the sample relaxes more, the resistance to plastic deformation becomes more similar to that of the as-melted mixed-alkali composition ($20Li_2O$-$10K_2O$-$70SiO_2$). Finally, the sample exchanged at 420 °C has the highest resistance to plastic deformation at the immediate edge, however, the 390 °C sample has the highest H^3/Y^{*2} further into the case depth (excluding the 450 °C sample). Once again, this result corresponds more closely with the compressive stress profile.

Although it is difficult to observe in Figs. 4.11 and 4.12, the resistance to plastic deformation improves 2–3 times more than the elastic recovery near the edge for samples exchanged at low IE temperatures, 390–420 °C. This result agrees with the

conclusion from the normalized Y/Y_0 and H/H_0 plots in Figs. 4.7 and 4.8. To better understand this result, it is important to realise H/Y^* is related to the maximum elastic strain, while H^3/Y^{*2} is related to the energy required for plastic deformation. Since brittle materials can only withstand small amounts of strain until fracture, it may simply be that there is little opportunity to improve their elastic recovery. In contrast, the amount of energy required for plastic deformation is more variable as it involves both stiffness and maximum strain. Nonetheless, it follows that in addition to arresting cracks due to compressive stress, IE also leads to the reduction in new flaws forming at the edge, which is expected from the high scratch resistance conferred by IE.

Additionally, unlike elastic recovery, H^3/Y^{*2} was found to be affected further away from the edge (> 30 μm) at high IE temperatures (435 and 480 °C). This is a result of high IE temperatures causing reduced hardness, likely because of having less compressive stress due to thermal relaxation. Overall, the improved scratch resistance, *i.e.* hardness, imparted from IE likely comes from the compressive stress at the edge mitigating tensile stresses, causing both crack closure and arresting in addition to decreasing shear flow. The MAE concurrently enhances hardness more than stiffness, thus, it may be improving mechanical properties by increasing elastic recovery and resistance to plastic deformation, in addition to increasing the fracture stress per Griffith's equation.[29]

The results from micro-indentation agree with those determined for elastic recovery and resistance to plastic deformation. Both H/Y and H^3/Y^{*2} displayed the most improvement nearest the edge (0–10 μm) in the samples exchanged at 405 and 420 °C, which are the same IE temperatures that saw enhanced micro-hardness. Additionally, IE temperature 390 °C did not show improvement in this region and the micro-hardness for this sample was found to be less than the untreated sample. Once

more these results indicate the importance of the first 10–15 microns in determining the performance of the material.

4.5 Summary

Following ion exchange, significant improvements in stiffness and hardness were seen near the edge (0–30 μm) when exchange was performed at temperatures (390–435 °C) below T_g (459 °C). Low IE temperatures (390 and 405 °C) resulted in better mechanical properties further into the case depth ($\geq$ 30 μm). Conversely, IE temperatures near or above T_g (450 and 480 °C) worsened mechanical properties near the edge as well as throughout the case depth. Low IE temperatures resulted in more compressive stress to oppose the concentrated tensile stress found at crack tips; this likely lead to a decrease in the importance of the surface condition and/or crack closure, causing an enhancement of mechanical properties near the edge. On the other hand, high IE temperatures caused relaxed structures similar to the as-melted, mixed-alkali series and little compressive stress; as a result, the surface condition is as important in these glasses as it is in the untreated composition, thus, the mechanical properties are not improved. Essentially, the IE process was observed to negate the free edge effect and restore the mechanical properties near the edge to those found in the middle of the specimen.

Overall, the hardness results from side-view nano-indentation were found to agree well with those from micro-indentation, namely the samples exchanged at 405 and 420 °C showed the most improved H near the edge. This agreement demonstrates the applicability of the stiffness results from nano-indentation measurements to the micron scale as well, which is an important, yet difficult property to measure in a thin layer. Considering that in the case of glass, the response at the edge is a large

predictor of the material performance, understanding which properties are improved near the edge may help model the mechanical response due to the IE process.

Despite the 405 and 420 °C samples having the most enhanced mechanical properties, they are known to have lower compressive stresses (over a larger case depth) than the sample exchanged at 390 °C. Consequently, the improvements in Y and H cannot be fully explained in terms of compressive stress and thermal relaxation alone. Hardness was seen to be greatly enhanced by the IE process, however, stiffness was improved beyond that which was expected from compressive stress alone, revealing that the MAE plays a role in the improvement of both mechanical properties. Given the composition dependence of the mechanical properties, it may be worth investigating the magnitude of the MAE in prospective IE materials.

The indent size was also found to effect stiffness and hardness, especially close to the edge due to the free edge effect. Interestingly, trends observed for shallow indents were more similar to those expected from compressive stress profiles, which may indicate release of compression with increasing indent depth. Moreover, this ISE-like behaviour was more pronounced for low IE temperatures in comparison to the untreated and high IE temperature samples, likely because low IE temperatures have more compression to be relaxed by indentation.

When the mechanical properties were evaluated in terms of elastic recovery (H/Y^*) and resistance to plastic deformation (H^3/Y^{*2}), the effect of IE temperature on these two responses matched the compression profiles: IE temperature 390 °C had the most enhanced mechanical response, while 420 °C had a less improved response over a larger case depth, especially near the edge. Overall, both responses were seen to improve by the IE process, however, the plastic response was found to be more enhanced compared to the elastic response. This likely contributes to the high scratch

resistance observed in IE glasses where a decrease in plastic flow reduces the likelihood of new flaws from occurring. Stiffness appears to act in two different ways: first by increasing the magnitude of compressive stress, yet also by decreasing elastic recovery and resistance to plastic deformation during indentation. Although the IE process improves hardness more than stiffness, only stiffness plays a role in the magnitude of compressive stress found in the IE layer; thus, stiffness is important when considering surface mechanics.

Chapter 5

Mixed Alkaline-Earth Effect in the xMgO-($50-x$)CaO-50SiO_2 System

5.1 Background

Although the MAE has been given considerable attention in the literature,[i] it is important to understand if the MAEE behaves the same way and therefore has the same structural origins (Sections 1.4 and 1.4.1). Part of the confusion regarding the existence of the MAEE stems from uncertainty about whether alkaline-earth ions act as modifiers or formers in the glass. Generally, addition of modifiers breaks up the 3-d network and results in degraded mechanical properties, yet MgO and CaO have been shown to increase elastic properties and hardness[54] and have been compared to intermediates like Al_2O_3.[286] However, addition of Li_2O is also known to increase elastic properties by behaving more covalently,[53,287] yet Li_2O-containing mixed-alkali glasses still exhibit the MME.[60,80,181]

To answer these questions, the xMgO-($50-x$)CaO-50SiO_2 glass series was chosen for this study; in addition to being of geologic importance, it also provides an opportunity to study the mixed alkaline-earth effect of the most commonly used alkaline-earth cations. Glasses containing MgO were chosen because of the small size

[i]The next Chapter, Chapter 6, explores the relationships between the *typical* MAE in ion conductivity and other properties using the analysis principles used here for the MAEE. Thus, this chapter serves as an example of the amount of detail which can be put into understanding one mixed-modifier glass series.

of Mg^{2+} and subsequently higher expected conductivity, however there is evidence that Ca^{2+} has a lower activation energy and more mobility (as will be discussed further in Section 6.1).[288,289]

Furthermore, the differences between the ions are extremely important, with larger differences resulting in large deviations from linearity.[58,64,83] Unfortunately, there is disagreement about whether Ca is 6[94] or 8-coordinate[16,54] and Mg coordination has been found to decrease from 6 to 4-fold with the addition of Ca in glasses and crystals,[81] so it is possible a range of size and field strength differences (Δr_c and ΔF_c, respectively) exists. If Mg^{2+} and Ca^{2+} are assumed to be 6-fold and 8-fold coordinated, then the Δr_c and ΔF_c are -0.28 and 0.13, while if Mg^{2+} converts to 4-fold coordination, Δr_c and ΔF_c are now -0.43 and 0.13.[22] Also, in the case of Mg and Ca, which are sufficiently similar in cationic strength, there is almost complete mixing, *i.e.*, each silicon atom is surrounded by equal parts of Mg and Ca, perhaps leading to an increased departure from linearity.[52,81,83]

An MME is expected for this system as it contains a high amount of modifier, which is known to increase the strength of the MME in many properties. Consequently, significant deviations in linearity in the properties studied are expected for this system, however, they may be diminished compared to the typical MAE.[95] The MME is expected to only have a small effect ($\approx$10%[58]) on static properties, for example, the molar volume (V_m) is usually treated as linear for ionic conduction models of MME.[290] On the hand, ionic conductivity has a departure from linearity of several orders of magnitude (10^2–10^6[58]), thus a larger MME is expected for dynamic properties. Mechanical properties will have MMEs somewhere between the two extremes depending on the influence of static vs. dynamic properties. Finally, Raman spectroscopy is also used to elucidate the Q^n-distribution (Section 1.1.4), in order to examine structure-property relationships.

5.2 Experimental

Samples in the xMgO-(50−x)CaO-50SiO_2 glass series were made per Section 2.1 from stoichiometric amounts of SiO_2 (purum p.a., Sigma-Aldrich), CaO (Aldrich Reagent Plus®99.9%) and MgO (Sigma-Aldrich m̃esh 98%) by melting at 1550 °C for 1–3 hours in a Pt crucible then quenching in air. Since thermal gravimetric anaylsis (TGA) measurements showed CaO and MgO to attract water and CO_2 from the atmosphere, both reagents were fully dried at temperatures greater than 600 °C for at least one hour before weighing. Generally compositions with high MgO or CaO content, *i.e.*, at either extreme of the mixed compositional range, took longer to melt fully and were very viscous, likely due to the high melting temperatures of MgO and CaO and the fact that the mixed-modifier compositions are in general significantly less viscous than their single-alkali counterparts.[58] In the case of 50MgO-50SiO_2 composition, the mixture would not melt fully at 1550 °C after any length of time. Glasses with large amounts of MgO crystallized easily making it difficult to obtain large pieces for further characterization; as a result, the highest MgO- or CaO-containing compositions studied within were 41.6MgO-8.3CaO-50SiO_2 and 8.3MgO-41.6CaO-50SiO_2.

The glasses were then annealed at temperatures between 650–700 °C for at least 16 hours, with higher MgO compositions needing higher annealing temperatures or longer annealing times. Since T_g measurements (reported to be between 720–766 °C for this series[99,291]) were not the focus of this study, annealing was done progressively, increasing the temperature incrementally and annealing overnight until stress-free glasses were obtained. All compositions were checked optically for proper annealing using strain-sensitive cross-polarizers. Finally, bulk glasses were cut into rectangular prisms and polished down to 1 μm grit using diamond paste.

The compositions of the samples were measured using WDS (Section 2.3.2). In this case, diopside ($MgCaSi_2O_6$) was used as an external standard. Five points were analyzed spaced throughout the sample to determine Mg, Ca, Si and O concentrations. Additionally, linescan type measurements were performed on the long-term conductivity samples to determine the ion migration after a long-term potential had been applied.

The density was measured using the Archimedean method at RT using absolute ethanol as the immersion fluid (Section 2.4). From there, molar volume (V_m), oxygen volume (V_o) and packing fraction (V_f) were determined using the density and compositional analysis (end of Sections 2.4 and 1.1.3, respectively). Mechanical properties (elastic moduli, hardness and fracture toughness) were measured using the appropriate procedure in Section 2.6. Finally, Raman spectroscopy of the bulk samples was performed at RT with a spectral resolution of 2 cm^{-1} (Section 2.5).

Activation energies were determined from ionic conductivity measurements as a function of composition and temperature (Section 2.7). Additionally, long-term conductivity experiments were performed to ascertain the mobile species and understand some unique conductivity results (Section 2.7.1).

Finally, powder X-ray diffraction (PXRD) was performed on the samples by Andy George using a Siemens D-500 powder diffractometer with a copper K-α X-ray source. The samples were ground into powder using a porcelain mortar and pestle. The diffraction pattern was collected for 8 scans for each sample to improve the counting statistics, since the amorphous peak of glass is low in intensity; this was done to ensure that the samples were thoroughly amorphous and had no nano-crystallites.

5.3 Results and Discussion

5.3.1 Sample Analysis

Compositional Analysis

Elemental analysis of the xMgO-(50−x)CaO-50SiO_2 series is shown in Table 5.1. All of the compositions are within 1.3% of their nominal values, except 0.28 and 0.84 MgO. The 0.28 MgO sample was contaminated by 2.1% K_2O, thus, any data from that sample is marked with the symbol "x", unlike the other compositions. The relative cation ratio is the dominant factor in ion conduction and the actual [MgO]/[MgO+CaO] ratios are used for the rest of this paper, for example 0.67 MgO refers to the 33.1MgO-16.7CaO-50.2SiO_2 sample.

Table 5.1: Glass compositions of the xMgO-(50−x)CaO-50SiO_2 series analyzed by WDS, compared to their nominal compositions. Instrumental error is 0.1–0.16 mol-%, while standard error of the five points was ≤0.3 mol-%. †Composition contains 2.1% K_2O contaminant.

[MgO]/[MgO+CaO]		MgO (mol-%)		CaO (mol-%)		SiO_2 (mol-%)	
Nominal	Actual	Nominal	Actual	Nominal	Actual	Nominal	Actual
0.17	0.17	8.3	8.5	41.7	41.6	50	49.7
0.25†	0.279	12.5	12.6	37.5	32.4	50	52.8
0.33	0.34	16.7	16.4	33.3	32.6	50	50.9
0.5	0.49	25	24.3	25	25.0	50	50.4
0.67	0.67	33.3	33.1	16.7	16.7	50	50.2
0.71	0.72	35.4	35.7	14.6	14.2	50	50.1
0.75	0.70	37.5	37.1	12.5	13.7	50	48.7
0.84	0.84	41.9	39.3	8.1	7.7	50	53.2

Phase Analysis

Although the average composition of a glass can be determined from WDS, it does not confirm whether a homogeneous amorphous phase exists. These glasses were

optically clear, however, Rayleigh scattering only occurs when particle size is on the order of the same size as the wavelength of the scattered light, thus, it is possible nucleation sites, *i.e*, nano-crystallites, on the order of 100 nm or less could be present without any interaction with visible light. It should be noted that this is true in polycrystalline materials with small enough grain sizes to appear optically clear, yet in that case, the refractive index remains constant, which may or may not be the case in a glass with small crystalline particles throughout. The same reasoning applies to same-phase separation, where there are glassy droplets within a glass the droplets vs. matrix usually have different refractive indices leading to cloudiness.

Nonetheless, PXRD was employed to determine whether the samples were completely amorphous; the diffraction patterns can be found in Fig. 5.1 for the highest MgO compositions, 0.71–0.84 relative MgO compared to the most mixed composition 0.5 relative MgO. Since high MgO compositions were observed to crystallize more easily (crystalline phase was removed by cutting), their diffraction patterns are compared with a composition that had no noticeably crystallization, the 0.5 relative MgO compositon.

It can be observed that all glasses, even ones with high MgO concentrations, only contain the broad amorphous peak without any high-intensity crystalline phase peaks being observed between 20–50° 2θ. The major differences between samples appear to be in peak intensity and position, with more relative MgO having a larger peak shifted to the left, perhaps indicating a larger d_{L} spacing, however it is difficult to make conclusions with this data. The important conclusion is that these glasses appear to be without any crystalline particles and are phase pure according to X-ray analysis. Thus, all of the following results can be assumed to not be due to nano-crystallites. It should be noted that glasses can be amorphous, yet still possess inhomogeneities, such as regions of one preferred cation versus another cation, thus, local structural

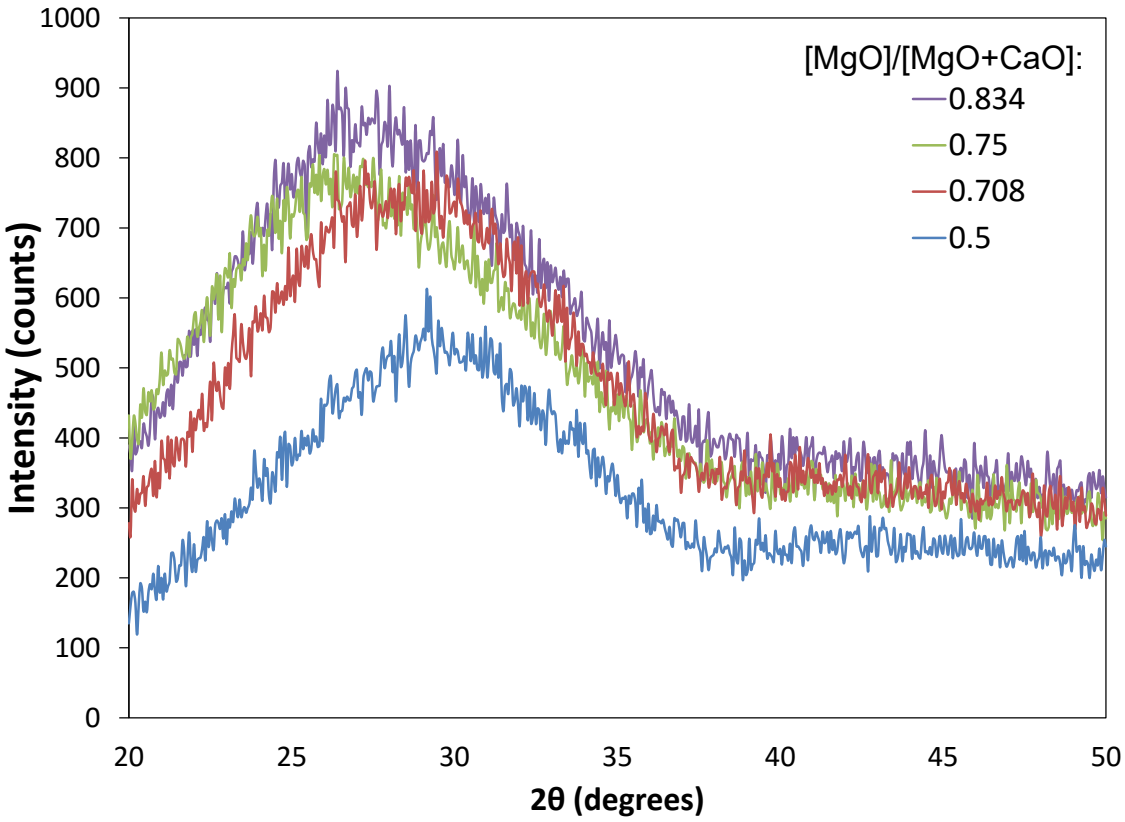

Figure 5.1: Powder X-ray diffraction patterns of four of the samples in the xMgO-$(50-x)$CaO-50SiO_2 series.

analysis such as NMR must also be used to confirm complete mixing.

5.3.2 Static Properties

One of the major questions about the MME regards its ability to affect both static and dynamic properties alike. Fig. 5.2 demonstrates the deviations from linearity for density (ρ) and molar volume (V_m), thus, proving static properties are also affected for purely alkaline-earth systems. The density data matches literature values.[52,83,99]

Both properties show a maximum deviation at 0.67 MgO, +2.9% for ρ and −2.7% for V_m. It is not uncommon for the MAE to produce ±10% and ≤ ±5% deviations in density and molar volume, respectively, so while the MAEE definitely can be

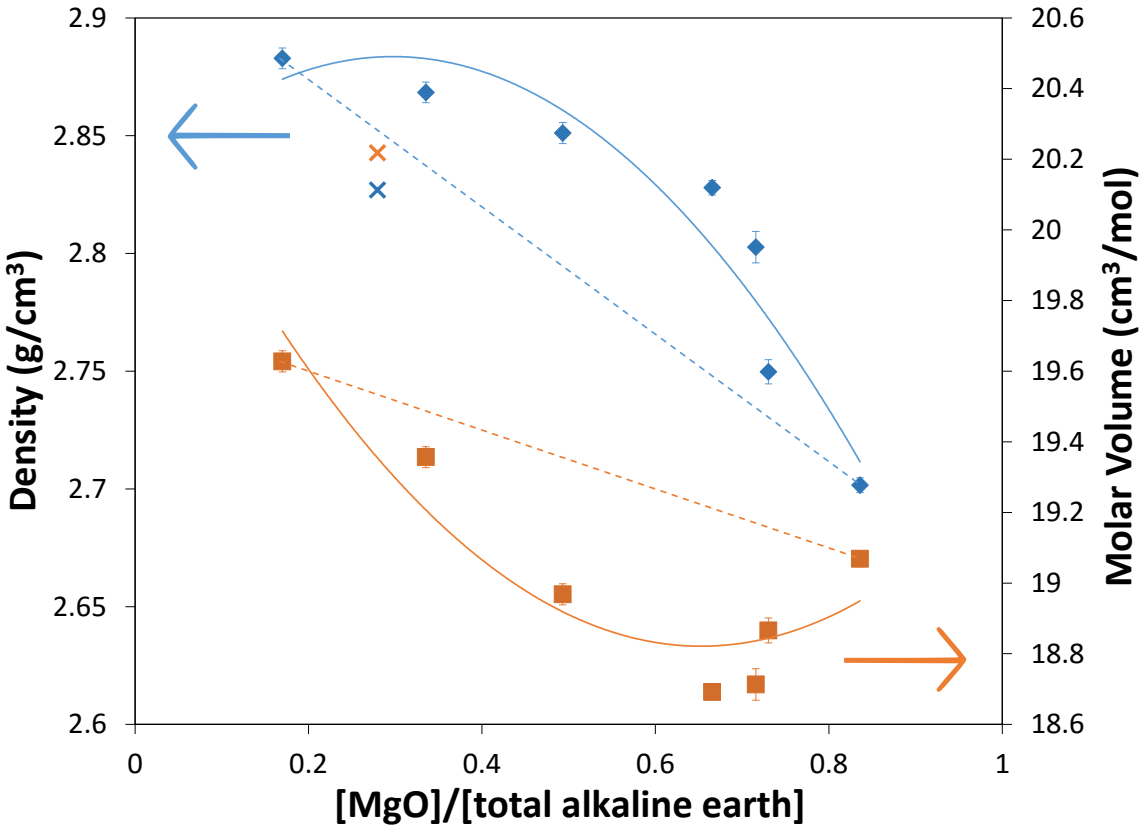

Figure 5.2: Density (ρ) and the corresponding molar volume (V_m) of the xMgO-(50−x)CaO-50SiO_2 series as a function of relative alkaline-earth ratio. Solid lines are the apparent trends fit with 2nd-order polynomials, while the dashed lines are linear fits between the two endmember compositions. Error of ρ determined from three trials, ≈0.01 g/cm^3.

seen in the static properties here, it is not as large as the MAE.[58] Nevertheless, the deviations found here are nearly twice those found previously for this system, however the previous reports were published almost 100 years ago.[83] There is evidence which indicates that if the molar volumes of the endpoint compositions are similar, as in this series, there is a larger departure from linearity.[63] Most alkali silicates cannot form glasses at such high modifier content; high modifier content has been linked to a stronger MME, so the MAEE seen here can be expected to be enhanced as a result.[65,67]

It can be seen in Fig. 5.3 that packing fraction follows generally the same trend

as density (Fig. 5.2). This system is more compact than the law of additivity states for the mixed compositions; this is likely because Ca^{2+} and Mg^{2+} are different sizes allowing for more efficient packing.[3] It is interesting that 0.67-0.71 MgO have the highest V_f, but this may because Mg is known to undergo a coordination change when Ca is present, thus, there are likely three sizes of ions (tetrahedral and octahedral Mg and Ca), allowing more packing configurations. Additionally, a positive deviation is contrary to what other authors have postulated: that the glass structure adapts to both ions, so packing is less efficient for both,[292] and the "loosening up of the structure" observed by mechanical loss experiments.[65,72]

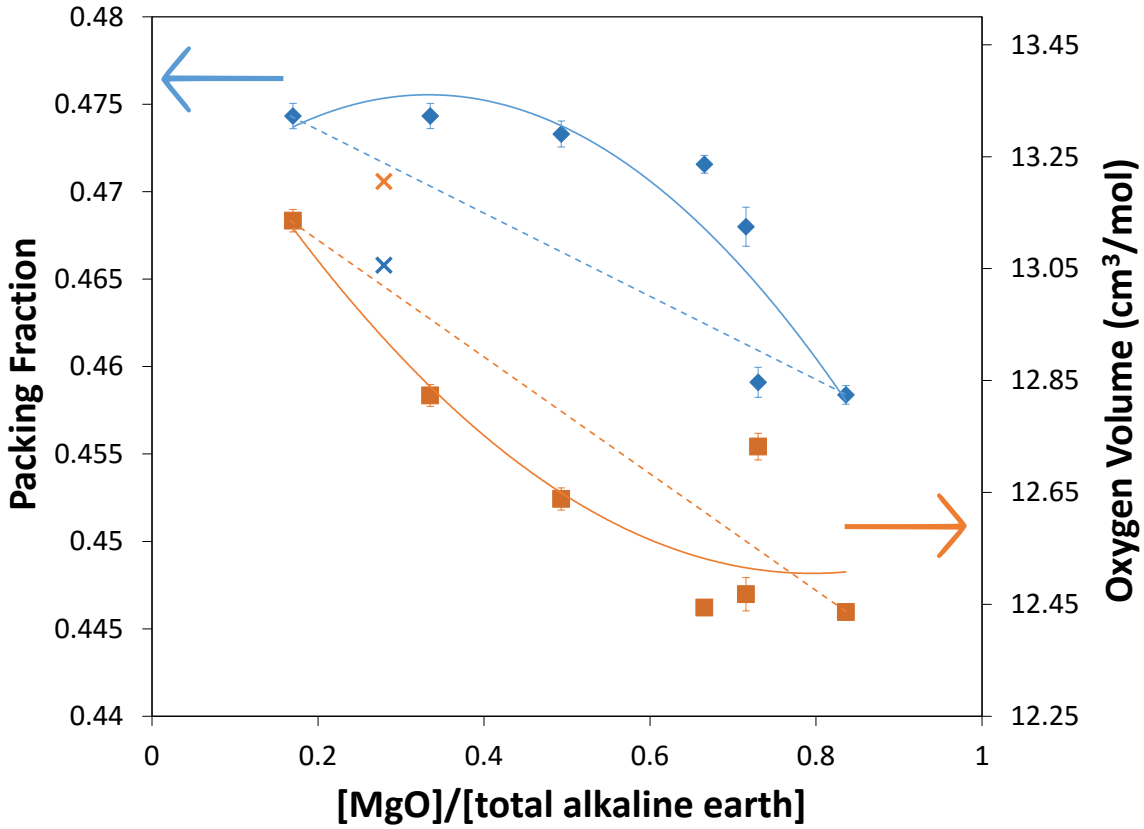

Figure 5.3: Packing fraction (V_f) and oxygen volume (V_O) of the xMgO-(50−x)CaO-50SiO_2 series as a function of relative alkaline-earth ratio, calculated using Eqs. 1.1 and 2.4, respectively. Solid lines are the apparent trends fit with 2nd-order polynomials, while the dashed lines are linear fits between the two endmember compositions.

The most interesting result comes from the oxygen volume, which shows that the

same samples, 0.28 and 0.73 MgO, which are below the additivity line for V_f also to have significantly higher oxygen volume than expected. The magnesium-calcium silicate system is likely to have substantial "free" O^{2-} (i.e., O^{2-} not bonded to Si) in the structure at high MgO-content;[293–296] free oxygen could give rise to large oxygen volumes since $V_{O^{2-}} > V_O$.

5.3.3 Structural Characterization

The Raman spectra in Fig. 5.4 were assigned to Q^n-unit stretches as outlined in previous papers;[147,193,297–299] Q^0, Q^1, Q^2, Q^3 and Q^4-units have been found near 850, 900, 950–1000, 1050–1100 and 1200 cm^{-1}, respectively. Full spectral deconvolution for the two endmember compositions can be found in Fig. C.10 in Appendix C. Other authors[147,193] used four peaks (Q^0–Q^3), while some used only three peaks, but assigned them to Q^0, Q^2, and Q^3.[297] In this case, at high [CaO] only three peaks were required to obtain a good fit, but were assigned to Q^1 (875 cm^{-1}), Q^2 (970 cm^{-1}), and Q^3 (1060 cm^{-1}) since Q^n-distributions from NMR spectroscopy for the endmember compositions show either none or 1% Q^0-species.[294,295,300] Only MgO-rich compositions (0.67–0.84 MgO) had an extra peak at 1170 cm^{-1}, which was assigned to Q^4-units.

Peaks in the low-frequency region (550–750 cm^{-1}) are assigned to Si-O-Si vibrations and changes in the Si-O-Si bond-angle, while the high-frequency region peaks (850–1200 cm^{-1}) are local intra-tetrahedral (O-Si-O) stretches related to Si-O bond length.[145,147,189,190] In both frequency regions, there is a broadening of the peaks with increased MgO content, due to the known effect of higher cationic strength ions inducing both more disperse Q^n distributions and wider lineshapes.[20,156,195,301,302] All low-frequency Raman shifts were found to increase linearly with MgO content,

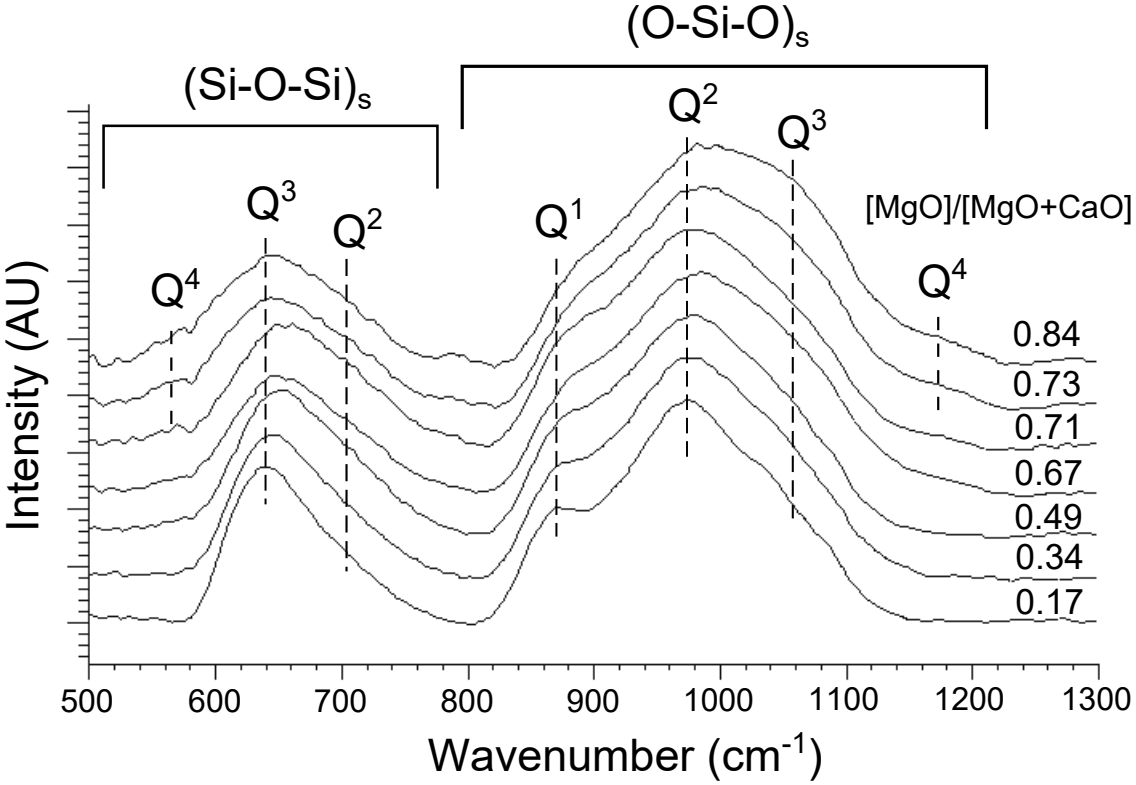

Figure 5.4: Raman spectra of xMgO-(50$-x$)CaO-50SiO$_2$ glasses as a function of relative alkaline-earth ratio. General positions of structural Q^n-units are marked with dashed lines. The low and high-frequency regions are separated by brackets which correspond to Si-O-Si stretches and O-Si-O stretches, respectively.

thereby indicating a decrease in average ∠Si-O-Si. On the other hand, in the high-frequency region, only the peak associated with Q^1 (880 cm^{-1}) was seen to be affected by alkaline-earth content, denoting a decrease in Si-O bond length. The Raman shifts of each peak vs. [MgO]/[MgO+CaO] plots can be found in the Appendices (Figs. C.11 and C.12). Since the high-frequency region peak vibrations are more localized, their intensities can be used to quantify the Q^n-distribution in the glass. Although Raman is a semi-quantitative technique, the peak areas can be compared within a spectrum. Furthermore, the cross-polarization ratios (efficiency of each type of vibration coupling to the incoming light) determined in Chapter 3 were used here to convert the raw Raman intensities into more physically reasonable Q^n-fractions,

however the cross-section for the Q^1 had to be calculated from NMR data of 50MgO-50SiO_2.[187,303] The processed Q^n-species and total non-bridging oxygen per silicon atom ratios ([NBO]/[Si]) can be found in Fig. 5.5. The error of the peak areas was ±10%, as estimated previously.[149,187]

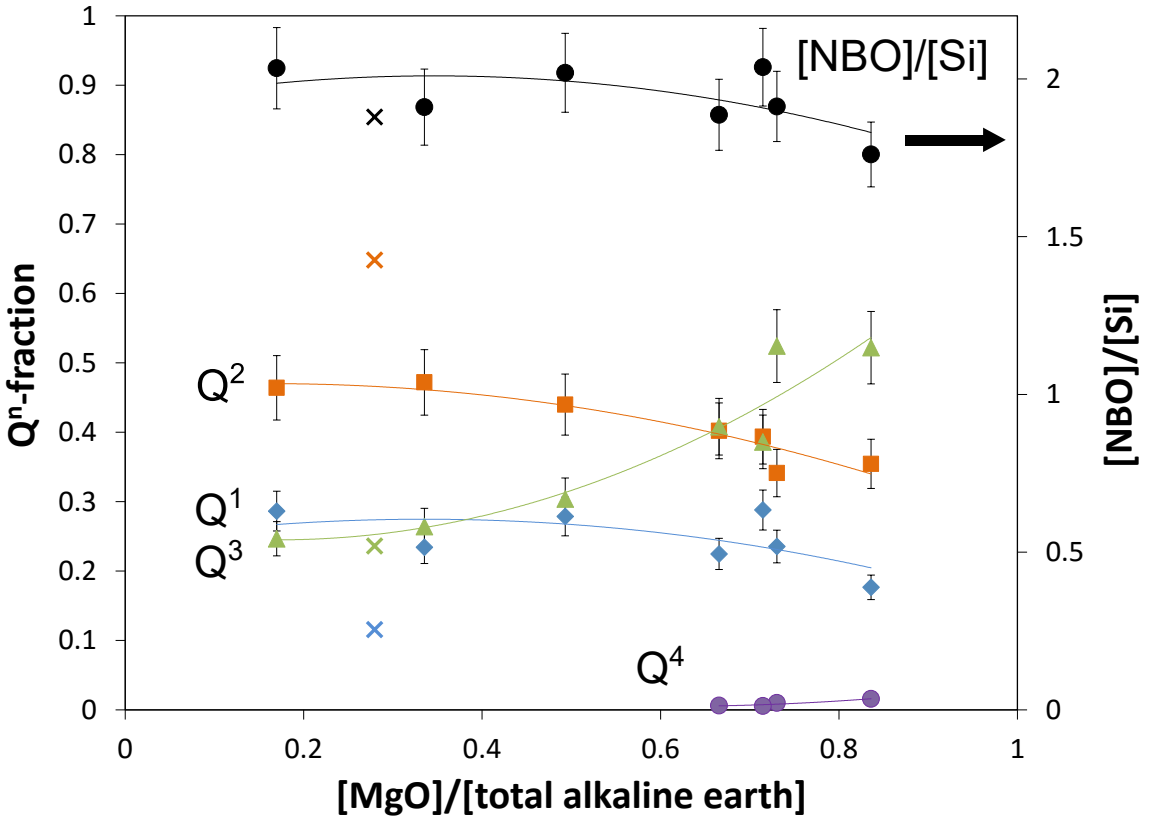

Figure 5.5: The Q^n-distribution (left) and non-bridging oxygen per silicon atom ([NBO]/[Si]) of xMgO-(50−x)CaO-50SiO_2 from Raman spectroscopy. Error from fitting was assumed to be 10% of peak intensity.

Unfortunately, there have not been many quantitative structural studies published on this mixed glass system, as it has been reported to be difficult to deconvolute with certainty.[304] Nonetheless, the highest CaO-containing composition, 8.3MgO-41.6CaO-50SiO_2, matches well with what has been reported for 50CaO-SiO_2[300] and the one reported mixed composition, 25MgO-25CaO-50SiO_2 agrees as well.[303] However, the Q^n-distribution reported for 50MgO-SiO_2,[294,295] disagrees with that for the highest MgO-containing composition here (41.6MgO-8.3CaO-50SiO_2); the Q^3-species here are

much higher in concentration, however, the Q^4 concentration is also much lower as well. Furthermore, only 50MgO-50SiO_2, not 50CaO-SiO_2, has been found to contain a signicant amount of Q^4-units, which agrees with the results observed here. If it is assumed that alkaline-earth silicate glasses are similar to alkali ones, then modifiers with higher cationic strengths are expected to decrease [NBO]/[Si][156] and that is what is observed for MgO-rich glasses. Additionally, 50MgO-50SiO_2 has been found to have a [NBO]/[Si] of 1.71–1.82,[294,295] while 50CaO-50SiO_2 was observed to have an [NBO]/[Si] of 1.99,[300] which again matches the present data.

Additionally, Mg coordination has been found to decrease from 6 to 4-fold with the addition of Ca in glasses and crystals,[81] which may be the reason for decreased network connectivity (increased NBOs) at Ca-rich compositions. Often local ordering of the lighter cation increases in presence of a heavier ion compared to single-alkali glasses.[61,82] Mg has been said to have more network-forming ability than Ca due to its lower ionicity[305] and tetrahedral Mg^{2+} has the same field strength as Y^{3+} and Zn^{2+} making it more like an intermediate.[16,22] Additionally, the ranking of the bonding energy (U) is thus: $|U_{[IV]\text{Mg-O}}| > |U_{\text{Ca-O}}| > |U_{[VI]\text{Mg-O}}|$,[54] so there is an exchange of increased bond strength and rigidity from the tetrahedral Mg for decreased network connectivity. However, tetrahdral Mg is also more former like and may increase the strength of the connections outside of the silica network. It appears that octahedral Mg is better at promoting the formation of Si-O-Si bonds, or it is removing oxygen from the network to form more Si-O-Si bonds and free oxygen. Furthermore, in Fig. 5.3 larger $^{[VI]}$Mg also decreases the compactness or packing fraction (V_f) of the glass structure. Thus, opposing trends are occuring between compactness and network connectivity of the glass structure similar to those observed elsewhere.[50]

The amount of free O^{2-} (see Section 2.5.2) as a function of MgO content is quantified in Fig. 5.6. The uncertainties are quite high since calculation of $N(O^{2-})$ requires

$[NBO]/[Si]_{obs}$, which itself has three Raman peak area fitting uncertainties. Most glass compositions have $N(O^{2-})$ of $\pm 1\%$, which within the uncertainty could be insignificant. The clear exception is 0.73 MgO, which has $3\pm 1\%$ free oxygen, while 0.28 MgO and 0.67 MgO may also have significant $N(O^{2-})$. The overall trend appears to be that MgO-rich compositions are more likely to contain free O^{2-}, with the exception of 0.28 MgO. Furthermore, the increase in oxygen volume seen in the previous section correlates well the compositions that have the highest $N(O^{2-})$. Overall, these results agree well with ^{17}O NMR results which directly observed free oxygen[293] as well as with indirect ^{29}Si studies which found 0.03–0.07 mole fraction of O^{-2} in magnesium silicate glasses.[294–296] Furthermore, elsewhere Raman data showed only xMgO-$(50-x)$CaO-50SiO_2 to have any free oxygen out of several alkali and alkaline-earth silicate systems.[193,298] Given that free oxygen is more likely to occur at high modifier content, it is unsurprising that it is found in this glass system.[193,298] It also would account for the reduction of [NBO]/[Si] seen in these compositions, since now the oxygen is no longer found attached to the network, yet since O^{2-} is larger it may reduce packing density. Finally, since free oxygen has a larger coordination sphere than bounded oxygen, it may be the reason that in some cases Mg^{2+} is octahedral instead of tetrahedrally-coordinated.

5.3.4 Ionic Conductivity

Only processed conductivity data is shown here, however, the Nyquist (Z" vs. Z'), also called Cole-Cole, and Bode (Z and θ vs. freq.) plots of several temperatures for the 0.49 MgO sample can be found in Appendix C (Figs. C.3 and C.4); several additional measured temperatures were removed from these plots for clarity. The centres of the semi-circles in the Bode plots are slightly above the axis, but still can be easily fit to obtain the conductivity (κ), where $Z" = 0$ as discussed in Section 2.7.

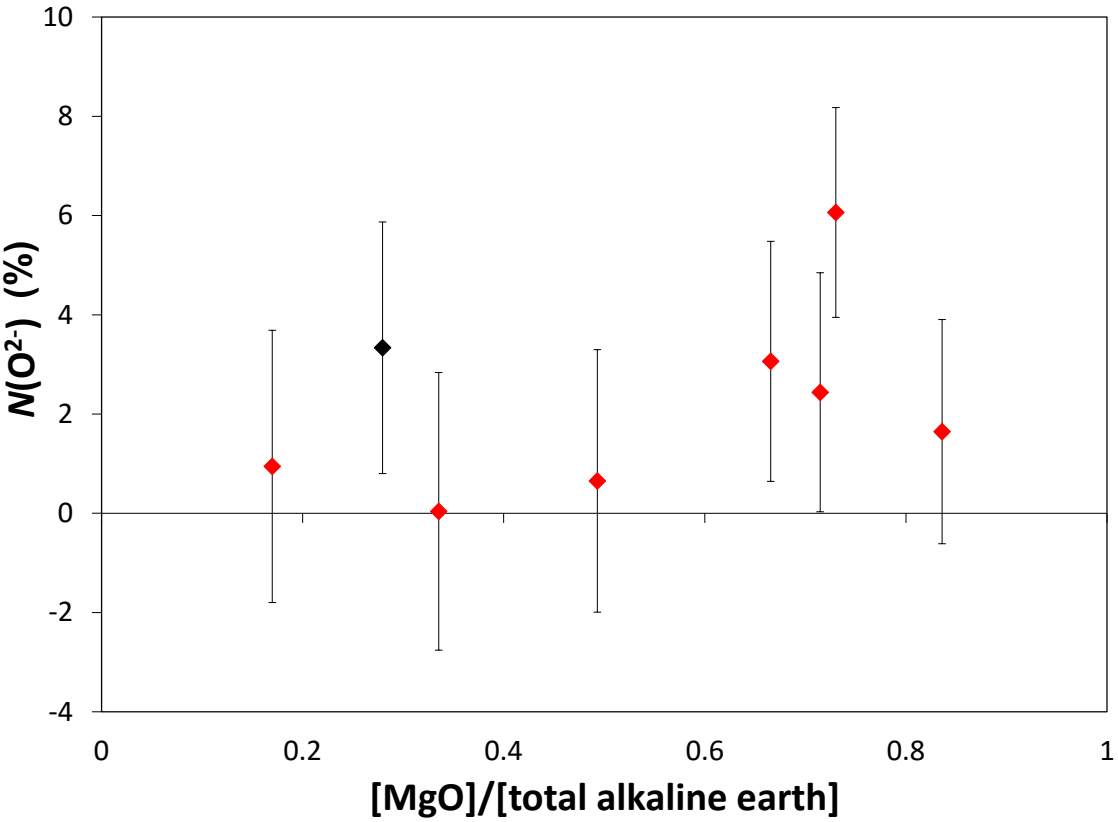

Figure 5.6: Percent of 'free' ionic oxygen, $N(O^{2-})$, of the xMgO-$(50-x)$CaO-50SiO_2 series as a function of relative alkaline-earth ratio. Large errors come from 10% fitting error for each Q^n-peak. The symbol in black represents the composition known to have ≈2% K_2O contaminant.

The plateau in the Bode plot (Fig. C.4a) is equal to the κ_{DC}; it is the frequency-independent region which corresponds to long-range movement of ions. The dispersion in the high frequency region is due to relaxation, caused by local motion of ions occurring at frequencies slower than the AC frequency.[171,306]

The conductivity isotherms shown in Fig. 5.7 clearly have a negative deviation with a maximum at approximately 0.63–0.73 MgO. Fig. 5.7 indicates that the MME in conductivity exists in mixed alkaline-earth glasses and is comparable in magnitude to the MAE, unlike what many previous studies have indicated.[95,99,100] The deviation from linearity appears smaller for this mixed-ion system than many that have been

reported for alkali systems (10^2–10^6 orders of magnitude),[58,60,184] however, this may be a result of the temperature which conductivity measurements were made in comparison to the glass transition temperature ($T_g \approx$720–770°C[99,291]). Many studies have been able to measure κ further from T_g[60,184] and the magnitude of the MME decreases with increasing temperature. The variation of the MME with T is explained by lower temperatures leading to slower structural relaxation, thus there are more restrictive parameters, *i.e*, hopping energy barriers, for diffusion.[71] Since the temperature plays a large role, it is more instructive to compare activation energies between glass series. Finally, the isotherms also exhibit the shift of the "cross-over" point (where total diffusion is at a minimum, while being equal for the two ions) towards the Mg-rich end with increased temperature, indicating that Mg is the less mobile ion.[64]

Unexpectedly, significant differences between cooling and heating were found for all compositions. Fig. 5.8 shows two compositions, 0.28 and 0.49 MgO; in the case of 0.49 MgO, there is one continuous cycle as well as separate heating and cooling curves. The initial dark red heating curves show discontinuous behaviour, while the blue cooling curves show large deviations from Arhennius behaviour (as shown more clearly in Fig. 5.9 below). Furthermore, the heating after cooling line (orange) does not show a discontinuity, only non-linear behaviour.

Deviations from Arrhenius behaviour have been reported in other systems,[60,307] yet, many authors gave no explanation or attributed it to the heating rate and thermal history of the glass. Thermal stress has been known to increase conductivity, leading to many authors noticing κ decreasing with annealing time until the samples are fully annealed.[171,307–310] Here, the conductivities of the samples were measured by heating the samples to the highest temperature measured, 650–675 °C, for an hour before slowly cooling down the samples and measuring κ at hold points. Consequently, there should be the least thermal stress at the highest temperature; stress would

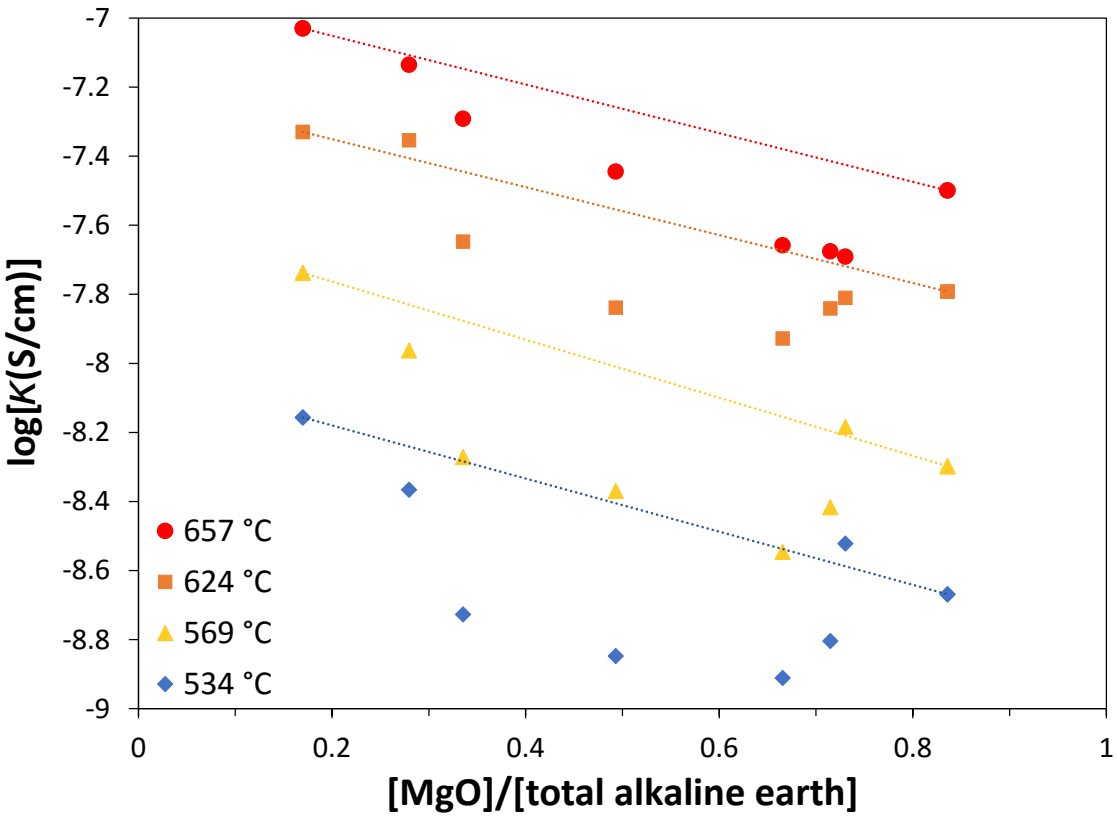

Figure 5.7: Conductivity (κ) of the xMgO-(50−x)CaO-50SiO_2 series as a function of relative alkaline-earth ratio and temperature. The actual measured temperature is ±4 °C from the reported temperature of the isotherm (not all samples were measured at exactly the same temperatures).

be introduced upon fast cooling. However, if that were the case, an increase in κ as stress is introduced would be observed during cooling—instead the opposite deviation occurred, thus, these trends are unlikely to be related to thermal stress. Due to the unexpected behaviour, many of the samples had their κ measured more than once, using different slices from the same (fully annealed) sample.

To further rule out the effect of stress, thermal expansion measurements were made on two of the samples; 24.3MgO-25CaO-50.4SiO_2 and 8.5MgO-41.6MgO-49.7SiO_2 have coefficients of thermal expansion (CTEs) of 9.0×10^{-6}/K and 7.3×10^{-6}/K, respectively. These values are not out of the ordinary for a silicate glass; they are

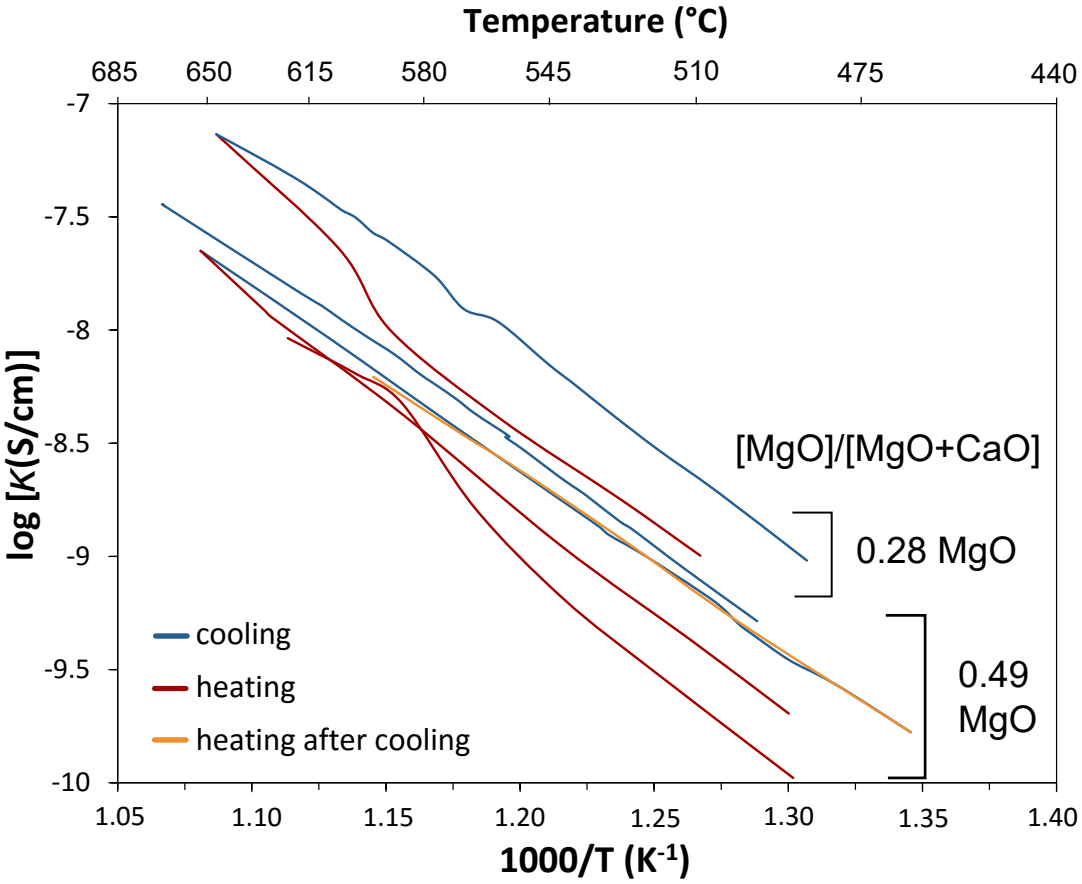

Figure 5.8: Conductivity heating and cooling curves for two samples, 0.28 and 0.49 MgO, in the xMgO-(50−x)CaO-50SiO_2 series.

on par with soda-lime glass (15Na_2O-10CaO-75SiO_2),[311] thus there is no reason to believe these glasses are more susceptible to thermal stress than other silicates. This hysteresis-like behaviour was found in all of the mixed xMgO-(50−x)CaO-50SiO_2 samples, yet the cooling portions were found to be more reliable and are shown in the following conductivity plots.

The conductivity cooling curves as a function of temperature for all compositions are also shown in Fig. C.5 in Appendix C. The data here is similar to what has been reported elsewhere.[99,289] Plots of lnκT vs. 1/T are shown in Fig. 5.9; as the composition becomes more mixed the conductivity decreases until around the 0.71 MgO composition, after which the system becomes less mixed and the conductivity

increases; this behaviour is typical of mixed-ion systems.[60] Unfortunately, this trend is to some degree obfuscated by the remarkable amount of deviation from the Arrhenius equation causing overlap between compositions. In order to better quantify the non-Arrhenius behaviour, a low and high temperature value of E_a were determined for each composition; the temperature region that applies to each is shown by connections between the points in the conductivity curves in Fig 5.9.

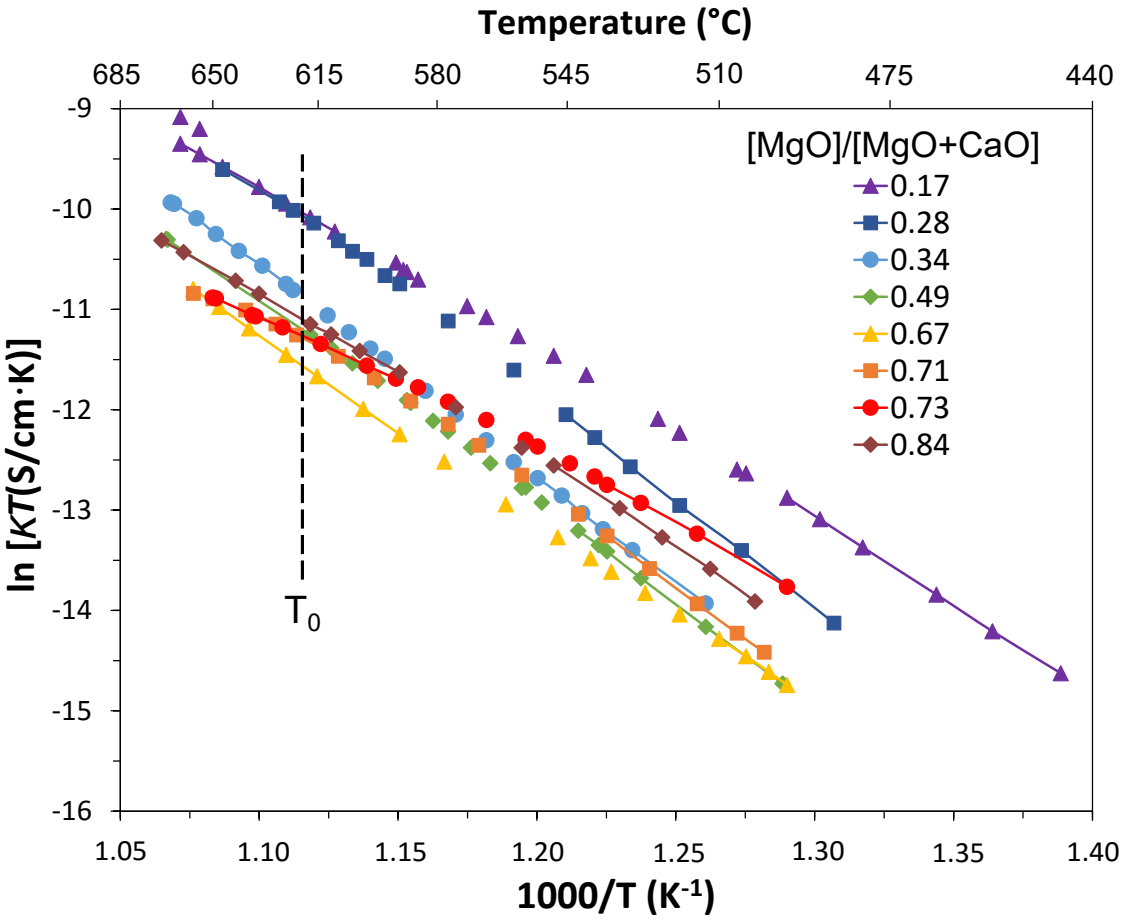

Figure 5.9: Arrhenius plot of $\ln\kappa T$ vs. 1000/T during cooling of the xMgO-$(50-x)$CaO-50SiO_2 series as a function of relative alkaline-earth ratio. Due to departure from Arrhenius behaviour, there are low-T and high-T linear fits for each composition. Common temperature point, T_0, is also plotted, where the plots are expected to overlap.

Despite possessing a smaller modifier cation, MgO-SiO_2 has been found elsewhere to have almost an order of magnitude lower conductivity than CaO-SiO_2 at the same

temperature (400 °C).[289] Furthermore, calculations of activation energies show conduction of Mg to require 1.3 times as much energy as conduction of Ca.[288] As a result, Ca^{2+} is expected to be the dominant ion carrier due to its higher mobility compared with Mg^{2+} in other systems.[312,313] This definitely appears to be the case as the higher CaO compositions possess higher κ in Fig. 5.9.

The quantified departure from Arrhenius behaviour is shown in Fig. 5.10; the experimental conductivity was compared to the theoretical value calculated from a *linear* least-squares fit of the data in Fig. 5.9. The difference data in Fig. 5.10 was fit with a 2nd-order polynomial and shows the deviations to span roughly +5% and −7.5% for all compositions. Departures from Arrhenius behaviour in glasses has been previously reported, however, the deviation was in the opposite direction for the $0.25(Li_2O\text{-}Na_2O)\text{-}0.75B_2O_3$ series.[60] Due to experimental error, a ±2% departure from linearity is expected, but it is expected to be random rather than only in one direction.[60] In this series, there is also free O^{2-} to consider and that appears to be the reason for 0.28 and 0.73 MgO having larger deviations from Arrhenius behaviour; they were also the compositions which showed more $N(O^{2-})$ from analysis of the Raman spectra, *see* Fig. 5.6.

Jain *et al.*[60] found that doping with F^- increased the deviation, while Cl^- and Br^- had the opposite effect; they attributed this to the fact that the Arrhenius equation may not apply exactly to a glass where there are distributions of saddle point energies in the structure. The low- and high-T activation energies determined from the Arrhenius plots in Fig. 5.9 are displayed in Fig. 5.11; the existence of disparate activation energies at different temperatures could be indicative of the possible range of activation energies within the glass structure. The most striking feature is how the low and high E_a differ most for the same compositions measured to have large amounts of free O^{2-} (0.28 and 0.73 MgO). It appears that at high temperatures O^{2-}

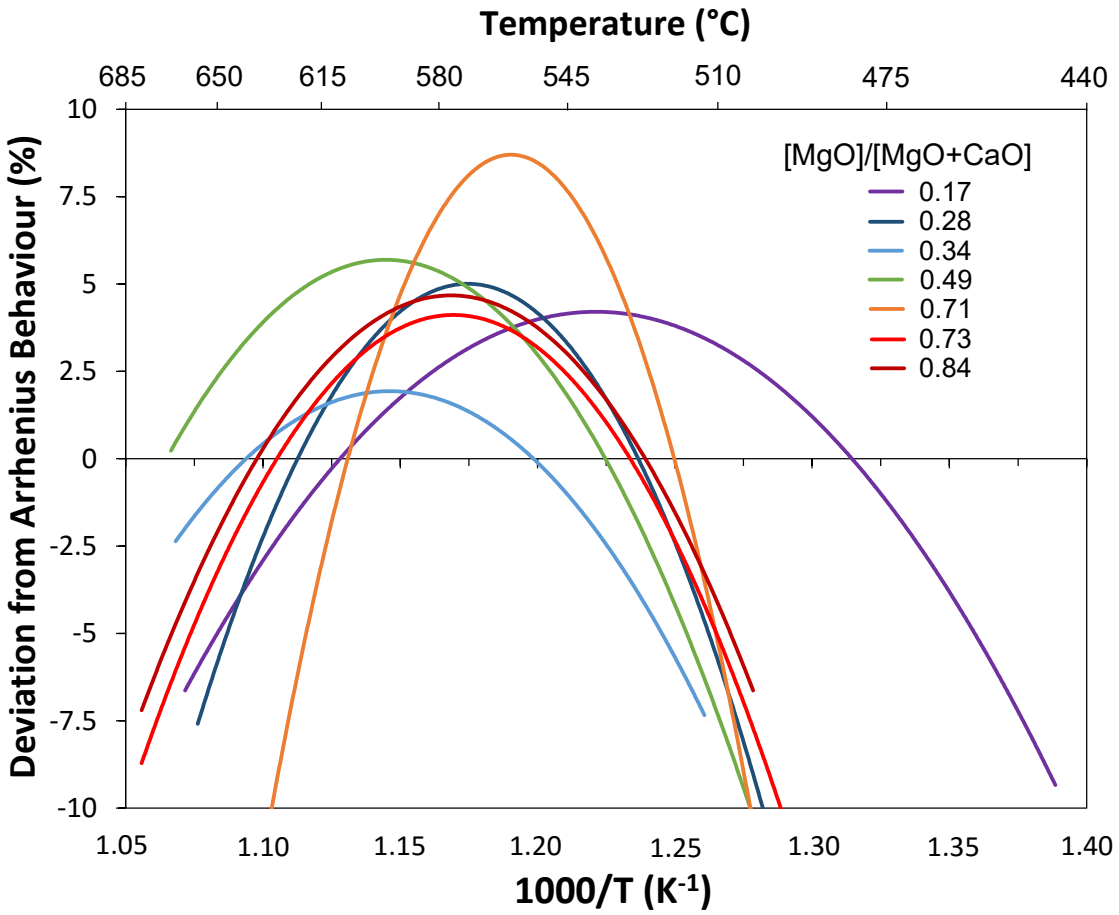

Figure 5.10: Departure from Arrhenius behaviour for conductivity data of the xMgO-$(50-x)$CaO-50SiO_2 series as a function of temperature and composition. Data is fit with a 2nd-order polynomial.

encourages mobility, yet curtails diffusion at low temperatures as well. Additionally, the outer edges of the compositional range, where less mixing has occurred, also have larger differences between low- and high-T E_a. This is opposite to the trend found elsewhere, where a higher activation energy was correlated with larger distributions and range of E_a's.[60]

If this result represents a range of activation energies, it follows that the most disparate structural environments should occur when a low amount of mixing has occurred; it must be assumed in a mostly MgO or CaO composition there is some

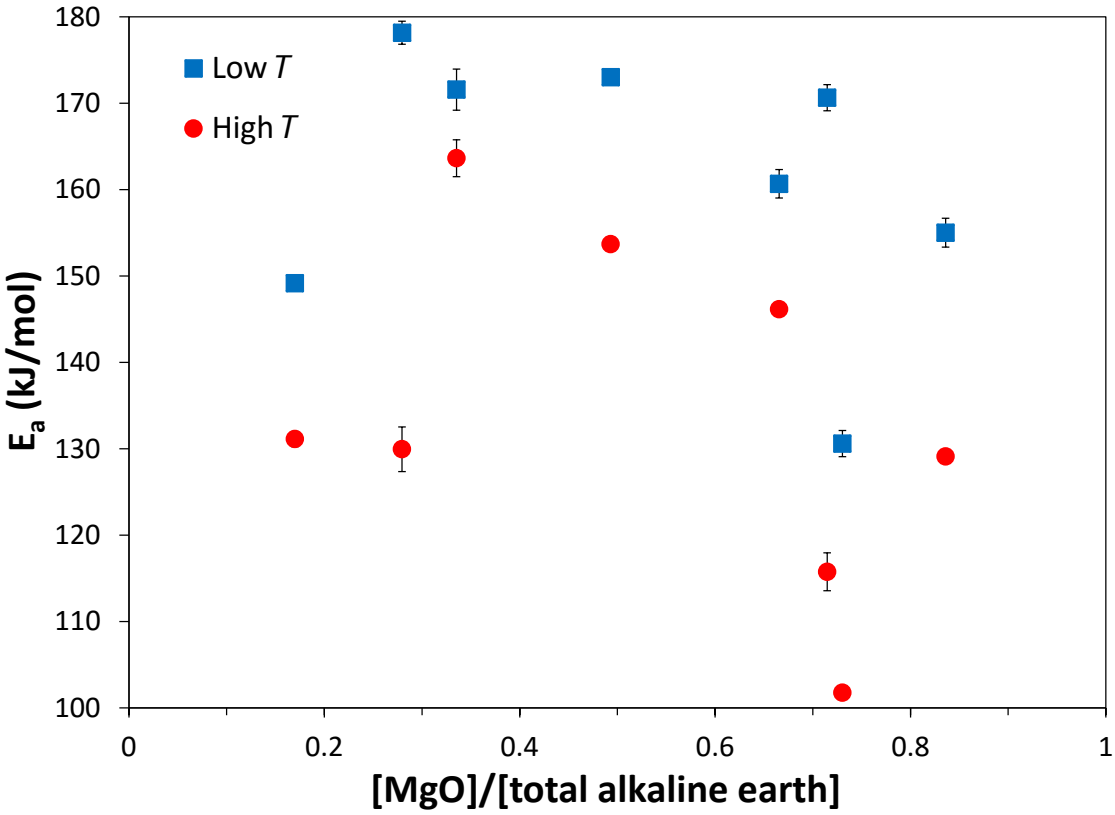

Figure 5.11: Activation energy (E_a) of the xMgO-(50−x)CaO-50SiO_2 series as a function of composition. Low and high-T values are from their corresponding regions of the Arrhenius plot (Fig. 5.9).

segregation, not full phase separation, but simply from ion proportions most of the ions in the glass will be surrounded by the largest component. For example, both Mg and Ca ions will be mostly surrounded by Mg in a high-MgO containing composition, however, in a more mixed system Mg and Ca would be surrounded by a similar combination of Mg and Ca throughout the system. These ranges of different environments likely exist in most mixed-ion systems, not only xMgO-(50−x)CaO-50SiO_2, so why this system displays more markedly non-linear behaviour is difficult to explain. It may be related to the inclination of this system to form free oxygen, but Ca-rich compositions have less proclivity to do so.[300] The fact that this system is known to be randomly mixed, *i.e.*, where Si atoms are equally likely to bond to either Mg or Ca, may also play a role, since that means high probability of diffusion paths interacting.

Additionally, the increase in packing density seems to indicate that ions are packing more efficiently than in a single-alkali glass, perhaps leading to a stronger dependence of the properties on T as the CTE would be expected to be higher as well.

As mentioned earlier, few studies have been published on mixed alkaline-earth glasses, however, the MME in E_a of alkali-containing mixed alkaline-earth silicate glasses has been reported to be approximately 22 kJ/mol (26% positive deviation).[95] The positive deviation in this system in Fig. 5.11 is 33 (25%) and 20 (13%) kJ/mol for the high-T and low-T E_a, respectively, which agree well with literature. Furthermore, the high-T E_a has a similar deviation to many mixed-alkali systems, such as Na-Rb silicate[314] and Li-Na borate,[60] indicating that the MAEE can be of comparable magnitude to the MAE. Finally, the dynamic structure model predicts the conductivity minimum to be at equal relative alkaline-earth concentrations,[72,315] but again lack of free oxygen in the Ca^{2+}-rich compositions may push the maximum towards magnesium silicate.

The pre-exponential factor (A) of the Arrhenius equation (Appendix C (Fig. C.6)) exhibits essentially the same trends as activation energies. A is commonly less explored for glass because it depends on many poorly characterized terms: the attempt frequency for ion jump, the jump distance, an ion concentration term, an entropy term and a geometrical factor.[171] Furthermore, it has a smaller role in the conductivity compared to E_a and can often have the opposite compositional trend of the conductivity, but is overwhelmed by the trend in activation energy.[60,316] Nonetheless, in this system, it appears that the pre-exponential factor is important and correlates to changes in the activation energy; this may indicate that the entropic portion of the conductivity is more important in this system than others (it is known to be well-mixed).[52,81]

Overall, the effects of static properties on the ionic conductivity are difficult to predict, in part because the static MME is small in comparison. The packing fraction and connectivity might be expected to relate inversely to ionic conductivity, simply because more open and flexible ion channels should encourage ion mobility. Indeed, Huang *et al.*[61] found molar volume to correlate negatively with conductivity in single-alkali germanate glasses, however, many authors have found the opposite to be true or no correlation between V_{m} and κ to exist, especially in mixed-ion systems.[63,64,79] Additionally, in silicate systems decreased connectivity has been correlated with reduced E_{a},[61,79,80,317] for example, the MME in ionic conduction has been observed to increase with the addition of Al_2O_3, which was attributed to the creation of BO and increased connectivity.[62]

As stated above, the difficulty of explaining the MME lies in reconciling mixing's effects of 'loosening of the structure' with 'the immobilization of the cations'.[65,72] Several AC impedance and mechanical loss experiments have shown stronger relaxation processes for mixed-modifier glasses,[65,318] assumed to be a result of 'loosening up of the structure', which may indicate a less efficient packing fraction and/or a less rigid network. Increased network connectivity is expected to introduce flexibility through introduction of Si-O-Si linkages, yet at high MgO concentration there likely exists octahedral Mg, which increases connectivity and reduces bond strength.

In Fig. 5.12, the deviation in packing fraction (which is correlated with density and molar volume) is shown to not correlate strongly with that in activation energy; only when a large amount of free oxygen is present do both V_{f} and E_{a} decrease. The amount of free oxygen correlates better with E_{a}; large amounts of $N(\mathrm{O}^{2-})$ lower the activation energy significantly. Usually, oxygen is treated as being immobile since it is larger (138 pm) than most mobile ions and more charged than alkalis.[22] However, in this case, higher connectivity of the network and 6-coordinated MgO result in a

more flexible structure, which would help both Ca^{2+} and O^{2-} diffuse through the network. Free oxygen is rarely found in a silicate glass, thus it is difficult to know its exact role in conduction, only that it lowers E_a and appears to reduce the dependence of conductivity on temperature at high temperatures.[156] O^{2-} could be participating directly in the ion conduction or perhaps creating ion clusters (where it is surrounded only by cations) which would likely increase the mobility of the surrounding ions.

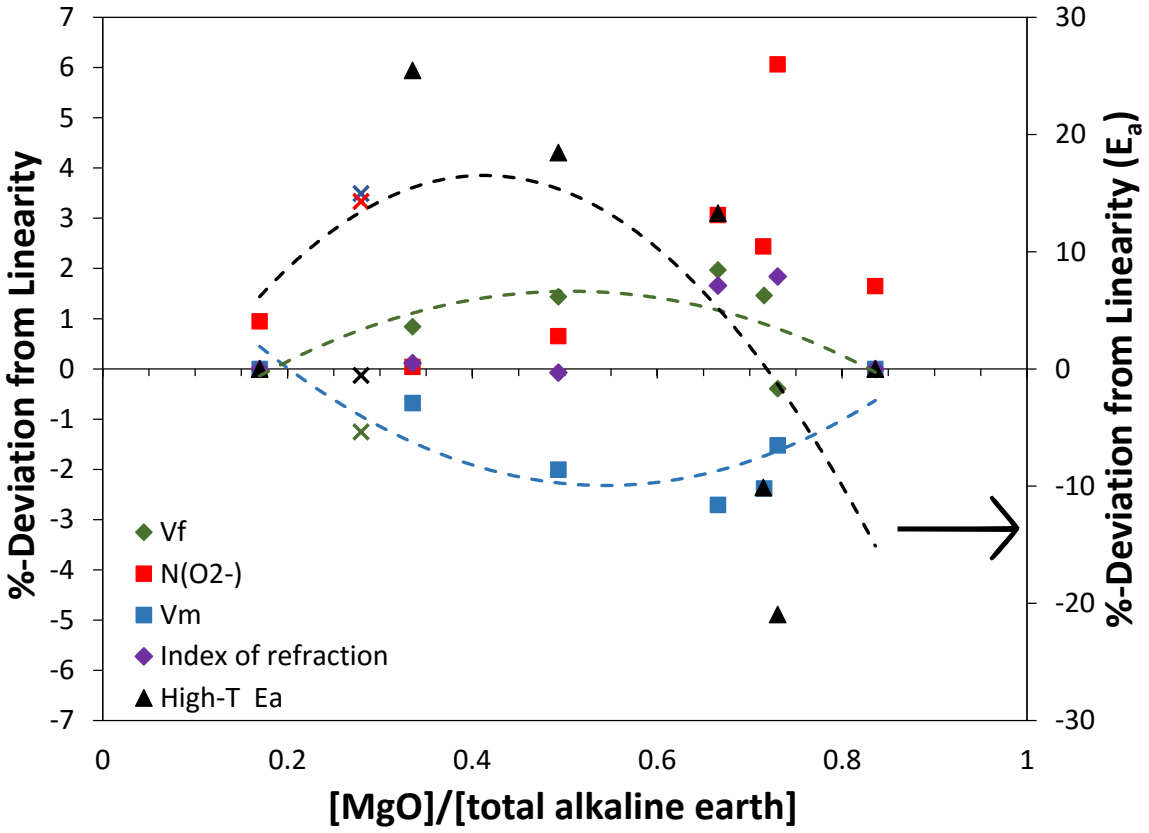

Figure 5.12: The MME in xMgO-$(50-x)$CaO-50SiO_2 as a function of relative MgO content. The static properties: density (ρ), molar volume (V_m), packing fraction (V_f), oxygen volume (V_O) and index of refraction are on the left axis, while the deviation from linearity for the high-T E_a is on the right axis. The dashed lines are fits to the apparent trends with 2nd-order polynomials. Error bars are not shown for clarity, but can be found in corresponding Figs. 5.2, 5.3, 5.6 and 5.11.

Many of the compositions, such as, 0.28, 0.66, and 0.73 MgO all have similar $N(O^{2-})$, yet differing E_a's; thus network connectivity also plays a role. Given the

curvature of [NBO]/[Si] shown in Fig. 5.5, network connectivity is lower than additivity predicts. By comparison to Fig. 5.12, this suggests that increased structural rigidity reduces ion mobility in the mixed compositions. On the other hand, the 0.84 MgO composition, which has the lowest [NBO]/[Si], should have the most flexible structure, yet it does not have the lowest E_a (Fig. 5.11), in fact, it is very similar to its compositional opposite 0.17 MgO. Perhaps, then, there is a structural mixing component as well, such as clustering vs. intercepting ion channels.

Long-Term Conductivity

In order to investigate which ion(s) was the mobile carrier, long-term DC conductivity measurements were performed in air at 600 °C (Fig. 5.13). The graphs are complicated somewhat because the silver from the electrodes played a role in addition to the glass components. Fig. C.8 in Appendix C shows the movement of Ag into the glass and the movement of Ca^{2+} and Mg^{2+} out into the electrode material (the electrodes are silver in an inorganic matrix). Although this is less than ideal, a similar experiment at higher temperatures with a protective thick coating of Au between the electrode and glass was performed, yet no appreciable movement of the ions was detected by WDS. This is likely because having an ion source and sink encourages conduction because there is no net build-up of charges at the electrodes.

The data are unusual because for the most part the WDS lineshapes are symmetric, however the plots show the following features (described from left to right in Fig. 5.13): first the more mobile Ag^{+} ions conduct into the glass from the cathode, thereby allowing Ca^{2+} and Mg^{2+} to move towards the anode. Additionally, the Ca^{2+} and Mg^{2+} transfer from the glass into the electrode sink at the anode, thus both ions are depleted at both ends of the sample. This is observable in Fig. 5.13b and c, which

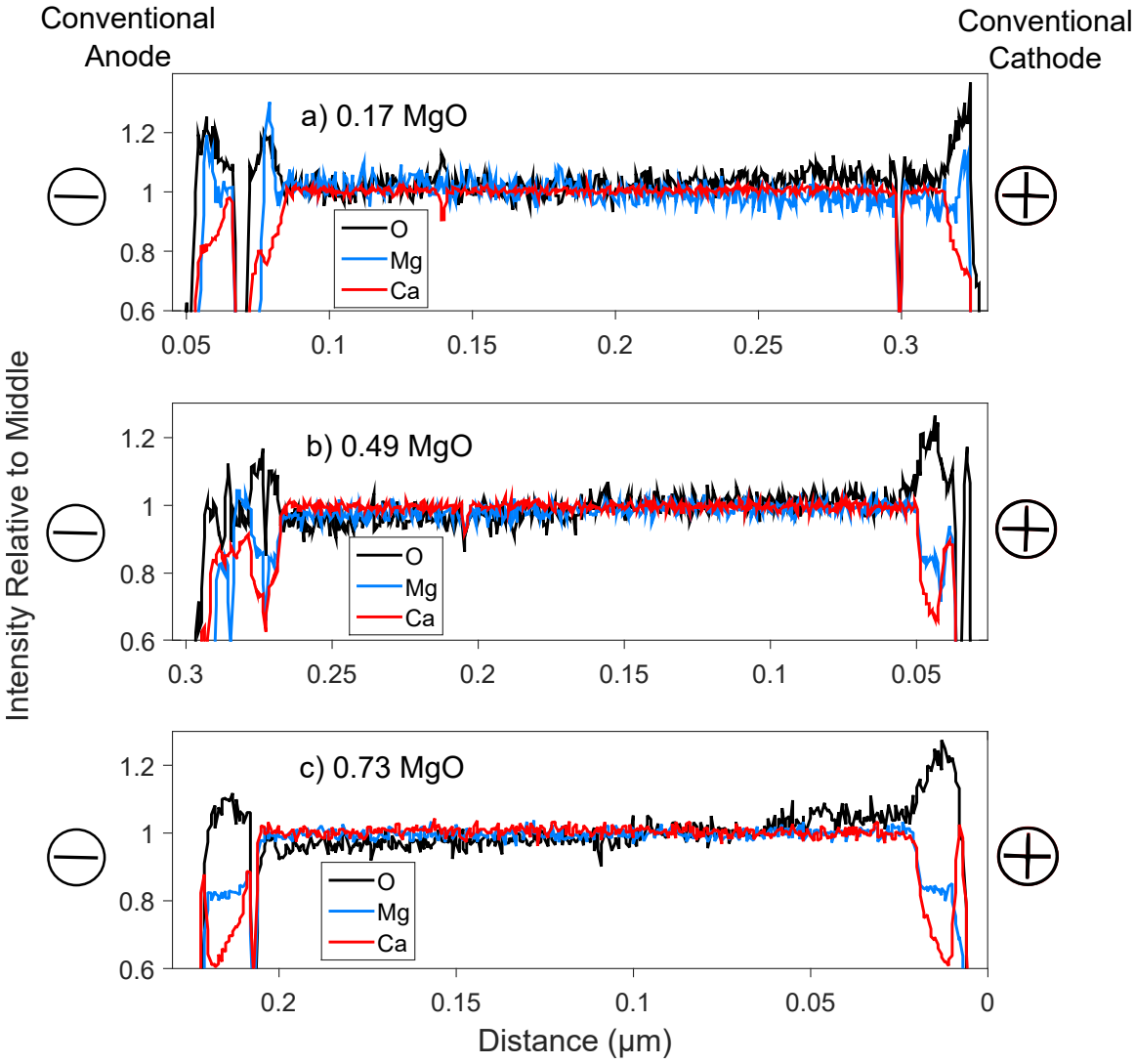

Figure 5.13: Relative compositional profiles measured by WDS from high temperature (600 °C) long-term conductivity experiments of the xMgO-(50−x)CaO-50SiO_2 series.. Intensity scale is relative to the middle of each corresponding element. Distance scale is small because only the sample edges were examined and "stitched" together, removing the less affected middle region. The error of the oxygen intensity is ±0.03, while the other elements are ±0.02.

show a slope of increased Ca^{2+} towards the anode. The other observation that can be made is regarding which ion is more mobile, Ca^{2+} or Mg^{2+}; in Fig. 5.13a, it is clearly Ca^{2+}, as Mg^{2+} is "playing catch-up" and has peaks where Ca^{2+} recently vacated in an attempt to balance charges. The "catch-up" peaks of Mg^{2+} are diminished in Fig. 5.13b and c, as Mg^{2+} conductivity is expected to increase with MgO content,

thus at 0.73 MgO, the two ions could be approaching comparable mobility. Finally, with Ag^{+} entering from the cathode, there can also be movement of Ca^{2+} or Mg^{2+} into the cathode to maintain charge balance. These plots also confirm that despite its larger size Ca^{2+} is, in general, more mobile.

An oxygen peak at either end of the sample was observed as well. An apparatus to vary the oxygen concentration of the atmosphere (which is required for oxygen mobility experiments) was unavailable to the author and thus these measurements were performed in air and O^{2-} has a source and sink. However, there is diffusion of Ag into the glass at both anode and cathode (Fig. C.8); the oxygen peaks imply that there must be some diffusion of Ag metal which becomes oxidized from the atmosphere. Nonetheless, based on the Raman and oxygen volume results, in addition to what is known from the literature[294,295] about this system, the oxygen is expected to be mobile and to be partly responsible for the sharp, larger O^{2-} peak at the cathode. The most confirming evidence comes from the slope of [O] across the sample, which shows a net migration towards the cathode, especially in Fig. 5.13c. This sample is predicted, given the Raman and conductivity results discussed above, to have the most free oxygen. It is interesting that oxygen appears to be mobile in all compositions given that $N(O^{2-})$ was below the margin of error in some cases (Fig. 5.6). However, in yttria-stabilized zirconia O^{2-} was found to be the charge carrier rather than Y^{3+} due to oxygen vacancies in the structure,[319] here Mg^{2+} has the same field strength as Y^{3+}, so it is possible that oxygen is somewhat mobile in all compositions.

5.3.5 Mechanical Properties

The MME in Young's modulus (Y) in Fig. 5.14 is quite small ($\approx$5%) relative to many mixed-alkali systems, which show $\pm$20% departure from linearity.[58] Similarly,

Poisson's ratio (μ) exhibits only a small MME, ≈5%. This may be to MgO and CaO having similar effects on the structure leading to similar mechanical properties. Indeed, other mechanical studies of Mg-Ca sodium aluminosilicates saw little change in Y with varied relative alkaline-earth concentration.[33,96]

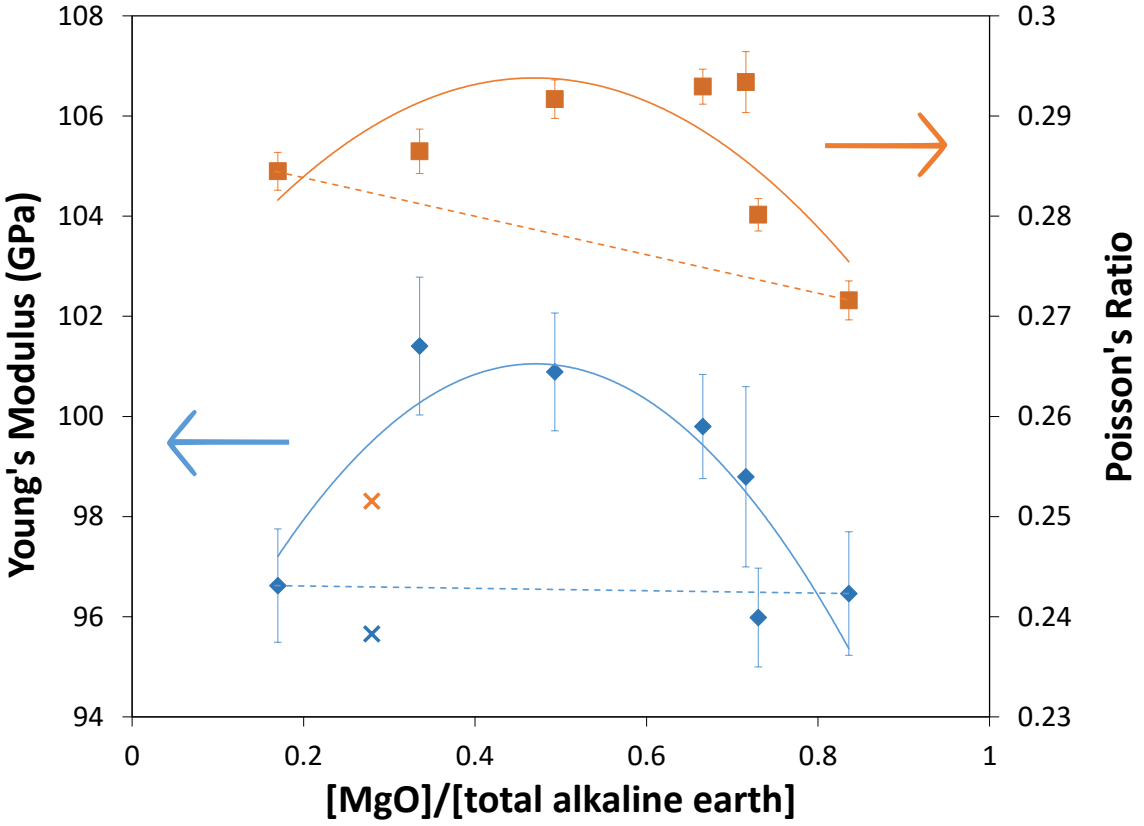

Figure 5.14: Young's modulus (Y) and Poisson's ratio (μ) of the xMgO-(50−x)CaO-50SiO_2 series as a function of relative alkaline-earth ratio. Solid lines are the apparent trends fit with 2nd-order polynomials, while the dashed lines are linear fits between the two endmember compositions.

This is further corroborated by the small deviation observed in shear modulus (G) in Fig. 5.15: approximately ≈5% once more. Bulk modulus (K) showed a somewhat larger departure from linearity, ≈10%. Again, G was shown elsewhere to be independent of alkaline-earth ratio in Mg-Ca sodium aluminosilicates.[96]

Values of the mechanical properties for the end-member compositions have not

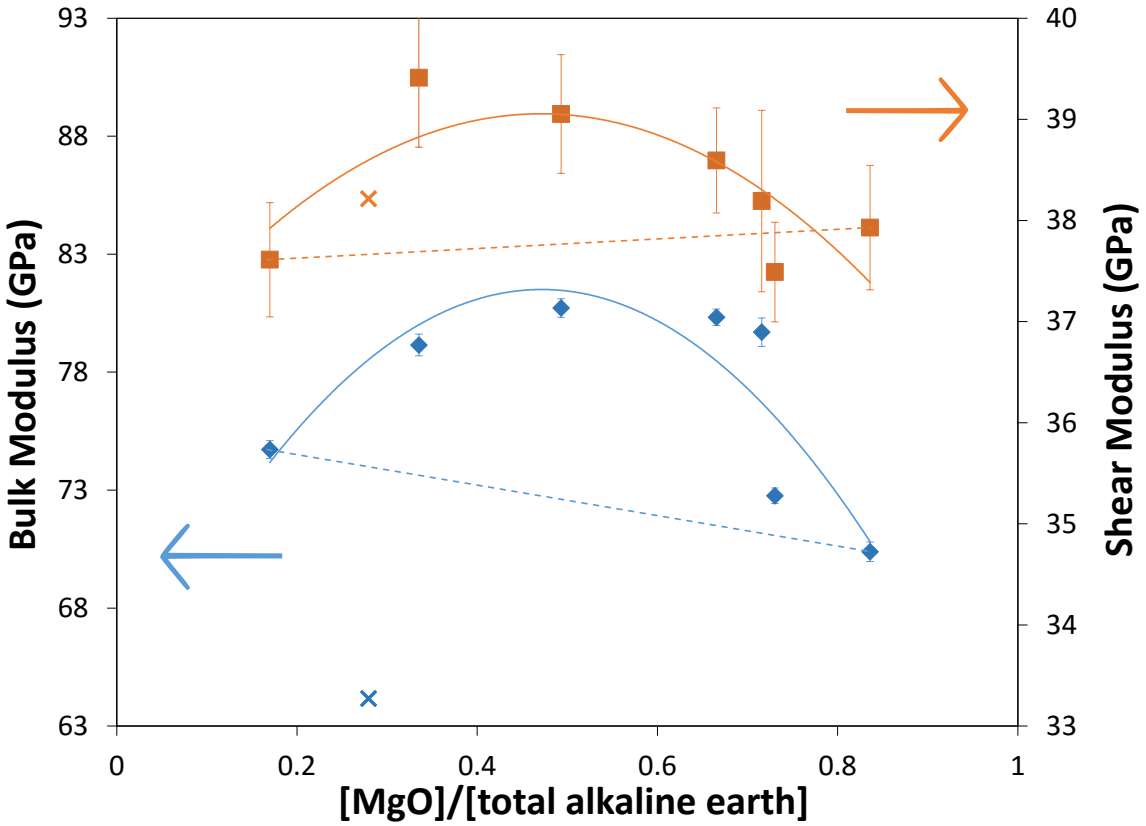

Figure 5.15: Bulk modulus (K) and shear Modulus (G) of the xMgO-(50$-x$)CaO-50SiO_2 series as a function of relative alkaline-earth ratio. Solid lines are the apparent trends fit with 2nd-order polynomials, while the dashed lines are linear fits between the two endmember compositions.

been reported in the literature, however, two mixed compositions reported have mechanical properties in the same range as these samples, only K was somewhat higher (5%) for the current results.[52] Additionally, as is seen here the replacement of MgO with CaO increases Y and μ.[54] Finally, it has been observed that μ and K are correlated with compactness of framework structure. Thus, the directionality of the MME, i.e., the fact that μ and K of the MgO 0.71–0.73 samples show the largest MME, could be significant as this follows the same trend as the packing fraction in Fig. 5.3. Conversely, the reverse is observed for Y and G, where the calcium-rich compositions show the largest MME, thus, it may be that these properties do not correlate as strongly with the compactness of the structure. G represents resistance to constant-volume strain, so perhaps bonding, rather than packing fraction, is more of a determinant. Although [NBO]/[Si] increases in the high CaO content region, fewer Si-O-Si bonds means less network flexibility; in addition, Mg^{2+} is also tetrahedral in this composition region, indicating that it is behaving more like a former and leading to an increase bond rigidity. Consequently, it appears bond rigidity rather than connectivity alone influences G.

Vickers hardness (H_V) shows a maximum of approximately 10% improvement, while toughness saw a maximum degradation of approximately 22% (Fig 5.16). The magnitude of the MME in H_V here is similar to that in mixed-alkali glasses, which has been reported as $\approx \pm 10\%$.[58] Although the deviation in H_V is similar in magnitude to that in mixed Mg-Ca sodium aluminosilicates,[33,96,98] in those materials the deviation was negative. Fracture toughness (K_{Ic}) exhibits a negative deviation, which is the opposite of those reported in mixed Li-Na glasses.[46] The large uncertainties in fracture toughness result from compounding of errors from Y, H_V and crack lengths.

Fig. 5.17 compares the mechanical properties to the static and dynamic properties; it only includes bulk and shear moduli for clarity (only two moduli are needed to

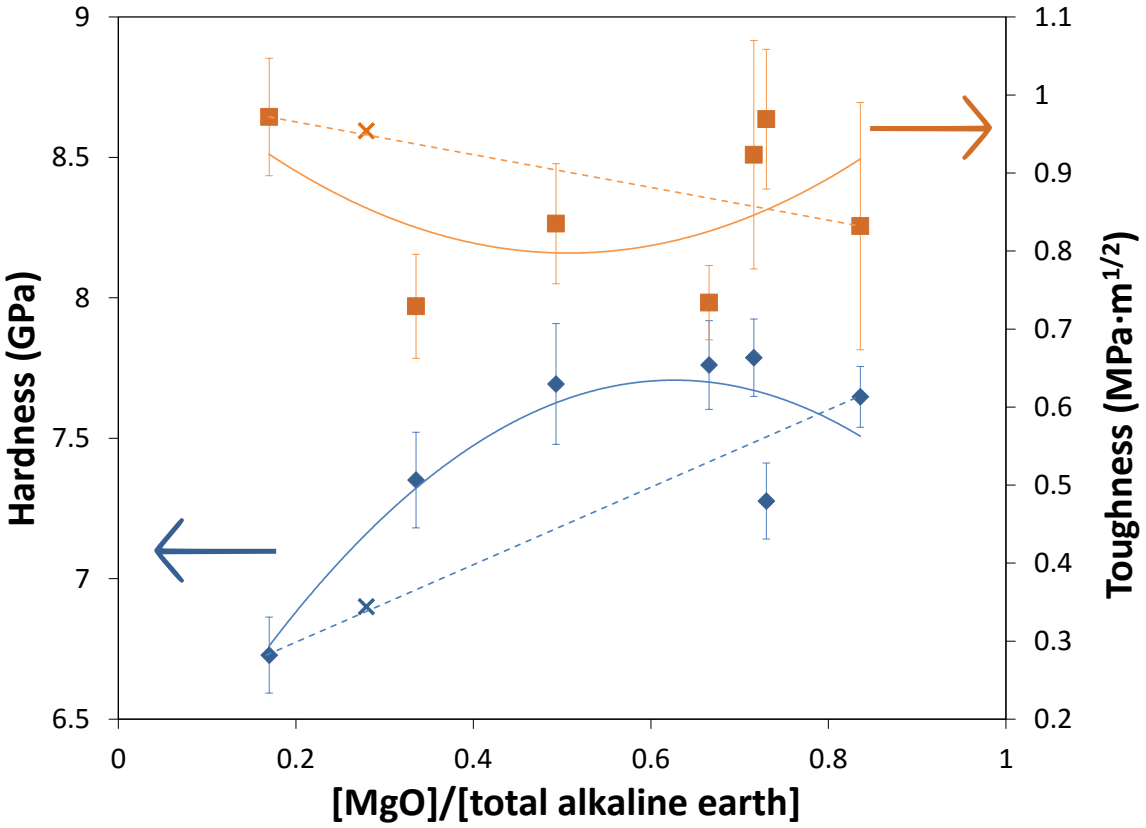

Figure 5.16: Vickers hardness (H_V) and fracture toughness (K_{Ic}) of the xMgO-(50−x)CaO-50SiO_2 series as a function of relative alkaline-earth ratio. Solid lines are the apparent trends fit with 2nd-order polynomials, while the dashed lines are linear fits between the two endmember compositions.

describe all four, μ can be found in Fig. C.13 in Appendix C). The effects of static properties, *i.e.*, packing fraction and connectivity, on the mechanical properties have been well studied.[3,26,50,52] Connectivity or network dimensionality is often described by [NBO]/[Si], but highly-coordinated modifiers have been said to increase cross-linking density as well, but usually bond strength is decreased. Additionally, silicates become *less* compressible with reduced connectivity; Si-O-Si linkages are known to be much more flexible compared to isolated SiO_4^{4-}-units.[53,54,296] Thus, as [Mg] increases, a more connected, yet flexible open framework appears. Finally, it has been suggested that oxygen stabilized by multiple types of alkaline-earth forms stronger bonds which should lead to improvements in properties which depend on bond strength; the Mg^{2+}

and Ca^{2+} cations should be well-mixed for this system.[81,83]

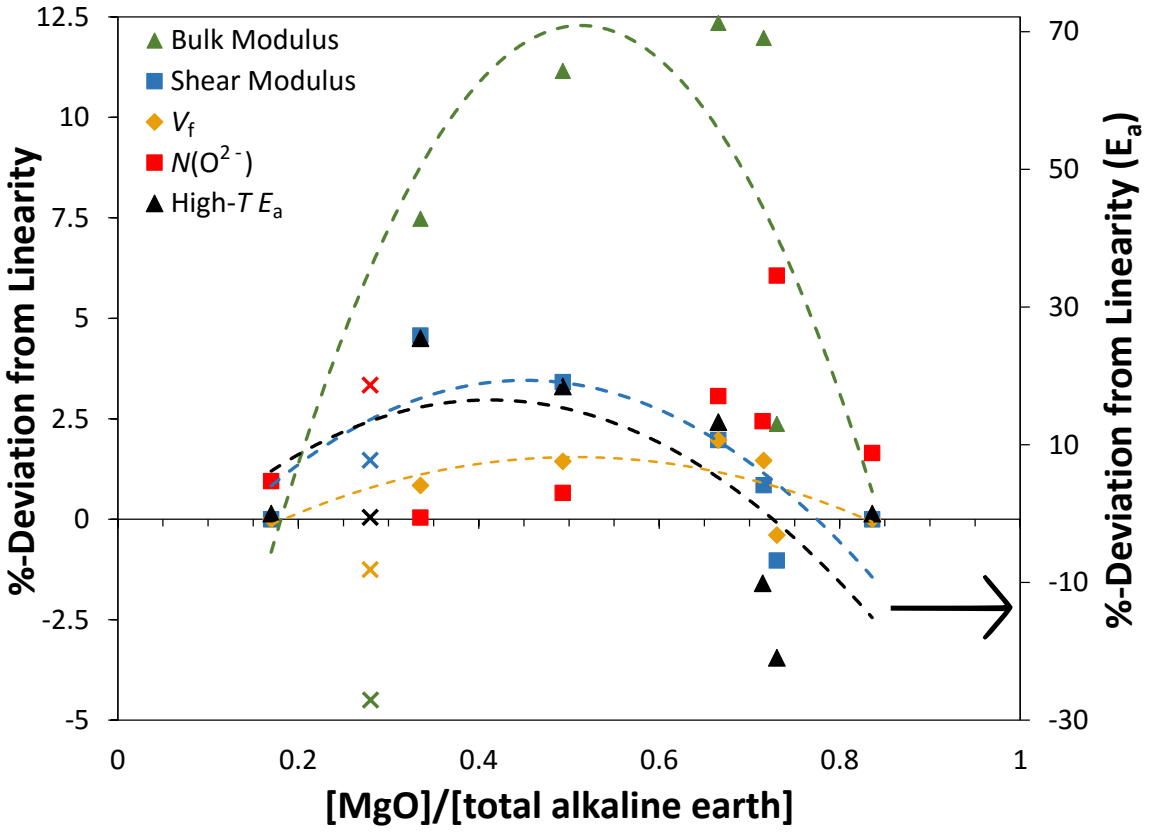

Figure 5.17: The MME in xMgO-(50−x)CaO-50SiO_2 as a function of relative MgO content. Mechanical properties (bulk, K, and shear moduli, G) and static properties (packing fraction, V_f, and free oxygen, $N(O^{2-})$) are on the left axis, while dynamic properties (high-T E_a) are on the right axis. The dashed lines are fits to the apparent trends with 2nd-order polynomials. Error bars are not shown for clarity, but can be found in corresponding Figs. 5.3, 5.6, 5.11 and 5.15.

As expected, K correlates strongly with V_f, however it has an unexpected relationship with [NBO]/[Si] (Fig. 5.5); in general K increases with increased network connectivity, except at MgO-rich compositions. μ (Fig. C.13 in Appendix C) has the similar trends and magnitude as K; like K, μ also depends heavily on V_f, but inversely with connectivity.[3,26,50,54] It is important to remember that with additional MgO, the coordination number of Mg should transition from four to six-fold leading to a decrease in bond strength and packing density (since octahedral Mg and Ca are more alike in size).[54,81,83] The sudden change in many properties at about 0.75

MgO could be due to this tetrahedral-octahedral transition. This would mean that while tetrahedral Mg exists, the packing fraction is high, *in addition* to there being fewer flexible Si-O-Si linkages and higher bond strength of Mg-O, but once octahedral Mg appears, the packing fraction decreases, and the flexible Si-O-Si bonds are more prevalent and lower strength Mg-O bonds are present.

Interestingly, bulk modulus and V_f (and μ in Fig. C.13 in Appendix C) have different maxima then does activation energy, contradicting the idea that increased free volume means more open ion channels and encourages ion conduction. The current explanation for the MME (DSM model[71]) includes a strain energy term, which is required to accommodate the motions of cations through the network; thus, the elastic moduli should be expected to influence the energy required for the glass structure to relax. An E_a increase with increasing Ca content was observed (Fig. 5.17), which indicates that [NBO]/[Si] (Fig. 5.5) and G, which show similar trends, are useful predictors of the structural rigidity here. However, as K exhibits the opposite trend, it appears to be a poor predictor of the structural rigidity, as is relevant to ion conduction, in these glasses. Tetrahedral Mg is more former-like and should increase the structural rigidity outside of the silica network, which appears to be correlated with the maximum deviation in G; this is interesting because it highlights how the modifier connectivity can be more important than the connectivity of the network, as [NBO]/[Si] shows the opposite compositional trend of modifier connectivity (however, both show the same trends in bond *rigidity*).

Fig. 5.18 compares static and dynamic properties to hardness, fracture toughness and Young's modulus. Hardness and resistance to densification are generally inversely correlated to network connectivity in silicates.[50,54,98,320] At the same time, densification is also less efficient if the packing fraction is higher.[98]

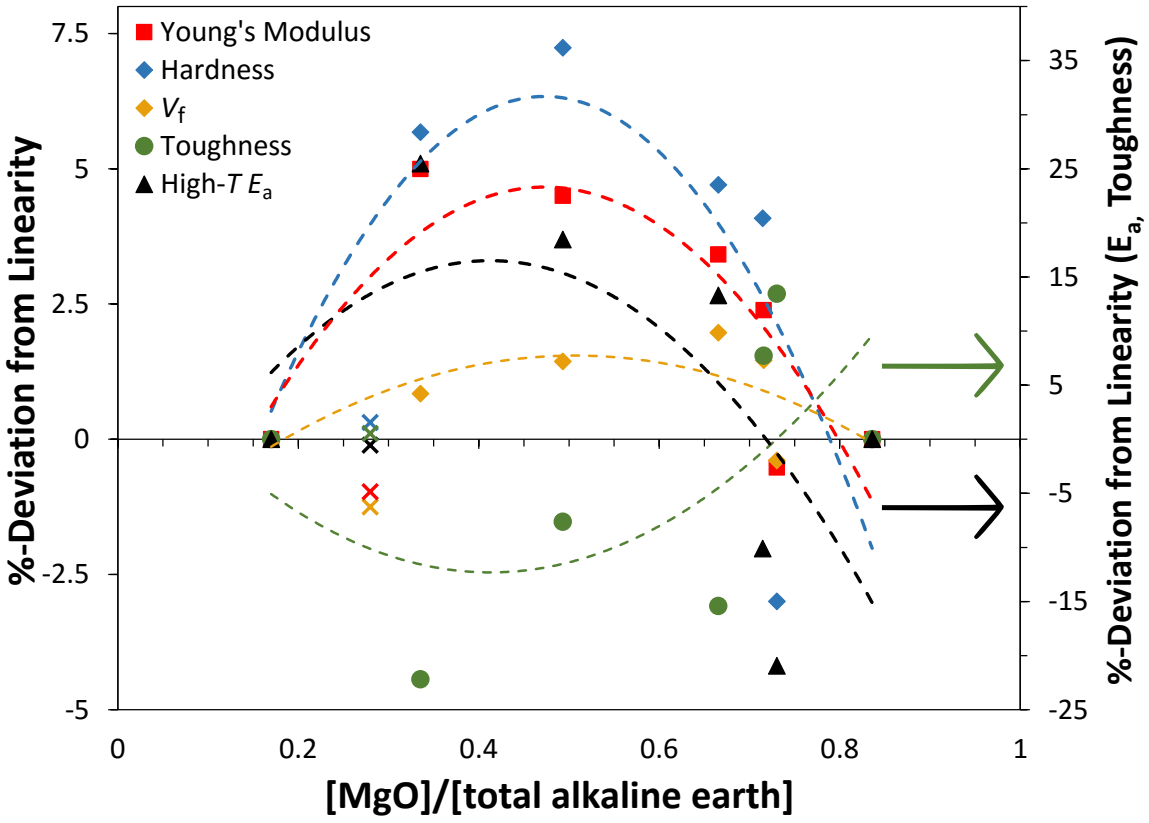

Figure 5.18: The MME in xMgO-(50−x)CaO-50SiO_2 as a function of relative MgO content. Mechanical properties (hardness, H_V, fracture toughness, K_{Ic} and Young's modulus, Y) and static properties (packing fraction, V_f, and free oxygen, $N(O^{2-})$) are on the left axis, while dynamic properties (high-T E_a) are on the right axis. The dashed lines are fits to the apparent trends with 2nd-order polynomials. Error bars are not shown for clarity, but can be found in corresponding Figs. 5.3, 5.11, 5.14 and 5.16.

Plastic flow (which affects hardness and toughness) has been reported to occur under stress in glasses with large modifier concentrations.[56] However, the introduction of two different alkali metals creates alkali-alkali interfaces within the material, thusly reducing slippage along NBOs, therefore, shear flow decreases and overall rigidity is increased.[24,46,77] Yet, measurements of plastic flow are necessarily obtained in an inelastic regime, so they may not apply to the elastic response which generally involves smaller energies. For a large (1%) strain, approximately 1 kJ/mol of energy is required, yet 100-200 kJ/mol is required for ion conduction, so it is uncertain whether

correlations between mechanical properties and E_a can be expected. Moreover, the extent to which the cations would need to move for their motion to affect the elastic moduli is unknown. The measured E_a is an average of the energies of possible ion "hops", but the energy required to shift the positions of the ions without moving them between sites ("ion settling") is not known, except that it is posited to occur well-below T_g ($\approx 0.3T_g$).[71] Consequently, it is not possible based on this series alone to conclude whether reduced cation conduction is responsible for the positive deviation observed in resistance to shear flow (seen in H_V and G) or if the rigidity of the more numerous NBOs is responsible.

Since negative deviations in H_V are generally attributed to increased μ and irreversible shear flow (plasticity), rather than densification,[33] the observed positive deviation in H_V here can be assumed to be due to increased rigidity of the anions and/or cation bonds. Resistance to deformation can be separated into an elastic densification component (K) and a plastic response component (αG), and has been found to be proportional to $(\alpha GK)^{1/2}$, where α is a material-dependent constant related to bond strength.[32,33] At lower MgO content, the trend in H_V is similar to that in V_f and K, however at MgO concentrations of 0.67 to 0.73, it appears that E_a and G play a larger role. Consequently, it may be that 0.67–0.73 MgO compositions also have lower bond strengths (from increased BOs and octahedral Mg) in addition to lower G.

Eq. 1.4 tells us that fracture toughness should vary with Y and $1/H_V$. K_{Ic} has mostly negative deviations, which would be expected to indicate some combination of decreased Y and increased H_V, however, in Fig. 5.18 it can be seen that both properties have increased at approximately the same magnitude. At a result, it appears that any gains made in Y are cancelled out by increases in H_V. Additionally, the K_{Ic} model of Eq. 1.4 has been found to overestimate fracture toughness when

densification takes place, which occurs more when packing density is lower,[26,45,46] and here tougher materials are observed to have low V_f's. It appears that fracture toughness follows E_a, where compositions with higher mobility have increased fracture toughness. Mohajerani *et al.*[46] also found the shorter crack lengths in mixed samples and attributed this finding in part to the indents introducing less residual stress to the bulk of the material. Therefore, the reduced crack lengths seen here for 0.28 and 0.71–0.73 MgO could be a result of lower E_a and increased ion mobility; ionic mobility is thought to partly relax applied stresses.[78]

5.4 Summary

First and foremost, it has been shown that the MME exists in pure mixed alkaline-earth systems, and is comparable in magnitude to the typical MAE. Unlike systems which included an alkali as well, xMgO-$(50-x)$CaO-50SiO_2 had large positive deviations from linearity in density, packing fraction, [NBO]/[Si], activation energies and all mechanical properties, except for toughness, which showed a negative deviation. Density measurements and Raman spectroscopy indicated that structural compactness was exchanged for increased network connectivity as MgO content increased, however, this was at odds with the behaviour of the mechanical properties G and K. Given the field strength and electronegativity of Mg^{2+} it may be acting more like a network former (especially in its 4-coordinate state) and increasing rigidity and G by creating stronger iono-covalent bonds. Additionally, free oxygen was observed indirectly for compositions with high MgO content.

Ionic conduction was found to significantly depart from Arrhenius behaviour well below T_g, resulting in different activation energies in different temperature regimes. Given both the sign and consistency of the non-Arrhenius behaviour (non-linear on

logarithmic scale) in all compositions it was attributed to the structure possessing a range of possible energetically-differing configurational states, some of which are not accessible at low temperatures. Surprisingly, larger deviations in E_a were found to correlate with smaller deviations in V_f, although both properties still had positive deviations indicating lower free volume is correlated with lower ionic conductivity. Increased network connectivity, and therefore, flexibility, are thought to play a role in ionic conductivity as well, where generally compositions with lower [NBO]/[Si] had lower E_a. Finally, it is difficult to know the precise role of free oxygen in conductivity, but its presence is associated with reduced activation energy.

The effects of packing fraction was easily discernible in μ and K, however the number of flexible Si-O-Si linkages did not have a significant effect on these elastic moduli. G and Y were more difficult to explain as they were correlated inversely with network connectivity, yet they followed trends in average bond strength and rigidity. The trend in E_a was the same as for G and Y, indicating that these elastic properties could affect ion conduction. Additionally, hardness and especially fracture toughness exhibited correlations with E_a, while H_V also correlated with V_f and K as well. For these two properties which involve large plastic deformations and have larger deviations than the elastic moduli, it is possible that the MME in dynamics plays a role. Overall, mechanically the best composition is 0.49 MgO, which does not have the lowest conductivity, thus, κ does not appear to, by itself, be a predictor of mechanical properties.

Clearly, the interplay between mechanical properties, structure and ionic conduction is complex and difficult to fully understand. However, it is likely that the increased former character of Mg at high Ca content is responsible for higher E_a and reduced ion mobility. This increased rigidity outside of the silicate network, in turn, reduces shear flow, thereby increasing hardness (plastic component) and decreasing

fracture toughness. Additionally, octahedral Mg^{2+} could be responsible for decreased packing fraction, which leads to lower K, μ and hardness (elastic component) as well. As a result, there may be a trade off between the more efficient packing fraction and that increased rigidity during plastic deformation that the MME can provide. Overall, the present data agrees that the MME is a dynamic process which depends on the ability of the network to dilate during ion conduction, which in turn is related to the nature of the chemical bonds in the system. Finally, since Y and G appear to be dependent on the same structural mechanism as E_{a}, they may be predictors of the compositional dependence of conduction.

Chapter 6

Evaluation of Mixed-Modifier Effect in Multiple Glass Series

6.1 Background

Chapter 5 focussed on mixed-modifier glasses containing only alkaline-earth ions in order to ascertain that the "pure" MAEE exists in static, dynamic and mechanical properties. In this chapter, several combinations of mixed alkali and/or alkaline earth silicate compositions were synthesized and studied to explore some of the many theories put forth about the MME, particularly by Dietzel[83] (see the end of Section 1.4), and to test whether they are generally applicable to systems where different types of modifiers are mixed.

Although the MME in mixed alkali systems has been the focus of considerable study previously, the interactions between the MAE in different properties is still not well-understood. The analysis presented in Chapter 5 to a mixed alkaline earth series was therefore applied to several mixed alkali series. $x\mathrm{Li_2O}$-$(30-x)\mathrm{K_2O}$-$70\mathrm{SiO_2}$ was characterized as the "baseline" mixed-modifier series; it contains only alkali ions with large differences in size and field strength, is completely within the glass-making region and had not been well-characterized, unlike mixed $\mathrm{Li_2O}$-$\mathrm{Na_2O}$-$\mathrm{SiO_2}$ compositions.[46,80] Next, $x\mathrm{Li_2O}$-$(30-x)\mathrm{Rb_2O}$-$70\mathrm{SiO_2}$ was studied to evaluate the effect of having larger differences in size and field strength between the two ions. Finally, the

effect of increasing the modifier content was investigated by characterization of the $x$$Li_2O$-$(40-x)$$K_2O-60SiO_2$ series and comparison to the $x$$Li_2O$-$(30-x)$$K_2O-70SiO_2$ series. It is known from many ionic conductivity studies that larger differences in size (or cationic strength in the case of only alkali ions) lead to larger deviations from linearity, additionally, more total alkali content should have a similar effect.[58,64,79,80] Understanding the effects of these modifications on static, dynamic, and mechanical properties in relatively simple mixed alkali series may shed light on the origins of the MME. Thereafter, the same type of analyses are applied to several different combinations of mixed alkali-alkaline earth silicate series.

Although authors have supposed that the differences between the ions are most important, it is possible that the identity of the ion is important as well.[64,83] In order to aid in the discussion, Table 6.1 shows the parameters of the cations, while Table 6.2 compares the parameters of each ion pair used to make mixed-modifier compositions in this work. The E_a of ionic oxygen is a range since the structure of the material greatly affects the energy needed to move from one site to another.[321] In fact, in pure silica glass the E_a of oxygen diffusion was found to be 155–293 kJ/mol, likely due to differences in purity[322], while depending on the crystal phase (α or β) and direction of diffusion, oxygen in crystalline SiO_2 has an E_a of 98–284 kJ/mol.[323,324] Indeed, O^{2-} in the presence of other cations in crystalline materials have E_a's of 83, 112, 122, 125 and 129 kJ/mol for CeO_2, ZrO_2, UO_2, $Zr_{0.85}Ca_{0.15}O_{1.85}$, and $DyAlO_3$, respectively.[321,325]

According to Dietzel[83], differences in coordination number (ΔCN) and cationic field strength (ΔF_c) should affect static and ionic transport properties, respectively. Ionic radii differences (Δr_c) have been known to affect ion transport and static properties as well, however, mostly studies have been performed on mixed-alkali glasses, where differences in size are equivalent to differences in F_c. Anderson and Stuart[288]

Table 6.1: Ion parameters for oxygen and the cations used in mixed-modifier compositions. Activation energies are calculated values from Anderson and Stuart [288]

Ion	Charge	CN$^{\alpha}$	r_c (Å)$^{\beta}$	F_c (Å^{-2})	Ea (kJ/mol)$^{\gamma}$	Electronegativity$^{\delta}$
O	−2	2–4	1.38	0.26	83–293$^{\epsilon}$	3.44
Li	+1	4	0.76	0.22	20	0.98
K	+1	8	1.51	0.12	25	0.82
	+1	9	1.55	0.12		
Rb	+1	9	1.63	0.11	31	0.82
Mg	+2	4	0.57	0.53	38.25	1.31
	+2	6	0.72	0.45		
Ca	+2	6	1.00	0.35	30	1
	+2	8	1.12	0.32		
Ba	+2	8	1.42	0.25	33.25	0.89
Zn	+2	4	0.74	0.44	35	1.65

$^{\alpha}$From ref [16], $^{\beta}$From ref [22], $^{\gamma}$From ref [288], $^{\delta}$From ref [326], $^{\epsilon}$From ref [321–325].

use the glass network properties (shear modulus, "hop" distance for ions) and ion properties (radius, valence and charge), along with empirical parameters derived from diffusion of gases in glasses, to predict the activation energies of cations in silica glasses. They go on to use their E_a's to calculate conductivities as a function of composition and temperature, which match well with several literature examples if one assumes a parameter related to the polarizability of the glasses changes with composition.[288] The differences between calculated activation energies of ionic conduction (ΔE_a) may correlate since E_a is directly related to ionic conductivity. Even though the exact E_a values calculated using this method may not correspond perfectly to experimental results, the difference between the E_a of the cations more important to this study.

The expected trends for the MME in Li-K vs. Li-Rb silicates match well with those in Table 6.2, ΔCN, Δr_c and ΔF_c are all larger in magnitude for Li-Rb. Within the xLi$_2$O-(50−x)MgO-50SiO$_2$ and xK$_2$O-(30−x)BaO-70SiO$_2$ series, which have very

Table 6.2: Comparison of cations parameters for the mixed-modifier compositions made within.

Ion Pair	ΔCN	Δr_c (Å)	ΔF_c (Å^{-2})	ΔE_a (kJ/mol)
Li-K	2–4	−0.75	0.10	−5
Li-Rb	5	−0.87	0.11	−11
Li-Mg	2	0.04	−0.24	−18.25
K-Ba	0	0.09	−0.14	−8.25
Li-Ba	4	−0.66	−0.04	−13.25
K-Mg	4	0.79	−0.33	−13.25
Li-Zn	0	0.02	−0.23	−15
Mg-Ca	0 to 2	−0.28 to −0.43	0.10 to 0.13	8.25

similar Δr_c, the effect of only ΔF_c can be evaluated separately. Furthermore, $x$$Li_2O$-$(30-x)$ZnO-70$SiO_2$ also has near zero Δr_c, yet a similar ΔF_c to $x$$Li_2O$-$(50-x)$MgO-50$SiO_2$, so therein the effect of a d-shell may be observed. Additionally, if ΔF_c is close to zero, while Δr_c and ΔCN are large, as in the case of $x$$Li_2O$-$(30-x)$BaO-70$SiO_2$, are only the static, not the dynamic properties affected, as Dietzel suggests[83,83]; if so how does that translate into mechanical properties? Also, many authors have suggested that only the differences between ions are important; for example $x$$Li_2O$-$(30-x)$$K_2O-70SiO_2$ and xMgO-$(50-x)$CaO-50SiO_2 have the same ΔF_c, but Li and K are more ionic, while Mg and Ca are more covalent, thus they could offer an opportunity to learn if F_c is important in addition to ΔF_c. Finally, $x$$K_2O$-$(40-x)$MgO-60$SiO_2$ has the largest ΔF_c and the more mobile ion (K^+) has a much larger ionic radius than Mg^{2+}. Unfortunately the total modifier content of these compositions varies from 30–50 mol-%, simply due to the requirement to use compositions in the glass-forming region. Although the MME increases with total modifier content, its growth diminishes with increasing modifier after 20 mol-%, thus, comparing between compositions should be reasonable.[61,79]

Furthermore, the directions and relationships between the deviations from linearity in all of the properties (static, dynamic and mechanical) within a series is more

important than comparing deviations directly between series. The goal is to establish whether the predicted trends are true for ionic conductivity in the mixed-modifier glasses and relate the trends observed in E_a to static and mechanical properties. Hopefully, this will indicate the relationship between the MME in ionic conductivity and static properties, and the role of ion transport in mechanical properties; with this knowledge, it will be possible to choose which ion combination will enhance the desired properties.

6.2 Experimental

Stoichiometric amounts of reagents were put into closed vials and shaken for a minute each to ensure thorough mixing. The regents used were SiO_2 (purum p.a., Sigma-Aldrich), Li_2CO_3 ($\geq$ 99%, Sigma-Aldrich), K_2CO_3 ($\geq$ 99%, ACP), Rb_2CO_3 (99% metal basis, Alfa-Aesar), MgO ($\approx$mesh 98%, Sigma-Aldrich), $BaCO_3$ (ACS reagent $\geq$99%, Sigma-Aldrich), and ZnO (<5 micron powder, 99.9%, Sigma-Aldrich); K_2CO_3 and MgO were always dried at 600 °C for at least an hour before weighing. All of the series were made using the conventional melt method, followed by quenching in air as discussed in detail in Section 2.1. The samples were annealed until they showed no birefringence under polarized light; the exact annealing temperatures are not known since often successive annealing was done at higher temperatures. In general, Li-K, Li-Rb, Li-Zn and Li-Ba were all annealed at starting temperatures of 400 °C, K-Ba at 450 °C, and Li-Mg at 500 °C, K-Mg at 600 °C, and Mg-Ca at 650 °C. It can be said that compositions containing MgO or BaO required higher annealing temperatures, while Li_2O-containing compositions required lower ones, and that more mixed compositions, *i.e.*, 0.5 modifier concentration relative to total modifier, required lower annealing temperatures (as expected from mixed-modifier compositions having lower T_g).

For each mixed-modifier series, density was measured (Section 2.4, and compositions were measured using ICP-OES for the $x\mathrm{Li_2O}$-$(30-x)\mathrm{K_2O}$-$70\mathrm{SiO_2}$ series and WDS for all other series (Sections 2.3.1 and 2.3.2, respectively). From there, molar volume (V_m), oxygen volume (V_O) and packing density (V_f) were calculated (end of Sections 2.4 and 1.1.3, respectively). Longitudinal and shear velocities of sound were measured using the ultrasonic method and the elastic moduli determined (Section 2.6.1). Vickers hardness (H_V) and fracture toughness (K_Ic) were investigated using a micro-indenter with a load of 1 kg for 15 s and then measuring the indent diagonals and crack lengths (Section 2.6.2). Ionic conductivity was measured starting at about 200 °C below the *starting* annealing temperature and at approximately 30 °C intervals every half an hour (Section 2.7). Generally, at least five temperatures or data points were collected for fitting the Arrhenius equation and obtaining the activation energy (E_a) and pre-exponential factor (A). Finally, Raman spectroscopy was used to obtain structural information, mainly network connectivity (amounts of NBOs), for each series (Section 2.5).

6.3 Results and Discussion

Since the relationships between the MME in all of the measured properties are more important than the values of the properties themselves, the next sections only include figures which compare the deviations from linearity; for the plots of the measured values see the appropriate section of the appendices. The only exception is Raman spectroscopic analyses, where the structural Q^n-units and NBOs are displayed directly (not the deviation), however, the Raman spectroscopic plots are available in the appendices. Finally, for all of the series the trends observed in V_m were mirrored in V_f, except V_m generally had a smaller deviation, approximately 1/2–2/3 of that seen in V_f; thus, only V_f and its relation to structural compactness is discussed.

6.3.1 Mixed-Alkali Series

$x\mathbf{Li_2O}$-$(\mathbf{30}-x)\mathbf{K_2O}$-$\mathbf{70SiO_2}$

The compositions of the $x\mathrm{Li_2O}$-$(30-x)\mathrm{K_2O}$-$70\mathrm{SiO_2}$ series were confirmed by ICP-OES and WDS, and can be found in Table D.1 in Appendix Section D.1. Furthermore, the Figures showing all measured properties (static, dynamic and mechanical) and Raman spectra can be found in Appendix Section D.1 as well.

Fig. 6.1 shows the Q^n population of the $x\mathrm{Li_2O}$-$(30-x)\mathrm{K_2O}$-$70\mathrm{SiO_2}$ series; in general, the network connectivity is seen to increase (decrease in [NBO]/[Si]) with increasing Li_2O content. This is expected as another study has shown only Li_2O-SiO_2, not K_2O-SiO_2, to have lower-than-expected [NBO]/[Si] from composition alone.[156] Additionally, there appears to be a negative deviation in linearity for [NBO]/[Si], but it is difficult to be certain in the given error limits. Finally, Fig. 6.2 shows the variance and possible MME in peak Raman shifts as a function of Li_2O concentration, where HF (>800 cm^{-1}) and LF (<700 cm^{-1}) peaks are attributed to Si-O bond lengths and ∠Si-O-Si, respectively (see Section 3.3.1 and Table 3.2 for details about Raman assignments).

The deviations from linearity for G, K and μ are shown in Fig. 6.3, while the MME in Y, H_V and K_Ic is found Fig 6.4; both Figures include V_f and E_a since they are representative of static and dynamic components, respectively. As expected from the many studies of the MME there is a positive deviation in the transport property E_a (conductivity plots can be found in Figs. D.4 and D.5 in the Appendix). Furthermore, in this series, there are also positive deviations in packing fraction (which is correlated with density in Fig. D.1) and all other mechanical properties except Poisson's ratio and fracture toughness. As discussed in Section 1.3, K and μ are expected to correlate

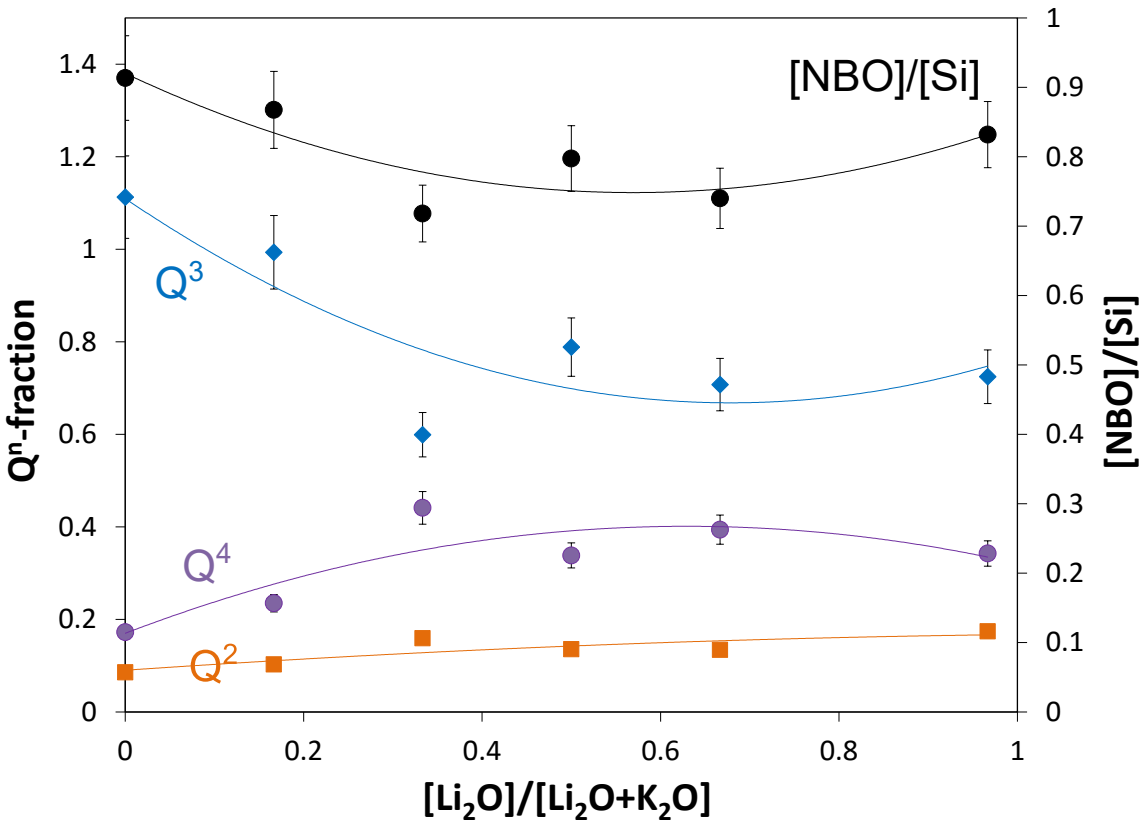

Figure 6.1: The Q^n-distribution (left) and non-bridging oxygen per silicon atom ([NBO]/[Si] on the right) of $x$$Li_2O$-$(30-x)$$K_2O$-$70SiO_2$ from Raman spectroscopy. Error from fitting was assumed to be 10% of peak intensity, if the error bars are not shown, they are smaller than the symbol.

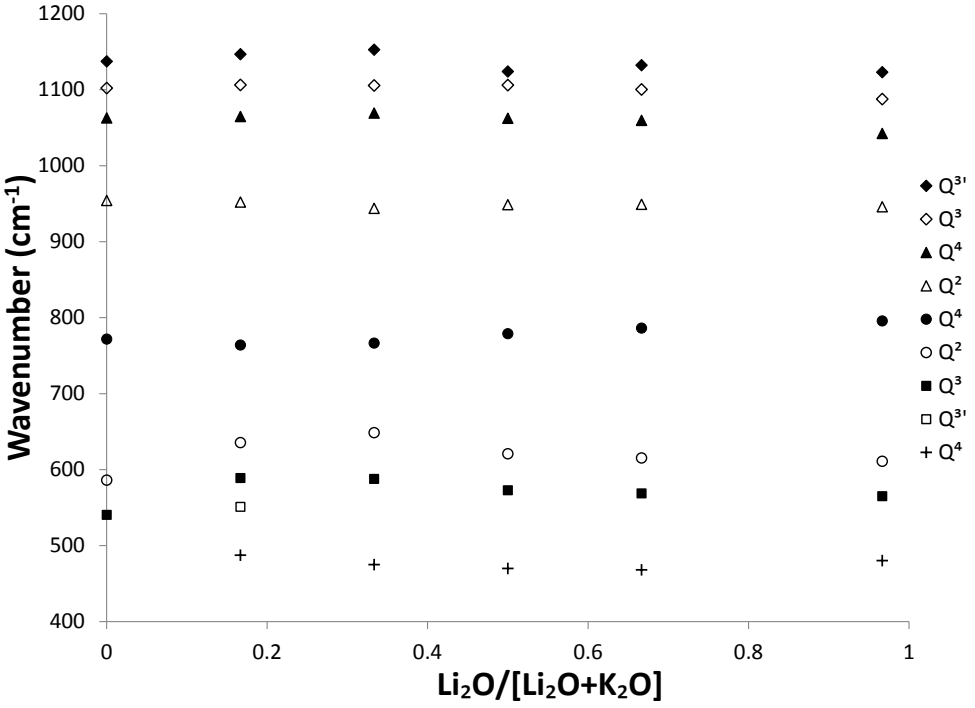

Figure 6.2: Raman shifts of $x$$Li_2O$-$(30-x)$$K_2O$-$70SiO_2$ glasses as a function of relative Li_2O ratio for the low-frequency (400-700 cm^{-1})peaks which correspond to Si-O-Si bond angles and high-frequency (>700 cm^{-1}) peaks which correspond to Si-O bond length.

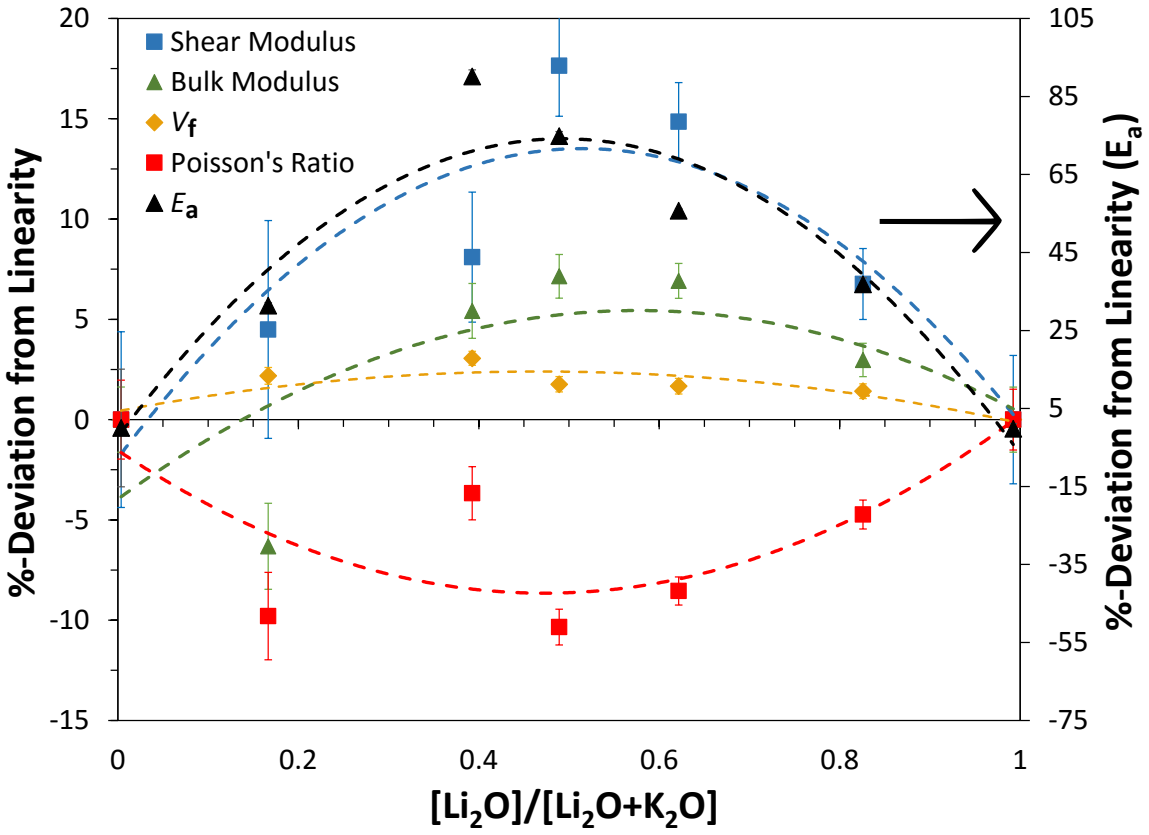

Figure 6.3: The MME in xLi$_2$O-(30$-x$)K$_2$O-70SiO$_2$ as a function of relative Li$_2$O content. Mechanical properties (bulk, K, and shear moduli, G) and static properties (packing fraction, V_f) are on the left axis, while ion transport (E_a) is on the right axis. The dashed lines are fits to the apparent trends with 2nd-order polynomials.

strongly with structural compactness (V_f), so it is somewhat surprising that μ has the opposite trend here. Since $\mu = Y/2G - 1$, if Y increases more than G, a higher μ is necessitated, while when Y increases less than G, a lower μ is needed; however, both xMgO-(50$-x$)CaO-50SiO$_2$ (Figs. 5.17 and 5.18, and this series have similar Y:G deviations, so this is likely not the reason for the opposite signs of MME for μ. Instead, it may be that the opposite deviations in network connectivity play a role (Figs. 5.5 and 6.1) in μ as well as the difference in magnitudes in the MME for Y and G between the Li-K and Ca-Mg series.

It is difficult to separate the dynamic vs. static components of the elastic moduli;

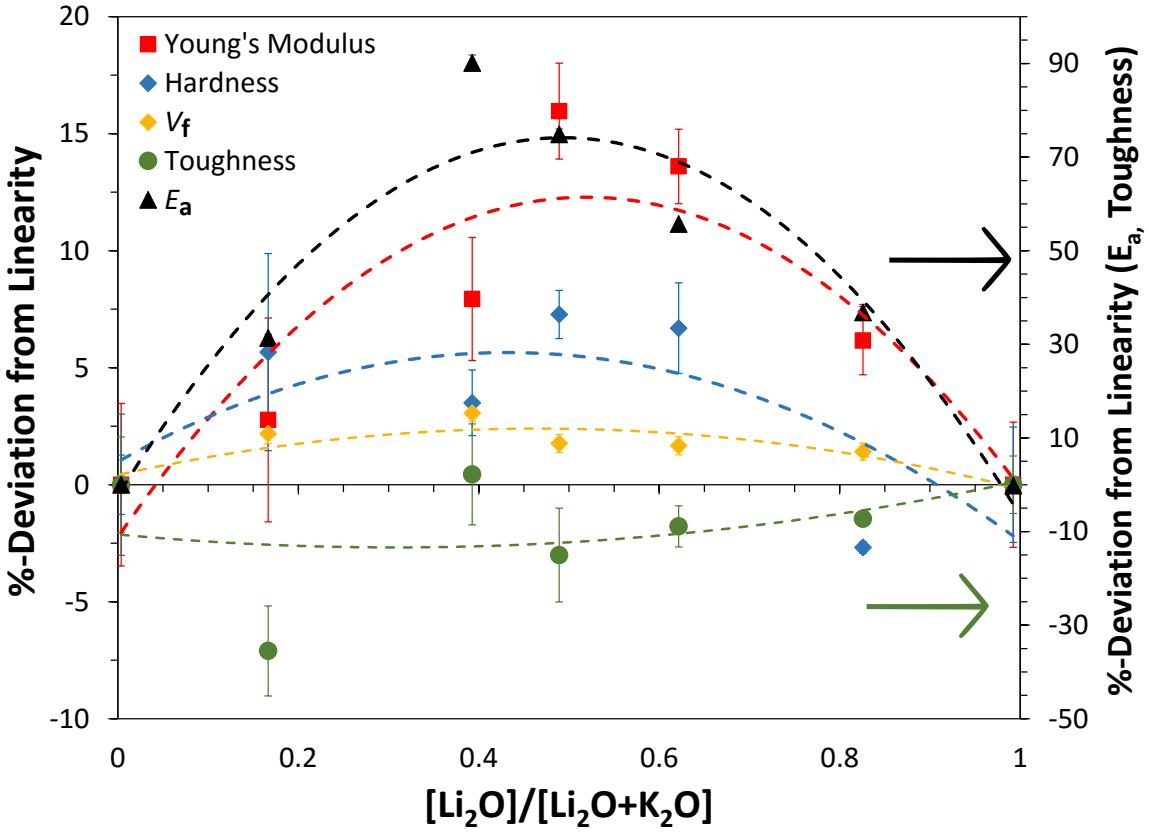

Figure 6.4: The MME in xLi$_2$O-(30$-x$)K$_2$O-70SiO$_2$ as a function of relative Li$_2$O content. Mechanical properties (hardness, H_{V}, fracture toughness, K_{Ic} and Young's modulus, Y) and static properties (packing fraction, V_{f}) are on the left axis, while ion transport (E_{a}) is on the right axis. The dashed lines are fits to the apparent trends with 2nd-order polynomials.

the MME in G, K and Y appear to mostly match those in V_{f} and E_{a}, however, increased network connectivity of mixed compositions may increase the deviations in G and Y, while reducing it in K. On the other hand, even though H_{V} and K_{Ic} involve plasticity, they appear to be more correlated with static properties. Additionally, since Li-K and Mg-Ca have similar ΔF_{c}'s, it can be said that either the MAE is undoubtedly larger than the MAEE, or that Δr_{c} and ΔCN also play a role in determining the magnitude of the MME. Finally, as the baseline mixed-alkali case, it is important to state that positive deviations from linearity in structural compactness and network connectivity were observed and explained most of the observed MME in mechanical properties.

$x\mathbf{Li_2O}$-$(\mathbf{40}-x)\mathbf{K_2O}$-$\mathbf{60SiO_2}$

For this glass series, $x\mathrm{Li_2O}$-$(40-x)\mathrm{K_2O}$-$60\mathrm{SiO_2}$, all relevant data, results from density, mechanical properties, and conductivity measurements can be found in Appendix D.2. Additionally, compositional analysis performed by WDS can be found in Table D.2 in Appendix D.2 as well, except only half of the results (those containing high amounts of lithium) were considered reliable; this is believed to be due to the hygroscopic nature of glasses containing high amounts of K_2O ($>$ 20 mol-%). This was observed to increase surface roughness during the measurement (leading to poor ZAF correction factors), while likely contributing to the inaccuracy of the oxygen count and therefore Li_2O concentrations as well. Nonetheless, the ρ and V_m results in Figure D.11 are reasonable for the high K_2O-containing compositions. Finally, Raman spectroscopy was not performed on this composition, however, the network connectivity trends are expected to be similar to the previous Section (6.3.1) on $x\mathrm{Li_2O}$-$(30-x)\mathrm{K_2O}$-$70\mathrm{SiO_2}$.

Now, from previous studies, it is known that larger amounts of total modifier, specifically alkali content in most cases, will increase the MME in conductivity; however, there are diminishing returns after ≈20 mol-%.[58,64,79,80] Indeed, this is the effect observed here in Fig. 6.5, where for this 40% total alkali series, the apparent deviation of E_a (dashed line fit with 2nd-order polynomial) is ≈40% higher compared to the corresponding 30% total alkali series (Section 6.3.1). It is more difficult to confirm with certainty if the deviations in elastic moduli, K and G, have increased similarly, however, the ordering of two has definitely reversed, where now the MME in K is larger then G, while the opposite was true for the 30% total alkali series. Additionally, the MME in μ is no longer negative, perhaps a result of the relation, $\mu = Y/2G - 1$. Finally, no reliable difference in the deviation of V_f is detectable.

Fig. 6.6 shows the MME in hardness to be nearly four times as large as the lower

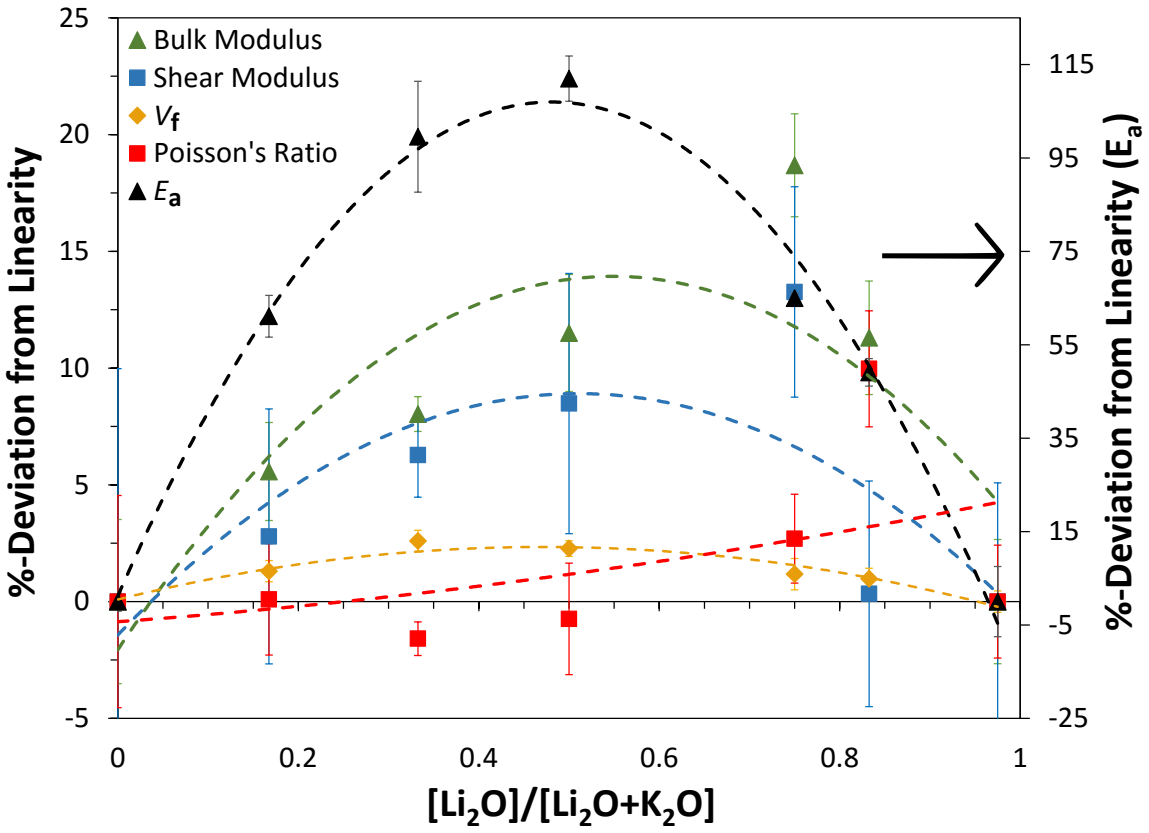

Figure 6.5: The MME in xLi$_2$O-(40$-x$)K$_2$O-60SiO$_2$ as a function of relative Li$_2$O content. Mechanical properties (bulk, K, and shear moduli, G) and static properties (packing fraction, V_f) are on the left axis, while ion transport (E_a) is on the right axis. The dashed lines are fits to the apparent trends with 2nd-order polynomials.

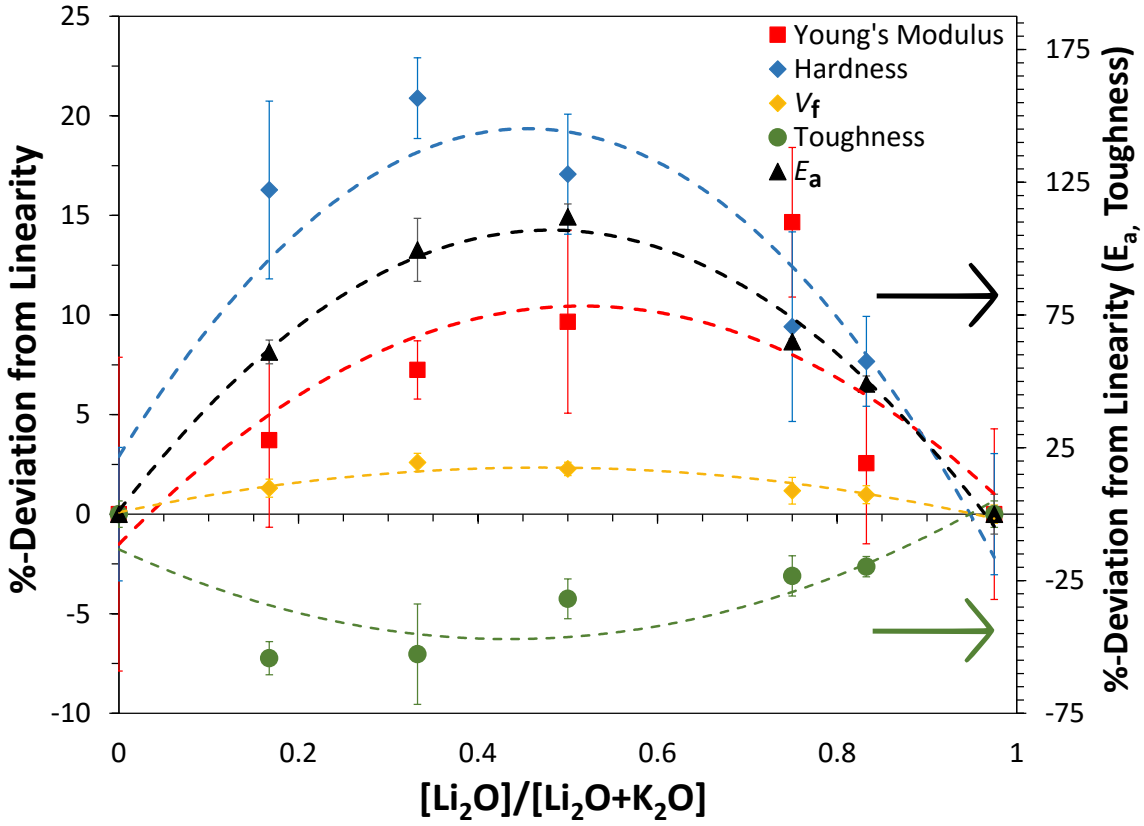

Figure 6.6: The MME in xLi$_2$O-(40$-x$)K$_2$O-60SiO$_2$ as a function of relative Li$_2$O content. Mechanical properties (hardness, H_V, fracture toughness, K_{Ic} and Young's modulus, Y) and static properties (packing fraction, V_f) are on the left axis, while ion transport (E_a) is on the right axis. The dashed lines are fits to the apparent trends with 2nd-order polynomials.

30% total alkali series. Furthermore, the deviation in K_{Ic} is negative. These two mechanical properties, H_V and K_{Ic}, have the highest dynamic components, where the material is deforming over time, thus, they are expected to be most correlated with changes in the ionic conductivity, so perhaps this is evidence of the properties' connections.

$x\mathbf{Li_2O}$-$(\mathbf{30}-x)\mathbf{Rb_2O}$-$\mathbf{70SiO_2}$

Once more, the relevant data for this series, $x\mathrm{Li_2O}$-$(30-x)\mathrm{Rb_2O}$-$70\mathrm{SiO_2}$, can be found in Appendix D.3. Additionally, the compositions were analyzed by ICP-OES and can be found in Table D.3 in Appendix D.3. Raman spectroscopy was not performed on this samples, as by the time it was considered the high $\mathrm{Rb_2O}$-containing samples were already affected by water; since Raman spectroscopy is a surface technique and is sensitive to Si-OH bonds which appear strongly at 970 $\mathrm{cm^{-1}}$,[327] the resulting spectra were found to have large hydroxyl peaks which obscured the important HF peaks of the material, nonetheless, the network connectivity is expected to be affected similarly by the addition of $\mathrm{K_2O}$ or $\mathrm{Rb_2O}$.

Comparing the differences between cations in this system $\mathrm{Li^+}$ vs. $\mathrm{Rb^+}$, they have larger differences in all parameters in Tables 6.1 and 6.2 (CN, r_c, F_c, E_a) compared with the $x\mathrm{Li_2O}$-$(30-x)\mathrm{K_2O}$-$70\mathrm{SiO_2}$ series in Section 6.3.1. Consequently, it is expected by most theories about the MME that this series, $x\mathrm{Li_2O}$-$(30-x)\mathrm{Rb_2O}$-$70\mathrm{SiO_2}$, should have a larger MME, however, as shown in Fig. 6.7, that was not found to be true here. In fact, the MME in E_a was roughly equal, if not smaller than that found in $x\mathrm{Li_2O}$-$(30-x)\mathrm{K_2O}$-$70\mathrm{SiO_2}$. This is somewhat surprising, the explanation may include the fact that the differences between $\mathrm{Rb^+}$ and $\mathrm{K^+}$ are quite small and may not be large enough to induce the expected increase in E_a due to the increased ionic radius of $\mathrm{Rb^+}$, or that the E_a measured for the $30\mathrm{Rb_2O}$-$70\mathrm{SiO_2}$ endpoint composition is less reliable than the corresponding $30\mathrm{K_2O}$-$70\mathrm{SiO_2}$ composition (due to water contamination). Nonetheless, like the 30 mol-% Li-K series, the MME in G is greater or at least equal to that in K and the deviation in μ is negative. Furthermore, like the MME in E_a, the deviation in V_f is smaller compared to the previous two series, perhaps indicating a correlation.

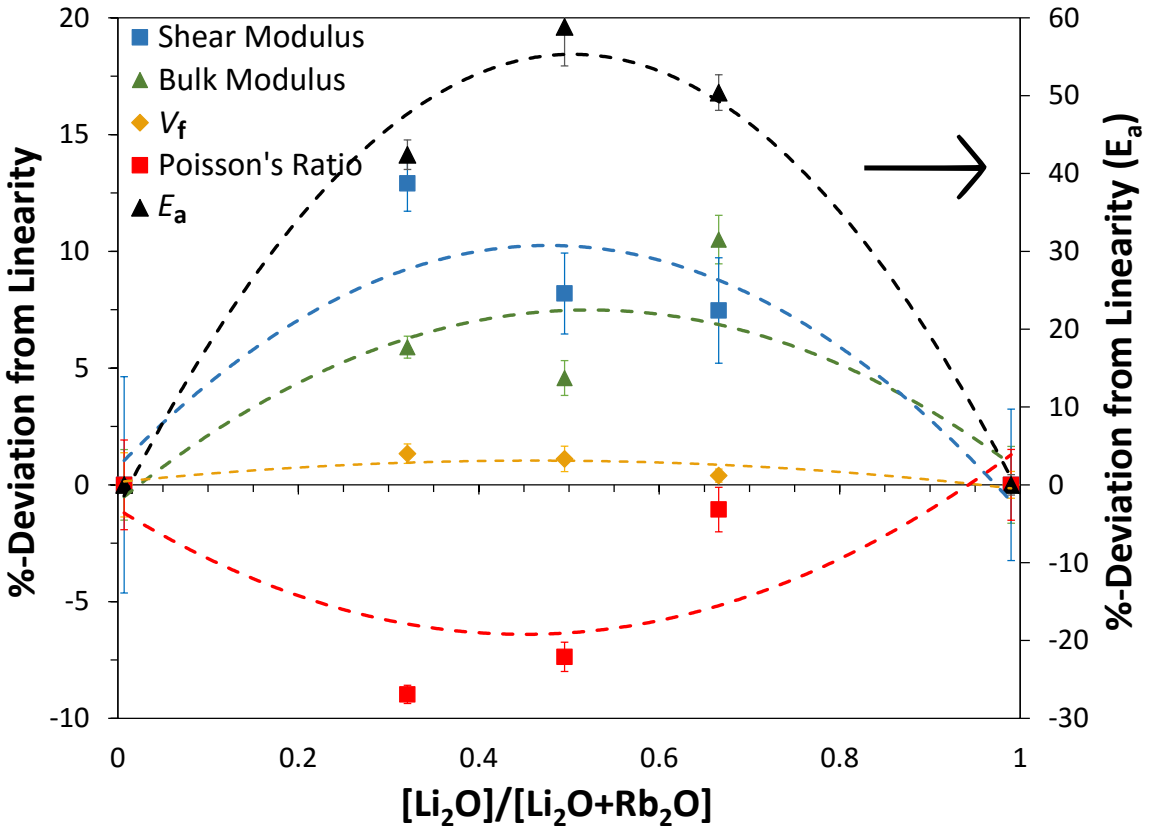

Figure 6.7: The MME in xLi$_2$O-(30$-x$)Rb$_2$O-70SiO$_2$ as a function of relative Li$_2$O content. Mechanical properties (bulk, K, and shear moduli, G) and static properties (packing fraction, V_f) are on the left axis, while ion transport (E_a) is on the right axis. The dashed lines are fits to the apparent trends with 2nd-order polynomials.

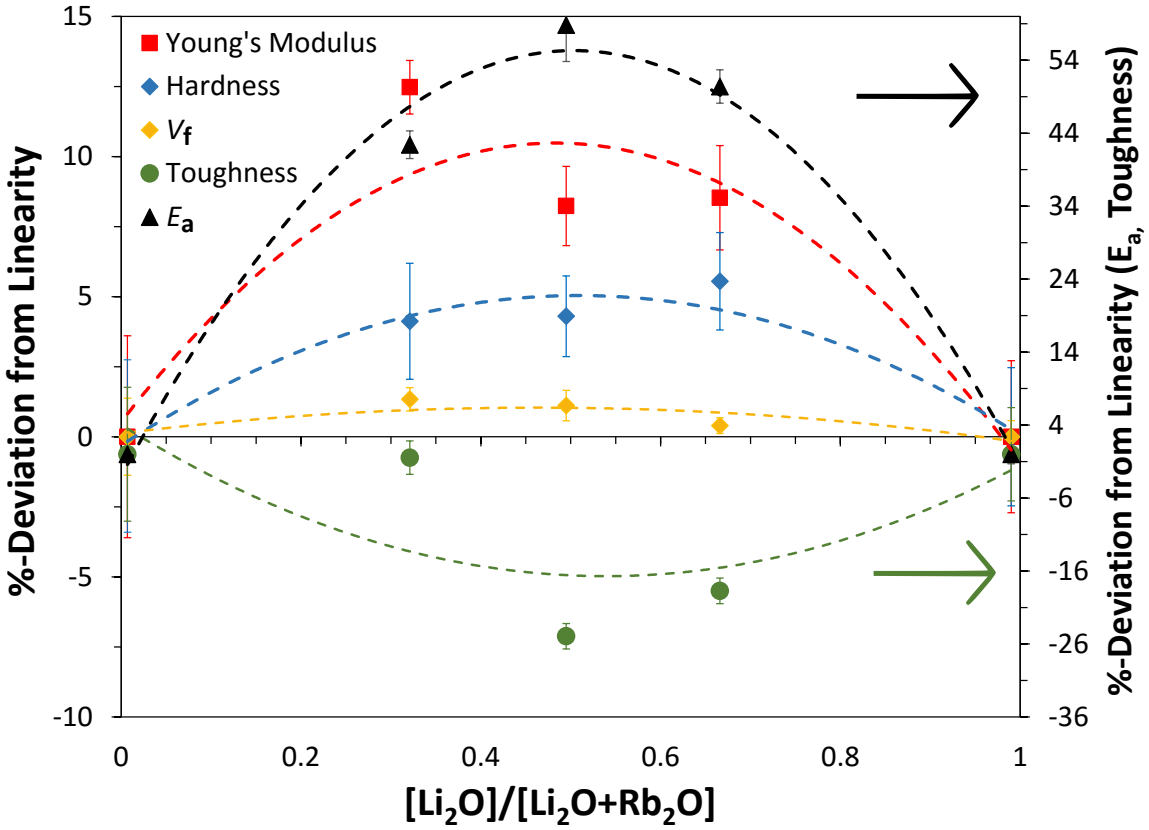

Figure 6.8: The MME in xLi$_2$O-(30$-x$)Rb$_2$O-70SiO$_2$ as a function of relative Li$_2$O content. Mechanical properties (hardness, H_{V}, fracture toughness, K_{Ic} and Young's modulus, Y) and static properties (packing fraction, V_{f}) are on the left axis, while ion transport (E_{a}) is on the right axis. The dashed lines are fits to the apparent trends with 2nd-order polynomials.

Fig. 6.8 displays very similar MMEs in Y, H_{V} and K_{Ic} as the corresponding 30 mol-% Li-K series. Overall, most mechanical properties have smaller deviations from linearity, but this may be a result of the smaller MME found in V_{f} and possibly E_{a}.

$x\mathbf{Li_2O}$-$(\mathbf{40}-x)\mathbf{Rb_2O}$-$\mathbf{60SiO_2}$

For all the relevant data for this series, $x\mathrm{Li_2O}$-$(40-x)\mathrm{Rb_2O}$-$60\mathrm{SiO_2}$, please see Appendix D.4. Again, Raman spectra were not collected of this series, and its compositions were not confirmed by WDS; it was thought to be of the least importance, but its results fit in with the preceding trends.

Since there is a larger or equal amounts of total alkali than the preceding glass series and the differences between the cations are equal or greater, $x\mathrm{Li_2O}$-$(40-x)\mathrm{Rb_2O}$-$60\mathrm{SiO_2}$ is expected to have the largest MME in E_a. Fig. 6.9 demonstrates this to be true, where the deviation in E_a is larger or at least equal to the corresponding 40% total alkali series, $x\mathrm{Li_2O}$-$(40-x)\mathrm{K_2O}$-$60\mathrm{SiO_2}$. This is somewhat surprising in light of the previous series, $x\mathrm{Li_2O}$-$(30-x)\mathrm{Rb_2O}$-$70\mathrm{SiO_2}$ not behaving as expected. Nonetheless, here the MME in K is the largest of all series, but more importantly, like the 40-mol% Li-K series K has a larger deviation than G and μ has zero to positive deviation, perhaps indicating that the amount of total alkali, in addition to the identity or differences between cations can also have an effect on the mechanical properties. Finally, the MME in V_f is also the largest of the previous mixed-alkali series. The MME in hardness in Fig 6.10 is also largest of the three preceding mixed-alkali series, while H_V and K_Ic are roughly equal to the corresponding 40 mol-% Li-K series.

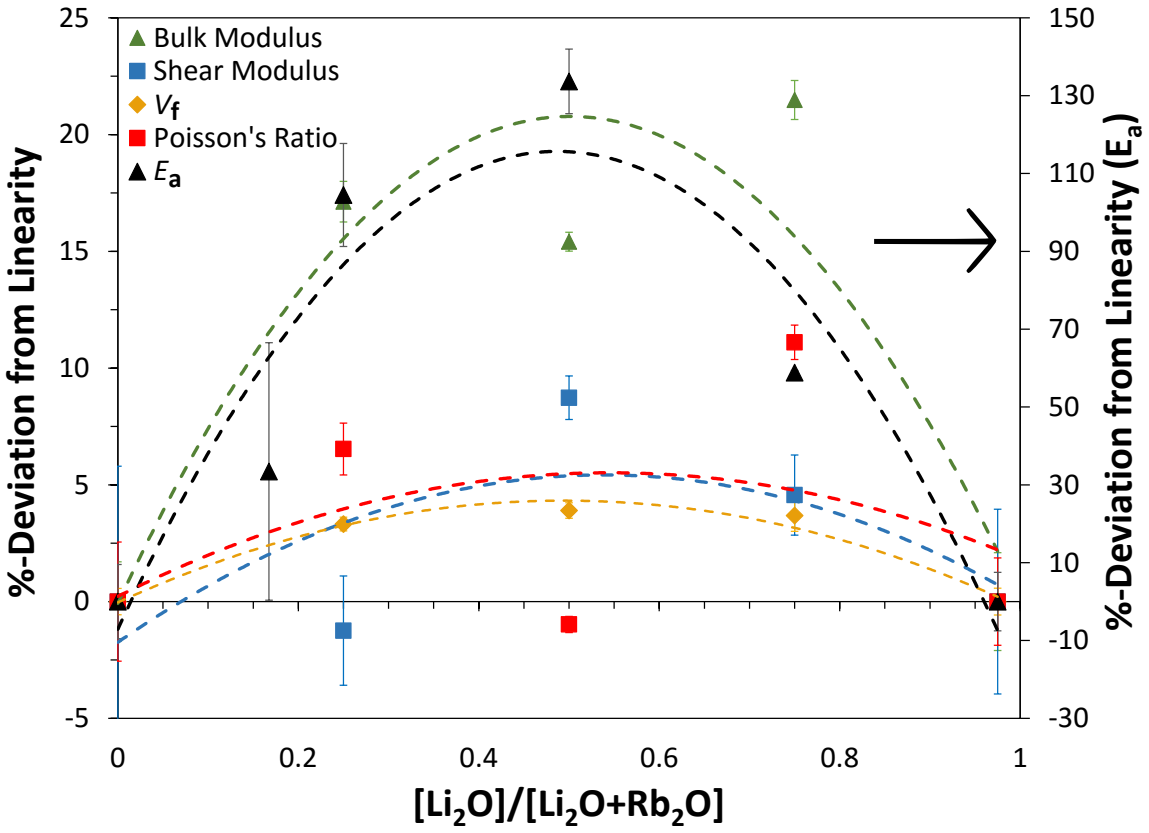

Figure 6.9: The MME in $x$$Li_2O$-(40−$x$)$Rb_2O-60SiO_2$ as a function of relative Li_2O content. Mechanical properties (bulk, K, and shear moduli, G) and static properties (packing fraction, V_f) are on the left axis, while ion transport (E_a) is on the right axis. The dashed lines are fits to the apparent trends with 2nd-order polynomials.

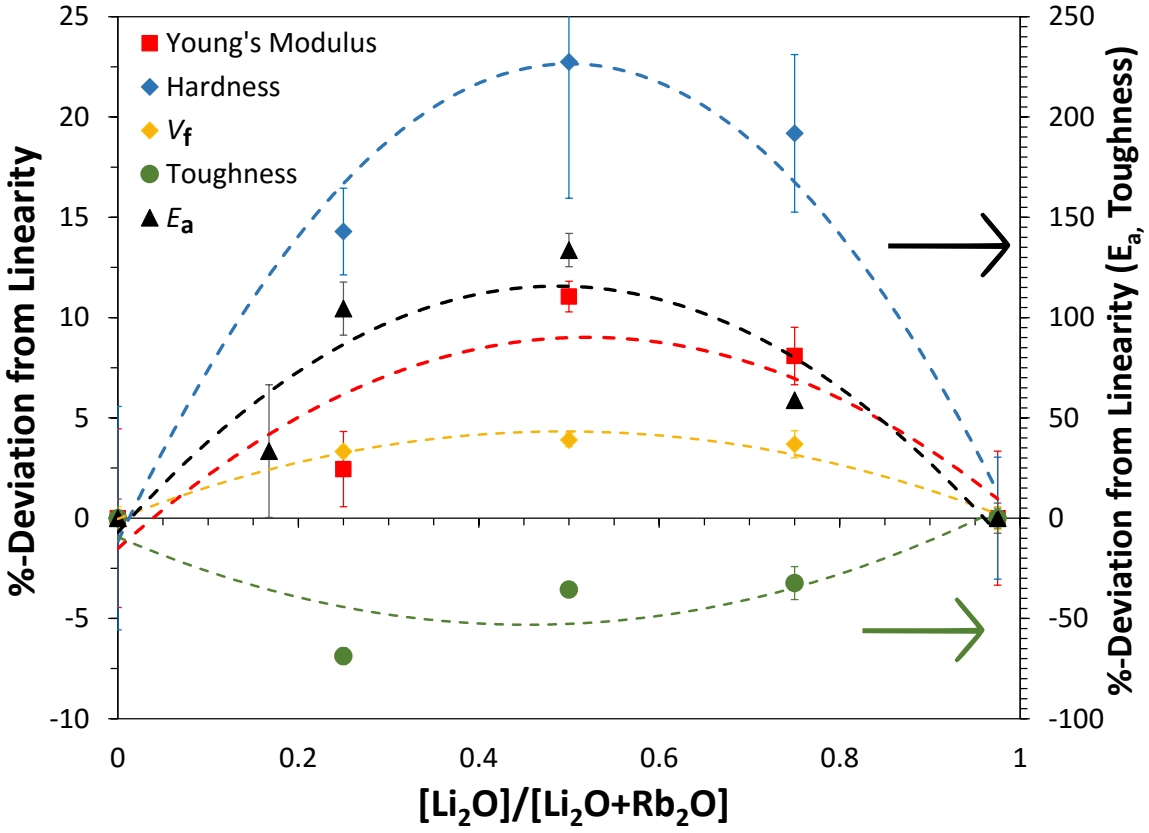

Figure 6.10: The MME in $x\mathrm{Li_2O}$-$(40-x)\mathrm{Rb_2O}$-$60\mathrm{SiO_2}$ as a function of relative $\mathrm{Li_2O}$ content. Mechanical properties (hardness, H_V, fracture toughness, K_Ic and Young's modulus, Y) and static properties (packing fraction, V_f) are on the left axis, while ion transport (E_a) is on the right axis. The dashed lines are fits to the apparent trends with 2nd-order polynomials.

6.4 Comparison of MME in Mixed-Alkali Series

In order to better understand the relationships between properties in the mixed-alkali series, the tabulated deviations from linearity in all studied properties can be found in Table 6.3; in all cases, significant deviations from linearity were found in most mechanical properties, μ being an exception in the $x\mathrm{Li_2O}$-$(40-x)\mathrm{K_2O}$-$60\mathrm{SiO_2}$ series. With the exception of the $x\mathrm{Li_2O}$-$(30-x)\mathrm{Rb_2O}$-$70\mathrm{SiO_2}$ series, the MME in E_a followed the expected trends: larger amounts of total alkali and/or large differences between the cations resulted in more pronounced MMEs. Additionally, both of the 40 mol-% total alkali series had larger MME in K compared with G, while the 30 mol-% total alkali series showed the opposite behaviour. The ratio of deviations from linearity in shear modulus over that in bulk modulus ($\delta G/\delta K$) is related to μ, which is turn related to plasticity;[3,26] glasses with lower ratios tend to be less brittle, which, as expected, are found in the higher total alkali series. Generally, glasses with more modifier are easier to permanently deform due to their lower network connectivity.[328] However, the MME was also found to be larger and *positive* in H_V, yet also larger and *negative* in K_Ic for the higher total alkali series, which indicates the increased plasticity due to higher modifier content has no effect on these properties and consequently the trend in E_a is much more important. Finally, the higher total alkali series had zero to positive deviation in μ, while the lower total alkali series always had negative MME in this property as result of the $\delta G/\delta K$ relationship.

Consequently, the amount of total modifier clearly has a significant effect on the MME in mechanical properties, but the same trends can be found for dynamic (E_a) and static (V_f) properties as well. For all of the series, the magnitude of the deviations in E_a correlated well with those observed in V_f, K, and H_V, indicating not only are these properties related fundamentally, but also suggests that these properties share a

Table 6.3: Comparison of MAE in the properties of the mixed-alkali glass series studied within, reporting the highest maximum value of the apparent 2nd-order polynomial fit. All values in percent.

Property	Li-K	40Li-K	Li-Rb	40Li-Rb
E_a	75	105	55	130
V_f	2.5	2.5	1.3	3.8
K	5	13.8	7.5	21.3
G	12.5	8.8	10	5
μ	−8.8	1.3	−6.3	5
Y	12.5	10	10	8.8
H_V	5	20	5	22.5
K_{Ic}	−15	−40	−16	−45

common mechanism of the MME. Additionally, the MME in μ appears to be directly related to that of E_a, but the relationship is less strong. Another interesting result is that Y and G appear to have little dependency on E_a, however, they do follow the same trends roughly; this is somewhat expected as both of these elastic moduli depend greatly on network connectivity and although E_a is dependent on amount of total modifier or [NBO]/[Si], it is not a simple relationship.[3,26,49,50,61,79,80]

6.4.1 $x\mathbf{Li_2O}$-$(\mathbf{50}-x)\mathbf{MgO}$-$\mathbf{50SiO_2}$

Appendix D.5 contains all of the relevant data and graphs for this series, including density, Raman spectra, mechanical properties, conductivity and compositional analysis. Although the phase diagram of this system shows this composition line to have the lowest-temperature eutectics,[131] the longer times needed to melt compositions with high MgO-content led to some compositions having lower-than-expected [MgO]/[Li_2O+MgO] content and caused a narrowing of the composition range over which this series was studied. The analyzed compositions were used to determined V_m and V_f as usual, however, it makes comparing the magnitudes of the MME to other series more difficult since the endpoints members are no longer 0 and 1.

This series, $x$$Li_2O$-$(50-x)$MgO-$50SiO_2$, was made to evaluate whether Δr_c or ΔF_c was more important in determining the behaviour of the MME in mechanical properties; Li^+ and Mg^{2+} are nearly the same size, yet the difference in cationic field strength is more than double that of Li^+ and K^+, thus according to Dietzel's[83] parameters, the MME should be twice as large in magnitude. Furthermore, this series has a large difference in E_a for the conductions of the cations. This system was also of interest because both Li and Mg are the most electronegative glass modifiers of their respective groups in the periodic table, thereby making their oxide bonds more covalent; in fact, Mg^{2+} has been called an intermediate cation between former and modifier,[16,54,286] and Li^+ can similarly stabilize free oxygen and has polarized bonds.[156,287]

The Raman results in Fig. 6.11 show increased MgO to shift the Q^n population towards more Q^3-units and fewer Q^2-units resulting in a lower net [NBO]/[Si], which is what is expected, since MgO is known to remove O^{2-} from the network via the creation of free oxygen.[294–296] There also appears to be a negative deviation

in [NBO]/[Si], similar to that observed in $x\mathrm{Li_2O}$-$(30-x)\mathrm{K_2O}$-$70\mathrm{SiO_2}$, however, once more the error bars are large due to the uncertainty of fitting peak areas.

The Raman shifts in Figs. 6.12 and 6.13 have a complex dependence on composition, but for the most populous Q^n-unit (Q^2 and Q^3), the HF peaks increase in frequency with $\mathrm{Li_2O}$ content and have a small positive deviation, while the LF peaks decrease in frequency with increasing $\mathrm{Li_2O}$ content and have a negative deviation only in the most mixed compositions. In conclusion, the Raman results indicate a positive MME in connectivity, along with an increase in Si-O bond lengths and widening of Si-O-Si angle (only for the most mixed compositions), perhaps leading to decreased V_f.

Looking at Fig. 6.14, the MME in E_a is smaller than expected from ΔF_c; although the compositional range is smaller, the deviation does not have twice the dependence on composition compared with $x\mathrm{Li_2O}$-$(30-x)\mathrm{K_2O}$-$70\mathrm{SiO_2}$ series in Section 6.3.1. Furthermore, the total modifier mol-% here is higher, so again the MME in E_a is expected to be higher. Nonetheless, the deviation in G is quite significant, especially compared to K, which again correlates with a large negative μ. Interestingly, V_f shows a large negative deviation, which agrees with the Raman shift results (specifically an increase of the $\angle$Si-O-Si), and is most likely responsible for the relatively small MME observed in K, and large negative deviation in μ as well.

Like the MME in G, Y has a large deviation from linearity, perhaps because of the increased connectivity for the middle compositions indicated by the Raman results. Additionally, H_V and K_Ic have much lower-than-expected deviations, which correlated with the smaller-than-expected MME in E_a.

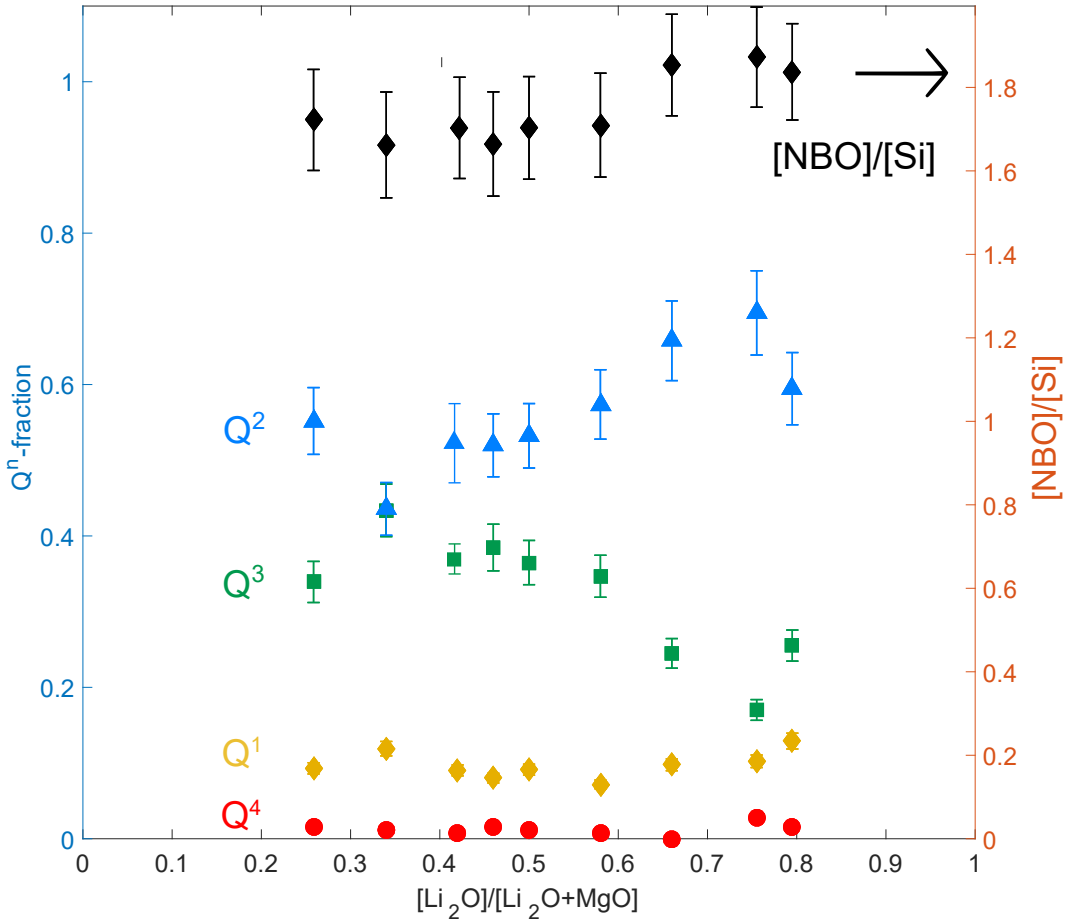

Figure 6.11: The Q^n-distribution (left) and non-bridging oxygen per silicon atom ([NBO]/[Si] on the right) of $x$$Li_2O$-(50$-x$)MgO-50$SiO_2$ from Raman spectroscopy. Error from fitting was assumed to be 10% of peak intensity, if the error bars are not shown, they are smaller than the symbol.

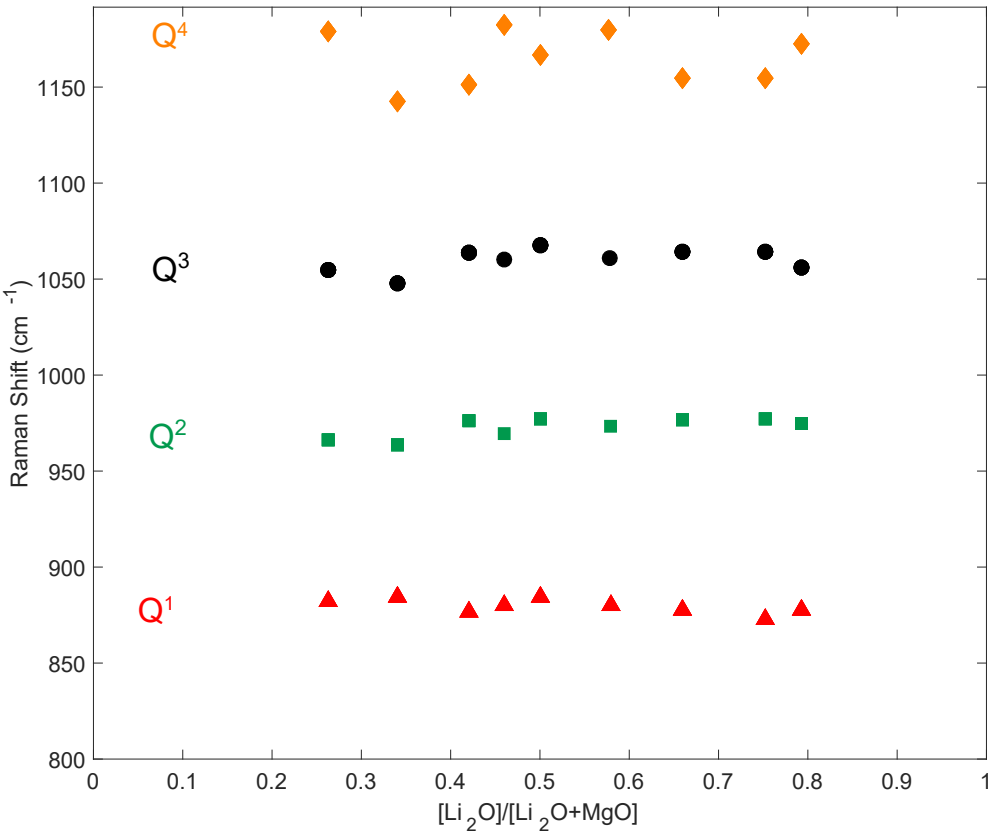

Figure 6.12: Raman shifts of xLi$_2$O-(50$-x$)MgO-50SiO$_2$ glasses as a function of relative Li$_2$O ratio for the high-frequency peaks which correspond to Si-O bond lengths.

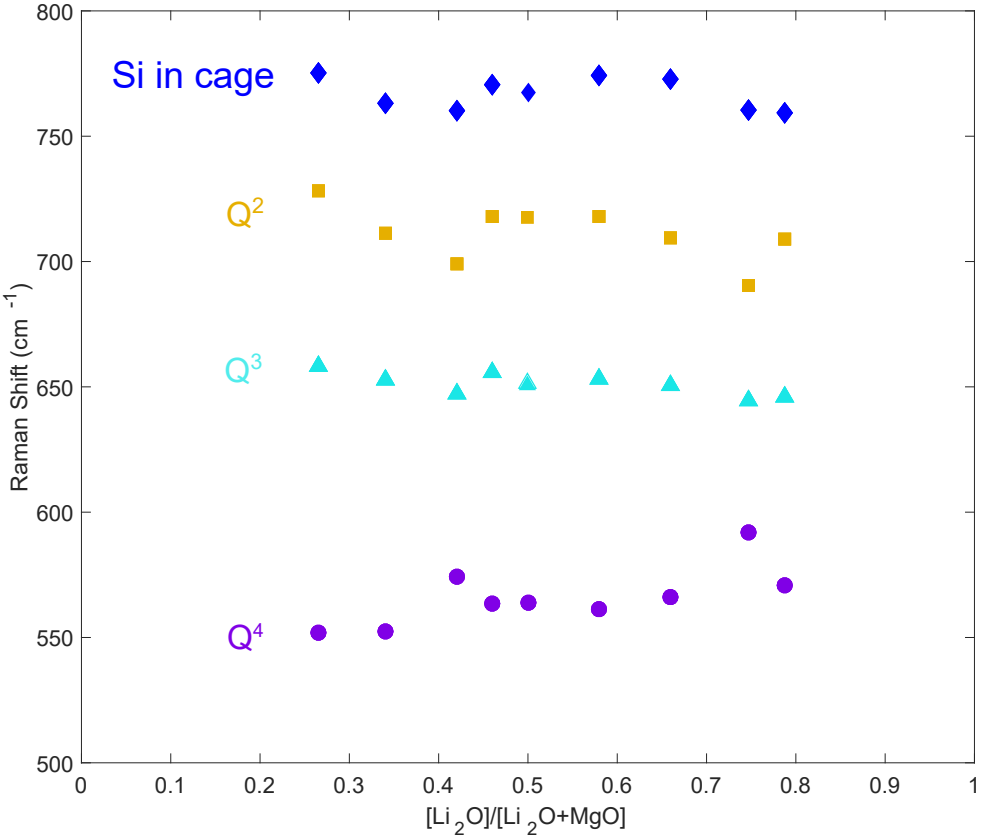

Figure 6.13: Raman shifts of $x$$Li_2O$-$(50-x)$MgO-50$SiO_2$ glasses as a function of relative Li_2O ratio for the low-frequency peaks which correspond to Si-O-Si bond angles.

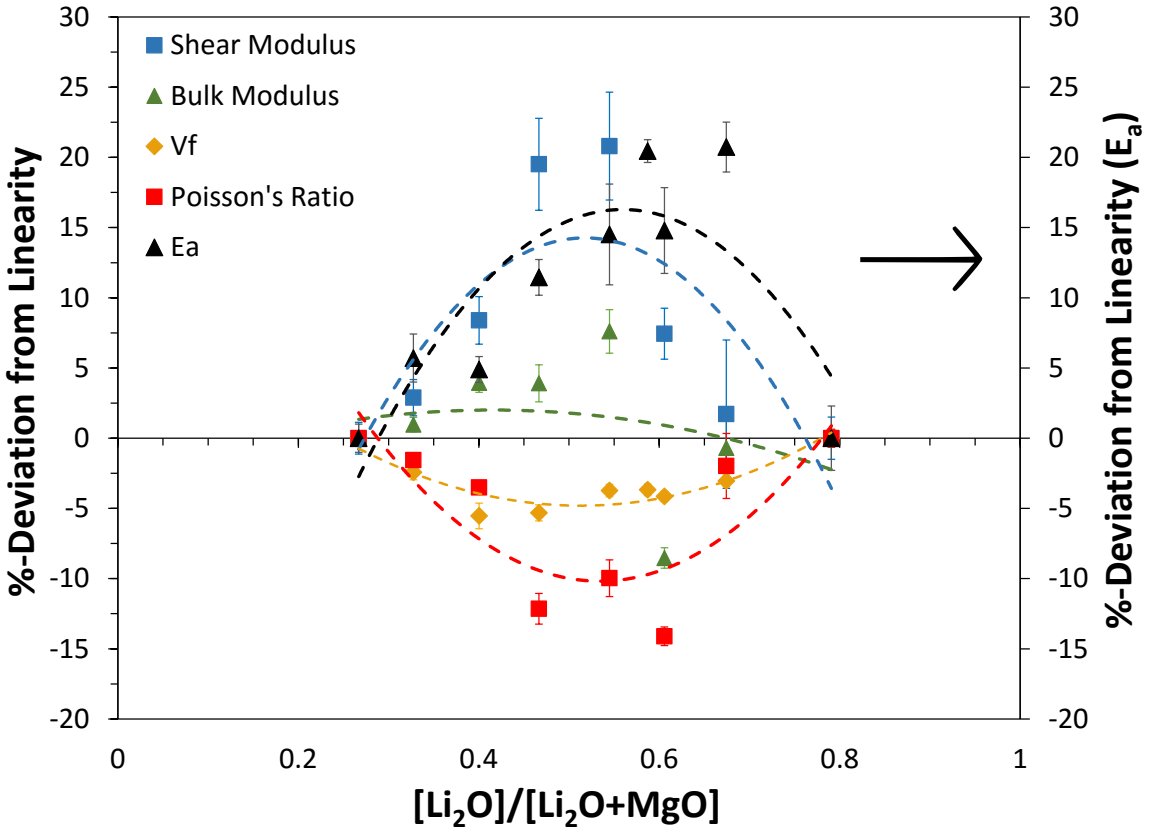

Figure 6.14: The MME in xLi$_2$O-(50$-x$)MgO-50SiO$_2$ as a function of relative Li$_2$O content. Mechanical properties (bulk, K, and shear moduli, G) and static properties (packing fraction, V_f) are on the left axis, while ion transport (E_a) is on the right axis. The dashed lines are fits to the apparent trends with 2nd-order polynomials.

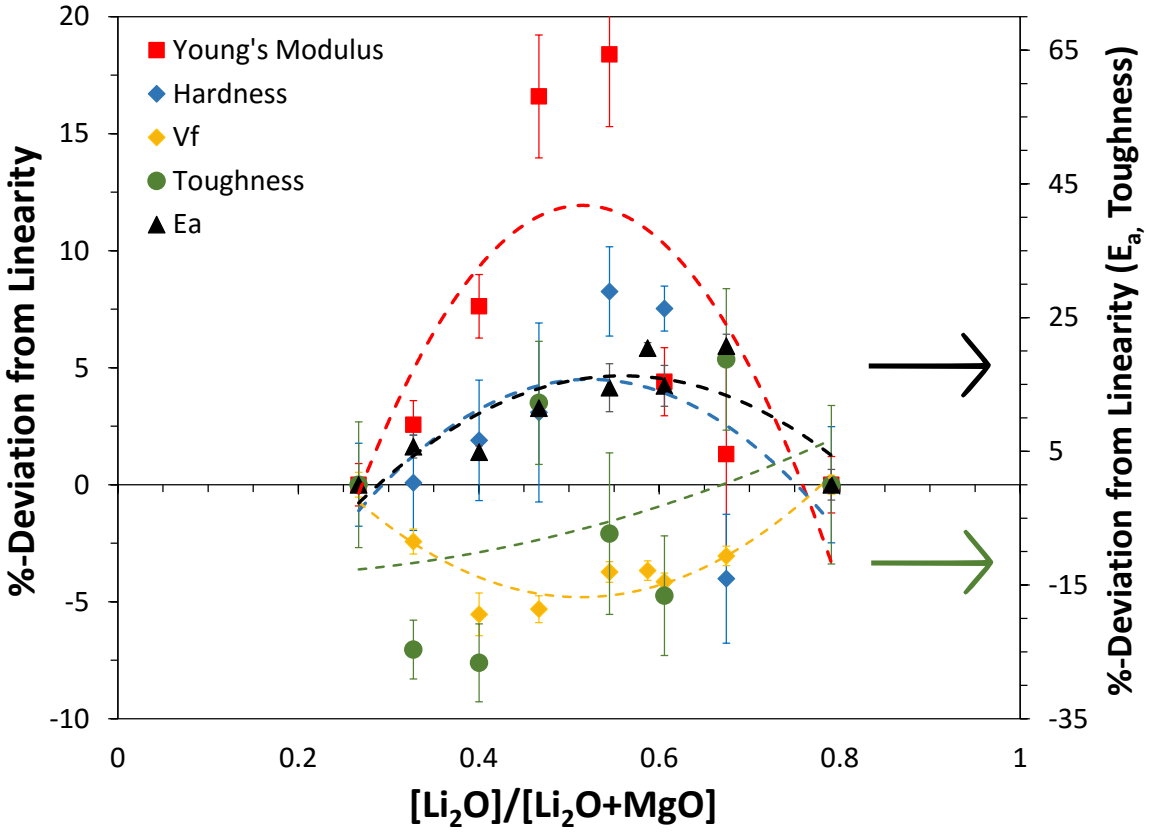

Figure 6.15: The MME in $x\mathrm{Li_2O}$-$(50-x)$MgO-$50\mathrm{SiO_2}$ as a function of relative $\mathrm{Li_2O}$ content. Mechanical properties (hardness, H_V, fracture toughness, K_Ic and Young's modulus, Y) and static properties (packing fraction, V_f) are on the left axis, while ion transport (E_a) is on the right axis. The dashed lines are fits to the apparent trends with 2nd-order polynomials.

6.4.2 xLi$_2$O-(30$-x$)BaO-70SiO$_2$

For this glass series, please refer to Appendix D.6 for structural, mechanical, conductivity and Raman spectra plots. Additionally, compositional analysis data can be found in Table D.5, however, only compositions with high amounts of Li_2O were considered reliable; it appears that high amounts of BaO lead to physically impossible low oxygen counts, thereby producing negative amounts of Li_2O. As a result, the nominal compositions are used for plotting and calculation of V_m and V_f. This glass series is of interest because despite being very different in size, Li^+ and Ba^{2+} have very similar cationic field strengths. Thus, it allows for a good opportunity to deconvolute the contribution of both factors.

Fig. 6.16 shows [NBO]/[Si] to increase with increasing Li_2O content, but more importantly there is a substantial negative deviation from linearity between 0.3–0.4 relative Li_2O content. This indicates a sharp increase in network connectivity at this compositions. In Fig. 6.17, the HF Raman shifts of the most populous Q^n-units (Q^3 and Q^4) show a positive deviation in frequency at the same composition range, indicating a strengthening of Si-O bonds, however, the Raman shifts at either endpoint composition are approximately equal. In contrast, the LF Raman shifts show more relative variation between the Li_2O- and BaO-rich regions; with increasing Li_2O concentration, the Q^4 peak migrates to lower wavenumbers, while the Q^2 and Q^3 peaks shift to higher wavenumbers. Interestingly, these changes are very similar to those observed in the IE glasses where Li^+ was exchanged for the large K^+ (see Fig. 3.7 in Section 3.4.5); here, these results also indicate the $\angle$Si-O-Si of the Q^2 and Q^3 tetrahedra are collapsing towards each other, while the Q^4-units are experiencing the opposite phenomenon. In retrospect, this phenomenon can be seen to occur in the baseline xLi$_2$O-(30$-x$)K$_2$O-70SiO$_2$ series, although to a lesser degree; the baseline

series saw much smaller changes in LF frequency peaks from one end of the composition range to the other, but also had much a larger deviation in the LF frequencies than that which is observed here.

Overall, the Raman results indicate a large positive deviation in connectivity, but not compactness, and a large variation in V_f with composition. This variation in V_f can easily be verified by the V_f plot for this 30% total modifier Li-Ba series in Fig. D.50, compared to that for the corresponding 30% total modifier Li-K series in Fig. D.2; it shows the V_f of the former series to vary from ≈0.37–0.44, while the latter only changes from 0.43–0.48 over the composition range. This is particularly interesting when one considers that Δr_c is actually larger for Li^+ vs. K^+ compared with Li^+ vs. Ba^{2+}. However, it is important to remember that two smaller Li^+ are being exchanged for only one larger Ba^{2+}.

In Fig. 6.19, the MME in V_f is very small as predicted by the Raman results. However, based on the large Δr_c, the MME in E_a is unexpectedly small and more surprisingly negative, however, it agrees well with Dietzel's[83] parameter ΔF_c. Interestingly, Dietzel studied this exact system, yet found there to be a significant MME in V_m, larger than any other glass series he studied.[83] Despite his earlier arguments about how Li-Ba interactions would not be stabilizing, as he expected them to have no reason to form Li^+–NBO–Ba^{2+} groups and *not* lead to an MME, he found one in the static properties and suggested it was due to a "packing effect" caused by their large differences in CN (not size). Moreover, he and others state that the Li^+ and Ba^{2+} are not uniformly distributed and form segregated regions of Li^+ and Ba^{2+} instead.[83]

If phase separation has occured and the size of the nucleated "droplets" or spinoids are on the order of the wavelength of visible light or smaller ($\leq$ 500 nm), light will

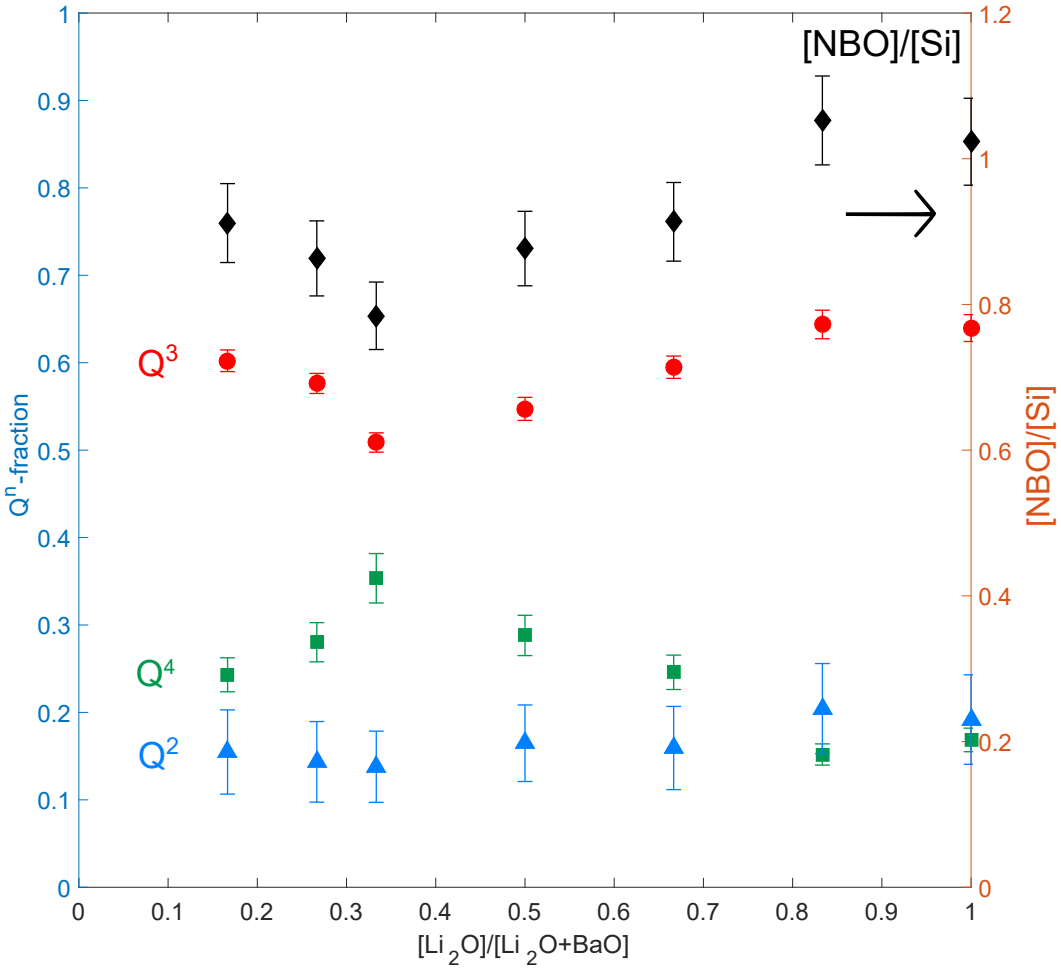

Figure 6.16: The Q^n-distribution (left) and non-bridging oxygen per silicon atom ([NBO]/[Si] on the right) of $x$$Li_2O$-(30−$x$)BaO-70$SiO_2$ from Raman spectroscopy. Error from fitting was assumed to be 10% of peak intensity.

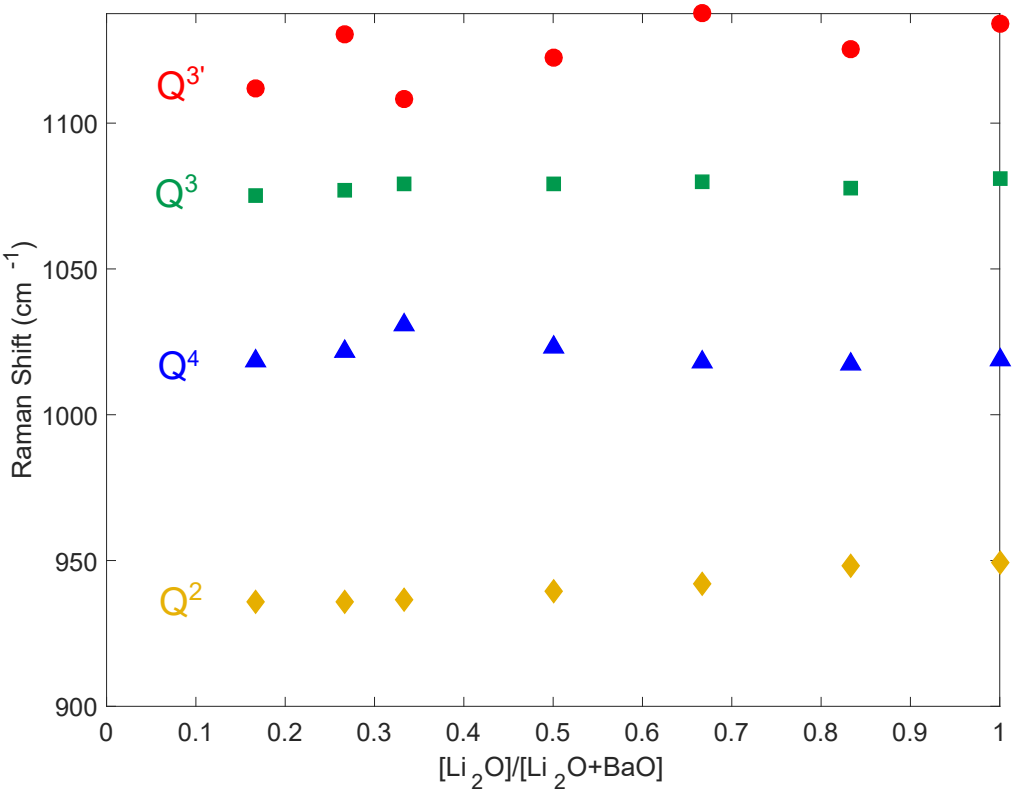

Figure 6.17: Raman shifts of xLi$_2$O-(30$-x$)BaO-70SiO$_2$ glasses as a function of relative Li$_2$O ratio for the high-frequency peaks which correspond to Si-O bond lengths.

interact through Rayleigh scattering and the sample would appear cloudy. In the present work, the glasses always had optically transparent parts which could be used; usually a cloudy layer formed on top and was able to be removed during the cutting process, except at the highest Li$_2$O mixed-composition, where more sample had to be removed to achieve a clear piece. The negative deviation in MME definitely indicates that regular mixing which occurs in most mixed-modifier glasses is not occurring here, however, that does no necessarily imply phase separation, rather a structure akin to intercalating ion channels.[81] Nonetheless, there does not appear to be the "packing effect" that Dietzel found as the MME for V_f is very small, perhaps indicating in this case the cations are more uniformly distributed. The small deviation in K is likely related to the small MME in V_f; in fact, this is the first time the deviation has been

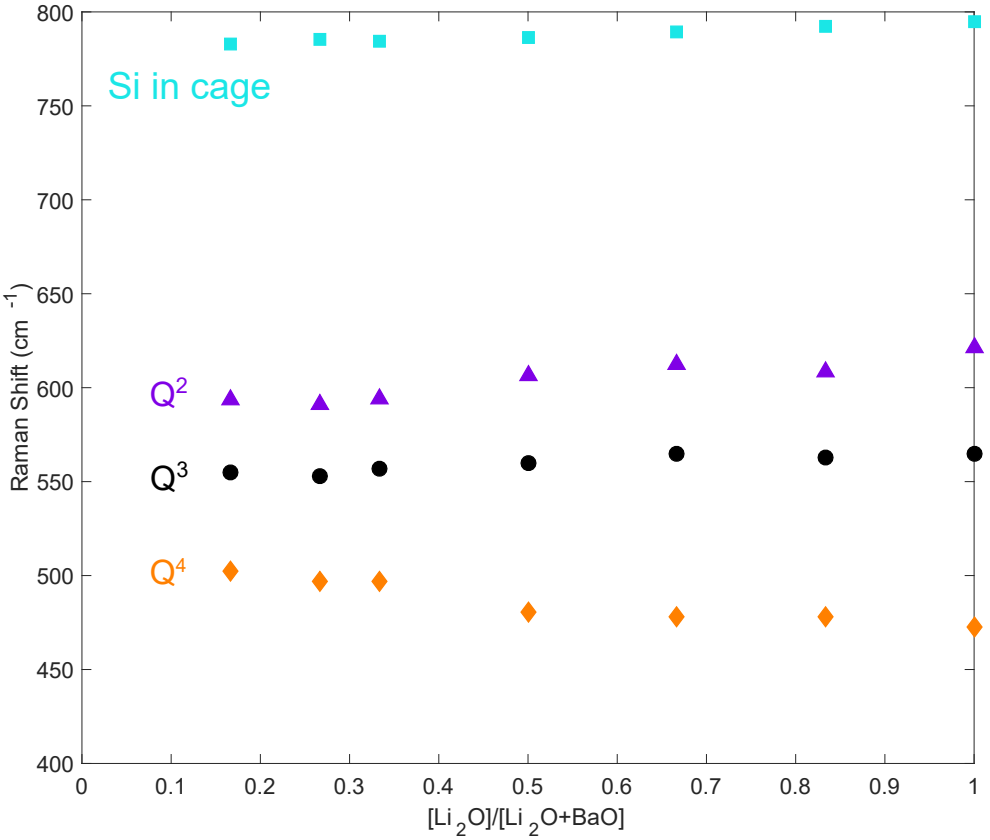

Figure 6.18: Raman shifts of xLi$_2$O-(30$-x$)BaO-70SiO$_2$ glasses as a function of relative Li$_2$O ratio for the low-frequency peaks which correspond to Si-O-Si bond angles.

negative, perhaps indicating that V_f and E_a are both playing a role. Conversely, the MME in G is relatively large as was predicted by the connectivity results from the Raman analysis. Finally, the MME in μ was negative once more when the MME in $G > K$.

The deviation in Y in Fig 6.20 is relatively small compared to the MME in H_V, unlike the baseline Li-K composition, where the opposite was true. This may also be indicative of Y being dependent on the MME in V_f and E_a. The magnitude of the deviation in H_V is perhaps the most surprising of all; since indentation involves plasticity, the mobility of ions should affect this mechanical property more, yet there is

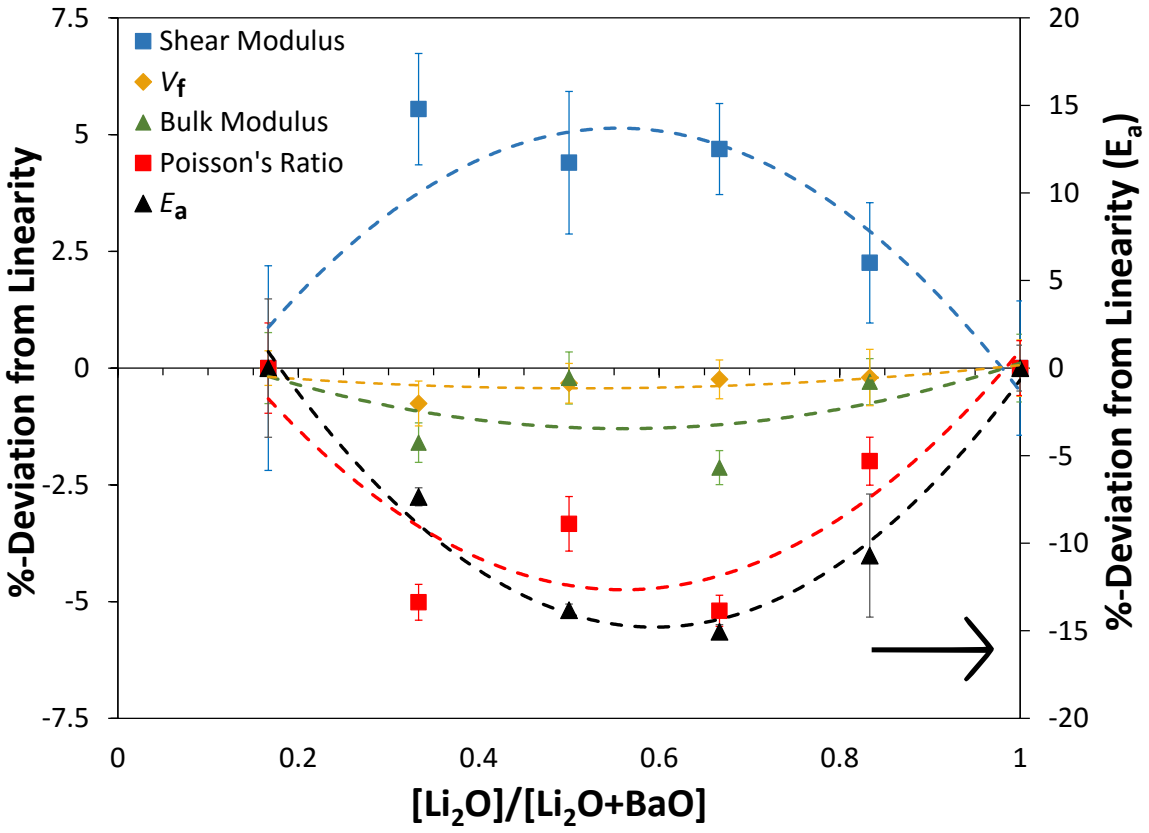

Figure 6.19: The MME in xLi$_2$O-(30$-x$)BaO-70SiO$_2$ as a function of relative Li$_2$O content. Mechanical properties (bulk, K, and shear moduli, G) and static properties (packing fraction, V_f) are on the left axis, while ion transport (E_a) is on the right axis. The dashed lines are fits to the apparent trends with 2nd-order polynomials.

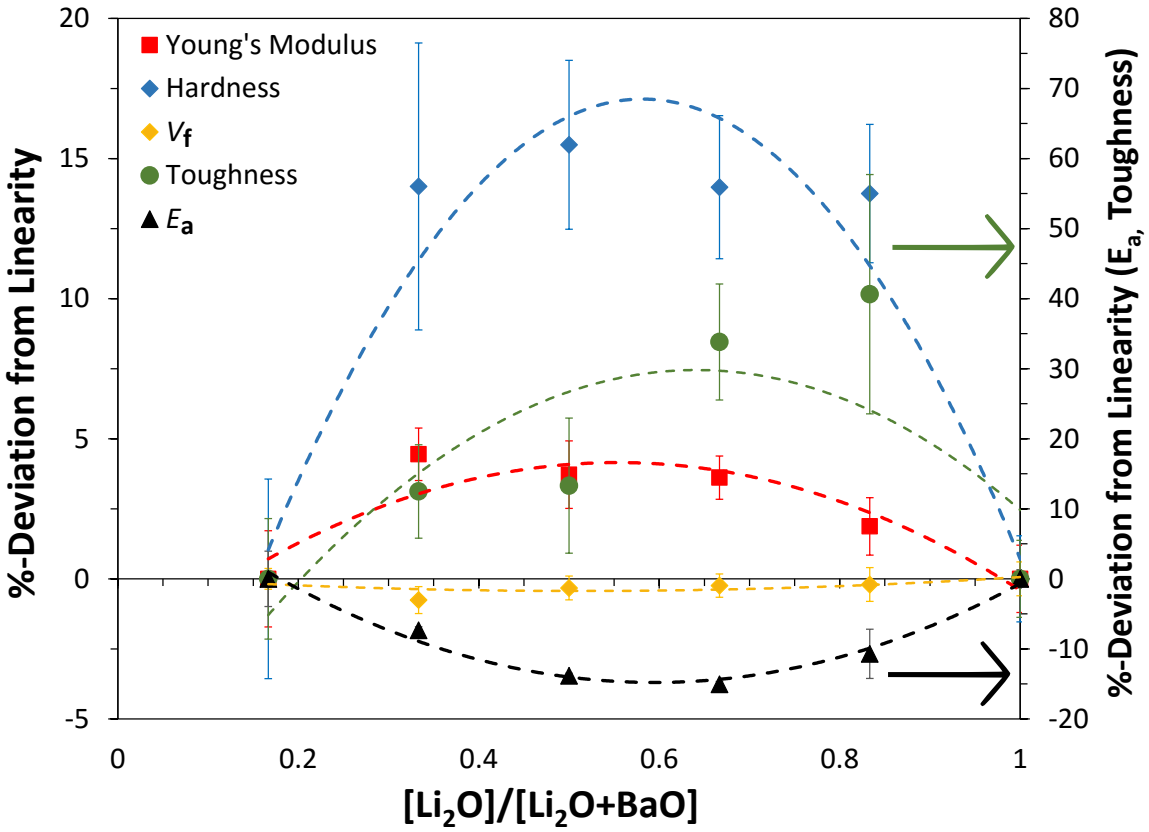

Figure 6.20: The MME in xLi$_2$O-(30$-x$)BaO-70SiO$_2$ as a function of relative Li$_2$O content. Mechanical properties (hardness, H_V, fracture toughness, K_{Ic} and Young's modulus, Y) and static properties (packing fraction, V_f) are on the left axis, while ion transport (E_a) is on the right axis. The dashed lines are fits to the apparent trends with 2nd-order polynomials.

a large positive deviation in H_V despite the negative deviation in E_a. One explanation could be that the increased network connectivity is very important to hardness, and the size difference between the two ions has affected the network connectivity and therefore hardness. Finally, this is the first time the deviation in toughness has been positive, which aligns with the idea that lower E_a will increase the capability for absorbing energy through the movement of ions.

6.4.3 $x\mathrm{K_2O}$-$(30-x)\mathrm{BaO}$-$70\mathrm{SiO_2}$

The other structural, Raman, conductivity and mechanical plots can be found in Appendix D.7. In this case, WDS was found to be unreliable due to the high sample ZAF, likely as a results of hygroscopicity at high K_2O concentrations and Ba being too heavy compared to the other elements of interest. As a result, the nominal compositions are used for plotting and calculation of V_f for this series. Nonetheless, the density data in Fig. D.59 matches well with that reported in literature.[83]

This series, $x\mathrm{K_2O}$-$(30-x)\mathrm{BaO}$-$70\mathrm{SiO_2}$, is of interest because like Li-Mg, the radius difference between the two cations is small, only 0.09 Å, while ΔF_c is larger than that of the Li-K series. Additionally, unlike the Li-Mg series, K^+ and Ba^{2+} both have relatively low electronegativities for cations and will form more ionic bonds with oxygen. Finally, both cations possess the same or near to the same CN (there is some debate about K being 8 or 9-fold coordinated).

The Q^n populations in Fig. 6.21 indicate that compositions with higher BaO concentration have a wider Q^n distribution, which agrees with what is expected for the more electronegative ion. The network connectivity is roughly constant at either end of the composition range, perhaps because of the similarity in size and electronegativity, however, there is a sharp increase in [NBO]/[Si] for the middle compositions (0.33–0.66 relative K_2O content). The significant increase in Q^2-units within that composition region is somewhat surprising, but at the same time, the Raman spectra for those compositions, especially the 0.5 relative K_2O content, in Fig. D.61 also show unique structural features.

Fig 6.22 shows all of the HF Raman shifts increasing with higher K_2O content, indicating shortening or strengthening of Si-O bonds. In order to fit the middle

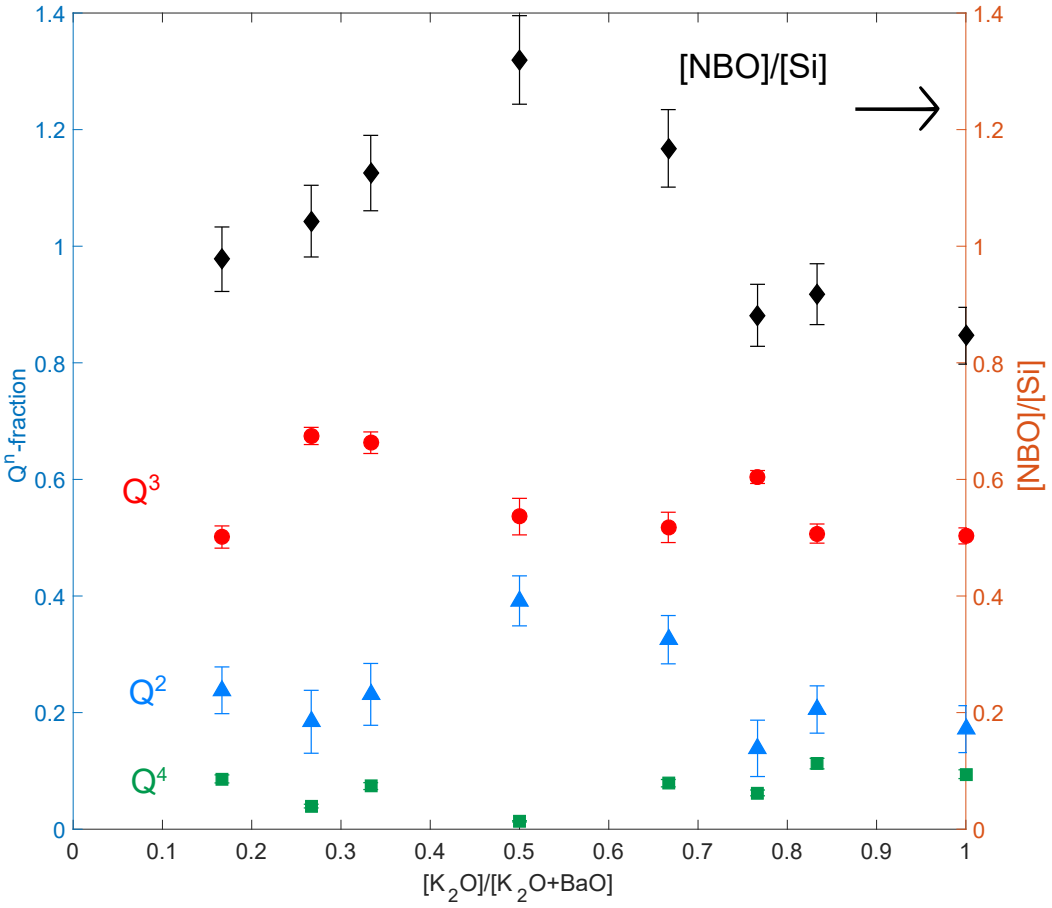

Figure 6.21: The Q^n-distribution (left) and non-bridging oxygen per silicon atom ([NBO]/[Si] on the right) of $x$$K_2O$-(30$-x$)BaO-70$SiO_2$ from Raman spectroscopy. Error from fitting was assumed to be 10% of peak intensity, if the error bars are not shown, they are smaller than the symbol.

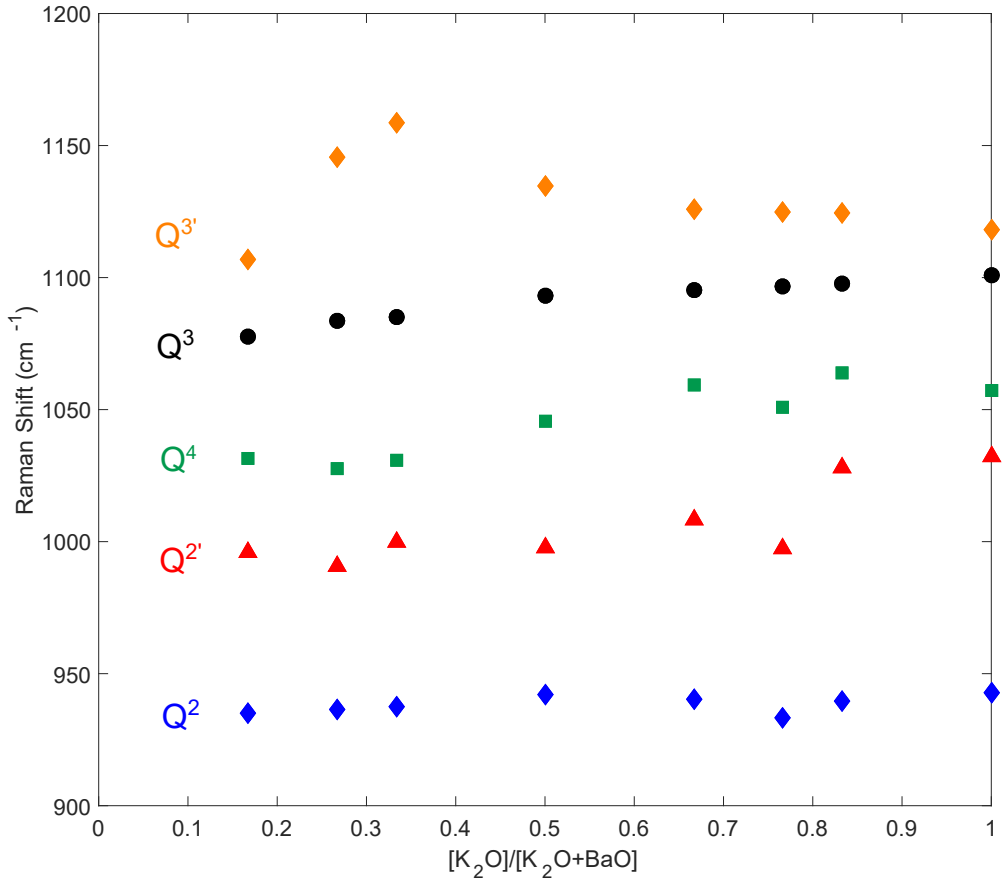

Figure 6.22: Raman shifts of $x$$K_2O$-$(30-x)$BaO-70$SiO_2$ glasses as a function of relative K_2O ratio for the high-frequency peaks which correspond to Si-O bond lengths.

region compositions, five peaks were required, which is reasonable as several authors have found K_2O-SiO_2 glass to contain second $Q^{2'}$ and $Q^{3'}$ peaks with discernibly unique environments,[329,330] however, it is only in this series that $Q^{2'}$ peaks have been detectable. There is not a clear MME for any of the peaks, except for $Q^{3'}$, which usually is the least reliable given its low intensity. In fact, there seems to be a negative deviation at high BaO content and a positive deviation when the relative K_2O concentration is high.

Fig. 6.23 contains the LF Raman peaks that correspond to ∠Si-O-Si; generally,

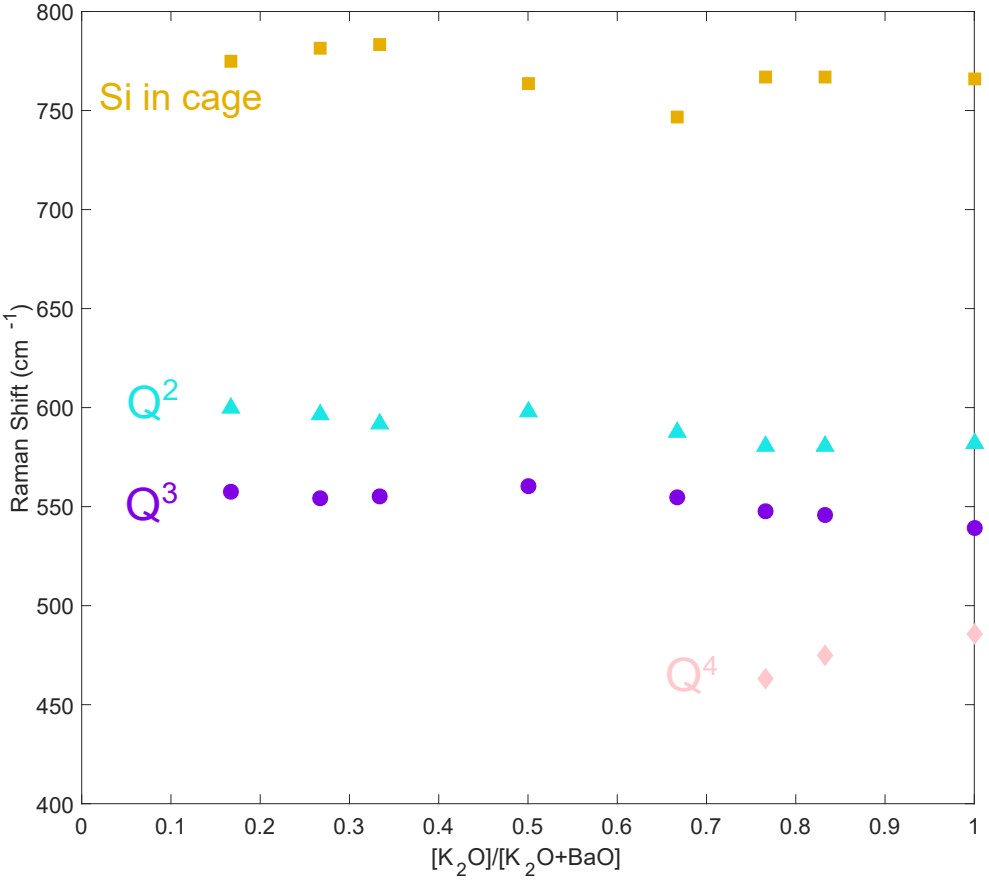

Figure 6.23: Raman shifts of xK$_2$O-(30$-x$)BaO-70SiO$_2$ glasses as a function of relative K$_2$O ratio for the low-frequency peaks which correspond to Si-O-Si bond angles.

the peak frequencies decrease with increasing K$_2$O content and there is a positive deviation, both indicative of narrowing of Si-O-Si bond angles. For this series, LF Q^4 peaks were not detectable at high BaO, yet HF Q^4 were; the LF peaks are due to longer range vibrations and have been shown to be poor probes of Q^n population.[145]

The MME in E_a shown in Fig. 6.24 is smaller-than-expected from the ΔF_c, (compared to the baseline series which has a smaller ΔF_c, yet a larger deviation in E_a), however, it may simply be that alkaline-earth cations induce a smaller MME even when paired with a alkali cation. More striking yet, is the fact that the MME in the

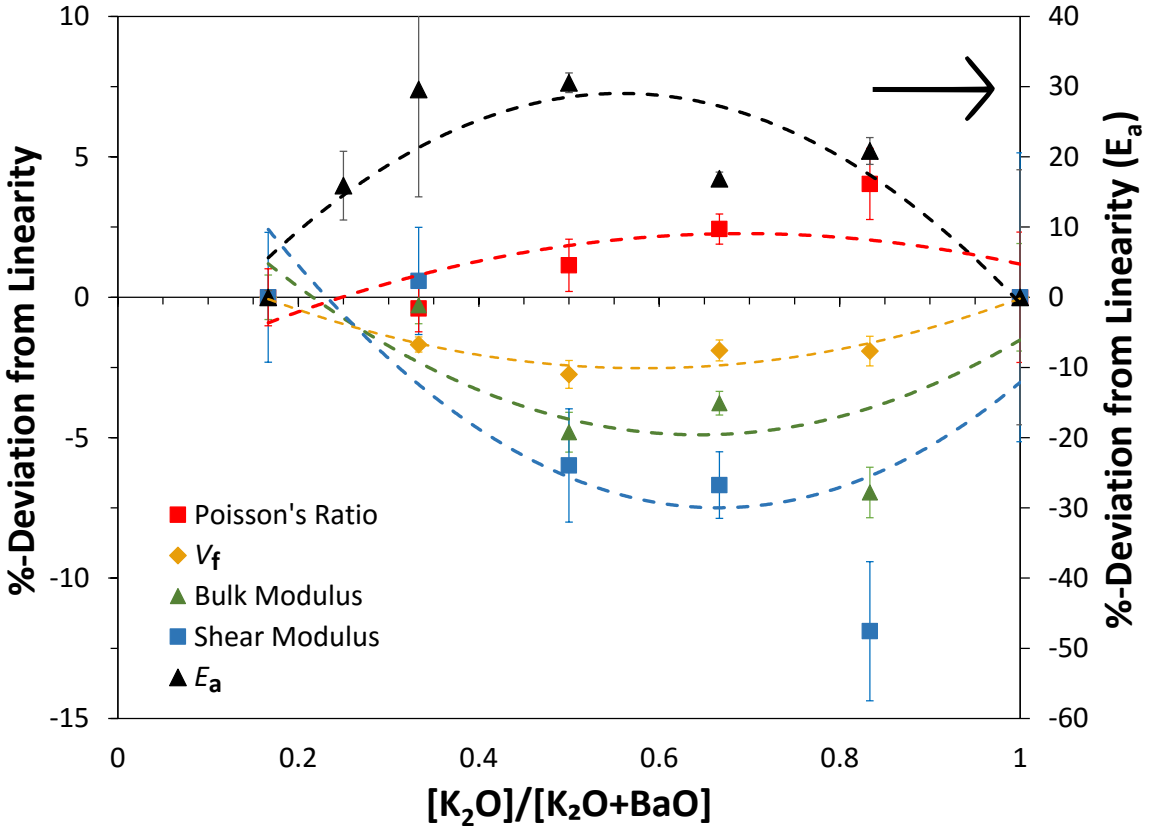

Figure 6.24: The MME in xK$_2$O-(30$-x$)BaO-70SiO$_2$ as a function of relative K$_2$O content. Mechanical properties (bulk, K, and shear moduli, G) and static properties (packing fraction, V_f) are on the left axis, while ion transport (E_a) is on the right axis. The dashed lines are fits to the apparent trends with 2nd-order polynomials.

mechanical properties has essentially been reversed; before, the deviations in K and G were always positive, while here both MMEs are negative. The relatively negative deviation in G likely is related to the sharp decrease in network connectivity observed in the Raman results. Nonetheless, it may still be able to extend the trend where if the deviation of G is greater than that of K, the deviation in μ is always the opposite direction. Finally, the deviation in V_f is negative, which thus far has only been found in this and the Li-Mg series, both where the Δr_c is very small; all of the Li-K and Li-Rb series had positive deviations, while the Li-Ba essentially had zero deviation from linearity.

Fig. 6.25 shows the fourth elastic modulus, Y, to also have a negative deviation, which could be a result of both decreased network connectivity and compactness. Yet despite G, K and Y having negative deviations, H_{V} still has a positive deviation, although it is smaller than most series. This appears to indicate that no matter the direction of the MME in dynamic properties (E_{a}), static properties (V_{f}) or the elastic moduli, H_{V} has a positive deviation, however, the magnitude of the deviation still depends on the identity of the cations. Conversely, fracture toughness appears to be correlated with E_{a} and the other elastic moduli. In the Li-Ba series a negative deviation in E_{a} was correlated with a positive one in K_{Ic}, while here the inverted deviations in elastic moduli are likely responsible for a positive deviation in fracture toughness. Although polymers are less stiff than glass, they are also tougher, which may be akin to the relationship between K_{Ic} and elastic moduli observed here.

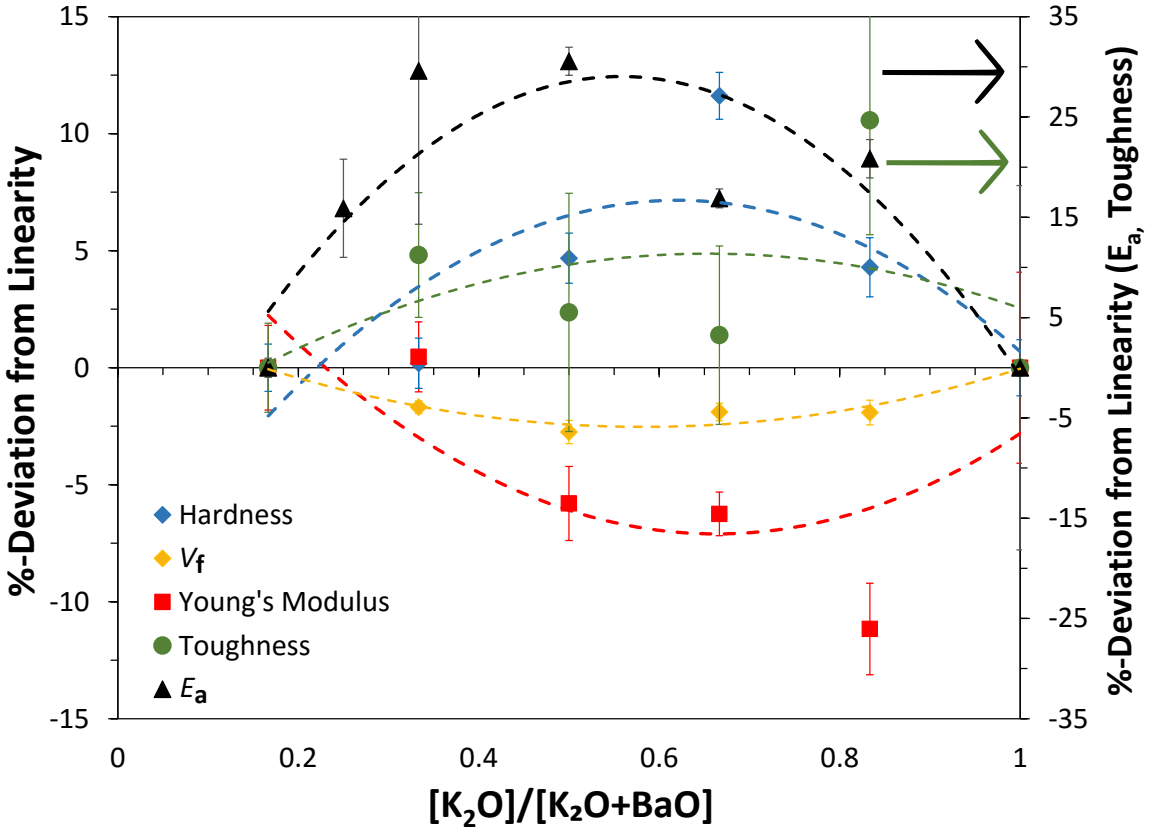

Figure 6.25: The MME in xK$_2$O-(30$-x$)BaO-70SiO$_2$ as a function of relative K$_2$O content. Mechanical properties (hardness, H_{V}, fracture toughness, K_{Ic} and Young's modulus, Y) and static properties (packing fraction, V_{f}) are on the left axis, while ion transport (E_{a}) is on the right axis. The dashed lines are fits to the apparent trends with 2nd-order polynomials.

6.4.4 $x\mathbf{K_2O}$-$(\mathbf{40}-x)\mathbf{MgO}$-$\mathbf{60SiO_2}$

Please see Appendix D.8 for all density, conductivity and mechanical plots. In this case, WDS was found to be suited only for the compositions with high MgO content ($\geq$ 20 mol-%), so those analyzed compositions can be in Table D.6, however, the nominal composition values were used for high K_2O compositions. For the same reason (surface water contamination) Raman spectroscopy could only be performed successfully on four samples and is not shown here.

This series is of interest because it possesses the largest ΔF_c between cations of all series studied within; moreover, it has nearly the largest Δr_c and ΔCN, thus by most metrics, it should have the largest MME. In fact, K^+ and Mg^{2+} are so different, there is evidence of incomplete mixing occurring, where the concentrated charge of Mg^{2+} outcompetes K^+ for charged NBOs and K^+ is left with only BOs creating regions where each type of oxygen is only bonded to a single type of cation.[81,331] In glasses with large cations and few NBOs, it is not uncommon for large, low-charge ions to bond to the oxygen of Si-O-Si linkages in order to maintain their desired coordination sphere.[332] Compared to a single modifier glass where NBOs and BOs both equally bond to the modifier, in this mixed-modifier glass with segregated bond types smaller ions, such as Mg^{2+} will end up having a smaller coordination sphere, while large cations such as K^+ must also increase their coordination spheres to satisfy the charge balance.[333] This is in direct conflict with the paper by Dietzel[83], who states that ions with larger ΔF_c are *more* likely to share a bond with NBO. Finally, the more mobile ion (K^+) is much larger than the less mobile ion (Mg^{2+}).

Before discussion of the MME in the mechanical properties vs. static and dynamic properties, it is worth noting that like the Mg-Ca series in Chapter 5, the high MgO content compositions showed evidence of free O^{2-} in the conductivity data (Figs. D.71

and D.72), where there are discontinuities at higher temperatures and both a low- and high-T E_a result (Fig. D.73). Like the Mg-Ca series, the high-T E_a fits better with the overall trend and is shown in Figs. 6.26 and 6.27. This phenomenon appears to be found in any silicate glass containing high amount of MgO, although the conductivity of the Li-Mg do not show strong evidence of this; it may be that the cations must be of different sizes to create conditions suitable for free O^{-2} to exist. Additionally, this series, specifically at high relative MgO content, had lower densities than those that had been reported for similar compositions;[334] since their compositions have been confirmed, it may be a result of the free oxygen, which lowered the density and V_f for the compositions suspected to have high $N(O^{2-})$ in the Ca-Mg series (Section 5.3.2).

Examining the MME in E_a in Fig. 6.26, the effect of the free oxygen can be observed: at high MgO concentration, the MME in E_a is very small, yet at higher K_2O content, the MME increases. Thus, it is likely that even though K^+ and Mg^{2+} are suspected of being somewhat separate within the glass structure, an MME in conductivity still exists. Nonetheless, given the small relative size of the deviation in E_a compared with that which is predicted for cations with such different ion parameters, it appears that the incomplete mixing may reduce the size of the MME in ion transport properties. This antagonism is interesting, it indicates that there may be a limit in how different the ions can be while still integrating sufficiently to obtain the MME.

Overall, this series has the largest negative deviation in V_f and all of the elastic moduli, including Poisson's ratio, have negative deviations as well. Only Mg-Ca and this series have had μ with the same direction of deviation as the other three moduli. However, for most of the elastic moduli, especially G in Fig. 6.26 and Y in Fig 6.27, there appears to be a different behaviour at high MgO content ($\geq$ 20 mol-% MgO) compared with that at high K_2O content. For example, the deviation in Y is quite

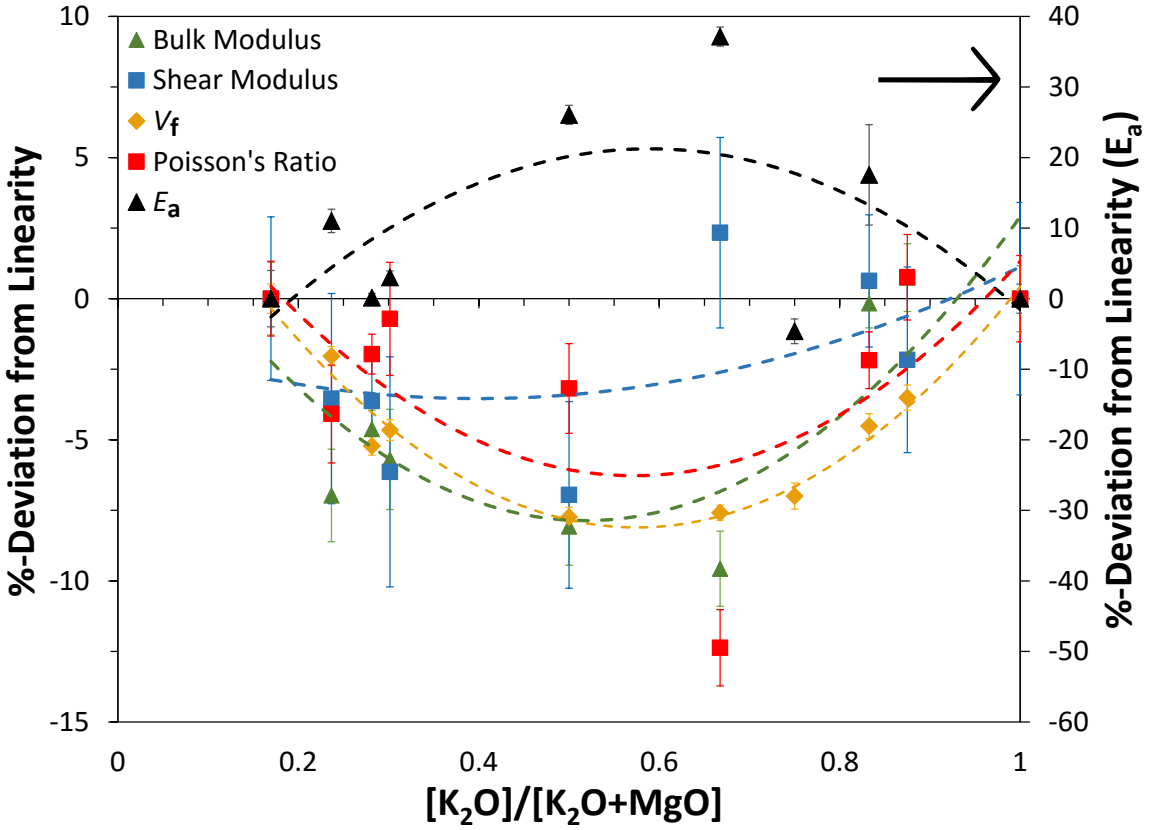

Figure 6.26: The MME in xK$_2$O-(40$-x$)MgO-60SiO$_2$ as a function of relative K$_2$O content. Mechanical properties (bulk, K, and shear moduli, G) and static properties (packing fraction, V_f) are on the left axis, while ion transport (E_a) is on the right axis. The dashed lines are fits to the apparent trends with 2nd-order polynomials.

negative between 0.16–0.5 relative K$_2$O mol-%, while it is near zero for compositions with greater than 0.5 relative K$_2$O mol-%. This inconsistency makes it difficult to comment upon this series, other than free O^{2-} appears to lower mechanical properties and this results in either a lower positive MME in the case of the Mg-Ca series, or in this case, a larger negative deviation from linearity. Once more, negative deviation in elastic moduli correlate with a positive MME in fracture toughness, while the MME in hardness is positive once more.

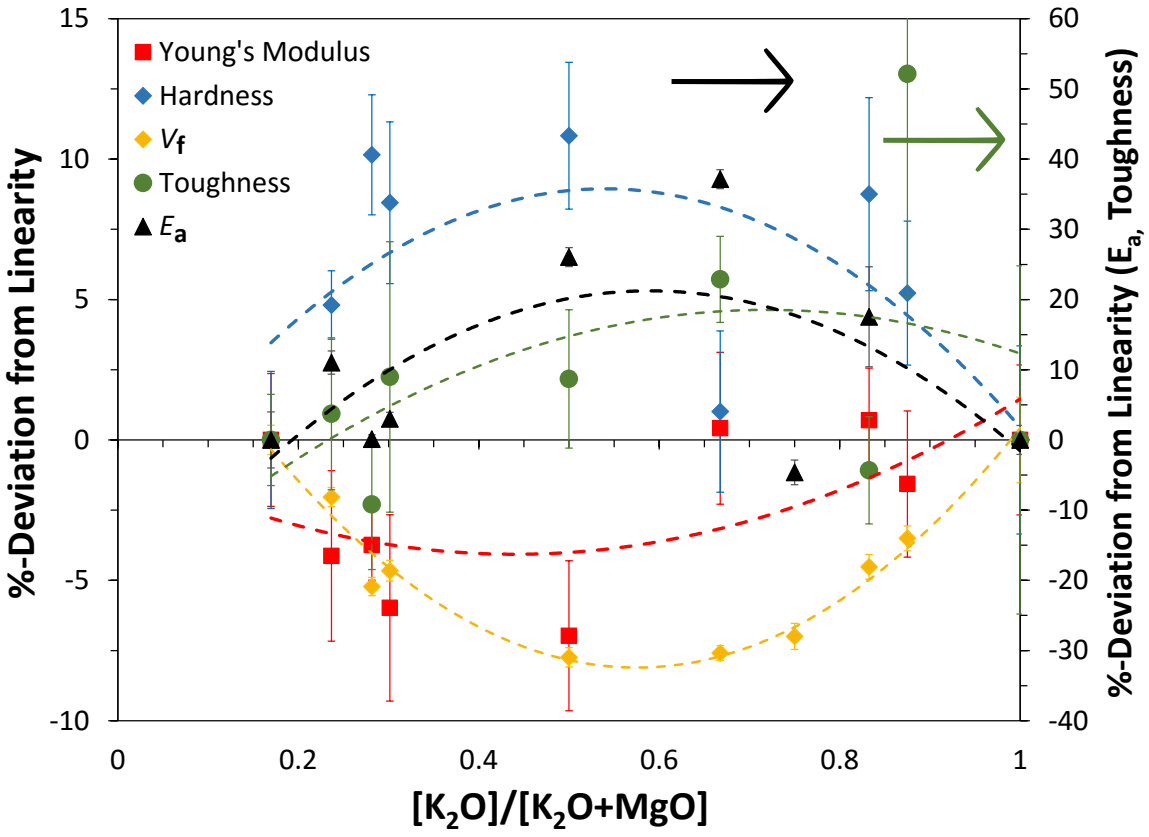

Figure 6.27: The MME in xK$_2$O-(40$-x$)MgO-60SiO$_2$ as a function of relative K$_2$O content. Mechanical properties (hardness, H_{V}, fracture toughness, K_{Ic} and Young's modulus, Y) and static properties (packing fraction, V_{f}) are on the left axis, while ion transport (E_{a}) is on the right axis. The dashed lines are fits to the apparent trends with 2nd-order polynomials.

6.4.5 $x\mathbf{Li_2O}$-$(\mathbf{30}-x)\mathbf{ZnO}$-$\mathbf{70SiO_2}$

The relevant plots (density, conductivity and mechanical) for this series, $x\mathrm{Li_2O}$-$(30-x)$ZnO-$70\mathrm{SiO_2}$, can be found in Appendix D.9. Additionally, WDS data and Raman spectra can be found in Table D.7 and Fig. D.80, respectively. As a result, the analyzed compositions were used to calculate V_f for this series.

This series is of interest because the second cation, Zn^{2+}, is definitively classified as an intermediate additive, and is close to being considered a glass former according to Sun's classification system based on cation-oxide bond strengths.[15] Of the series studied thus far, only Mg^{2+} has been thought to be a intermediate, rather than a modifier, but there are disagreeing classifications and also it depends on the nature of the second cation, since tetrahedral Mg is much more likely to act as an intermediate than octahedral. Consequently, this system was studied in order to determine whether deviations from linearity occur in a mixed modifier-intermediate series. Moreover, Li^+ and Zn^{2+} are identical in CN, very similar in size (only 0.02 Å different), yet due to difference in charge have a ΔF_c of -0.23, making the cation pair very similar to Li-Mg, only here Zn^{2+} is an intermediate and has a d-shell valence active in bonding making it the most electronegative cation studied by far. Zn^{2+} also has the ability to behave more like a glass modifier or former, where at low ZnO mostly tetrahedral zinc forms, yet more octahedral zinc forms at higher ZnO concentration indicating a shift towards more modifier-like attributes.[335] However, the same study found tetrahedral zinc to be disruptive to the silica network in the same way a modifier would be. Finally, zinc was found to create sodium depleted regions in the silica network in sodium-zinc silicate glasses.[335]

This glass series was prone to "cloudiness" or translucency rather than transparency, care was taken to "cut away" opaque regions, since they usually formed on

top (likely due to slower cooling), or in some cases (high ZnO content), a "squash" melt method was adopted, where the melt was quickly pressed between two metal plates at RT for increased cooling rate; in the latter case, likely the fictive temperature is changed. The cloudiness seemed to be more akin to phase separation rather than crystallization (which forms noticeably white crystals), however, that is in contradiction to the current theories which predict cations with not-too-large Δr_c and not–too-small ΔF_c should mix easily, yet have a stabilising interaction with NBO in the glass network.

Fig. 6.28 indicates that ZnO forces the Q^n population towards having more Q^4 and less Q^2-units, thereby increasing the network connectivity (lower [NBO]/[Si]), likely due to oxygen being sequestered in Zn-O-Zn linkages (since zinc is behaving more like a glass former) and no longer playing a role in the silica network. There is no evidence to indicate mobile free oxygen in the conductivity data (Figs. D.81 and D.5). Additionally, there is a negative MME in [NBO]/[Si], indicating increased connectivity for mixed compositions.

The Raman shifts in Figs. 6.29 and 6.30 show both the HF and LF peaks increasing with more Li_2O content. Interestingly there appears to be a large positive deviation in the HF peaks, indicating a shortening of Si-O bonds, while the LF peaks have the opposite deviation and indicate a widening of the Si-O-Si angle between silica tetrahedra. Thus, there are two opposite mechanisms occurring in reference to compactness. This could be due to the ability of Zn^{2+} to act as a modifier or former, depending on the amount of ZnO.

First and foremost, there is a clear deviation in E_a in Fig. 6.31, indicating that even combinations of modifier and intermediate ions can induce behaviour akin to the MME. This may be because of the generally modifier-like behaviour of zinc found in

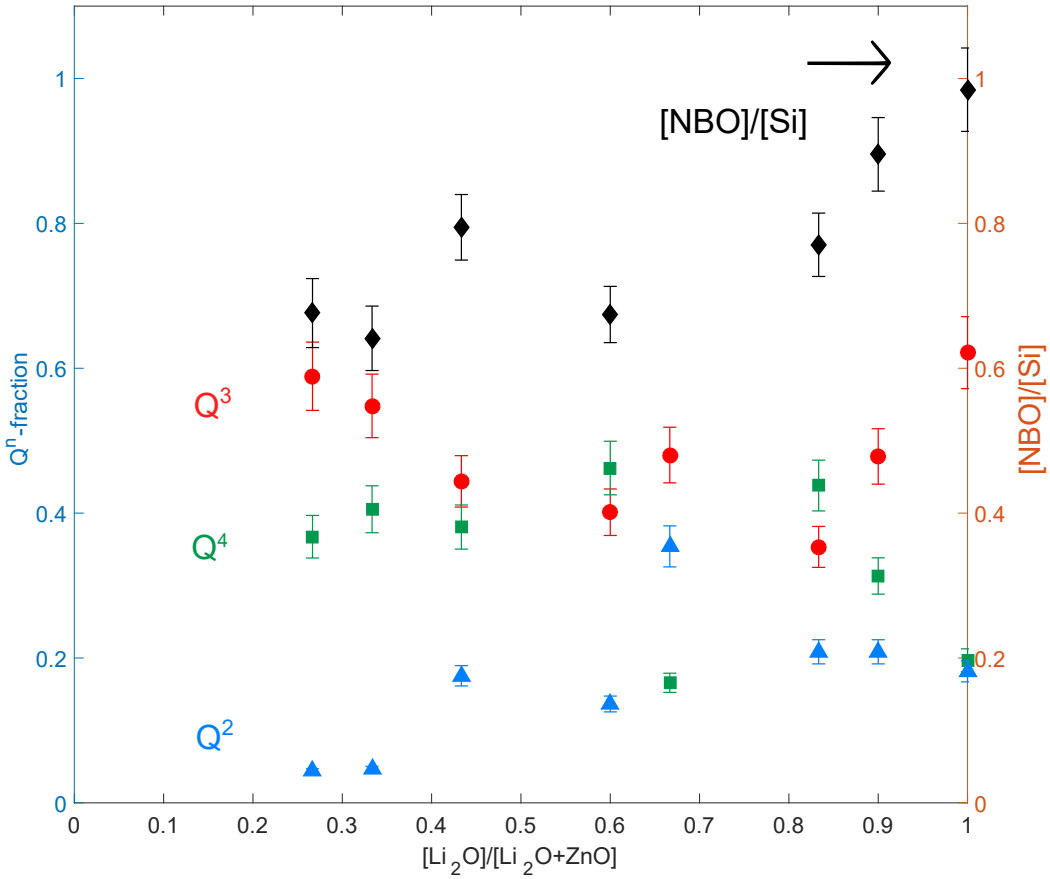

Figure 6.28: The Q^n-distribution (left) and non-bridging oxygen per silicon atom ([NBO]/[Si] on the right) of $x$$Li_2O$-(30−$x$)ZnO-70$SiO_2$ from Raman spectroscopy. Error from fitting was assumed to be 10% of peak intensity.

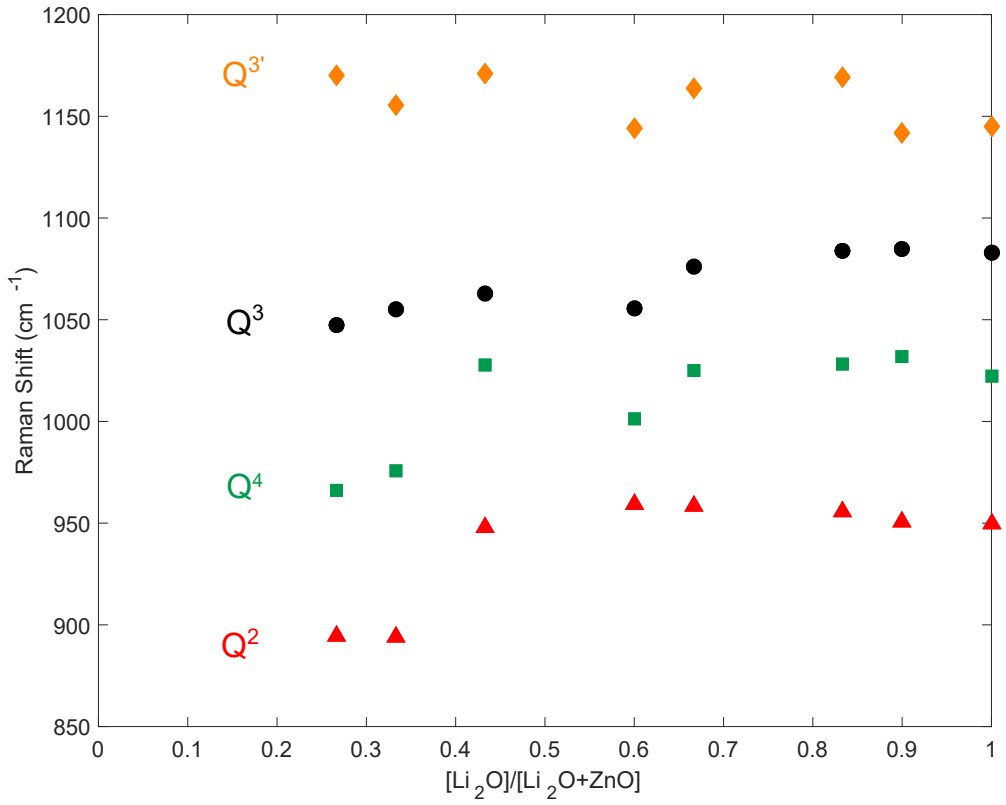

Figure 6.29: Raman shifts of $x\mathrm{Li_2O}$-$(30-x)$ZnO-70$\mathrm{SiO_2}$ glasses as a function of relative $\mathrm{Li_2O}$ ratio for the high-frequency peaks which correspond to Si-O bond lengths.

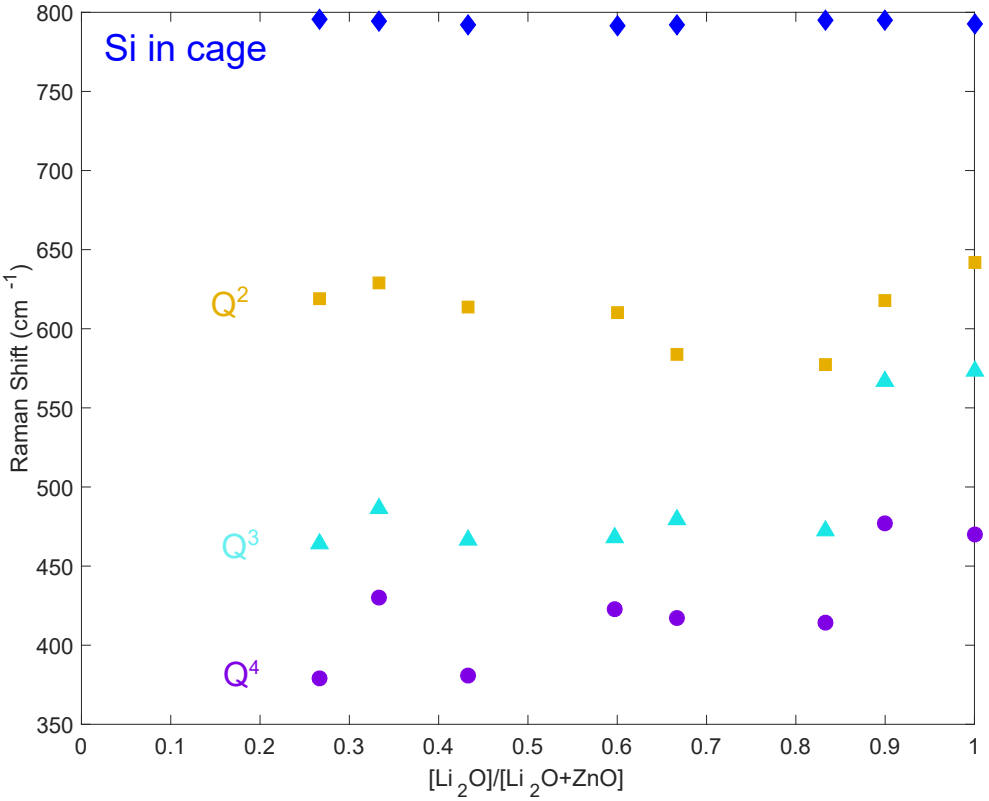

Figure 6.30: Raman shifts of $x$$Li_2O$-$(30-x)$ZnO-70$SiO_2$ glasses as a function of relative Li_2O ratio for the low-frequency peaks which correspond to Si-O-Si bond angles.

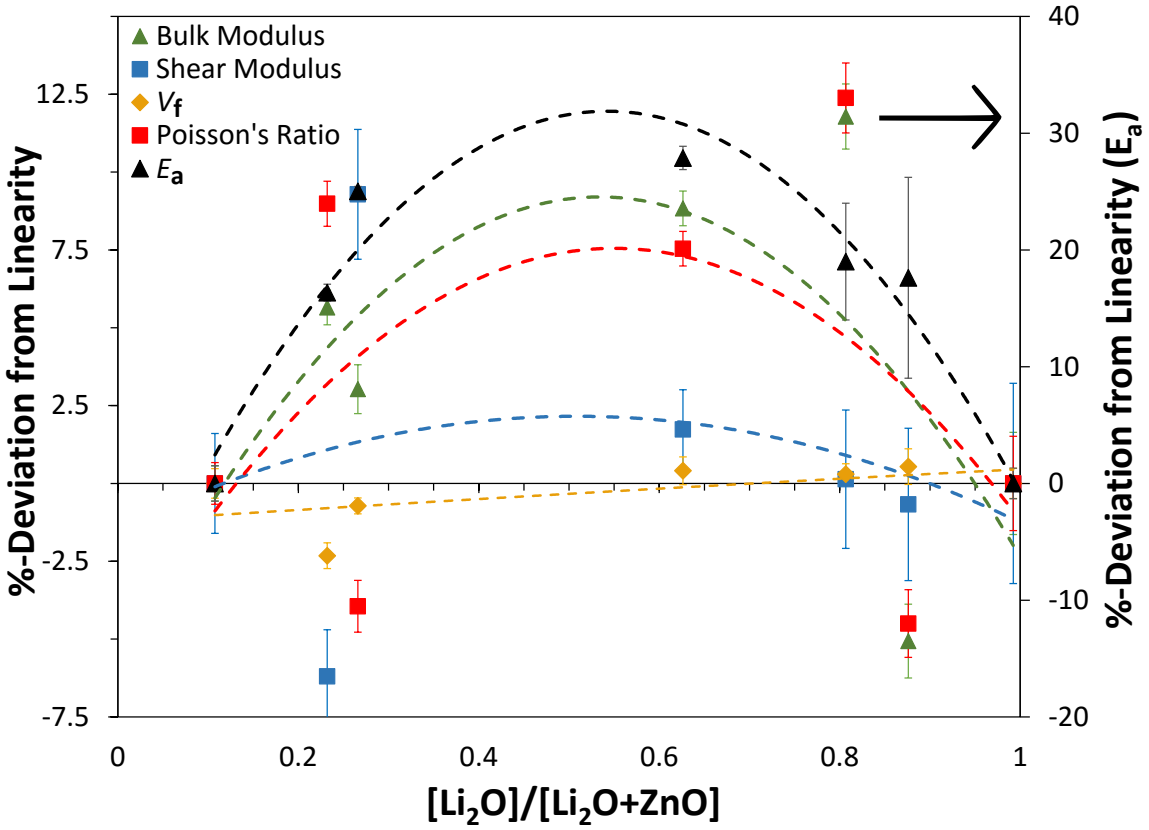

Figure 6.31: The MME in xLi$_2$O-(30$-x$)ZnO-70SiO$_2$ as a function of relative Li$_2$O content. Mechanical properties (bulk, K, and shear moduli, G) and static properties (packing fraction, V_f) are on the left axis, while ion transport (E_a) is on the right axis. The dashed lines are fits to the apparent trends with 2nd-order polynomials.

zinc silicates.[335] The trends in the other properties are less obvious; the deviation in K appears to mostly be positive, the deviation in V_f goes from negative to positive with increasing Li$_2$O content, but it is so close to zero for the most part that the deviation is likely negligible (agreement with the Raman results), while the MME in G and μ have data points far below and above zero that the overall trend is difficult to discern. In the past series, when the MME in K was greater than G, μ had a deviation in the same direction as K, so the MME in μ may indeed be positive.

The trend in Y in Fig. 6.32 is very similar to that observed for G in the previous Figure, which has become an expected correlation. Once more, the deviation in H_V

is positive and fairly large for the relatively small deviation in E_a. Interestingly K_{Ic} also has a positive MME which has only been related to either a negative deviation in E_a or a negative deviation in most other elastic moduli, consequently, this may be something unique to adding an intermediate rather than second modifier cation. Finally, there are similar trends in K, H_V and K_{Ic} (and perhaps in G and Y, but only one data point) where the deviation goes from being large at high Li_2O to being much smaller at high ZnO content. Again this "switch" may be due to zinc behaving more modifier-like at high ZnO and decreasing the mechanical properties. In retrospect, this is very similar to the behaviour observed in the Mg-Ca and K-Mg series which both saw significantly decreased MME at high MgO content; Mg^{2+} is known to undergo a octahedral-tetrahedral transition in the presence of a second modifier[81] and evidence of free oxygen, likely involved in Mg-O-Mg linkages was found in the conductivity data of both of those series as well (Figs. 5.9 and D.43).

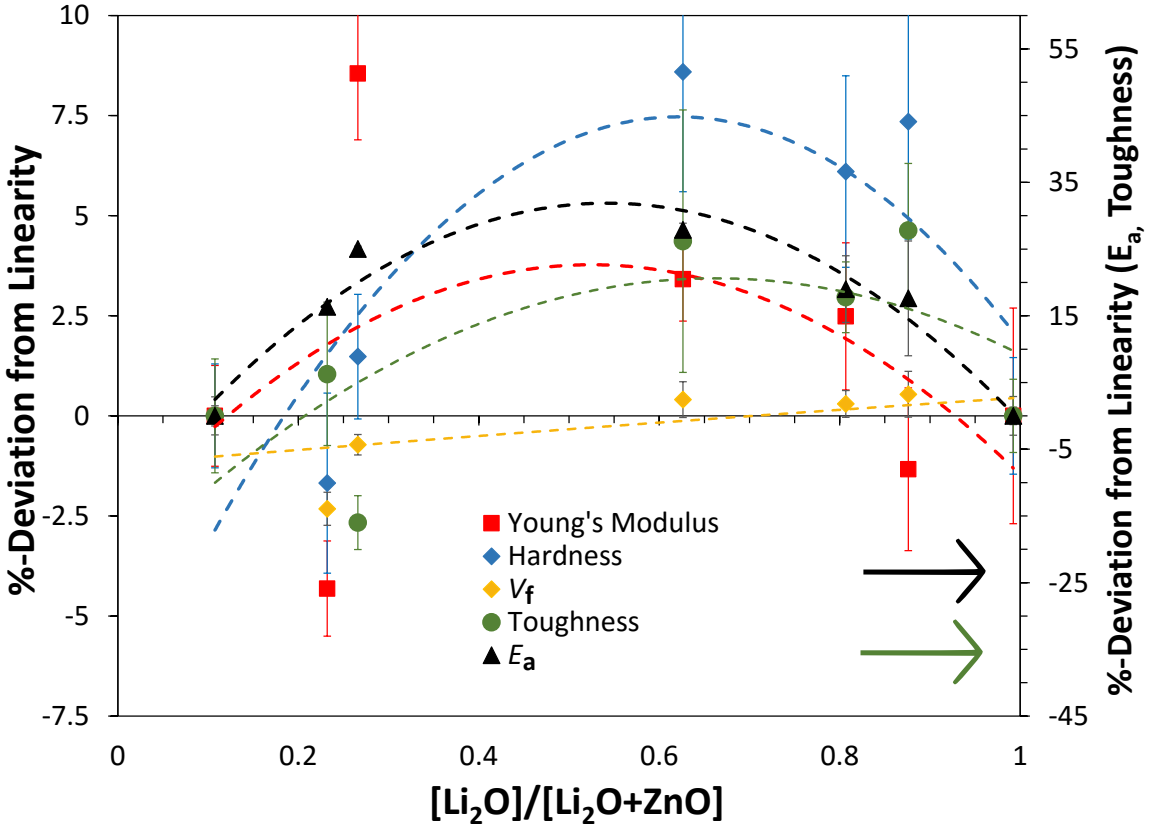

Figure 6.32: The MME in $x\mathrm{Li_2O}$-$(30-x)$ZnO-70$\mathrm{SiO_2}$ as a function of relative $\mathrm{Li_2O}$ content. Mechanical properties (hardness, H_V, fracture toughness, K_Ic and Young's modulus, Y) and static properties (packing fraction, V_f) are on the left axis, while ion transport (E_a) is on the right axis. The dashed lines are fits to the apparent trends with 2nd-order polynomials.

6.5 Comparison of MME in All Properties of the Mixed-Modifier Series

Table 6.4 displays the MME for all properties and series studied in this chapter; for comparisons between the mixed-alkali series only, please see Section 6.4. Perhaps the most striking quality of Table 6.4 is the variation which can be achieved depending upon the combination of modifier; almost all properties can have positive or negative deviations and the relationships between the properties vary as well.

Table 6.4: Comparison of MME in the properties of all glass series studied within, reporting the highest maximum value of the apparent 2nd-order polynomial fit. All values in percent.

Property	Mg-Ca	Li-K	40Li-K	Li-Rb	40Li-Rb	Li-Mg	Li-Ba	K-Ba	K-Mg	Li-Zn
E_a	17.5	75	105	55	130	15	−5	30	20	30
V_f	1.3	2.5	2.5	1.3	3.8	−3.8	−0.5	−2.5	−7.5	0
G	3.8	12.5	8.8	10	5	15	5	−7.5	−3.8	2.5
K	12.5	5	13.8	7.5	21.3	2.5	−1.3	−5	−7.5	8.3
μ	6.8	−8.8	1.3	−6.3	5	10	−5	2.5	−6.3	7.5
Y	5	12.5	10	10	8.8	11.3	3.8	−7.5	−3.8	3.8
H_V	6.3	5	20	5	22.5	5	17.5	6.3	8.8	7.5
K_{Ic}	−12.5	−15	−40	−16	−45	−5	30	10	20	20

First and foremost, previous studies of the MME state[58,61,64,79] that the magnitude of the deviation should depend on the differences between ions, thus Table 6.5 again shows the differences between ion pairs studied here. The expected outcomes for the mixed-alkali series were observed; a greater total alkai content and large differences between ions produced a more pronounced deviation from linearity in E_a. It is abundantly clear that for E_a the "pure" MAE in mixed-alkali series is much larger than the MME in mixed alkali-alkaline earth or "pure" mixed alkaline-earth series, even after other differences between the ions are accounted for. Thus, it appears that the MME in conductivity depends heavily on the periodic group(s) of the mixed ions. For example, alkalis tend to be much more mobile than alkaline-earths, leading to more opportunities for the "hopping" of cations to be discouraged by the extra energy required to relax the ion site to the identity of a different ion. Nonetheless,

Table 6.5: Comparison of cations parameters for the mixed-modifier compositions made within.

Ion Pair	ΔCN	Δr_c (Å)	ΔF_c (Å^{-2})	ΔE_a (kJ/mol)
Li-K	4	−0.75	0.10	−5
Li-Rb	5	−0.87	0.11	−11
Li-Mg	2	0.04	−0.24	−18.25
K-Ba	0	0.09	−0.14	−8.25
Li-Ba	4	−0.66	−0.04	−13.25
K-Mg	4	0.79	−0.33	−13.25
Li-Zn	0	0.02	−0.23	−15
Mg-Ca	0 to 2	−0.28 to −0.43	0.10 to 0.13	8.25

if the mobility of the ions are similar, *e.g.* K^+ and Rb^+, the differences between the ions becomes important. Essentially, all mixed-alkali series (Li-K, 40Li-K, Li-Rb and 40Li-Rb) have similar magnitudes of E_a at the point of maximum mixing, thus the mobility of the ions is similar at the maximum E_a and the differences between the ions should determine the MME in these series.

An interesting trend among the other mixed-modifier series is that neither the difference in cationic strength (ΔF_c) nor size (Δr_c) appear to correlate with the MME in E_a. Based on ΔF_c, K-Mg should have the largest deviation, while based on Δr_c, Li-Ba should. Although neither classification appears to be true, ΔF_c does predict almost no deviation in E_a for the Li-Ba series and that was confirmed experimentally, which may prove that ΔF_c is a better predictor than Δr_c of the strength of the MME. Part of the difficulty in using these metrics comes from the fact that some cations, namely Mg^{2+}, Zn^{2+} and perhaps Ca^{2+} can behave more glass former-like, leading to questions about their participation in ion conductivity. Thus, it might be unfair to claim that ΔF_c is not a good predictor of the MME as most of the series studied contain MgO, CaO or ZnO; in fact, the only mixed alkali-alkaline earth series without one of those cations are the Li-Ba and K-Ba series, whose MME in E_a does follow the trend in ΔF_c. Consequently, it may be in the absence of any cations that behave more

like glass formers, the strength of the MME *is* dependent on ΔF_c between the cations, rather than having no clear trend such as observed when considering a broader group of cations. Still, this is important as the identity of the modifier *clearly* matters; if one desires to create a series containing an alkaline earth and a large deviation in E_a, Ba or Sr should be chosen *in combination* with a large ΔF_c. However, there is evidence that indicates too large of a ΔF_c may not translate into a larger MME for E_a as in the case of K-Mg, where incomplete mixing occurs;[81] yet, this could still be due to the ability of Mg to behave more like a glass former. Most importantly, ΔF_c is only considered influential to the MME in E_a *if* the conductivities of the series are similar.

The mechanical properties of the mixed alkali-alkaline earth series appear to have entirely different trends than the MME in the E_a. Uniquely, the only " pure" mixed alkaline-earth series (Mg-Ca) has trends in the deviations of the mechanical properties that were very similar to those in the 40Li-K and 40Li-Rb series. All three series have deviations in the same directions (positive deviations in every property except K_{Ic}, which is negative). Like the 40Li-K and 40Li-Rb series, Mg-Ca has a large amount of total modifier (50 mol-%) thus it may be that the MAE and MAEE are similar in mechanism but the MAE is much stronger than the MAEE (possibly due to increased ion mobility in the alkali case). Similarly for the Mg-Ca series, V_f and perhaps H_V do correlate with the weaker MME in E_a as it did in the mixed-alkali series, however, the deviation in K is larger in the Mg-Ca series despite the smaller deviation in E_a. Additionally, the deviation in G is smaller than K and μ is positive (like the 40Li-K and 40 Li-Rb series again) indicating higher plasticity, yet, the deviations in H_V and K_{Ic} are smaller (as would expected from more plastic behaviour) compared with the 40Li-K and 40 Li-Rb series. This may reveal that when the deviation in E_a is small, the deviation from linearity in shear modulus over that in bulk modulus

($\delta G/\delta K$) ratio becomes more important in determining the more dynamic mechanical properties.

It is interesting that despite the much weaker MME in E_{a} for the alkali-alkaline earth series, the deviations in the mechanical and static properties of all the series are comparable if not larger than those in the "pure" MAE. This seems to indicate that the MME behaves very differently once cations of different charges are involved, since no clear trend exists between E_{a}, V_{f} and mechanical properties for the mixed alkali-alkaline earth series. Firstly, the deviation in V_{f} is normally negative (or near zero in the case of Li-Zn) for the mixed alkali-alkaline earth series unlike the mixed alkali series. Additionally, four of the five mixed alkali-alkaline earth systems have the larger cation also being the more mobile one, only Li-Ba goes against the trend. Since Li-Ba goes against this trend, yet still has a negative deviation in V_{f}, it indicates that difference in charge is an important factor in determining the static properties, such as density and refractive index. It appears that the perhaps the role of the modifier, a 1+ or 2+ charged site, affect how the glass network responds and forms during cooling. Nonetheless, if the Li-Zn series is excluded, the V_{f} of the other four mixed alkali-alkaline earth series follow the trend in ΔF_{c}, where the largest ΔF_{c} has the most negative deviation in V_{f}. Consequently, it appears to be a similar situation to above, where after a parameter, in this case charge difference, is accounted for ΔF_{c} is a good predictor of the trends in V_{f}.

The negative deviation in V_{f} for the mixed alkali-alkaline earth series is counter-intuitive; before in the mixed-alkali and mixed alkaline-earth series, when V_{f} increased, so did E_{a}, likely due to less free space in the structure making it more difficult for ions to move throughout. However, in the mixed alkali-alkaline earth series the opposite trend occurs, where despite the lower V_{f}, there is still a positive deviation, albeit smaller MME in E_{a}. As a result, this indicates that the decrease in conductivity is

affected by more than just the packing fraction, that the simple fact of having two types of ions will increase E_a; this result is in line with the DSM which claims that extra energy is required to rearrange the ion site when a different type of ion settles there, leading to a positive MME in E_a always. The exception is the Li-Ba series, but it may be the size difference and near-zero ΔF_c leads the migration paths of each ion not interacting. Nonetheless, the MME in V_f appears to be a large predictor of the MME in E_a, while the V_f can be predicted using charge difference, followed by ΔF_c. This result indicates that having differently sized spheres does increase packing fraction, but ions of different charges may affect the silica network in a way which leads to non-optimal packing for either cation.

In the mixed-alkali series, the strength of the MME in E_a was correlated with that in K, which may be true for Li-Ba, where almost no deviation in conductivity is found with a small deviation in K, but the other four series do not show this trend, so it seems unlikely. In fact, the reason Li-Mg and Li-Zn would have positive deviations in K, while the others (Li-Ba, K-Ba and K-Mg) would have negative deviations is not located anywhere in Table 6.5. At first it appears that only cation combinations with small ΔF_c have positive deviations in K, however, K-Ba also has a small ΔF_c, yet a negative deviation in K. Perhaps then, the type of ion pair is important, as both cations in the Li-Mg and Li-Zn series are relatively electronegative and form relatively covalent bonds, while Li-Ba, K-Ba and K-Mg all involve at least one low-electronegativity cation. At least for those three series with negative deviations in K (Li-Ba, K-Ba and K-Mg), the trend in ΔF_c or V_f does appears to be correlated with K. Thus, for bulk modulus, there appears to be an extra consideration after total conductivity and charge difference, the type of bonding of the ion pair may affect the packing density of the atoms as well.

The trends in G are even more difficult to nail down than those in K; unlike K,

shear modulus did not follow the trends observed in E_a even for the mixed-alkali series. Although perhaps a similar claim as K can be made, where in this case Li-Mg and Li-Zn have positive deviations in G, while K-Ba and K-Mg have negative (Li-Ba may be an outlier due its near-zero ΔF_c). Despite Li-Mg and Li-Zn having very similar ΔF_c and mostly similar deviations for mechanical properties, G and K_{Ic} are major exceptions. Moreover, the trends in ΔF_c also indicate K-Mg should have larger deviations than K-Ba and that is not the case for most compositions. Thus, there must be another reason for the trends in G which are unrelated to the metrics in Table 6.5. Interestingly, the trends in Y essentially follow those in G; the deviation in Y is always the same direction and at most different by only a 1/3 (40Li-Rb is an exception). Generally, the deviation in Y is larger than or equal to that in G, the 40Li-Rb, Li-Mg and Li-Ba series are exceptions.

Nevertheless, the K-Ba series was the only one found to have a positive deviation in [NBO]/[Si], and it is likely K-Mg would be found to be the same, indicating that decreased network connectivity is correlated with negative deviations in G. In Chapter 5 however, bond rigidity was found to be more important than network connectivity in determining G and Y. Thus, there could potentially be competing mechanisms, bond connectivity vs. rigidity, and it is difficult to know without further information if any changes in the cation environment are occurring, as it did in the Mg-Ca series. One of the interesting aspects of the MME is the ability of the second cation to affect the bonding environment of the first cation, for example in the Mg-Ca system, the larger, less electronegative ion, Ca^{2+} forces Mg^{2+} to adopt a more ordered tetrahedral environment. This has been found to be generally true of ion pairs where small cations shift to smaller sites and large cations to larger ones.[81]

Thus, in terms of bonding, it is worthwhile to consider the effect of the small ion becoming more ordered, possibly decreasing in coordination, forming fewer, but

stronger bonds similar to a glass former. Conversely, the large ion should be becoming more modifier like and reducing overall rigidity. Additionally, the electronegativity of the cation affects the network connectivity as well. Thus, perhaps the trends in G and Y are a compromise between the changes in bond rigidity, positive from small ion and negative from large ion, as well as the network connectivity. It may be the increase in former-like behaviour of the small ion in Li-K and Li-Mg is much more stabilizing that the increased modifier-like behaviour of the large ion. Alternatively, the reduced bond rigidity occurring in the large ion in the K-Ba and K-Mg series could have a larger influence on G and Y.

Overall, no single parameter can easily determine the deviations in G and Y, the bonding environment of the modifier appears to be important, like whether it is more covalent, or former-like. This complex behaviour is made more interesting by the fact that Makishima and Mackenzie[48] successfully calculated Y of glasses from the weighted fundamental properties of crystals; it indicates that the MME influences the structure to be different than the sum of its parts, such as affecting the [NBO]/[Si] and cation bonding environments in a non-additive way.

As a result of the E_a and G not correlating, the idea that the MME would reduce ion mobility and increase rigidity appears to be only a small contribution to the overall picture. Indeed, quite often the opposite trend is observed, for example, the Li-K and Li-Mg have the highest deviation in G and Y, while fairly low MME in E_a compared to the other series. This also runs counter-intuitive to the DSM which highlights the importance of including the strain energy required for the network to dilate and relax during ion conduction, which implies that more rigid bonding should lead to higher E_a for ion movement. This result definitely indicates that packing fraction is larger determinant of E_a, rather than bond rigidity. Structural compactness and connectivity have been found elsewhere to be antagonistic.[3] The trends found here

agree, considering Y and G are measures of glass connectivity; a weaker deviation in E_a is correlated with weaker deviations in Y and G is clear for most of the series (excluding K-Ba and K-Mg).

Another trend which was found in the "pure" mixed-alkali and mixed alkaline-earth series was when the deviations of G and K were compared and the $\delta G/\delta K$ ratio is greater than one, μ is negative and the mechanical response of the glass should be more brittle and the opposite is true is $\delta G/\delta K < 1$. If the deviations in K and G are both in the same direction (excluding Li-Ba due to its small deviations and Li-Zn is excluded due to having a strong intermediate cation), the other three series, Li-Mg, K-Ba and K-Mg do follow this trend in regards to the sign of μ.

Most striking is that all of the systems with near-zero Δr_c have small negative or positive correlations in K_{Ic}. Granted, Li-Ba and K-Mg also have a positive MME in fracture toughness, but those two systems have been found elsewhere to have ion channels or regions which do not fully interact. Furthermore, the series with negative MMEs in μ (Li-K, Li-Rb, Li-Ba and K-Mg) also have the most positive (or least negative in the case of mixed-alkali series) deviation in K_{Ic}, while the series with positive deviations in μ (Li-Mg and K-Ba) have lower or negative deviations in K_{Ic}. Thus, it appears there are consistent relationships between these four mechanical properties, G, K, μ and K_{Ic}, no matter the identity of the ion, the only exception being the Li-Zn series. Although a higher G/K ratio in glass has been associated with brittleness upon fracture,[3] this result was found for metallic glasses. In the case of the mixed-modifier series studied here, the very opposite is true in most cases, where $\delta G/\delta K \geq 1$ correlates with more positive deviations in fracture toughness, meaning more energy is able to be absorbed through plastic deformation rather than cracking. This is definitely counter-intuitive, as a higher resistance to shear *should* make plasticity less likely and brittle fracture more likely.

Overall, the trends in E_a clearly have some influence on K_{Ic}, for example Li-Ba has almost no deviation in E_a and the most positive deviation in K_{Ic}, while 40Li-K and 40Li-Rb have the largest deviations in both properties. Although, not all series follow this trend, Mg-Ca and Li-Mg are outliers, there may be other reasons for these exceptions. Since K_{Ic} is the ability of the material to absorb energy under stress, an increase in the likelihood of the ions in a material moving and forcing the material around the ion site to rearrange to fit the new occupant may help reduce residual stress and material fracture. Thus, it appears in Table 6.4 that having a small deviation in E_a dictates that the material is more able to absorb energy under stress, clearly because of the ability of ions to move and force network relaxation.

The easiest trend to spot is that all series have positive deviations in H_V, no matter the identity of the ions, simply having more than one type of cation improves the hardness. Additionally, the three largest deviations in H_V, twice as much as the other series, have the largest size differences; the MME in hardness clearly seems influenced by Δr_c or ΔCN rather than ΔF_c. The only exception is K-Mg, which should a similarly large "double-digits" deviation in H_V, yet it still has the next largest deviation in H_V after the top three series and has been found elsewhere to lack the complete ion mixing required of the MME.[81] Since indentation adds energy to the system and deforms the structure, perhaps ions are forced to hop into site of the other type ion. Even when the structure, such as separate, yet intercalating ion channels would otherwise prevent the MME from occurring, the Li-Ba series is indicating indentation forces the deviation from linearity to occur nonetheless. Additionally, the MME in H_V should be affected by that in the V_f, where less free space leads to higher resistance to densification. However, the deviation of V_f in K-Mg is the most negative by far, yet the H_V has a large positive deviation.

6.6 Summary

One of the clearest conclusions to be drawn from this study is that the mixed alkali, mixed alkaline-earth and mixed alkali-alkaline earth series have different behaviour; factors such as the charge of the modifier cations and total conductivity of the system must be considered before applying a simple metric such as Δr_c or ΔF_c. For example, the MME in pure mixed-alkali systems was much stronger in E_a, while the mixed alkali-alkaline earth series saw only negative deviations in V_f, no matter the differences in size or cationic strength. However, when similar series were compared, V_f could be related to E_a, where generally compositions with more free space also had smaller deviations in E_a. All series, except for Li-Ba, experienced positive deviations in E_a, a finding in accordance with Dietzel's ΔF_c parameter.[83] Thus, the DSM (where energy is required to relax a site to a different type of ion)[71] works well for E_a, as long the same type of series are compared.

Additionally, another clear finding was that H_V was always improved by mixing as well, but depended on Δr_c, not ΔF_c or E_a. With only two exceptions, K_{Ic} was found to strongly correlate with Δr_c as well, where pairs with near zero had positive deviations in fracture toughness. Thus, the mechanical properties which contain more of a dynamic component appear to depend more on Δr_c, while E_a depended more on ΔF_c. Several series went against many of the trends for different reasons. Li-Ba and K-Mg are known to likely have intercalating ion channels or incomplete mixing (more like pockets rather than channels), respectively.[81,83] Li-Zn is likely unique due to the ability of Zn to behave more like a former at high ZnO content.[335] Finally, Li-Mg and Mg-Ca sometimes were different as well, likely due to Mg undergoing a change in coordination.

Other trends found included that the $\delta G/\delta K$ ratio determined the sign of the

deviation in μ, where a ratio over one meant a negative μ, while the opposite was found for a ratio of less than one. This was found to be true for all series except Li-Mg and Li-Zn. Additionally, K was found to correlate well with E_{a} and V_{f} in the mixed alkali series, however, in the mixed alkali alkaline-earth series, the type of bonding seemed to matter as well, where the more covalent series Li-Mg and Li-Zn had to be compared separately from the Li-Ba, K-Ba and K-Mg series (contain at least one more ionic cation).

The trends in G and Y were less clear, but may have something to do with the increase or decrease in connectivity and/or rigidity of bonding caused by the changes in modifier ion. Additionally, the Raman results showed non-additivity in [NBO]/[Si], where only K-Ba was observed to have lower-than-expected network connectivity, yet, K-Mg might as well (Raman was not collected), confirming that decreased connectivity degrades shear and Young's modulus. However, no explanation for why K-Ba and K-Mg are different can be found in Δr_{c} or ΔF_{c}. Even within mixed-alkali series, the best that can be said is the least modifier-like cation pair and least total modifier will have the highest improvement in G and Y. Since no reliable correlations between of G and Y with E_{a} could be found, the strain energy component of the DSM is not validated, instead packing fraction appears to be more deterministic of the E_{a}. Additionally, the idea where decreased conductivity will lead to less slippage along the ion channels and thereby increase resistance to shear has also been refuted. Thus, there appears to be something more complex at work for these two mechanical properties, such as the changes in bonding environments of the ion pair.

Overall, it appears that the Li-Zn series has the best mechanical properties, it series has positive deviations in all properties, including K_{Ic}. Yet, the 40Li-Rb series has the highest deviations in elastic mechanical properties, while Li-Ba is the best for mechanical properties involving plasticity. On the other hand, the K-Mg series

is the worst series in terms of mechanical properties; it has negative deviations in all elastic moduli. However, similar to the Li-Ba series, K-Mg does have fairly large improvements in H_{V} and K_{Ic}, which are often the more important properties for applications where scratch resistance is important such as cell-phone screens. Thus, having large Δr_{c} and ΔF_{c} may lead to incomplete mixing and poor V_{f} and elastic moduli as a result, but at the same time, it will lead to improved H_{V} and K_{Ic} as well. In fact, to only improve these two mechanical properties, the goal should be to have the largest Δr_{c}, and the smallest ΔF_{c}, to discourage ions sharing the same channels and resulting in a higher E_{a} and lower K_{Ic}, but yet still discourage plasticity under stress and increase H_{V}, like that which is seen in the Li-Ba series. It is very interesting that both mechanical properties which involve the most plasticity can be improved while having near to zero change in E_{a}. Alternatively, if the goal is to only improve bulk moduli or only H_{V}, than a mixed-alkali series with the largest ion difference is the best choice, but nevertheless, E_{a} and K_{Ic} will change accordingly. It is difficult to know how to improve G and Y; it is not clear why Li-K and Li-Mg offer the most improvement in these properties.

Chapter 7

Conclusions

First and foremost, the goal of this work was to explore the fundamental relationships between composition, molecular structure and mechanical properties of glass in order to broaden the high-stress applications in which the material can be used. The structural and compositional qualities of glasses with desirable mechanical properties were studied in order to understand their origins and in hopes of aiding the choice of the best composition for a given application. One method used was to investigate a type of glass already commonly used in high-strength applications, IE glass, in order to elucidate the molecular structure which gives it its superior mechanical properties. Moreover, evaluating how mechanical properties were affected as a function of the IE case depth was undertaken to further refine the relationship between compressive stress and the mechanical response. The other avenue explored was to fully characterize the MME by cataloguing several series with differing cation pairs, allowing for a comprehensive examination of the effect of Δr_c, ΔF_c, charge and electronegativity on the mechanical properties.

The micro-Raman study of the IE glass revealed several modifications of the network structure compared to the corresponding "as-melted" composition. Most importantly, the Q^2 and Q^3 SiO_4^{4-} tetrahedra were seen to collapse towards each other, along with the lengthening of Si-O bonds in the Q^4-units, which overall led to a reduction in the Si$\cdots$Si distance, which was then equated to network volume contraction

and compressive stress. The compressive stress was seen to depend on IE temperature, with IE temperatures well-below T_g which had significant IE to have the most strain, while IE temperatures near or at T_g experienced no contraction or even expansion of the network volume in comparison to the untreated composition. This latter result was attributed to thermal relaxation at the surface and the exchange of smaller lithium for larger potassium. Once the change in volume of the cations was accounted for, the LNDC was calculated from the compressive stress profiles, which matched those reported in literature. However, when the stresses were calculated using the LNDC, there was a mismatch between them and the compressive stress profiles found from the Raman data; by replacing the usual reference state composition (lithium silicate glass) with that corresponding to the invading ion (potassium silicate glass) different LNDCs were calculated which produced stress profiles much more similar in behaviour to those obtained experimentally. Thus, the difference between how the invading ion is found in the IE glass versus in the corresponding "as-melted" composition as well as the stiffness of the network are important to achieving an IE glass with the most compressive stress and therefore, enhanced mechanical properties.

The mechanical response of the IE layer as a function of IE temperature was explored using nano-indentation; the hardness results were found to match well to those from micro-indentation indicating the validity of the Y measurements of this thin IE layer. IE temperatures below T_g saw significant increases in stiffness and hardness in the first 30 μm of the layer, while IE temperatures near or above T_g saw decreases in mechanical properties throughout the material. Only low IE temperatures where significant IE occurred had improved mechanical properties further (> 30 μm) into the IE layer, likely due to the increased compressive stress found to occur at these IE temperatures. Overall, the compressive stress appeared to remove the degradation of the mechanical properties which occurs near a free edge. Nonetheless, the sample

with maximum improvement in Y and H did not match perfectly with those known to have the most compressive stress, indicating the presence of the MAE playing a role, especially in Y. However, once the mechanical properties were evaluated in terms of elastic recovery and resistance to plastic deformation, the changes in these mechanical responses agreed with the compression profiles. Both mechanical responses were improved by the IE process, yet the plastic response increased more than the elastic, likely giving rise to the high scratch resistance offered by IE glass. Although hardness is usually considered as more important for applications such as phone screens, stiffness proved to have several effects on the properties of the IE glass; stiffness increased the amount of compressive stress but also decreased the elastic recovery and resistance to plastic deformation as the surface.

The "pure" MAEE was shown to exist, although weaker than the "pure" MAE, in xMgO-(50$-x$)CaO-50SiO_2 for all properties studied: static, dynamic and mechanical, and the relationships between these properties were explored thoroughly. Mg^{2+} exhibited unusual behaviour, whereby it likely underwent a coordination change from tetrahedral to octahedral and became more modifier-like at high MgO content, leading to oxygen anions being stabilized by Mg^{2+} outside of the silica network. WDS, in combination with Raman spectroscopy, revealed the presence of this free oxygen outside of the silica network, which was later confirmed by long-term conductivity experiments. The free oxygen was associated with lowering E_a in the compositions with high MgO content, while also likely being responsible for the departure from Arrhenius behaviour observed in the conductivity plots. Furthermore, it degraded many of the mechanical properties, as network connectivity was exchanged for structural compactness at high MgO and created "lop-sided" deviations which were much lower on the high MgO concentration end of the series. If the compositions with high amounts of free oxygen were excluded, the MAEE in E_a was found to be inversely

correlated with V_f and the MME in V_f was strongly correlated with those in μ and K, as expected from literature. The trends in Y and G are more complicated, however, the MME was stronger when Mg^{2+} acted more like a glass former and was less easily distorted (as tetrahedral Mg), indicating the importance of connectivity to these two mechanical properties. Since both E_a and V_f have positive deviations, it is difficult to separate the static vs. dynamic contributions to the mechanical properties, especially hardness or fracture toughness. Overall, the MME in E_a does not match perfectly with those in the mechanical properties, indicating complex relationships between conductivity, V_f, network connectivity and bond strength.

A comprehensive study of the MME in static, dynamic and mechanical properties in multiple mixed-modifier series revealed several clear correlations. First, a distinction between the "pure" mixed-alkali, "pure" mixed-alkaline and mixed alkali-alkaline earth series was found, where the MAE is the strongest in E_a and only mixed-alkaline earth series saw negative deviations in V_f. Nonetheless, when only like series were compared, V_f and E_a correlated positively, indicating the amount of unoccupied space is important to conductivity in mixed-modifier glasses. Although not all series agreed with Dietzel's predictions,[83] Li-Ba which has near-zero ΔF_c was found to have near-zero deviations in V_f and E_a. The DSM model was found to predict E_a pretty well, as it too predicts ions with larger ΔF_c will have large E_a, but it failed to correlate with variation in strain energy expected from deviations in G and Y. Trends in K and μ were fairly strong, with K being related to V_f and type of bonding, while μ depended on the $\delta G/\delta K$ ratio. However, the MME in the mechanical properties associated with connectivity, G and Y, was difficult to understand. Finally, H_V and K_{Ic} were both correlated with Δr_c, indicating this to be a more important parameter to mechanical properties with a dynamic component. Thus, ΔF_c appears to predict V_f and E_a, pure static and dynamic properties, respectively, while Δr_c is a predictor of mechanical

properties containing both components.

A direct measurement of the changes in the structure when IE occurred allowed for calculation of contraction in volume and compressive stress; this was the first time a mechanism for the compressive stress was measured. With the knowledge of how the structure responds to the replacement of smaller ions with larger ones, it should be possible to better model the structural mechanisms which give IE glasses their enhanced mechanical properties. For much of the same reason, measuring the mechanical properties directly in the IE layer gives further insight into understanding and more accurate modelling of the IE process. Perhaps it will be possible to use these insights to make stronger, harder IE glass, but it is also important in simply understanding the aspects of the IE structure which confer it these properties. In the case of the many mixed-modifier series studied, several trends were observed which depended on Δr_c and ΔF_c, thus, making it easier to predict the properties of a composition and allow for maximum exploitation of ion pairs by simply choosing the correct two cations. Additionally, relationships between the MME of different properties were observed, allowing the MME in some properties to be assigned as having the same or different origins as each other. This data and review of the MME may help understand the structural origins of the MME further and lead to compositions of glass with structures with desired mechanical properties.

Previously, the mechanical behaviour at the surface of the glass was shown to have a disproportionately large effect on the mechanical response of the bulk. Thus, as shown in the overview of several ion pairs in Chapter 6, it is important to understand if different ion pairs used in the IE process confer different mechanical properties to the IE layer and/or bulk material. Thus far, only Δr_c has been considered for inducing the most compressive strain, yet, ΔF_c may have a role to play as well. Thus, making an ion exchange glass where the size difference is negligible, yet, ΔF_c is large, could

make for an interesting study on the effect of difference in charge of the cations in IE glasses. Conversely, two cations with a large Δr_c and small ΔF_c could be used as well; it is expected a large difference in size would lead to more compression. However, a difficulty with comparing any of these results would be the amount of exchange as it would likely change depending of the amount of difference between the two cations. Consequently, a metric similar to the LNDC, where the amount of change in molar volume per exchanged cation would have to be used. Furthermore, the mechanical responses of these other IE glasses could be measured and the trends compared to the ones found in Chapter 6.

Although the presence of the compressive stress in the IE glasses was measured by Raman spectroscopy and nano-indentation, the stress profiles were never verified in the typical optical fashion. Although ellipsometry was attempted by the author, it did not yield reliable results and the common methods, such as observing stress fringe lines using a modified refractometer or Brillouin scattering were unavailable.

The Mg-Ca series ended up having complex structure and properties; confirming the presence of free oxygen using ^{29}Si or ^{17}O NMR would be helpful in understanding the "lop-sided" MME in most of the properties. Additionally, performing long-term conductivity measurements not in air, where the source and sink of oxygen would be removed would also confirm the increased mobility of oxygen at high MgO content. Alternatively, isotopically enriched oxygen could be used to a similar effect. Finally, a detailed understanding of at which composition Mg undergoes a coordination transition from tetrahedral to octahedral would be most useful in explaining the bonding and connectivity of this series, and hopefully some of the trends in mechanical properties, specifically, G and Y. Unfortunately, ^{25}Mg NMR suffers from poor sensitivity and would require isotopic enrichment, high magnetic fields and spinning speeds;[336,337] even then the lineshapes are fairly featureless and even crystals with

known $^{[IV]}$Mg and $^{[VI]}$Mg sites only differed by 30 ppm, yet the FWHM of the glass peaks was on the order of 150 ppm.[338] Thus, it would be challenging if not impossible to achieve the spectral resolution needed to answer these questions in NMR and a different technique such as EXAFS or total neutron scattering would need to be undertaken to determine changes in coordination of Mg.

Although many different combination of cations were explored, when it came to analyzing trends in the properties, there remain still some gaps. For example, only one "pure" mixed alkaline-earth series was studied, so all conclusions were made about only that one system (although the pure MAE, particularly in conductivity has been extensively studied in the literature). Additionally, four of the five mixed alkali-alkaline earth systems have the larger cation also being the more mobile one, so it could be important to create more mixed alkali-alkaline earth glasses where the smaller ion is also the more mobile one, as was the case in the Li-Ba series. Additionally, often the size difference was small for many of mixed alkali-alkaline earth series, so the effect of Δr_c could be evaluated more thoroughly.

Experimentally, there was a problem with using WDS to confirm the composition when high amounts of K_2O or BaO were present, leading to some uncertainty in the reliability of the results. Thus, another route of chemical analyses could be used for these systems, such as ICP-OES or X-ray photoelectron spectroscopy. Additionally, Raman spectroscopy also suffered when high K_2O or Rb_2O was present due to the hygroscopicity. However, it still may be possible to cut or polish the water-logged layer away and expose a fresh surface for Raman or WDS to be successful; in the future, it would be wise to do measurements which depend on surface quality immediately after the glass has been synthesized.

An interesting exercise would be to test some of the trends tabulated in Section 6.5;

for example, if Δr_c in combination with a medium ΔF_c (as to avoid creation of separate ion-rich regions) would always return the strongest deviation in H_V, thus, Cs-Ca with a Δr_c of 0.73 and a ΔF_c of 0.23 should be expected to have deviation in H_V larger than Li-Ba. Additionally, Li-Cs should have a larger deviations in E_a, V_f, K, H_V and K_{Ic} than all series studied here. The elastic moduli are much more difficult to understand, particularly the trends in the MME G and Y are unresolved. More complete understanding of the molecular structures of these series, such as through EXAFS or ^{29}Si and ^{17}O NMR could help evaluate the connectivity and changes in cation environment as result of the addition of a second different ion. To be honest, the structural origins of the MME in these properties are difficult to understand and may benefit from modelling such as molecular dynamic simulations.

Finally, although many properties were explored, the MME manifests in many other properties not studied here, such as thermal expansion, T_g, viscosity, and index of refraction; thus, it would be interesting to see if the trends produced here extend to those properties as well. It is somewhat surprising that the MME lowers conductivity, viscosity and T_g, so perhaps completing a similar comprehensive overview of those properties as done here could shed some light on the shared mechanisms.

Appendix A

Structural Mechanisms of Compression in the Ion-Exchanged Layer in Lithium Silicate

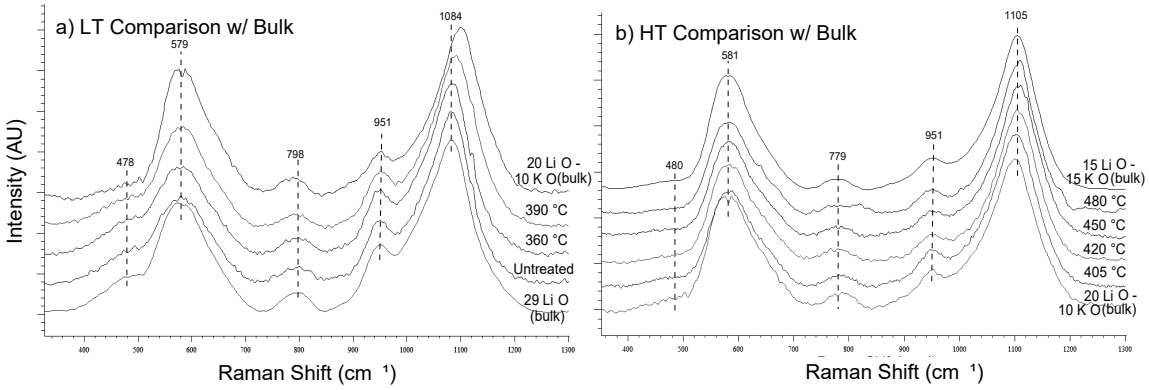

Figure A.1: (a)Micro-Raman spectra collected at the edge (highest K^+ conc.) of low-temperature IE specimens, untreated and 360 °C–390 °C, in comparison with similar spectra in the bulk xLi_2O–$(1\text{-}x)K_2O$–70SiO2 series, indicative of a mixed composition between $30Li_2O$–70SiO2 and $20Li_2O$–$10K_2O$–70SiO2 for the LT specimens. (b)Micro-Raman spectra collected at the edge (highest K^+ conc.) of high-temperature IE specimens, 405 °C–480 °C, in comparison with the similar spectra in the bulk xLi_2O–$(1\text{-}x)K_2O$–70SiO2 series, indicating a mixed composition between $20Li_2O$–$10K_2O$–70SiO2 and $15Li_2O$–$15K_2O$–70SiO2 for the HT specimens.

Table A.1: Raman shifts (ν) and peak areas (AU) for fitted peaks

Wavenumber (cm^{-1})				Peak Area Fraction			
$30Li_2O$	$20Li_2O$-$10K_2O$	$15Li_2O$-$15K_2O$	$30K_2O$	$30Li_2O$	$20Li_2O$-$10K_2O$	$15Li_2O$-$15K_2O$	$30K_2O$
480	468	470	297				
565	569	572	541				
611	615	621	586				
795	786	779	772				
945	949	949	954	0.17	0.13	0.14	0.09
1042	1060	1062	1063	0.34	0.39	0.34	0.17
1088	1100	1106	1102	0.24	0.18	0.19	0.61
1123	1132	1124	1137	0.24	0.29	0.34	0.14

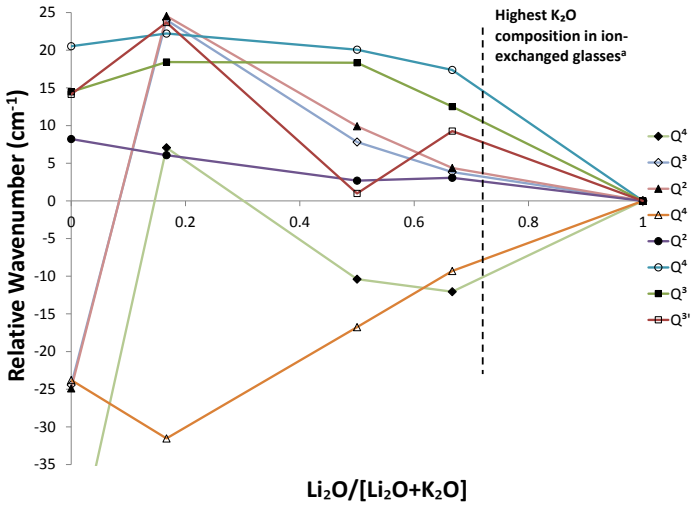

Figure A.2: Shifted Raman shift ($\Delta\nu$), where the major Raman peak positions of each mixed composition (ν_s) are compared to the corresponding Raman shift in the Li_2O-rich end member (ν_{30Li_2O}) according to $\nu_r = \nu_s - \nu_{30Li_2O}$, as a function of $[Li_2O]/[Li_2O+K_2O]$ ratio in the bulk series, xLi_2O-$(30-x)K_2O$-$70SiO_2$. The highest K_2O-containing composition in the IE glasses as determined by WDS is plotted on the bulk-series to show the expected Raman peak positions for an as-melted mixed sample of the same composition as the edge of the IE glasses, $20Li_2O$-$10K_2O$-$70SiO_2$.

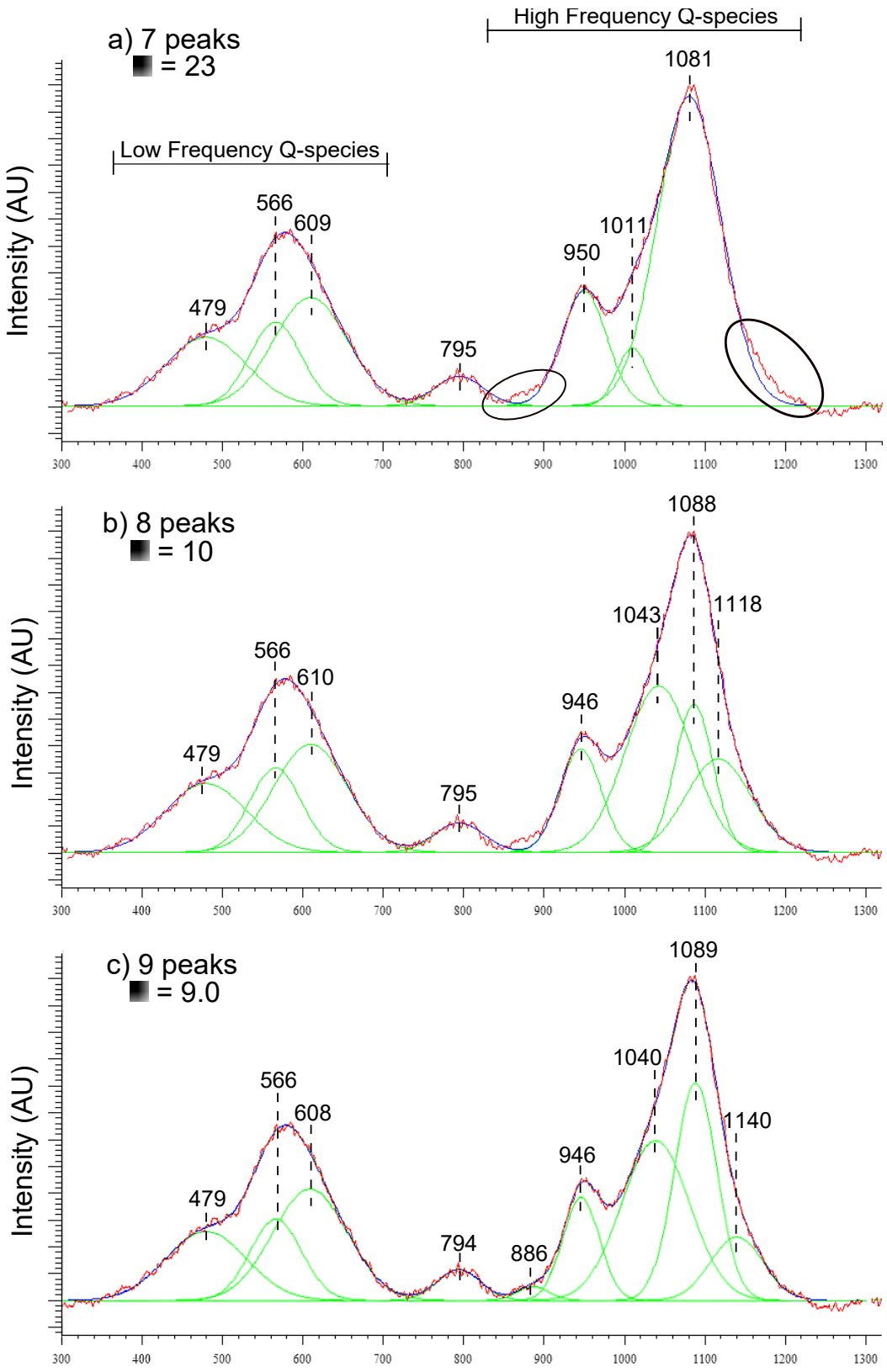

Figure A.3: Comparison of possible fits for the untreated, parent glass, $30Li_2O$-$70SiO_2$ using (a) 7 peaks, $\chi^2 = 23$ (b 8 peaks, $\chi^2 = 10$ and (c) 9 peaks, $\chi^2 = 9.0$. Lines are to guide eyes only.

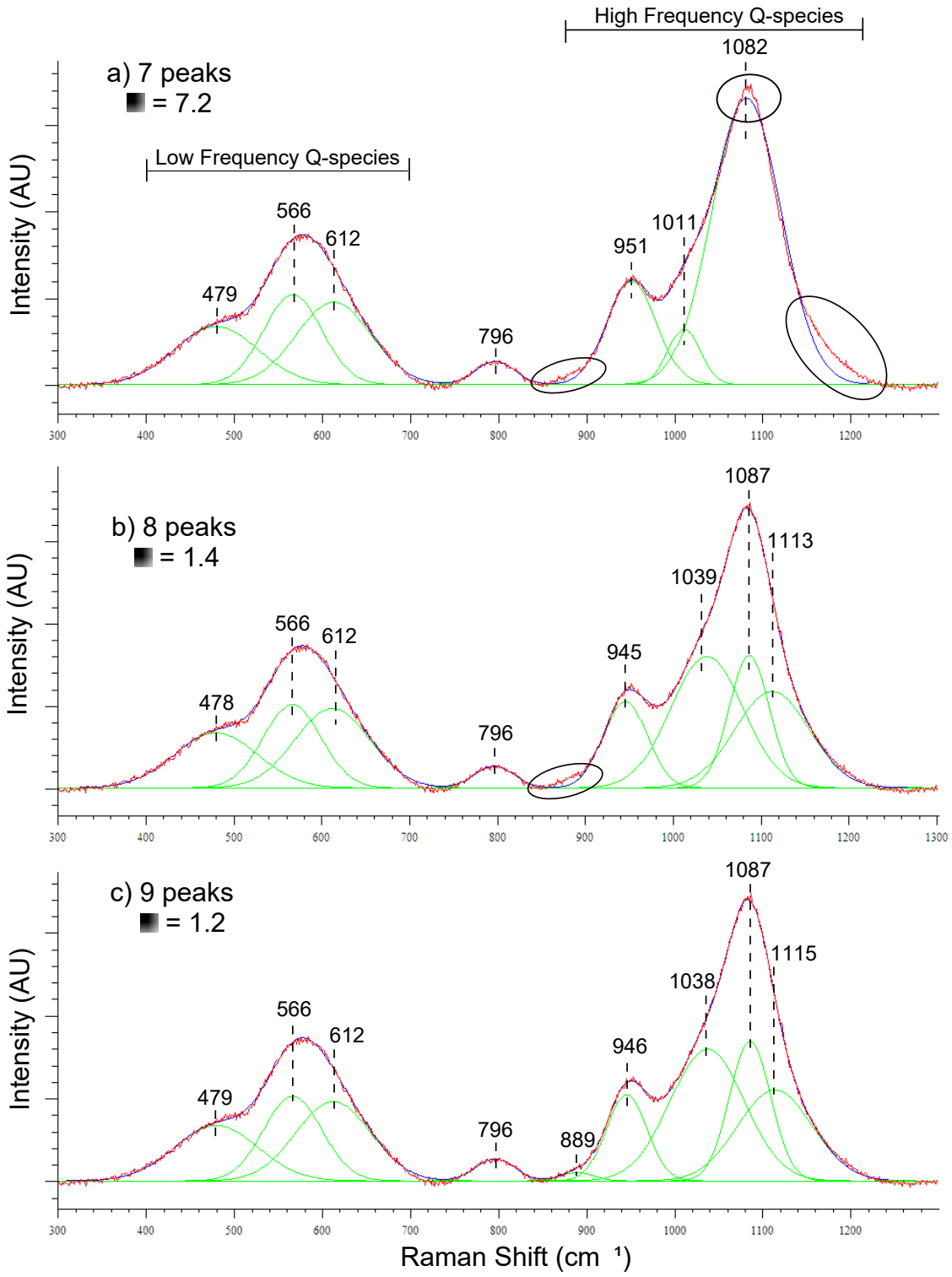

Figure A.4: Comparison of possible fits for sample ion-exchanged at 360 °C using (a) 7 peaks, $\chi^2 = 7.2$ (b) 8 peaks, $\chi^2 = 1.4$ and (c) 9 peaks, $\chi^2 = 1.2$. Lines are to guide eyes only.

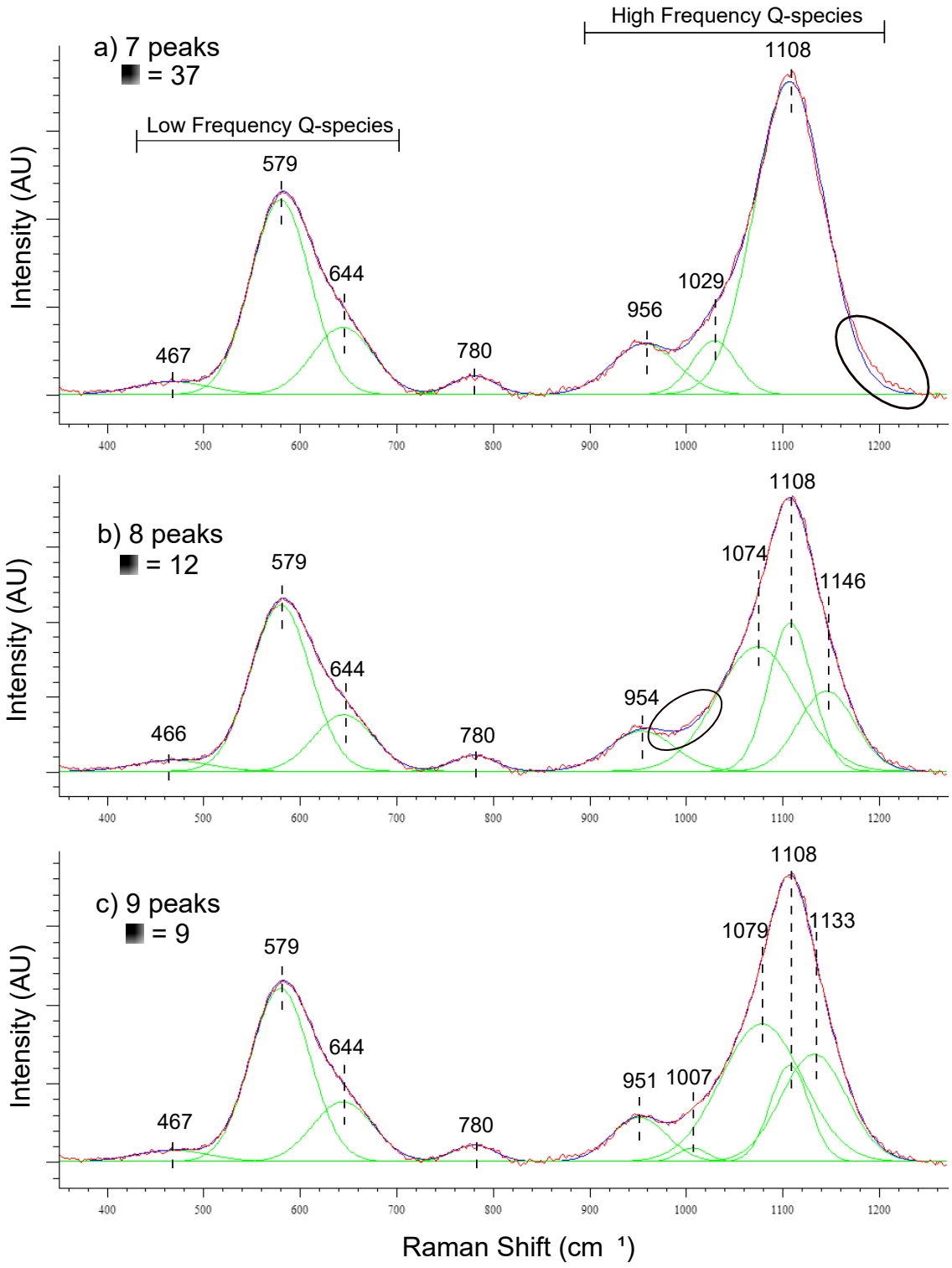

Figure A.5: Comparison of possible fits for sample ion-exchanged at 450 °C using (a) 7 peaks, $\chi^2 = 37$ (b 8 peaks, $\chi^2 = 12$ and (c) 9 peaks, $\chi^2 = 9$. Lines are to guide eyes only.

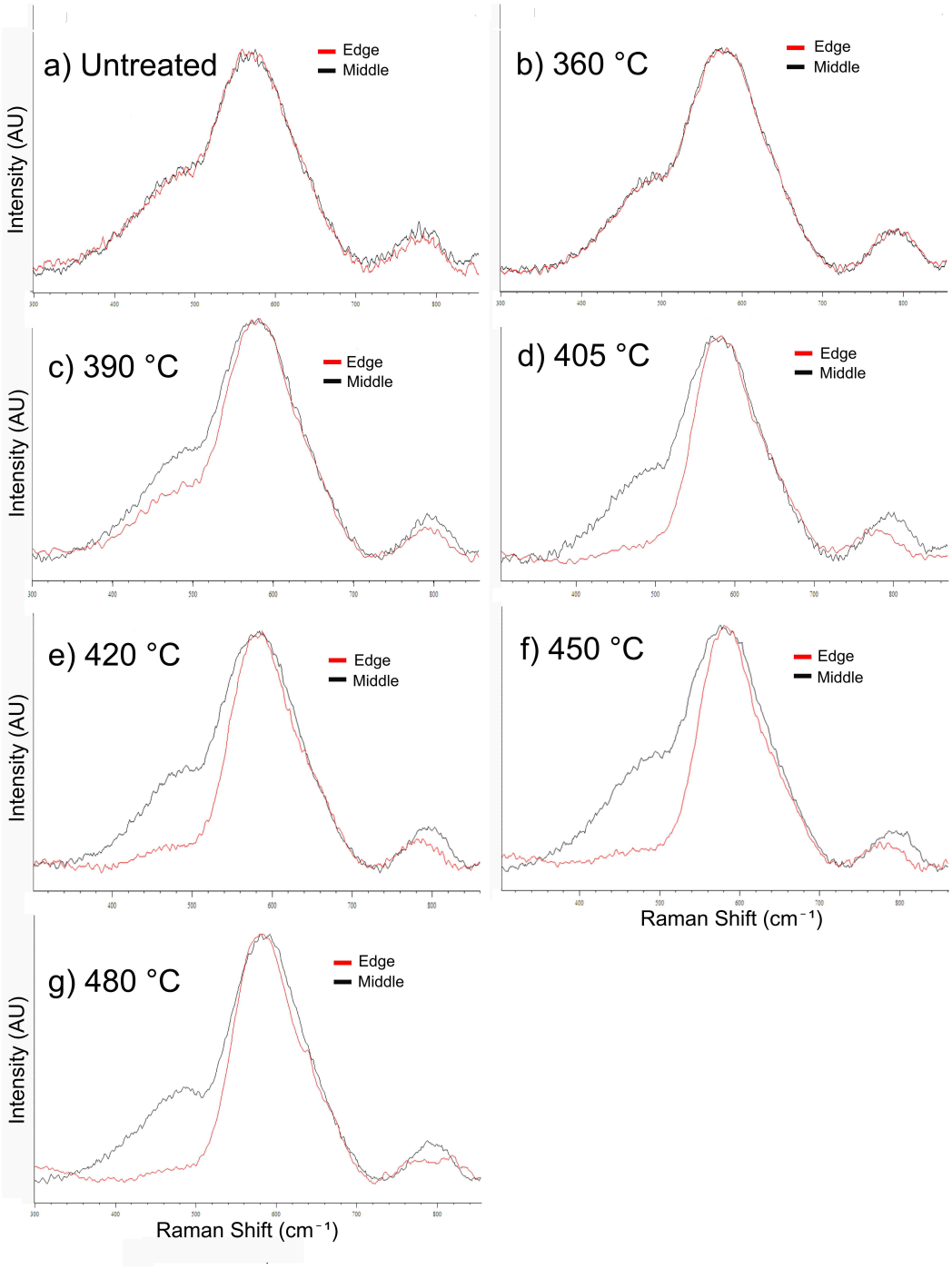

Figure A.6: Low-frequency region of the Raman spectra of each IE heat treatment collected near the edge (black) in comparison to the same LF-region collected far from the edge, or middle (red). Close-up demonstrates the separation of the LF $Q^2(\approx 570\ cm^{-1})$ and $Q^3(\approx 630\ cm^{-1})$ peaks with increasing-temperature IE conditions, in addition to the decrease of the $Q^4(\approx 470\ cm^{-1})$ peak observed at the edge (highest K^+ conc.) in the HT samples.

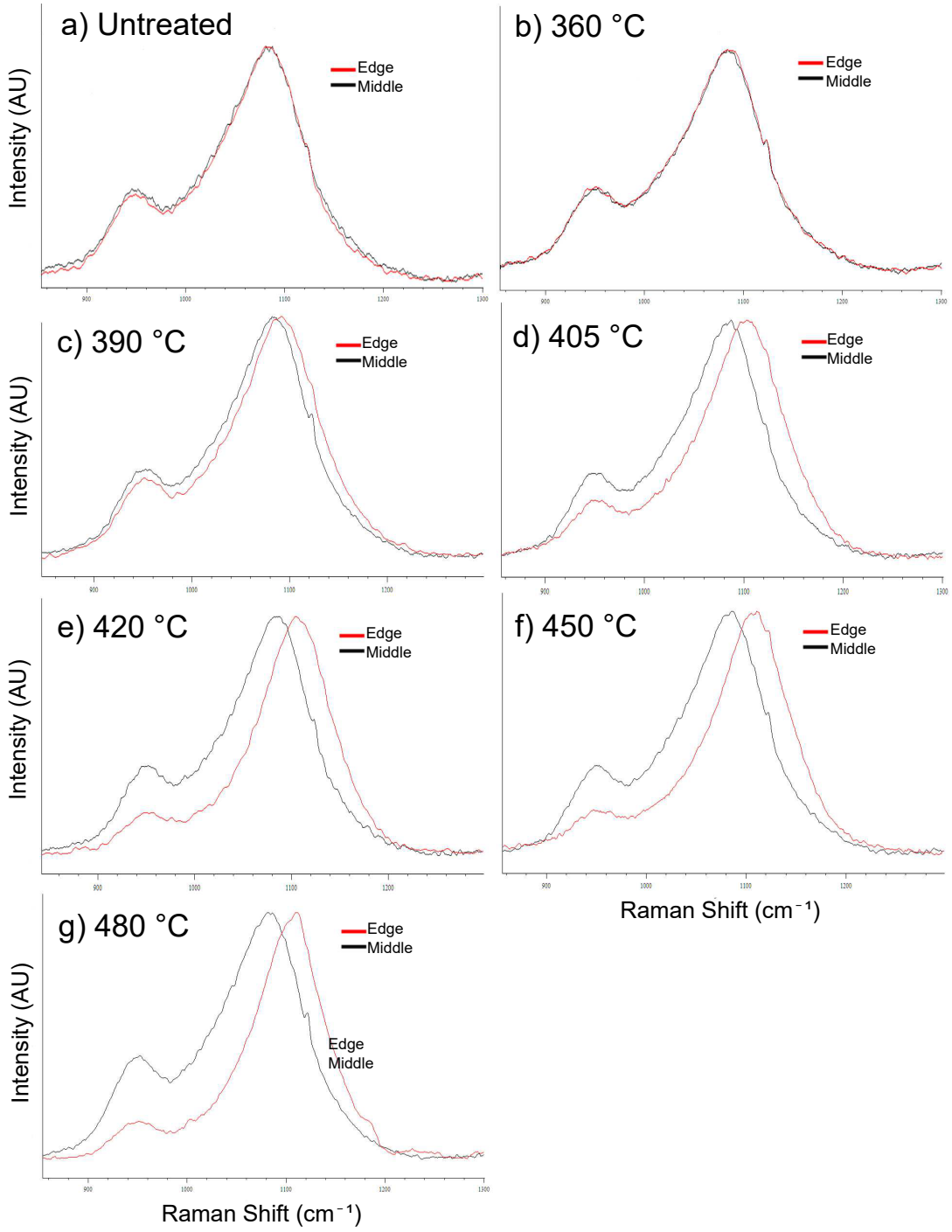

Figure A.7: High-frequency region of the Raman spectra of each IE heat treatment collected near the edge (black) in comparison to the same LF-region collected far from the edge, or middle (red). Close-up demonstrates the migration of the $Q^4(\approx 1040\ cm^{-1})$, $Q^3(\approx 1090\ cm^{-1})$ and $Q^{3'}(\approx 1115\ cm^{-1})$ peaks with increasing-temperature IE conditions, in contrast to the relative insensitive $Q^2(\approx 950\ cm^{-1})$ peak.

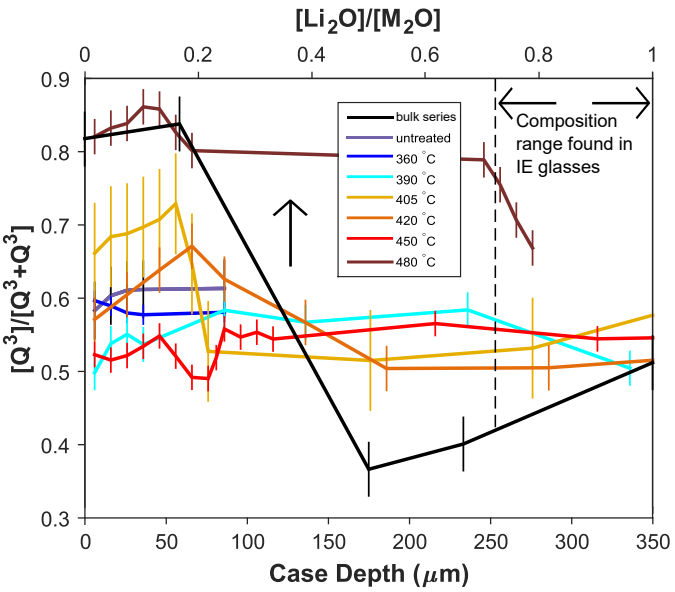

Figure A.8: Relative Q^3-fraction, $[Q^3]/[Q^3+Q^{3'}]$, for ion-exchanged glasses, untreated (purple) and 360–480 °C (dark blue–red) as a function of depth from IE surface (bottom axis) in comparison with $[Q^3]/[Q^3+Q^{3'}]$ in the bulk series (black) as a function of composition (top axis). The range of $[Li_2O]/[M_2O]$ found in the IE glasses from WDS is also marked for comparison.

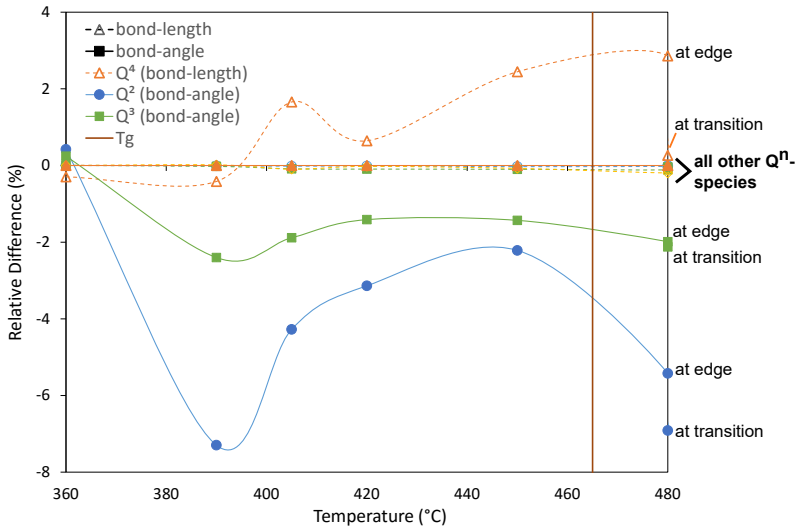

Figure A.9: The relative difference in bond lengths and angles compared to the untreated sample for each Q^n-unit, as a function of IE processing temperature. All of the data is *at the edge* of the sample, i.e., the first collection, except 480 °, where the transition from IE layer to pristine glass is shown in addition the the edge of the sample. Bond lengths have open symbols, bond angles closed symbols. T_g is shown as a straight line. Only the bond length of the Q^4-units and the bond angles of the Q^2 and Q^3-units were observed to change significantly; all other Q^n-units bond lengths and angles have relative differences near zero.

A.1 Elemental Analysis

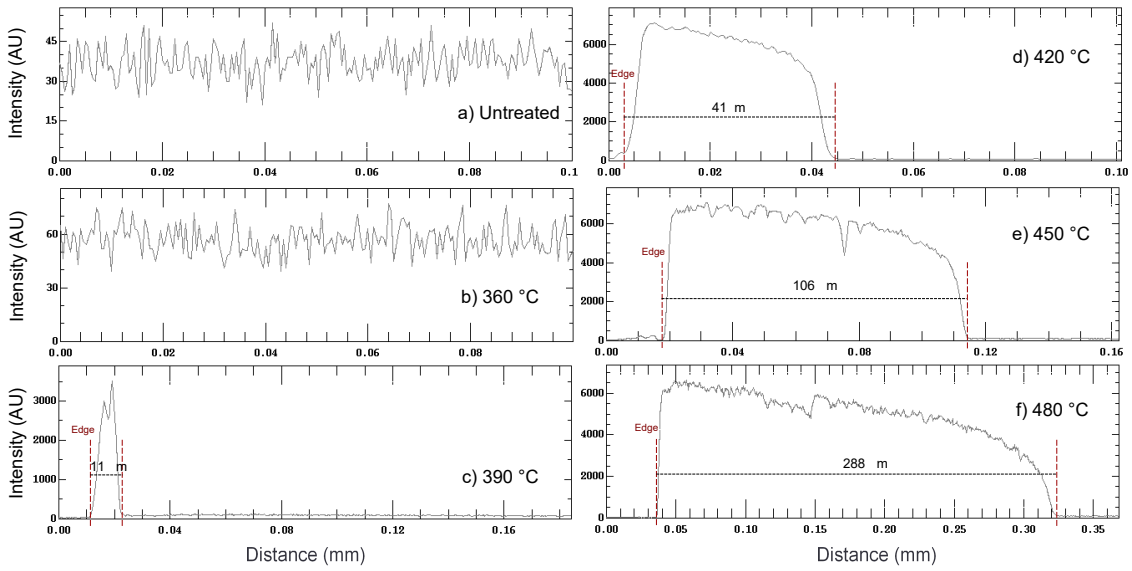

Figure A.10: Composition linescans from WDS instrument of all ion-exchanged samples at temperatures between 360-480 °C and the untreated, parent glass.

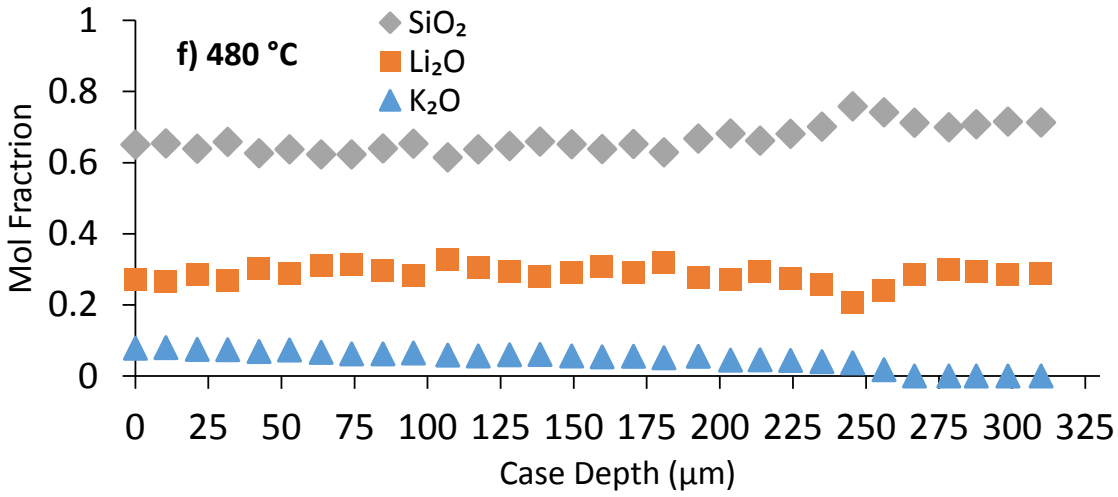

Figure A.11: Composition of IE glasses as a function of distance from the IE surface or edge of the 480 °C sample. Determined from Wavelength-Dispersive Spectroscopy (WDS). Error depends on the concentration and mass of the analyte, for elements with wt-% $\geq$2, error is 0.2–0.3 wt-% and mol-% <2, error is 0.05 wt-%. In this case, all error bars are smaller than the symbols. Diopside was used as the standard to accurately determine K, Si and O concentrations, which allowed the calculation of Li content from simple charge balance.

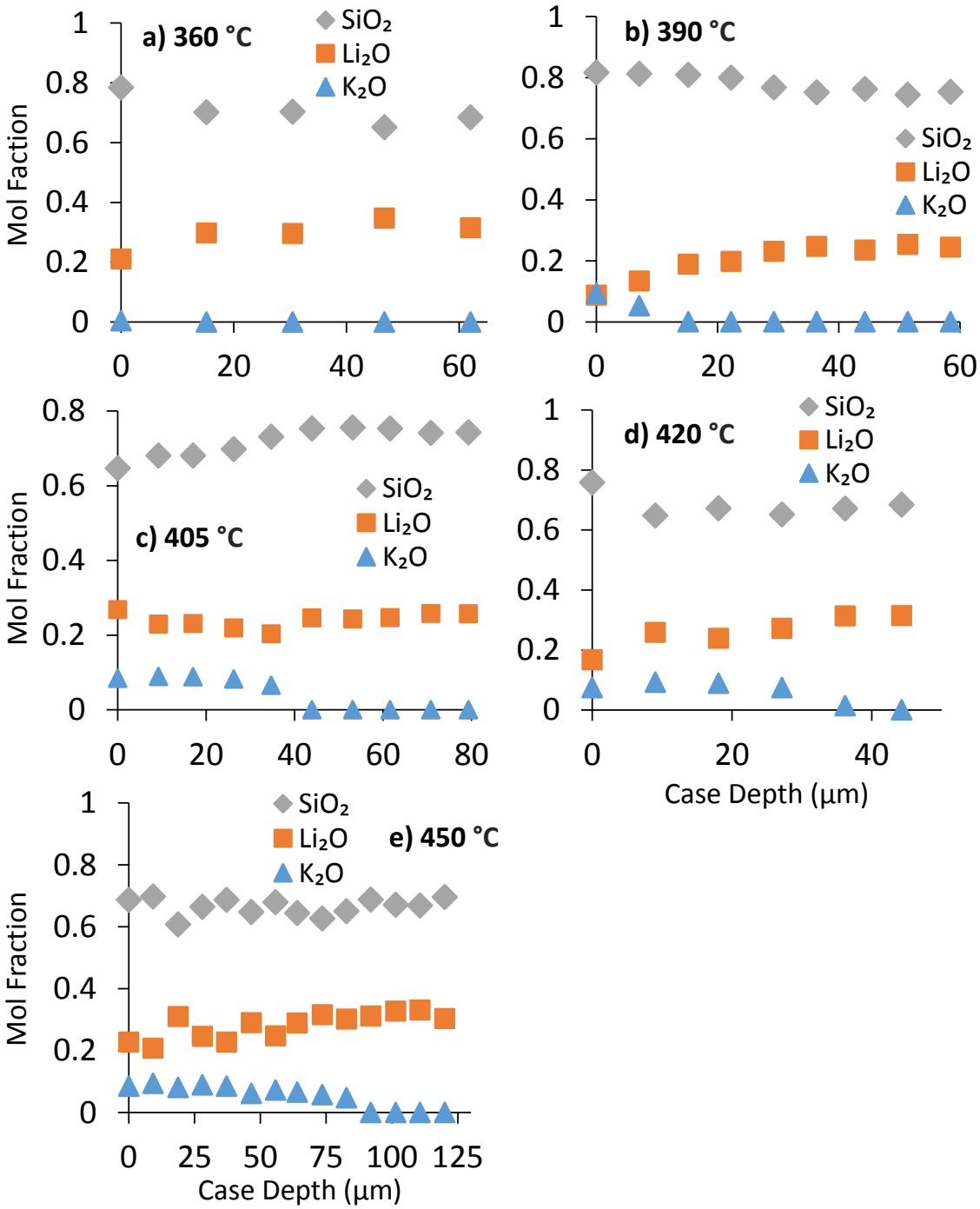

Figure A.12: Composition of IE glasses as a function of distance from the IE surface or edge. Determined from Wavelength-Dispersive Spectroscopy (WDS). Error depends on the concentration and mass of the analyte, for elements with wt-% $\geq$2, error is 0.2–0.3 wt-% and mol-% <2, error is 0.05 wt-%. In this case, all error bars are smaller than the symbols. Diopside was used as the standard to accurately determine K, Si and O concentrations, which allowed the calculation of Li content from simple charge balance.

A.2 Literature Raman Data of Crystals

Table A.2: Crystal structure parameters, namely Si-O-Si bond-angle, from publications

Crystal Structure	Reference	Si-O-Si [°]	⟨Si-O⟩ [Å]	Si-Si [Å]
α-quartz	Dusek (2001)[221]	142.006	1.6169	3.0577
	Glinneman (1992)[223]	144.167	1.60935	3.0626
	Gualtieri (2000)[222]	143.767	1.6093	3.0591
	Hazen (1989)[224]	143.642	1.6092	3.0576
	Ogata (1987)[225]	143.675	1.6081	3.056
	D'amour (1979)[220]	142.294	1.6155	3.0577
	Norby (1997)[217]	144.337	1.6055	3.0568
β-quartz	Wright (1981)[218]	153.404	1.58785	3.0905
	Tucker (2001)[245]	153.795	1.5862	3.0898
	kihara (1990)[246]	153.282	1.5881	3.0903
α-cristobalite	Downs (1994)[234]	146.496	1.603	3.0699
	Dollase (1965)[233]	146.771	1.6049	3.0758
β-cristobalite	Wyckoff (1925)[239]	146.616	1.6068	3.0782
	Peacor (1973)[240]	149.543	1.59935	3.0864
α-Tridymite	Baur (1977)[241]	150.034	1.59694	3.07903
	Hirose (2005)[242]	150.006	1.6001	3.08515
β-tridymite	Hirose (2005)[242]	159.792	1.57577	3.08837
	Graetsch (1996)[247]	157.06	1.57593	3.07075
Coesite	Araki (1969)[212]	151.074	1.61075	3.09144
	Levien (1981)[213]	150.833	1.60896	3.08652
Shistovite	Ross (1990)[339]	114.707	1.77058	2.9553
Li_2SiO_3	Seemann (1956)[204]	133.035	1.5981	2.9318
	Voellenkle (1981)[205]	124.664	1.67785	2.972
	Hesse (1977)[206]	124.116	1.6797	2.9678
Na_2SiO_3	Liu (1993)[202]	130.2 62	1.6728	3.0354
	McDonald (1967)[201]	133.715	1.67225	3.0754
$Li_2Si_2O_5$	Smith (1990)[210]	144.377	1.61905	3.06625
	Smith (1990)[211]	143.978	1.62555	3.06525
	de Jong (1998)[23]	145.465	1.6255	3.0753
$Na_2Si_2O_5$	Pant (1968)[208]	149.486	1.62463	3.12065
β-$Na_2Si_2O_5$	Pant (1968)[340]	136.239	1.63892	3.04163
$K_2Si_2O_5$	de Jong (1998)[23]	144.45	1.64517	3.12537

Table A.3: Crystal structure parameters, namely Si-O-Si bond-length, from publications

Crystal Structure	Reference	O-Si-O [°]	$\langle$Si-O$\rangle$ [Å]	O-O [Å]
α-quartz	Dusek (2001)[221]	109.487217	1.617	2.65072
	Glinneman (1992)[223]	109.472383	1.60935	2.62936
	Gualtieri (2000)[222]	109.472633	1.6094	2.62974
	Hazen (1989)[224]	109.472783	1.608	2.62773
	Ogata (1987)[225]	109.472783	1.60823	2.62615
	D'amour (1979)[220]	109.472917	1.60915	2.6277
	Norby (1997)[217]	109.4729	1.6056	2.62192
β-quartz	Wright (1981)[218]	109.478717	1.58785	2.59283
	Tucker (2001)[245]	109.476367	1.5862	2.59013
	kihara (1990)[246]	109.479583	1.5881	2.59327
α-cristobalite	Downs (1994)[234]	109.4693	1.603	2.61753
	Dollase (1965)[233]	109.469983	1.6049	2.62065
β-cristobalite	Wyckoff (1925)[239]	109.466983	1.6068	2.62363
	Peacor (1973[240])	109.4669	1.59935	2.61152
α-Tridymite	Baur (1977)[241]	109.470397	1.59697	2.60773
	Hirose (2005)[242]	109.469043	1.6001	2.61283
β-tridymite	Hirose (2005)[242]	109.470939	1.57577	2.57308
	Graetsch (1996)[247]	109.454667	1.57594	2.57306
Coesite	Araki (1969)[212]	109.468992	1.61275	2.6335
	Levien (1981)[213]	109.469167	1.61053	2.62989
Shistovite	Ross (1990)[339]	90	1.76585	2.4925
Li_2SiO_3	Seemann (1956)[204]	109.4636	1.6091	2.6274
	Voellenkle (1981)[205]	109.327233	1.63463	2.66472
	Hesse (1977)[206]	109.32625	1.6359	2.66668
Na_2SiO_3	Liu (1993)[202]	109.22775	1.63665	2.66537
	McDonald (1967)[201]	109.293967	1.63228	2.66005
$Li_2Si_2O_5$	Smith (1990)[210]	109.383683	1.61663	2.63712
	Smith (1990)[211]	109.402067	1.61975	2.64272
	de Jong (1998)[23]	109.419267	1.616	2.63682
$Na_2Si_2O_5$	Pant (1968)[208]	109.418467	1.61695	2.63848
β-$Na_2Si_2O_5$	Pant (1968)[340]	109.3754	1.62426	2.63812
$K_2Si_2O_5$	de Jong (1998)[23]	109.354656	1.62348	2.64667

Table A.4: Raman shifts for the low-frequency peaks assigned from publications to Si-O-Si stretch

Crystal Structure	Reference	ν_s (Si-O) [cm^{-1}]	Symmetry	Intensity
α-quartz	Bates (1972)[227] 25 °C	464	A1	vs
	Bates (1972)[227] 382 °C	462	A1	
	Gillet (1990)[216]	464	A1	vs
	Scott and Porto (1967)[226,232]	464	A1	
	Sharma (1981)[215]	465		vs
	Shapiro (1967)[228]	466	A1	
	McMillan (1992)[229]	464	A1	vs
	Hemley (1986)[230]	464	A1	
β-quartz (845K)	Bates (1972)[227]	464		
	Shapiro (1967)[228]	459	A1	
α-cristobalite	Palmer (1994)[236]	419.9	A1	s
	Bates (1972)[235,238]	416	A1	
	Swainson (2003)[237]	418		
β-cristobalite	Bates (1972)[235]	292	B1	
	Swainson (2003)[237]	279.5		vb
α-Tridymite	kihara (2005)[243]	433	A	
	kihara (2005) calculated[243]	432.3	A	
β-tridymite	kihara (2005)[243]	444	A	
	kihara (2005) calculated[243]	455.3	A	
coesite	Gillet (1990)[216]	521		vs
	Hemley (1986)[230]	521		vs
	Sharma (1981)[215]	521		
	Boyer (1985)[248]	520	A1	vs
	Boyer (1985)[248]	521	A1	vs
shistovite	Gillet (1990)[216]	589		
	Hemley (1986)[230]	589		
Li_2SiO_3	Richet (1996)[203]	610		
	Fuss (2006)[189,207]	612		
Na_2SiO_3	Richet (1996)[203,231]	589		
	Brawer (1975)[189,231]	587		
$Li_2Si_2O_5$	Fuss (2006)[207]	530		s
	Brawer (1975)[189]	553		
$Na_2Si_2O_5$	You (2001)[209,341]	517		
	Brawer (1975)[189]	525		
$K_2Si_2O_5$	Brawer (1975)[189]	505		vs

Table A.5: Raman shifts for the high-frequency peaks from publications assigned to Si-O stretch

Crystal Structure	Reference	ν_s (Si-O-Si) [cm^{-1}]	Symm.	Intens.
α-quartz	Bates (1972)[227] 25 °C	1072	E	
	Bates (1972)[227] 382 °C	1070	E	
	Gillet (1990)[216]	1085	A1	
	Scott and Porto (1967)[226,232]	1085	A1	
	Sharma (1981)[215]	1083	A2	w
	Shapiro (1967)[228]	1081	A1	
	McMillan (1992)[229]	1082		
	Hemley (1986)[230]	1085	A1	
β-quartz (845K)	Bates (1972)[227]	1065	E1	m
	Shapiro (1967)[228]	absent		
α-cristobalite	Palmer (1994)[236]	1069	A1	
	Bates 1972[235,238]	1079	A1	
	Swainson (2003)[237]	1083	B1	vb
β-cristobalite	Bates (1972)[235]	1077	A1	
	Swainson (2003)[237]	1076		
α-Tridymite	kihara (2005)[243]	1078	A	
	kihara (2005) calculated[243]	1080.6	A	
β-tridymite	kihara (2005)[243]	1074	A	
	kihara (2005) calculated[243]	1056	A	
coesite	Gillet (1990)[216]	1065		
	Hemley (1986)[230]	1065		w
	Sharma (1981)[215]	1065		w
	Boyer (1985)[248]	not reported		
	Boyer (1985)[248]	not reported		
shistovite	Gillet (1990)[216]	753	A1	
	Hemley (1986)[230]	753	A2	
Li_2SiO_3	Richet (1996)[203]	975		
	Fuss (2006)[189,207]	976		vs
Na_2SiO_3	Richet (1996)[203,231]	965	A1	
	Brawer (1975)[189,231]	973	A1	vs
$Li_2Si_2O_5$	Fuss (2006)[207]	1101		vs
	Brawer (1975)[189]	1110		
$Na_2Si_2O_5$	You (2001)[209,341]	1072		
	Brawer (1975)[189]	1060		
$K_2Si_2O_5$	Brawer (1975)[189]	1105		vs

Table A.6: Average LF Raman shift and ∠Si-O-Si used for shift/angle correlation.

Crystal Structure	average ν_s (Si-O-Si) [cm^{-1}]	$\langle\angle$Si-O-Si$\rangle$ [°]
α-quartz	464.1	143.4
β-quartz (845K)	461.5	153.4
α-cristobalite	418.0	146.6
β-cristobalite	285.8	148.1
α-tridymite	432.6	150.0
β-tridymite (413K)	449.7	158.4
shistovite	589	114.7
coesite	520.8	151.0
Li_2SiO_3	611	127.3
Na_2SiO_3	588	132.0
$Li_2Si_2O_5$	541.5	144.6
$Na_2Si_2O_5$	521	149.5
$K_2Si_2O_5$	505	144.5

Table A.7: Average HF Raman shift and $\langle$Si-O$\rangle$ used for shift/bond-length correlation.

Crystal Structure	average ν_s (Si-O) [cm^{-1}]	$\langle$Si-O$\rangle$ [Å]
α-quartz	1079.7	1.610
β-quartz (845K)	1065	1.587
α-cristobalite	1077	1.604
β-cristobalite	1076.5	1.603
α-tridymite	1079.3	1.599
β-tridymite (413K)	1065	1.576
shistovite	753	1.766
coesite	1065	1.611
Li_2SiO_3	975.5	1.627
Na_2SiO_3	969	1.634
$Li_2Si_2O_5$	1105.5	1.617
$Na_2Si_2O_5$	1066	1.617
$K_2Si_2O_5$	1105	1.623

Table A.8: Quantitative $\langle$Si-O$\rangle$ bond-length changes and relative difference compared to the untreated sample for each Q^n-unit based on shift/bond-length correlation. Each Raman peak is the value at the edge, i.e., the first collection, for each sample.

Q^n-unit	Sample	Shift [cm^{-1}]	$\langle$Si-O$\rangle$ [Å]	Diff. [Å]	Rel. Diff (%)
Q^2	Li_2O-SiO_2	946.2	1.632		
	IE 360 °C	945.5	1.632	0.0001	0.00
	IE 390 °C	947.8	1.632	-0.0001	-0.01
	IE 405 °C	949.7	1.632	-0.0003	-0.02
	IE 420 °C	948.9	1.632	-0.0002	-0.01
	IE 450 °C	951.8	1.632	-0.0005	-0.03
	IE 480 °C-edge	950.6	1.632	-0.0004	-0.02
	IE 480 °C-transition	946.8	1.632	0.0000	0.00
	K_2O-SiO_2	954.3	1.631	-0.0007	-0.04
Q^3	Li_2O-SiO_2	1088.4	1.620		
	IE 360 °C	1088.2	1.620	0.0000	0.00
	IE 390 °C	1092.7	1.620	-0.0004	-0.02
	IE 405 °C	1105.1	1.619	-0.0014	-0.09
	IE 420 °C	1106.3	1.619	-0.0015	-0.09
	IE 450 °C	1107.4	1.618	-0.0016	-0.10
	IE 480 °C-edge	1110.2	1.618	-0.0018	-0.11
	IE 480 °C-transition	1095.6	1.619	-0.0006	-0.04
	K_2O-SiO_2	1102.3	1.619	-0.0012	-0.07
$Q^{3'}$	Li_2O-SiO_2	1125.7	1.617		
	IE 360 °C	1125.4	1.617	0.0000	0.00
	IE 390 °C	1122.5	1.617	0.0003	0.02
	IE 405 °C	1144.1	1.615	-0.0016	-0.10
	IE 420 °C	1130.0	1.617	-0.0004	-0.02
	IE 450 °C	1139.9	1.616	-0.0012	-0.07
	IE 480 °C-edge	1163.0	1.614	-0.0032	-0.20
	IE 480 °C-transition	1149.7	1.615	-0.0020	-0.13
	K2O-SiO2	1137.2	1.616	-0.0010	-0.06
Q^4	Li_2O-SiO_2	1045.2	1.549		
	IE 360 °C	1042.4	1.545	-0.0046	-0.30
	IE 390 °C	1041.3	1.543	-0.0064	-0.42
	IE 405 °C	1060.7	1.575	0.0257	1.66
	IE 420 °C	1051.2	1.559	0.0100	0.64
	IE 450 °C	1068.1	1.587	0.00379	2.44
	IE 480 °C-edge	1072.0	1.593	0.0443	2.86
	IE 480 °C-transition	1047.7	1.553	0.0041	0.27
	K_2O-SiO_2	1062.9	1.579	0.0293	1.89

Table A.9: Quantitative Si-O-Si bond-angle changes and relative difference compared to the untreated sample for each Q^n-unit using the shift/angle correlation. Each Raman peak is the value at the edge, i.e., the first collection, for each sample.

Q^n-unit	Sample	Shift [cm^{-1}]	∠Si-O-Si [°]	Diff. °]	Rel. Diff (%)
Q^2	Li_2O-SiO_2	608.25	128.7		
	IE 360 °C	605.497	129.3	0.5432	0.42
	IE 390 °C	655.849	119.3	-9.3918	-7.30
	IE 405 °C	636.136	123.2	-5.5022	-4.27
	IE 420 °C	628.721	124.7	-4.0392	-3.14
	IE 450 °C	622.697	125.9	-2.8506	-2.21
	IE 480 °C-edge	643.625	121.7	-6.9799	-5.42
	IE 480 °C-transition	653.357	119.8	-8.9001	-6.91
	K_2O-SiO_2	586.157	133.1	4.3591	3.39
Q^3	Li_2O-SiO_2	563.98	137.5		
	IE 360 °C	562.29	137.8	0.3334	0.24
	IE 390 °C	580.71	134.2	-3.3015	-2.40
	IE 405 °C	577.11	134.9	-2.5902	-1.88
	IE 420 °C	573.82	135.5	-1.9410	-1.41
	IE 450 °C	573.95	135.5	-1.9673	-1.43
	IE 480 °C-edge	577.83	134.7	-2.7318	-1.99
	IE 480 °C-transition	578.77	134.5	-2.9187	-2.12
	K_2O-SiO_2	540.59	142.1	4.6146	3.36
Q^4	Li_2O-SiO_2	480.948	148.6		
	IE 360 °C	478.551	148.6	0.0000	0.00
	IE 390 °C	465.647	148.6	0.0000	0.00
	IE 405 °C	472.554	148.6	0.0000	0.00
	IE 420 °C	475.293	148.6	0.0000	0.00
	IE 450 °C	472.819	148.6	0.0000	0.00
	IE 480 °C-edge	469.708	148.6	0.0000	0.00
	IE 480 °C-transition	465.169	148.6	0.0000	0.00
	K_2O-SiO_2	461.756	148.6	0.0000	0.00

Appendix B

Mechanical Response of the Surface of Ion-Exchanged Lithium Silicate Glass

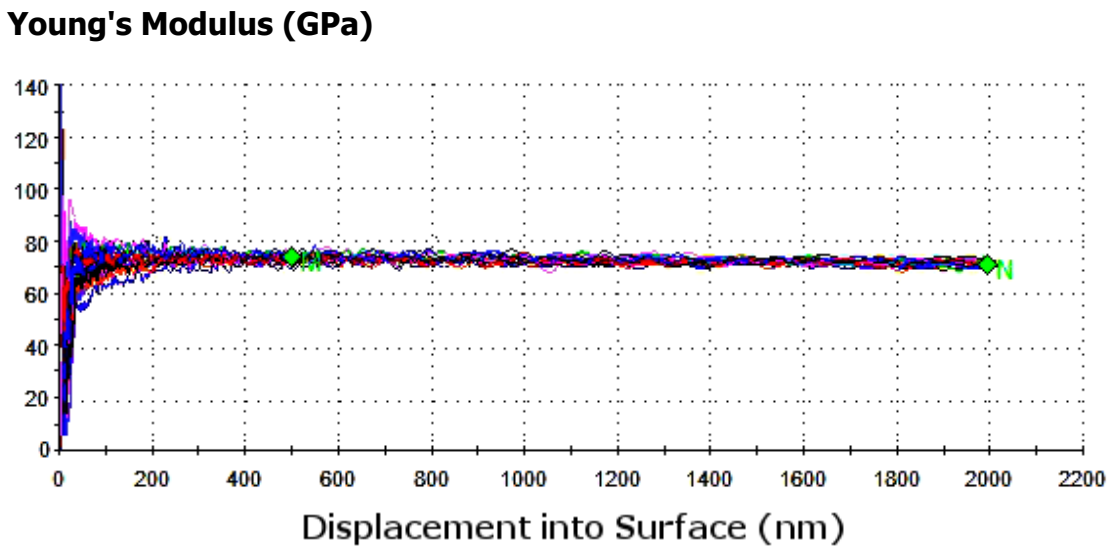

Figure B.1: Typical graph of Young's modulus (Y) vs. displacement into surface produced from nano-indentation. Approximately 20 indents done in the middle of the untreated sample demonstrate the reliability of the technique. Note the consistent value of Y after indenting approximately 200 nm into the surface.

======== ”””””””””””””””””””””””””’4

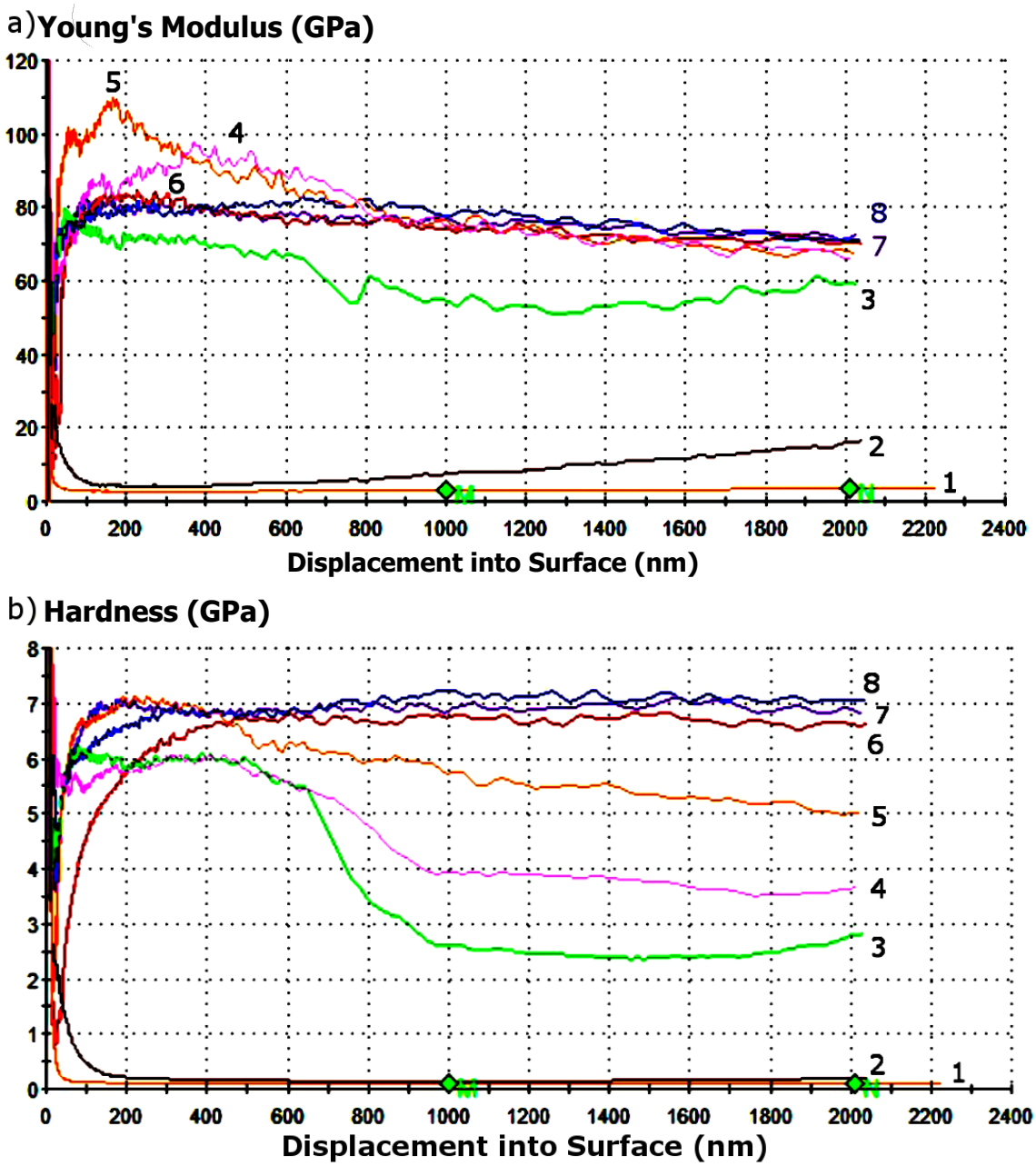

Figure B.2: Young's modulus (a) and hardness (b) vs. displacement into surface for the 420 °C IE sample. Near the bottom, indent 1, the stiffness and hardness of the epoxy can be seen to be $\leq$ 10 GPa and $\leq$ 0.25 GPa, respectively. Then there is a transition from epoxy to glass demonstrated by indents 2 (black) and 3 (green). Indent 2 is on the epoxy, yet near enough the glass that the indenter begins to measure the glass stiffness as the tip goes further into the epoxy. Indent 3 appears to be on the glass, at most 5 μm from the sample edge; likely the indenter tip measures glass at first until the material yields and a value somewhere between glass and epoxy is measured. Finally, indents 4–8 probe the case depth of the IE glass; both mechanical properties exhibit an ISE-like behaviour when the indent is near the edge of the sample (indents 4–6) however, at higher indents numbers (7 & 8) or further from the edge, *only* stiffness exhibits an ISE-like behaviour despite these last indents being within the IE layer (known from WDS results).

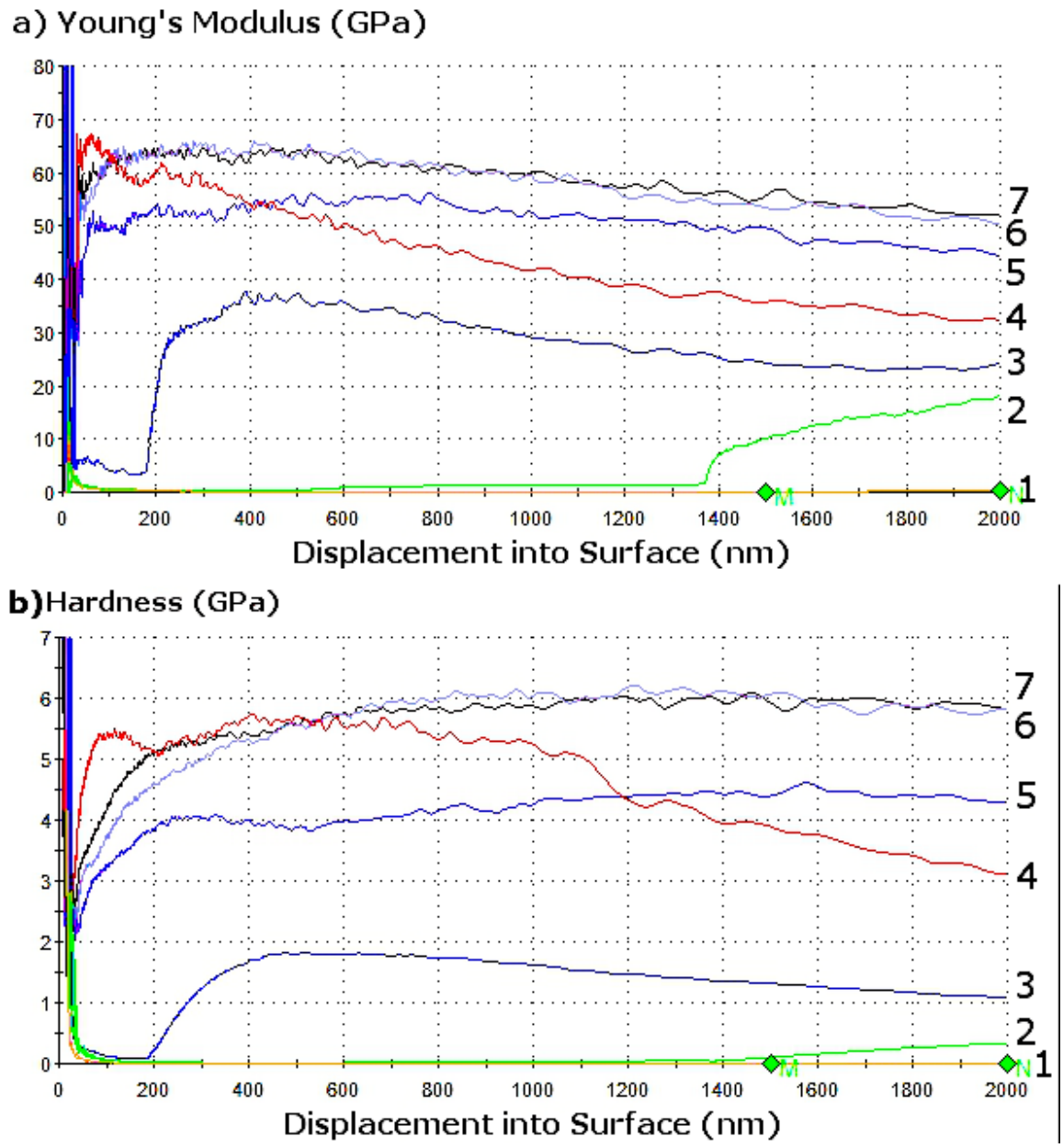

Figure B.3: Young's modulus (a) and hardness (b) vs. displacement into surface for the 450 °C IE sample. Near the bottom, indent 1, the stiffness and hardness of the epoxy can be seen to be $\leq$ 10 GPa and $\leq$ 0.25 GPa, respectively. Then there is a transition from epoxy to glass demonstrated by indents 2 (green) and 3 (dark blue). Indent 2 is on the epoxy, yet near enough the glass that the indenter begins to measure the glass stiffness as the tip goes further into the epoxy. Indent 3 appears to be on the glass, at most 5 μm from the edge; likely the indenter tip measures glass at first until the material yields and a stiffness somewhere between glass and epoxy is measured. Finally, indents 4–7 probe the case depth of the IE glass; only indent 4 shows an ISE-like behaviour for both mechanical properties, at higher indents numbers (5–7) or further from the edge, *only* stiffness exhibits an ISE-like behaviour despite these last indents being within the IE layer (known from WDS results).

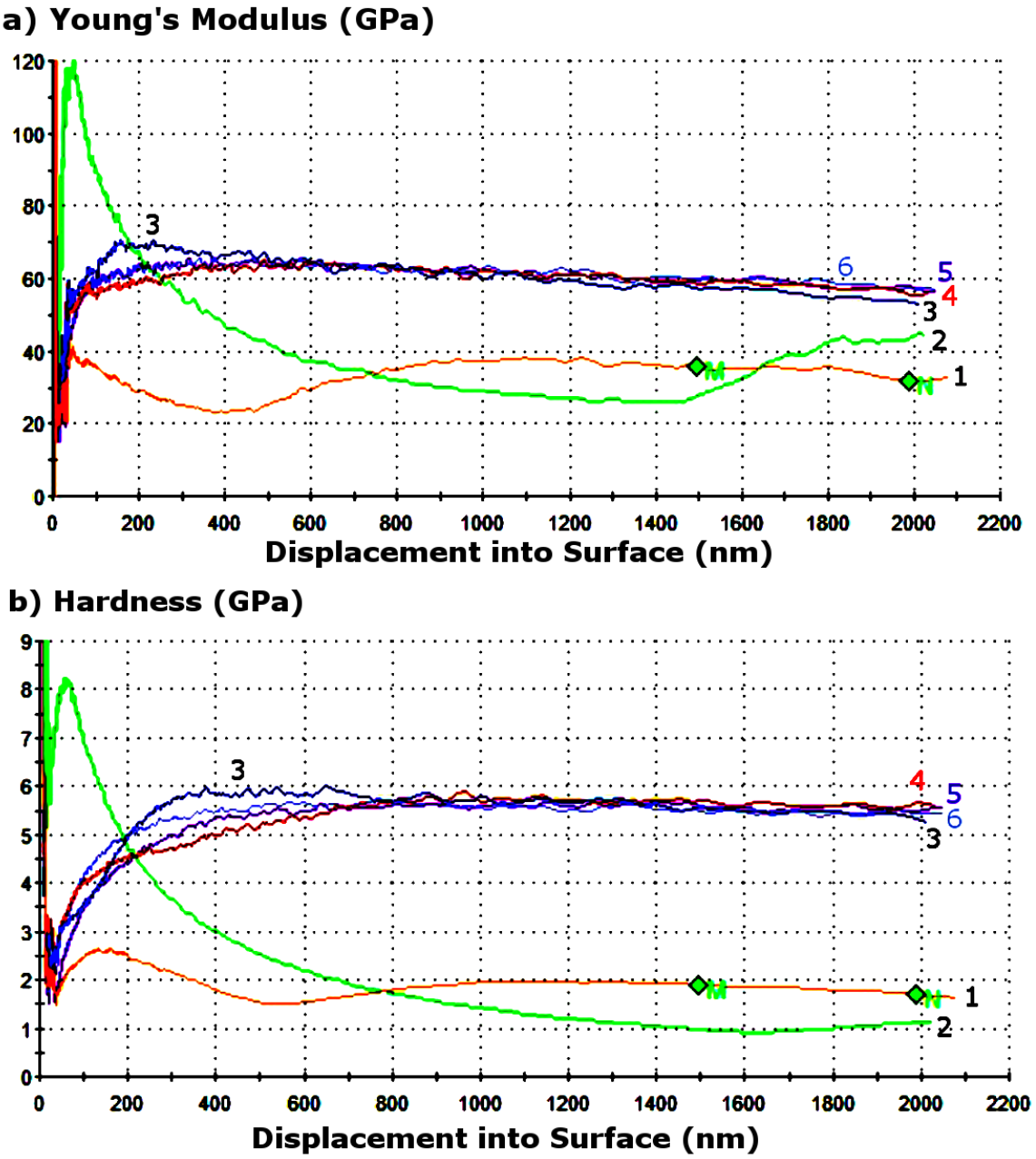

Figure B.4: Young's modulus (a) and hardness (b) vs. displacement into surface for the 480 °C IE sample. Indents 1 (beige) and 2 (green) demonstrate the transition from epoxy to glass. Indent 1 is on the epoxy, yet near enough the glass that the indenter begins to measure the glass stiffness as the tip goes further into the epoxy. Conversely, indent 2 is on the glass, at most 5 μm from the edge, which likely leads to the material yielding and a stiffness somewhere between glass and epoxy is measured. Additionally, based on the shape indent 2 is clearly on a large incline, $\geq 10°$, which can be expected to occur during polishing. Indents 3–6 are within the case depth of the IE glass (known from WDS results); only indent 3 shows an ISE-like behaviour for both mechanical properties, at higher indents numbers (4–6) or further from the edge, *only* stiffness exhibits an ISE-like behaviour.

Appendix C

Mixed Alkaline-Earth Effect in xMgO-$(50-x)$CaO-50SiO_2 System

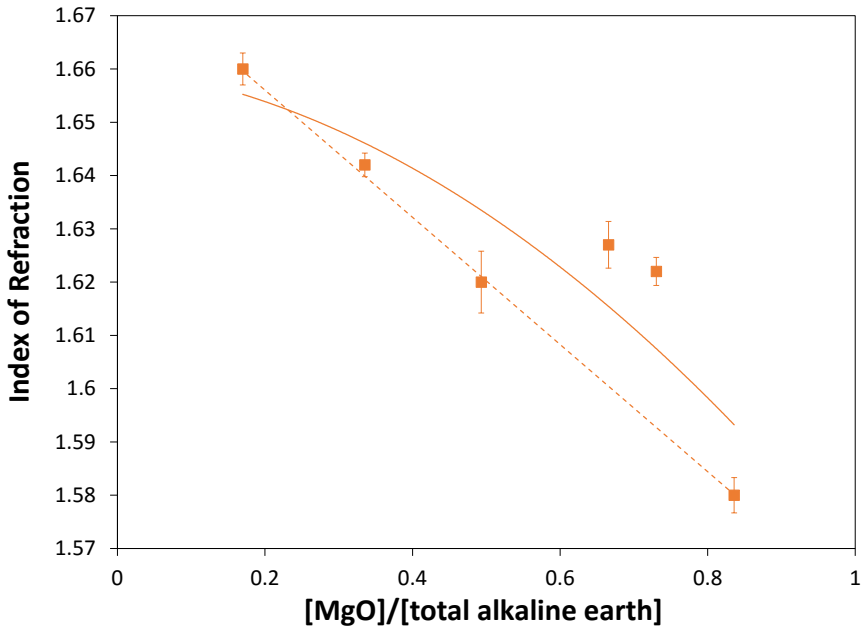

Figure C.1: Index of refraction of the xMgO-$(50-x)$CaO-50SiO_2 series as a function of relative alkaline-earth ratio. Some samples were not measured.

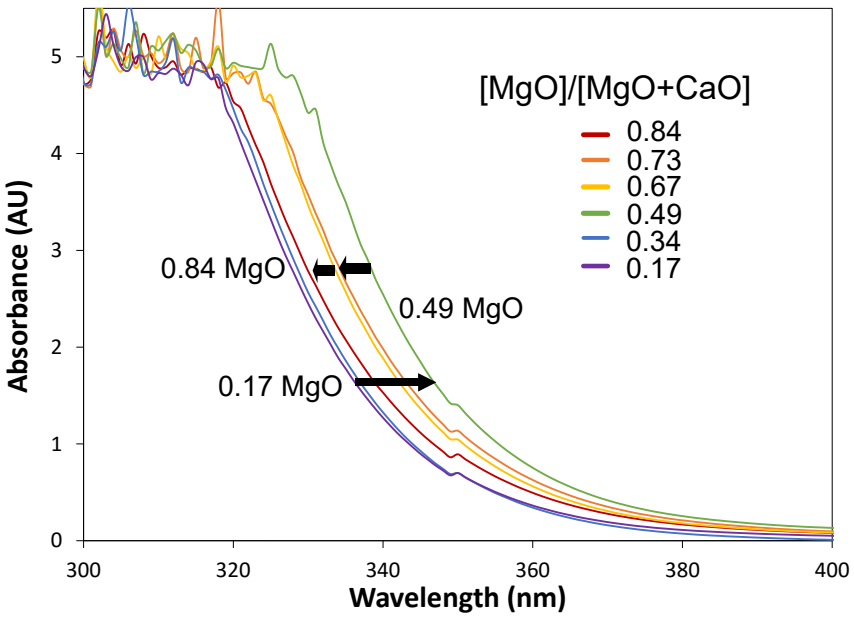

Figure C.2: Migration of the band-gap of the xMgO-$(50-x)$CaO-50SiO_2 series as a function of relative alkaline-earth ratio.

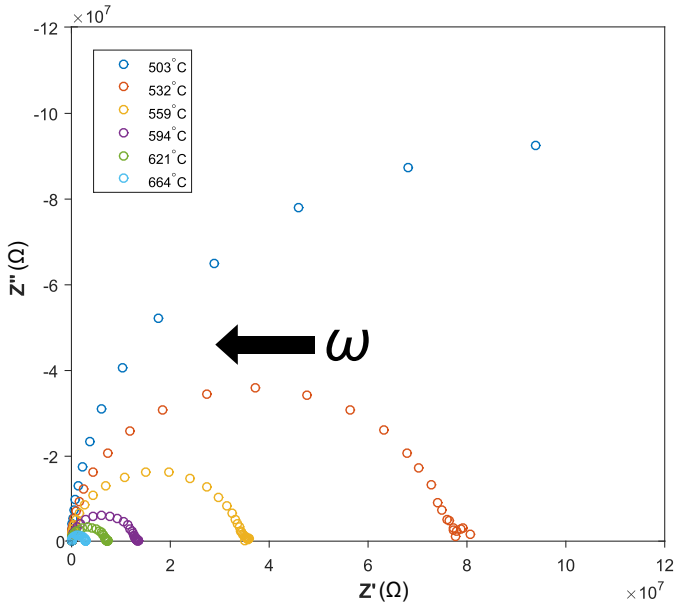

Figure C.3: Nyquist or Cole-Cole plots of the 0.49 MgO sample at several different temperatures of the xMgO-$(50-x)$CaO-50SiO_2 series.

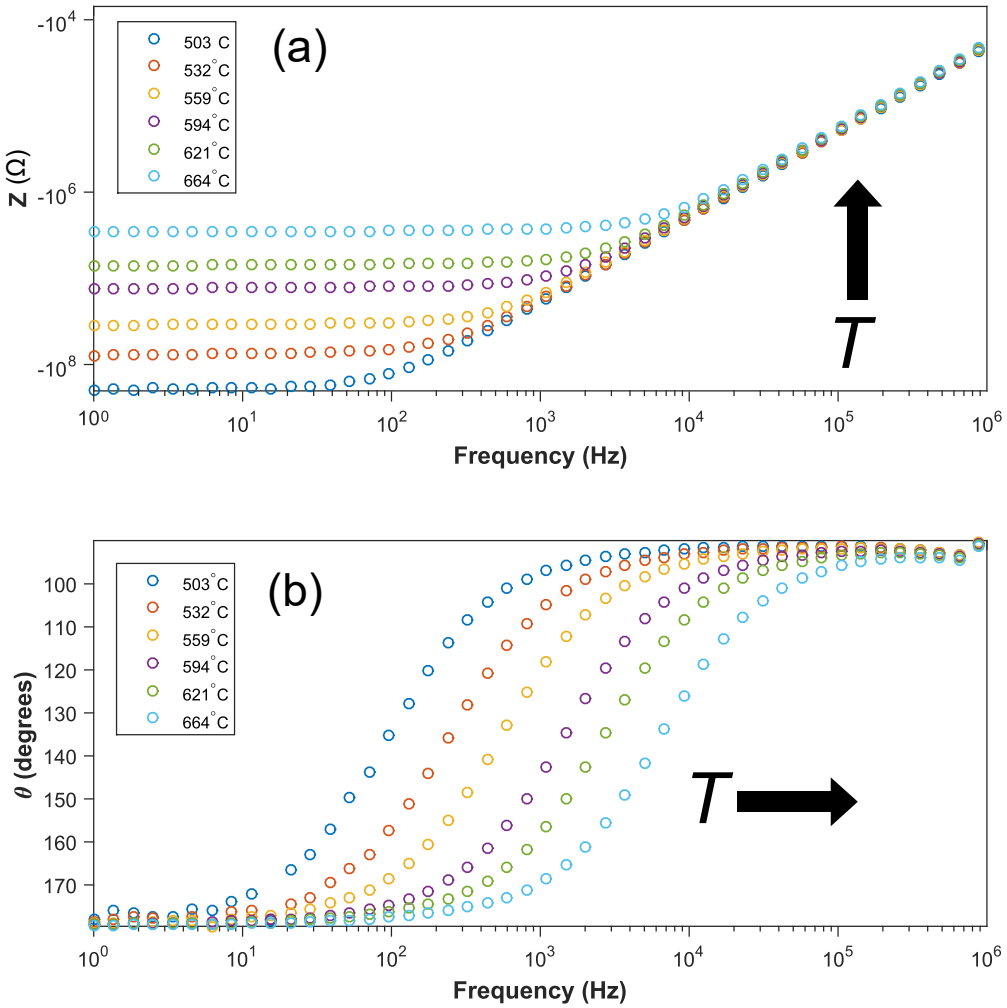

Figure C.4: Bode plots of the 0.49 MgO sample from the xMgO-(50$-x$)CaO-50SiO_2 series at several different temperatures.

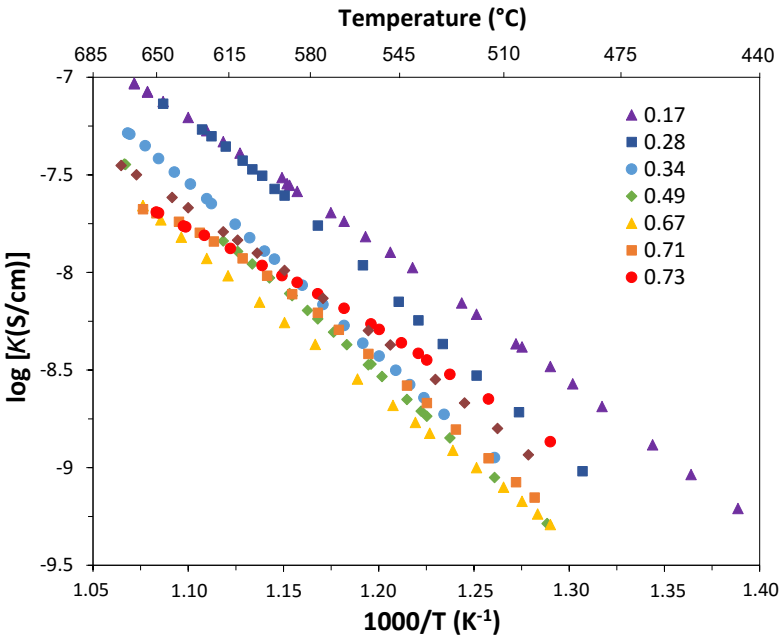

Figure C.5: Conductivity Arrhenius plots of logκ vs. 1000/T of the xMgO-(50−x)CaO-50SiO_2 series as a function of relative alkaline-earth ratio.

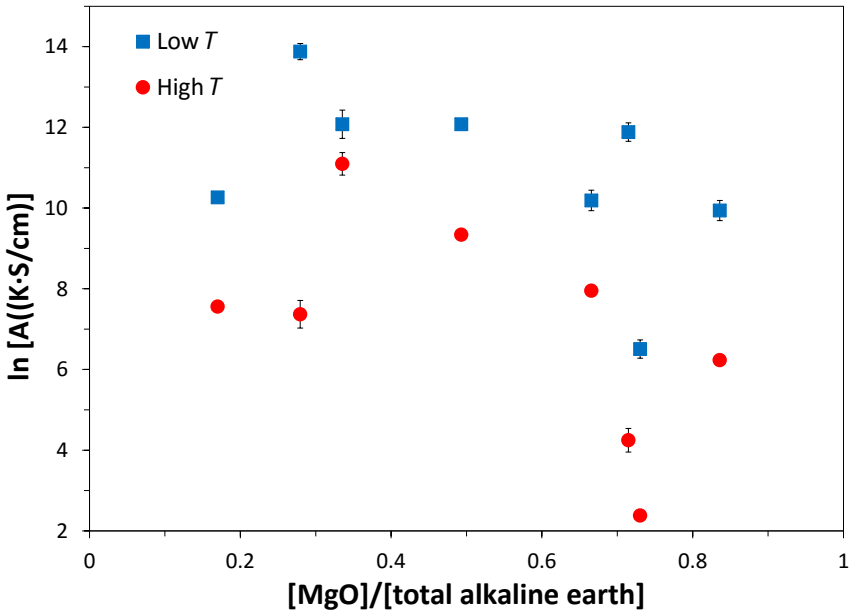

Figure C.6: Pre-exponential factor (A) of the xMgO-(50−x)CaO-50SiO_2 series as a function of relative alkaline-earth ratio. High and low temperature data is taken from the respective region in the Arrhenius plot (Fig. 5.9).

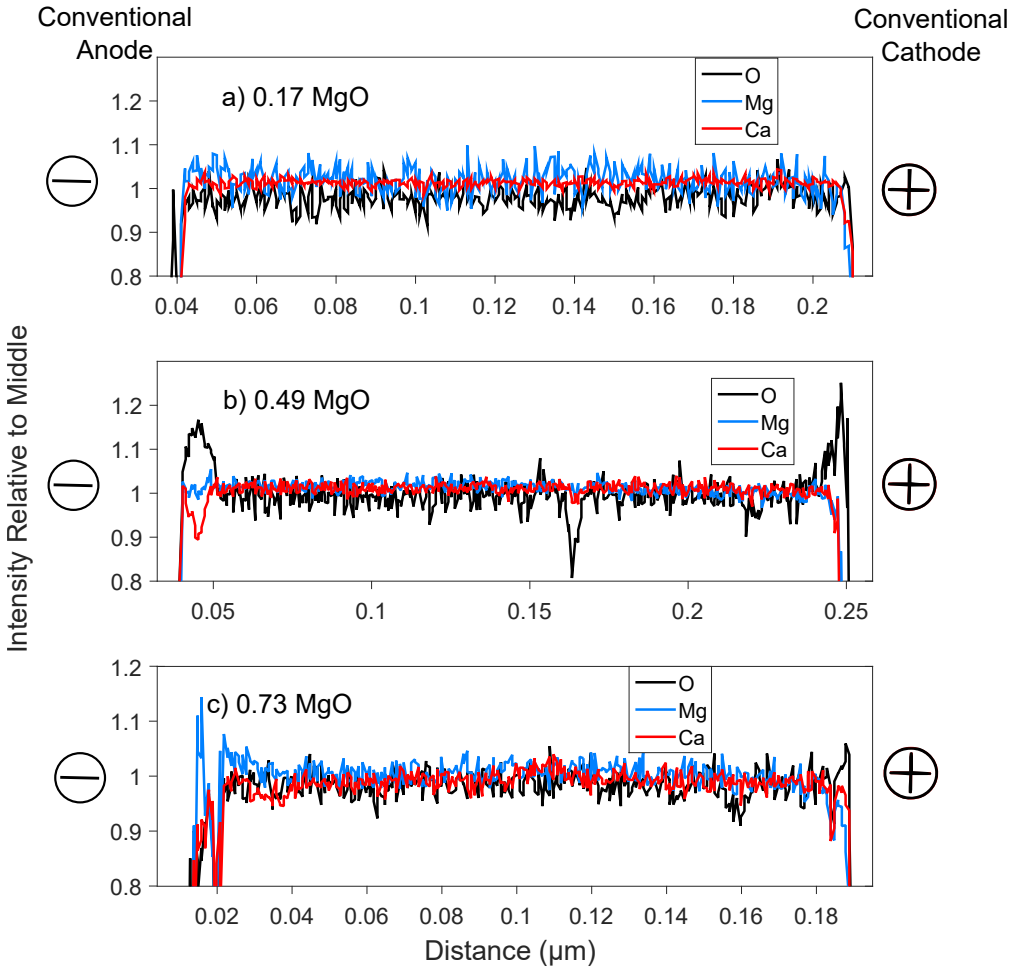

Figure C.7: Relative compositional profiles measured by WDS from low temperature (500 °C) long-term conductivity experiments. Intensity scale is relative to the middle of each corresponding element. Distance scale is small because only the sample edges were examined and "stitched" together, removing the less affected middle region. The error of the oxygen is ±0.03, while the other elements are ±0.02.

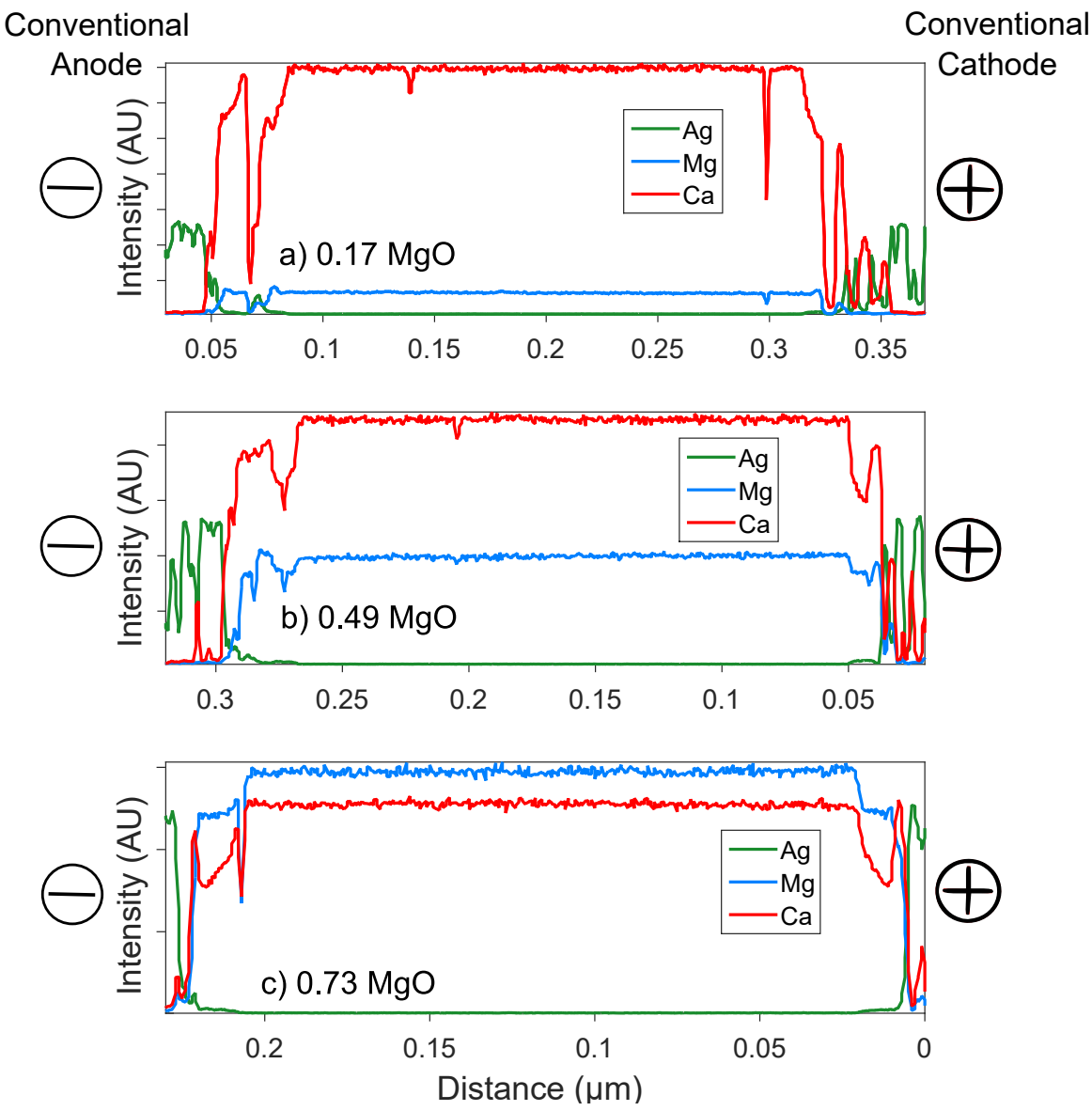

Figure C.8: Absolute intensity compositional profiles measured by WDS from high temperature (600 °C) long-term conductivity experiments, includes Ag from the electrode material. Distance scale is small because only the sample edges were examined and "stitched" together, removing the less affected middle region. The error of the oxygen is ±0.03, while the other elements are ±0.02.

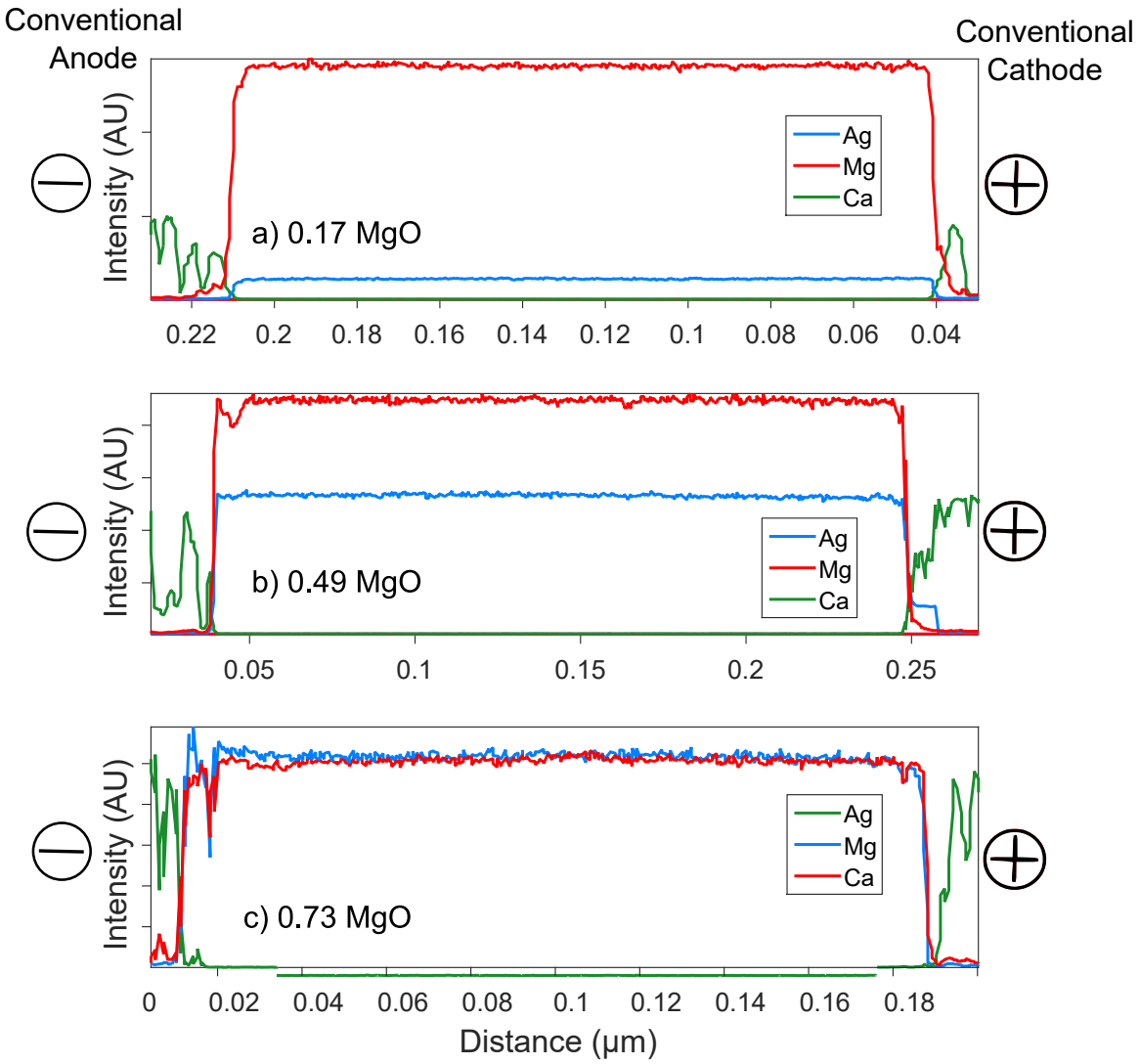

Figure C.9: Absolute intensity compositional profiles measured by WDS from low temperature (500 °C) long-term conductivity experiments, includes Ag from the electrode material. Distance scale is small because only the sample edges were examined and "stitched" together, removing the less affected middle region. The error of the oxygen is ±0.03, while the other elements are ±0.02.

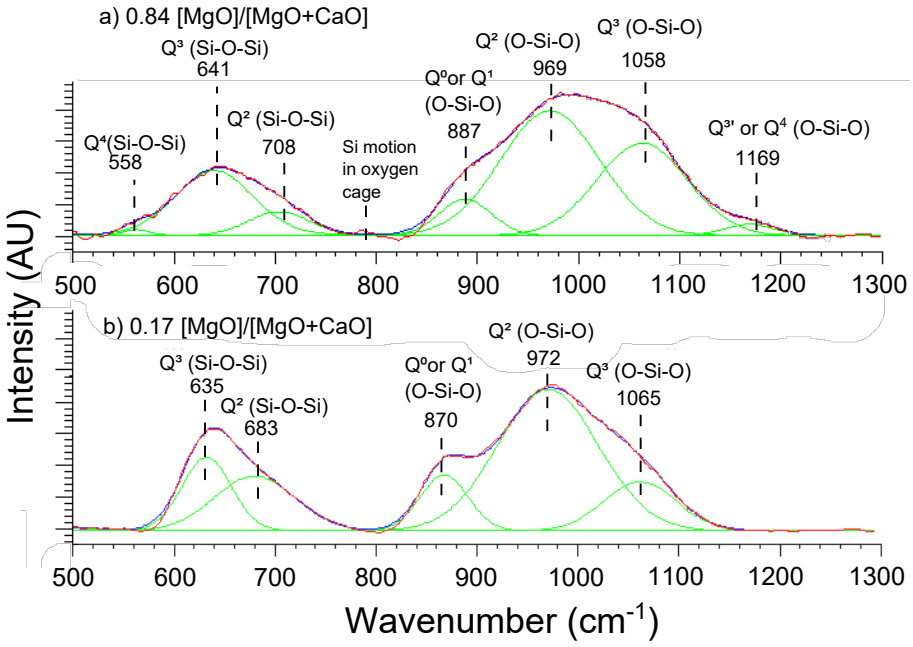

Figure C.10: Peak deconvolution for the two endmember compositions of the xMgO-$(50-x)$CaO-50SiO_2 series: (a) 0.84 relative alkaline-earth ratio and (b) 0.17 relative alkaline-earth ratio. Lines are only guides for the eyes.

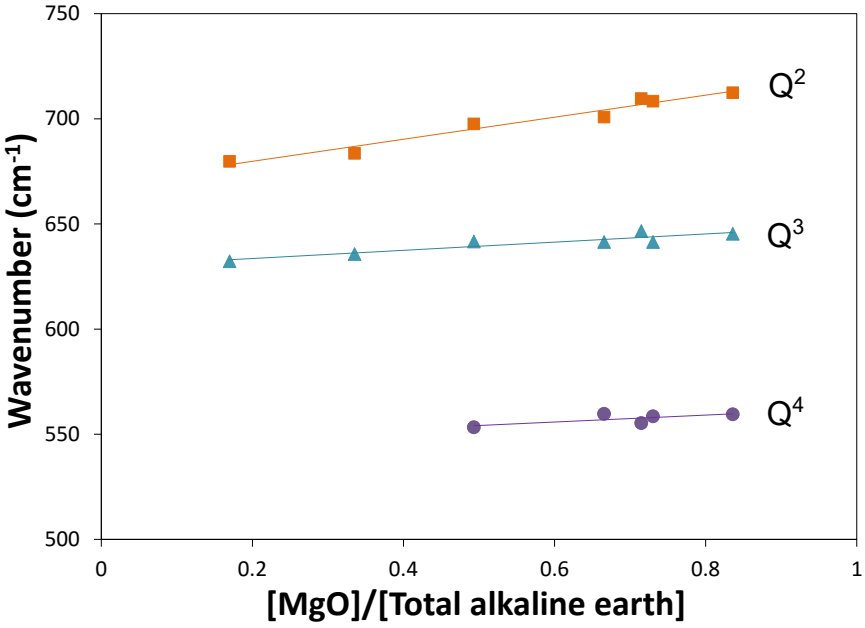

Figure C.11: Raman shifts of the xMgO-$(50-x)$CaO-50SiO_2 series an a function of relative alkaline-earth ratio for the low-frequency peaks which correspond to Si-O-Si bond angles.

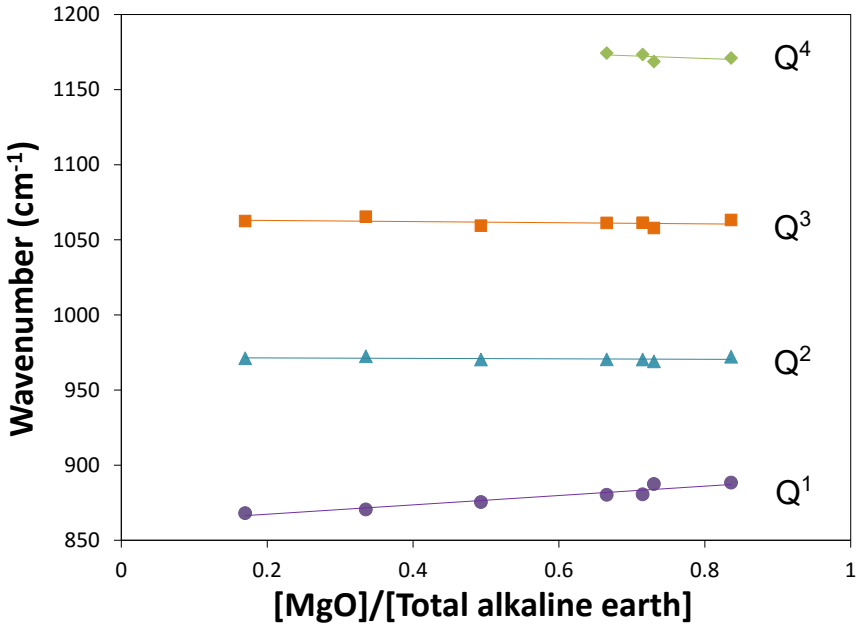

Figure C.12: Raman shifts of the xMgO-$(50-x)$CaO-50SiO_2 series an a function of relative alkaline-earth ratio for the high-frequency peaks which correspond to Si-O bond lengths.

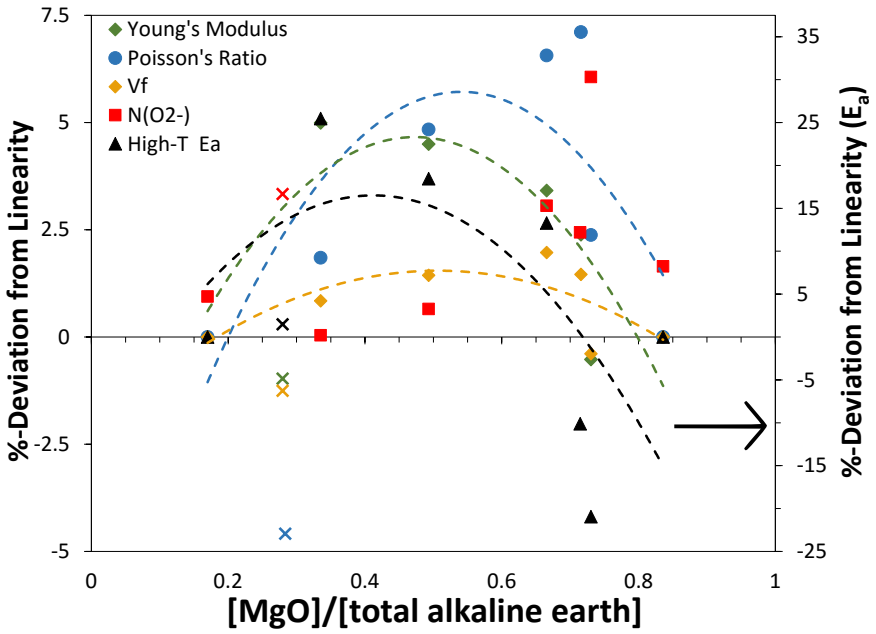

Figure C.13: The MME in of the xMgO-(50$-x$)CaO-50SiO$_2$ series as a function of relative alkaline-earth ratio. Mechanical properties (Young's modulus, Y, and Poisson's ratio, μ) and static properties (packing fraction, V_f, and free oxygen, $N(\mathrm{O}^{2-})$) are on left axis, while dynamic properties (high-T E_a) are on the right side. The dashed lines are fits to the apparent trends with 2nd-order polynomials.

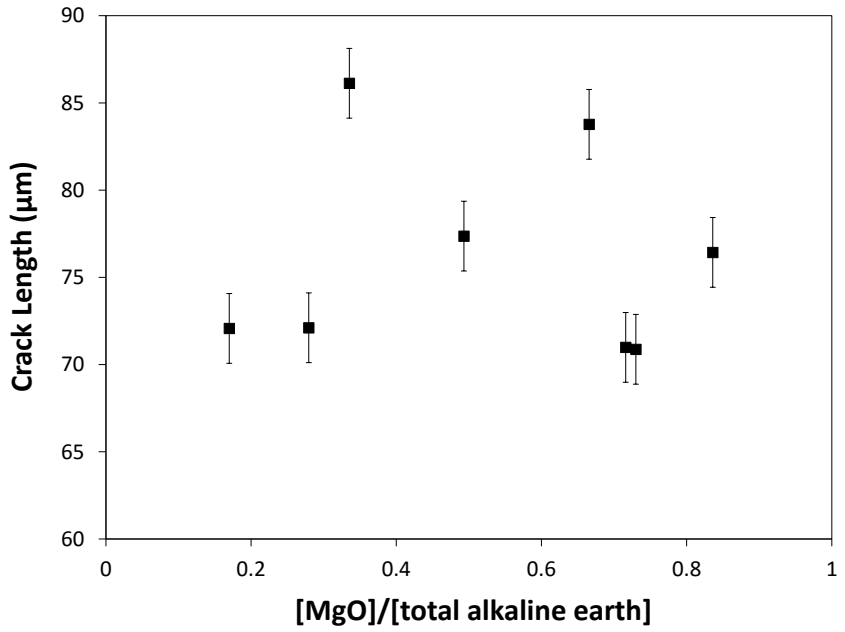

Figure C.14: Cracks lengths of the xMgO-(50$-x$)CaO-50SiO$_2$ series measured during Vickers indentation, used to calculate K_Ic

Appendix D

Evaluation of Mixed-Modifier Effect in Multiple Glass Series

D.1 $x\mathbf{Li_2O}$-$(\mathbf{30}-x)\mathbf{K_2O}$-$\mathbf{70SiO_2}$

Table D.1: Glass compositions of the $x\mathrm{Li_2O}$-$(30-x)\mathrm{K_2O}$-$70\mathrm{SiO_2}$ series analyzed by ICP-OES, compared to their nominal compositions. Errors of 1% or less.

$[Li_2O]/[Li_2O+K_2O]$		Li_2O (mol-%)		K_2O (mol-%)		SiO_2 (mol-%)	
Nominal	Actual	Nominal	Actual	Nominal	Actual	Nominal	Actual
0.0	0.00	0	0.1	30	28.0	70	72.0
0.33	0.32	10	11.6	20	25.0	70	63.4
0.5	0.49	15	14.5	15	15.2	70	70.3
0.67	0.62	20	19.5	10	11.9	70	68.7
[a]0.83	0.83	25	25.6	5	5.4	70	69.0
[a]1	0.99	30	31.4	0	0.4	70	68.5

[a] Analyzed by WDS.

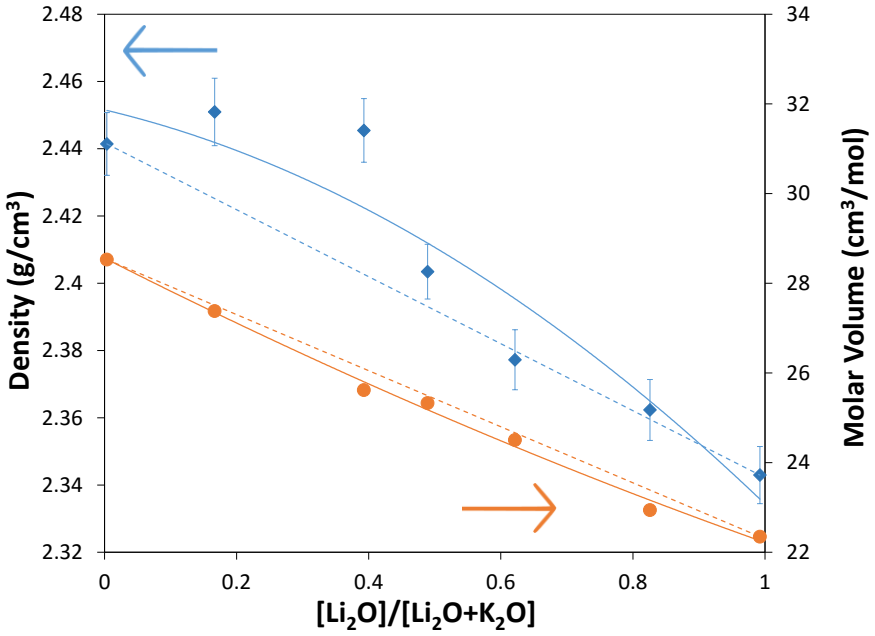

Figure D.1: Density (ρ) and the corresponding molar volume (V_{m}) aof the $x$$Li_2O$-(30−$x$)$K_2O-70SiO_2$ series as a function of relative Li_2O fraction. Solid line is the apparent trend, fit using a 2nd-order polynomial, while the dashed line is the linear fit between the two endmember compositions. Error of ρ determined from three trials, ≈0.01 g/cm^3.

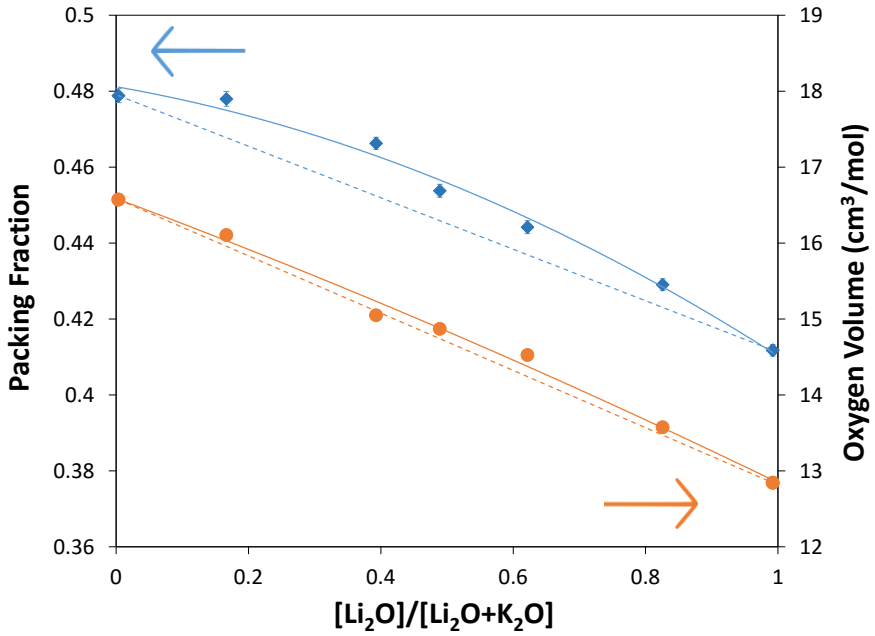

Figure D.2: Packing fraction (V_{f}) and oxygen volume (V_{O}) of the $x$$Li_2O$-(30−$x$)$K_2O-70SiO_2$ series as a function of relative Li_2O fraction, calculated using Eqs. 1.1 and 2.4, respectively. The solid line is the apparent trend, fit using a 2nd-order polynomial, while the dashed line is the linear fit between the two endmember compositions. Error is derived from density measurements.

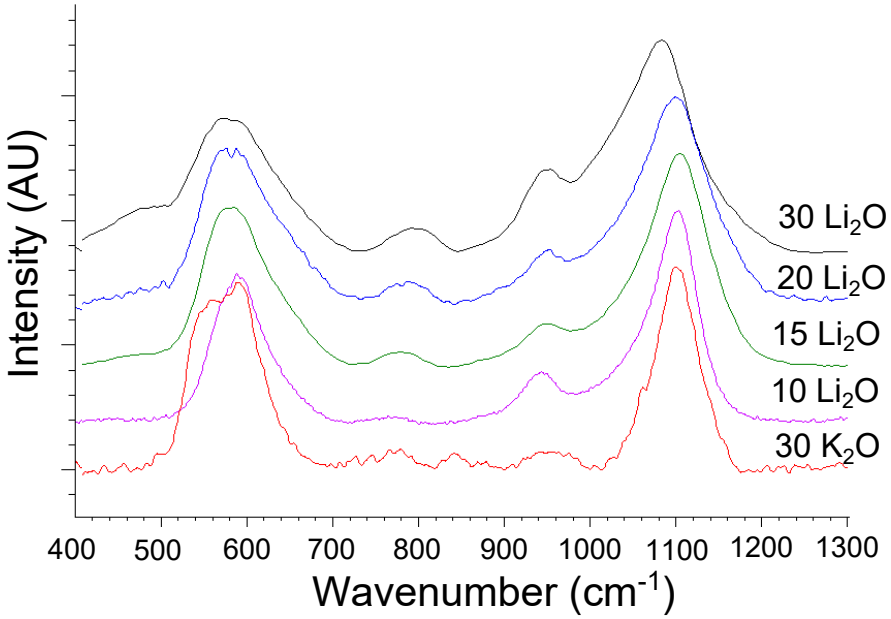

Figure D.3: Raman spectra of xLi$_2$O-(30−x)K$_2$O-70SiO$_2$ glasses as a function of relative Li$_2$O ratio. General positions of structural Q^n-units are marked with dashed lines. The low and high-frequency regions are separated by brackets which correspond to Si-O-Si stretches and O-Si-O stretches, respectively.

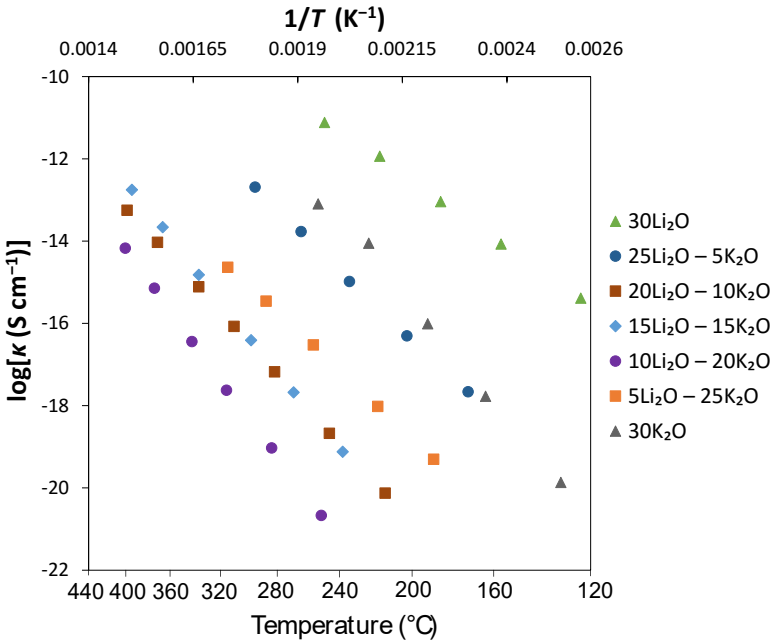

Figure D.4: Conductivity Arrhenius plots of logκ vs. 1000/T of the xLi$_2$O-(30−x)K$_2$O-70SiO$_2$ series as a function of relative Li$_2$O fraction.

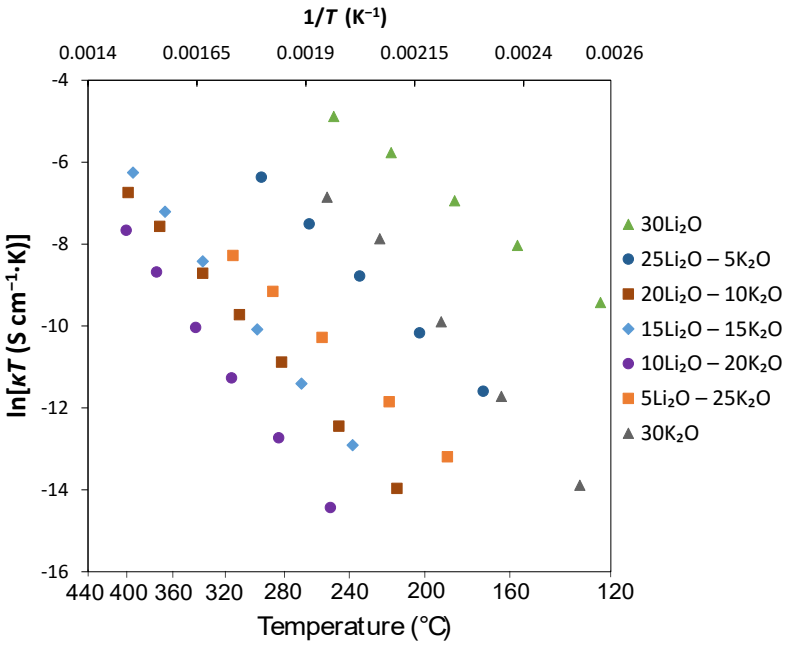

Figure D.5: Arrhenius plot of $\ln\kappa T$ vs. 1000/T of the $x\mathrm{Li_2O}$-$(30-x)\mathrm{K_2O}$-$70\mathrm{SiO_2}$ series as a function of relative $\mathrm{Li_2O}$ fraction. Due to departure from Arrhenius behaviour, there are low-T and high-T linear fits for each composition. Common temperature point, T_0, is also plotted and is discussed later in the text.

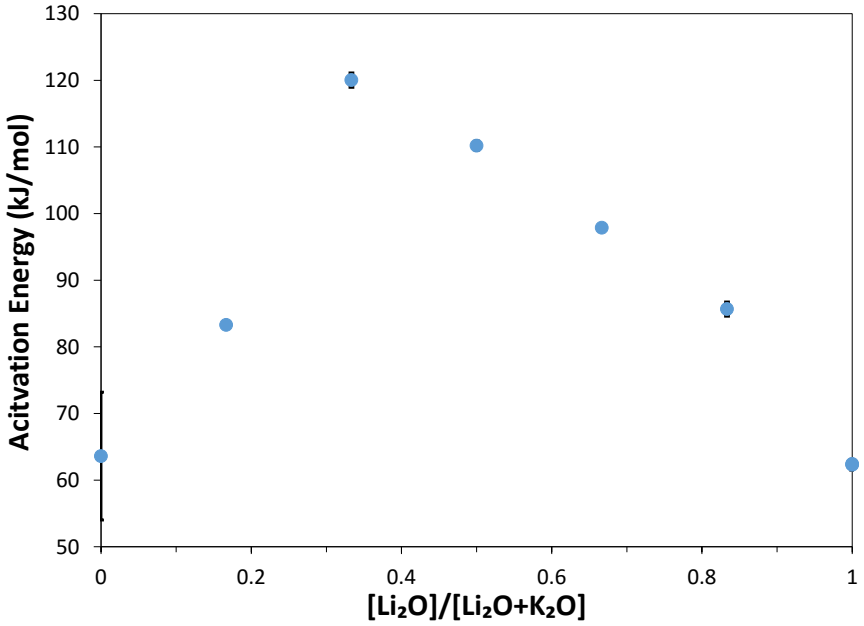

Figure D.6: Activation energy (E_a) of the $x\mathrm{Li_2O}$-$(30-x)\mathrm{K_2O}$-$70\mathrm{SiO_2}$ series as a function of relative $\mathrm{Li_2O}$ fraction. Low and high-T values are from their corresponding regions of the Arrhenius plot (Fig. 5.9).

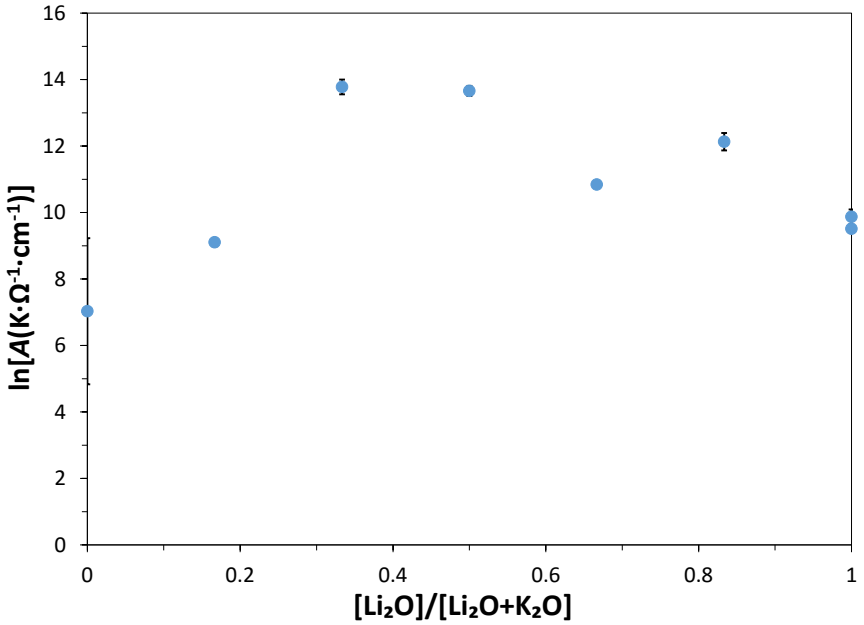

Figure D.7: Pre-exponential factor (A) of the xLi$_2$O-(30$-x$)K$_2$O-70SiO$_2$ series as a function of relative Li$_2$O fraction. High and low temperature data is taken from the respective region in the Arrhenius plot (Fig. 5.9).

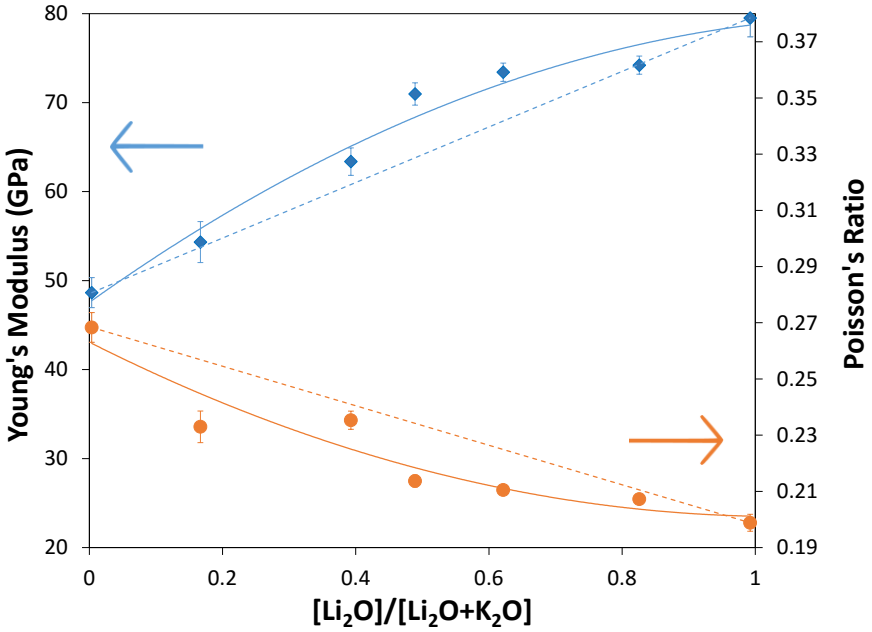

Figure D.8: Young's modulus (Y) and Poisson's ratio (μ) of the xLi$_2$O-(30$-x$)K$_2$O-70SiO$_2$ series as a function of relative Li$_2$O fraction. Solid lines are the apparent trends fit with 2nd-order polynomials, while the dashed lines are linear fits between the two endmember compositions.

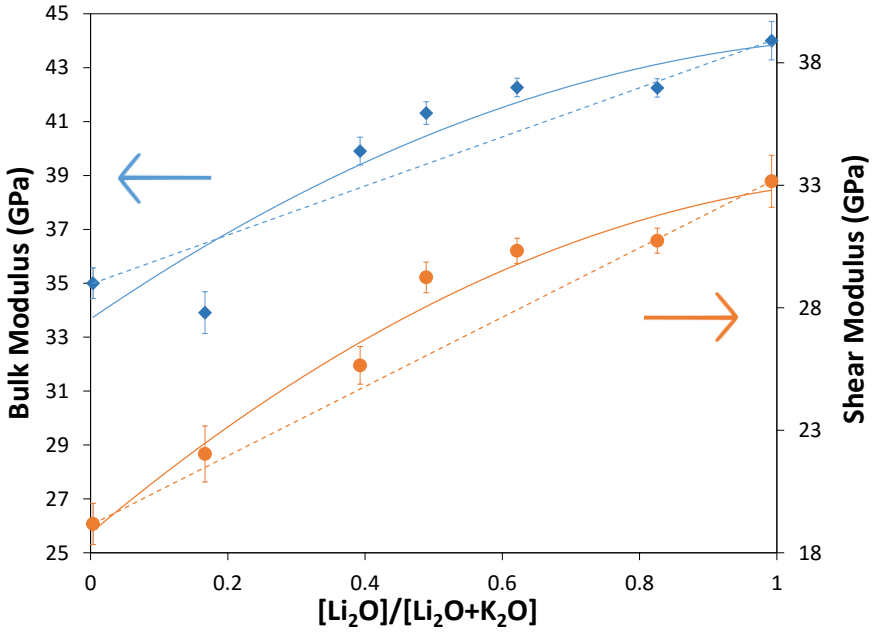

Figure D.9: Bulk modulus (K) and shear Modulus (G) of the $x$$Li_2O$-(30−$x$)$K_2O-70SiO_2$ series as a function of relative Li_2O fraction. Solid lines are the apparent trends fit with 2nd-order polynomials, while the dashed lines are linear fits between the two endmember compositions.

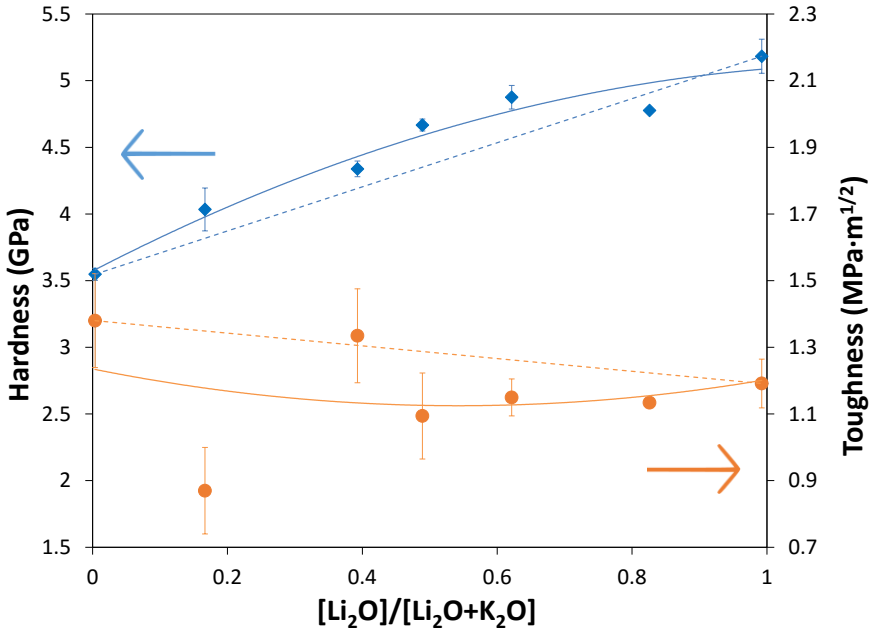

Figure D.10: Vickers hardness (H_V) and fracture toughness (K_{Ic}) of the $x$$Li_2O$-(30−$x$)$K_2O-70SiO_2$ series as a function of relative Li_2O fraction. Solid lines are the apparent trends fit with 2nd-order polynomials, while the dashed lines are linear fits between the two endmember compositions.

D.2 $x\mathrm{Li_2O}$-$(40-x)\mathrm{K_2O}$-$60\mathrm{SiO_2}$

Table D.2: Glass compositions of the $x\mathrm{Li_2O}$-$(40-x)\mathrm{K_2O}$-$60\mathrm{SiO_2}$ series analyzed by WDS, compared to their nominal compositions. Instrumental error is 0.1–0.16 mol-%, while standard error of the five points was ≤0.3 mol-%.

$[Li_2O]/[Li_2O+K_2O]$		Li_2O (mol-%)		K_2O (mol-%)		SiO_2 (mol-%)	
Nominal	Actual	Nominal	Actual	Nominal	Actual	Nominal	Actual
0.50	0.49	60	62.3	20	18.6	20	19.2
0.67	0.37	60	59.4	13.3	14.9	26.7	25.6
0.75	0.20	60	62.2	10	7.5	30	30.3
0.83	0.13	60	62.3	6.7	4.9	33.3	32.8
0.98	0.01	60	67.7	1	0.0	39	32.2

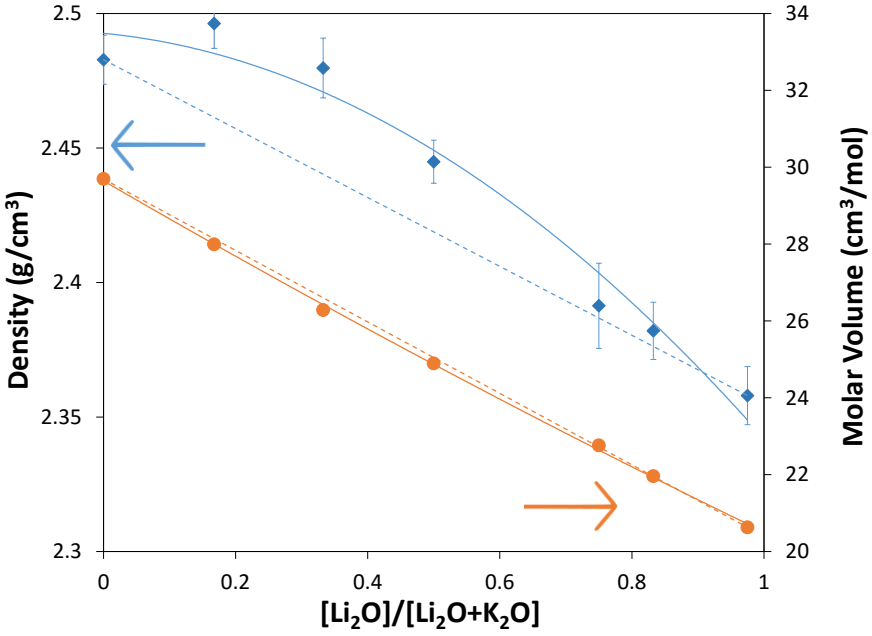

Figure D.11: Density (ρ) and the corresponding molar volume (V_m) aof the $x\mathrm{Li_2O}$-$(40-x)\mathrm{K_2O}$-$60\mathrm{SiO_2}$ series as a function of relative Li_2O fraction. Solid line is the apparent trend, fit using a 2nd-order polynomial, while the dashed line is the linear fit between the two endmember compositions. Error of ρ determined from three trials, ≈0.01 g/cm^3.

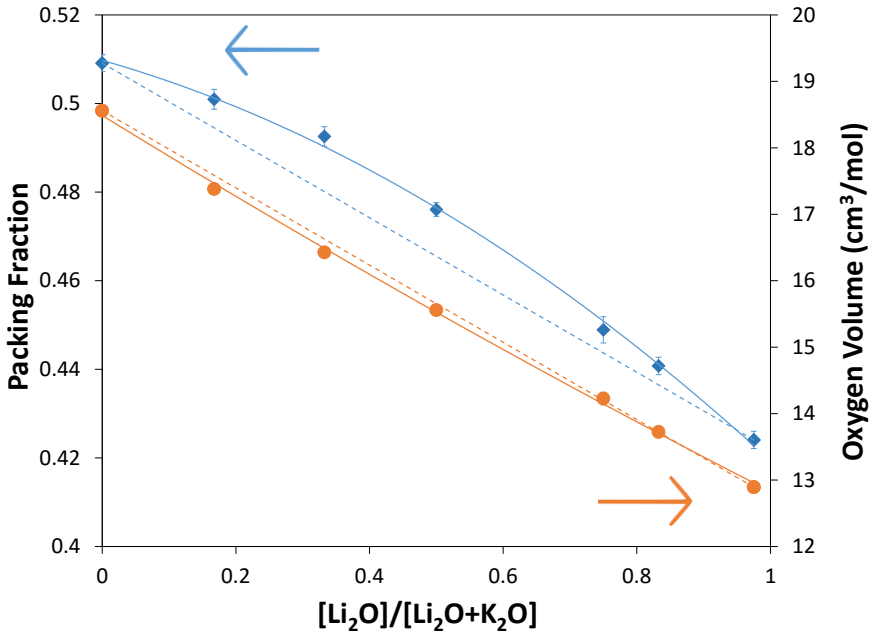

Figure D.12: Packing fraction (V_f) and oxygen volume (V_O) of the xLi$_2$O-(40−x)K$_2$O-60SiO$_2$ series as a function of relative Li$_2$O fraction, calculated using Eqs. 1.1 and 2.4, respectively. The solid line is the apparent trend, fit using a 2nd-order polynomial, while the dashed line is the linear fit between the two endmember compositions. Error is derived from density measurements.

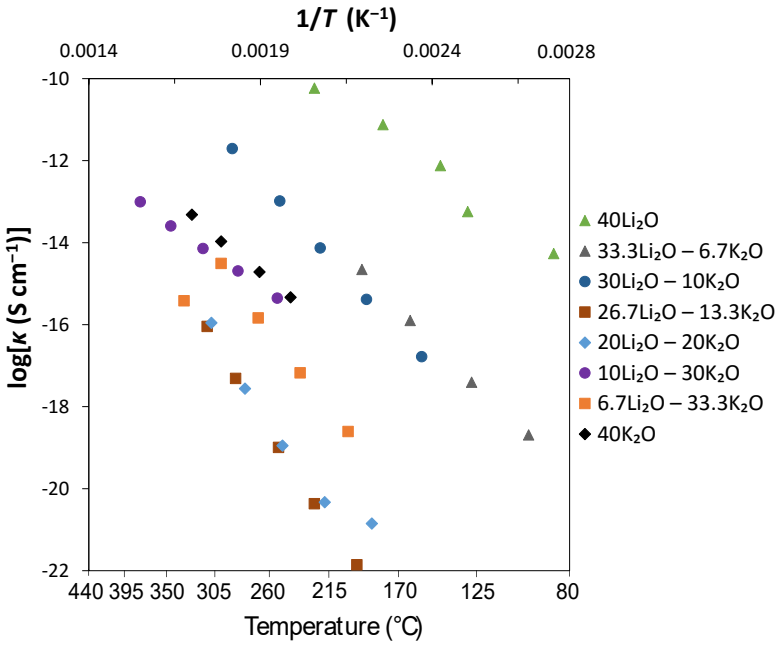

Figure D.13: Conductivity Arrhenius plots of logκ vs. 1000/T of the xLi$_2$O-(40−x)K$_2$O-60SiO$_2$ series as a function of relative Li$_2$O fraction.

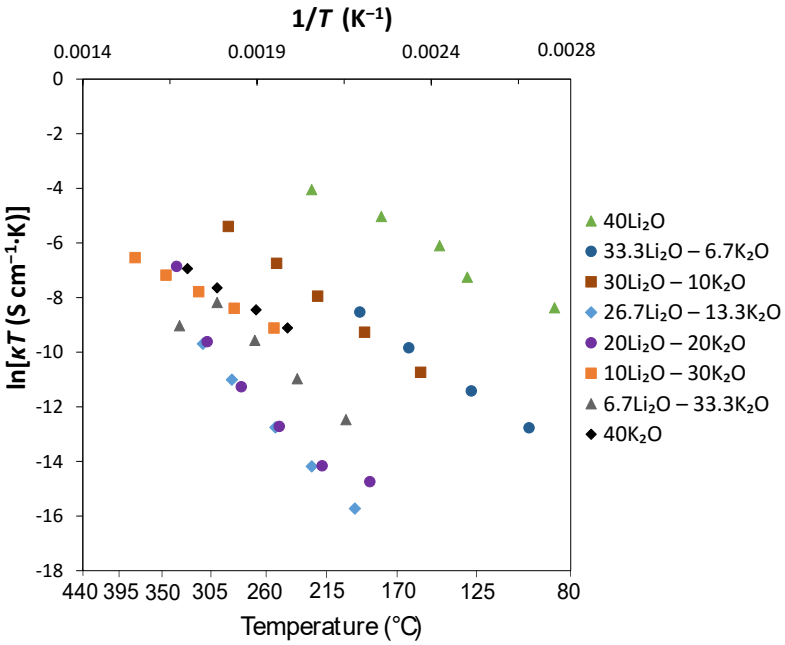

Figure D.14: Arrhenius plot of lnκT vs. 1000/T of the xLi$_2$O-(40$-x$)K$_2$O-60SiO$_2$ series as a function of relative Li$_2$O fraction. Due to departure from Arrhenius behaviour, there are low-T and high-T linear fits for each composition. Common temperature point, T_0, is also plotted and is discussed later in the text.

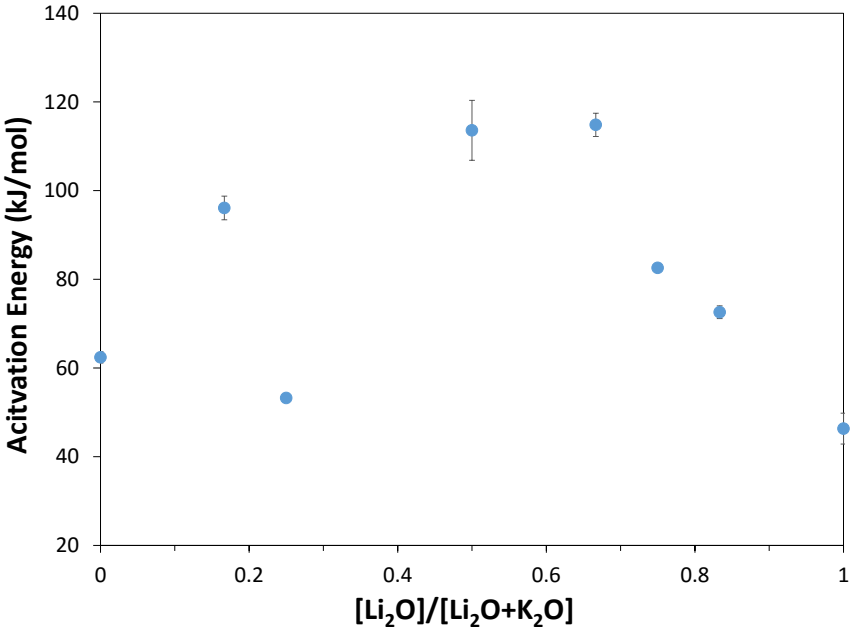

Figure D.15: Activation energy (E_a) of the xLi$_2$O-(40$-x$)K$_2$O-60SiO$_2$ series as a function of relative Li$_2$O fraction. Low and high-T values are from their corresponding regions of the Arrhenius plot (Fig. 5.9).

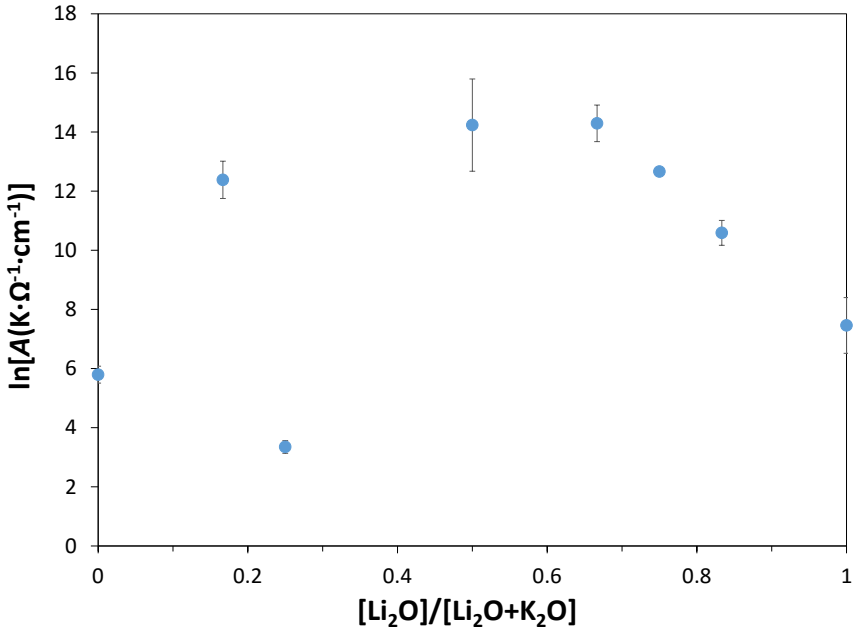

Figure D.16: Pre-exponential factor (A) of the xLi$_2$O-(40−x)K$_2$O-60SiO$_2$ series as a function of relative Li$_2$O fraction. High and low temperature data is taken from the respective region in the Arrhenius plot (Fig. 5.9).

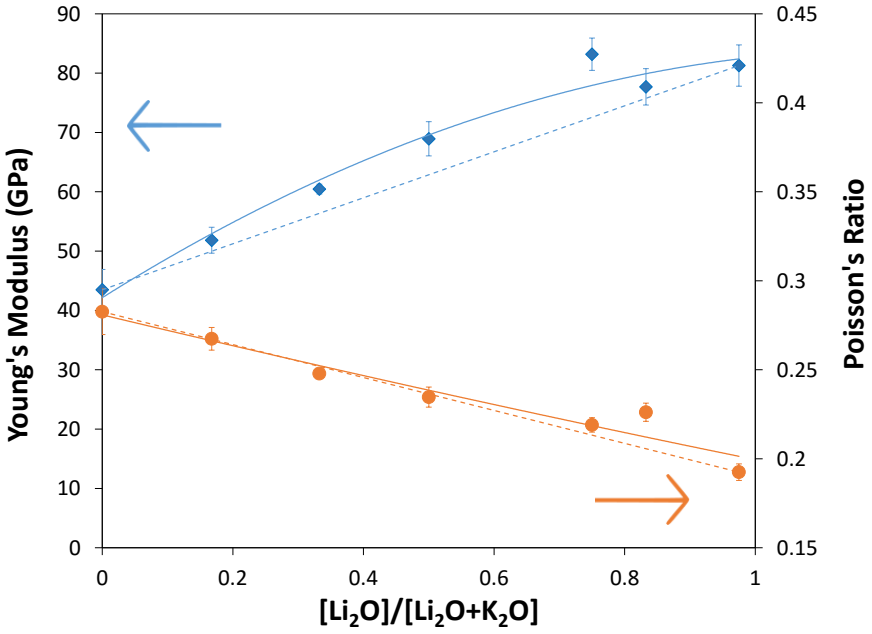

Figure D.17: Young's modulus (Y) and Poisson's ratio (μ) of the xLi$_2$O-(40−x)K$_2$O-60SiO$_2$ series as a function of relative Li$_2$O fraction. Solid lines are the apparent trends fit with 2nd-order polynomials, while the dashed lines are linear fits between the two endmember compositions.

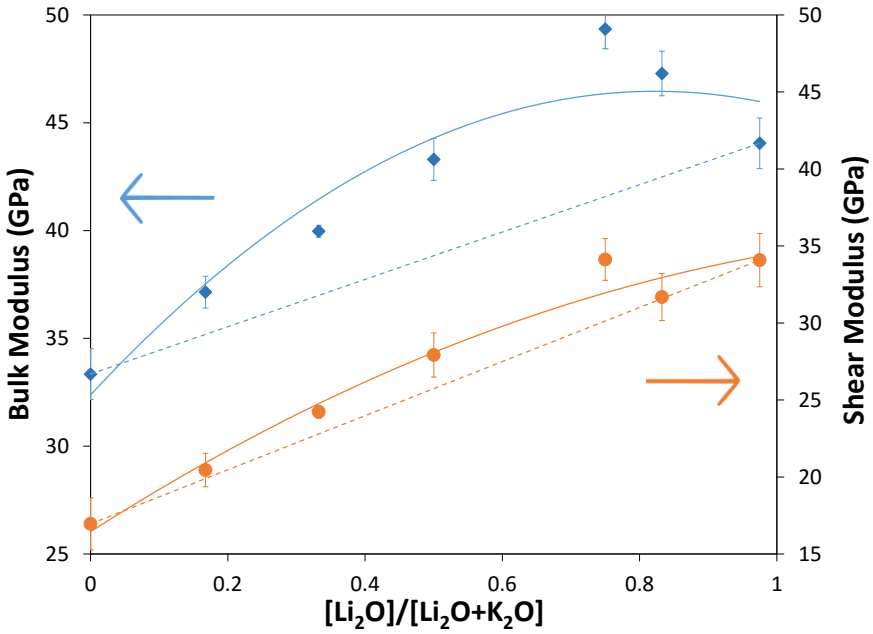

Figure D.18: Bulk modulus (K) and shear Modulus (G) of the $x$$Li_2O$-(40−$x$)$K_2O-60SiO_2$ series as a function of relative Li_2O fraction. Solid lines are the apparent trends fit with 2nd-order polynomials, while the dashed lines are linear fits between the two endmember compositions.

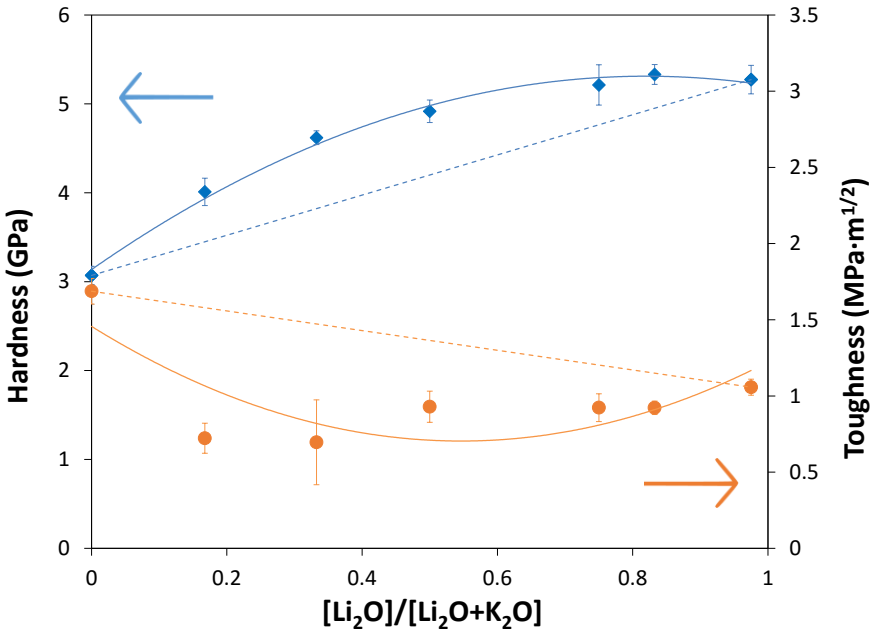

Figure D.19: Vickers hardness (H_V) and fracture toughness (K_{Ic}) of the $x$$Li_2O$-(40−$x$)$K_2O-60SiO_2$ series as a function of relative Li_2O fraction. Solid lines are the apparent trends fit with 2nd-order polynomials, while the dashed lines are linear fits between the two endmember compositions.

D.3 $x\mathrm{Li_2O}$-$(30-x)\mathrm{Rb_2O}$-$70\mathrm{SiO_2}$

Table D.3: Glass compositions of the $x\mathrm{Li_2O}$-$(30-x)\mathrm{Rb_2O}$-$70\mathrm{SiO_2}$ series analyzed by ICP-OES, compared to their nominal compositions. Errors of 1% or less.

$[Li_2O]/[Li_2O+Rb_2O]$		Li_2O (mol-%)		Rb_2O (mol-%)		SiO_2 (mol-%)	
Nominal	Actual	Nominal	Actual	Nominal	Actual	Nominal	Actual
0	0.01	0	0.2	30	28.6	70	71.2
0.33	0.32	10	8.7	20	18.3	70	72.7
0.5	0.50	15	14.2	15	14.5	70	71.1
0.67	0.67	20	18.3	10	9.2	70	72.5
[a]1	0.99	30	31.4	0	0.4	70	68.5

[a] Remade, analyzed by WDS.

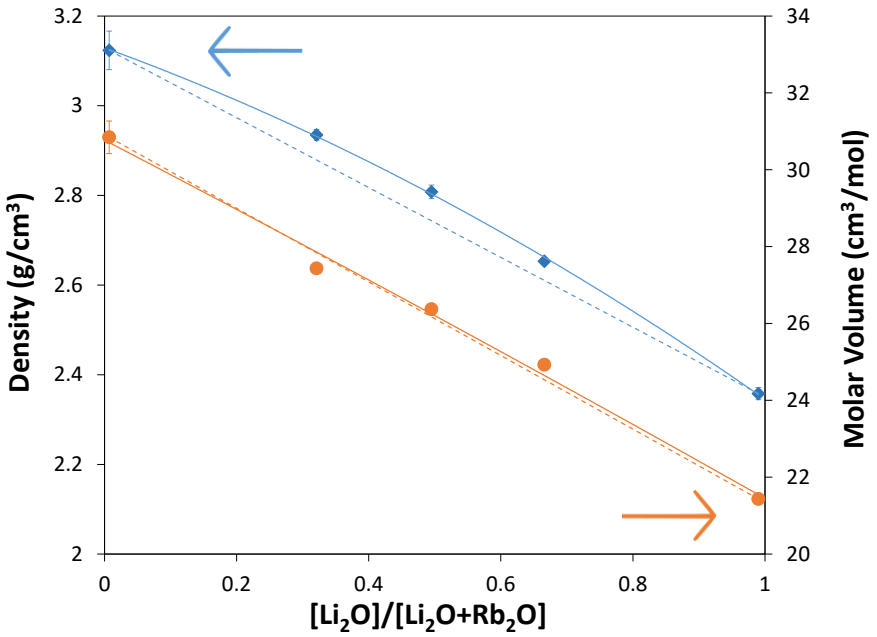

Figure D.20: Density (ρ) and the corresponding molar volume (V_m) of the $x\mathrm{Li_2O}$-$(30-x)\mathrm{Rb_2O}$-$70\mathrm{SiO_2}$ series as a function of relative Li_2O fraction. Solid line is the apparent trend, fit using a 2nd-order polynomial, while the dashed line is the linear fit between the two endmember compositions. Error of ρ determined from three trials, $\approx$0.01 g/cm^3.

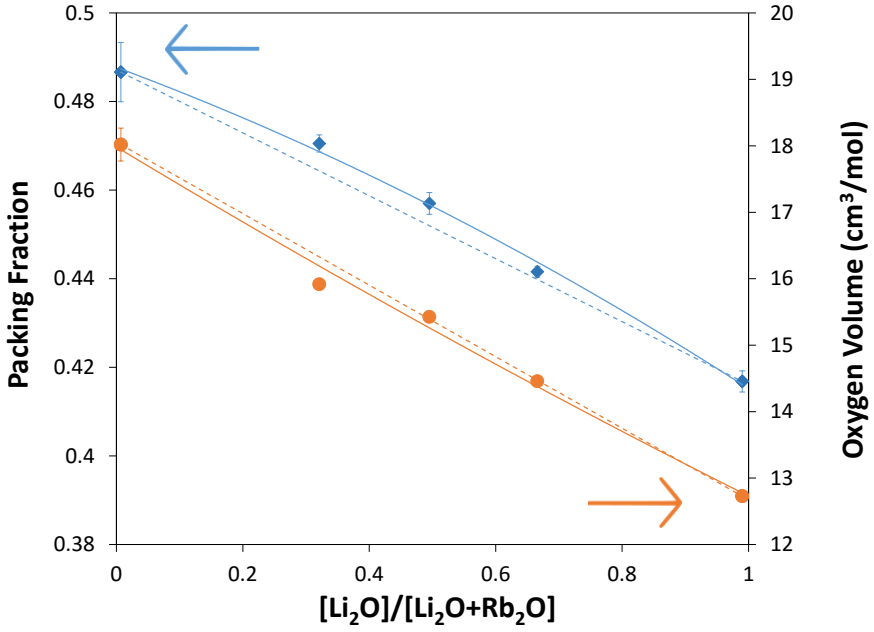

Figure D.21: Packing fraction (V_f) and oxygen volume (V_O) of the $x$$Li_2O$-$(30-x)$$Rb_2O$-$70SiO_2$ series as a function of relative Li_2O fraction, calculated using Eqs. 1.1 and 2.4, respectively. The solid line is the apparent trend, fit using a 2nd-order polynomial, while the dashed line is the linear fit between the two endmember compositions. Error is derived from density measurements.

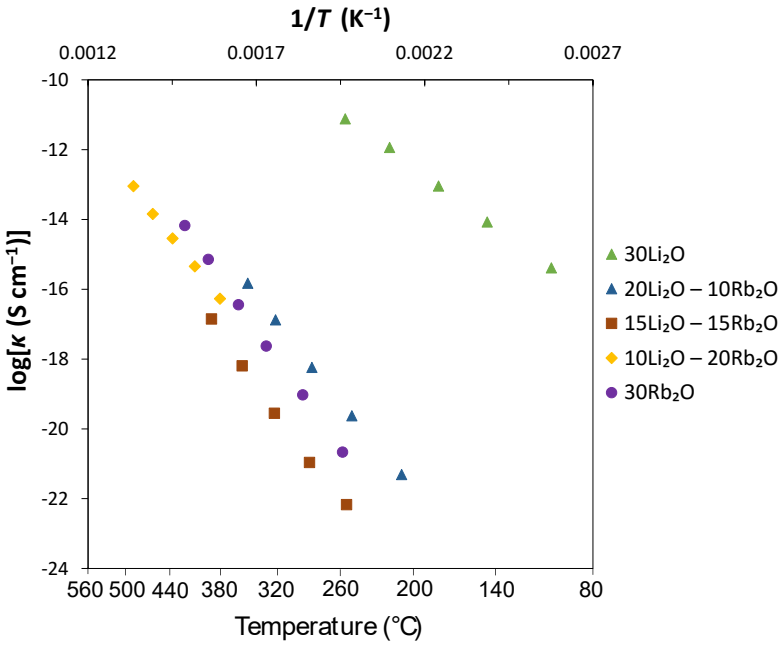

Figure D.22: Conductivity Arrhenius plots of logκ vs. 1000/T of the $x$$Li_2O$-$(30-x)$$Rb_2O$-$70SiO_2$ series as a function of relative Li_2O fraction.

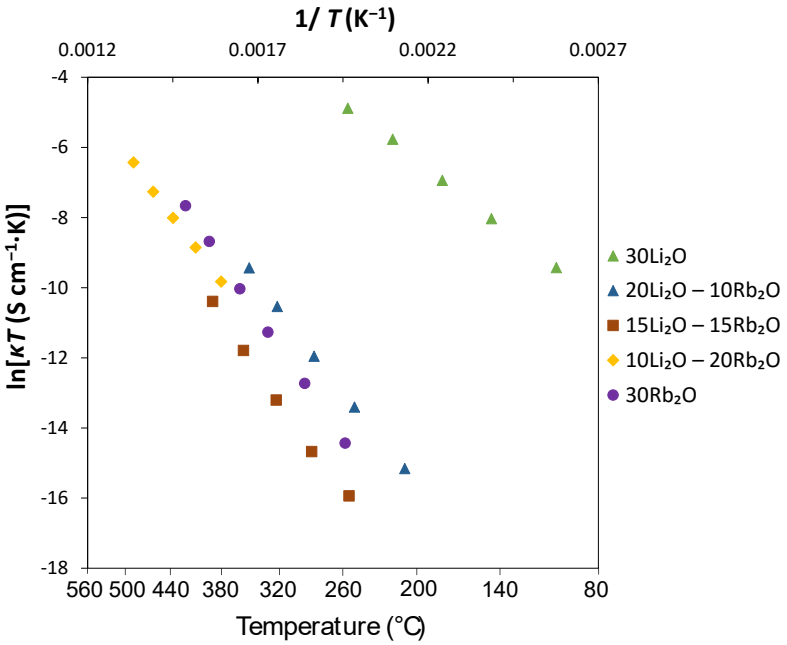

Figure D.23: Arrhenius plot of $\ln\kappa T$ vs. 1000/T of the $x\mathrm{Li_2O}$-$(30-x)\mathrm{Rb_2O}$-$70\mathrm{SiO_2}$ series as a function of relative $\mathrm{Li_2O}$ fraction. Due to departure from Arrhenius behaviour, there are low-T and high-T linear fits for each composition. Common temperature point, T_0, is also plotted and is discussed later in the text.

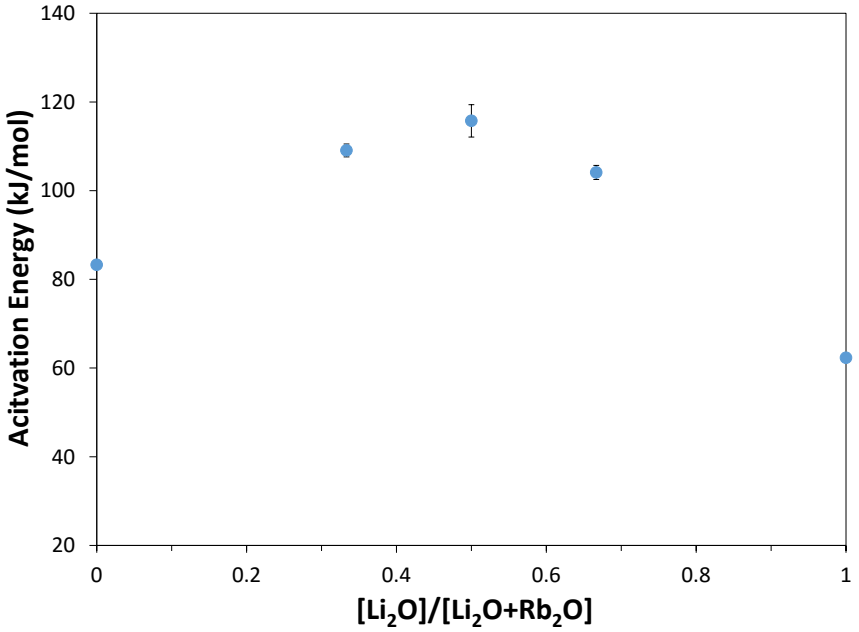

Figure D.24: Activation energy (E_a) of the $x\mathrm{Li_2O}$-$(30-x)\mathrm{Rb_2O}$-$70\mathrm{SiO_2}$ series as a function of relative $\mathrm{Li_2O}$ fraction. Low and high-T values are from their corresponding regions of the Arrhenius plot (Fig. 5.9).

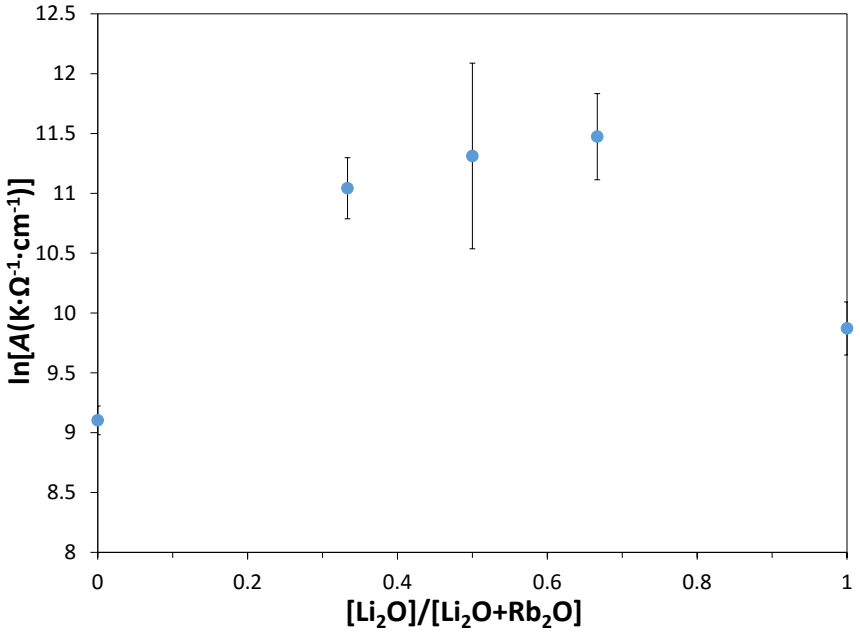

Figure D.25: Pre-exponential factor (A) of the xLi$_2$O-(30$-x$)Rb$_2$O-70SiO$_2$ series as a function of relative Li$_2$O fraction. High and low temperature data is taken from the respective region in the Arrhenius plot (Fig. 5.9).

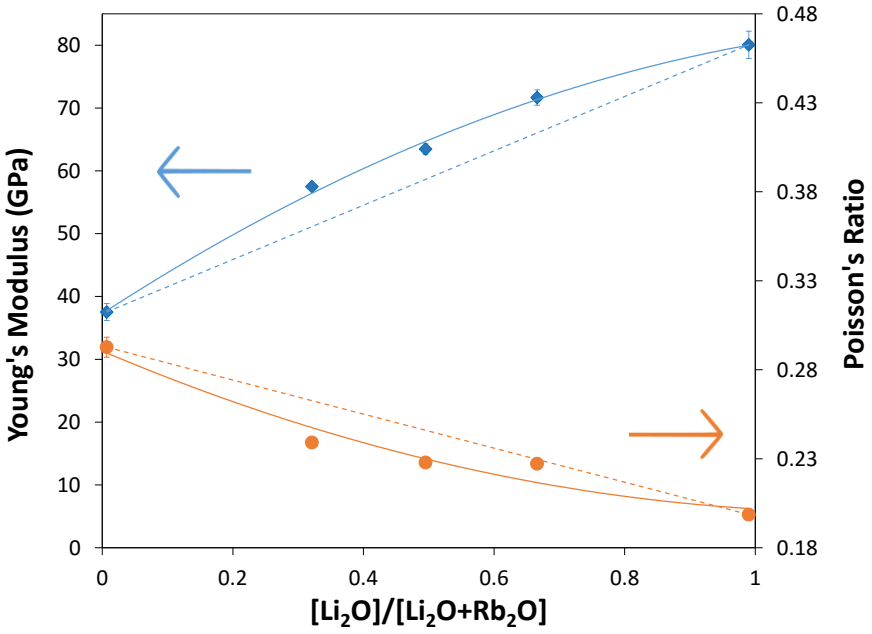

Figure D.26: Young's modulus (Y) and Poisson's ratio (μ) of the xLi$_2$O-(30$-x$)Rb$_2$O-70SiO$_2$ series as a function of relative Li$_2$O fraction. Solid lines are the apparent trends fit with 2nd-order polynomials, while the dashed lines are linear fits between the two endmember compositions.

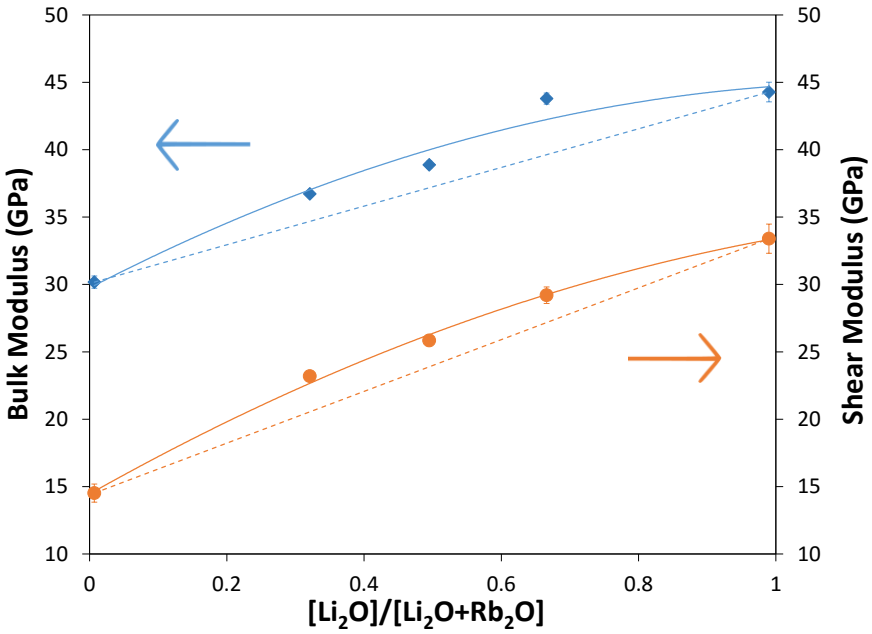

Figure D.27: Bulk modulus (K) and shear Modulus (G) of the $x$$Li_2O$-(30−$x$)$Rb_2O-70SiO_2$ series as a function of relative Li_2O fraction. Solid lines are the apparent trends fit with 2nd-order polynomials, while the dashed lines are linear fits between the two endmember compositions.

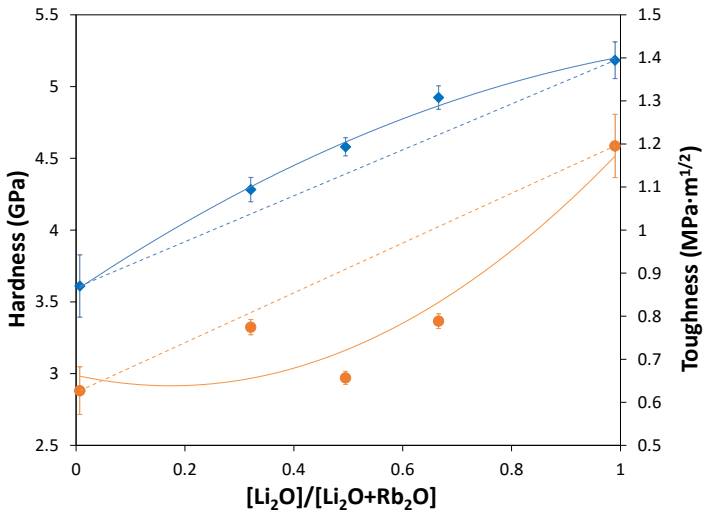

Figure D.28: Vickers hardness (H_V) and fracture toughness (K_{Ic}) of the $x$$Li_2O$-(30−$x$)$Rb_2O-70SiO_2$ series as a function of relative Li_2O fraction. Solid lines are the apparent trends fit with 2nd-order polynomials, while the dashed lines are linear fits between the two endmember compositions.

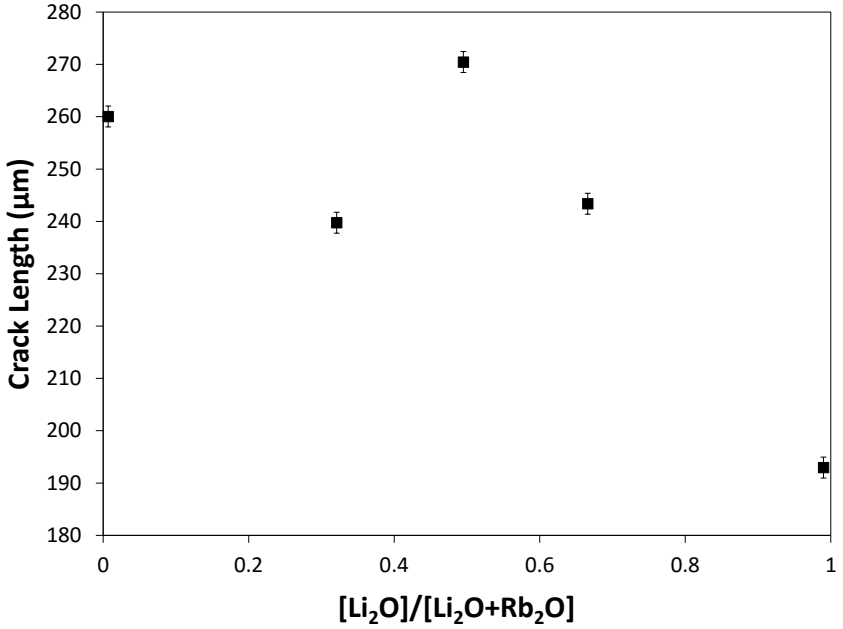

Figure D.29: Cracks lengths of the $x\mathrm{Li_2O}$-$(30-x)\mathrm{Rb_2O}$-$70\mathrm{SiO_2}$ series as a function of relative $\mathrm{Li_2O}$ fraction measured during Vickers indentation, used to calculate K_{Ic}

D.4 $x\mathrm{Li_2O}$-$(40-x)\mathrm{Rb_2O}$-60$\mathrm{SiO_2}$

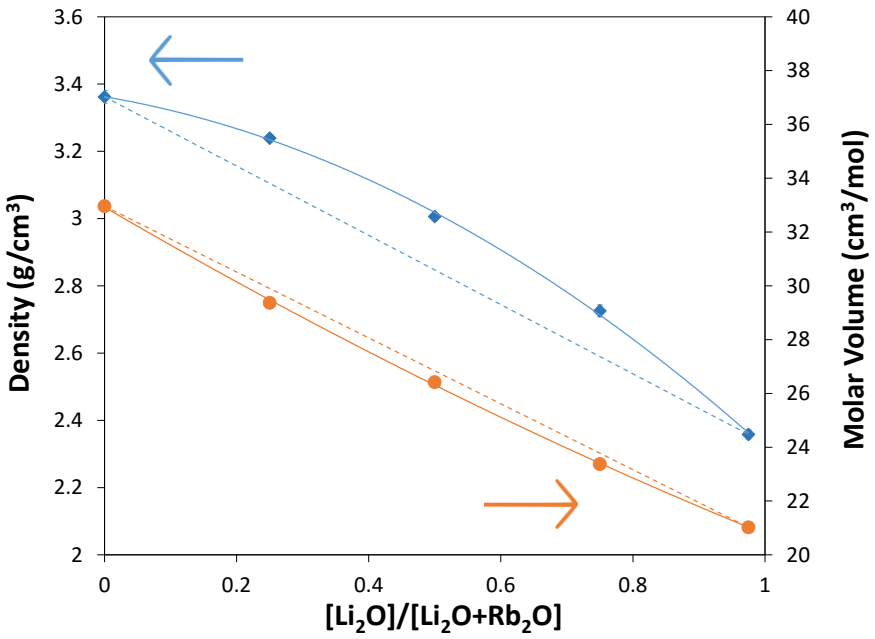

Figure D.30: Density (ρ) and the corresponding molar volume (V_m) of the $x\mathrm{Li_2O}$-$(40-x)\mathrm{Rb_2O}$-70$\mathrm{SiO_2}$ series as a function of relative $\mathrm{Li_2O}$ fraction. Solid line is the apparent trend, fit using a 2nd-order polynomial, while the dashed line is the linear fit between the two endmember compositions. Error of ρ determined from three trials, $\approx$0.01 g/cm^3.

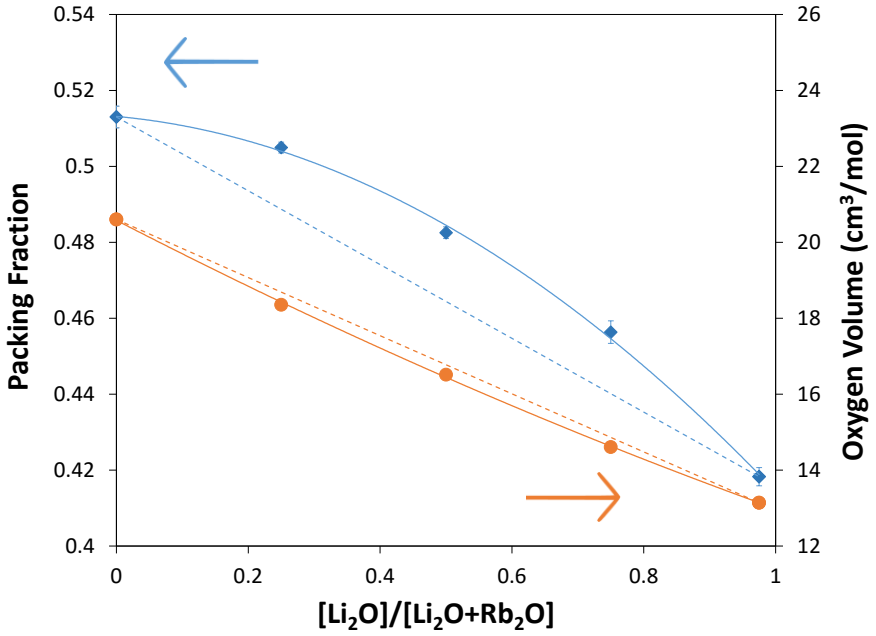

Figure D.31: Packing fraction (V_f) and oxygen volume (V_O) of the xLi$_2$O-(40−x)Rb$_2$O-70SiO$_2$ series as a function of relative Li$_2$O fraction, calculated using Eqs. 1.1 and 2.4, respectively. The solid line is the apparent trend, fit using a 2nd-order polynomial, while the dashed line is the linear fit between the two endmember compositions. Error is derived from density measurements.

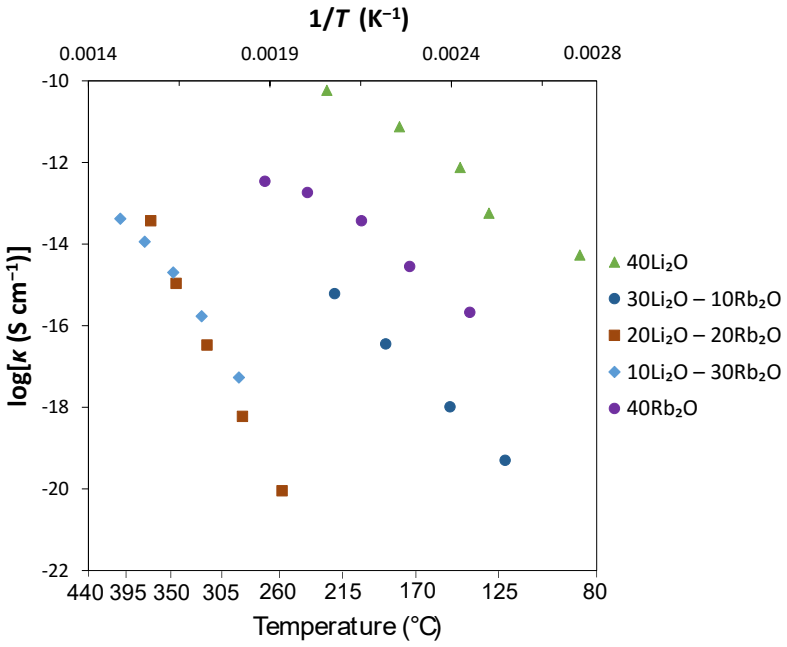

Figure D.32: Conductivity Arrhenius plots of logκ vs. 1000/T of the xLi$_2$O-(40−x)Rb$_2$O-60SiO$_2$ series as a function of relative Li$_2$O fraction.

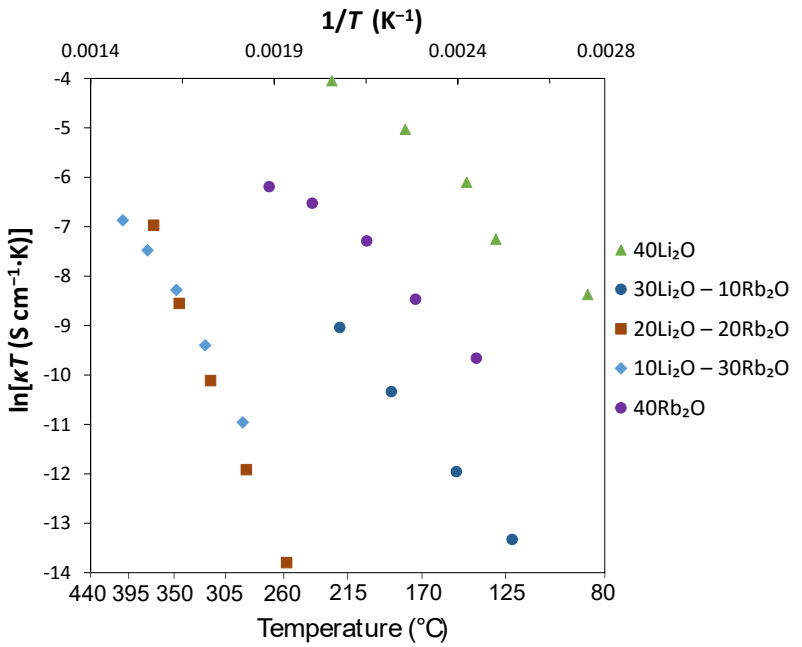

Figure D.33: Arrhenius plot of $\ln\kappa T$ vs. 1000/T of the $x\mathrm{Li_2O}$-$(40-x)\mathrm{Rb_2O}$-$60\mathrm{SiO_2}$ series as a function of relative $\mathrm{Li_2O}$ fraction. Due to departure from Arrhenius behaviour, there are low-T and high-T linear fits for each composition. Common temperature point, T_0, is also plotted and is discussed later in the text.

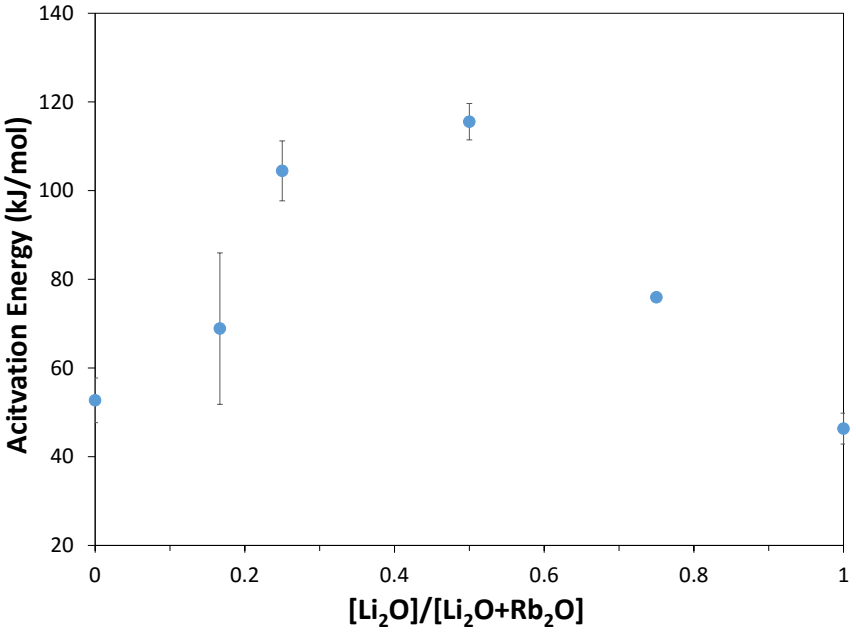

Figure D.34: Activation energy (E_a) of the $x\mathrm{Li_2O}$-$(40-x)\mathrm{Rb_2O}$-$60\mathrm{SiO_2}$ series as a function of relative $\mathrm{Li_2O}$ fraction. Low and high-T values are from their corresponding regions of the Arrhenius plot (Fig. 5.9).

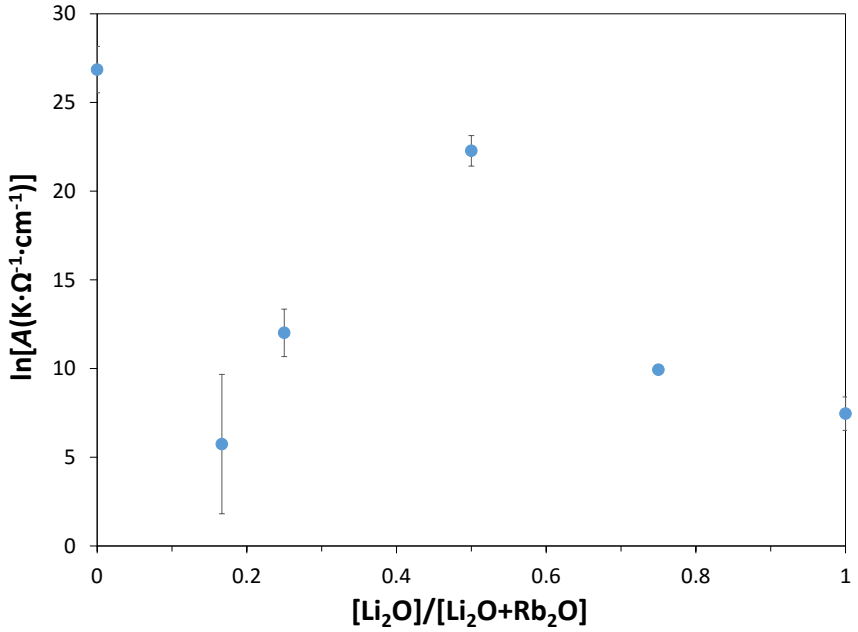

Figure D.35: Pre-exponential factor (A) of the xLi$_2$O-(40$-x$)Rb$_2$O-60SiO$_2$ series as a function of relative Li$_2$O fraction. High and low temperature data is taken from the respective region in the Arrhenius plot (Fig. 5.9).

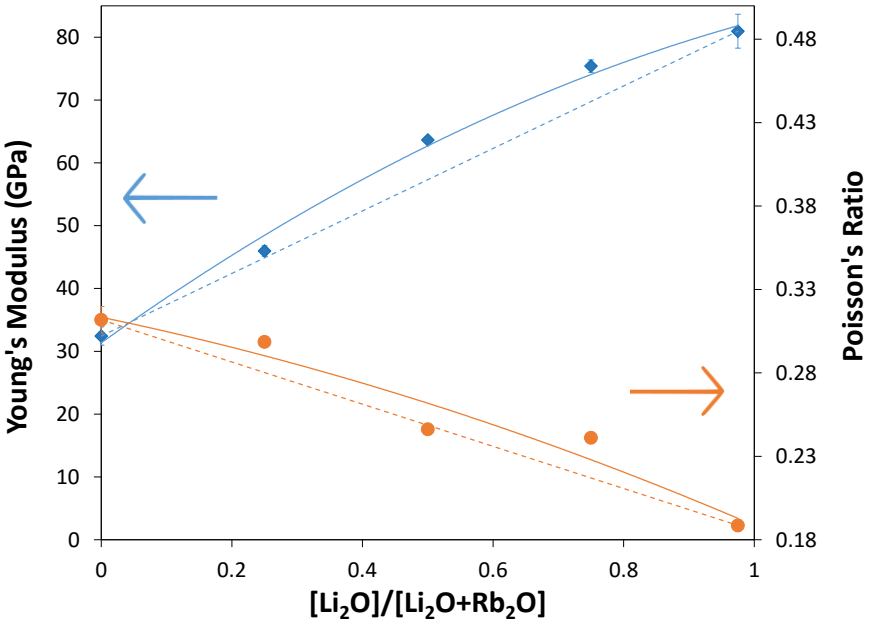

Figure D.36: Young's modulus (Y) and Poisson's ratio (μ) of the xLi$_2$O-(40$-x$)Rb$_2$O-60SiO$_2$ series as a function of relative Li$_2$O fraction. Solid lines are the apparent trends fit with 2nd-order polynomials, while the dashed lines are linear fits between the two endmember compositions.

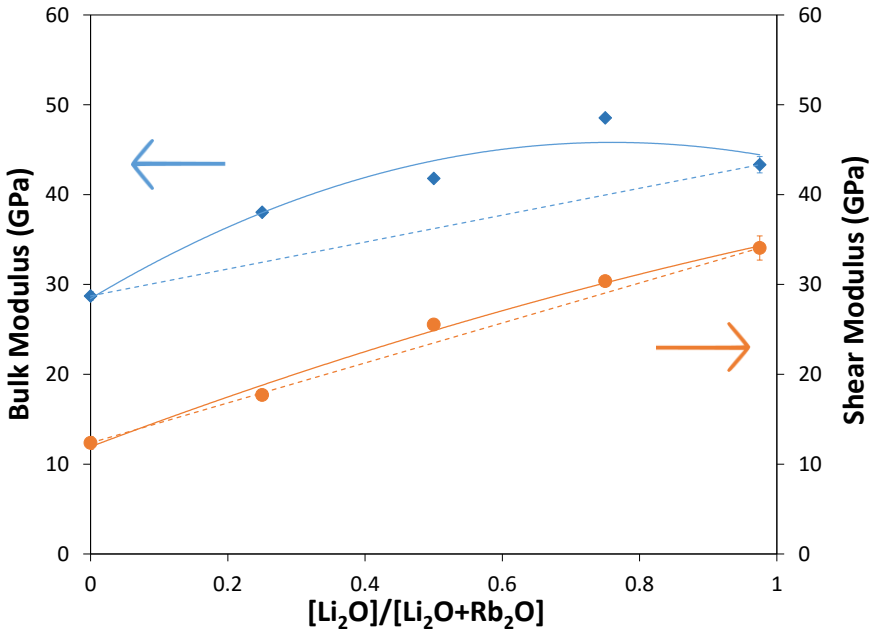

Figure D.37: Bulk modulus (K) and shear Modulus (G) of the $x$$Li_2O$-(40−$x$)$Rb_2O-60SiO_2$ series as a function of relative Li_2O fraction. Solid lines are the apparent trends fit with 2nd-order polynomials, while the dashed lines are linear fits between the two endmember compositions.

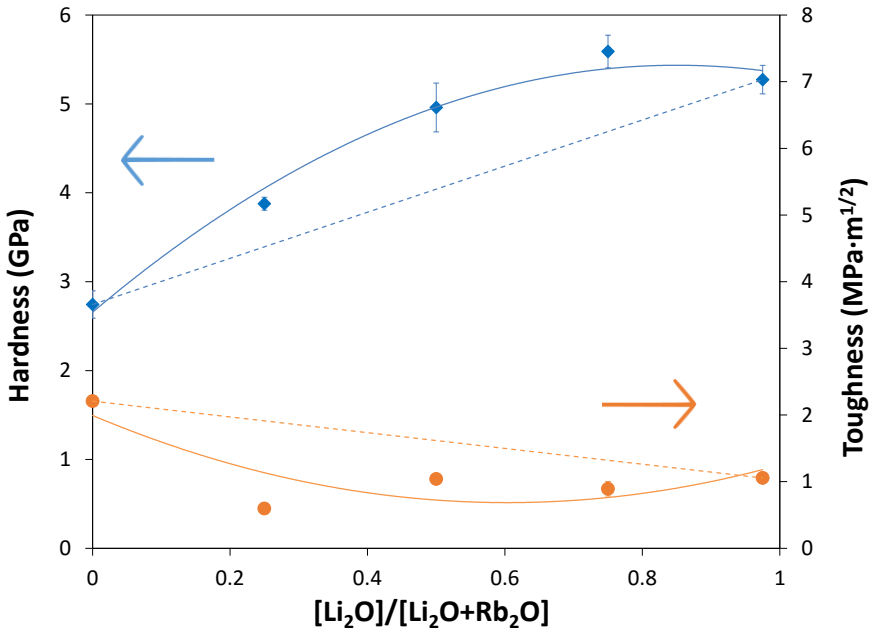

Figure D.38: Vickers hardness (H_V) and fracture toughness (K_{Ic}) of the $x$$Li_2O$-(40−$x$)$Rb_2O-60SiO_2$ series as a function of relative Li_2O fraction. Solid lines are the apparent trends fit with 2nd-order polynomials, while the dashed lines are linear fits between the two endmember compositions.

D.5 xLi$_2$O-(50−x)MgO-50SiO$_2$

Table D.4: Glass compositions of the xLi$_2$O-(50−x)MgO-50SiO$_2$ series analyzed by ICP-OES, compared to their nominal compositions. Instrumental error is 0.1–0.16 mol-%, while standard error of the five points was ≤ 0.3, 0.6 and 1.1 mol-% for MgO, SiO$_2$ and Li$_2$O, respectively.

[Li$_2$O]/[Li$_2$O+MgO]		SiO$_2$ (mol-%)		MgO (mol-%)		Li$_2$O (mol-%)	
Nominal	Actual	Nominal	Actual	Nominal	Actual	Nominal	Actual
0.208	0.27	50	46.0	39.6	39.5	10.4	14.4
0.34	0.33	50	47.2	33	35.4	17	17.3
0.416	0.40	50	51.0	25	29.3	25	19.6
0.456	0.47	50	51.6	29.2	25.8	22.8	22.6
0.5	0.54	50	49.0	22.2	23.2	27.8	27.7
0.556	0.59	50	50.0	27.2	20.6	22.8	29.3
0.584	0.61	50	51.0	20.8	19.3	29.2	29.7
0.66	0.67	50	50.4	17	16.1	33	33.4
0.792	0.79	50	53.6	8.4	9.7	41.6	36.6

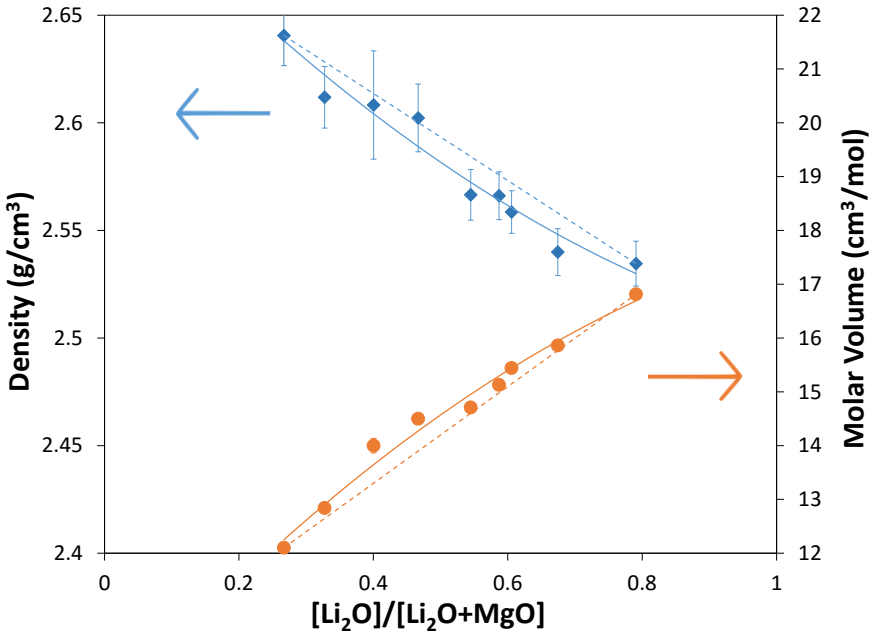

Figure D.39: Density (ρ) and the corresponding molar volume (V_m) aof the xLi$_2$O-(50−x)MgO-50SiO$_2$ series as a function of relative Li$_2$O fraction. Solid line is the apparent trend, fit using a 2nd-order polynomial, while the dashed line is the linear fit between the two endmember compositions. Error of ρ determined from three trials, ≈0.01 g/cm^3.

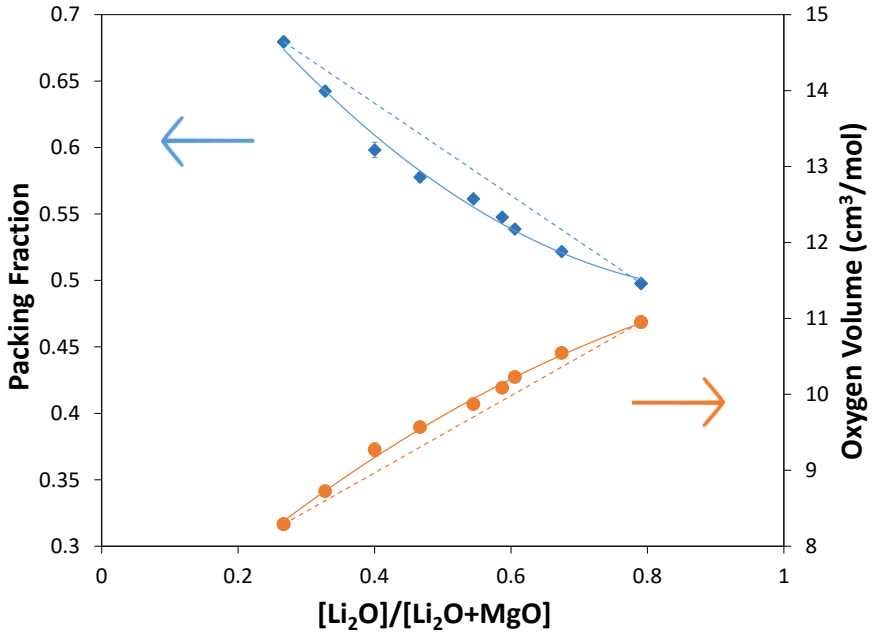

Figure D.40: Packing fraction (V_f) and oxygen volume (V_O) of the $x$$Li_2O$-(50−$x$)MgO-50$SiO_2$ series as a function of relative Li_2O fraction, calculated using Eqs. 1.1 and 2.4, respectively. The solid line is the apparent trend, fit using a 2nd-order polynomial, while the dashed line is the linear fit between the two endmember compositions. Error is derived from density measurements.

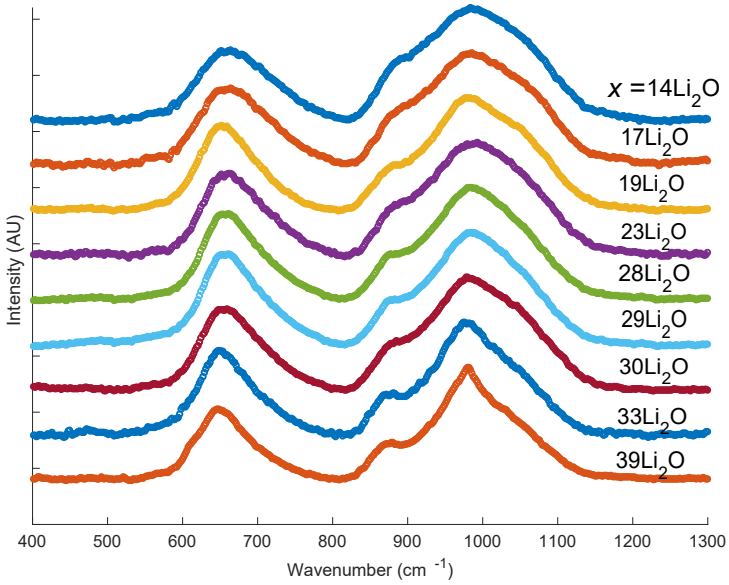

Figure D.41: Raman spectra of $x$$Li_2O$-(50−$x$)MgO-50$SiO_2$ glasses as a function of relative Li_2O ratio. General positions of structural Q^n-units are marked with dashed lines. The low and high-frequency regions are separated by brackets which correspond to Si-O-Si stretches and O-Si-O stretches, respectively.

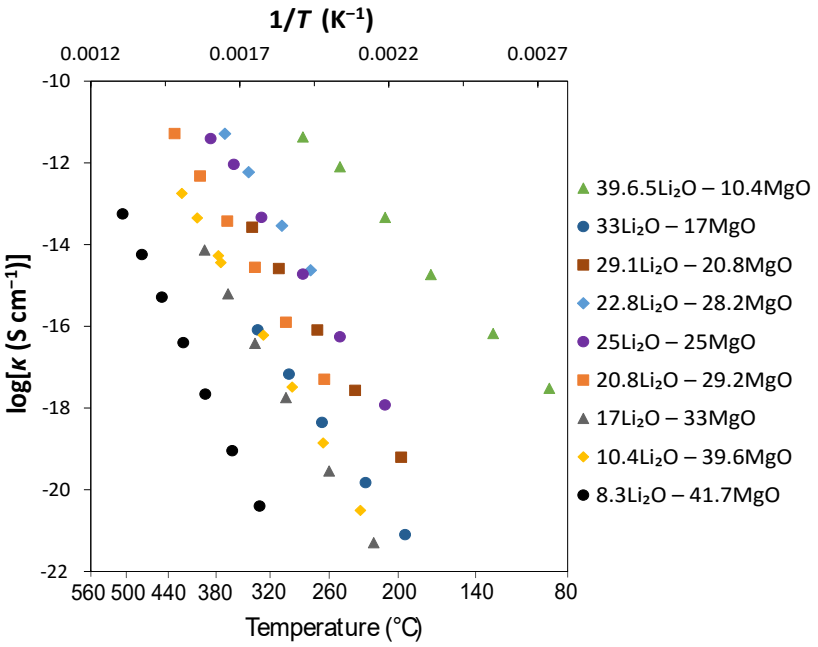

Figure D.42: Conductivity Arrhenius plots of logκ vs. 1000/T of the xLi$_2$O-(50$-x$)MgO-50SiO$_2$ series as a function of relative Li$_2$O fraction.

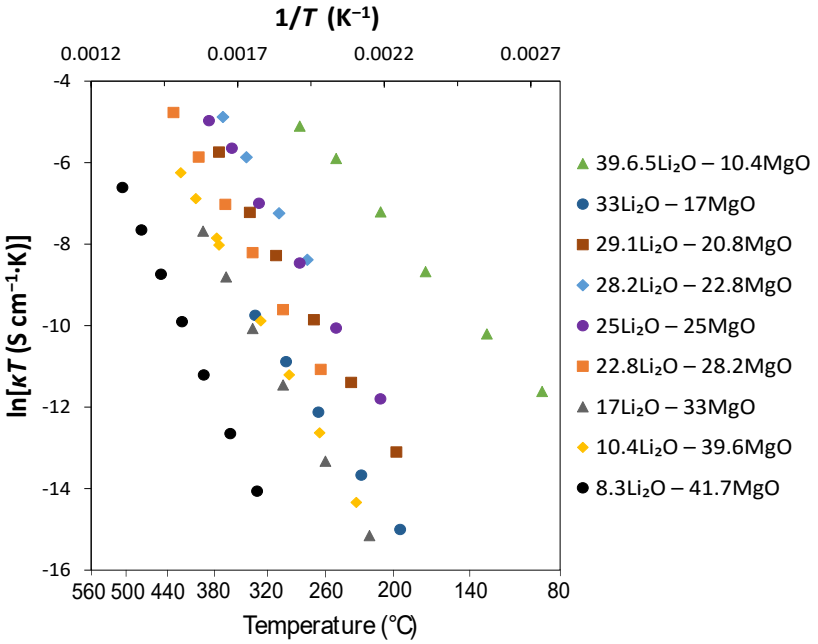

Figure D.43: Arrhenius plot of lnκT vs. 1000/T of the xLi$_2$O-(50$-x$)MgO-50SiO$_2$ series as a function of relative Li$_2$O fraction. Due to departure from Arrhenius behaviour, there are low-T and high-T linear fits for each composition. Common temperature point, T_0, is also plotted and is discussed later in the text.

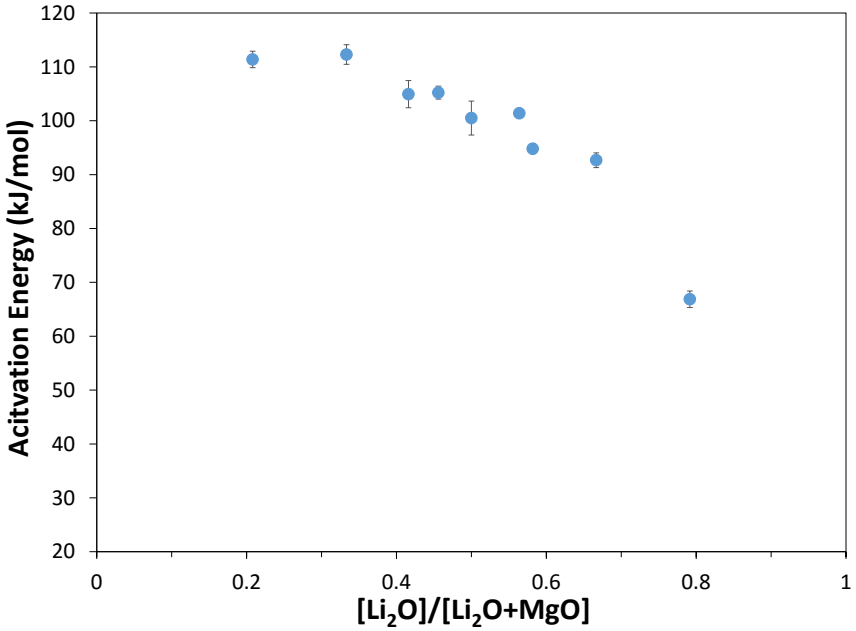

Figure D.44: Activation energy (E_a) of the xLi$_2$O-(50$-x$)MgO-50SiO$_2$ series as a function of relative Li$_2$O fraction. Low and high-T values are from their corresponding regions of the Arrhenius plot (Fig. 5.9).

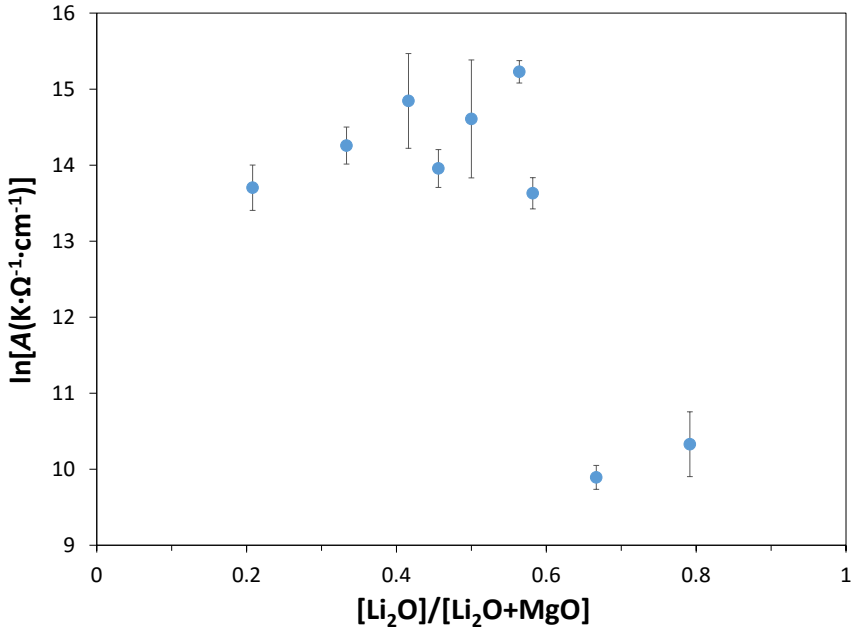

Figure D.45: Pre-exponential factor (A) of the xLi$_2$O-(50$-x$)MgO-50SiO$_2$ series as a function of relative Li$_2$O fraction. High and low temperature data is taken from the respective region in the Arrhenius plot (Fig. 5.9).

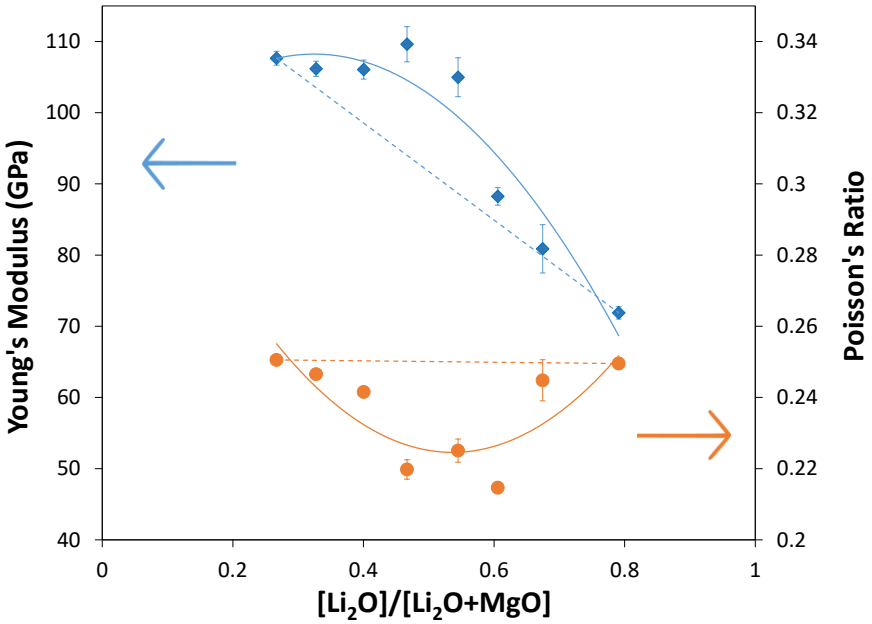

Figure D.46: Young's modulus (Y) and Poisson's ratio (μ) of the xLi$_2$O-(50$-x$)MgO-50SiO$_2$ series as a function of relative Li$_2$O fraction. Solid lines are the apparent trends fit with 2nd-order polynomials, while the dashed lines are linear fits between the two endmember compositions.

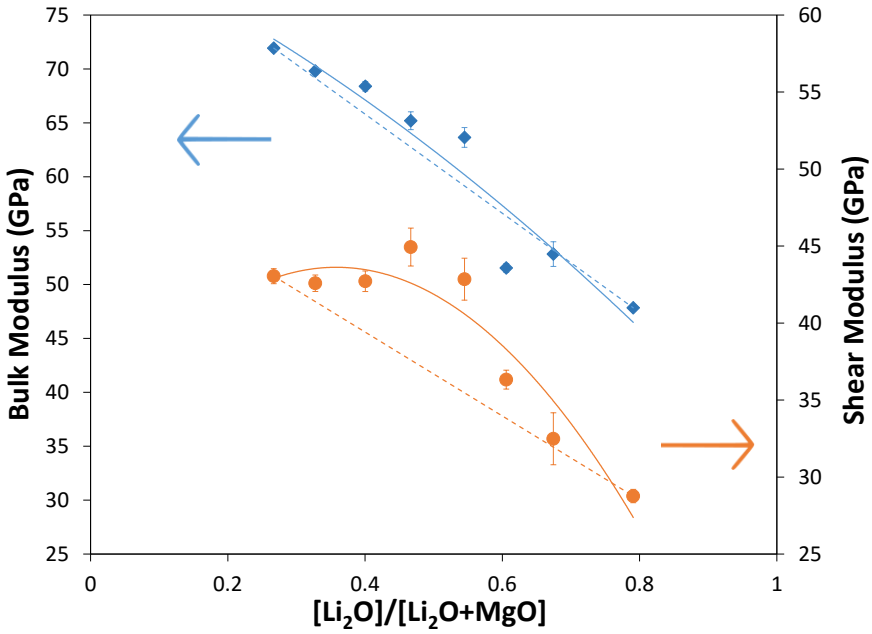

Figure D.47: Bulk modulus (K) and shear Modulus (G) of the xLi$_2$O-(50$-x$)MgO-50SiO$_2$ series as a function of relative Li$_2$O fraction. Solid lines are the apparent trends fit with 2nd-order polynomials, while the dashed lines are linear fits between the two endmember compositions.

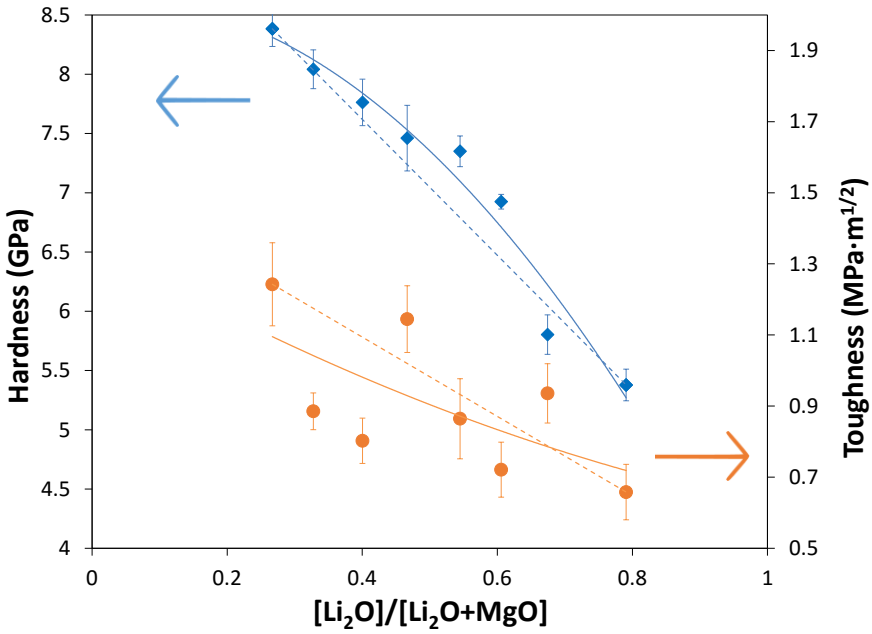

Figure D.48: Vickers hardness (H_{V}) and fracture toughness (K_{Ic}) of the $x\mathrm{Li_2O}$-$(50-x)\mathrm{MgO}$-$50\mathrm{SiO_2}$ series as a function of relative $\mathrm{Li_2O}$ fraction. Solid lines are the apparent trends fit with 2nd-order polynomials, while the dashed lines are linear fits between the two endmember compositions.

D.6 xLi$_2$O-(30−x)BaO-70SiO$_2$

Table D.5: Glass compositions of the xLi$_2$O-(30−x)BaO-70SiO$_2$ series analyzed by WDS, compared to their nominal compositions. Average errors of 1.5%, 1.3% and 2.7% for SiO$_2$, BaO and Li$_2$O, respectively.

[Li$_2$O]/[Li$_2$O+BaO]		SiO$_2$ (mol-%)		BaO (mol-%)		Li$_2$O (mol-%)	
Nominal	Actual	Nominal	Actual	Nominal	Actual	Nominal	Actual
0.50	0.49	70	75.7	15	12.4	15	11.8
0.67	0.61	70	73.0	10	10.4	20	16.4
0.83	0.80	70	74.2	5	5.2	25	20.5
1	0.99	70	68.5	0	0.4	30	31.4

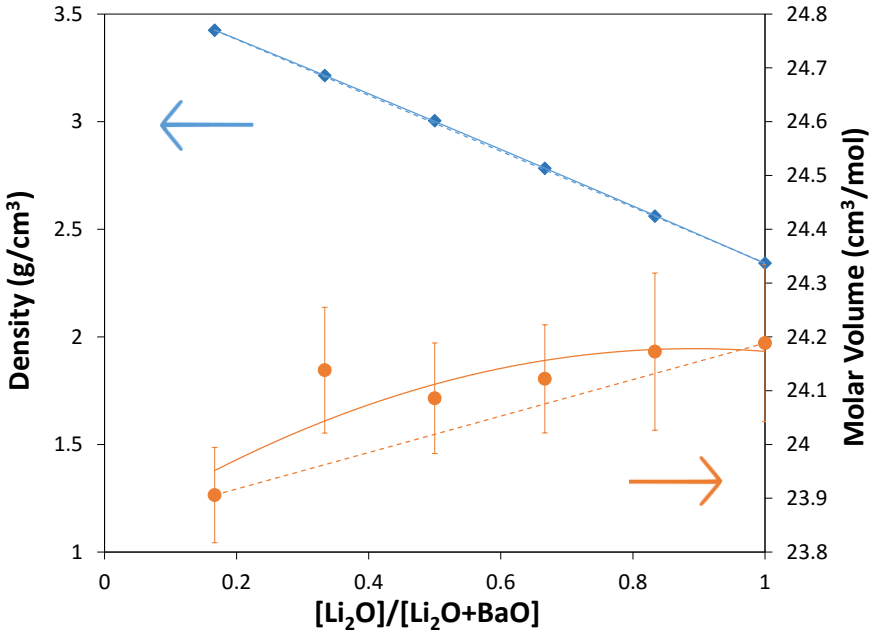

Figure D.49: Density (ρ) and the corresponding molar volume (V_m) aof the xLi$_2$O-(30−x)BaO-70SiO$_2$ series as a function of relative Li$_2$O fraction. Solid line is the apparent trend, fit using a 2nd-order polynomial, while the dashed line is the linear fit between the two endmember compositions. Error of ρ determined from three trials, ≈0.01 g/cm^3.

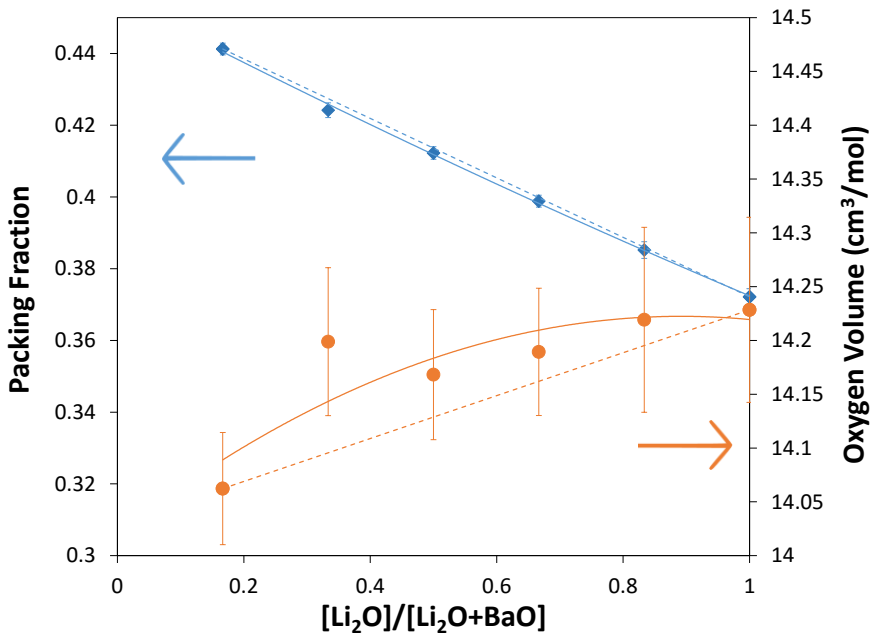

Figure D.50: Packing fraction (V_f) and oxygen volume (V_O) of the xLi$_2$O-(30−x)BaO-70SiO$_2$ series as a function of relative Li$_2$O fraction, calculated using Eqs. 1.1 and 2.4, respectively. The solid line is the apparent trend, fit using a 2nd-order polynomial, while the dashed line is the linear fit between the two endmember compositions. Error is derived from density measurements.

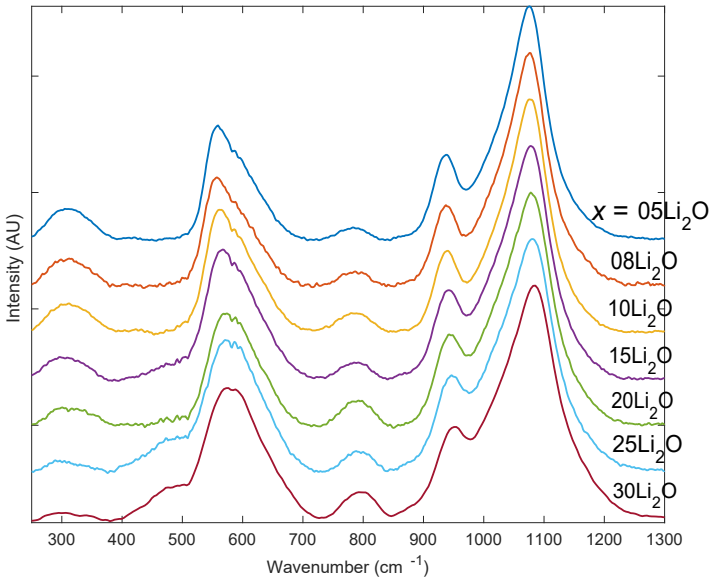

Figure D.51: Raman spectra of xLi$_2$O-(30−x)BaO-70SiO$_2$ glasses as a function of relative Li$_2$O ratio. General positions of structural Q^n-units are marked with dashed lines. The low and high-frequency regions are separated by brackets which correspond to Si-O-Si stretches and O-Si-O stretches, respectively.

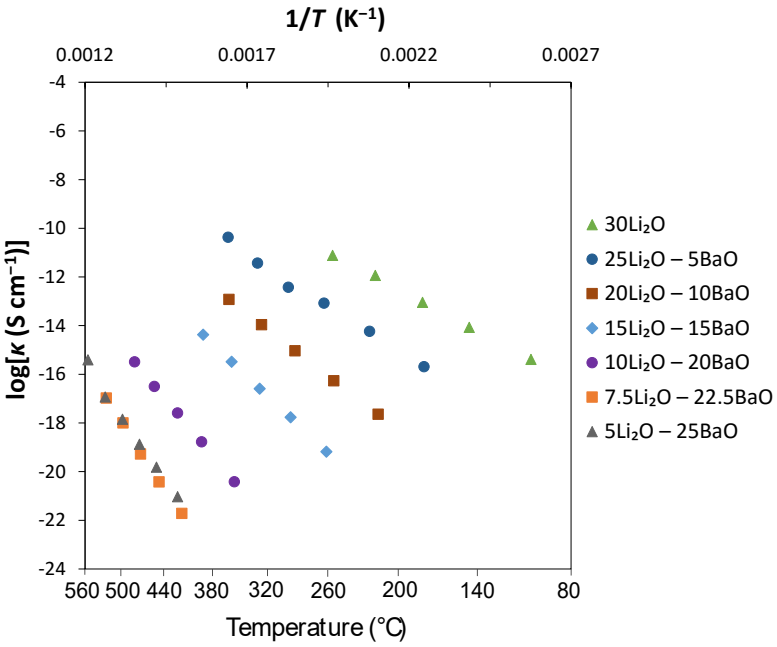

Figure D.52: Conductivity Arrhenius plots of logκ vs. 1000/T of the xLi$_2$O-(30−x)BaO-70SiO$_2$ series as a function of relative Li$_2$O fraction.

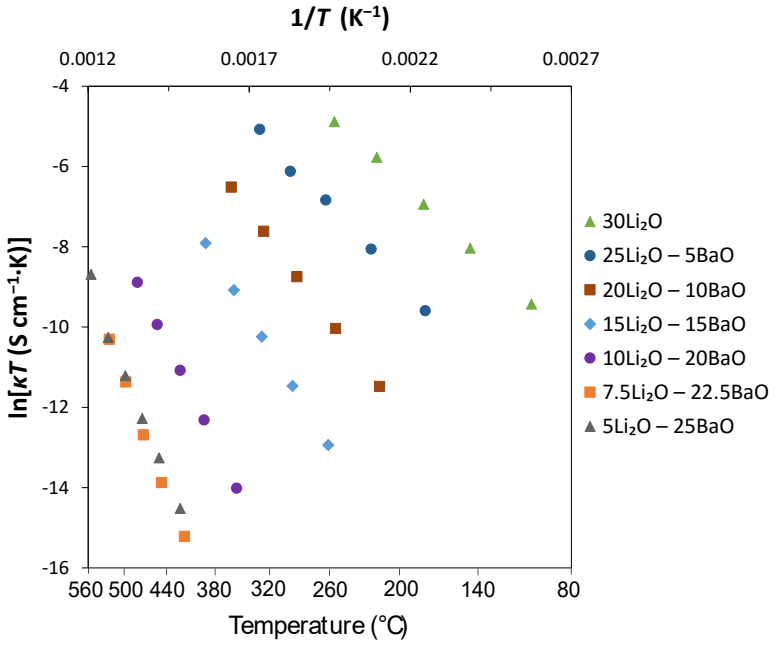

Figure D.53: Arrhenius plot of lnκT vs. 1000/T of the xLi$_2$O-(30−x)BaO-70SiO$_2$ series as a function of relative Li$_2$O fraction. Due to departure from Arrhenius behaviour, there are low-T and high-T linear fits for each composition. Common temperature point, T_0, is also plotted and is discussed later in the text.

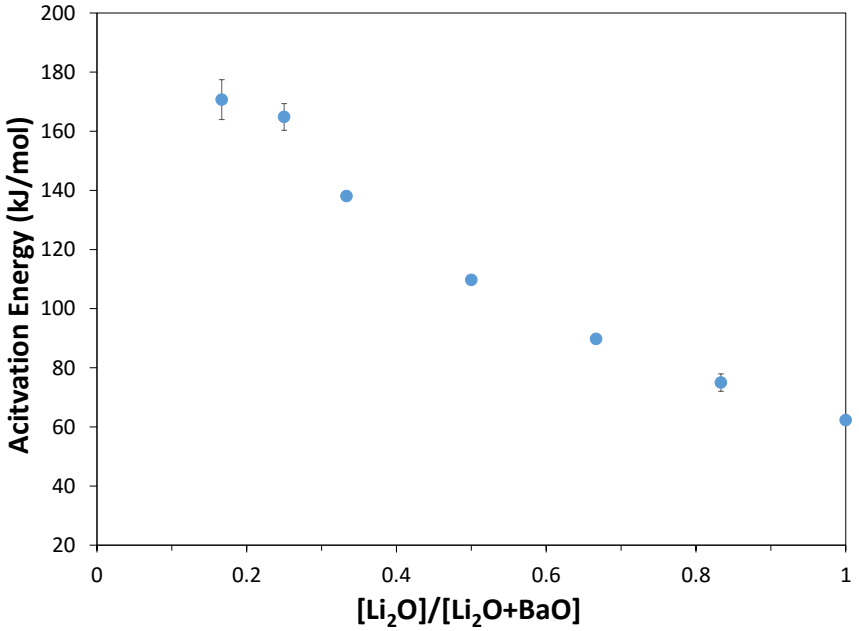

Figure D.54: Activation energy (E_a) of the xLi$_2$O-(30$-x$)BaO-70SiO$_2$ series as a function of relative Li$_2$O fraction. Low and high-T values are from their corresponding regions of the Arrhenius plot (Fig. 5.9).

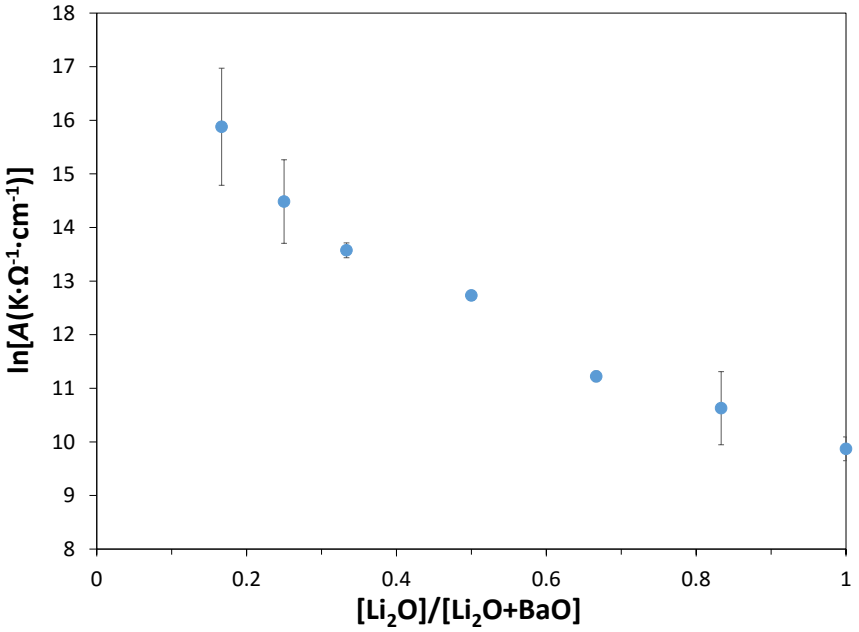

Figure D.55: Pre-exponential factor (A) of the xLi$_2$O-(30$-x$)BaO-70SiO$_2$ series as a function of relative Li$_2$O fraction. High and low temperature data is taken from the respective region in the Arrhenius plot (Fig. 5.9).

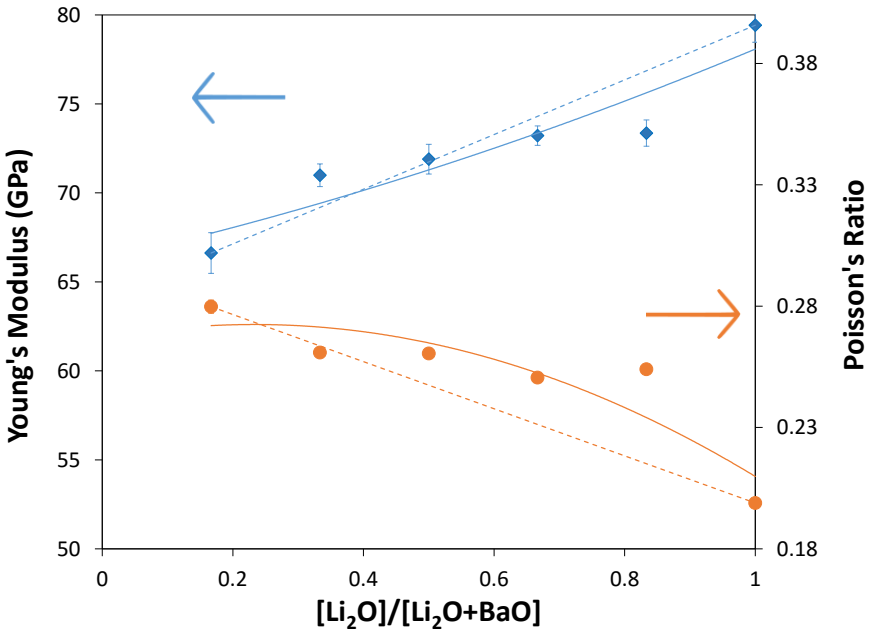

Figure D.56: Young's modulus (Y) and Poisson's ratio (μ) of the $x$$Li_2O$-(30−$x$)BaO-70$SiO_2$ series as a function of relative Li_2O fraction. Solid lines are the apparent trends fit with 2nd-order polynomials, while the dashed lines are linear fits between the two endmember compositions.

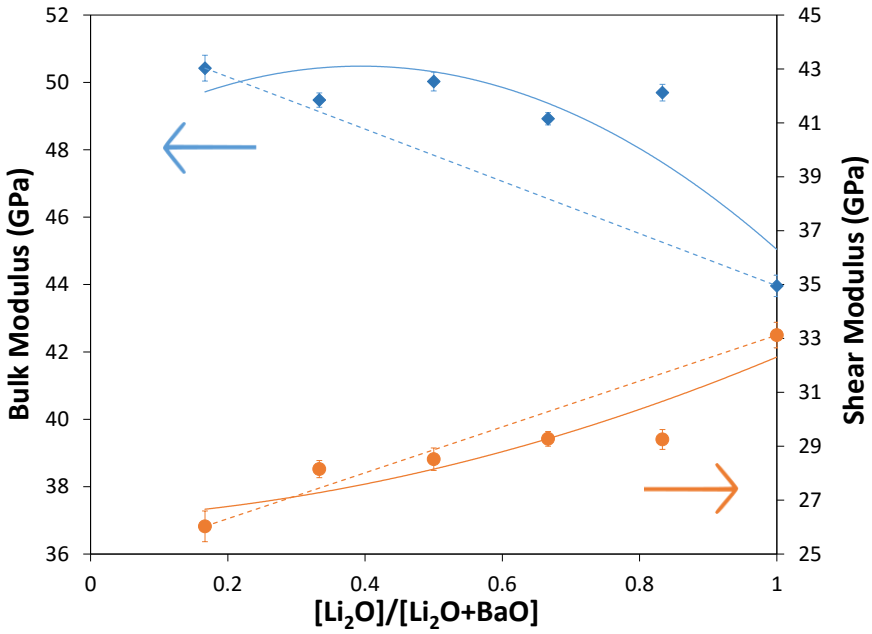

Figure D.57: Bulk modulus (K) and shear Modulus (G) of the $x$$Li_2O$-(30−$x$)BaO-70$SiO_2$ series as a function of relative Li_2O fraction. Solid lines are the apparent trends fit with 2nd-order polynomials, while the dashed lines are linear fits between the two endmember compositions.

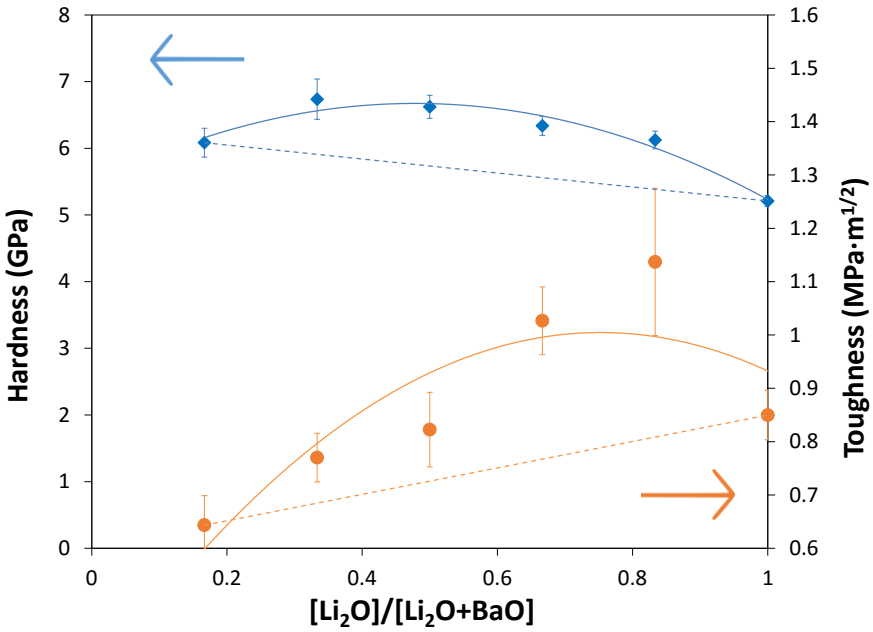

Figure D.58: Vickers hardness (H_{V}) and fracture toughness (K_{Ic}) of the $x\mathrm{Li_2O}$-$(30-x)\mathrm{BaO}$-$70\mathrm{SiO_2}$ series as a function of relative $\mathrm{Li_2O}$ fraction. Solid lines are the apparent trends fit with 2nd-order polynomials, while the dashed lines are linear fits between the two endmember compositions.

D.7 $x\mathrm{K_2O}$-$(30-x)$BaO-70$\mathrm{SiO_2}$

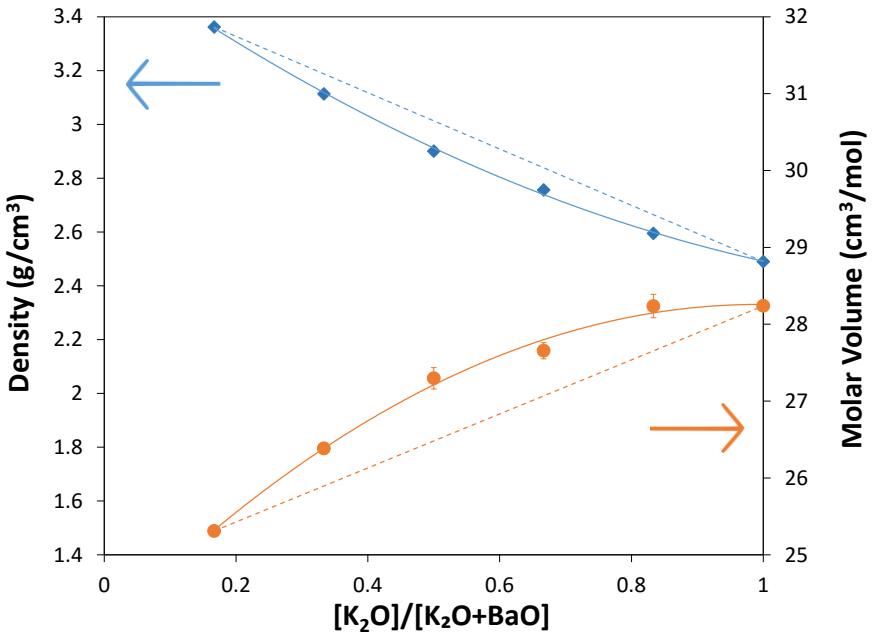

Figure D.59: Density (ρ) and the corresponding molar volume (V_m) aof the $x\mathrm{K_2O}$-$(30-x)$BaO-70$\mathrm{SiO_2}$ series as a function of relative $\mathrm{K_2O}$ fraction. Solid line is the apparent trend, fit using a 2nd-order polynomial, while the dashed line is the linear fit between the two endmember compositions. Error of ρ determined from three trials, $\approx$0.01 g/cm^3.

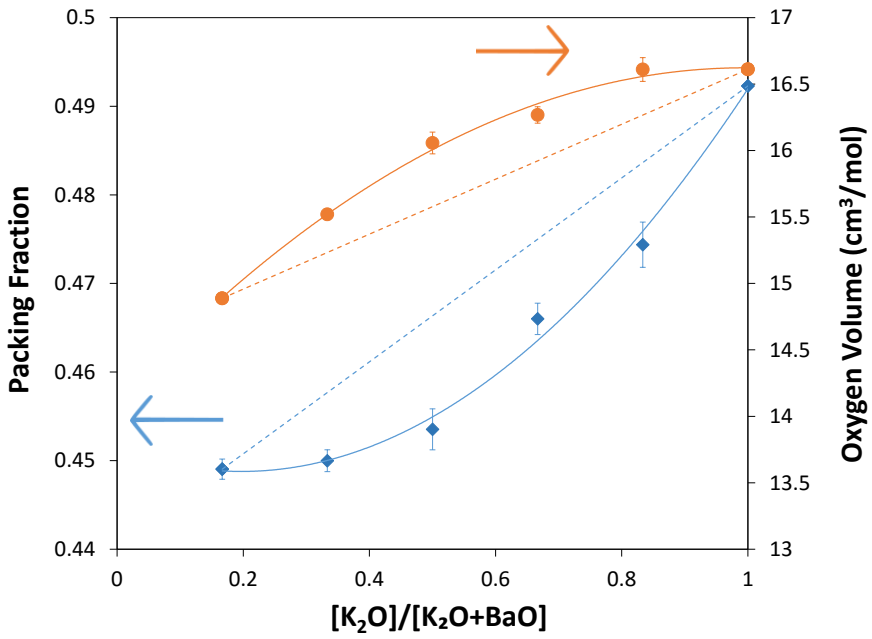

Figure D.60: Packing fraction (V_f) and oxygen volume (V_O) of the xK$_2$O-(30−x)BaO-70SiO$_2$ series as a function of relative K$_2$O fraction, calculated using Eqs. 1.1 and 2.4, respectively. The solid line is the apparent trend, fit using a 2nd-order polynomial, while the dashed line is the linear fit between the two endmember compositions. Error is derived from density measurements.

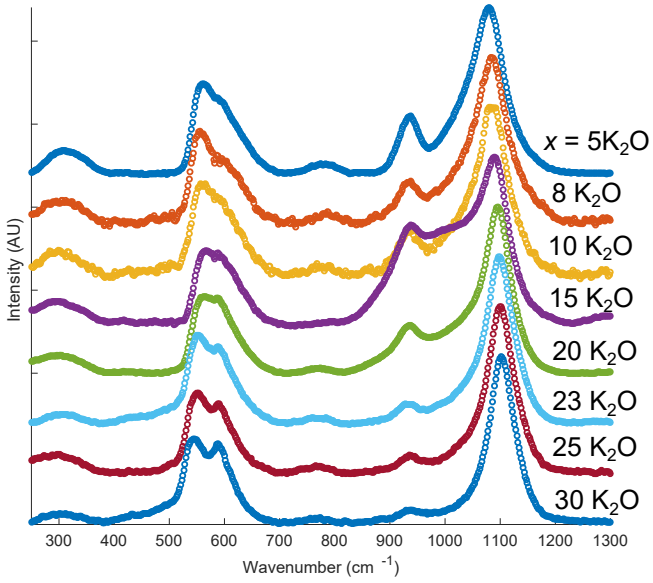

Figure D.61: Raman spectra of xK$_2$O-(30−x)BaO-70SiO$_2$ glasses as a function of relative K$_2$O ratio. General positions of structural Q^n-units are marked with dashed lines. The low and high-frequency regions are separated by brackets which correspond to Si-O-Si stretches and O-Si-O stretches, respectively.

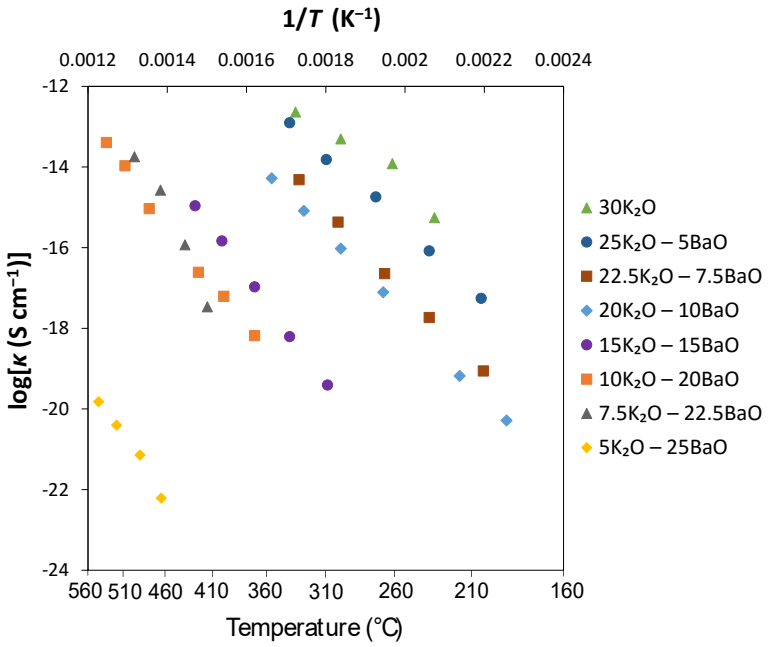

Figure D.62: Conductivity Arrhenius plots of logκ vs. 1000/T of the xK$_2$O-(30−x)BaO-70SiO$_2$ series as a function of relative K$_2$O fraction.

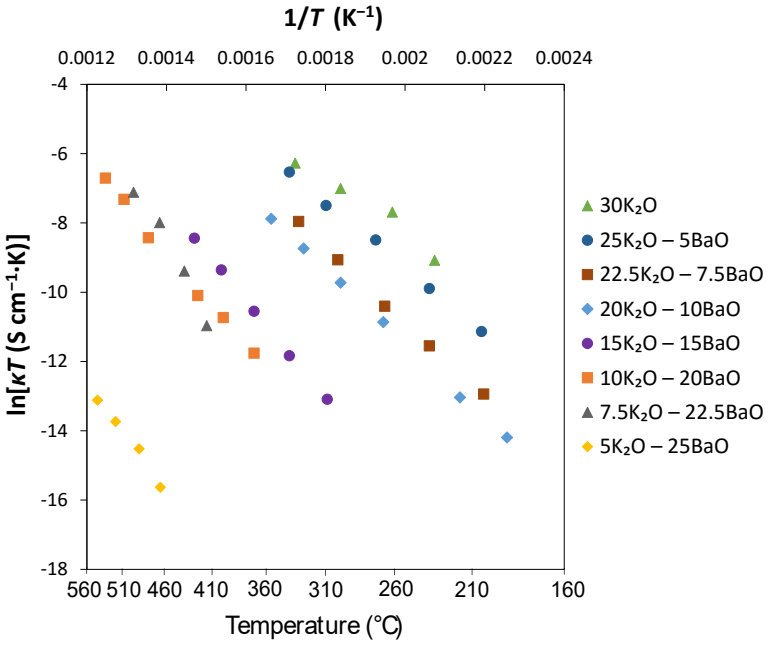

Figure D.63: Arrhenius plot of lnκT vs. 1000/T of the xK$_2$O-(30−x)BaO-70SiO$_2$ series as a function of relative K$_2$O fraction. Due to departure from Arrhenius behaviour, there are low-T and high-T linear fits for each composition. Common temperature point, T_0, is also plotted and is discussed later in the text.

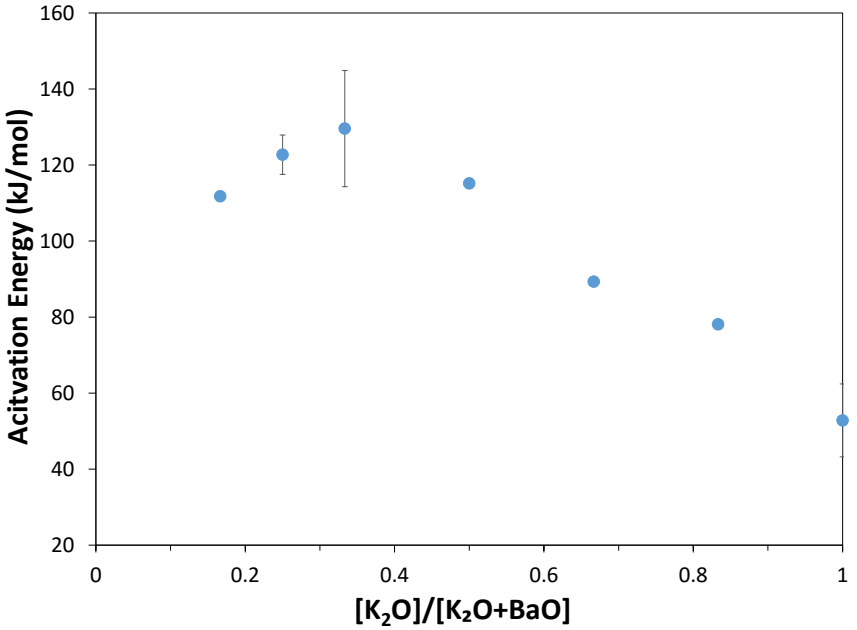

Figure D.64: Activation energy (E_a) of the xK$_2$O-(30−x)BaO-70SiO$_2$ series as a function of relative K$_2$O fraction. Low and high-T values are from their corresponding regions of the Arrhenius plot (Fig. 5.9).

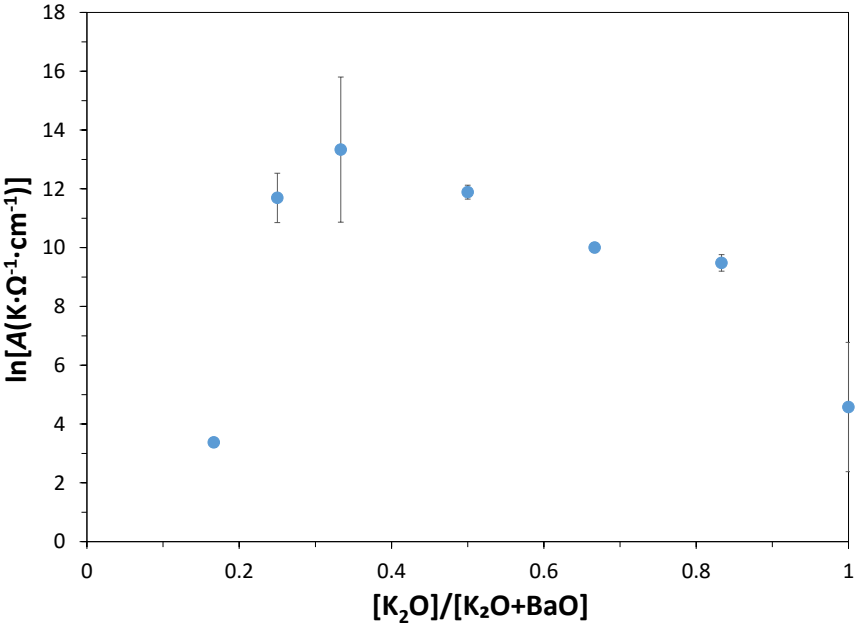

Figure D.65: Pre-exponential factor (A) of the xK$_2$O-(30−x)BaO-70SiO$_2$ series as a function of relative K$_2$O fraction. High and low temperature data is taken from the respective region in the Arrhenius plot (Fig. 5.9).

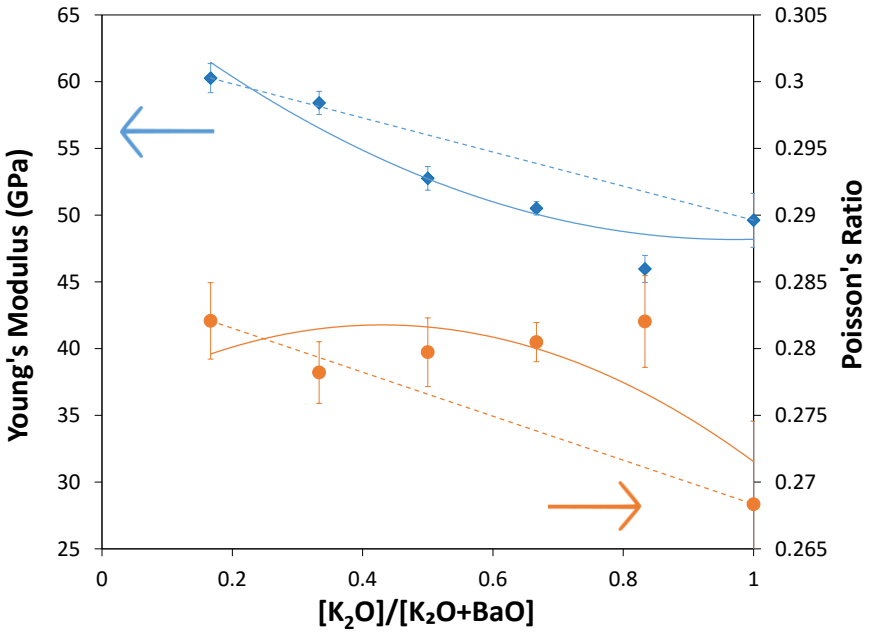

Figure D.66: Young's modulus (Y) and Poisson's ratio (μ) of the xK$_2$O-(30$-x$)BaO-70SiO$_2$ series as a function of relative K$_2$O fraction. Solid lines are the apparent trends fit with 2nd-order polynomials, while the dashed lines are linear fits between the two endmember compositions.

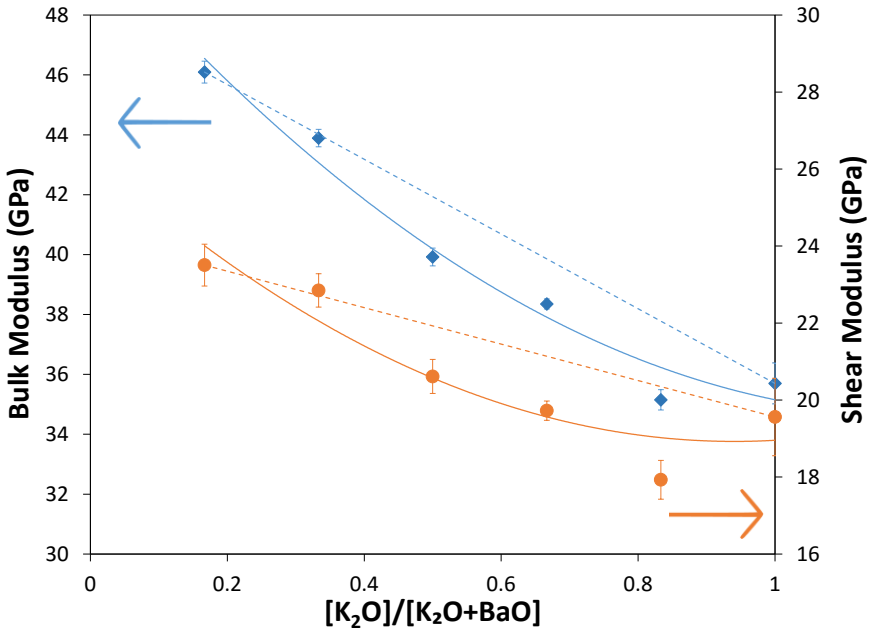

Figure D.67: Bulk modulus (K) and shear Modulus (G) of the xK$_2$O-(30$-x$)BaO-70SiO$_2$ series as a function of relative K$_2$O fraction. Solid lines are the apparent trends fit with 2nd-order polynomials, while the dashed lines are linear fits between the two endmember compositions.

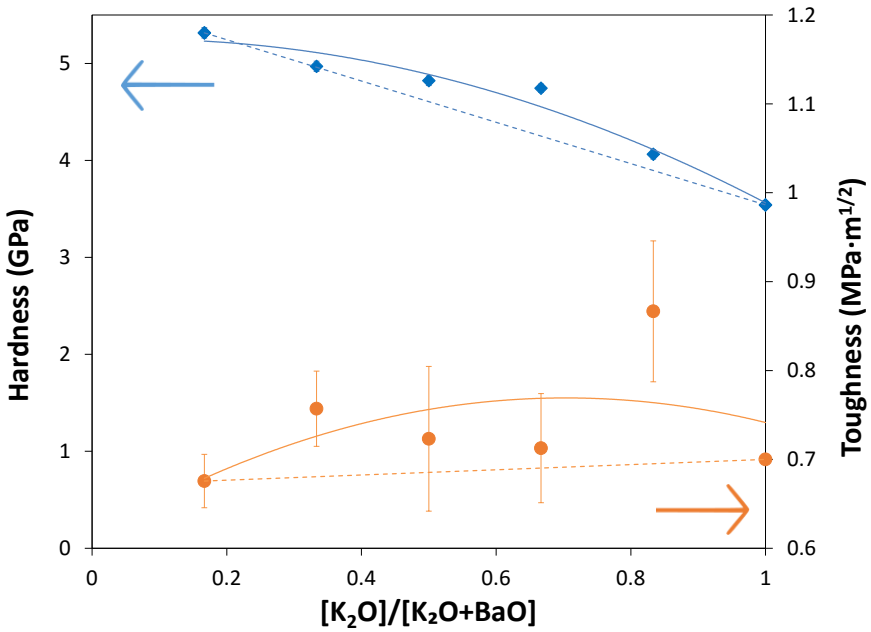

Figure D.68: Vickers hardness (H_{V}) and fracture toughness (K_{Ic}) of the $x\mathrm{K_2O}$-$(30-x)\mathrm{BaO}$-$70\mathrm{SiO_2}$ series as a function of relative $\mathrm{K_2O}$ fraction. Solid lines are the apparent trends fit with 2nd-order polynomials, while the dashed lines are linear fits between the two endmember compositions.

D.8 $x\mathrm{K_2O}$-$(40-x)$MgO-60$\mathrm{SiO_2}$

Table D.6: Glass compositions of the $x\mathrm{K_2O}$-$(40-x)$MgO-60$\mathrm{SiO_2}$ series analyzed by WDS, compared to their nominal compositions. Instrumental error is 0.1–0.16 mol-%, while standard error of the five points was $\leq$ 0.6, 0.9 and 0.4 mol-% for MgO, $\mathrm{SiO_2}$ and $\mathrm{K_2O}$, respectively.

[$\mathrm{K_2O}$]/[$\mathrm{K_2O}$+MgO])		$\mathrm{SiO_2}$ (mol-%)		MgO (mol-%)		$\mathrm{K_2O}$ (mol-%)	
Nominal	Actual	Nominal	Actual	Nominal	Actual	Nominal	Actual
0.17	0.17	60	59.1	33.3	33.9	6.7	6.9
0.21	0.24	60	62.0	31.6	29.0	8.3	9.0
0.25	0.28	60	58.8	30	29.6	10	11.6
0.33	0.30	60	60.6	26.7	27.5	13.3	11.9

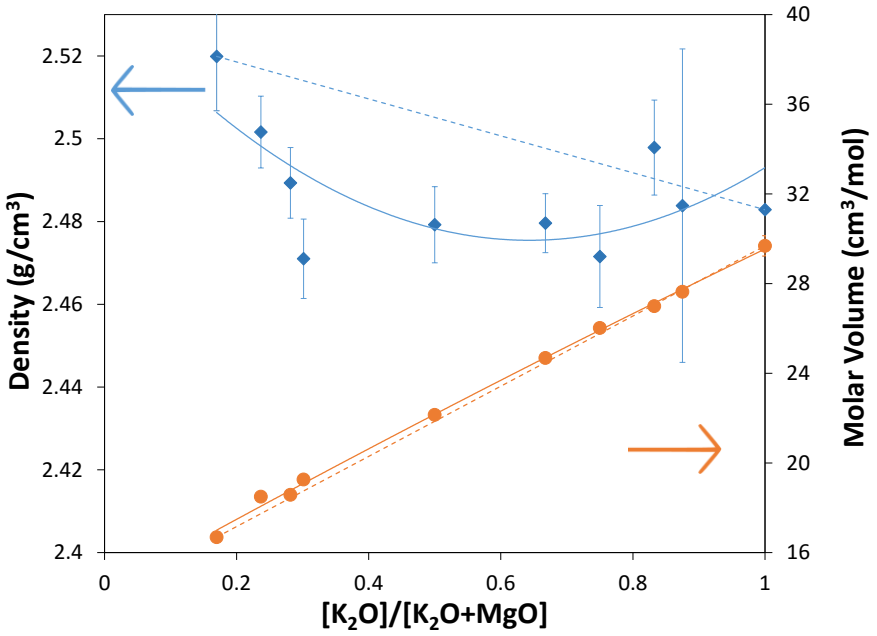

Figure D.69: Density (ρ) and the corresponding molar volume (V_m) aof the $x\mathrm{K_2O}$-$(40-x)$MgO-60$\mathrm{SiO_2}$ series as a function of relative $\mathrm{K_2O}$ fraction. Solid line is the apparent trend, fit using a 2nd-order polynomial, while the dashed line is the linear fit between the two endmember compositions. Error of ρ determined from three trials, $\approx$0.01 g/cm^3.

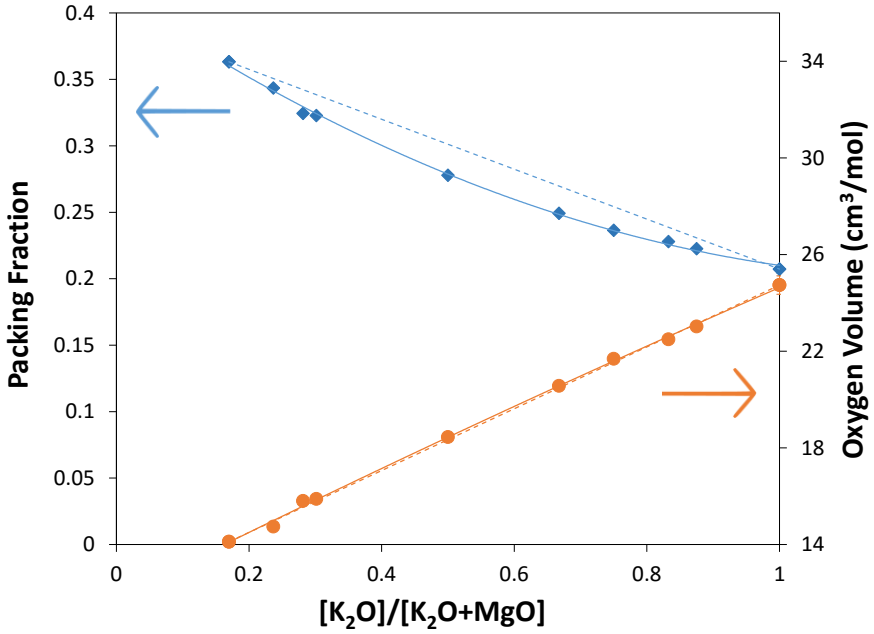

Figure D.70: Packing fraction (V_f) and oxygen volume (V_O) of the xK$_2$O-(40−x)MgO-60SiO$_2$ series as a function of relative K$_2$O fraction, calculated using Eqs. 1.1 and 2.4, respectively. The solid line is the apparent trend, fit using a 2nd-order polynomial, while the dashed line is the linear fit between the two endmember compositions. Error is derived from density measurements.

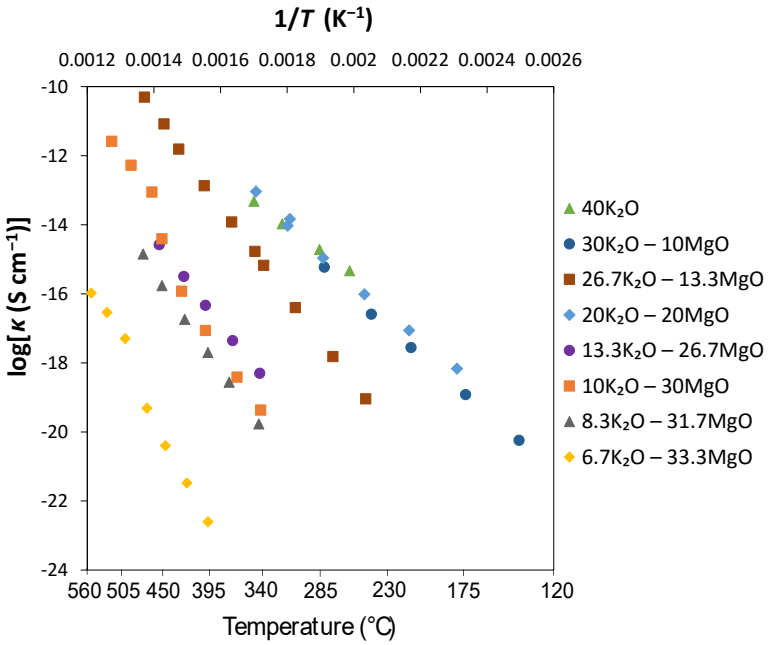

Figure D.71: Conductivity Arrhenius plots of logκ vs. 1000/T of the xK$_2$O-(40−x)MgO-60SiO$_2$ series as a function of relative K$_2$O fraction.

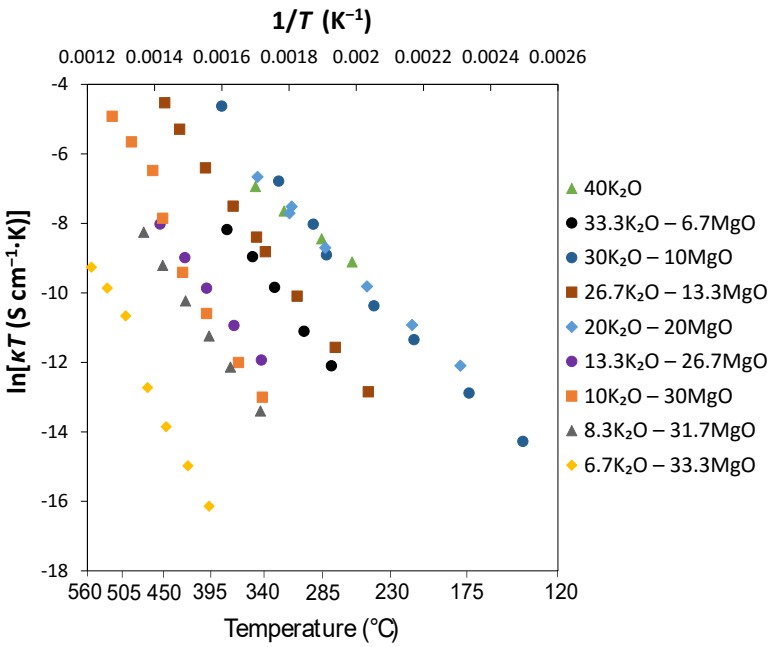

Figure D.72: Arrhenius plot of lnκT vs. 1000/T of the xK$_2$O-(40$-x$)MgO-60SiO$_2$ series as a function of relative K$_2$O fraction. Due to departure from Arrhenius behaviour, there are low-T and high-T linear fits for each composition. Common temperature point, T_0, is also plotted and is discussed later in the text.

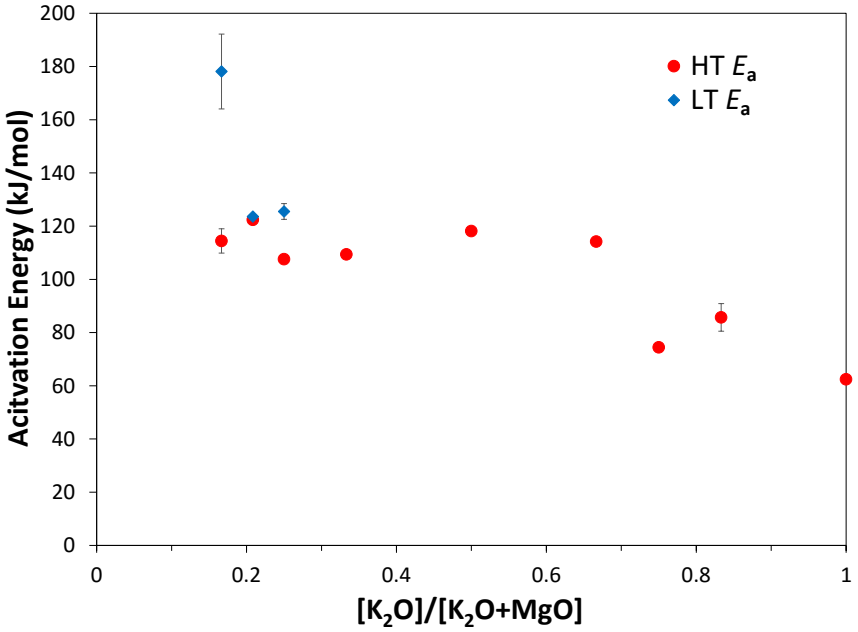

Figure D.73: Activation energy (E_a) of the xK$_2$O-(40$-x$)MgO-60SiO$_2$ series as a function of relative K$_2$O fraction. Low and high-T values are from their corresponding regions of the Arrhenius plot (Fig. 5.9).

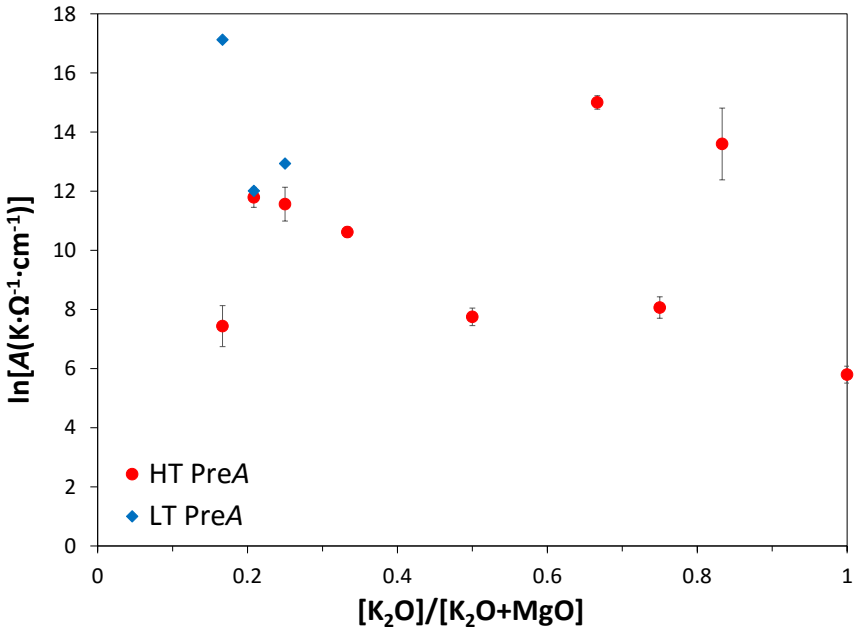

Figure D.74: Pre-exponential factor (A) of the xK$_2$O-(40$-x$)MgO-60SiO$_2$ series as a function of relative K$_2$O fraction. High and low temperature data is taken from the respective region in the Arrhenius plot (Fig. 5.9).

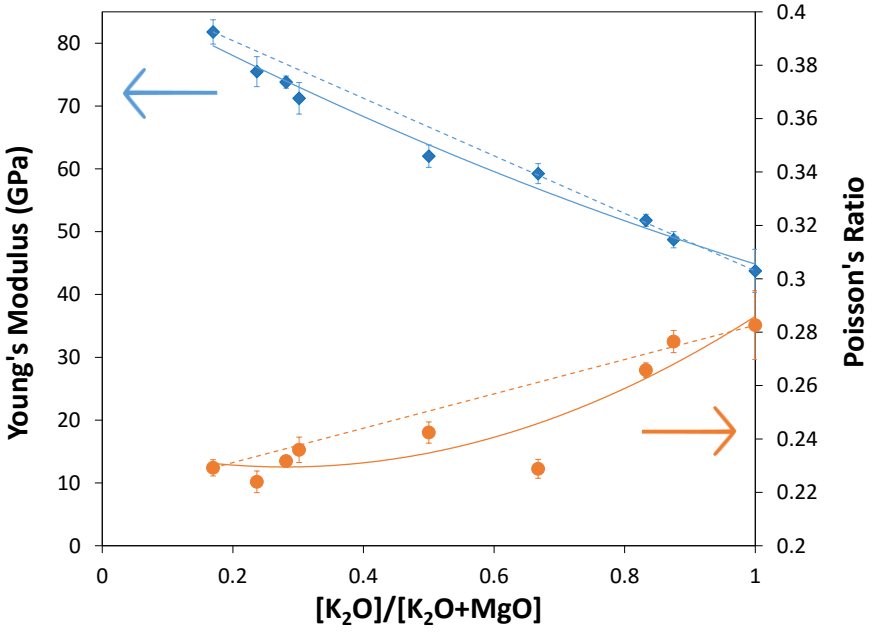

Figure D.75: Young's modulus (Y) and Poisson's ratio (μ) of the xK$_2$O-(40$-x$)MgO-60SiO$_2$ series as a function of relative K$_2$O fraction. Solid lines are the apparent trends fit with 2nd-order polynomials, while the dashed lines are linear fits between the two endmember compositions.

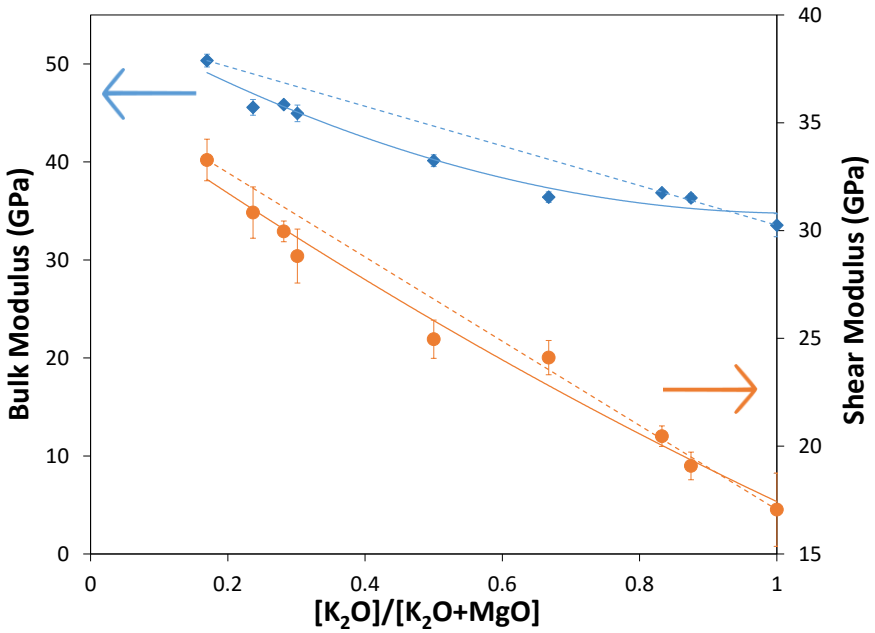

Figure D.76: Bulk modulus (K) and shear Modulus (G) of the xK$_2$O-(40$-x$)MgO-60SiO$_2$ series as a function of relative K$_2$O fraction. Solid lines are the apparent trends fit with 2nd-order polynomials, while the dashed lines are linear fits between the two endmember compositions.

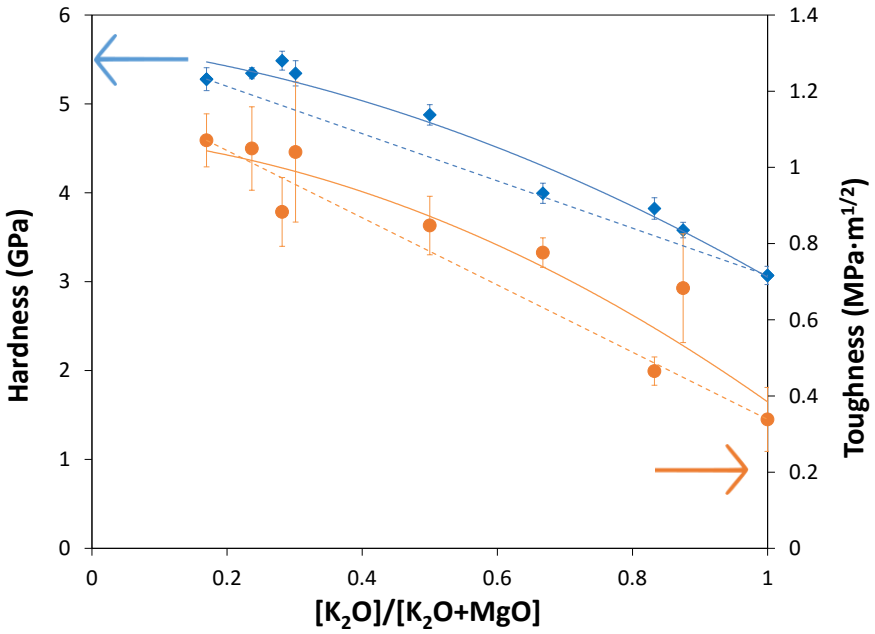

Figure D.77: Vickers hardness (H_V) and fracture toughness (K_Ic) of the xK$_2$O-(40$-x$)MgO-60SiO$_2$ series as a function of relative K$_2$O fraction. Solid lines are the apparent trends fit with 2nd-order polynomials, while the dashed lines are linear fits between the two endmember compositions.

D.9 xLi$_2$O-(30−x)ZnO-70SiO$_2$

Table D.7: Glass compositions of the xLi$_2$O-(30−x)ZnO-70SiO$_2$ series analyzed by WDS, compared to their nominal compositions. Average errors of 1.2%, 1.1% and 1.9% for SiO$_2$, ZnO and Li$_2$O, respectively.

[Li$_2$O]/[Li$_2$O+ZnO]		SiO$_2$ (mol-%)		ZnO (mol-%)		Li$_2$O (mol-%)	
Nominal	Actual	Nominal	Actual	Nominal	Actual	Nominal	Actual
0.25	0.11	70	74.8	22.5	22.4	7.5	2.7
0.33	0.23	70	70.6	20	22.5	10	6.8
0.42	0.27	70	73.9	17.5	19.1	12.5	6.9
0.50	0.46	70	67.2	15	17.5	15	15.2
0.67	0.63	70	69.2	10	11.5	20	19.3
0.83	0.81	70	69.2	5	5.9	25	24.8
0.90	0.88	70	72.1	3	3.4	27	24.4
1.00	0.99	70	74.0	0	0.2	30	25.8

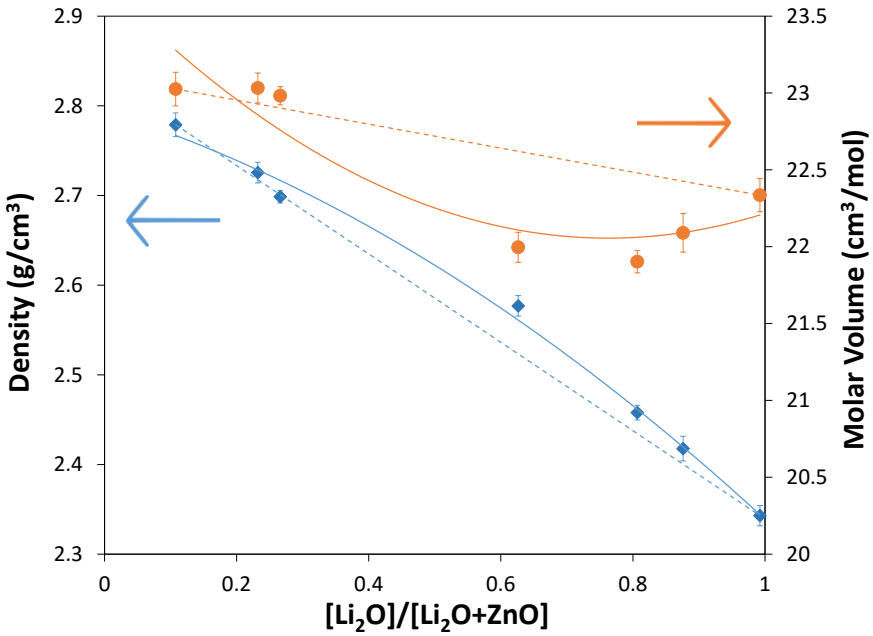

Figure D.78: Density (ρ) and the corresponding molar volume (V_m) aof the xLi$_2$O-(30−x)ZnO-70SiO$_2$ series as a function of relative Li$_2$O fraction. Solid line is the apparent trend, fit using a 2nd-order polynomial, while the dashed line is the linear fit between the two endmember compositions. Error of ρ determined from three trials, ≈0.01 g/cm^3.

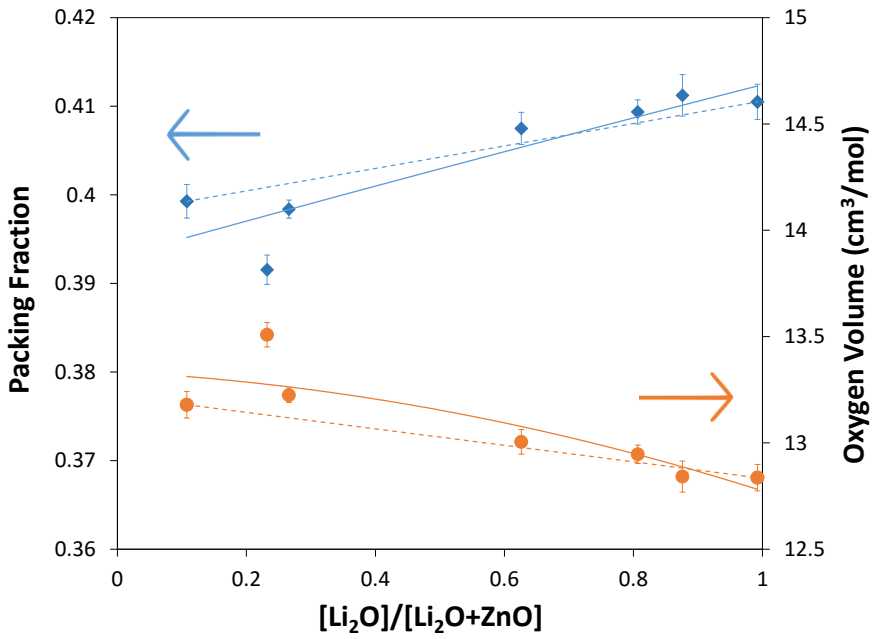

Figure D.79: Packing fraction (V_f) and oxygen volume (V_O) of the xLi$_2$O-(30−x)ZnO-70SiO$_2$ series as a function of relative Li$_2$O fraction, calculated using Eqs. 1.1 and 2.4, respectively. The solid line is the apparent trend, fit using a 2nd-order polynomial, while the dashed line is the linear fit between the two endmember compositions. Error is derived from density measurements.

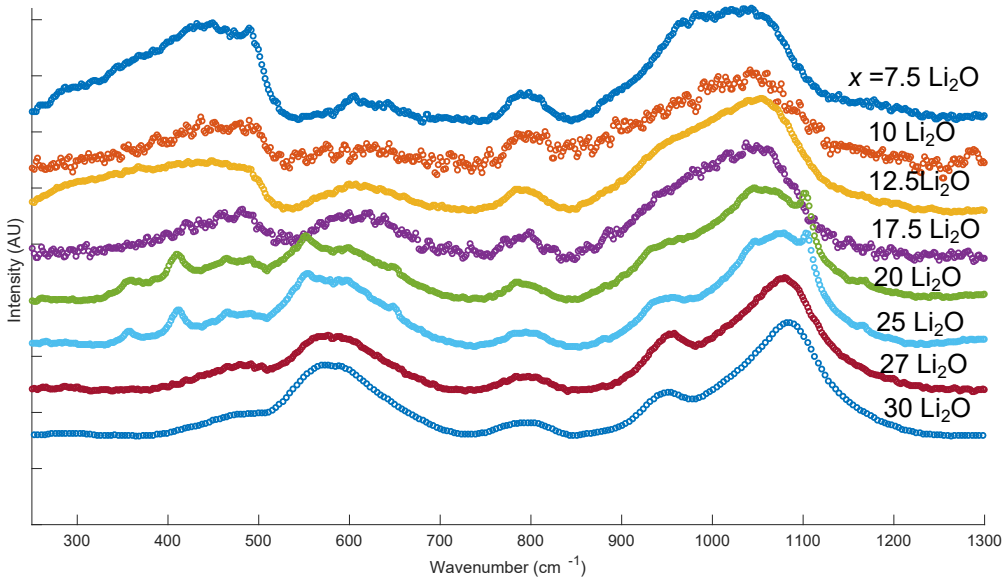

Figure D.80: Raman spectra of xLi$_2$O-(30−x)ZnO-70SiO$_2$ glasses as a function of relative Li$_2$O ratio. General positions of structural Q^n-units are marked with dashed lines. The low and high-frequency regions are separated by brackets which correspond to Si-O-Si stretches and O-Si-O stretches, respectively.

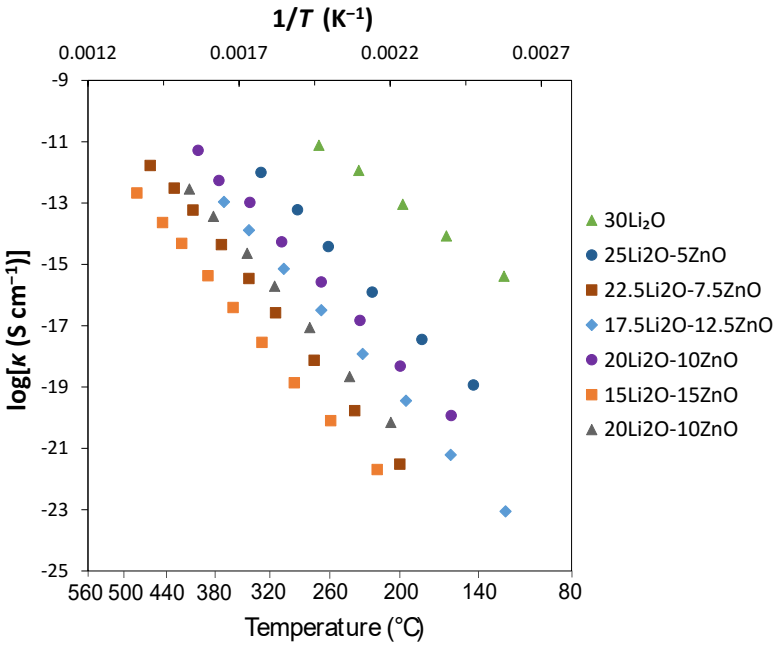

Figure D.81: Conductivity Arrhenius plots of logκ vs. 1000/T of the xLi$_2$O-(30$-x$)ZnO-70SiO$_2$ series as a function of relative Li$_2$O fraction.

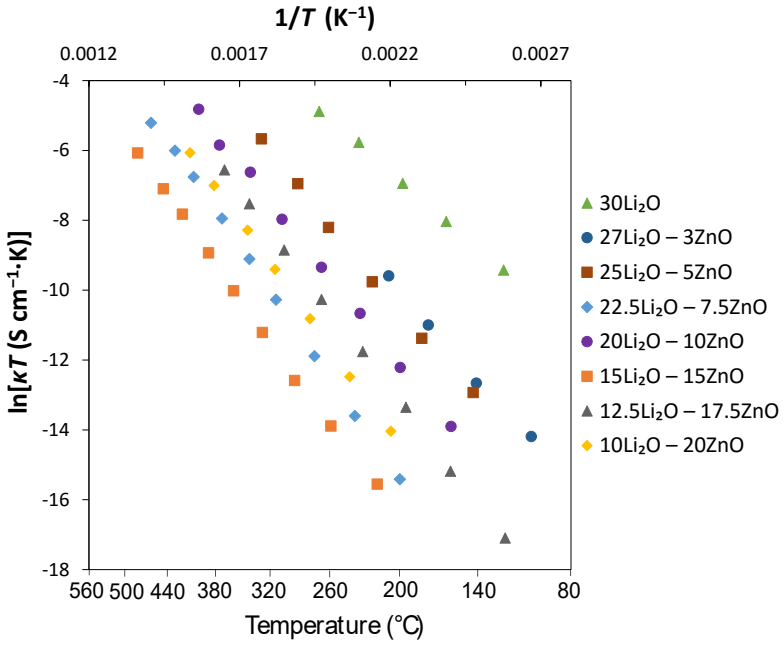

Figure D.82: Arrhenius plot of lnκT vs. 1000/T of the xLi$_2$O-(30$-x$)ZnO-70SiO$_2$ series as a function of relative Li$_2$O fraction. Due to departure from Arrhenius behaviour, there are low-T and high-T linear fits for each composition. Common temperature point, T_0, is also plotted and is discussed later in the text.

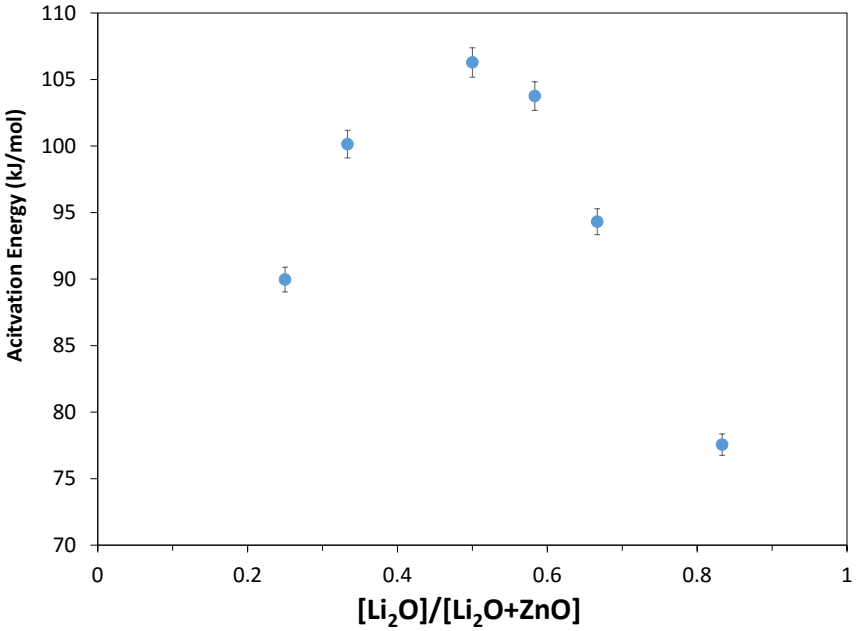

Figure D.83: Activation energy (E_a) of the xLi$_2$O-(30$-x$)ZnO-70SiO$_2$ series as a function of relative Li$_2$O fraction. Low and high-T values are from their corresponding regions of the Arrhenius plot (Fig. 5.9).

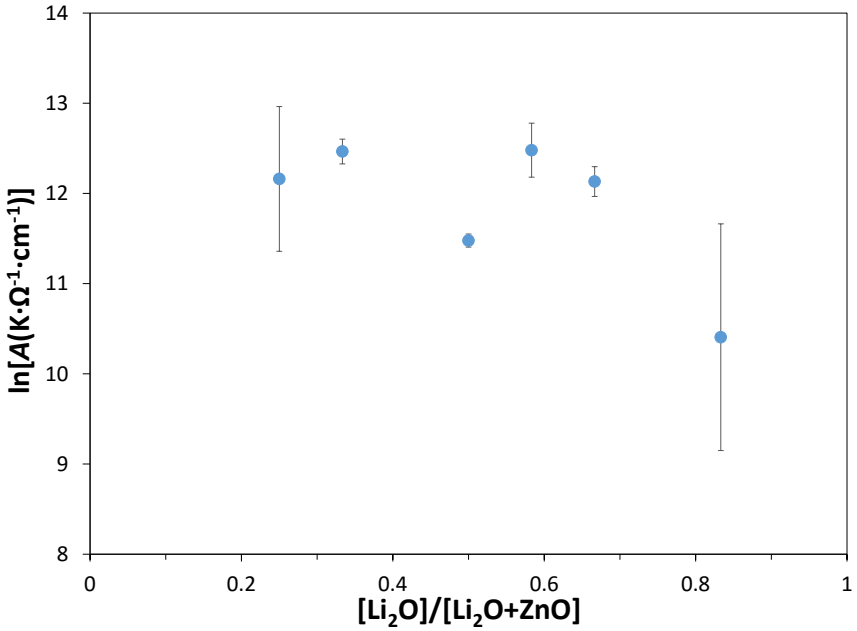

Figure D.84: Pre-exponential factor (A) of the xLi$_2$O-(30$-x$)ZnO-70SiO$_2$ series as a function of relative Li$_2$O fraction. High and low temperature data is taken from the respective region in the Arrhenius plot (Fig. 5.9).

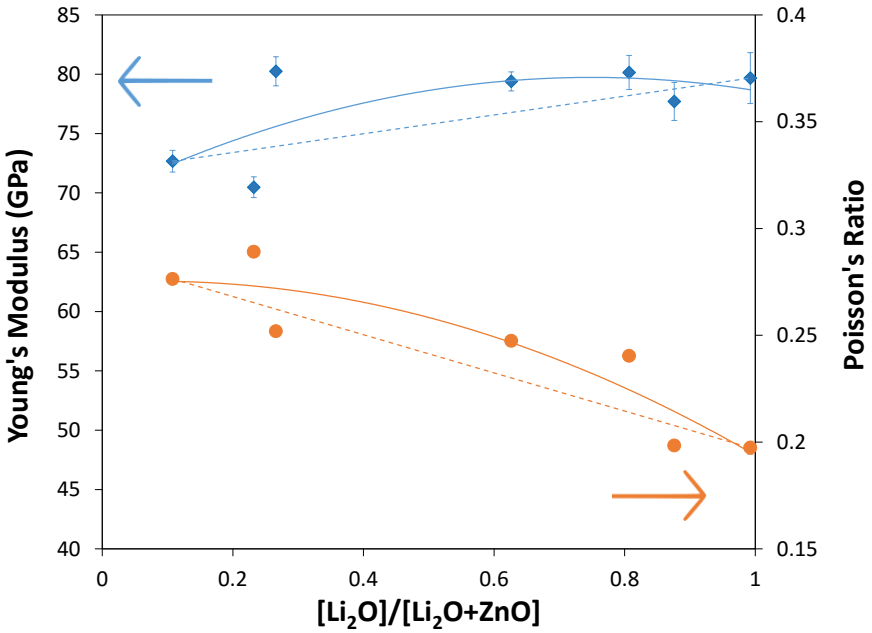

Figure D.85: Young's modulus (Y) and Poisson's ratio (μ) of the $x$$Li_2O$-(30−$x$)ZnO-70$SiO_2$ series as a function of relative Li_2O fraction. Solid lines are the apparent trends fit with 2nd-order polynomials, while the dashed lines are linear fits between the two endmember compositions.

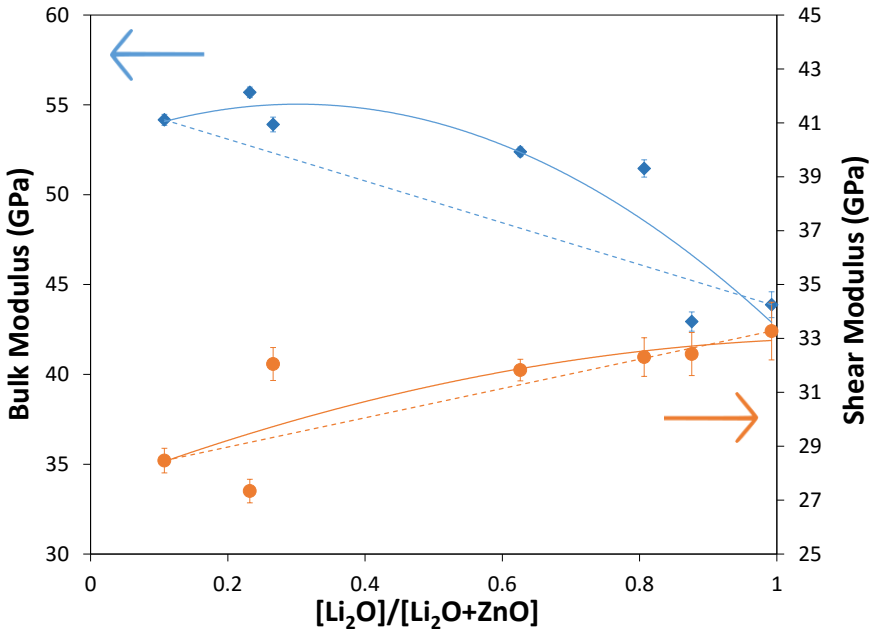

Figure D.86: Bulk modulus (K) and shear Modulus (G) of the $x$$Li_2O$-(30−$x$)ZnO-70$SiO_2$ series as a function of relative Li_2O fraction. Solid lines are the apparent trends fit with 2nd-order polynomials, while the dashed lines are linear fits between the two endmember compositions.

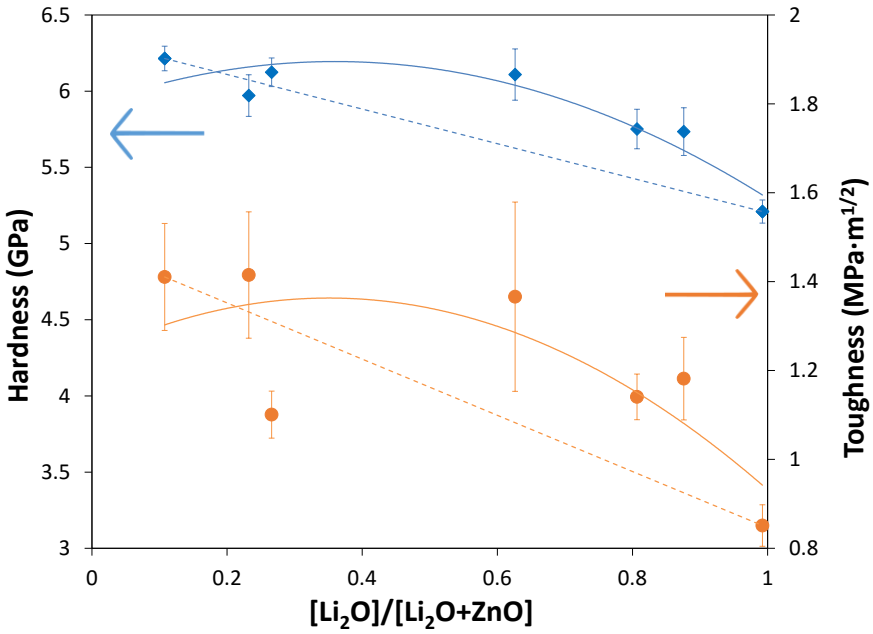

Figure D.87: Vickers hardness (H_{V}) and fracture toughness (K_{Ic}) of the $x\mathrm{Li_2O}$-$(30-x)\mathrm{ZnO}$-$70\mathrm{SiO_2}$ series as a function of relative $\mathrm{Li_2O}$ fraction. Solid lines are the apparent trends fit with 2nd-order polynomials, while the dashed lines are linear fits between the two endmember compositions.

D.10 Permissions to Reproduce Copywritten Materials

My Orders My Library My Profile

Welcome etchersketcher@gmail.com Log out | Help

My Orders > Orders > All Orders

License Details

This Agreement between Courtney M Calahoo ("You") and Elsevier ("Elsevier") consists of your license details and the terms and conditions provided by Elsevier and Copyright Clearance Center.

Get the printable license.

License Number	3856001507556
License date	Apr 19, 2016
Licensed Content Publisher	Elsevier
Licensed Content Publication	Elsevier Books
Licensed Content Title	Fundamentals of Inorganic Glasses
Licensed Content Author	Arun K. Varshneya
Licensed Content Date	1994
Licensed Content Volume	n/a
Licensed Content Issue	n/a
Type of Use	reuse in a thesis/dissertation
Portion	figures/tables/illustrations
Number of figures/tables/illustrations	1
Format	both print and electronic
Are you the author of this Elsevier chapter?	No
Will you be translating?	No
Order reference number	
Original figure numbers	Figure 2.1
Title of your thesis/dissertation	Structure-Property Relations of Mixed-Alkali and Ion-Exchange Silicate Glasses
Expected completion date	Jun 2016
Elsevier VAT number	GB 494 6272 12
Requestor Location	Courtney M Calahoo 1240 Church St., Apt. D Halifax, NS B3J2E8 Canada Attn: Courtney M Calahoo
Billing Type	Invoice
Billing address	Courtney M Calahoo 1240 Church St., Apt. D Halifax, NS B3J2E8 Canada Attn: Courtney M Calahoo
Total	**0.00 USD**
Total	**0.00 USD**

BACK

Figure D.88: Permission to reproduce Figure 1.1.

My Orders My Library My Profile

Welcome etchersketcher@gmail.com Log out | Help

My Orders > Orders > All Orders

License Details

This Agreement between Courtney M Calahoo ("You") and John Wiley and Sons ("John Wiley and Sons") consists of your license details and the terms and conditions provided by John Wiley and Sons and Copyright Clearance Center.

Get the printable license.

License Number	3852641110205
License date	Apr 19, 2016
Licensed Content Publisher	John Wiley and Sons
Licensed Content Publication	Advanced Materials
Licensed Content Title	Towards Ultrastrong Glasses
Licensed Content Author	Lothar Wondraczek,John C. Mauro,Jürgen Eckert,Uta Kühn,Jürgen Horbach,Joachim Deubener,Tanguy Rouxel
Licensed Content Date	Sep 8, 2011
Licensed Content Pages	9
Type of Use	Dissertation/Thesis
Requestor type	University/Academic
Format	Print and electronic
Portion	Figure/table
Number of figures/tables	1
Original Wiley figure/table number(s)	Figure 2
Will you be translating?	No
Title of your thesis / dissertation	Structure-Property Relations of Mixed-Alkali and Ion-Exchange Silicate Glasses
Expected completion date	Jun 2016
Expected size (number of pages)	300
Requestor Location	Courtney M Calahoo 1240 Church St., Apt. D Halifax, NS B3J2E8 Canada Attn: Courtney M Calahoo
Publisher Tax ID	EU826007151
Billing Type	Invoice
Billing address	Courtney M Calahoo 1240 Church St., Apt. D Halifax, NS B3J2E8 Canada Attn: Courtney M Calahoo
Total	**0.00 CAD**

BACK

Figure D.89: Permission to reproduce Figure 1.4.

Gmail Courtney Calahoo <etchersketcher@gmail.com>

Permission to use phase diagrams

2 messages

Courtney Calahoo <cr469900@dal.ca> Tue, Apr 19, 2016 at 5:24 PM
To: mmecklenborg@ceramics.org

Hello,

I recently got off the phone with you, it was one of those rare cases where calling someone was easier than searching around the website. If I may be so bold, it could be helpful in the future for people like myself to know who to call/email on the website, I just was really lucky!

I'm interested in reproducing two figures in my thesis entitled, "Structure-Property Relations of Mixed-Alkali and Ion-Exchange Silicate Glasses" to be submitted in June. Also, my name is Courtney Calahoo. (Sorry don't know what info you need!)

The two figures from "Phase diagrams for ceramicists" 1964 are:
Fig. 377 ---System Li2OSiO2--K2OSiO2--SiO2
Fig. 598 ----System CaO-MgO-SiO2

Thanks in advance, so easy!

Courtney

Mark Mecklenborg <mmecklenborg@ceramics.org> Tue, Apr 19, 2016 at 5:28 PM
To: Courtney Calahoo <cr469900@dal.ca>

Dear Courtney:

Thank you very much. We hereby grant you permission to use figures 377 and 598 in your thesis. Please include a complete reference to Phase Diagrams for Ceramists and indicate reprinted with permission of The American Ceramic Society.

Regards and good luck,

Mark

Mark J. Mecklenborg, MBA

Director of Membership, Meetings, and Technical Publications

The American Ceramic Society

Figure D.90: Permission to reproduce Figures 2.2 and 2.3.

CAMBRIDGE UNIVERSITY PRESS

Home / **About Us /** **Rights & Permissions /** Permissions

Permissions

If you wish to reproduce excerpts from a Cambridge book or journal (text extracts, figures, etc.) in another publication you should submit your request in writing by completing the Permissions Request Form.

Cambridge University Press grants permission freely for the reproduction in another work of a short prose extract (less than 400 words), a single figure or a single table in which it holds rights (see the important caveat in the Notes below). In such cases a request for permission need not be submitted, but the reproduced material must be accompanied by a full citation of the original source.

Note also that Cambridge University Press may not be able to grant permission for the use of all the material it publishes. In particular, illustrations, tables, poetry or other extensive quotations included in Cambridge publications may have been reproduced by Cambridge with the permission of another rights holder. Always check the caption or citation to ensure that Cambridge is the rights holder before proceeding.

In the case of some journals published by Cambridge on behalf of a learned society, permission may need to be obtained directly from the society. Check the cover of the journal before proceeding.

For some of our journal articles you may be able to clear permission using the Copyright Clearance Center's Rightslink® Service.

In these pages, you can find out how to submit the following permissions requests:

PERMISSIONS REQUESTS

Reproduction or translation of a chapter, journal article, text extract, audio extract.

PERMISSIONS REQUESTS FROM CAMBRIDGE AUTHORS

Re-use of material from their own works.

NETWORKING REQUESTS

For education institutions to enable them to make all or part of certain Cambridge publications available via a secure Intranet for teaching purposes.

PERFORMANCE REQUESTS

If you wish to perform a play in which Cambridge administers performance rights.

Figure D.91: Permission to reproduce Figure 2.5.

Bibliography

[1] M. F. Ashby. *Materials and the environment: eco-informed material choice*. Elsevier, 2012.

[2] Nippon Sheet Glass Co. Ltd. About NSG Group, The Glass Industry. Technical report, 2016. URL `http://www.nsg.com/en/about-nsg/whatwedo`. [Online; accessed 22-March-2016].

[3] L. Wondraczek, J. C. Mauro, J. Eckert, U. Kühn, J. Horbach, J. Deubener, and T. Rouxel. Towards ultrastrong glasses. *Adv. Mater.*, 23:4578–4586, 2011.

[4] Schott. Schott Robax, In Front, Glass ceramic for fireplaces and stoves. Technical report, 2007. URL `http://www.us.schott.com/hometech/english/products/robax/index.html`. [Online; accessed 25-April-2016].

[5] Corning. Corning Gorilla Glass 4 Product Information. Technical report, 2014. URL `www.corninggorillaglass.com`. [Online; accessed 25-April-2016].

[6] Pliny the Elder. *Naturalis Historia*. Taylor and Francis, RedLion Court, Fleet Street, London, 1885. Editions and translations: English. J. Bostock, M.D., F.R.S. H.T. Riley, Esq.

[7] A. K. Varshneya. *Fundamentals of Inorganic Glasses*. Academic Press, San Diego, 1994.

[8] J. Zarzycki. *Glasses and the vitreous state*. Cambridge University Press, 1991.

[9] C. Phillips. The strength and weakness of brittle materials. *Am. Sci.*, 53:20–51, 1965.

[10] E. Porai-Koshits. Genesis of concepts on structure of inorganic glasses. *J. Non-Cryst. Solids*, 123:1–13, 1990.

[11] A. A. Lebedev. Polymorphism and tempering of glass. Preliminary communication. *J. Russ. Phys. Chem. Soc., physical sect.*, 50:57, 1921.

[12] W. H. Zachariasen. The atomic arrangement in glass. *J. Am. Chem. Soc.*, 54: 3841–3851, 1932.

[13] V. Martin. *Composition and Structure Dependence of the Photoelastic Response of Oxide Glass*. PhD thesis, Dalhousie University, Halifax, Canada, 8 2011.

[14] T. Charpentier, S. Ispas, M. Profeta, F. Mauri, and C. Pickard. First-principles calculation of O-17, Si-29, and Na-23 NMR spectra of sodium silicate crystals and glasses. *J. Phys. Chem. B*, 108:4147–4161, 2004.

[15] K.-H. Sun. Fundamental condition of glass formation. *J. Am. Ceram. Soc.*, 30: 277–281, 1947.

[16] A. Dietzel. Die Kationenfeldstärken und ihre Beziehungen zu Entglasungsvorgängen, zur Verbindungsbildung und zu den Schmelzpunkten von Silicaten. *Z. Electrochem.*, 48:9–23, 1942.

[17] L. Linati, G. Lusvardi, G. Malavasi, L. Menabue, M. C. Menziani, P. Mustarelli, A. Pedone, and U. Segre. Medium-range order in phospho-silicate bioactive glasses: Insights from MAS-NMR spectra, chemical durability experiments and molecular dynamics simulations. *J. Non-Cryst. Solids*, 354:84–89, 2008.

[18] N. J. Clayden, S. Esposito, P. Pernice, and A. Aronne. Solid state ^{29}Si and ^{31}P NMR study of gel derived phosphosilicate glasses. *J. Mater. Chem.*, 11: 936–943, 2001.

[19] B. Warren and J. Biscob. Fourier analysis of X-ray patterns of soda-silica glass. *J. Am. Ceram. Soc.*, 21:259–265, 1938.

[20] G. Greaves. EXAFS and the structure of glass. *J. Non-Cryst. Solids*, 71:203–217, 1985.

[21] A. Makishima and J. Mackenzie. Direct calculation of Young's modulus of glass. *J. Non-Cryst. Solids*, 12:35–45, 1973.

[22] R. Shannon and C. Prewitt. Effective ionic radii in oxides and fluorides. *Acta Crystallogr. B*, 25:925–946, 1969.

[23] B. de Jong, H. Super, A. Spek, N. Veldman, G. Nachtegaal, and J. Fischer. Structure and ^{29}Si MAS NMR of $Li_2Si_2O_5$ and $Ki_2Si_2O_5$. *Acta. Cryst. B*, 54: 568–577, 1998.

[24] G. N. Greaves, S. J. Gurman, C. R. A. Catlow, A. V. Chadwick, S. Houde-Walter, C. Henderson, and B. Dobson. A structural basis for ionic diffusion in oxide glasses. *Philos. Mag. A*, 64:1059–1072, 1991.

[25] A. C. Hannon, B. Vessal, and J. M. Parker. The structure of alkali silicate glasses. *J. Non-Cryst. Solids*, 150:97–102, 1992.

[26] T. Rouxel. Elastic properties of glasses: A multiscale approach. *C. R. Mec.*, 334:743–753, 2006.

[27] C. J. Phillips and S. DiVita. Similarities in the impact behavior of glasses and polycrystalline ceramics. *Am. Ceram. Soc. Bull.*, 42:685–687, 1963.

[28] C. Inglis. Stress in a plate due to the presence of sharp corners and cracks. *Trans. Roy. Inst. Naval Architects*, 60:219–241, 1913.

[29] A. A. Griffith. The phenomena of rupture and flow in solids. *Philos. Trans. R. Soc., A*, 221:163–198, 1921.

[30] W. F. Hosford. *Mechanical behavior of materials*. Cambridge University Press, 2010.

[31] V. L. Popov. *Contact Mechanics and Friction, Physical Principle and Applications*. Springer-Verlag Berlin Heidelberg, Berlin, Germany, 2010.

[32] M. Yamane and J. Mackenzie. Vicker's hardness of glass. *J. Non-Cryst. Solids*, 15:153–164, 1974.

[33] J. Kjeldsen, M. M. Smedskjaer, J. C. Mauro, and Y. Yue. Hardness and incipient plasticity in silicate glasses: Origin of the mixed modifier effect. *Appl. Phys. Lett.*, 104:051913, 2014.

[34] G. M. Pharr, E. G. Herbert, and Y. Gao. The indentation size effect: A critical examination of experimental observations and mechanistic interpretations. *Annu. Rev. Mater. Res.*, 40:271–292, 2010.

[35] M. Kaji, M. Stevenson, and R. Bradt. Knoop microhardness anisotropy and the indentation size effect on the basal plane of single-crystal alumina (sapphire). *J. Am. Ceram. Soc.*, 22:415–422, 2002.

[36] J.-I. Jang, B.-G. Yoo, Y.-J. Kim, J.-H. Oh, I.-C. Choi, and H. Bei. Indentation size effect in bulk metallic glass. *Scr. Mater.*, 64:753–756, 2011.

[37] N. Li, L. Liu, and M. Zhang. The role of friction to the indentation size effect in amorphous and crystallized Pd-based alloy. *J. Mater. Sci.*, 44:3072–3076, 2009.

[38] Y. Huang, J. Shen, Y. Sun, and J. Sun. Indentation size effect of hardness of metallic glasses. *Mater. Design*, 31:1563–1566, 2010.

[39] I. Manika and J. Maniks. Size effects in micro- and nano-scale indentation. *Acta Mater.*, 54:2049–2056, 2006.

[40] W. C. Oliver and G. M. Pharr. An improved technique for determining hardness and elastic modulus using load and displacement sensing indentation experiments. *J. Mater. Res.*, 7:1564–1583, 1992.

[41] H. Li and R. C. Bradt. The indentation load/size effect and the measurement of the hardness of vitreous silica. *J. Non-Cryst. Solids*, 146:197–212, 1992.

[42] T. Ebisu and S. Horibe. Analysis of the indentation size effect in brittle materials from nanoindentation load-displacement curve. *J. Eur. Ceram. Soc.*, 30:2419–2426, 2010.

[43] G. Anstis, P. Chantikul, B. R. Lawn, and D. Marshall. A critical evaluation of indentation techniques for measuring fracture toughness: I, direct crack measurements. *J. Am. Ceram. Soc.*, 64:533–538, 1981.

[44] P. Chantikul, G. Anstis, B. R. Lawn, and D. Marshall. A critical evaluation of indentation techniques for measuring fracture toughness: II, strength method. *J. Am. Ceram. Soc.*, 64:539–543, 1981.

[45] B. R. Lawn, A. Evans, and D. Marshall. Elastic/plastic indentation damage in ceramics: the median/radial crack system. *J. Am. Ceram. Soc.*, 63:574–581, 1980.

[46] A. Mohajerani and J. Zwanziger. Mixed alkali effect on Vickers hardness and cracking. *J. Non-Cryst. Solids*, 358:1474–1479, 2012.

[47] Z. Burghard, A. Zimmermann, J. Rödel, F. Aldinger, and B. R. Lawn. Crack opening profiles of indentation cracks in normal and anomalous glasses. *Acta Mater.*, 52:293–297, 2004.

[48] A. Makishima and J. D. Mackenzie. Calculation of bulk modulus, shear modulus and Poisson's ratio of glass. *J. Non-Cryst. Solids*, 17:147–157, 1975.

[49] B. Bridge, N. Patel, and D. Waters. On the elastic constants and structure of the pure inorganic oxide glasses. *Physica Status Solidi A*, 77:655–668, 1983.

[50] G. N. Greaves, A. Greer, R. Lakes, and T. Rouxel. Poisson's ratio and modern materials. *Nat. Mater.*, 10:823–837, 2011.

[51] H. Scholze. *Glass: Nature, Structure, and Properties.* Springer, 1991.

[52] N. Soga, H. Yamanaka, C. Hisamoto, and M. Kunugi. Elastic properties and structure of alkaline-earth silicate glasses. *J. Non-Cryst. Solids*, 22:67–76, 1976.

[53] D. J. Burkhard. Elastic properties of alkali silicate glasses with iron oxide: Relation to glass structure. *Solid State Commun.*, 101:903–907, 1997.

[54] S. Deriano, T. Rouxel, M. LeFloch, and B. Beuneu. Structure and mechanical properties of alkali-alkaline earth-silicate glasses. *Phys. Chem. Glasses*, 45:37–44, 2004.

[55] E. Le Bourhis. *Glass: mechanics and technology.* John Wiley & Sons, 2008.

[56] K. Peter. Densification and flow phenomena of glass in indentation experiments. *J. Non-Cryst. Solids*, 5:103–115, 1970.

[57] B. Epstein. Statistical aspects of fracture problems. *J. Appl. Phys.*, 19:140–147, 1948.

[58] D. E. Day. Mixed alkali glasses–their properties and uses. *J. Non-Cryst. Solids*, 21:343–372, 1976.

[59] G. Walter, U. Hoppe, A. Barz, R. Kranold, and D. Stachel. Intermediate range structure of mixed phosphate glasses by X-ray diffraction. *J. Non-Cryst. Solids*, 263:48–60, 2000.

[60] H. Jain, H. Downing, and N. Peterson. The mixed alkali effect in lithium-sodium borate glasses. *J. Non-Cryst. Solids*, 64:335–349, 1984.

[61] W. Huang and H. Jain. Correlation between local structure and electrical response of Rb and (Rb, Ag) germanate glasses: DC conductivity. *J. Non-Cryst. Solids*, 188:254–265, 1995.

[62] J. C. Lapp and J. E. Shelby. The mixed alkali effect in lithium-sodium aluminosilicate glasses. *J. Non-Cryst. Solids*, 95:889–896, 1987.

[63] R. V. Caporali. Volume changes in mixed-alkali silicate glasses. *J. Am. Ceram. Soc.*, 47:412–412, 1964.

[64] J. O. Isard. The mixed alkali effect in glass. *J. Non-Cryst. Solids*, 1:235–261, 1969.

[65] D. Sidebottom. Evidence for site memory effects in the ionic relaxation of $(Li_2O)_x(Na_2O)_y(GeO_2)_{1-x-y}$ glasses. *J. Non-Cryst. Solids*, 255:67–77, 1999.

[66] Y. Gao. Dependence of the mixed alkali effect on temperature and total alkali oxide content in $y[x\mathrm{Li_2O}\cdot(1-x)\ \mathrm{Na_2O}]\cdot(1-y)\mathrm{B_2O_3}$ glasses. *J. Sol. St. Chem.*, 178:3376–3380, 2005.

[67] H. Jain and X. Lu. Is there a mixed alkali effect in the low temperature AC conductivity of glasses? *J. Non-Cryst. Solids*, 196:285–290, 1996.

[68] T. Fujii. Correlation of some physical properties and chemical composition of solid solution. *Am. Miner.*, 45:370–382, 1960.

[69] J. C. Dyre, P. Maass, B. Roling, and D. L. Sidebottom. Fundamental questions relating to ion conduction in disordered solids. *Rep. Prog. Phys.*, 72:046501, 2009.

[70] G. N. Greaves and K. L. Ngai. Reconciling ionic-transport properties with atomic structure in oxide glasses. *Phys. Rev. B*, 52:6358, 1995.

[71] A. Bunde, M. D. Ingram, and P. Maass. The dynamic structure model for ion transport in glasses. *J. Non-Cryst. Solids*, 172:1222–1236, 1994.

[72] A. Bunde, M. D. Ingram, P. Maass, and K. L. Ngai. Mixed alkali effects in ionic conductors: a new model and computer simulations. *J. Non-Cryst. Solids*, 131: 1109–1112, 1991.

[73] M. D. Ingram and A. J. Robertson. Ion transport in glassy electrolytes. *Solid State Ionics*, 94:49–54, 1997.

[74] M. Ingram, C. T. Moynihan, and A. Lesikar. Ionic conductivity and the weak electrolyte theory of glass. *J. Non-Cryst. Solids*, 38:371–376, 1980.

[75] M. L. F. Nascimento and S. Watanabe. Test of the Anderson–Stuart model and correlation between free volume and the universal conductivity in potassium silicate glasses. *Mater. Chem. Phys.*, 105:308–314, 2007.

[76] J. Mundy. Models for ionic transport in glass. *Solid State Ionics*, 28:671–676, 1988.

[77] A. Faivre, F. Despetis, F. Guillaume, P. Solignac, and M. Ramonda. Role of mobile cations on microplasticity in alumino-phosphate glasses. *J. Am. Ceram. Soc.*, 93:2986–2989, 2010.

[78] A. Bunde, K. Funke, and M. D. Ingram. Ionic glasses: History and challenges. *Solid State Ionics*, 105:1–13, 1998.

[79] R. M. Hakim and D. R. Uhlmann. Electrical conductivity of alkali silicate glasses. *Phys. Chem. Glasses*, 12:132–138, 1971.

[80] B. Wright and J. Shelby. Phase separation and the mixed alkali effect. *Phys. Chem. Glasses*, 41:192–198, 2000.

[81] J. R. Allwardt and J. F. Stebbins. Ca-Mg and K-Mg mixing around non-bridging O atoms in silicate glasses: An investigation using ^{17}O MAS and 3QMAS NMR. *Am. Mineral.*, 89:777–784, 2004.

[82] W. Hater, W. Müller-Warmuth, M. Meier, and G. Frischat. High-resolution solid-state NMR studies of mixed-alkali silicate glasses. *J. Non-Cryst. Solids*, 113:210–212, 1989.

[83] A. H. Dietzel. On the so-called mixed alkali effect. *Phys. Chem. Glasses*, 24: 172–180, 1983.

[84] J. Hendrickson and P. Bray. A theory for the mixed alkali effect in glass. *Phys. Chem. Glasses*, 13:107–115, 1972.

[85] M. Abou El–leil, J. Heasley, and M. Omar. A mixed isotope effect in lithium borate glasses. *Phys. Chem. Glasses*, 19:37–40, 1978.

[86] W. Weyl and E. Marboe. The constitution of glasses, a dynamic interpretation, vol II, parts I and II. *New York, Interscience Publishers*, 2:778–779, 1967.

[87] H. Van Ass and J. Stevels. Internal friction of mixed alkali metaphosphate glasses: (I). Results. *J. Non-Cryst. Solids*, 15:215–238, 1974.

[88] H. Van Ass and J. Stevels. Internal friction of mixed alkali metaphosphate glasses: (II). Discussion. *J. Non-Cryst. Solids*, 16:27–45, 1974.

[89] J. E. Shelby and D. E. Day. Mechanical relaxations in mixed-alkali silicate glasses: I, Results. *J. Am. Ceram. Soc.*, 52:169–173, 1969.

[90] J. E. Shelby and D. E. Day. Mechanical relaxations in mixed alkali silicate glasses: II, Discussion. *J. Am. Ceram. Soc.*, 53:182–187, 1970.

[91] W. T. Van Gemert, H. Van Ass, and J. Stevels. Internal friction and dielectric losses of mixed alkali borate glasses. *J. Non-Cryst. Solids*, 16:281–293, 1974.

[92] J. Stevels. The electrical properties of glass. In *Electrical Conductivity II/Elektrische Leitungsphänomene II*, pages 350–391. Springer, 1957.

[93] R. Kirchheim. On the mobility of alkaline earth ions in mixed alkali alkaline earth silicate glasses. *J. Non-Cryst. Solids*, 328:157–163, 2003.

[94] F. J. Valle-Fuentes, M. Garza-García, J. López-Cuevas, C. A. Gutiérrez Chavarría, and J. Rendón-Angeles. Study of a mixed alkaline–earth effect on some properties of glasses of the CaO-MgO-Al_2O_3-SiO_2 system. *Bol. Soc. Esp. Ceram. Vidrio*, 2007.

[95] B. Roling and M. Ingram. Mixed alkaline–earth effects in ion conducting glasses. *J. Non-Cryst. Solids*, 265:113–119, 2000.

[96] J. Kjeldsen, M. M. Smedskjaer, J. C. Mauro, R. E. Youngman, L. Huang, and Y. Yue. Mixed alkaline earth effect in sodium aluminosilicate glasses. *J. Non-Cryst. Solids*, 369:61–68, 2013.

[97] K.-D. Kim. Influence of BaO/(SrO+ BaO) on melt properties in R_2O–RO–SiO_2 glasses for plasma display panel substrates. *Glass Technol.*, 41:161–164, 2000.

[98] M. M. Smedskjaer, S. J. Rzoska, M. Bockowski, and J. C. Mauro. Mixed alkaline earth effect in the compressibility of aluminosilicate glasses. *J. Chem. Phys.*, 140:054511, 2014.

[99] O. V. Mazurin, editor. *Handbook of Glass Data*. Elsevier. Distributors for the US and Canada, Elsevier Science Pub. Co., 1983.

[100] J. P. Poole. Low-temperature viscosity of alkali silicate glasses. *J. Am. Ceram. Soc.*, 32:230–233, 1949.

[101] R. Gy. Ion exchange for glass strengthening. *Mater. Sci. Eng. B*, 149:159–165, 2008.

[102] A. K. Varshneya. Chemical strengthening of glass: Lessons learned and yet to be learned. *Int. J. Appl. Glass Sci.*, 1:131–142, 2010.

[103] R. Rogoziński. Ion exchange in glass–changes of glass refraction. In A. Kilislioğlu, editor, *Ion Exchange Technologies*, pages 154–190. Intech, 2012.

[104] E. Stavrou, D. Palles, E. I. Kamitsos, A. Lipovskii, D. Tagantsev, Y. Svirko, and S. Honkanen. Vibrational study of thermally ion-exchanged sodium aluminoborosilicate glasses. *J. Non-Cryst. Solids*, 401:232–236, 2014.

[105] A. Sane and A. Cooper. Stress buildup and relaxation during ion exchange strengthening of glass. *J. Am. Ceram. Soc.*, 70:86–89, 1987.

[106] A. K. Varshneya. Method for making strengthened glass, 2015. US Patent 8,959,953.

[107] M. Huang. Stress effects on the performance of optical waveguides. *Int. J. Solids Struct.*, 40:1615–1632, 2003.

[108] K. Saitoh, M. Koshiba, and Y. Tsuji. Stress-analysis method for optical waveguides composed of elastically anisotropic materials and its application to strain-induced optical waveguides. *Electron. Comm. Jpn. 2*, 81:16–23, 1998.

[109] C. R. Kurkjian, G. W. Kammlott, and M. M. Chaudhri. Indentation behavior of soda-lime silica glass, fused silica, and single-crystal quartz at liquid nitrogen temperature. *J. Amer. Ceram. Soc.*, 78:737–744, 1995.

[110] F. Gonella and A. Quaranta. On the recovery of refractive-index profiles of ion-exchanged glass waveguides. *Pure Appl. Opt.*, 2:405–409, 1993.

[111] F. Gonella, F. Caccavale, A. Quaranta, and J. Sambo. Copper-doped ion-exchanged waveguide characterization. *J. Mod. Opt.*, 45:837–845, 1998.

[112] J. C. Lee. *Effects of exchange temperature on properties in field-assisted ion-exchanged glass*. PhD thesis, Iowa State University, Ames, Iowa, 1986.

[113] J. Varner and R. Lang-Egelkraut. Influences of ion-exchange temperature and time on stress profiles and strengths of chemically strengthened glass. In G. Frischat, editor, *Proc. Fourth Intl. Conf. on the Physics of Non-Crystalline Solids*, pages 465–470, Aedermannsdorf, 1977. Trans. Tech. A.A.

[114] B. Varughese, Y.-K. Lee, and M. Tomozawa. Effect of fictive temperature on mechanical strength of soda-lime glasses. *J. Non-Cryst. Solids*, 241:134–139, 1998.

[115] V. Jain and A. Varshneya. Finite-element analysis of network dilatation in ion-exchanged glass rods after slicing. *J. Am. Ceram. Soc.*, 70:2–5, 1987.

[116] A. Tandia, K. D. Vargheese, J. C. Mauro, and A. K. Varshneya. Atomistic understanding of network dilation anomaly in ion-exchanged glass. *J. Non-Cryst. Solids*, 358:316–320, 2012.

[117] P. K. Kreski, A. K. Varshneya, and A. N. Cormack. Investigation of ion-exchanged 'stuffed' glass structures by MD. *J. Non-Cryst. Solids*, 358:3539–3545, 2012.

[118] A. I. Fu and J. C. Mauro. Mutual diffusivity, network dilation, and salt bath poisoning effects in ion-exchanged glass. *J. Non-Cryst. Solids*, 363:199–204, 2013.

[119] O. Richmond, W. Leslie, and H. Wriedt. Theory of residual stresses due to chemical concentration gradients. *Trans. ASM*, 57:294–300, 1964.

[120] A. Cooper and D. Krohn. Strengthening of glass fibers II: ion exchange. *J. Am. Ceram. Soc.*, 52:665–669, 1969.

[121] A. Tandia, K. D. Vargheese, and J. C. Mauro. Elasticity of ion stuffing in chemically strengthened glass. *J. Non-Cryst. Solids*, 358:1569–1574, 2012.

[122] V. Tyagi and A. K. Varshneya. Measurement of progressive stress buildup during ion exchange in alkali aluminosilicate glass. *J. Non-Cryst. Solids*, 238: 186–192, 1998.

[123] K. D. Vargheese, A. Tandia, and J. C. Mauro. Molecular dynamics simulations of ion-exchanged glass. *J. Non-Cryst. Solids*, 403:107–112, 2014.

[124] S. N. Houde-Walter, J. M. Inman, A. J. Dent, and G. N. Greaves. Sodium and silver environments and ion-exchange processes in silicate and aluminosilicate glasses. *J. Phys. Chem.*, 97:9330–9336, 1993.

[125] A. Quaranta, A. Rahman, G. Mariotto, C. Maurizio, E. Trave, F. Gonella, E. Cattaruzza, E. Gibaudo, and J. E. Broquin. Spectroscopic investigation of structural rearrangements in silver ion-exchanged silicate glasses. *J. Phys. Chem. C*, 116:3757–3764, 2012.

[126] M. Ingram, J. Davidson, A. Coats, E. Kamitsos, and J. Kapoutsis. Origins of anomalous mixed-alkali effects in ion-exchanged glasses. *Glastech. Ber. Glass Sci. Technol.*, 73:89–104, 2000.

[127] A. K. Varshneya. The physics of chemical strengthening of glass: Room for a new view. *J. Non-Cryst. Solids*, 356:2289–2294, 2010.

[128] D. K. Hale. Strengthening of silicate glasses by ion exchange. *Nature*, 217: 1115–1118, 1968.

[129] A. Varshneya. Kinetics of ion exchange in glass. *J. Non-Cryst. Solids*, 19: 355–365, 1975.

[130] H. Garfinkel and C. King. Ion concentration and stress in a chemically tempered glass. *J. Am. Ceram. Soc.*, 53:686–691, 1970.

[131] E. Levin, C. R. Robbins, H. F. McMurdie, and M. Reser. *Phase Diagrams For Ceramists*. American Ceramic Society Inc., 1964.

[132] F. P. Miller, A. F. Vandome, and J. McBrewster. *Birefringence*. VDM Publishing House Ltd New York, USA, 2009.

[133] C. B. Boss and K. J. Fredeen. *Concepts, Instrumentation and Techniques in Inductively Coupled Plasma Optical Emission Spectroscopy*. PerkinElmer Inc., USA, 2004.

[134] J. Goldstein, D. E. Newbury, D. Joy, C. Lyman, P. Echlin, E. Lifshin, L. Sawyer, and J. Michael. *Scanning electron microscopy and X-ray microanalysis*. 2003.

[135] L. Reimer. *Scanning electron microscopy: physics of image formation and microanalysis*. IOP Publishing, 2000.

[136] R. Egerton. *Physical principles of electron microscopy: an introduction to TEM, SEM, and AEM*. Springer Science & Business Media, 2006.

[137] S. J. B. Reed. *Electron microprobe analysis and scanning electron microscopy in geology*. Cambridge University Press, 2005.

[138] C. P. Romao. *Thermoelastic Properties of Materials with Negative Coefficients of Thermal Expansion*. PhD thesis, Dalhousie University, Halifax, Nova Scotia, July 2015.

[139] H. Unuma, T. Kokubo, and S. Sakka. Crystallization of Li-Si-ON oxynitride glasses. *J. Mat. Sci.*, 23:4399–4405, 1988.

[140] A. deOliveira, L. Barbieri, C. Leonelli, T. Manfredini, and G. Pellacani. Physical properties of quenched glasses in the Li_2O-ZrO_2-SiO_2 system. *J. Am. Ceram. Soc.*, 79:1092, 1996.

[141] J. Shelby and S. Shelby. Phase separation and the properties of lithium calcium silicate glasses. *Phys. Chem. Glasses*, 41:59–64, 2000.

[142] I. Gee, D. Holland, and C. McConville. Atomic environments in binary lead silicate and ternary alkali lead silicate glasses. *Phys. Chem. Glasses*, 42:339–348, 2001.

[143] R. H. Perry. *Perry's Chemical Engineers Handbook*. McGraw Hill, New York, 6 edition, 1984.

[144] K. Ferraro. *Introductory Raman spectroscopy*. Academic Press, 1994.

[145] D. W. Matson, S. K. Sharma, and J. A. Philpotts. The structure of high-silica alkali-silicate glasses. A Raman spectroscopic investigation. *J. Non-Cryst. Solids*, 58, 1983.

[146] B. O. Mysen, D. Virgo, and F. A. Seifert. The structure of silicate melts: Implications for chemical and physical properties of natural magma. *Rev. Geophys.*, 20:353, 1982.

[147] P. McMillan. A Raman spectroscopic study of glasses in the system CaO-MgO-SiO_2. *Am. Mineral.*, 69:645–659, 1984.

[148] T. Furukawa, K. E. Fox, and W. B. White. Raman spectroscopic investigation of the structure of silicate glasses. III. Raman intensities and structural units in sodium silicate glasses. *J. Chem. Phys.*, 75:3226, 1981.

[149] M. Bliss, P. M. Aker, and C. F. Windisch. Further investigations of the effect of replacing lithium by sodium on lithium silicate scintillating glass efficiency. *J. Non-Cryst. Solids*, 358:751–757, 2012.

[150] P. R. Griffiths and J. A. De Haseth. *Fourier transform infrared spectrometry*, volume 171. John Wiley & Sons, 2007.

[151] E. Burstein, F. Johnson, and R. Loudon. Selection rules for second-order infrared and Raman processes in the rocksalt structure and interpretation of the raman spectra of NaCl, KBr, and NaI. *Phys. Rev.*, 139:A1239–A1245, 1965.

[152] D. A. Long. *Raman Spectroscopy*. McGraw-Hill, New York, 1977.

[153] E. O. Potma and S. Mukamel. *Theory of Coherent Raman Scattering*. CRC Press, Taylor & Francis Group, 2013.

[154] N. Zotov. Effects of composition on the vibrational properties of sodium silicate glasses. *J. Non-Cryst. Solids*, 287:231–236, 2001.

[155] M. Wojdyr. Fityk: a general-purpose peak fitting program. *J. Appl. Crystallogr.*, 43:1126–1128, 2010.

[156] H. Maekawa, T. Maekawa, K. Kawamura, and T. Yokokawa. The structural groups of alkali silicate glasses determined from ^{29}Si MAS-NMR. *J. Non-Cryst. Solids*, 127:53–64, 1991.

[157] OlympusNDT. *Ultrasonic Transducers Technical Notes*. 48 Woerd Avenue Waltham, MA, 02453, USA, 2011. URL `http://www.olympus-ims.com/en/resources/white-papers/ultrasonic-transducer-technical-notes/`.

[158] Agilent. How to Select the Correct Indenter Tip. Technical report, 5301 Stevens Creek Blvd Santa Clara, CA 95051 United States, 2009. URL `http://cp.literature.agilent.com/litweb/pdf/5990-4907EN.pdf`.

[159] G. D. Quinn, P. Green, and K. Xu. Cracking and the indentation size effect for Knoop hardness of glasses. *J. Am. Ceram. Soc.*, 86:441–448, 2003.

[160] X. Li and B. Bhushan. A review of nanoindentation continuous stiffness measurement technique and its applications. *Mater. Charact.*, 48:11–36, 2002.

[161] G. Pharr. Measurement of mechanical properties by ultra-low load indentation. *Mater. Sci. Eng. A*, 253:151–159, 1998.

[162] M. Suszynska. Load dependence of hardness of the doped soda-lime silicate glasses. *Opt. Appl.*, 42:399–406, 2012.

[163] Agilent. Indentation Rules of Thumb – Applications and Limits. Technical report, 5301 Stevens Creek Blvd Santa Clara, CA 95051 United States, 2010. URL `http://cp.literature.agilent.com/litweb/pdf/5990-5700EN.pdf`.

[164] N. Ong and V. Venkatesh. Semi-ductile grinding and polishing of Pyrex glass. *J. Mater. Process. Tech.*, 83:261–266, 1998.

[165] Z. Zhong and V. C. Venkatesh. Semi-Ductile Grinding and Polishing of Ophthalmic Aspherics and Spherics*. *CIRP Annals - Manu. Tech.*, 44:339–342, 1995.

[166] J. E. Jakes and D. S. Stone. The edge effect in nanoindentation. *Philos. Mag.*, 91:1387–1399, 2011.

[167] M. Jebahi, D. André, F. Dau, J. L. Charles, and I. Iordanoff. Simulation of Vickers indentation of silica glass. *J. Non-Cryst. Solids*, 378:15–24, 2013.

[168] G. N. Greaves. Poisson's ratio over two centuries: Challenging hypotheses. *Notes Rec. R. Soc.*, 21:1–22, 2012.

[169] Solartron Analytical. *1260 Impedance/Gain-Phase Analyzer, Operating Manual*. Unit B1 Armstrong Mall, Southwood Business Park, Farnborough, Hampshire, UK, 01 2001.

[170] Scribner Associates Inc. *Zplot for Windows, Electrochemical Impedance Software*. 150 East Connecticut Ave., Southern Pines, NC, USA, 10 2001.

[171] H. Jain. Measurement of electrical conductivity of glasses. In C. J. Simmons and O. H. El-Bayoumi, editors, *Experimental Techniques of Glass Science*. American Ceramic Society, 1993.

[172] C. P. Romao, F. A. Perras, U. Werner-Zwanziger, J. A. Lussier, K. J. Miller, C. M. Calahoo, J. W. Zwanziger, M. Bieringer, B. A. Marinkovic, D. L. Bryce, *et al.* Zero thermal expansion in $ZrMgMo_3O_{12}$: NMR crystallography reveals origins of thermoelastic properties. *Chem. Mater.*, 27:2633–2646, 2015.

[173] M. Orazem and B. Tribollet. *Electrochemical impedance spectroscopy*. John Wiley & Sons, Inc, 2008.

[174] V. S. Bagotsky. *Fundamentals of electrochemistry*. John Wiley & Sons, 2 edition, 2006.

[175] E. Barsoukov and J. R. Macdonald. *Impedance spectroscopy: theory, experiment, and applications*. John Wiley & Sons, 2005.

[176] A. Nowick, W. Lee, and H. Jain. Survey and interpretation of pre-exponentials of conductivity. *Solid State Ionics*, 28:89–94, 1988.

[177] A. Nowick and W. Lee. The conductivity pre-exponential of solid electrolytes. *Superionic Solids And Solid Electrolytes Recent Trends*, pages 381–405, 1989.

[178] J. Weston and B. Steele. Effects of inert fillers on the mechanical and electrochemical properties of lithium salt-poly (ethylene oxide) polymer electrolytes. *Solid State Ionics*, 7:75–79, 1982.

[179] M. Watanabe, S. Nagano, K. Sanui, and N. Ogata. Estimation of Li^+ transport number in polymer electrolytes by the combination of complex impedance and potentiostatic polarization measurements. *Solid State Ionics*, 28:911–917, 1988.

[180] Y. Kawamoto and M. Nishida. Ionic conduction in As_2S_3–Ag_2S, GeS_2–GeS–Ag_2S and P_2S_5–Ag_2S glasses. *J. Non-Cryst. Solids*, 20:393–404, 1976.

[181] A. A. Pronkin. Transfer numbers and mobility of alkali metal ions in two-alkali metal glasses (M'$_2$O + M"$_2$O).2SiO_2. *Fiz. Khim. Stekla*, page 573, 1979.

[182] X. Zhang, J. Ganguly, and M. Ito. Ca–Mg diffusion in diopside: tracer and chemical inter-diffusion coefficients. *Contrib. Mineral. Petrol.*, 159:175–186, 2010.

[183] M. Thomas and N. Peterson. Electrical conductivity and tracer diffusion in sodium germanate glasses. *Solid State Ionics*, 14:297–307, 1984.

[184] H. Jain, N. L. Peterson, and H. Downing. Tracer diffusion and electrical conductivity in sodium-cesium silicate glasses. *J. Non-Cryst. Solids*, 55:283–300, 1983.

[185] U. Schoo, C. Cramer, and H. Mehrer. Tracer diffusion in sodium–rubidium borate glasses: An unconventional mixed-alkali effect? *Solid State Ionics*, 138: 105–114, 2000.

[186] N. Imanaka, Y. Kobayashi, K. Fujiwara, T. Asano, Y. Okazaki, and G.-y. Adachi. Trivalent rare earth ion conduction in the rare earth tungstates with the $Sc_2(WO_4)_3$-type structure. 10:2006–2012, 1998.

[187] C. M. Calahoo, J. W. Zwanziger, and I. S. Butler. Mechanical-structural investigation of ion-exchanged lithium silicate glass using micro-raman spectroscopy. *J. Phys. Chem. C*, 120:7213–7232, 2016.

[188] Renishaw. inVia Raman microscopes: Upgradeable, automated Raman microscopes. Technical report, New Mills, Wotton-under-Edge, Gloucestershire, GL12 8JR, UK, 2006. URL `resources.renishaw.com/en/download/invia-raman-microscopes--5866`.

[189] S. A. Brawer and W. B. White. Raman spectroscopic investigation of the structure of silicate glasses. I. The binary akali silicates. *J. Chem. Phys.*, 63: 2421–2432, 1975.

[190] P. McMillan. Structural studies of silicate glasses and melts-applications and limitations of Raman spectroscopy. *Am. Miner.*, 69:622–644, 1984.

[191] Société des Produits Chimiques Harbonnières. MSDS: Potassium carbonate. Technical report, 2010. URL `http://www.spch-chemicals.com`.

[192] B. Hering and H. Bliss. Diffusion in ion exchange resins. *AIChE J.*, 9:495–503, 1963.

[193] B. O. Mysen, L. W. Finger, D. Virgo, and F. A. Seifert. Curve-fitting of Raman spectra of silicate glasses. *Am. Miner.*, 67:686–695, 1982.

[194] X. Xue, J. F. Stebbins, M. Kanzaki, P. F. McMillan, and B. Poe. Pressure-induced silicon coordination and tetrahedral structural changes in alkali oxide-silica melts up to 12 GPa: NMR, Raman, and infrared spectroscopy. *Am. Miner.*, 76:8–26, 1991.

[195] A. A. Osipov and L. M. Osipova. New approach to modeling of a local structure of silicate glasses and melts. volume 410, pages 012–019, 2013.

[196] R. A. B. Devine, R. Dupree, I. Farnan, and J. J. Capponi. Pressure-induced bond-angle variation in amorphous SiO_2. *Phys. Rev. B*, 35:2560–2562, 1987.

[197] M. Newton and G. Gibbs. Ab initio calculated geometries and charge distributions for H_4SiO_4 and $H_6Si_2O_7$ compared with experimental values for silicates and siloxanes. *Phys. Chem. Miner.*, 6:221–246, 1980.

[198] A. Revesz and G. Gibbs. *The Physics of MOS insulators*. Pergamon Press, Elsevier Inc., London, UK, 1980.

[199] Q. Williams, R. J. Hemley, M. B. Kruger, and R. Jeanloz. High-pressure infrared spectra of α-quartz, coesite, stishovite and silica glass. *J. Geophys. Res*, 98: 22157–22170, 1993.

[200] K. Kihara, T. Hirose, and K. Shinoda. Raman spectra, normal modes and disorder in monroclinic tridymite and its higher temperature orthorhombic modification. *J. Miner. Petrol. Sci.*, 100:91–103, 2005.

[201] W. S. McDonald and D. W. J. Cruickshank. A reinvestigation of the structure of sodium metasilicate, Na_2SiO_3. *Acta. Cryst.*, 22:37–43, 1967.

[202] F. Liu, S. H. Garofalini, R. D. King-Smith, and D. Vanderbilt. Structural and electronic properties of sodium metasilicate. *Chem. Phys. Lett.*, 215:401–404, 1993.

[203] P. Richet. Melting and premelting of silicates: Raman spectroscopy and X-ray diffraction of Li_2SiO_3 and Na_2SiO_3. *Phys. Chem. Miner.*, 23:157–172, 1996.

[204] H. Seemann. Die Kristallstruktur des Lithiummetasilikates, $(Li_2SiO_3)_x$. *Acta. Cryst.*, 9:251–252, 1956.

[205] H. Voellenkle. Verfeinerung der Kristallstrukturen von Li_2SiO_3 und Li_2GeO_3. *Z. Kristallogr.*, 154:77–81, 1981.

[206] K. F. Hesse. Refinement of the crystal structure of lithium polysilicate. *Acta. Cryst. B*, 33:901–902, 1977.

[207] T. Fuss, A. Moguš-Milanković, C. S. Ray, C. E. Lesher, R. Youngman, and D. E. Day. Ex situ XRD, TEM, IR, Raman and NMR spectroscopy of crystallization of lithium disilicate glass at high pressure. *J. Non-Cryst. Solids*, 352:4101–4111, 2006.

[208] A. K. Pant and D. W. J. Cruickshank. The crystal structure of α-$Na_2Si_2O_5$. *Acta. Cryst. B*, 24:13–19, 1968.

[209] J. You, G.-C. Jiang, and K.-D. Xu. High temperature Raman spectra of sodium disilicate crystal, glass and its liquid. *J. Non-Cryst. Solids*, 282:125–131, 2001.

[210] R. I. Smith, A. R. West, I. Abrahams, and P. G. Bruce. Rietveld structure refinement of metastable lithium disilicate using synchrotron X-ray powder diffraction data from the Daresbury SRS 8.3 diffractometer. *Powder Diffr.*, 5:137–143, 1990.

[211] R. I. Smith, R. A. Howie, A. R. West, A. Aragon Pina, and M. E. Villafuerte Castrejon. The structure of metastable lithium disilicate, $Li_2Si_2O_5$. *Act. Cryst. C*, 46:363–365, 1990.

[212] T. Araki and T. Zoltai. Refinement of a coesite structure. *Z. Kristallogr.*, 129: 381–387, 1969.

[213] L. Levien and C. Prewitt. High-pressure crystal structure and compressibility of coesite. *Am. Miner.*, 66:324–333, 1981.

[214] R. Hemley. Pressure dependence of Raman spectra of SiO_2 polymorphs α-quartz, coesite and stishovite. *High Pressure Research in Mineral Physics, Geophys. Monogr. Ser.*, 39:347–359, 1987.

[215] S. K. Sharma, J. F. Mammone, and M. F. Nicol. Raman investigation of ring configurations in vitreous silica. *Nature*, 292:140–141, 1981.

[216] P. Gillet, A. Le Cléac'h, and M. Madon. High-temperature Raman spectroscopy of SiO_2 and GeO_2 polymorphs: Anharmonicity and thermodynamic properties at high-temperatures. *J. Geophys. Res*, 95:21635–21655, 1990.

[217] P. Norby. Synchrotron powder diffraction using imaging plates: Crystal structure determination and Rietveld refinement. *J. Appl. Crystallogr.*, 30:21–30, 1997.

[218] A. F. Wright and M. S. Lehmann. The structure of quartz at 25 and 590 °C determined by neutron diffraction. *J. Sol. St. Chem.*, 36:371–380, 1981.

[219] F. Hanic and L. Sumichrast. α-β phase transition in quartz. *Ceram. Silik.*, 18: 1–9, 1974.

[220] H. D'Amour, W. Denner, and H. Schulz. Structure determination of α-quartz up to 68×10^8 Pa. *Acta. Cryst. B*, 35:550–555, 1979.

[221] M. Dusek, V. Petricek, M. Wunschel, R. E. Dinnebier, and S. van Smaalen. Refinement of modulated structures against X-ray powder diffraction data with JANA2000. *J. Appl. Crystallogr.*, 34:398–404, 2001.

[222] A. F. Gualtieri. Accuracy of XRPD QPA using the combined Rietveld-RIR method. *J. Appl. Crystallogr.*, 33:267–278, 2000.

[223] J. Glinnemann, H. E. King Jr., H. Schulz, T. Hahn, S. la Placa, and F. Dacol. Crystal structures of the low-temperature quartz-type phases of SiO_2 and GeO_2 at elevated pressure. *Z. Kristallogr.*, 198:177–212, 1992.

[224] R. M. Hazen, L. W. Finger, R. J. Hemley, and H. K. Mao. High-pressure crystal chemistry and amorphization of α-quartz. *Solid State Commun.*, 72:507–511, 1989.

[225] K. Ogata, Y. Takeuchi, and Y. Kudoh. Structure of α-quartz as a function of temperature and pressure. *Z. Kristallogr.*, 179:403–413, 1987.

[226] J. F. Scott and S. Porto. Longitudinal and transverse optical lattice vibrations in quartz. *Phys. Rev.*, 161:903, 1967.

[227] J. B. Bates and A. Quist. Polarized Raman spectra of β-quartz. *J. Chem. Phys.*, 56:1528, 1972.

[228] S. M. Shapiro, D. C. O'Shea, and H. Z. Cummins. Raman scattering study of the α-β phase transition in quartz. *Phys. Rev. Lett.*, 19:361–364, 1967.

[229] P. F. McMillan, G. H. Wolf, and P. Lambert. A Raman spectroscopic study of shocked single crystalline quartz. *Phys. Chem. Miner.*, 19:71–79, 1992.

[230] R. J. Hemley, H. K. Mao, and E. C. T. Chao. Raman spectrum of natural and synthetic stishovite. *Phys. Chem. Miner.*, 13:285–290, 1986.

[231] N. Zotov, I. Ebbsjö, D. Timpel, and H. Keppler. Calculation of Raman spectra and vibrational properties of silicate glasses: Comparison between $Na_2Si_4O_9$ and SiO_2 glasses. *Phys. Rev. B*, 60:6383–6397, 1999.

[232] J. Etchepare. Vibrational normal modes of SiO_2. I. α- and β-quartz. *J. Chem. Phys.*, 60:1873, 1974.

[233] W. A. Dollase. Reinvestigation of the structure of low cristobalite. *Z. Kristallogr.*, 121:369–377, 1965.

[234] R. T. Downs and C. Palmer D. The pressure behavior of α-cristobalite. *Am. Miner.*, 79:9–14, 1994.

[235] J. B. Bates. Raman spectra of α- and β-cristobalite. *J. Chem. Phys.*, 57: 4042–4047, 1972.

[236] D. C. Palmer, J. Russell, and C. T. Prewitt. Raman spectroscopic study of high-pressure phase transitions in cristobalite. *Phys. Chem. Miner.*, 21:481–488, 1994.

[237] I. P. Swainson, M. T. Dove, and D. C. Palmer. Infrared and Raman spectroscopy studies of the α–β phase transition in cristobalite. *Phys. Chem. Miner.*, 30:353–365, 2003.

[238] J. Etchepare, M. Merian, and P. Kaplan. Vibrational normal modes of SiO_2. II. Cristobalite and tridymite. *J. Chem. Phys.*, 68:1531, 1978.

[239] R. W. G. Wyckoff. Crystal structure of high temperature cristobalite. *Am. J. Sci.*, 9:448–459, 1925.

[240] D. Peacor. High-temperature single-crystal study of the cristobalite inversion. *Z. Kristallogr.*, 138:274–298, 1973.

[241] W. H. Baur. Silicon-oxygen bond lengths, bridging angles Si-O-Si and synthetic low tridymite. *Acta. Cryst. B*, 33:2615–2619, 1977.

[242] T. Hirose, K. Kihara, M. Okuno, S. Fujinami, and K. Shinoda. X-ray, DTA and Raman studies of monoclinic tridymite and its higher temperature orthorhombic modification with varying temperature. *J. Miner. Petrol. Sci.*, 100:55–69, 2005.

[243] K. Kihara, T. Hirose, and K. Shinoda. Raman spectra, normal modes and disorder in monoclinic tridymite and its higher temperature orthorhombic modification. *J. Miner. Petrol. Sci.*, 100:91–103, 2005.

[244] R. W. G. Wyckoff. XXIX. Kriterien für hexagonale Raumgruppen und die Kristallstruktur von β-Quarz. *Z. Kristallogr.*, 63:507–537, 1926.

[245] M. G. Tucker, D. A. Keen, and M. T. Dove. A detailed structural characterization of quartz on heating through the α-β transition. *Mineral. Mag.*, 65: 489–507, 2001.

[246] K. Kihara. An X-ray study of the temperature dependence of the quartz structure. *Eur. J. Mineral.*, 2:63–77, 1990.

[247] H. Graetsch and I. Topalović-Dierdorf. ^{29}Si MAS NMR spectrum and superstructure of modulated tridymite L3-T_O(MX-1). *Eur. J. Mineral.*, 8:103–113, 1996.

[248] H. Boyer, D. C. Smith, C. Chopin, and B. Lasnier. Raman microprobe (RMP) determinations of natural and synthetic coesite. *Phys. Chem. Miner.*, 12:45–48, 1985.

[249] M. Sato. X-ray study of tridymite. *Mineral. J. (Japan)*, 4:115–130, 1964.

[250] F. Galeener. A model for the distribution of dihedral angles in SiO_2-like glasses. *J. Non-Cryst. Solids*, 75:399–405, 1985.

[251] R. J. Hill and G. V. Gibbs. Variation in $d(T\text{-O})$, $d(T\cdots T)$ and $\angle TOT$ in silica and silicate minerals, phosphates and aluminates. *Acta Crystallogr. Sect. B-Struc. Sci.*, 35:25–30, 1979.

[252] E. Birtch, M. Mesko, and J. Shelby. Phase separation and properties of lithium barium silicate glasses. *Phys. Chem. Glasses*, 44:319–324, 2003.

[253] R. Tickle. Electrical conductance of molten alkali silicates. 2. Theoretical discussion. *Phys. Chem. Glasses*, 8:113, 1967.

[254] H. Ledbetter, S. Kim, and D. Balzar. Elastic properties of mullite. *J. Am. Ceram. Soc.*, 28:1025–1028, 1998.

[255] F. Schilling, M. Hauser, S. Sinogeikin, and J. Bass. Compositional dependence of elastic properties and density of glasses in the system anorthite-diopside-forsterite. *Contrib. Mineral. Petrol.*, 141:297–306, 2001.

[256] J. C. Mauro and R. J. Loucks. Forbidden glasses and the failure of fictive temperature. *J. Non-Cryst. Solids*, 355:676–680, 2009.

[257] C. M. Calahoo, X. Zhang, and J. W. Zwanziger. Nano-indentation study of the surface of ion-exchanged lithium silicate glass. *J. Phys. Chem. C*, 120: 5585–5598, 2016.

[258] J. Glass, R. Tandon, A. K. Varshneya, and I. Spinelli. Processing and properties of ion exchanged glasses. *Glass and Optical Materials Division Fall Meeting, Am. Ceram. Soc.*, 2004.

[259] T. Sakai and M. Suzuki. Distribution characteristics of mechanical properties and correlation between the respective properties on S35C carbon steel. *J. Mater. Sci.*, 26:1755–1761, 1991.

[260] M. L. Oyen. Nanoindentation hardness of mineralized tissues. *J. Biomech.*, 39: 2699–2702, 2006.

[261] C. Moyhihan, N. Saad, D. Tran, and A. Lessikar. Mixed-alkali effect in the dilute foreign–alkali region. Failure of the strong electrolyte. *J. Am. Ceram. Soc.*, 63:458–464, 1980.

[262] T. B. Ballaran. Equations of state and their applications in geosciences. In E. Boldyreva and P. Dera, editors, *High-Pressure Crystallography: From Fundamental Phenomena to Technological Applications*, pages 135–145. Springer Science, Berlin, 2010.

[263] A. M. Hofmeister. Pressure derivatives of the bulk modulus. *J. Geophys. Res.*, 96:21893–21907, 1991.

[264] H. Yaghoubi, N. Taghavinia, E. K. Alamdari, and A. A. Volinsky. Nanomechanical properties of TiO_2 granular thin films. *ACS Appl. Mater. Inter.*, 2: 2629–2636, 2010.

[265] D. Newey, M. Wilkins, and H. Pollock. An ultra-low-load penetration hardness tester. *J. Phys. E: Sci. Instr.*, 15:119, 1982.

[266] J. Jakes, C. Frihart, J. Beecher, R. Moon, and D. Stone. Experimental method to account for structural compliance in nanoindentation measurements. *J. Mater. Res.*, 23:1113–1127, 2008.

[267] J. Jakes, C. Frihart, J. Beecher, R. Moon, P. Resto, Z. Melgarejo, O. Suárez, H. Baumgart, A. Elmustafa, and D. Stone. Nanoindentation near the edge. *J. Mater. Res.*, 24:1016–1031, 2009.

[268] T. Downing, R. Kumar, W. Cross, L. Kjerengtroen, and J. Kellar. Determining the interphase thickness and properties in polymer matrix composites using phase imaging atomic force microscopy and nanoindentation. *J. Adhes. Sci. Technol.*, 14:1801, 2000.

[269] A. Hodzic, Z. H. Stachurski, and J. K. Kim. Nano-indentation of polymer–glass interfaces part I. experimental and mechanical analysis. *Polymer*, 41:6895–6905, 2000.

[270] Z. Zong, J. Lou, O. O. Adewoye, A. A. Elmustafa, F. Hammad, and W. O. Soboyejo. Indentation size effects in the nano- and micro-hardness of fcc single crystal metals. *Mater. Sci. Eng. A*, 434:178–187, 2006.

[271] R. G. Wellman, A. Dyer, and J. R. Nicholls. Nano and Micro indentation studies in bulk zirconia and EB PVD TBCs. *Surf. Coat. Tech.*, 176:720–724, 2003. doi: 10.1016/S0257-8972.

[272] M. N. Svenson, L. M. Thirion, R. E. Youngman, J. C. Mauro, S. J. Rzoska, M. Bockowski, and M. M. Smedskjær. Pressure-induced changes in interdiffusivity and compressive stress in chemically strengthened glass. *ACS Appl. Mater. Inter.*, 6:10436–44, 2014.

[273] D. J. Green. Compressive surface strengthening of brittle materials by a residual stress distribution. *J. Am. Ceram. Soc.*, 66:807–810, 1983.

[274] S. Striepe, M. M. Smedskjær, J. Deubener, U. Bauer, H. Behrens, M. Potuzak, R. E. Youngman, J. C. Mauro, and Y. Yue. Elastic and micromechanical properties of isostatically compressed soda-lime-borate glasses. *J. Non-Cryst. Solids*, 364:44–52, 2013.

[275] J. Wu, J. Deubener, J. F. Stebbins, L. Grygarova, H. Behrens, L. Wondraczek, and Y. Yue. Structural response of a highly viscous aluminoborosilicate melt to isotropic and anisotropic compressions. *J. Chem. Phys.*, 131:104504, 2009.

[276] M. M. Smedskjaer, D. J. Mauro, S. Sen, and Y. Yue. Quantitative Design of Glassy Materials Using Temperature-Dependent Constraint Theory. *Chem. Mater.*, 2:445–452, 2010. ISSN 0897-4756. doi: 10.1021/cm1016799.

[277] P. W. Bridgman and I. Simon. Effects of Very High Pressures on Glass. *J. Appl. Phys.*, 24:405, 1953.

[278] S. Bull. On the origins of the indentation size effect. *Z. Metallkd.*, 94:787–792, 2003.

[279] Y. Liu and A. Ngan. Depth dependence of hardness in copper single crystals measured by nano-indentation. *Scr. Mater.*, 44:237–241, 2001.

[280] K. Durst, B. Backes, and M. Göken. Indentation size effect in metallic materials: Correcting for the size of the plastic zone. *Scr. Mater.*, 52:1093–1097, 2005.

[281] S. Pathak, D. Stojakovic, R. Doherty, and S. Kalidindi. Importance of surface preparation on the nano-indentation stress-strain curves measured in metals. *J. Mater. Res.*, 24:1142–1155, 2009.

[282] J. Musil, F. Kunc, H. Zeman, and H. Poláková. Relationships between hardness, Young's modulus and elastic recovery in hard nanocomposite coatings. *Surf. Coat. Tech.*, 154:304–313, 2002.

[283] S. S. Chiang, D. B. Marshall, and A. G. Evans. The response of solids to elastic/plastic indentation. I. stresses and residual stresses. *J. Appl. Phys.*, 53: 298–311, 1982.

[284] K. L. Johnson. *Contact Mechanics*. Cambridge University Press, Cambridge, UK, 1985.

[285] T. Y. Tsui, G. M. Pharr, W. C. Oliver, C. S. Bhatia, R. L. White, S. Anders, A. Anders, and I. G. Brown. Mechanical behaviour of diamond and other forms of carbon. *Mat. Res. Soc. Symp. Proc.*, 383:447–452, 1995.

[286] J. Shelby. Effect of morphology on the properties of alkaline earth silicate glasses. *J. Appl. Phys.*, 50:8010–8015, 1979.

[287] D. Bellert, D. K. Winn, and W. Breckenridge. Dispersed fluorescence studies of linear LiOLi: a strongly bound, but very 'floppy' ionic molecule. *Chem. Phys. Lett.*, 348:39–46, 2001.

[288] O. Anderson and D. Stuart. Calculation of activation energy of ionic conductivity in silica glasses by classical methods. *J. Am. Ceram. Soc.*, 37:573–580, 1954.

[289] M. Schwartz and J. Mackenzie. Ionic conductivity in calcium silicate glasses. *J. Am. Ceram. Soc.*, 49:582–585, 1966.

[290] R. Kirchheim. The mixed alkali effect as a consequence of network density and site energy distribution. *J. Non-Cryst. Solids*, 272:85–102, 2000.

[291] A. Costantini, F. Branda, and A. Buri. Thermal properties and devitrification behaviour of $(1+x)$CaO·$(1-x)$MgO·2SiO$_2$ glasses. *J. Mater. Sci.*, 30:1561–1564, 1995.

[292] J. Swenson and S. Adams. Mixed alkali effect in glasses. *Phys. Rev. Lett.*, 90: 155507, 2003.

[293] N. Nasikas, T. Edwards, S. Sen, and G. Papatheodorou. Structural characteristics of novel Ca–Mg orthosilicate and suborthosilicate glasses: Results from ^{29}Si and ^{17}O NMR spectroscopy. *J. Phys. Chem. B*, 116:2696–2702, 2012.

[294] S. Sen, H. Maekawa, and G. Papatheodorou. Short-range structure of invert glasses along the pseudo-binary join MgSiO$_3$-Mg$_2$SiO$_4$: Results from ^{29}Si and ^{25}Mg MAS NMR spectroscopy. *J. Phys. Chem. B*, 113:15243–15248, 2009.

[295] M. C. Davis, K. J. Sanders, P. J. Grandinetti, S. J. Gaudio, and S. Sen. Structural investigations of magnesium silicate glasses by ^{29}Si 2D Magic-Angle Flipping NMR. *J. Non-Cryst. Solids*, 357:2787–2795, 2011.

[296] S. Sen and J. Tangeman. Evidence for anomalously large degree of polymerization in Mg$_2$SiO$_4$ glass and melt. *Am. Mineral.*, 93:946–949, 2008.

[297] K. Shimoda, H. Miyamoto, M. Kikuchi, K. Kusaba, and M. Okuno. Structural evolutions of CaSiO$_3$ and CaMgSi$_2$O$_6$ metasilicate glasses by static compression. *Chem. Geol.*, 222:83–93, 2005.

[298] B. O. Mysen. The Structure of Silicate Melts. *Annual Review of Earth and Planetary Sciences*, 11:75–97, 1983.

[299] D. Virgo, B. Mysen, and I. Kushiro. Anionic constitution of 1-atmosphere silicate melts: Implications for the structure of igneous melts. *Science*, 208: 1371–1373, 1980.

[300] P. Zhang, P. J. Grandinetti, and J. F. Stebbins. Anionic species determination in $CaSiO_3$ glass using two-dimensional ^{29}Si NMR. *J. Phys. Chem. B*, 101: 4004–4008, 1997.

[301] S. A. Brawer and W. B. White. Raman spectroscopic investigation of the structure of silicate glasses. I. the binary akali silicates. *J. Chem. Phys.*, 63: 2421–2432, 1975.

[302] B. O. Mysen, D. Virgo, and C. M. Scarfe. Relations between the anionic structure and viscosity of silicate meltsa Raman spectroscopic study. *Am. Mineral.*, 65:690–710, 1980.

[303] J. Schneider, V. Mastelaro, E. Zanotto, B. A. Shakhmatkin, N. M. Vedishcheva, A. C. Wright, and H. Panepucci. Q^n distribution in stoichiometric silicate glasses: Thermodynamic calculations and ^{29}Si high resolution NMR measurements. *J. Non-Cryst. Solids*, 325:164–178, 2003.

[304] E. Schneider, J. Stebbins, and A. Pines. Speciation and local structure in alkali and alkaline earth silicate glasses: Constraints from ^{29}Si NMR spectroscopy. *J. Non-Cryst. Solids*, 89:371–383, 1987.

[305] G. Hauret, Y. Vaills, Y. Luspin, F. Gervais, and B. Coté. Similarities in the behaviour of magnesium and calcium in silicate glasses. *J. Non-Cryst. Solids*, 170:175–181, 1994.

[306] K. Funke. Jump relaxation in solid electrolytes. *Prog. Solid State Chem.*, 22: 111–195, 1993.

[307] J. Littleton and W. Wetmore. The electrical conductivity of glass in the annealing zone as a function of time and temperature. *J. Am. Ceram. Soc.*, 19: 243–245, 1936.

[308] K. Otto and M. Milberg. Ionic conduction in alkali and thallium silicate glasses. *J. Am. Ceram. Soc.*, 51:326–329, 1968.

[309] M. Milberg, K. Otto, and T. Kushida. Electrical conductivity and nuclear magnetic resonance chemical shift in caesium silicate glasses. *Phys. Chem. Glasses*, 7:14, 1966.

[310] M. Mulligan. A study of the conductivity of annealed and unannealed soda-lime glasses. *Trans. R. Soc. Can.*, 7:120, 1933.

[311] G. Ghosh. Dispersion of thermooptic coefficients of soda–lime–silica glasses. *J. Am. Ceram. Soc.*, 78:218–220, 1995.

[312] F. Natrup, H. Bracht, C. Martiny, S. Murugavel, and B. Roling. Diffusion of calcium and barium in alkali alkaline-earth silicate glasses. *Phys. Chem. Chem. Phys.*, 4:3225–3231, 2002.

[313] F. Natrup, M. Grofmeier, and H. Bracht. Self-and foreign alkaline-earth diffusion in mixed cation silicate glasses. *Solid State Ionics*, 180:109–115, 2009.

[314] G. McVay and D. E. Day. Diffusion and internal friction in Na-Rb silicate glasses. *J. Am. Ceram. Soc.*, 53:508–513, 1970.

[315] P. Maass and R. Peibst. Ion diffusion and mechanical losses in mixed alkali glasses. *J. Non-Cryst. Solids*, 352:5178–5187, 2006.

[316] A. Grandjean, M. Malki, and C. Simonnet. Effect of composition on ionic transport in SiO_2–B_2O_3–Na_2O glasses. *J. Non-Cryst. Solids*, 352:2731–2736, 2006.

[317] A. Hunt. Statistical and percolation effects on ionic conduction in amorphous systems. *J. Non-Cryst. Solids*, 175:59–70, 1994.

[318] M. Yoshiyagawa and M. Tomozawa. Electrical properties of rapidly quenched lithium-silicate glasses. *J. Phys. Colloq.*, 43:C9–411, 1982.

[319] H. L. Tuller. Ionic conduction in nanocrystalline materials. *Solid State Ionics*, 131:143–157, 2000.

[320] R. Kuryaeva. Compressibility of magnesium silicate glasses in comparison with those of aluminosilicate glasses. *Solid State Sci.*, 24:133–139, 2013.

[321] J. Kilner and R. Brook. A study of oxygen ion conductivity in doped non-stoichiometric oxides. *Solid State Ionics*, 6:237–252, 1982.

[322] E. W. Sucov. Diffusion of oxygen in vitreous silica. *J. Am. Ceram. Soc.*, 46: 14–20, 1963.

[323] B. J. Giletti and R. A. Yund. Oxygen diffusion in quartz. *J. Geophys. Res.: Solid Earth*, 89:4039–4046, 1984.

[324] S. Elphick, P. Dennis, and C. Graham. An experimental study of the diffusion of oxygen in quartz and albite using an overgrowth technique. *Contrib. Mineral. Petrol.*, 92:322–330, 1986.

[325] W. Kingery, J. Pappis, M. Doty, and D. Hill. Oxygen ion mobility in cubic $Zr_{0.85}Ca_{0.15}O_{1.85}$. *J. Am. Ceram. Soc.*, 42:393–398, 1959.

[326] E. J. Little Jr and M. M. Jones. A complete table of electronegativities. *J. Chem. Educ.*, 37:231, 1960.

[327] P. F. McMillan and R. L. Remmele. Hydroxyl sites in SiO_2 glass: A note on infrared and Raman spectra. *Am. Mineral.*, 71:772–778, 1986.

[328] T. Miura, Y. Benino, R. Sato, and T. Komatsu. Universal hardness and elastic recovery in Vickers nanoindentation of copper phosphate and silicate glasses. *J. Eur. Ceram. Soc.*, 23:409–416, 2003.

[329] H. Maekawa, T. Maekawa, K. Kawamura, and T. Yokokawa. Si-29 MAS NMR investigation of the Na_2O-Al_2O_3-SiO_2 glasses. *J. Phys. Chem.*, 95:6822–6827, 1991.

[330] W. J. Malfait, W. E. Halter, Y. Morizet, B. H. Meier, and R. Verel. Structural control on bulk melt properties: single and double quantum ^{29}Si NMR spectroscopy on alkali-silicate glasses. *Geochim. Cosmochim. Acta*, 71:6002–6018, 2007.

[331] I. Farnan, P. J. Grandinetti, J. H. Baltisberger, J. F. Stebbins, U. Werner, M. A. Eastman, and A. Pines. Quantification of the disorder in network-modified silicate glasses. *Nature*, 358:2, 1992.

[332] B. De Jong and G. E. Brown. Polymerization of silicate and aluminate tetrahedra in glasses, melts and aqueous solutionsII. the network modifying effects of Mg^{2+}, K^+, Na^+, Li^+, H^+, OH^-, F^-, Cl^-, H_2O, CO_2 and H_3O^+ on silicate polymers. *Geochim. Cosmochim. Acta*, 44:1627–1642, 1980.

[333] J. F. Stebbins. Cation sites in mixed-alkali oxide glasses: correlations of NMR chemical shift data with site size and bond distance. *Solid State Ionics*, 112: 137–141, 1998.

[334] Y. Nageno, H. Takebe, K. Morinaga, and T. Izumitani. Effect of modifier ions on fluorescence and absorption of Eu^{3+} in alkali and alkaline earth silicate glasses. *J. Non-Cryst. Solids*, 169:288–294, 1994.

[335] A. B. Rosenthal and S. H. Garofalini. Structural role of zinc oxide in silica and soda-silica glasses. *J. Am. Ceram. Soc.*, 70:821–826, 1987.

[336] S. Kroeker, P. S. Neuhoff, and J. F. Stebbins. Enhanced resolution and quantitation from 'ultrahigh' field NMR spectroscopy of glasses. *J. Non-Cryst. Solids*, 293:440–445, 2001.

[337] K. Shimoda, T. Nemoto, and K. Saito. Local structure of magnesium in silicate glasses: a ^{25}Mg 3QMAS NMR study. *J. Phys. Chem. B*, 112:6747–6752, 2008.

[338] S. Kroeker and J. F. Stebbins. Magnesium coordination environments in glasses and minerals: New insight from high-field magnesium-25 MAS NMR. *Am. Mineral.*, 85:1459–1464, 2000.

[339] N. L. Ross, J.-F. Shu, R. M. Hazen, and T. Gasparik. High-pressure crystal chemistry of stishovite. *Am. Miner.*, 75:739–747, 1990.

[340] A. K. Pant. A reconsideration of the crystal structure of β-$Na_2Si_2O_5$. *Acta. Cryst. B*, 24, 1968.

[341] J. L. You, G.-C. Jiang, and K.-D. Xu. Temperature dependence of the Raman spectra of $Na_2Si_2O_5$. *Chin. Phys. Lett.*, 18:408–410, 2001.